

DISSERTATION

**Search for Neutral MSSM Higgs Bosons
Decaying to $\tau_{\text{had}}\tau_{\text{had}}$ in $\sqrt{s} = 7$ TeV
Proton–Proton Collisions with the ATLAS
Detector**

Julian Glatzer

CERN-THESIS-2013-439
17/10/2013



Fakultät für Mathematik und Physik
Albert-Ludwigs-Universität Freiburg

**Search for Neutral MSSM Higgs Bosons
Decaying to $\tau_{\text{had}}\tau_{\text{had}}$ in $\sqrt{s} = 7$ TeV
Proton–Proton Collisions with the ATLAS
Detector**

DISSERTATION

zur Erlangung des Doktorgrades der
Fakultät für Mathematik und Physik der

ALBERT-LUDWIGS-UNIVERSITÄT
Freiburg im Breisgau

vorgelegt von
Julian Glatzer

August 2013

Dekan: Prof. Dr. Michael Růžička
Betreuer der Arbeit: Prof. Dr. Jochen Dingfelder
Prof. Dr. Karl Jakobs
Referent: Prof. Dr. Karl Jakobs
Koreferent: Prof. Dr. Thomas Filk
Prüfer: Prof. Dr. Jochen Dingfelder
Prof. Dr. Gregor Herten
JProf. Dr. Harald Ita

Datum der mündlichen Prüfung:

17. Oktober 2013

Contents

1. Introduction	1
2. Theory Overview and Experimental Status	3
2.1. The Standard Model of Particle Physics	3
2.1.1. Particle Content and Interactions	3
2.1.2. Field Theory and Lagrange Density Functions	4
2.1.3. Quantum Electrodynamics	5
2.1.4. Quantum Chromodynamics	6
2.1.5. Electroweak Unification and the Glashow-Weinberg-Salam Model . . .	6
2.1.6. Spontaneous Symmetry Breaking and the Higgs Mechanism	9
2.1.7. Quark and Lepton Mixing	11
2.1.8. The Standard Model Lagrangian	11
2.1.9. Open Questions	12
2.2. Supersymmetry	14
2.2.1. Supersymmetry Transformations and the Lagrange Density Function of the MSSM	15
2.2.2. R -Parity	18
2.2.3. The Hierarchy Problem and Supersymmetry Breaking	18
2.2.4. Constrained Models Based on the Minimal Supersymmetric Standard Model	19
2.2.5. Motivation for Supersymmetry	21
2.2.6. Two-Higgs-Doublet Models	21
2.2.7. The Higgs Sector of the Minimal Supersymmetric Standard Model . .	25
2.3. Calculation of Cross Sections and Simulation of Hadron Collisions	26
2.3.1. The Factorisation Theorem, Parton Distribution and Fragmentation Functions	27
2.3.2. Partonic Cross Section	28
2.3.3. Simulation of Hadron Collisions	30
2.3.4. Simulation of the Partonic Process	30
2.3.5. Parton Shower and Matching	31
2.3.6. Hadronisation	32
2.3.7. Underlying Event and Multiple Parton Interactions	33
2.3.8. Pile-up	33
2.3.9. Detector Simulation and Event Reweighting	34
2.4. Phenomenology of the Production and the Decay of Higgs Bosons	34
2.4.1. Production and Decay of Higgs Bosons in the Standard Model	35
2.4.2. Higgs Boson Masses in the MSSM and the m_h^{\max} Scenario	35
2.4.3. Production and Decay of Higgs Bosons in the MSSM	38
2.5. Experimental Status	39
2.5.1. Observation of a Massive Particle Consistent With the Standard Model Higgs Boson	41

2.5.2.	Searches for Neutral MSSM Higgs Bosons at LEP	41
2.5.3.	Searches for Neutral MSSM Higgs Bosons at the Tevatron	42
2.5.4.	Searches for Neutral MSSM Higgs Bosons at the LHC	43
2.5.5.	Searches for Charged MSSM Higgs Bosons	44
2.5.6.	Indirect Constraints on the Higgs Sector	45
3.	The Large Hadron Collider and the ATLAS Experiment	49
3.1.	The Injector Chain and the Large Hadron Collider	50
3.2.	The ATLAS Experiment	51
3.2.1.	The ATLAS Coordinate System	52
3.2.2.	The Inner Detector	52
3.2.3.	The Calorimeter System	55
3.2.4.	The Muon Spectrometer	58
3.2.5.	The Luminosity Counters and the Forward Detectors	60
3.2.6.	The Trigger and Data Acquisition System	60
3.3.	LHC Operation and ATLAS Data-Taking	61
4.	Calibration of the Semiconductor Tracker	63
4.1.	Response Curve Test	63
4.2.	Trim Range Test	64
4.3.	Noise Occupancy Test	65
4.4.	Summary of the Calibration Results	66
5.	Object Reconstruction and Identification	67
5.1.	Tracks	67
5.2.	Vertices	68
5.3.	Jets and Flavour Tagging	69
5.3.1.	Jet Reconstruction	70
5.3.2.	Jet Energy Scale and Resolution	72
5.3.3.	Tagging of b -jets	73
5.4.	τ Leptons	76
5.4.1.	Reconstruction of Hadronic τ -Lepton Decays	77
5.4.2.	Energy Calibration for Hadronic τ -Lepton Decays	79
5.4.3.	Identification of Hadronic τ -Lepton Decays	79
5.4.4.	Measurement of the Identification Efficiency of Hadronic τ -Lepton Decays	83
5.5.	Electrons and Muons	85
5.5.1.	Electron Reconstruction and Identification	85
5.5.2.	Muon Reconstruction and Identification	86
5.6.	Missing Transverse Momentum	87
6.	The Search for the Higgs Bosons $h/A/H$ in the $\tau_{\text{had}}\tau_{\text{had}}$ Decay Channel	89
6.1.	Signal Processes and Event Samples	89
6.1.1.	Simulation of Higgs Boson Production in b -quark Annihilation	89
6.1.2.	Simulation of Higgs Boson Production in Gluon Fusion	91
6.1.3.	The MSSM Signal Hypothesis	92
6.1.4.	The Generic Higgs Boson Production Model	92
6.2.	Background Processes and Event Samples	93
6.2.1.	Multi-jet Production	93
6.2.2.	Production of Z/γ^* and W Bosons	95
6.2.3.	Production of Top-Quark Pairs and Single Top Quarks	99

6.2.4.	Diboson Production	101
6.3.	Event Selection	104
6.3.1.	Data Sample and Trigger	104
6.3.2.	Additional Data Quality Requirements	106
6.3.3.	Electron and Muon Vetoes	106
6.3.4.	Selection of the Hadronic τ -lepton Decays	107
6.3.5.	Categorisation into Events With and Without b -jet	108
6.4.	Mass Reconstruction for Di- τ Final States	110
6.4.1.	Visible Mass, Effective Mass and Transverse Mass	112
6.4.2.	Collinear Mass Approximation	113
6.4.3.	Missing Mass Calculator	115
6.5.	Signal and Background Estimation	117
6.5.1.	Estimation of the Multi-jet Background	119
6.5.2.	Trigger Correction Factors	124
6.5.3.	Estimation of the Background From Events With Misidentified Jets	128
6.5.4.	Studies With τ -embedded $Z/\gamma^* \rightarrow \mu^+\mu^-$ and $W \rightarrow \mu\nu$ Data	132
6.5.5.	Estimation of the Fraction of Events With Identified b -jet	135
6.5.6.	Validation and Results of the Combined Background Estimate	139
6.6.	Systematic Uncertainties	139
6.6.1.	Systematic Uncertainties for Generator-level Distributions	143
6.6.2.	Experimental Uncertainties	149
6.7.	Results	155
7.	Statistical Analysis of the Results of the Search for $h/A/H$	159
7.1.	Results of the $h/A/H \rightarrow \mu\mu$ and $\tau\tau$ Search Channels	159
7.1.1.	Results of the Search for $h/A/H \rightarrow \mu\mu$ Decays	159
7.1.2.	Results of the Search for $h/A/H \rightarrow \tau_e\tau_\mu$ Decays	161
7.1.3.	Results of the Search for $h/A/H \rightarrow \tau_{\text{lep}}\tau_{\text{had}}$ Decays	162
7.1.4.	Results of the Search for $h/A/H \rightarrow \tau_{\text{had}}\tau_{\text{had}}$ Decays	163
7.2.	Definition of the Likelihood Function	165
7.2.1.	Nuisance Parameters for Systematic Uncertainties	167
7.2.2.	Nuisance Parameters for Statistical Uncertainties	170
7.2.3.	Nuisance Parameters for Backgrounds Normalised in Control Regions	171
7.2.4.	Functional Form of the Likelihood	172
7.3.	Hypothesis Tests	172
7.3.1.	Calculation of Exclusion Limits and Discovery Significances	173
7.3.2.	Characterisation of the Experimental Sensitivity	175
7.3.3.	Calculation of Trial Factors	175
7.4.	Validation of the Likelihood Function	176
7.4.1.	Validation of the Model for the Systematic Uncertainties	176
7.4.2.	Validation of the Likelihood Minimisation Procedure	177
7.4.3.	Comparison to Results Obtained From Pseudo Experiments	179
7.5.	Results of the Calculation of Exclusion Limits	180
7.5.1.	Event Yield and MMC Mass Distributions for the $h/A/H \rightarrow \tau_{\text{had}}\tau_{\text{had}}$ Channel After the Minimisation Procedure	181
7.5.2.	Exclusion Limit on the Parameter Space of the Minimal Supersymmetric Standard Model	181
7.5.3.	Exclusion Limits on the Cross Section and Branching Ratio	185
7.5.4.	Discovery Significances for the Minimal Supersymmetric Standard Model	186

8. Summary	189
A. Auxiliary Information for the Theory Overview	191
A.1. The Dirac and Gell-Mann Matrices	191
A.2. The QCD Lagrange Density Function	192
A.3. Lagrange Density Function of the Glashow-Weinberg-Salam Model	192
B. Auxiliary Figures for the Background Estimation	195
B.1. Estimation of the Multi-jet Background	195
B.2. Estimation of the Background From Events With Misidentified Jets	199
B.3. Comparison of τ -embedded $Z/\gamma^* \rightarrow \mu^+\mu^-$ Data and Simulated $Z/\gamma^* \rightarrow \tau^+\tau^-$ Events	204
B.4. Comparison of τ -embedded $W \rightarrow \mu\nu$ Data and Simulated $W \rightarrow \tau\nu$ Events	208
B.5. Validation of the Combined Background Estimate	210
C. Auxiliary Information for the Statistical Analysis	215
C.1. Binning of the Mass Distributions	215
C.2. Names and Functions of the Nuisance Parameters	217
C.3. Validation of the Nuisance Parameter Values Obtained in the Likelihood Minimisation Procedure	223
Bibliography	229
Acknowledgements	247

“There are many hypotheses in science which are wrong. That’s perfectly all right; they’re the aperture to finding out what’s right. Science is a self-correcting process. To be accepted, new ideas must survive the most rigorous standards of evidence and scrutiny.”

Carl Sagan

in “Cosmos: A Personal Voyage”, episode 4 “Heaven and Hell”

Particle physics is the branch of fundamental science in which the constituents of matter and their interactions are studied at a fundamental level. The idea that all visible matter is composed of a small number of fundamental particles was probably developed several hundred years B.C, however these ideas were the result of philosophical reasoning rather than experimental observation. The modern concept of atoms was established in the 19th century based on the law of the conservation of mass and the law of multiple proportions in chemical reactions. Today it is known that atoms are not elementary, but instead consist of protons, neutrons and electrons. Schematically the neutrons and protons in turn are composed of three valence quarks, however the model of quantum fluctuations does not allow for a strict interpretation of composition. The elementary particles that make up matter take part in four fundamental types of interactions, the electromagnetic, weak, strong and gravitational interactions. With the exception of gravity, the fundamental particles and their interactions are described by the Standard Model of particle physics. The gravitational interaction can usually be neglected for particle interactions at high energies.

In order to probe new physics, particles are collided and high energy densities are created, so that interactions can take place that are not possible at lower energy densities and particles with high masses can be created. The highest-energy particle collider is the Large Hadron Collider (LHC) [1] that is located near Geneva, Switzerland. The LHC is designed to collide two proton beams at a centre-of-mass energy $\sqrt{s} = 14$ TeV per proton pair. In 2011 and 2012 it was operated with $\sqrt{s} = 7$ TeV and 8 TeV, respectively. With the recorded data the Standard Model is tested and searches for new physics are performed.

The Standard Model of particle physics predicts and describes a large variety of experimental results with high precision. In its formulation without Higgs fields only massless particles are described, however particle masses can be generated by the Higgs mechanism. The Higgs mechanism predicts the Higgs field and its quantum, the Higgs boson. On July 4, 2012 the ATLAS and CMS collaborations announced the observation of a new boson [2, 3]. The measurements have since then been refined and are consistent with the hypothesis that the observed boson is the Standard Model Higgs boson. To date, however, other models that include a boson with the observed mass and the measured decay modes are not excluded and the true nature of the observed boson is still unknown.

In spite of the success of the Standard Model in describing the current experimental data, it is considered an effective theory that does not describe matter and its interactions at much higher energies. In the Standard Model the Higgs boson mass is subject to large radiative corrections that induce a huge difference between the Higgs mass parameter and the measured Higgs boson mass. Without further explanation this difference can be perceived as unnatural

due to its size [4]. It was established by the WMAP and Planck satellite missions that the ordinary matter contributes only 4.9% to the matter and energy distribution of the universe, 68.3% are due to dark energy and 26.8% due to dark matter [5]. The Standard Model does not provide a particle that could make up this dark matter.

Models based on the concept of supersymmetry [4] address these problems. Supersymmetry is a symmetry between bosons, particles with integer spin, and fermions, particles with half-integer spin, and for $N = 1$ supersymmetry a heavier superpartner is introduced for every Standard Model particle.

In supersymmetric models an extended Higgs sector compared to the Standard Model is necessary. In the Minimal Supersymmetric Standard Model (MSSM) two Higgs doublets, which lead to five physical Higgs bosons, are introduced. The five physical states are the electrically neutral CP-even Higgs bosons, h and H , the neutral and CP-odd Higgs boson, A , and the electrically charged Higgs bosons, H^\pm .

In this thesis a search for the neutral Higgs bosons, h , A and H , in the decay channel $h/A/H \rightarrow \tau_{\text{had}}\tau_{\text{had}}$, where τ_{had} denotes a hadronic τ -lepton decay, is documented. The search is based on data recorded with the ATLAS detector and complements the searches for the Standard Model Higgs boson. It is optimised for general models with two Higgs doublets, but with a special focus on supersymmetric models. In supersymmetric models the decay into down-type fermions can be enhanced and the $\tau\tau$ decay channel provides a particular sensitivity to such models.

The $\tau_{\text{had}}\tau_{\text{had}}$ decay channel includes approximately 42% of all events in the $\tau\tau$ channel [6] and complements the searches in the $\tau\tau$ decay channels with electrons or muons. The search in the $\tau_{\text{had}}\tau_{\text{had}}$ channel is complicated by the fact that no electrons and muons exist in the final state and that events with $\tau\tau$ production need to be separated from the overwhelming background from events with multi-jet production based on the identification of τ_{had} decays at the trigger and the analysis level. After the selection the expected and observed distributions of the reconstructed di- τ mass are compared for background and data.

In Chapter 2 of this thesis a brief review of the Standard Model of particle physics is given together with an introduction to the concepts of supersymmetry focussing on the Minimal Supersymmetric Standard Model. An overview of the methods used to calculate interaction rates and the experimental constraints on Higgs boson production in the context of supersymmetric models follows. In Chapter 3 the Large Hadron Collider and the ATLAS experiment are described. For this thesis detailed work on the calibration of the semiconductor tracking detector was performed and is described in Chapter 4. The reconstruction and identification of particles and other objects used in the analysis based on information read out from the ATLAS detector is described in Chapter 5. In Chapter 6 the selection of events with MSSM Higgs bosons decaying into two τ leptons which in turn decay hadronically is described together with the methods for the estimation of backgrounds from Standard Model processes and their uncertainties. The expected distribution of the di- τ mass for background and MSSM Higgs boson production is used together with the distribution in data to evaluate the sensitivity of the presented search in Chapter 7.

The work that is documented in this thesis was executed within the ATLAS collaboration and all results were obtained in close collaboration with other members of the ATLAS collaboration.

2 Theory Overview and Experimental Status

In this chapter an overview of the theoretical framework of modern particle physics is given. In Section 2.1 the Standard Model of particle physics (SM), which describes the known elementary particles and their non-gravitational interactions, is briefly reviewed. In Section 2.2 supersymmetry, a hypothetical extension of the Standard Model, is described. The methods for the calculation of interaction rates and the simulation of hadron collisions are summarised in Section 2.3 and the phenomenology of Higgs bosons is detailed in Section 2.4. In Section 2.5 an overview of direct and indirect searches for Higgs bosons from non-minimal Higgs sectors is given.

2.1. The Standard Model of Particle Physics

The Standard Model of particle physics is the established theoretical framework that describes properties of the known particles and their interactions using quantum field theory. The Standard Model was first formulated in the time from 1960 to 1974 and has successfully predicted the discovery of the b quark [7], the top quark [8, 9], and the τ neutrino [10]. In addition, the Standard Model predicts the existence of a Higgs boson. In 2012 a new boson that seems to be consistent with the Standard Model Higgs boson was found by the ATLAS and CMS experiments [2, 3]. However, more measurements are needed for a final confirmation that the observed boson is indeed the Standard Model Higgs boson. The review of the Standard Model of particle physics in this thesis starts with an overview of the Standard Model particles in Section 2.1.1. The theory describing electromagnetic interactions is introduced in Section 2.1.3, the theory that describes the strong interactions in Section 2.1.4 and the unification of the electromagnetic and weak interactions is described in Section 2.1.5. In Section 2.1.8 the separate theories are combined and open questions are discussed in Section 2.1.9. This overview follows References [11, 12, 13].

2.1.1. Particle Content and Interactions

All observed particles can be divided into fermions with half-integer spin, $s \in \left\{n + \frac{1}{2} \mid n \in \mathbb{N}_0\right\}$, and bosons with integer spin, $s \in \mathbb{N}_0$. The elementary fermions can be further divided into three generations with two quarks (colour-charged fermions) and two leptons (fermions without colour charge) per generation. In addition the corresponding anti-particles exist. In this thesis particle names usually refer to the particle and its anti-particle. The six quarks are the up, charm and top quarks with electric charge $+2/3$ and the down, strange and bottom quarks with electric charge $-1/3$. The six leptons are the electron, the muon and the τ lepton with unit electric charge and the corresponding neutrinos which are not electrically charged. In this thesis electric charge, color charge and hypercharge are discussed. If the type of the charge is not explicitly specified, charge refers to the electric charge.

Interactions between these particles can be associated with four forces: gravity, the electromagnetic, the weak and the strong force. The gravitational interaction is not described by the Standard Model. In particle physics the effects of the gravitational interaction can usually be neglected. In Table 2.1 the electromagnetic, weak and strong forces are compared

Force	Boson	Mass
Electromagnetic	photon γ	$< 1 \cdot 10^{-18}$ eV
Weak	gauge bosons W^+, W^-, Z^0	80.385 ± 0.015 GeV, 91.1876 ± 0.0021 GeV
Strong	gluons g_1, \dots, g_8	< 0.0002 eV

Table 2.1.: Forces and the corresponding force-mediating bosons of the Standard Model of particle physics together with the mass of the bosons. All gauge bosons have spin 1. Gravity and its hypothetical spin-2 graviton G are not included in this table because they are not theorised within the framework of the Standard Model. The values of the masses are the experimental values/upper bounds recommended or referenced by the Particle Data Group [6, 14].

and the corresponding force carriers and their masses are given. The electromagnetic interaction is present between electrically charged particles and has an infinite range due to the zero mass of the photon. The strength of the electromagnetic force falls off $\propto r^2$, where r is the distance between the charges. The effective coupling constant for electromagnetism decreases for increasing distance to the charge due to the screening by vacuum polarisation effects, the creation of virtual electron–positron pairs. The weak force is mediated by the massive W^\pm and Z gauge bosons and can be observed in the radioactive β decay. The strong force is mediated by the massless gluons and has an infinite range. As the gluons itself carry a colour charge the strong interaction couples to quarks and gluons. Colour-charged particles have only been observed in their bound states, the colour-neutral hadrons. Hadrons can either be mesons, which are made of two quarks ($q_1\bar{q}_2$), e.g. pions, or baryons, which are made of three quarks ($q_1q_2q_3$ or $\bar{q}_1\bar{q}_2\bar{q}_3$), e.g. protons or neutrons. Contrary to the electromagnetic force the effective strong coupling increases for increasing distance to the charge. For small distances this effect is known as asymptotic freedom and for large distances this results in the so-called confinement. Confinement refers to the observation that quarks are confined inside hadrons. If the constituents of the hadrons are separated new quark–anti-quark pairs can be observed in the form of new colour-neutral hadrons. Experimentally high- p_T quarks and gluons and their hadronisation can be observed in the form of highly directed sprays of hadrons, the jets. The reconstruction of jets is described in detail in Section 5.3.

2.1.2. Field Theory and Lagrange Density Functions

In modern particle physics theories are formulated as field theories based on a Lagrange density function. Lagrange density functions \mathcal{L} are action densities in Minkowski space and defined by

$$S = \int \mathcal{L}(\phi_i, \partial_\mu \phi_i) d^4x, \quad (2.1)$$

where S refers to the action, ∂_μ to the Minkowski space derivative and ϕ_i are fields. Here the Einstein notation

$$a^\mu b_\mu = a_0 b_0 - \sum_{i=1}^3 a_i b_i \quad (2.2)$$

is used. One field exists for each type of particle described by a field theory and particles are excited states, the quanta, of a field. According to the principle of least action the equations

of motion for the fields can be derived from

$$0 = \partial_\mu \left(\frac{\partial \mathcal{L}}{\partial (\partial_\mu \phi_i)} \right) - \frac{\partial \mathcal{L}}{\partial \phi_i} \quad (2.3)$$

for each of the fields ϕ_i . The equation of motions for a single scalar field ϕ and a Dirac field ψ with Lagrange density functions

$$\mathcal{L}_\phi = \frac{1}{2} \partial_\mu \phi \partial^\mu \phi - \frac{1}{2} m^2 \phi^2 \quad \text{and} \quad \mathcal{L}_\psi = \bar{\psi} (i \not{\partial} - m) \psi, \quad m \in \mathbb{R} \quad (2.4)$$

are the Klein-Gordon and the Dirac equations

$$(\partial_\mu \partial^\mu + m^2) \phi = 0 \quad \text{and} \quad (i \not{\partial} - m) \psi = 0, \quad (2.5)$$

respectively. In the Lagrange density functions the imaginary unit is denoted by i , and the notations $\bar{\psi} = \psi^\dagger \gamma^0$ and $\not{\partial} = \gamma^\mu \partial_\mu$, where γ^μ denote the Dirac matrices defined in Appendix A.1, have been used. In particle physics it is commonly accepted to use units which are determined up to powers of \hbar and c ($\hbar = c = 1$). In this thesis powers of \hbar and c are only explicitly specified in special cases. In the following the term Lagrangian refers to a Lagrange density function.

2.1.3. Quantum Electrodynamics

The theory of Quantum Electrodynamics (QED) is the quantum field theory which describes the electromagnetic interaction of electrically charged particles. The Lagrange density function for a Dirac fermion $\psi(x)$ is

$$\mathcal{L}_\psi = i \bar{\psi}(x) \not{D} \psi(x) - m \bar{\psi}(x) \psi(x), \quad (2.6)$$

where m is the tree-level mass of the fermion and \not{D} the covariant derivative. The covariant derivative is defined by

$$\not{D} \psi(x) = \gamma^\mu D_\mu \psi(x) = \gamma^\mu (\partial_\mu + ieQ A_\mu(x)) \psi(x), \quad (2.7)$$

where A_μ is a spin-1 field and eQ the electric charge of the fermion. The Lagrangian is invariant under the translations, rotations and boosts that form the Poincaré group and under local $U(1)_{\text{EM}}$ gauge transformations

$$\begin{aligned} \psi(x) &\rightarrow \psi(x) + \delta \psi(x) = \exp(iQ\theta(x)) \psi(x) \\ A_\mu(x) &\rightarrow A_\mu(x) + \delta A_\mu(x) = A_\mu(x) - \frac{1}{e} \partial_\mu \theta(x), \quad \theta(x) \in \mathbb{R}. \end{aligned} \quad (2.8)$$

Theories that are invariant under $U(1)$ or other groups of continuous local transformations are called gauge theories.

The kinetic term for the spin-1 field A_μ has the form

$$\mathcal{L}_A = -\frac{1}{4} F_{\mu\nu}(x) F^{\mu\nu}(x) \quad \text{with} \quad F_{\mu\nu} = \partial_\mu A_\nu(x) - \partial_\nu A_\mu(x). \quad (2.9)$$

A mass term for the field A_μ would violate the local $U(1)_{\text{EM}}$ gauge invariance. If the kinetic term \mathcal{L}_A is added to the Lagrange density function \mathcal{L}_ψ , the Lagrangian

$$\begin{aligned} \mathcal{L}_{\text{QED}} &= \bar{\psi}(x) (i \not{D} - m) \psi(x) - \frac{1}{4} F_{\mu\nu}(x) F^{\mu\nu}(x) \\ &= \underbrace{i \bar{\psi}(x) \not{\partial} \psi(x) - \frac{1}{4} F_{\mu\nu}(x) F^{\mu\nu}(x)}_{\text{kinetic term}} - \underbrace{m \bar{\psi}(x) \psi(x)}_{\text{mass term}} - \underbrace{eQ \bar{\psi}(x) \not{A}(x) \psi(x)}_{\text{interaction term}}, \end{aligned} \quad (2.10)$$

is obtained. The spin-1 field A_μ can be identified with the massless photon. For multiple fermions the kinetic and mass terms of the fermion and the interaction term are repeated and the Lagrange density function is

$$\mathcal{L}'_{\text{QED}} = \sum_{\psi} \mathcal{L}_{\psi} + \mathcal{L}_A. \quad (2.11)$$

2.1.4. Quantum Chromodynamics

The theory of Quantum Chromodynamics (QCD) describes the strong interaction of the colour-charged quarks and gluons. Every quark is a triplet in the colour-charge space and eight gluons are introduced in order to make the Lagrangian invariant under $\text{SU}(3)_C$ transformations. With the definition of the covariant derivative

$$D_\mu q_f = \left(\partial_\mu + ig_S \frac{\lambda_a}{2} G_{a,\mu}(x) \right) q_f, \quad (2.12)$$

where q_f is a quark of flavour f with tree-level mass m_f , g_S the QCD gauge coupling, which is related to the strong coupling constant via $4\pi\alpha_S = g_S^2$, λ_a the generators of the group $\text{SU}(3)$, the Gell-Mann matrices defined in Appendix A.1, and $G_{a,\mu}(x)$ the gluon fields with colour index a , the Lagrangian of Quantum Chromodynamics is

$$\mathcal{L}_{\text{QCD}} = \sum_f \bar{q}_{f,\alpha} (i\not{D} - m_f) q_f^\alpha + \mathcal{L}_g \quad (2.13)$$

$$\text{with } \mathcal{L}_g = -\frac{1}{4} G_a^{\mu\nu} G_{\mu\nu}^a. \quad (2.14)$$

In this definition the field strength tensor

$$G_a^{\mu\nu}(x) = \partial^\mu G_a^\nu - \partial^\nu G_a^\mu - g_S f_{abc} G_b^\mu G_c^\nu \quad (2.15)$$

is used. The symbol f_{abc} denotes the structure functions of QCD as defined in Appendix A.1. The QCD Lagrangian is invariant under infinitesimal $\text{SU}(3)_C$ transformations that are defined by

$$\begin{aligned} q_f^\alpha(x) &\rightarrow q_f^\alpha(x) + \delta q_f^\alpha(x) = q_f^\alpha(x) + \frac{i}{2} (\lambda_a)^{\alpha\beta} \delta\theta_a(x) q_{f,\beta}(x), \\ G_a^\mu(x) &\rightarrow G_a^\mu(x) + \delta G_a^\mu(x) = G_a^\mu(x) - \frac{1}{g_S} \partial^\mu (\delta\theta_a(x)) - f_{abc} \delta\theta_b(x) G_c^\mu(x), \end{aligned} \quad (2.16)$$

where $\delta\theta_1(x), \dots, \delta\theta_8(x)$ are the parameters of the transformation.

Contrary to QED, an abelian gauge theory, QCD is a non-abelian gauge theory and the generators of the $\text{SU}(3)_C$ group, λ_a , do not commute. As shown in Appendix A.2 the non-commutativity leads to 3-gluon and 4-gluon interaction terms, which in turn are the reason for the confinement and the asymptotic freedom in QCD.

2.1.5. Electroweak Unification and the Glashow-Weinberg-Salam Model

In Section 2.1.3 the QED Lagrange density function that describes the electromagnetic interaction of photons and fermions was introduced. In the Standard Model Lagrange density function, however, the weak and electromagnetic interactions are described with a unified theory that builds on the the group $\text{SU}(2)_L \otimes \text{U}(1)_Y$. Based on the eigenvalues of the chirality operator,

$$\gamma^5 = i\gamma^0\gamma^1\gamma^2\gamma^3 = \begin{pmatrix} -\mathbb{1} & 0 \\ 0 & \mathbb{1} \end{pmatrix} \quad (2.17)$$

in Weyl notation, fields can be grouped into left-handed (eigenvalue -1) and right-handed (eigenvalue $+1$) fields. Massless particles have chirality $+1$ if the spin is parallel to the momentum and chirality -1 if the spin is anti-parallel to the momentum. To be able to reflect the experimental observation that only left-handed fermions (right-handed anti-fermions) take part in the weak interaction, the left-handed fermions are grouped into SU(2) doublets and the right-handed fermions into SU(2) singlets according to Table 2.2. It should be noted that in general for fermions the interaction eigenstates can be different from the mass eigenstates. By definition the interaction eigenstates form the SU(2) doublets, while the mass eigenstates are the eigenstates that describe freely propagating particles with a definite mass.

	Particles	Colour multiplet, T_3 , Y
Left-handed fields	$L_L = \begin{pmatrix} \nu_e \\ e \end{pmatrix}_L, \begin{pmatrix} \nu_\mu \\ \mu \end{pmatrix}_L, \begin{pmatrix} \nu_\tau \\ \tau \end{pmatrix}_L$	$\mathbf{1}, 1/2, -1/2$ $\mathbf{1}, -1/2, -1/2$
	$Q_L = \begin{pmatrix} u \\ d \end{pmatrix}_L, \begin{pmatrix} c \\ s \end{pmatrix}_L, \begin{pmatrix} t \\ b \end{pmatrix}_L$	$\mathbf{3}, 1/2, 1/6$ $\mathbf{3}, -1/2, 1/6$
Right-handed fields	$l_R = e_R, \mu_R, \tau_R$	$\mathbf{1}, 0, 1$
	$q_{u,R} = u_R, c_R, t_R$	$\bar{\mathbf{3}}, 0, -2/3$
	$q_{d,R} = d_R, s_R, b_R$	$\bar{\mathbf{3}}, 0, 1/3$

Table 2.2.: Grouping of the left-handed fermions into SU(2) doublets and the right-handed fermions into SU(2) singlets. Right-handed anti-fermions are grouped into SU(2) doublets and left-handed anti-fermions into SU(2) singlets accordingly. In the table interaction eigenstates are shown together with the SU(3)_C representations and the eigenvalues of the T_3 and hypercharge operators. Mass eigenstates are discussed in Section 2.1.7. Right-handed neutrinos would be non-interacting (“sterile”) and are neglected. The symbols $\mathbf{1}$, $\mathbf{3}$ and $\bar{\mathbf{3}}$ refer to the singlet, the triplet and the anti-triplet representation of SU(3)_C.

The covariant derivative is defined by

$$\begin{aligned}
D_\mu Q_L &= \left(\partial_\mu + ig\tilde{W}_\mu(x) + ig'y_1 B_\mu(x) \right) Q_L, \\
D_\mu q_{u,R} &= \left(\partial_\mu + ig'y_2 B_\mu(x) \right) q_{u,R}, \\
D_\mu q_{d,R} &= \left(\partial_\mu + ig'y_3 B_\mu(x) \right) q_{d,R},
\end{aligned} \tag{2.18}$$

where

$$\tilde{W}_\mu(x) = \frac{\sigma^i}{2} W_\mu^i(x) = \frac{1}{2} \begin{pmatrix} W_\mu^3 & \sqrt{2}W_\mu^+ \\ \sqrt{2}W_\mu^- & -W_\mu^3 \end{pmatrix}, \tag{2.19}$$

$$W_\mu^\pm = \frac{1}{\sqrt{2}} \left(W_\mu^1 \mp iW_\mu^2 \right) \tag{2.20}$$

and $W_\mu^i(x)$, $B_\mu(x)$ and g , g' are the SU(2)_L and U(1)_Y spin-1 gauge fields and gauge couplings. For leptons it is defined accordingly. The Lagrangian is $\mathcal{L}_{\text{EW}} = \mathcal{L}_{\text{matter}} + \mathcal{L}_{\text{W,B}}$

with

$$\mathcal{L}_{\text{matter}} = \sum_{\text{generations}} \left[i\bar{Q}_L \not{D} Q_L + i\bar{q}_{u,R} \not{D} q_{u,R} + i\bar{q}_{d,R} \not{D} q_{d,R} + i\bar{L}_L \not{D} L_L + i\bar{l}_R \not{D} l_R \right], \quad (2.21)$$

$$\mathcal{L}_{\text{W,B}} = -\frac{1}{4} W_{\mu\nu}^i W^{\mu\nu i} - \frac{1}{4} B_{\mu\nu} B^{\mu\nu}, \quad (2.22)$$

where

$$B_{\mu\nu} = \partial_\mu B_\nu - \partial_\nu B_\mu, \quad (2.23)$$

$$\text{and } W_{\mu\nu}^i = \partial_\mu W_\nu^i - \partial_\nu W_\mu^i - g\epsilon^{ijk} W_\mu^j W_\nu^k. \quad (2.24)$$

The Lagrange density function is shown in terms of mass eigenstates in Equation A.10.

The Lagrangian is invariant under the local transformations

$$Q_L(x) \rightarrow Q_L(x) + \delta Q_L(x) = \exp(iy_1\beta(x)) U_L(x) Q_L(x),$$

$$q_{u,R}(x) \rightarrow q_{u,R}(x) + \delta q_{u,R}(x) = \exp(iy_2\beta(x)) q_{u,R}(x),$$

$$q_{d,R}(x) \rightarrow q_{d,R}(x) + \delta q_{d,R}(x) = \exp(iy_3\beta(x)) q_{d,R}(x),$$

$$B_\mu(x) \rightarrow B_\mu(x) + \delta B_\mu(x) = B_\mu(x) - \frac{1}{g'} \partial_\mu \beta(x),$$

$$\tilde{W}_\mu(x) \rightarrow \tilde{W}_\mu(x) + \delta \tilde{W}_\mu(x) = U_L(x) \tilde{W}_\mu(x) U_L^\dagger(x) + \frac{i}{g} \partial_\mu U_L(x) U_L^\dagger(x), \quad (2.25)$$

where the transformations for $Q_L(x)$ and $q_{u,R}(x)$ are applied to $L_L(x)$ and $l_R(x)$ accordingly and

$$U_L(x) = \exp\left(i\frac{1}{2}\sigma^i\alpha^i(x)\right), \quad i = 1, 2, 3 \quad \text{and} \quad (2.26)$$

$$\tilde{W}_\mu(x) = \frac{\sigma^i}{2} W_\mu^i(x). \quad (2.27)$$

The transformations are parameterised by $\beta(x) \in \mathbb{R}$ and $\alpha^i(x) \in \mathbb{R}$ for $i = 1, 2, 3$.

A fermion mass term that gives different masses to the electron and the electron neutrino would be of the form

$$-m_e \bar{e} e = -m_e \bar{e} \left[\frac{1}{2} (\mathbb{1} - \gamma^5) + \frac{1}{2} (\mathbb{1} + \gamma^5) \right] e = -m_e (\bar{e}_R e_L + \bar{e}_L e_R), \quad (2.28)$$

because $1/2(\mathbb{1} \pm \gamma^5)$ are the left- and right-handed chirality projection operators, but the fields belong to different SU(2) representations and the term violates gauge invariance. A possible solution to this problem is discussed in Section 2.1.6.

The gauge fields in Equation 2.21 are interaction eigenstates that do not coincide with the mass eigenstates. The charged gauge bosons W_μ^\pm take the form defined in Equation 2.20. The gauge bosons B_μ and W_μ^3 are both electrically neutral and mixing can occur, so that $U(1)_Y \neq U(1)_{\text{EM}}$. This mixing is parameterised by the Weinberg angle θ_W , so that

$$\begin{pmatrix} W_\mu^3 \\ B_\mu \end{pmatrix} = \begin{pmatrix} \cos \theta_W & \sin \theta_W \\ -\sin \theta_W & \cos \theta_W \end{pmatrix} \begin{pmatrix} Z_\mu \\ A_\mu \end{pmatrix}. \quad (2.29)$$

The Lagrangian is shown in Equation A.11 as a function of these mass eigenstates, so that the kinetic and interaction terms can be identified.

In comparison to the QED Lagrangian in Equation 2.6 the couplings and the electric charges are

$$g \sin \theta_W = g' \cos \theta_W = e \quad \text{and} \quad Q_1 = y_1 + T_3, Q_{2,3} = y_{2,3} \quad \text{with} \quad T_3 = \sigma_3/2, \quad (2.30)$$

where Q is a matrix in the $SU(2)$ space. The weak hypercharges y_1, y_2 and y_3 are

$$\begin{aligned} y_1 = Q_\nu - \frac{1}{2} = Q_e + \frac{1}{2} = -\frac{1}{2}, \quad y_2 = Q_\nu = 0, \quad y_3 = Q_e = -1 \quad \text{for leptons and} \\ y_1 = Q_u - \frac{1}{2} = Q_d + \frac{1}{2} = \frac{1}{6}, \quad y_2 = Q_u = \frac{2}{3}, \quad y_3 = Q_d = -\frac{1}{3} \quad \text{for quarks.} \end{aligned} \quad (2.31)$$

2.1.6. Spontaneous Symmetry Breaking and the Higgs Mechanism

While the photon is massless, the W and Z bosons are massive and masses of

$$m_W = (80.385 \pm 0.015) \text{ GeV} \quad (2.32)$$

$$m_Z = (91.1876 \pm 0.0021) \text{ GeV} \quad (2.33)$$

have been measured. For the electrically charged fermions masses between 511 keV (electron) and 173 GeV (top quark) have been measured [6]. It is established that neutrino flavour oscillations exist and thus that neutrinos are massive. The experimental constraints on the neutrino masses are discussed in Section 2.1.9. With Equation 2.21 it is possible to describe the weak and electromagnetic interactions, but the gauge bosons and fermions are massless in this theory. Explicit mass terms for the gauge bosons and fermions violate the gauge invariance. In addition, the theory predicts a vertex with four W bosons. For the calculation of the cross section for WW scattering the Feynman diagrams based on this vertex and the Feynman diagrams with s- or t-channel Z/γ^* exchange need to be considered. Without further diagrams, this process violates unitarity, the condition that the probability sum for all outcomes of a physical process is 1.

However, masses can be generated with the spontaneous breaking of a gauge symmetry. For this reason a spin-0 $SU(2)$ doublet, the Higgs field $\phi = (\phi_1, \phi_2)^T$, is introduced. The corresponding part of the Lagrangian is

$$\mathcal{L}_{\text{Higgs}} = (D_\mu \phi)^\dagger D^\mu \phi - V(\phi) = (D_\mu \phi)^\dagger D^\mu \phi - \mu^2 \phi^\dagger \phi - \lambda (\phi^\dagger \phi)^2, \quad (2.34)$$

where μ^2 and λ are model parameters and

$$D^\mu \phi = \left[\partial^\mu + ig \tilde{W}^\mu + ig' y_\phi B^\mu \right] \phi, \quad y_\phi = Q_\phi - T_3 = \frac{1}{2}. \quad (2.35)$$

For $\mu^2 < 0$ and $\lambda > 0$ the potential of the Higgs field, V , has minima at

$$|\phi_0| = \sqrt{\frac{-\mu^2}{2\lambda}} = \frac{v}{\sqrt{2}}, \quad \text{with values} \quad V(\phi_0) = -\frac{\mu^4}{4\lambda} = -\lambda \frac{v^4}{4} \quad (2.36)$$

as illustrated in Figure 2.1 for an $SU(2)$ singlet. The vacuum expectation value of the Higgs field is parameterised by v to obtain a simpler notation. The parameter v is defined by Equation 2.36. Without knowledge of the Higgs boson mass, the parameter λ is unknown. However, the vacuum expectation value v can be inferred from measurements of the muon lifetime. Based on the Fermi coupling constant, G_F , the Higgs vacuum expectation value can be determined as

$$v = \left(\sqrt{2} G_F \right)^{-1/2} \approx 246 \text{ GeV} [6]. \quad (2.37)$$

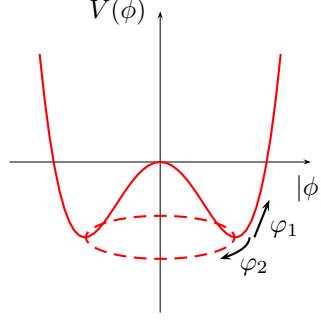


Figure 2.1.: The Higgs potential $V(\phi)$ is shown as a function of $|\phi|$. As four degrees of freedom cannot be shown a SU(2) singlet ϕ that can be written as $\phi = 1/\sqrt{2}[v + \varphi_1 + i\varphi_2]$ is used. The field $\varphi_1(x)$ corresponds to the Higgs boson with a mass $m_H = -\frac{\mu^2}{2}$, the field $\varphi_2(x)$ to the massless Nambu-Goldstone boson. For a SU(2) doublet there are three Nambu-Goldstone bosons. The dashed line illustrates the minimum for a three-dimensional representation.

The Higgs field can now be parameterised around an arbitrary point in the minimum as

$$\phi(x) = \exp\left(i\frac{\sigma_i}{2}\theta^i(x)\right) \frac{1}{\sqrt{2}} \begin{pmatrix} 0 \\ v + H(x) \end{pmatrix}, \quad (2.38)$$

where $H(x)$ and $\theta^1(x)$, $\theta^2(x)$ and $\theta^3(x)$ are real fields, so that in the unitarity gauge ($\theta^i = 0$) the Lagrangian is

$$\begin{aligned} \mathcal{L}_{\text{Higgs}} = & \frac{1}{2}\partial_\mu H(x)\partial^\mu H(x) + \frac{1}{8}m_H^2 v^2 \\ & + m_W^2 W_\mu^- W^{+\mu} \left(1 + \frac{2}{v}H(x) + \frac{H^2(x)}{v^2}\right) + \frac{1}{2}m_Z^2 Z_\mu Z^\mu \left(1 + \frac{2}{v}H(x) + \frac{H^2(x)}{v^2}\right) \\ & - \frac{1}{2}m_H^2 H^2(x) - \frac{m_H^2}{2v}H^3(x) - \frac{m_H^2}{8v^2}H^4, \end{aligned} \quad (2.39)$$

where $m_W = \frac{1}{2}vg$, $m_Z = \frac{1}{2}v\sqrt{g^2 + g'^2}$ and $m_H = \sqrt{2\lambda}v$ are the W , the Z and the Higgs boson tree-level masses, respectively. Equation 2.39 shows that with the Higgs field mass terms for the gauge bosons can be introduced into a Lagrangian that is invariant under $\text{SU}(2)_L \otimes \text{U}(1)_Y$ transformations.

The Higgs doublet corresponds to three massless Nambu-Goldstone bosons, $\theta^i(x)$, and a scalar particle with tree-level mass m_H , $H(x)$. In general the Goldstone theorem [15, 16, 17] states that if a Lagrangian is invariant under a symmetry group G while the vacuum is only invariant under a symmetry group $U \subset G$, then there are $\dim(U \setminus G)$ mass- and spinless Nambu-Goldstone bosons.

Fermion masses can be added to the Lagrangian with the following so-called Yukawa interaction terms

$$\begin{aligned} \mathcal{L}_{\text{Yukawa}} = & - \sum_{i,j=1}^3 \left[(c_d)_{ij} \bar{Q}_{L,i} \phi q_{d,R,j} + (c_u)_{ij} \bar{Q}_{L,i} \phi^C q_{u,R,j} + (c_e)_{ij} L_{L,i} \phi l_{R,j} \right] + \text{h.c.} \\ = & - \sum_{i,j=1}^3 \left[(m_d)_{ij} \bar{d}_{L,i} d_{R,j} + \frac{(m_d)_{ij}}{v} \bar{d}_{L,i} H d_{R,j} + (m_u)_{ij} \bar{u}_{L,i} u_{R,j} + \frac{(m_u)_{ij}}{v} \bar{u}_{L,i} H u_{R,j} \right. \\ & \left. + (m_l)_{ij} \bar{l}_{L,i} l_{R,j} + \frac{(m_l)_{ij}}{v} \bar{l}_{L,i} H l_{R,j} \right] + \text{h.c.} \end{aligned} \quad (2.40)$$

The indices i, j denote generation indices, $\phi^C = i\sigma_2\phi^*$, $\mathbf{m}_d = \mathbf{c}_d v/\sqrt{2}$, $\mathbf{m}_u = \mathbf{c}_u v/\sqrt{2}$ and $\mathbf{m}_l = \mathbf{c}_l v/\sqrt{2}$ are matrices in generation space. The coupling constants $(c_d)_{ij}$, $(c_u)_{ij}$ and $(c_l)_{ij}$ are model parameters. A mass term for the right-handed neutrino is neglected.

2.1.7. Quark and Lepton Mixing

The masses for quarks and charged leptons have been generated by the Yukawa interaction defined in Equation 2.40. The mass matrices $\mathbf{m}_d = \mathbf{c}_d v/\sqrt{2}$, $\mathbf{m}_u = \mathbf{c}_u v/\sqrt{2}$ and $\mathbf{m}_l = \mathbf{c}_l v/\sqrt{2}$, however, are in general not diagonal. With unitary matrices $\mathbf{V}_{d,L}$, $\mathbf{V}_{d,R}$ the mass matrix \mathbf{m}_d can be diagonalised,

$$\mathbf{V}_{d,L}\mathbf{m}_d\mathbf{V}_{d,R}^\dagger = \text{diag}(m_d, m_s, m_b) \quad (2.41)$$

and the mass eigenstates, d_L^m and d_R^m , corresponding to the interaction eigenstates, d_L^m and d_R^m , are

$$\begin{aligned} d_L^m &= \mathbf{V}_{d,L} d_L, \\ d_R^m &= \mathbf{V}_{d,R} d_R. \end{aligned} \quad (2.42)$$

The terms for up-type quarks and leptons are defined accordingly. Terms involving only up-type quarks, down-type quarks or leptons, $\bar{f}_L f_L$ and $\bar{f}_R f_R$ are invariant under $f_L \rightarrow f_L^m$. The weak interaction via W^\pm -boson exchange, however, contains terms of the form $\bar{u}_L d_L$ that are not invariant, i.e.

$$\bar{u}_L d_L = \bar{u}_L^m \mathbf{V}_{u,L} \mathbf{V}_{d,L}^\dagger d_L^m. \quad (2.43)$$

The matrix $\mathbf{V} = \mathbf{V}_{u,L} \mathbf{V}_{d,L}^\dagger$ is the Cabibbo-Kobayashi-Maskawa (CKM) matrix [18, 19] that is defined by three angles and one complex phase. The complex phase leads to a violation of the CP symmetry in the weak interaction. In the Standard Model only massless left-handed neutrinos are described and the neutrino flavours can be redefined, so that no mixing matrix is needed. For a theory that describes neutrino masses and neutrino flavour oscillations a leptonic mixing matrix, the Maki-Nakagawa-Sakata (MNS) matrix, is needed [20].

2.1.8. The Standard Model Lagrangian

The QCD, the electroweak, the Higgs and the Yukawa Lagrangians can be combined to the Standard Model Lagrangian

$$\mathcal{L}_{\text{SM}} = \mathcal{L}_{\text{matter}} + \mathcal{L}_{\text{W,B}} + \mathcal{L}_{\text{gluons}} + \mathcal{L}_{\text{Higgs}} + \mathcal{L}_{\text{Yukawa}}, \quad (2.44)$$

where the matter and the Yukawa parts include terms for all generations of fermions. The covariant derivative is defined by

$$\begin{aligned} D_\mu Q_L &= \left(\partial_\mu + ig\tilde{W}_\mu(x) + g'y_1 B_\mu(x) + ig_S \frac{\lambda^a}{2} G_{a,\mu}(x) \right) Q_L, \\ D_\mu q_{u,R} &= \left(\partial_\mu + ig'y_2 B_\mu(x) + ig_S \frac{\lambda^a}{2} G_{a,\mu}(x) \right) q_{u,R}, \\ D_\mu q_{d,R} &= \left(\partial_\mu + ig'y_3 B_\mu(x) + ig_S \frac{\lambda^a}{2} G_{a,\mu}(x) \right) q_{d,R} \end{aligned} \quad (2.45)$$

for quarks and without the term proportional to g_S for leptons. The Standard Model Lagrangian is invariant under

$$\text{SU}(3)_C \otimes \text{SU}(2)_L \otimes \text{U}(1)_Y \quad (2.46)$$

transformations. After spontaneous symmetry breaking the vacuum is invariant under

$$\mathrm{SU}(3)_C \otimes \mathrm{U}(1)_{\mathrm{EM}} \quad (2.47)$$

transformations.

2.1.9. Open Questions

In the course of the last decades the Standard Model of particle physics has proven its predictive power in numerous experimental tests and has become widely accepted. There are, however, some observations from particle physics experiments that are not explained by the Standard Model and the underlying reasons for the structure of the Standard Model are not completely known. These open questions include

- **Neutrino masses and oscillations:** If neutrinos have mass, it is possible that oscillations between the three flavour eigenstates occur. The first hint to neutrino flavour oscillations is called the solar neutrino problem, the question why the flux of electron neutrinos from the sun is smaller than 1/2 of the expected flux [6, 21]. By now neutrino oscillations have been observed for accelerator, atmospheric, reactor and solar neutrinos and the mass differences of the neutrinos were measured to be

$$\Delta m_{21}^2 = (7.50 \pm 0.20) \cdot 10^{-5} \text{ eV}^2, \quad (2.48)$$

$$\Delta m_{32}^2 = (2.32^{+0.12}_{-0.08}) \cdot 10^{-3} \text{ eV}^2 [6], \quad (2.49)$$

where $\Delta m_{ij}^2 = m_i^2 - m_j^2$ and m_1 and m_2 are the masses of the neutrinos of which the mass difference is smaller compared to the differences to the third neutrino. In the Standard Model neutrinos are massless and in order to explain massive neutrinos the Standard Model needs to be extended. The mechanism that is responsible for the generation of neutrino masses, however, is still unknown.

- **Dark matter and dark energy:** The WMAP [22] and Planck [23] satellite missions have measured the spectrum of the cosmic microwave background (CMB). The cosmic microwave background is the radiation that is left from the period of recombination, the period when the temperature dropped to below the hydrogen ionisation temperature. The anisotropy of the temperature and the angular power spectrum as measured by the Planck satellite are shown in Figure 2.2. The multipole spectrum is fit with a six-parameter cosmological model, Λ CDM [24]. The models includes a cosmological constant due to dark energy, Λ , dark matter and baryonic matter. In contrast to dark matter, baryonic matter is affected by the radiation pressure. From a fit with this model it is extracted that the fraction of baryonic matter contributes only 4.9% to the total matter and energy distribution, 68.3% is due to dark energy and 26.8% is due to dark matter [5]. The Standard Model does not provide an explanation for dark energy or a particle that can make up dark matter.
- **Hierarchy problem and fine-tuning problem:** Due to the renormalisation procedure of which an overview is available in Section 2.3.2 the bare mass parameter for the Higgs boson is corrected by loop contributions to obtain the observable mass. The loop contributions are proportional to Λ_{UV}^2 , where Λ_{UV} is the ultraviolet momentum cutoff that is introduced in the renormalisation procedure. As the contributions to the Higgs boson mass after renormalisation from fermion-anti-fermion loops are up to 30 orders of magnitude larger than the observable Higgs boson mass [4], the bare mass

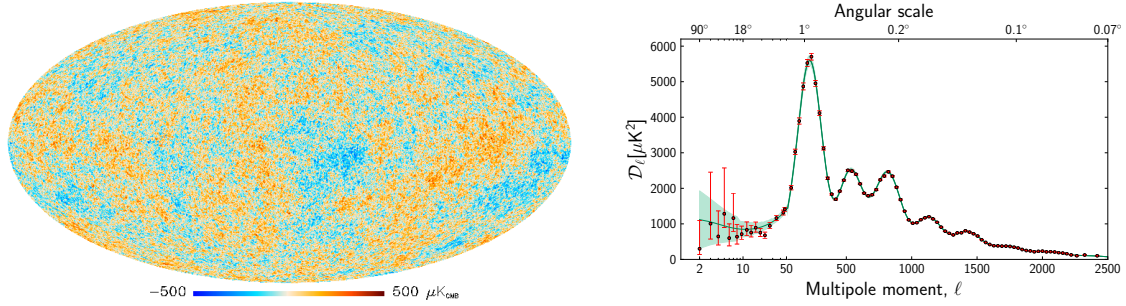


Figure 2.2.: The temperature anisotropy (left-hand side) and the temperature angular power spectrum (right-hand side) of the Cosmic Microwave Background (CMB) as measured by the Planck satellite. The green line shows the best-fit of the six-parameter Λ CDM theory model (taken from Reference [23]).

parameter has to be fine-tuned to balance the loop contributions with high precision. This extreme fine-tuning can be regarded as unnatural.

- **Gravity:** The Standard Model does not include the theory of general relativity or any other description of gravity.
- **Parameters and structure of the Standard Model of particle physics:** The Standard Model contains three generations of quark and lepton families and 19 parameters which are a priori unknown and have to be measured with experiments. These parameters can be chosen to be nine charged lepton and quark masses, 3 CKM mixing angle, 1 CKM CP-violating phase, the 3 gauge couplings, the QCD vacuum angle θ , the Higgs field vacuum expectation value and the Higgs boson mass. The origin of these parameters and the number of generations is unknown and there is no explanation why the non-zero masses of the Standard Model range from 0.511 MeV for the electron to 173.5 GeV for the top quark. There is no widely accepted reason known why the Cabibbo-Kobayashi-Maskawa matrix is close to 1l.
- **Baryon asymmetry and CP violation:** The baryon asymmetry is the asymmetry between the amount of baryonic matter and anti-matter in the observable universe. To ensure that during the evolution of the universe unequal amounts of matter and anti-matter are created the three Sakharov conditions [25] need to be fulfilled:
 - baryon number violation, so that a baryon excess over anti-baryons can be generated,
 - C- and CP-symmetry violation, so that an excess of (left-handed, right-handed) baryons over (right-handed, left-handed) anti-baryons can be generated,
 - interactions out of thermal equilibrium, so that the CPT symmetry does not lead to a compensation between baryon number increasing and decreasing processes.

In the Standard model the baryon number is conserved. Complex phases in the CKM matrix induce CP violation, but the effect of the known CP violation is too small by many orders of magnitude. In order to explain the baryon asymmetry a further source of CP violation is needed.

- **The strong CP problem:** In the Standard Model Lagrange density function a term

proportional to

$$\mathcal{L}_{\text{SCP}} = \frac{\theta g_S^2}{32\pi^2} \epsilon^{\mu\nu\rho\sigma} G_{\mu\nu}^a G_{\rho\sigma}^a, \quad (2.50)$$

where θ is the QCD vacuum angle, is neglected. The term violates CP symmetry and leads to an electric dipole moment of the neutron (nEDM). Measurements of the nEDM lead to the constraint $|\theta| < 1.5 \cdot 10^{-10}$ [26]. The strong CP problem is the question why the QCD vacuum angle is so small.

- **Unification of forces:** In order to obtain finite results in the calculation of interaction rates renormalisation procedures as described in detail in Section 2.3.2 have to be applied. These renormalisation procedures replace the bare couplings of the Lagrangian by energy-scale dependent physical couplings. The evolution of the couplings as a function of the energy scale Q depends on all particles that can be present in loop contributions to these couplings, so that an indirect sensitivity to unknown particles is present. These couplings are shown as a function of the energy scale Q in Figure 2.3. The fact that the couplings have only very roughly, but not exactly, the same value for $Q \approx 10^{15}$ GeV can be interpreted as a hint to new physics.

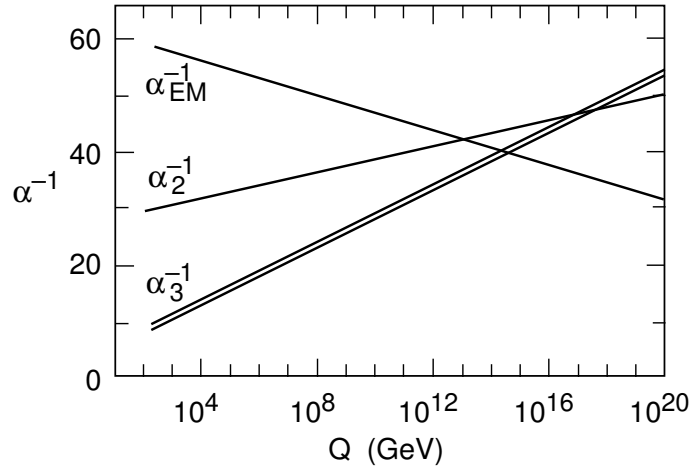


Figure 2.3.: Evolution of the Standard Model gauge coupling constants according to the renormalisation group equations. The gauge couplings are defined by $\alpha_i = \frac{g_i^2}{2\pi}$, where $g_1 = \sqrt{5/3}g'$, $g_2 = g$ and $g_3 = g_S$ (taken from Reference [27]).

2.2. Supersymmetry

Supersymmetry (SUSY) is a symmetry that relates bosons and fermions. Based on work by Coleman and Mandula [28] it was shown in the Haag-Lopuszański-Sohnius theorem [29] that supersymmetry is the only non-trivial extension for consistent four-dimensional quantum field theories with internal and Poincaré symmetries. In the following sections an overview of minimal $N = 1$ and global supersymmetry with four space-time dimensions, the Minimal Supersymmetric Standard Model, is given based on References [4] and [30]. Unbroken supersymmetry with $N = 1$ kind of transformations implies that for every boson a fermion and for every fermion a boson that is identical in all properties except for their spin exists. As it is not possible to relate two Standard Model particles with a supersymmetry transformation, for

every Standard Model particle, one superpartner has to be introduced¹. The superpartners of the boson interaction states are the Winos, the Bino, the gluinos and the Higgsinos. The superpartners of the fermions are called squarks and sleptons. All supersymmetric particles are referred to as sparticles, the superpartners of the gauge bosons are referred to as gauginos.

2.2.1. Supersymmetry Transformations and the Lagrange Density Function of the MSSM

A general, infinitesimal supersymmetry transformation is defined as

$$\hat{S} = \exp \left(\epsilon \hat{Q} + \epsilon^\dagger \hat{Q}^\dagger \right), \quad (2.51)$$

where ϵ is an infinitesimal, anti-commuting Weyl spinor. The symbols \hat{Q} and \hat{Q}^\dagger denote the SUSY operators, for which

$$\left\{ \hat{Q}_\alpha, \hat{Q}_\beta^\dagger \right\} = 2i\sigma_{\alpha\beta}^\mu \partial_\mu = -2\sigma_{\alpha\beta}^\mu \hat{P}_\mu, \quad \left\{ \hat{Q}_\alpha, \hat{Q}_\beta \right\} = 0, \quad \left\{ \hat{Q}_\alpha^\dagger, \hat{Q}_\beta^\dagger \right\} = 0 \quad (2.52)$$

holds. The symbol \hat{P}_μ denotes the momentum operator, so that the SUSY operators connect the spacetime structure and the internal degrees of freedom of a particle. A Standard Model fermion, ψ , and the corresponding supersymmetric boson, ϕ , are combined in a chiral superfield together with an auxiliary field F . In addition, the scalar MSSM Higgs bosons and the fermionic Higgsinos are combined in a chiral superfield with auxiliary fields. The auxiliary fields do not constitute physical particles and can be removed from the Lagrange density function with their equations of motion. They are, however, important to retain the invariance of the Lagrange density function under supersymmetry transformations. The mathematical form of a chiral superfield is

$$\Phi(x_\mu, \theta, \theta^\dagger) = \phi + i\theta^\dagger \bar{\sigma}^\mu \theta \partial_\mu \phi + \frac{1}{4} \theta \theta^\dagger \theta^\dagger \partial_\mu \partial^\mu \phi + \sqrt{2} \theta \psi + \frac{i}{\sqrt{2}} \theta \theta^\dagger \bar{\sigma}^\mu \partial_\mu \psi + \theta \theta F, \quad (2.53)$$

where θ is a two-component, anti-commuting Grassmann spinor [13]. In the superfield formalism \hat{Q} and \hat{Q}^\dagger can be expressed with the chiral covariant derivatives

$$\begin{aligned} \hat{Q}_\alpha &= iD_\alpha, \quad \hat{Q}^{\dagger\dot{\alpha}} = iD^{\dagger\dot{\alpha}} \\ \text{with } D_\alpha &= \frac{\partial}{\partial \theta^\alpha} - \left(\sigma^\mu \theta^\dagger \right)_\alpha \partial_\mu, \quad D^{\dagger\dot{\alpha}} = \frac{\partial}{\partial \theta_{\dot{\alpha}}^\dagger} - (\bar{\sigma}^\mu \theta)^{\dot{\alpha}} \partial_\mu, \end{aligned} \quad (2.54)$$

so that the supersymmetry transformations for these fields are

$$\begin{aligned} \phi &\rightarrow \hat{S}\phi = \phi + \delta_\epsilon \phi = \phi + \epsilon \psi, \\ \psi &\rightarrow \hat{S}\psi = \psi_\alpha + \delta_\epsilon \psi = \psi - i \left(\sigma^\mu \epsilon^\dagger \right) \partial_\mu \phi, \\ F &\rightarrow \hat{S}F = F + \delta_\epsilon F = F - i\epsilon^\dagger \bar{\sigma}^\mu \partial_\mu \psi. \end{aligned} \quad (2.55)$$

The Standard Model vector bosons and their superpartners are combined into vector superfields which have the form

$$V(x_\mu, \theta, \theta^\dagger) = \theta^\dagger \bar{\sigma}^\mu \theta A_\mu + \theta^\dagger \theta^\dagger \theta \lambda + \theta \theta \theta^\dagger \lambda^\dagger + \frac{1}{2} \theta \theta \theta^\dagger \theta^\dagger D, \quad (2.56)$$

¹It will be shown in Section 2.2.7 that in addition a second Higgs doublet and its superpartner doublet have to be introduced.

in the Wess-Zumino gauge [31]. The symbol A_μ denotes a Standard Model spin-1 boson and λ the corresponding gaugino. Similar to F in Equation 2.53, D is an auxiliary field that can be removed as no corresponding kinetic term is present. The supersymmetry transformations of the component fields and more details on the superfield formulation of supersymmetric theories are available in Reference [4].

Based on the chiral and vector superfields real supersymmetric terms that can be included in the Lagrange density function can be constructed. In the following, two supersymmetric terms, the D-term of the so-called Kähler potential and a term based on the so-called superpotential are described. The D-term of the Kähler potential is a term based on the chiral superfields Φ . The term is invariant under gauge symmetry and supersymmetry transformations. For renormalisable theories the D-term of the Kähler potential is

$$\left[K \left(\Phi_i, \tilde{\Phi}^{*j} \right) \right]_D = \left[\Phi_i \tilde{\Phi}^{*j} \right]_D$$

with $\tilde{\Phi}^{*j} = \Phi^{*k} (\exp(2T^a g_a V^a))_k^j$,

(2.57)

where V_a denote vector superfields, T_a the generators of the corresponding gauge group and g_a the corresponding gauge couplings. The notation $[S]_D$ refers to the term of a superfield S proportional to $\theta\theta\theta^\dagger\theta^\dagger$, the D-term. The Kähler potential provides the kinetic terms for the fields that make up chiral superfields and a part of the interaction terms for fields that make up chiral and vector superfields.

Similar $[S]_F$ refers to the term proportional to $\theta\theta$. The F-term of a chiral superfield and, as any linear combination of chiral superfields is a chiral superfield, the F-term of any linear combination W is supersymmetric. A general linear combination W can be parameterised by

$$W = L_i \Phi_i + M_{ij} \Phi_i \Phi_j + y_{ijk} \Phi_i \Phi_j \Phi_k.$$
(2.58)

The symbols L_i , M_{ij} and y_{ijk} denote complex numbers and only terms of $\mathcal{O}(\Phi^3)$ are considered to retain the renormalisability. For the Minimal Supersymmetric Standard Model only the minimal number of supersymmetry generators and the minimal field content is considered. Based on these fields the superpotential is

$$W_{\text{MSSM}} = -\bar{u} \mathbf{y}_u Q \cdot H_u - \bar{d} \mathbf{y}_d H_d \cdot Q - \bar{e} \mathbf{y}_e H_d \cdot L + \mu H_u \cdot H_d,$$
(2.59)

where the superfields are defined according to Table 2.3 and \mathbf{y}_u , \mathbf{y}_d , \mathbf{y}_e are the Yukawa couplings. The Yukawa couplings are matrices in the 3×3 generation space and the lepton and quark superfields are vectors in generation space. The terms of the form $\bar{u} \mathbf{y}_u Q \cdot H_u$ include SU(2)-doublet products $Q \cdot H_u$, that can be written as

$$\bar{u} \mathbf{y}_u Q \cdot H_u = \bar{u} \mathbf{y}_u Q_\alpha (H_u)_\beta i\sigma_2^{\alpha\beta} = \bar{u}^{ia} (y_u)_i^j Q_{ja\alpha} (H_u)_\beta i\sigma_2^{\alpha\beta},$$
(2.60)

where $\alpha, \beta = 1, 2$ are weak isospin indices, $i, j = 1, 2, 3$ generation indices and $a = 1, 2, 3$ colour indices.

The F-term of the superpotential is used in the Lagrange density function. However, to obtain a real and gauge-invariant function the complex conjugate of the F-term of the superpotential has to be added

$$[W(\Phi)]_F + \text{h.c.}$$
(2.61)

The superpotential term accounts for the Yukawa interactions of the fermions and the Higgs doublets and the mass term for the Higgsinos. The kinetic terms and self-interaction terms

Chiral superfield Φ	ϕ	ψ	Vector superfield V	λ	A_μ
Q	$\begin{pmatrix} \tilde{u}_L \\ \tilde{d}_L \end{pmatrix}$	$\begin{pmatrix} u_L \\ d_L \end{pmatrix}$	\tilde{g}	\tilde{g}	g
\bar{u}	\tilde{u}_R^*	u_R^\dagger	\tilde{W}	\tilde{W}^1	W^1
\bar{d}	\tilde{d}_R^*	d_R^\dagger		\tilde{W}^2	W^2
L	$\begin{pmatrix} \tilde{\nu}_L \\ \tilde{e}_L \end{pmatrix}$	$\begin{pmatrix} \nu_L \\ e_L \end{pmatrix}$		\tilde{W}^3	W^3
e	\tilde{e}_R^*	e_R^\dagger	\tilde{B}	\tilde{B}	B
H_u	$\begin{pmatrix} H_u^+ \\ H_u^0 \end{pmatrix}$	$\begin{pmatrix} \tilde{H}_u^+ \\ \tilde{H}_u^0 \end{pmatrix}$			
H_d	$\begin{pmatrix} H_d^0 \\ H_d^- \end{pmatrix}$	$\begin{pmatrix} \tilde{H}_d^0 \\ \tilde{H}_d^- \end{pmatrix}$			

Table 2.3.: Particle and superfield content of the Minimal Supersymmetric Standard Model. The fields ϕ and ψ are combined to form a chiral superfield according to Equation 2.53. The fields A_μ and λ are combined into a vector superfield, the form of which is given in the Wess-Zumino gauge in Equation 2.56.

for the gauge bosons and their superpartners are introduced in the supersymmetric gauge kinetic function. The form of the gauge kinetic function is

$$\left(\frac{1}{4} - i\frac{g_a^2\Theta_a}{32\pi^2}\right) [\mathcal{W}^{a\alpha}, \mathcal{W}_\alpha^a]_F + \text{h.c.}, \quad (2.62)$$

where $\mathcal{W}^{a\alpha}$ is a field strength tensor defined by

$$\mathcal{W}^{a\alpha} = -\frac{1}{4}D^\dagger D^\dagger [\exp(-2g_a T^a V^a) D_\alpha \exp(2g_a T^a V^a)] \quad (2.63)$$

and Θ_a parameterises the CP-violating effect of the coupling g_a . With the gauge kinetic function the supersymmetric Lagrange density function can be constructed. It is given by

$$\mathcal{L}_{\text{SUSY}} = \left[K(\Phi_i, \tilde{\Phi}^{*j})\right]_D + \left[\left(\frac{1}{4} - i\frac{g_a^2\Theta_a}{32\pi^2}\right) \mathcal{W}^{a\alpha} \mathcal{W}_\alpha^a + W(\Phi_i)\right]_F + \text{h.c.} \quad (2.64)$$

For a realistic theory of supersymmetry additional supersymmetry-breaking terms have to be included, as will be discussed in Section 2.2.3. The interaction eigenstates of the MSSM particles are shown in Table 2.3. Similar to the Standard Model some of the interaction eigenstates can mix and the mass eigenstates are different. In particular the charged Higgsino components and the charged Wino components form the so-called charginos, $\tilde{\chi}_1^\pm$ and $\tilde{\chi}_2^\pm$. The neutral Bino and Wino interaction eigenstates form the so-called neutralinos, $\tilde{\chi}_i$, $i = 1, 2, 3, 4$. In addition the superpartners of the left- and right-handed fermions can mix. However, in practice it is often a good approximation to consider only the mixing of the stop, sbottom and stau bosons. The Higgs sector and the mixing of the interaction eigenstates therein is described in detail in Sections 2.2.6 and 2.2.7.

2.2.2. R -Parity

In general it is possible to include terms in the superpotential which lead to vertices that violate the baryon number B or the total lepton number L . Couplings proportional to $L_1 Q_1 \bar{d}_{2,3}$ (lepton number violating) and $\bar{u}_1 \bar{d}_1 \bar{d}_{2,3}$ (baryon number violating), where the indices denote the generation, would for example lead to proton decay via $p \rightarrow e^+ \pi^0$. The lifetime of the proton was measured to be $> 2.1 \cdot 10^{29}$ years (partial mean lifetime for $p \rightarrow e^+ \pi^0 > 8.2 \cdot 10^{33}$ years) [6], so that the relevant products of coupling constants have to be zero or very small.

To retain a proton lifetime of $> 10^{29}$ years it is possible to postulate B and L conservation. It is, however, more elegant to postulate R -parity conservation for the Lagrange density function. The postulation of R -parity removes all B - and L -violating terms. R -parity is defined as

$$P_R = (-1)^{3(B-L)+2s}, \quad (2.65)$$

where s refers to the spin. Standard Model particles have R -parity $P_R = +1$ and superpartners $P_R = -1$. By definition R -parity is a multiplicative quantum number.

In the MSSM, R -parity is assumed to be conserved, so that only interaction vertices that contain even numbers of superpartners are possible. In consequence superpartners are produced in pairs and the lightest supersymmetric particle (LSP) is stable as there are no lighter supersymmetric particles it can decay to. The LSP is a candidate particle for cold dark matter if it is electrically and colour neutral. In many searches for supersymmetry the fact that electrically and colour neutral stable particles are created in the decay chains of supersymmetric particles is used by searching for signatures with an imbalance of transverse momentum in the event, the missing transverse momentum. As particle detectors can not be fully hermetic and as in hadron-hadron collisions the z -component of the colliding parton momenta is unknown the longitudinal momentum imbalance can not be observed. In many models of supersymmetry the lightest supersymmetric particle is the lightest neutralino, $\tilde{\chi}_1^0$, a mixture of the Wino, the Bino and the Higgsinos. In other supersymmetric models, such as gauge-mediated supersymmetry breaking (GMSB), the gravitino is the LSP.

2.2.3. The Hierarchy Problem and Supersymmetry Breaking

The hierarchy problem of the Standard Model is the question for an explanation of the fine-tuning of the bare Higgs boson mass and the loop contributions, as was discussed in Section 2.1.9. The leading-order loop contributions of a fermion to the Higgs boson mass are proportional to Λ_{UV}^2 . In supersymmetric models for every fermion f two complex scalars \tilde{f}_L and \tilde{f}_R are introduced. The sfermions can couple to the Higgs boson as shown in the Feynman diagram in Figure 2.4 and induce corrections to the Higgs boson mass. If no other contributions exist, the quadratic divergencies of each fermion f and the sfermions \tilde{f}_L and \tilde{f}_R cancel at leading order if $\lambda_{\tilde{f}} = -\lambda_f^2$, where λ_f ($\lambda_{\tilde{f}}$) is the coupling constant of the Higgs boson to a pair of fermions (sfermions). In theories with unbroken supersymmetry it is $\lambda_{\tilde{f}} = -\lambda_f^2$ and the quadratic divergencies even cancel at all orders of perturbation theory.

As the superpartners have not yet been observed by experiments, supersymmetry needs to be broken, so that superpartners can obtain higher masses than Standard Model particles. For the spontaneous breaking of supersymmetry a field needs to acquire a non-zero vacuum expectation value. In the MSSM there is no field available whose vacuum expectation value would break supersymmetry and could lead to an acceptable particle spectrum [4]. For the breaking of supersymmetry a wide variety of models exists. In most models of supersymmetry a particle in a so-called hidden sector has a non-zero vacuum expectation value. The hidden sector consists of new particles that are only weakly coupled to the Standard Model parti-

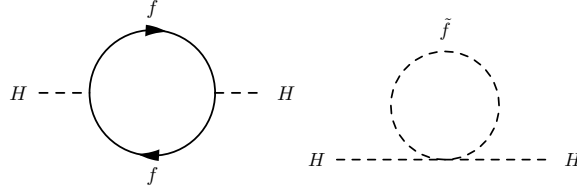


Figure 2.4.: Feynman diagrams for loop corrections to the Higgs boson mass due to fermions (left-hand side) and scalars (right-hand side). For supersymmetric models the quadratic part of the divergencies introduced by the fermion corrections can cancel with the quadratic divergencies introduced by the scalar corrections.

cles. In gravity-mediated supersymmetry breaking, e.g. minimal supergravity (mSUGRA), the gravitino, the superpartner of the gravity-mediating graviton, obtains a mass and the supersymmetry breaking is communicated to the visible sector by the gravitational interaction. In other models supersymmetry breaking is gauge-mediated, which means that the breaking is communicated to the sector with the visible particles by the Standard Model gauge interactions, or anomaly-mediated, which means that the breaking is communicated by the gravitational interaction through the so-called conformal anomaly.

In the MSSM no special mechanism to break supersymmetry is assumed, but the effect of supersymmetry breaking is parameterised. Only soft breaking terms are considered for the Lagrange density function. Terms that break supersymmetry are called soft if the inclusion of the term into the Lagrange density function does not spoil the cancellation of fermion and scalar contributions (i.e. does not lead to divergencies other than logarithmic divergencies) to the Higgs boson mass as needed to mitigate the hierarchy problem. The soft terms of the MSSM are

$$\begin{aligned}
\mathcal{L}_{\text{soft}} = & -\frac{1}{2} \left(M_3 \tilde{g} \tilde{g} + M_2 \tilde{W} \tilde{W} + M_1 \tilde{B} \tilde{B} + \text{h.c.} \right) \\
& - \left(\tilde{u} \mathbf{a}_u \tilde{Q} \cdot H_u + \tilde{d} \mathbf{a}_d H_d \cdot \tilde{Q} + \tilde{e} \mathbf{a}_e H_d \cdot \tilde{L} + \text{h.c.} \right) \\
& - \tilde{Q}^\dagger \mathbf{m}_Q^2 \tilde{Q} - \tilde{L}^\dagger \mathbf{m}_L^2 \tilde{L} - \tilde{u} \mathbf{m}_u^2 \tilde{u}^\dagger - \tilde{d} \mathbf{m}_d^2 \tilde{d}^\dagger - \tilde{e} \mathbf{m}_e^2 \tilde{e}^\dagger \\
& - m_{H_u}^2 H_u^* H_u - m_{H_d}^2 H_d^* H_d - (b H_u \cdot H_d + \text{h.c.}) ,
\end{aligned} \tag{2.66}$$

where M_1 , M_2 and M_3 are the gaugino mass parameters, m_Q^2 , m_u^2 , m_d^2 , m_e^2 the mass parameters for the sfermions, a_u , a_d and a_e the trilinear couplings of the sfermions to the Higgs doublets and $m_{H_u}^2$, $m_{H_d}^2$ and b the Higgs mass parameters. It should be noted that the supersymmetry-breaking terms are formulated in terms of particle and sparticle fields instead of superfields.

2.2.4. Constrained Models Based on the Minimal Supersymmetric Standard Model

In addition to the 19 parameters of the Standard Model for the MSSM 105 parameters [4] are introduced mostly due to the parameterisation of the effects of the supersymmetry breaking. In practice it is not possible to consider the parameter space of all 105 parameters and more constrained models are used. One of these constrained models is mSUGRA which is inspired by grand unified theories. Grand unified theories (GUT) are theories in which at a high scale, the GUT scale, the three gauge interactions unify. In mSUGRA it is in addition assumed that at the unification scale

- the gaugino masses are degenerate,

$$M_3 = M_2 = M_1 =: m_{1/2} \quad (2.67)$$

- the sfermion mass matrices and trilinear couplings are diagonal, universal for all generations and real,

$$(m_Q^2)_{ij} = (m_u^2)_{ij} = (m_d^2)_{ij} = (m_L^2)_{ij} = (m_e^2)_{ij} =: m_0^2 \cdot \delta_{ij} \quad (2.68)$$

$$(a_u)_{ij} = A_0 (y_u)_{ij}, \quad (a_d)_{ij} = A_0 (y_d)_{ij}, \quad (a_e)_{ij} = A_0 (y_e)_{ij} \quad (2.69)$$

- the Higgs mass parameters are real,

$$m_{H_u}^2 = m_{H_d}^2 = m_0^2 \quad (2.70)$$

$$b = B_0 \mu. \quad (2.71)$$

The symbols $m_{1/2}$, m_0 and A_0 denote parameters of the model which are defined by the above relations. Even though the sfermions and gauginos are degenerate in mass at the GUT scale, the particles that could be measured in experiment are not degenerate due to the different evolution provided by the renormalisation group equations. In Figure 2.5 the evolution of the masses is shown for an exemplary parameter point.

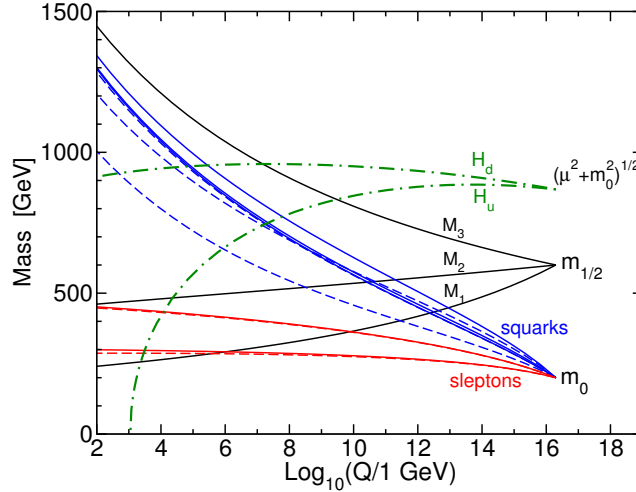


Figure 2.5.: Evolution of the squark, slepton, gaugino and Higgs mass parameters according to the MSSM renormalisation group equations as a function of the energy scale Q . At $Q_0 = 2 \cdot 10^{16}$ GeV the mSUGRA boundary conditions $m_0 = 200$ GeV, $m_{1/2} = -A_0 = 600$ GeV, $\tan \beta = 10$ and $\mu > 0$ are applied (taken from Reference [4]).

For the mSUGRA model instead of $m_{1/2}$, m_0 , A_0 , b and μ the parameters $m_{1/2}$, m_0 , A_0 , $\tan \beta$ and the sign of μ are used. The parameter $\tan \beta$ is the ratio of the vacuum expectation values of the first and the second Higgs doublets. In Section 2.2.7 the conditions for the electroweak symmetry breaking are derived and b and μ can be replaced by $\tan \beta$ and the sign of μ by using Equation 2.92 from Section 2.2.7.

2.2.5. Motivation for Supersymmetry

Supersymmetry was initially considered because it is an elegant and the only non-trivial extension of the Standard Model for a consistent 4-dimensional quantum field theory with internal and Poincaré symmetries. However, it turned out that supersymmetry is able to solve several of the problems of the Standard Model that were introduced in Section 2.1.9. In the following it is described how supersymmetry addresses some of the open questions of the Standard Model.

- **Hierarchy problem:** It was discussed in Section 2.2.3 that the quadratic divergencies to the Higgs boson mass due to fermion loop contributions are cancelled by contributions of the corresponding bosonic superpartners. To provide a solution to the hierarchy problem supersymmetry can only be broken by soft supersymmetry breaking terms.
- **Dark matter:** If R -parity is conserved the lightest supersymmetric particle is stable. If the LSP is electrically and colour neutral, it is a candidate for dark matter. It can be shown that the relic density of the LSP is close to the measured relic density for a significant part of the MSSM parameter space [32].
- **Coupling unification:** The evolution of the gauge couplings as a function of the considered energy scale is governed by the MSSM renormalisation group equations. For the Standard Model the evolution of the inverse gauge couplings is shown in Figure 2.3. The renormalisation group equations for the gauge couplings $g = \sqrt{5/3}g'$, $g_2 = g$ and $g_3 = g_S$ are

$$\frac{d}{dt}g_a = \frac{1}{16\pi^2}b_ag_a^3, \quad \text{where } t = \ln(Q/Q_0) \quad (2.72)$$

and Q and Q_0 are the considered scale and the reference scale, respectively. The parameters b_1 , b_2 and b_3 [4] are given by

$$(b_1, b_2, b_3) = \begin{cases} (41/10, -19/6, -7) & \text{for the Standard Model} \\ (33/5, 1, -3) & \text{for the MSSM} \end{cases}. \quad (2.73)$$

The evolution of the inverse gauge couplings is shown for the MSSM in Figure 2.6. Within the uncertainties of the gauge coupling evolution due to unknown sparticle masses and the uncertainty of the strong coupling constant $\alpha_S(m_Z)$ the values of the coupling constants are unified at $Q \approx 10^{16}$ GeV.

2.2.6. Two-Higgs-Doublet Models

The MSSM is an example of a model where a second Higgs doublet is introduced, but two Higgs doublets also exist in a wide variety of other models. In fact, the addition of a second Higgs doublet is one of the simplest possible extensions of the Standard Model. The details of the Higgs sector and the reasons for the introduction of a second Higgs doublet in the MSSM are discussed in details in Section 2.2.7. In this section a brief review of two-Higgs-doublet models is given based on Reference [33]. In general two-Higgs-doublet models can lead to additional sources of CP violation compared to the Standard Model. These stronger CP violation effects could help to explain the baryon-antibaryon symmetry obtained in the baryogenesis [34].

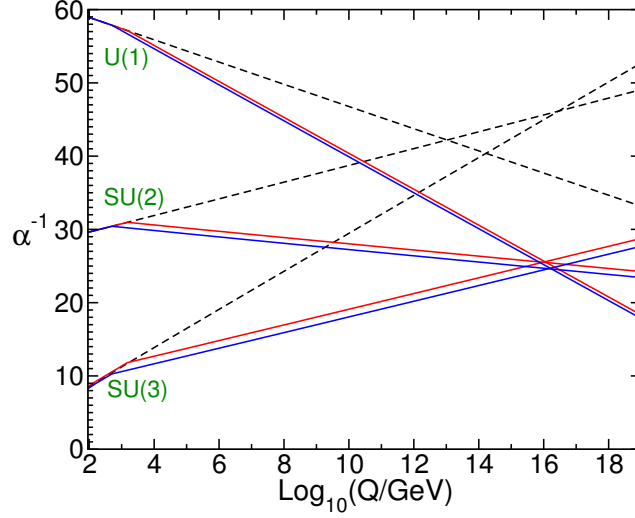


Figure 2.6.: Evolution of the inverse gauge couplings α^{-1} according to the renormalisation group equations as a function of the energy scale Q for the MSSM (solid lines) and the Standard Model (dashed lines). The inverse gauge couplings α_i^{-1} corresponding to the Standard Model gauge groups U(1), SU(2) and SU(3) are shown (taken from Reference [4]).

A general two-Higgs-doublet model has 14 parameters. Usually the number of parameters is reduced and scalar potential is written as

$$\begin{aligned}
 V(\phi_1, \phi_2) = & \lambda_1 \left(\phi_1^\dagger \phi_1 - \frac{v_1^2}{2} \right)^2 + \lambda_2 \left(\phi_2^\dagger \phi_2 - \frac{v_2^2}{2} \right)^2 + \lambda_3 \left[\left(\phi_1^\dagger \phi_1 - \frac{v_1^2}{2} \right) + \left(\phi_2^\dagger \phi_2 - \frac{v_2^2}{2} \right) \right]^2 \\
 & + \lambda_4 \left[\left(\phi_1^\dagger \phi_1 \right) \left(\phi_2^\dagger \phi_2 \right) - \left(\phi_1^\dagger \phi_2 \right) \left(\phi_2^\dagger \phi_1 \right) \right] \\
 & + \lambda_5 \left[\text{Re} \left(\phi_1^\dagger \phi_2 \right) - \frac{v_1 v_2}{2} \right]^2 + \lambda_6 \left[\text{Im} \left(\phi_1^\dagger \phi_2 \right) \right]^2, \quad (2.74)
 \end{aligned}$$

where it is assumed that the theory is gauge invariant, that the Higgs sector is conserving CP and that a symmetry $\phi_1 \rightarrow -\phi_1$ exists which is only softly violated by dimension-two terms [33]. This symmetry ensures that flavor-changing neutral currents are small.

The scalar potential is given for two $y = +1/2$ Higgs doublets ϕ_1, ϕ_2 . For one $y = -1/2$ Higgs doublet H_1 and one $y = +1/2$ Higgs doublet H_2 the replacements $\phi_1 = i\sigma_2 H_1^*$ and $\phi_2 = H_2$ have to be performed. The parameters of the potential have to be chosen such that the potential is bounded from below for every value of the Higgs doublets. In order to spontaneously break the $SU(2) \times U(1)$ symmetry to the $U(1)_{\text{EM}}$ symmetry additional constraints have to be fulfilled. These constraints are explicitly given for the MSSM in Section 2.2.7. If the electroweak symmetry is broken in the minimum of the Higgs potential the vacuum expectation values $\langle \phi_1 \rangle$ and $\langle \phi_2 \rangle$ have the form

$$\langle \phi_1 \rangle = \begin{pmatrix} 0 \\ v_1/\sqrt{2} \end{pmatrix}, \quad \langle \phi_2 \rangle = \begin{pmatrix} 0 \\ v_2/\sqrt{2} \end{pmatrix}, \quad (2.75)$$

with $v_1, v_2 \in \mathbb{R}^+$ and $v^2 = v_1^2 + v_2^2 \approx (246 \text{ GeV})^2$ to be consistent with experimental obser-

vations. The Higgs doublets can be reparameterised as

$$\phi_a = \begin{pmatrix} \phi_a^+ \\ (v_a + \rho_a + i\eta_a)/\sqrt{2} \end{pmatrix}, \quad a = 1, 2 \quad (2.76)$$

with real fields ρ_a and η_a .

The ratio of v_1 and v_2 is $\tan \beta$, so that $v_1 = v \cos \beta$ and $v_2 = v \sin \beta$. Altogether, the two Higgs doublets correspond to eight degrees of freedom, which are distributed to three Nambu-Goldstone bosons and five observable Higgs bosons, of which two are electrically charged, H^\pm , two are electrically neutral and CP-even, h , H , and one is electrically neutral and CP-odd, A . By convention the lighter of the two neutral and CP-even Higgs bosons is denoted by h . At tree level, the masses of the fields ϕ_a , corresponding to the charged Nambu-Goldstone bosons and the charged Higgs bosons, are 0 and

$$m_{H^\pm}^2 = \frac{\lambda_4}{2} v^2. \quad (2.77)$$

The tree-level masses for the CP-even neutral bosons η_a , corresponding to a neutral Nambu-Goldstone boson and the Higgs boson A , are 0 and

$$m_A^2 = \frac{\lambda_6}{2} v^2 \quad (2.78)$$

and the masses of the Higgs bosons h and H , corresponding to the scalar bosons ρ_a , are the eigenvalues of the mass matrix \mathcal{M} ,

$$m_{h,H}^2 = \text{Eigenvalues}[\mathcal{M}] \quad \text{with} \quad \mathcal{M} = \begin{pmatrix} 2v_1^2(\lambda_1 + \lambda_3) + v_2^2 \frac{\lambda_5}{2} & v_1 v_2 \left(2\lambda_3 + \frac{\lambda_5}{2}\right) \\ v_1 v_2 \left(2\lambda_3 + \frac{\lambda_5}{2}\right) & 2v_2^2(\lambda_2 + \lambda_3) + v_1^2 \frac{\lambda_5}{2} \end{pmatrix}. \quad (2.79)$$

The mixing angle α for the CP-even, neutral Higgs bosons is determined by the eigenvectors of \mathcal{M} . The mixing angle α can be calculated with

$$\tan 2\alpha = \frac{2\mathcal{M}_{12}}{\mathcal{M}_{11} - \mathcal{M}_{22}}. \quad (2.80)$$

For general two-Higgs-doublet models Yukawa interactions of down-type quarks exist with both Higgs doublets. The Yukawa interactions are

$$\mathcal{L}_{\text{Yukawa}} = -c_1 \bar{d} \phi_1 d - c_2 \bar{d} \phi_2 d \quad (2.81)$$

for down-type quarks and correspondingly for up-type quarks and leptons. The parameters c_1 and c_2 are 3×3 matrices in generation space. In general the quark mass matrix and the Yukawa interaction matrices cannot be diagonalised simultaneously and thus flavour-changing neutral currents occur. Two-Higgs-doublet models are called type III models if both Higgs fields couple to all Standard Model fermions asymmetrically, so that strong restrictions can arise from B -physics analyses of flavour-changing neutral currents. Type I two-Higgs-doublet models are invariant under the transformation $\phi_2 \rightarrow -\phi_2$, so that only the first doublet couples to quarks and leptons. Type II models are invariant under the transformation

$$\phi_2 \rightarrow -\phi_2 \quad \text{and} \quad d_R \rightarrow -d_R. \quad (2.82)$$

Thus the left-handed fermions couple to ϕ_1 only and the right-handed fermions couple to ϕ_2 only. Supersymmetric models with two Higgs doublets, such as the MSSM, and most axion

models² are examples for type II two-Higgs-doublet models. In type II models the Yukawa interaction contribution to the Lagrange density function [33, 37] is

$$\begin{aligned} \mathcal{L}_{\text{Yukawa Type II}} = & -m_d \bar{d}d - m_u \bar{u}u - m_e \bar{e}e \\ & - \frac{m_d}{v \cos \beta} \bar{d}d (H \cos \alpha - h \sin \alpha) + \frac{im_d \tan \beta}{v} \bar{d} \gamma_5 d A \\ & - \frac{m_u}{v \sin \beta} \bar{u}u (H \sin \alpha + h \cos \alpha) + \frac{im_u \cot \beta}{v} \bar{u} \gamma_5 u A \\ & - \frac{m_e}{v \cos \beta} \bar{e}e (H \cos \alpha - h \sin \alpha) + \frac{im_e \tan \beta}{v} \bar{e} \gamma_5 e A \\ & + \frac{1}{\sqrt{2}v} \left(H^+ \bar{u} [\cot \beta m_u V (1 - \gamma_5) + \tan \beta V m_d (1 + \gamma_5)] d + \text{h.c.} \right), \quad (2.83) \end{aligned}$$

where V is the CKM matrix. The tree-level ratio of the couplings of the Higgs bosons h , A , H to fermions and W and Z bosons and the couplings of the Standard Model Higgs boson to fermions and bosons given in Equation 2.40 is shown in Table 2.4. In addition to these couplings, tree-level couplings with multiple Higgs bosons exist.

Two-Higgs-doublet model type I			
	h	H	A
$u\bar{u}$	$\frac{\cos \alpha}{\sin \beta}$	$\frac{\sin \alpha}{\sin \beta}$	$i\gamma^5 \cot \beta$
$d\bar{d}$	$\frac{\cos \alpha}{\sin \beta}$	$\frac{\sin \alpha}{\sin \beta}$	$-i\gamma^5 \cot \beta$
WW/ZZ	$\sin(\beta - \alpha)$	$\cos(\beta - \alpha)$	0

Two-Higgs-doublet model type II			
	h	H	A
$u\bar{u}$	$\frac{\cos \alpha}{\sin \beta}$	$\frac{\sin \alpha}{\sin \beta}$	$i\gamma^5 \cot \beta$
$d\bar{d}$	$-\frac{\sin \alpha}{\cos \beta}$	$\frac{\cos \alpha}{\sin \beta}$	$-i\gamma^5 \tan \beta$
WW/ZZ	$\sin(\beta - \alpha)$	$\cos(\beta - \alpha)$	0

Table 2.4.: Ratios of the tree-level couplings of the neutral Higgs bosons to fermions, W and Z bosons in two-Higgs-doublet models and in the Standard Model [38]. The ratios are shown for type I models, where only the first doublet couples to fermions, and for type II models, where the first doublet couples only to up-type and the second doublet only to down-type fermions. The angle α is the mixing angle for the neutral Higgs bosons, $\tan \beta$ is the ratio of the Higgs doublet vacuum expectation values. The CP-even Higgs boson A does not couple to W or Z bosons at tree level.

²In Peccei-Quinn theories [35, 36] the QCD vacuum angle θ is a field. The quantum of this hypothetical field is called axion. The axion is the Nambu-Goldstone boson (pseudo-Nambu-Goldstone boson) that results from a spontaneously and explicitly broken symmetry and the expectation value of θ is small. Thus axions provide a solution to the strong CP problem.

A theoretically interesting parameter configuration is the so-called decoupling limit, in which the Higgs bosons H and A are much heavier than the Higgs boson h . By removing the Higgs bosons H and A it is possible to build an effective theory with a Higgs sector that – up to small corrections to the couplings – is very similar to the one of the Standard Model [39].

2.2.7. The Higgs Sector of the Minimal Supersymmetric Standard Model

In contrast to the Standard Model, two Higgs doublets are required in the MSSM. In the Yukawa interactions of the Standard Model as shown in Equation 2.40 the fields ϕ and ϕ^C with hypercharges $y = +1/2$ and $y = -1/2$ are used to give mass to the up- and down-type quarks. In the MSSM the Yukawa interactions are generated by the superpotential given in Equation 2.59. The introduction of ϕ^C into the superpotential would lead to a non-holomorphic superpotential and this in turn to a non-supersymmetric Lagrange density function. A mass for up- and down-type quarks can thus only be obtained with the introduction of two Higgs doublets H_d and H_u .

The two Higgs doublets are conventionally chosen as

$$H_d = \begin{pmatrix} \phi_1^{0*} \\ -\phi_1^- \end{pmatrix}, \quad H_u = \begin{pmatrix} \phi_2^+ \\ -\phi_2^0 \end{pmatrix} \quad (2.84)$$

and the Higgs potential consists of terms from the D-term, V_D , the F-term, V_F , and the soft SUSY breaking Lagrange density function, V_{soft} ,

$$V(H_d, H_u) = V_D(H_d, H_u) + V_F(H_d, H_u) + V_{\text{soft}}(H_d, H_u) \quad (2.85)$$

with

$$V_D(H_d, H_u) = \frac{1}{8} (g^2 + g'^2) (H_d^\dagger H_d - H_u^\dagger H_u)^2 + \frac{1}{2} g^2 |H_d^\dagger H_u|^2, \quad (2.86)$$

$$V_F(H_d, H_u) = |\mu|^2 (H_d^\dagger H_d + H_u^\dagger H_u), \quad (2.87)$$

$$V_{\text{soft}}(H_d, H_u) = m_{H_d}^2 H_d^\dagger H_d + m_{H_u}^2 H_u^\dagger H_u - b (H_d^\dagger H_u + \text{h.c.}) \quad [40]. \quad (2.88)$$

The MSSM Higgs potential [33] is equivalent to the potential for more general two-Higgs-doublet models, as specified in Equation 2.74 with

$$\begin{aligned} \tan^2 \beta &= \frac{2m_{H_u}^2 + m_Z^2 + 2|\mu|^2}{2m_{H_d}^2 + m_Z^2 + 2|\mu|^2}, \\ \lambda_1 &= \frac{m_{H_d}^2 + m_{H_u}^2 + m_Z^2 + 2|\mu|^2}{v^2}, \\ \lambda_2 &= \lambda_1, \\ \lambda_3 &= \frac{1}{8} (g^2 + g'^2) - \lambda_1, \\ \lambda_4 &= 2\lambda_1 - \frac{1}{2} g'^2, \\ \lambda_5 &= 2\lambda_1 - \frac{1}{2} (g^2 + g'^2), \\ \lambda_6 &= \lambda_5. \end{aligned} \quad (2.89)$$

The quartic interactions ensure that the potential is bounded from below, except for the so-called D-flat directions with $|H_u^0| = |H_d^0|$. Under the condition

$$2|\mu|^2 + m_{H_u}^2 + m_{H_d}^2 - 2b > 0 \quad (2.90)$$

the potential is bounded from below for arbitrary directions. The electroweak symmetry is broken if a linear combination of H_u^0 and H_d^0 has a negative squared mass near $H_u^0 = H_d^0 = 0$. For potentials that fulfil Equation 2.90 this condition is equivalent to

$$\left(|\mu|^2 + m_{H_u}^2\right) \left(|\mu|^2 + m_{H_d}^2\right) - b^2 < 0. \quad (2.91)$$

In addition

$$\lambda_5 = \frac{2b}{v_1 v_2} \quad \Leftrightarrow \quad \frac{2b}{\sin(2\beta)} = m_{H_d}^2 + m_{H_u}^2 + 2|\mu|^2 \quad (2.92)$$

has to be fulfilled to ensure electroweak symmetry breaking with a minimum at the known value $v \approx 246$ GeV.

Using Equations 2.89 and 2.92 it can be shown that μ is either on the order of the electroweak scale or a fine-tuned cancellation between $m_{H_d}^2$, $m_{H_u}^2$ and μ^2 is needed. If fine-tuning was present, the constants m_{H_d} , m_{H_u} need to be roughly on the order of the Planck scale. As m_{H_d} , m_{H_u} are parameters of the supersymmetry breaking and thus expected to be on the order of the electroweak scale, it is usually assumed that μ is on the order of the electroweak scale. The parameter μ respects supersymmetry and is therefore expected to be on the order of the Planck scale. The “ μ -problem” is the question why μ is on the order of the electroweak scale or if fine-tuning is present, why m_{H_d} , m_{H_u} are on the order of the Planck scale.

The tree-level masses of the Higgs bosons can be inferred from Equations 2.77, 2.78 and 2.79 and are

$$\begin{aligned} m_A^2 &= \frac{\lambda_5}{2} v^2 = m_{H_d}^2 + m_{H_u}^2 + 2|\mu|^2, \\ m_{H^\pm}^2 &= \frac{\lambda_4}{2} v^2 = m_A^2 + m_W^2, \\ m_{h/H} &= \frac{1}{2} \left(m_A^2 + m_Z^2 \mp \sqrt{(m_A^2 - m_Z^2)^2 + 4m_Z^2 m_A^2 \sin^2(2\beta)} \right). \end{aligned} \quad (2.93)$$

Thus at tree level it is $m_h \leq m_Z$. However, the mass of the lightest CP-even Higgs boson, h , is subject to radiative corrections, which can increase the mass m_h up to $m_h \approx 135$ GeV [4]. It is shown in Equation 2.93 that at tree level the mass spectrum of the MSSM Higgs bosons is determined by two parameters, m_A and $\tan\beta$.

2.3. Calculation of Cross Sections and Simulation of Hadron Collisions

In Sections 2.1 and 2.2 the Lagrange density functions of the Standard Model and the MSSM were discussed. With Lagrange density functions theories can be defined, however they are not directly observable. In this section the process of deriving physical observables, like the interaction rate for a given process, and the simulation of hadron collisions is described on the basis of References [12, 13].

The number of interactions for a given physics process, N_{int} , is determined by the cross section, σ , and the integrated luminosity, $\int \mathcal{L} dt$:

$$N_{\text{int}} = \sigma \int \mathcal{L} dt. \quad (2.94)$$

For a synchrotron in which proton beams are collided with negligible crossing angle, the instantaneous luminosity can be approximated by

$$\mathcal{L} = \frac{fnN_1N_2}{2\pi\Sigma_x\Sigma_y}, \quad (2.95)$$

where f is the revolution frequency in the storage ring, n the number of colliding bunches, N_1 and N_2 the number of protons per bunch for beam 1 and 2 and Σ_x and Σ_y characterise the horizontal convolved beam widths [41]. It is shown in Equation 2.95 that for a synchrotron the time-integrated luminosity depends on the machine parameters and the length of the data-taking only. The cross section for hard-scattering events, such as events with Higgs boson production, is process-specific, but independent on the machine conditions.

2.3.1. The Factorisation Theorem, Parton Distribution and Fragmentation Functions

While it is possible to calculate high-energy cross sections at e^+e^- colliders with perturbation theory, this is not possible for most processes at pp colliders, as low-energy QCD effects govern the proton structure. It is, however, possible to factorise the effects that can be described by perturbation theory from non-perturbative low-energy effects. Schematically the factorisation theorem states that observables can be approximately calculated from the convolution of a low-energy, long-range function and a high-energy, short-range function. The scale that is used to distinguish low- from high-energy effects is called factorisation scale, $\mu_F = Q^2$. A more detailed overview of the factorisation theorem and its applicability is available in Reference [42]. The factorisation scale is a property of the calculation and the physical value of an observable is not expected to depend on the factorisation scale. As the factorisation scale is not a physical parameter, it is conventionally varied and the variation of the result is used as a systematic uncertainty. At hadron colliders the factorisation theorem is employed for the parton distribution functions (PDF) and the process of hadronisation described in Section 2.3.6.

Partons, i.e. quarks and gluons, are the point-like constituents of hadrons. According to the factorisation theorem the differential cross section for an observable \mathcal{O} in a collision of hadron h_1 with hadron h_2 can be written as

$$\frac{d\sigma}{d\mathcal{O}} = \sum_{a,b} \int_0^1 dx_a \int_0^1 dx_b \sum_F \int d\Phi_F f_a^{h_1}(x_a, \mu_F) f_b^{h_2}(x_b, \mu_F) \frac{d\hat{\sigma}_{ab \rightarrow F}}{d\hat{\mathcal{O}}} D_F(\hat{\mathcal{O}} \rightarrow \mathcal{O}, \mu_F) \quad [43], \quad (2.96)$$

where in the sums a and b run over all partonic constituents of hadrons h_1 and h_2 . The inner sum includes all possible final states F in the process $ab \rightarrow F$ with phase space Φ_F . The functions $f_a^{h_1}(x_a, \mu_F)$ and $f_b^{h_2}(x_b, \mu_F)$ are the non-perturbative parton distribution functions, $\hat{\sigma}$ is the perturbative partonic cross section and $D_F(\hat{\mathcal{O}} \rightarrow \mathcal{O}, \mu_F)$ is a non-perturbative fragmentation function, which describes the transition from the quantity $\hat{\mathcal{O}}$ based on the partons from final state F to the observable \mathcal{O} . The fragmentation function includes effects from hadronisation, bremsstrahlung and other low-energy processes as described in Section 2.3.3. At leading order of α_S the parton distribution function $f_a^{h_1}(x_a, \mu_F)$ represents the probability to find a parton of type a with momentum fraction x_a in the hadron h_1 .

The parton distribution and fragmentation functions are universal and within a given factorisation scheme they can be measured in other processes. The value of the parton distribution and the fragmentation functions at a scale Q'^2 can be obtained from the value

at Q^2 with the DGLAP equations [44, 45, 46]. In Figure 2.7 the phase space of parton distribution functions that is probed by collisions at the LHC is shown together with the phase space for some of the measurements from the experiments at HERA and the fixed-target experiments that are used to determine the parton distribution functions. The parton distribution functions used for this thesis are based on these data and a variety of other data. The details of the used data are available in the references for the CTEQ [47, 48, 49], MSTW [50] and MRST [51] parton distribution functions. The parton distribution functions and their 68% confidence level uncertainties for the MSTW2008 set are illustrated in Figure 2.7 for $Q^2 = 10 \text{ GeV}^2$ and 10^4 GeV^2 .

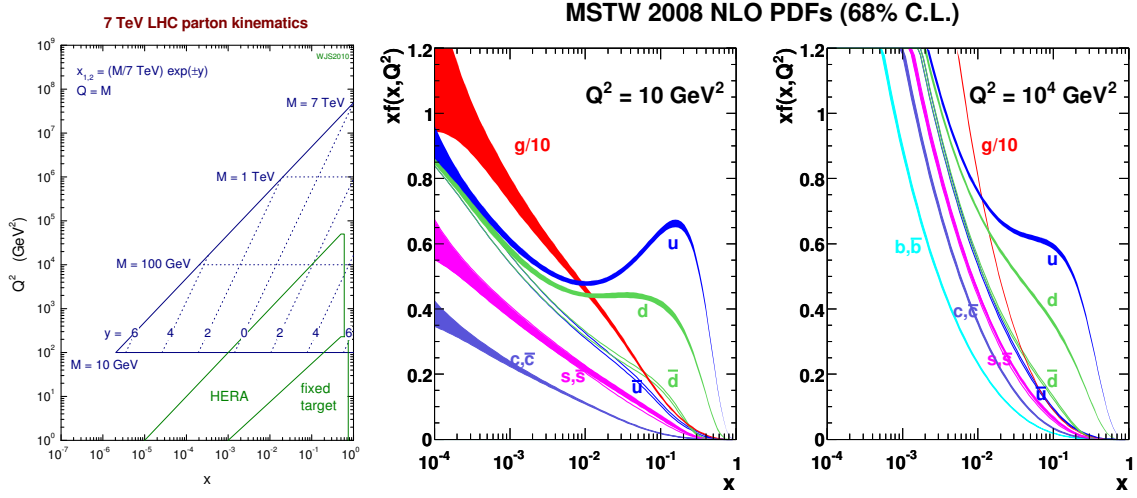


Figure 2.7.: Illustration of the parton phase space in the x - Q^2 plane that is accessible by LHC collisions with $\sqrt{s} = 7 \text{ TeV}$ (left-hand side) and MSTW 2008 parton distribution functions at $Q^2 = 10 \text{ GeV}^2$ (middle) and $Q^2 = 10^4 \text{ GeV}^2$ (right-hand side) together with their 68% confidence level uncertainty bands. The product of the proton momentum fraction of the quark or gluon, x , and the parton distribution function $f(x, Q^2)$ is shown. The parton distribution functions for gluons are scaled down by a factor of 10 (taken from References [50, 52]).

2.3.2. Partonic Cross Section

The partonic cross section for inclusive production of a final state F is the non-physical cross section for a hard interaction at energies exceeding the factorisation scale. It is

$$\frac{d\sigma_{ab \rightarrow F}}{d\hat{\mathcal{O}}} = \int d\Phi_F |\mathcal{M}_F|^2 \delta(\hat{\mathcal{O}} - \hat{\mathcal{O}}(\Phi_F)) \quad (2.97)$$

$$= \sum_{k=0}^{\infty} \int d\Phi_{F+k} \left| \sum_{l=0}^{\infty} \mathcal{M}_{F+k}^l \right|^2 \delta(\hat{\mathcal{O}} - \hat{\mathcal{O}}(\Phi_{F+k})) \quad [43], \quad (2.98)$$

where \mathcal{M}_F is the matrix element for the production of the final state F with phase space Φ_F . In Equation 2.98 the matrix element is perturbatively expanded in α_S . The sum over k runs over the additional partons in the final state (“real emissions” from QCD interactions), the sum over l over the virtual corrections (“loops” from QCD interactions) and \mathcal{M}_{F+k}^l is the matrix element for the final state F with real emissions k , loops l and phase space Φ_{F+k} . If the sums include only the terms for

- $k = 0, l = 0$, the result is the leading order of α_S approximation (LO),
- $k = n, l = 0$, the result is the leading order of α_S approximation for $F + n$ jets if all real emissions are quarks or gluons (LO),
- $k + l \leq n$, the result is the N^{n-1} LO approximation.

The processes used for the calculation of the matrix element can be illustrated by the so-called Feynman diagrams. An example Feynman diagram for the matrix element for Higgs boson production in the MSSM is shown in Figure 2.8. In practice calculations can also additionally include the Feynman diagrams with the leading logarithmic divergences (LL) of a higher order, e.g. NLO+NNLL. For the calculation of the matrix element for the final state F with k real emissions and l loops, \mathcal{M}_{F+k}^l , Feynman rules can be derived from the Lagrange density functions in Sections 2.1 and 2.2. The derivation of Feynman rules from Lagrange density functions cannot be described in this thesis; a detailed explanation can be found in References [12, 13, 53]. In this thesis the partonic process that is calculated based on perturbation theory is also referred to as “hard-scattering process” or “ x partons to y partons” scattering process for different values of x and y .

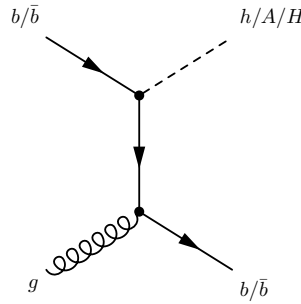


Figure 2.8.: Example of a Feynman diagram for Higgs boson production with one additional b quark. The shown Feynman diagram contributes to the matrix element with $k = 1$ and $l = 0$. The decay of the Higgs boson and non-perturbative contributions are not shown.

If observables are calculated at fixed order in α_S with perturbation theory it is possible that the result is divergent. Examples for these divergencies are the fermion- or gluon-loop corrections to the gauge boson and gluon propagator, where the divergence is introduced in the integration over the momentum vector of the fermion or gluon in the loop. Even though the calculated value of a physical observable is expected to be non-divergent for a non-perturbative calculation, a fixed order calculation can feature divergencies if these divergencies are counterbalanced by divergencies that are introduced at even higher orders that have not been considered in the calculation. As it is not possible to calculate all orders in the perturbation theory, the divergencies are removed by renormalising the theory. In the renormalisation the masses, charges and fields, e.g. the electron charge and mass, in the Lagrange density function (“bare quantities”) are replaced by observable quantities that formally include divergencies. The formally included divergencies cancel with loop-induced divergencies of the bare quantities, so that the observable quantities are finite. In the renormalisation process an unnatural scale, the renormalisation scale μ_R , is introduced. Similar to the factorisation scale, calculated quantities depend on the renormalisation scale μ_R and as the renormalisation scale is regarded as unnatural, it is conventionally varied and the variation of the result is used as a systematic uncertainty. A more detailed overview of renormalisation is available in Reference [13].

2.3.3. Simulation of Hadron Collisions

The simulation of particle collisions is an essential tool for high-energy physics. In this section a general overview of the methods used for the simulation of hadron collisions is given. The used samples of simulated events are described in Sections 6.1 and 6.2. A schematic overview of the various steps in the simulation of events is shown in Figure 2.9. Based on the parton distribution functions for the collided hadrons, partons and their corresponding four-momenta for the partonic process (hard subprocess) are selected. The partonic process can be simulated based on perturbative calculations and is described in Section 2.3.4. Non-perturbative effects from parton showers, initial and final state photon radiation and hadronisation are described in the following sections.

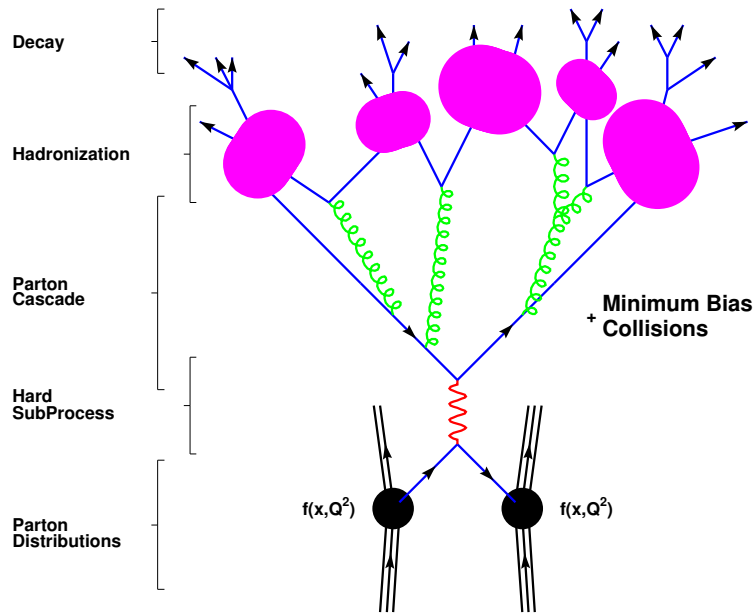


Figure 2.9.: Illustration of the perturbative and non-perturbative subprocesses for the simulation of hadron collisions. The term “minimum bias” generally refers to events that are selected with the smallest possible trigger and selection bias. In ATLAS usually more than one collision happens during a bunch crossing. In this illustration the term “minimum-bias collisions” more specifically refers to the additional collisions in a bunch crossing, the so-called pile-up collisions (taken from Reference [54]).

2.3.4. Simulation of the Partonic Process

The initial state partons for the partonic process are selected based on parton distribution functions. The different parton final states and the corresponding four-momenta are produced with probability density functions that are proportional to the differential cross sections based on fixed-order calculations. The resulting event samples are normalised to the number of events expected for the cross section of the generated process. For this thesis the partonic process event generators that are based on leading-order calculations for the final state F , leading-order calculations for the final state $F + n$ jets, and next-to-leading order calculations are used. For $F + n$ jets and NLO generators the additional partons that are generated based

on the fixed-order calculation are required to have a minimum transverse momentum p_T and minimum angular separation ΔR , so that soft and collinear divergencies are avoided. Other partons are generated by the parton shower algorithm. The event generator handles the prompt decay of non-hadronic particles with the exception of τ leptons. The radiation of photons from the initial and final state partons is simulated with PHOTOS [55]. For the initial and final state radiation of photons similar methods as for the radiation of gluons are used. The radiation of gluons as simulated with a parton shower algorithm is described in Section 2.3.5. The perturbative results used in the partonic process are valid if the strong coupling α_S is small and if the corrections from higher-order processes become successively smaller. The second condition effectively restricts the phase space to hard and well-separated jets [43].

2.3.5. Parton Shower and Matching

Parton showers are complementary to the simulation of the partonic process. It is tried to approximately simulate hadronic activity close to high- p_T partons, primarily the emission of soft and collinear gluons, which cannot be simulated with methods that are based on fixed-order perturbation series. In a perturbative calculation logarithmic divergencies from soft and collinear emissions would appear. Logarithmic divergencies are terms that – if regulated by a cut-off scale – feature a logarithm of this cut-off scale. Parton showers are based on the resummation of the leading soft and collinear logarithms, in principle include all orders of perturbation theory and avoid the divergencies.

Parton showers build on a relation of the differential cross section for a final state with n partons, $d\sigma_n$, and the differential cross section of a final state with $n + 1$ partons,

$$d\sigma_{n+1} = \sigma_n \sum_{\substack{\text{possible} \\ \text{splittings} \\ i \rightarrow jk}} \frac{\alpha_S}{2\pi} \frac{d\theta^2}{\theta^2} dz P_{i \rightarrow jk}(z, \phi) d\phi, \quad (2.99)$$

where z is the energy ratio of parton k and the parent parton i , θ the angle between the partons k and i , ϕ the azimuthal angle of parton j around the axis defined by parton i and $P_{i \rightarrow jk}(z, \phi)$ are the spin-averaged splitting functions [56]. They are defined by

$$P_{q \rightarrow qg} = C_F \frac{1+z^2}{1-z}, \quad (2.100)$$

$$P_{q \rightarrow gq} = C_F \frac{1+(1-z)^2}{z}, \quad (2.101)$$

$$P_{g \rightarrow gg} = C_A \frac{z^4 + 1 + (1-z)^4}{z(1-z)}, \quad (2.102)$$

$$P_{g \rightarrow q\bar{q}} = \frac{1}{2} (z^2 + (1-z)^2) \quad (2.103)$$

with

$$C_F = \frac{N_C^2 - 1}{2N_C}, \quad C_A = N_C \quad \text{and} \quad \frac{d\theta^2}{\theta^2} = \frac{dq^2}{q^2} = \frac{dk_T^2}{k_T^2}, \quad (2.104)$$

where N_C refers to the number of colours, q is the virtuality of the propagator and k_T is the transverse momentum of the parton k with respect to the parton i . The relation is derived with the Feynman rules for a $1 \rightarrow 2$ parton splitting. Practically, parton showers are implemented as successive parton splittings with a probability (“Sudakov form factor”)

proportional to the differential cross section as a function of k_T , θ or virtuality depending on the implementation. For virtuality-ordered parton showers the parton splitting is stopped when the virtuality of the parton is below a cut-off that corresponds to the hadronisation scale. Other parton showers, e.g. the parton showers in SHERPA and PYTHIA 8, build on the Catani-Seymour dipole factorisation, which is described in detail in Reference [57].

If parton showers are used together with generators for NLO or LO $F+n$ jets production, a phase space overlap between jets created by the parton shower and the fixed-order generator exists. This overlap can be removed with matching algorithms, e.g. the MLM algorithm [58] that is used by ALPGEN and the CKKW algorithm [59, 60] that is used by SHERPA. Parton shower-parton matching for NLO calculations is implemented in the POWHEG [61] and MC@NLO [62] generators.

The CKKW algorithm is based on the resolution of the k_T jet algorithm [63] that is described in more detail in Section 5.3. For the k_T jet algorithm two jets i and j are resolved if the distance parameter y_{ij} is greater than the resolution parameter y_{cut} , i.e.

$$y_{ij} = 2 \min \{E_i^2, E_j^2\} (1 - \cos \theta_{ij}) / Q^2 > y_{\text{cut}}, \quad (2.105)$$

where E_i is the energy of jet i , θ_{ij} the angular difference of jets i and j , y_{cut} is the predefined resolution and Q^2 the scale of the interaction [60]. Conceptually the fixed-order calculation is used for parton splittings with $y_{ij} > y_{\text{cut}}$ and the parton shower for $y_{ij} < y_{\text{cut}}$. An event for $F+n$ jets production is generated and the resolution parameters y_{cut} to obtain $2, 3, \dots, n$ jets are determined. In the clustering procedure a backward parton shower is performed and only particle combinations that can result from a parton splitting are clustered, i.e. a quark and a gluon can be clustered, but two anti-quarks cannot be clustered. For the events based on the perturbative calculation a weight based on the Sudakov form factor for the back-ward parton shower is applied and a parton shower is initiated. The weight is a function of a cut-off of the parton shower evolution variable, the merging scale, and ensures that partons are only generated with values of the evolution variable higher than the cut-off by the fixed-order generator. The parton shower emissions are only generated below the cut-off for the evolution variable.

For the MLM matching a hard-scattering event based on a fixed-order calculation is generated with partons with a minimum transverse momentum, $p_{T,\text{min}}(\text{parton})$, and a minimum angular distance in the η - ϕ plane, $\Delta R_{\text{min}}(\text{parton})$. Different event samples with $0, 1, 2, \dots, n-1$ and $\geq n$ final state partons are generated. The sample with $\geq n$ partons is called inclusive sample, all other samples are called exclusive samples. For these parton-scattering events a parton shower is initiated and a jet-clustering algorithm (k_T algorithm) with a distance parameter ΔR_{clus} is run to obtain jets with $p_T > p_{T,\text{clus}}$. These jets are matched to the partons from the fixed-order generator within $\Delta R < 1.5 \Delta R_{\text{clus}}$ and events, where two partons are matched to the same jet or where one parton is not matched to a jet are rejected. For the exclusive event sample also events where a jet is not matched to a parton are rejected.

2.3.6. Hadronisation

Due to the confinement property of QCD, no free colour-charged particles exist at low energies. Hadronisation is the transition of a parton event with colour-charged quarks and gluons into an event with colour-neutral hadrons. The hadronisation is governed by non-perturbative effects and phenomenological models are applied. The most commonly used models are the Lund String model [64], which is for example used in PYTHIA, and the cluster model [56], which is for example used in HERWIG. More details about the hadronisation models are available in the references, in the following only a schematic overview is given.

The Lund String model builds on the observation that the potential between a colour charge and the corresponding anti-colour charge grows linearly with distance in lattice QCD simulations [43]. Quarks and anti-quarks are the end-points of strings whose potential energy rises with their length. Gluons are kinks in these strings. Conceptually if the two quarks move apart their kinetic energy is converted into potential energy of the string until the string breaks and a new quark-anti-quark pair is produced. This procedure is repeated until the quarks have lost their kinetic energies and the particles connected with strings form mesons and baryons.

Schematically in the cluster model gluons are forced to split into quark-anti-quark pairs and colourless groups of particles, referred to as clusters, are created. These clusters decay into the final state hadrons.

The hadronisation is followed by the decay of the produced hadrons and the τ leptons if they are present in the event. The decay of τ leptons is handled by the program TAUOLA [65] for all generators with the exception of SHERPA. The use of TAUOLA is necessary if τ -lepton polarisation effects influence the result. Top quarks have a short lifetime and decay before the hadronisation.

2.3.7. Underlying Event and Multiple Parton Interactions

The underlying event is the hadronic activity from collisions between partons from the colliding hadrons that do not take part in the hard subprocess. The underlying event includes effects from the hadronisation of the beam remnant and multiple $2 \rightarrow 2$ parton interactions. For event samples generated with PYTHIA the multi-parton model implemented therein is used, for event samples generated with HERWIG the multi-parton model from JIMMY [66] is used. The underlying event models include free parameters for non-perturbative effects that are tuned with data. In this thesis the underlying event tunes AUET2B LO** [67] and PERUGIA 2011 [68] are used. The number of multi-parton interactions and their energy scale depends on the impact parameter of the proton-proton collision. Triggered events are biased towards lower impact parameter, so that the underlying event on average features higher- p_T jets than minimum-bias events (“pedestal effect”).

2.3.8. Pile-up

At the LHC protons are collided in beams with up to $1.1 \cdot 10^{11}$ protons per beam [69]. The protons in the beams are organised in bunches, small groups of protons that are within one wave length of the accelerating AC field. The details of the LHC filling scheme are described in Section 3.1. Due to the large number of protons per beam bunch and the small bunch separation in the LHC beam, more than one proton-proton collision is expected per bunch crossing. The term “in-time pile-up” refers to additional interactions from protons in the same bunches as the protons of the hard-scattering event. If the bunch separation is small enough, additional “out-of-time pile-up” events can affect an event. Out-of-time pile-up effects are due to collisions in other bunch crossings that are recorded in the hard-scattering bunch crossing. Due to the relatively long read-out time of the calorimeters out-of-time pile-up effects are especially important for energy measurements.

The effects of in-time and out-of-time pile-up interactions are taken into account in the simulation together with effects from beam halo, beam gas and cavern background. For in-time pile-up additional collisions (“minimum-bias events”) are generated with PYTHIA and added to the hard-scattering event. As the number of pile-up interaction changes with the operating conditions of the accelerator, events corresponding to different sets of conditions are simulated. The distribution of the average number of interactions per bunch crossing is

shown in Figure 2.10 for simulation and in Figure 3.8 for data. For the analysis simulated events are reweighted to match the distributions of the number of interactions per bunch crossing in data.

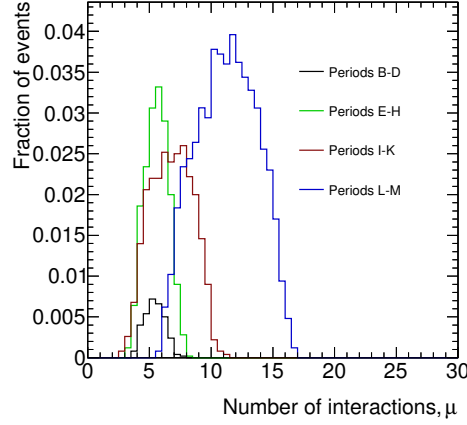


Figure 2.10.: Distribution of the average number of interactions per bunch crossing for four different sets of accelerator conditions (periods B-D, E-H, I-K and L-M) used in the production of simulated event samples. For the analysis simulated events are reweighted to match the distributions of the number of interactions per bunch crossing in data.

2.3.9. Detector Simulation and Event Reweighting

After the steps described above all generated events are passed through the simulation of the ATLAS detector. The “full simulation” of the ATLAS detector is based on GEANT4 [70] and can take up to several minutes per event. In addition a “fast simulation” based on a parameterised detector response is available, but not used in this thesis. The production of simulated event samples is performed on the World-wide LHC Computing Grid (WLCG) [71].

The simulation of the detector includes the simulation of the trigger and the conditions of the detector. In particular for a fraction of the data a crate controller in the LAr calorimeter failed (see Section 3.2). As a consequence it is not possible to get energy information for jets that point into the direction of this non-functioning region of the LAr calorimeter. In order to obtain an unbiased jet and τ_{had} reconstruction the failed crate controller is turned off in the simulation for the events from the relevant data-taking period. A summary of the detector and pile-up conditions for simulated event samples is available in Table 2.5. As the fraction of events corresponding to the different data-taking periods is different in data and simulation, the simulated events are reweighted. An additional reweighting is performed based on the distribution of the average number of interactions per bunch crossing in data and simulation.

2.4. Phenomenology of the Production and the Decay of Higgs Bosons

In this section the production and the decay of Higgs bosons is described for the Standard Model and the MSSM. The relevant Feynman diagrams, the cross sections and the decay branching ratios for Higgs boson production in pp collisions with $\sqrt{s} = 7$ TeV are presented.

Period	MC run	Average μ	LAr controller failed	Fraction of MC events	Fraction of data events
B-D	180164	5.4	no	3.2%	3.7%
E-H	183003	5.6	yes	17.4%	21.1%
I-K	186169	6.8	no	25.8%	23.9%
L-M	189751	11.3	no	53.5%	51.3%

Table 2.5.: Summary of the detector and accelerator conditions used for the simulated data samples corresponding to data-taking periods B-D, E-H, I-K and L-M. Events are simulated with pile-up distributions and with or without information from the partially failed LAr crate controller. The corresponding Monte Carlo run number, the average number of interactions per bunch-crossing μ , the relative fraction of Monte Carlo events corresponding to these data-taking periods and the fraction of events in data are shown. It is also indicated, whether all LAr controllers are functional.

2.4.1. Production and Decay of Higgs Bosons in the Standard Model

In the Standard Model the production and the decay of Higgs bosons is determined by the Yukawa and the Higgs–gauge boson interactions. The coupling to fermions is proportional to m_f/v and the coupling to gauge bosons is proportional to m_V^2/v , where m_f and m_V are the fermion and gauge boson masses, respectively. The relevant Feynman diagrams for the production of Standard Model Higgs bosons are shown in Figure 2.11. The production cross sections for the different production mechanisms and the decay branching ratios of the Higgs boson are shown in Figure 2.12 as a function of the Higgs boson mass. As the analysis documented in this thesis is based on proton–proton collisions at a centre-of-mass energy $\sqrt{s} = 7$ TeV, the production cross sections are shown for this centre-of-mass energy.

The production in the gluon-fusion process dominates over the other processes. However, the vector-boson fusion process (VBF), the vector-boson-associated (VH) and the $t\bar{t}$ -associated production ($t\bar{t}H$) provide more complex final states and searches in more complex final states can be beneficial. For low masses the Higgs boson preferentially decays to fermions, $b\bar{b}$, $\tau\tau$ and $c\bar{c}$, for higher masses the diboson decay channels, WW and ZZ , are dominant. The decay to two photons is experimentally relevant for lower Higgs boson masses.

In this thesis a search for MSSM Higgs bosons in the $\tau\tau$ decay channel is documented. The decay width is determined by the Yukawa interaction term and at tree level the decay width of a Standard Model Higgs boson to a fermion–anti-fermion pair is

$$\Gamma(H \rightarrow f\bar{f}) = \frac{g^2}{32\pi} N_C \left(\frac{m_f}{m_W} \right)^2 m_H \left(1 - \frac{4m_f^2}{m_H^2} \right)^{\frac{3}{2}}. \quad (2.106)$$

This value is modified by sizable higher-order corrections.

2.4.2. Higgs Boson Masses in the MSSM and the m_h^{\max} Scenario

Altogether the MSSM has 105 additional parameters and even constrained models such as mSUGRA have five parameters. To first order the phenomenology of Higgs boson production and decays in the context of the MSSM is determined by the masses of the three Higgs bosons, h, A, H , and the ratio of the vacuum expectation values of the two Higgs doublets,

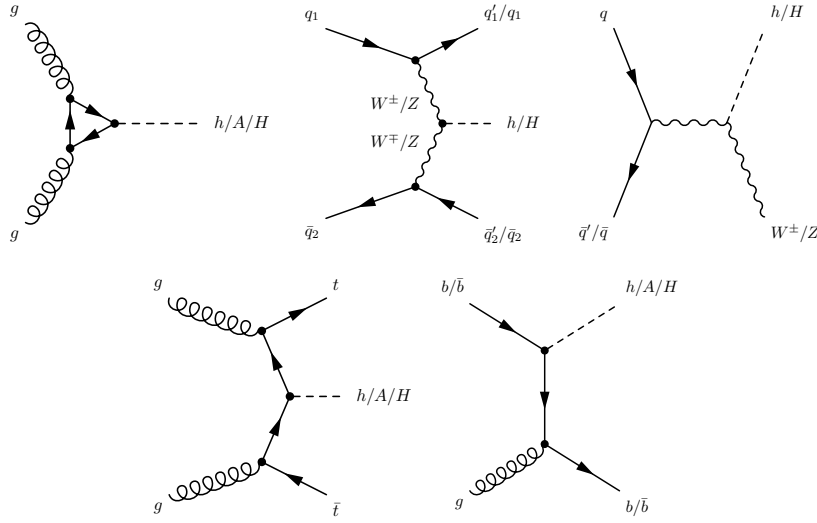


Figure 2.11.: Feynman diagrams for the production of Higgs bosons in the Standard Model and the MSSM. From left to right the production in gluon fusion, the production in vector-boson fusion, the associated production with a W^\pm or Z boson, the $t\bar{t}$ -associated production and the production in association with a b quark are shown. The CP-odd Higgs boson, A , cannot be produced in W -boson fusion or in association with a W boson. Due to the relatively small mass of the b quark the Higgs boson production in association with a b quark is only relevant in the MSSM with intermediate or high $\tan\beta$.

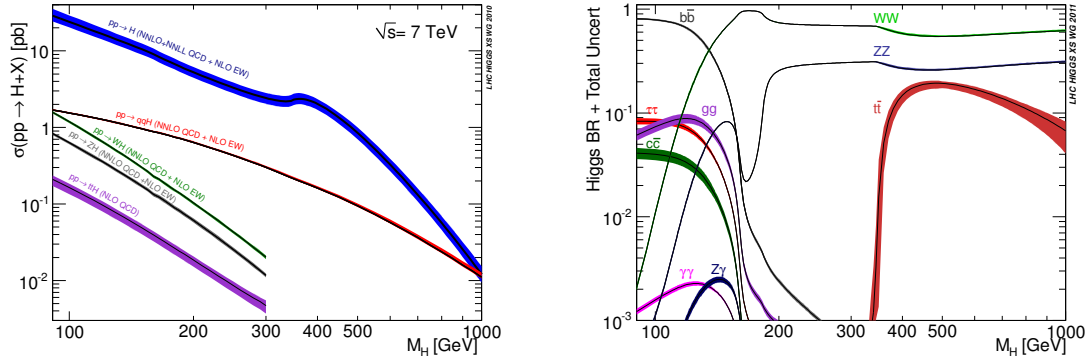


Figure 2.12.: Production cross sections (left-hand side) and decay branching ratios (right-hand side) for a Standard Model Higgs boson in pp collisions at $\sqrt{s} = 7$ TeV (taken from References [72, 73]). The theory uncertainty is shown as a coloured band. The processes $pp \rightarrow H$, $pp \rightarrow q\bar{q}H$, $pp \rightarrow W/ZH$ and $pp \rightarrow t\bar{t}H$ are dominated by Higgs production in gluon fusion, production in vector-boson fusion, associated production with a W/Z boson and $t\bar{t}$ -associated production. The Higgs boson decays to $\gamma\gamma$ and $Z\gamma$ are mediated by a fermion or W -boson loop.

$\tan \beta$, which determines the couplings to massive particles. It is shown in Equation 2.93 that the masses of the Higgs bosons h and H are determined by m_A and $\tan \beta$ at tree level. At tree level $m_h \leq m_Z$, but the Higgs boson mass m_h is subject to sizable radiative corrections, which mainly stem from the t - \tilde{t} and the b - \tilde{b} sectors.

The m_h^{\max} scenario is a benchmark model that depends on the two parameters m_A and $\tan \beta$. A scan over other parameters is performed and the values of the relevant parameters are set so that the mass of the Higgs boson h is maximised. With this choice conservative exclusion bounds from the LEP experiments in the m_A - $\tan \beta$ plane were obtained [74, 75]. As the most important corrections to m_h stem from the t - \tilde{t} and the b - \tilde{b} sectors, the parameters that are most relevant for the value of m_h and their values obtained from the scan are

- $X_t = A_t - \mu / \tan \beta = 2$ TeV with $A_b = A_t$, where A_t and A_b are the top and bottom quark trilinear couplings³,
- the Wino mass parameter, $M_2 = 200$ GeV,
- the Higgs mixing parameter⁴, $\mu = 200$ GeV and
- the gluino mass parameter, $M_3 = 0.8 \cdot M_{\text{SUSY}} = 800$ GeV.

In addition, the following Standard Model and MSSM parameters have been used as constant values in the scan:

- the SUSY breaking scale, which is assumed to be equal for the third generation squark mass parameters and set to the constant value

$$m_{\tilde{t}_L} = m_{\tilde{b}_L} = m_{\tilde{t}_R} = m_{\tilde{b}_R} = M_{\text{SUSY}} = 1 \text{ TeV}, \quad (2.107)$$

- the CP-odd Higgs boson mass m_A , which is set to the constant value of 1 TeV,
- the Bino mass parameter M_1 , which is fixed by the relation

$$M_1 = \frac{5}{3} \left(\frac{\sin \theta_W}{\cos \theta_W} \right)^2 M_2, \quad (2.108)$$

- the mass of the top quark, $m_{\text{top}} = 172.5$ GeV,
- the mass of the bottom quark, $m_b = 4.213$ GeV and
- the strong coupling constant, $\alpha_s(M_Z) = 0.119$.

The masses of the Higgs bosons h , A and H are shown for the m_h^{\max} scenario and different values of $\tan \beta$ as a function of m_A in Figure 2.13. The figure shows that for high values of $\tan \beta$ two almost mass-degenerate Higgs bosons, A and H , and one Higgs boson, h , with $m_h \approx 130$ GeV exist. For lower values of $\tan \beta$ the mass difference between the Higgs bosons A and H increases.

It should be noted that the m_h^{\max} scenario does not take any information related to the new boson that was discovered by the ATLAS and CMS collaborations in 2012 [2, 3] into account. In the light of the discovery of the new boson, new benchmark scenarios have been proposed in Reference [78]. These benchmark scenarios could not be considered in this thesis.

³The exact value of X_t depends on the performed calculation. The given value is obtained for the Feynman-diagrammatic calculation [75].

⁴The m_h^{\max} scenario was originally derived with $\mu = -200$ GeV. However, for this thesis the value $\mu = 200$ GeV is chosen as $\mu > 0$ is favored by measurements of the anomalous magnetic dipole moment of the muon [76].

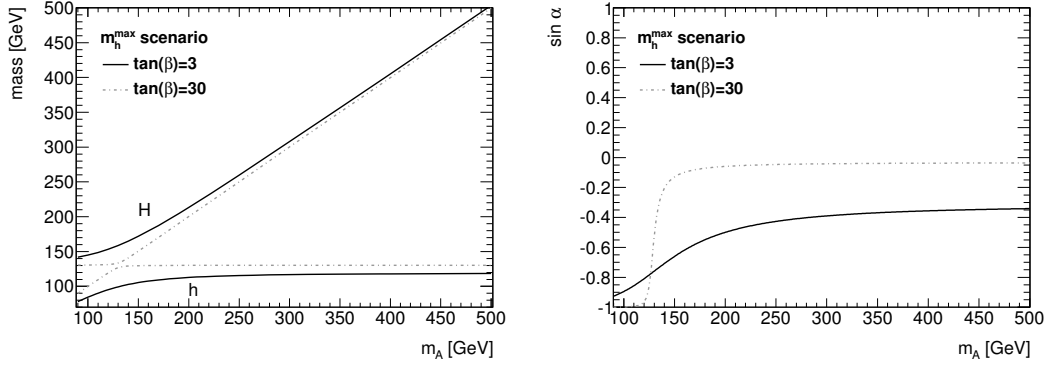


Figure 2.13.: Masses and mixing angle α of the MSSM Higgs bosons h and H as a function of the mass of the neutral CP-odd Higgs boson A for $\tan \beta = 3$ and 30. The masses have been calculated in the m_h^{\max} scenario with $\mu > 0$ with FEYNHIGGS [77].

2.4.3. Production and Decay of Higgs Bosons in the MSSM

The CP-odd Higgs boson A does not couple to gauge bosons at tree level, but for the MSSM Higgs bosons h and H all the production and decay channels of the Standard Model are possible. However, the tree-level couplings are modified by the factors documented in Table 2.4. In addition, couplings of the Higgs bosons that involve three Higgs bosons or two Higgs bosons and a gauge boson exist. The couplings to down-type quarks are enhanced with increasing $\tan \beta$, so that in addition to the SM production processes, the production in b -quark annihilation is relevant for medium and high values of $\tan \beta$. The dominant Feynman diagram for this process is shown in Figure 2.11. The production of MSSM Higgs bosons in gluon fusion and b -quark annihilation is most important in searches for MSSM Higgs bosons over a wide range of model parameters. The cross sections for these production channels are shown for all neutral Higgs bosons as a function of the Higgs boson mass for $\sqrt{s} = 7$ TeV proton–proton collisions and $\tan \beta = 3$ and $\tan \beta = 30$ in Figure 2.14. The production of Higgs bosons in the decay of supersymmetric particles is possible, but the cross section for this production mode heavily depends on the exact parameters of the supersymmetric model and a large variety of final states can be produced.

For the decay of MSSM Higgs bosons h and H the same modes as for the Standard Model Higgs boson exist, but the decay widths are modified. For the CP-odd Higgs boson A all decay modes except for the decays to gauge bosons exist. The decay width for the Standard Model Higgs boson into a pair of fermions is given at tree level in Equation 2.106, for the MSSM Higgs bosons the decay widths are

$$\begin{aligned}
 \Gamma(h \rightarrow f\bar{f}) &= \frac{g^2}{32\pi} N_C \left(\frac{m_f}{m_W} \right)^2 m_h \left(1 - \frac{4m_f^2}{m_h^2} \right)^{\frac{3}{2}} \begin{cases} \frac{\cos^2 \alpha}{\sin^2 \beta}, & \text{for an up-type fermion,} \\ \frac{\sin^2 \alpha}{\cos^2 \beta}, & \text{for a down-type fermion,} \end{cases} \\
 \Gamma(A \rightarrow f\bar{f}) &= \frac{g^2}{32\pi} N_C \left(\frac{m_f}{m_W} \right)^2 m_A \left(1 - \frac{4m_f^2}{m_A^2} \right)^{\frac{3}{2}} \begin{cases} \cot^2 \beta, & \text{for an up-type fermion,} \\ \tan^2 \beta, & \text{for a down-type fermion,} \end{cases} \\
 \Gamma(H \rightarrow f\bar{f}) &= \frac{g^2}{32\pi} N_C \left(\frac{m_f}{m_W} \right)^2 m_H \left(1 - \frac{4m_f^2}{m_H^2} \right)^{\frac{3}{2}} \begin{cases} \frac{\sin^2 \alpha}{\sin^2 \beta}, & \text{for an up-type fermion,} \\ \frac{\cos^2 \alpha}{\cos^2 \beta}, & \text{for a down-type fermion,} \end{cases}
 \end{aligned} \tag{2.109}$$

where N_C is a colour factor that is 3 for quarks and 1 for leptons. The branching ratios for

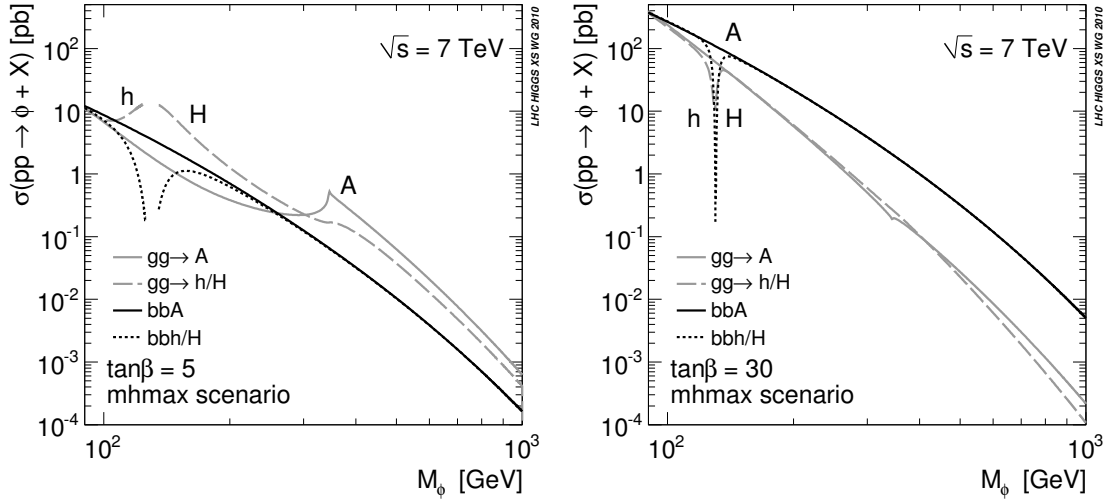


Figure 2.14.: The cross sections for the production of the MSSM Higgs bosons, $\phi = h, A, H$, in $\sqrt{s} = 7$ TeV proton–proton collisions as a function of the Higgs boson mass, m_ϕ , for $\tan\beta = 5$ (left-hand side) and $\tan\beta = 30$ (right-hand side). The cross sections have been calculated in the m_h^{\max} scenario (taken from Reference [72]).

all relevant decay channels and the three neutral MSSM Higgs bosons h , A and H are given as a function of the Higgs boson mass in Figure 2.15. Especially for high values of $\tan\beta$ the Higgs bosons almost exclusively decay to fermion pairs, $b\bar{b}$ and $\tau^+\tau^-$. For low values of $\tan\beta$ the decay into a pair of gauge bosons is relevant for the Higgs bosons h and H . Due to CP conservation the Higgs boson A does not decay into pairs of gauge bosons. For high masses of the Higgs bosons A and H the decay into $t\bar{t}$ is relevant. It can be seen that in addition to the Standard Model decay modes, for the heavier Higgs bosons A and H the decays into two Higgs bosons and a Higgs boson and a gauge boson are possible.

As shown in Figure 2.15 the decay into a pair of down-type fermions is dominant over a wide range of parameters. The decay width is proportional to m_f^2 . As the mass of the bottom quark, $m_b = 4.18$ GeV, is larger than the mass of the τ lepton, $m_\tau = 1.78$ GeV, the branching ratio into $b\bar{b}$ is larger than the branching ratio into $\tau^+\tau^-$. The $b\bar{b}$ channel, however, is subject to high background rates from di-jet production and the selection of signal events is challenging. As τ leptons decay leptonically or hadronically the background rates are dependent on the $\tau\tau$ decay channels. In general the Higgs boson decay mode into $\tau^+\tau^-$ provides a good compromise between a large decay width and a high selection efficiency with acceptable background rates.

2.5. Experimental Status

In the previous section an overview of the Higgs sector and the physical Higgs bosons in the Standard Model and two-Higgs-doublet models like the Minimal Supersymmetric Standard Model was given. Direct searches for these Higgs bosons have been performed by several experiments. In addition, constraints from indirect measurements exist. In this section searches for Higgs bosons with a focus on Higgs bosons from two-Higgs-doublet models and supersymmetry are described.

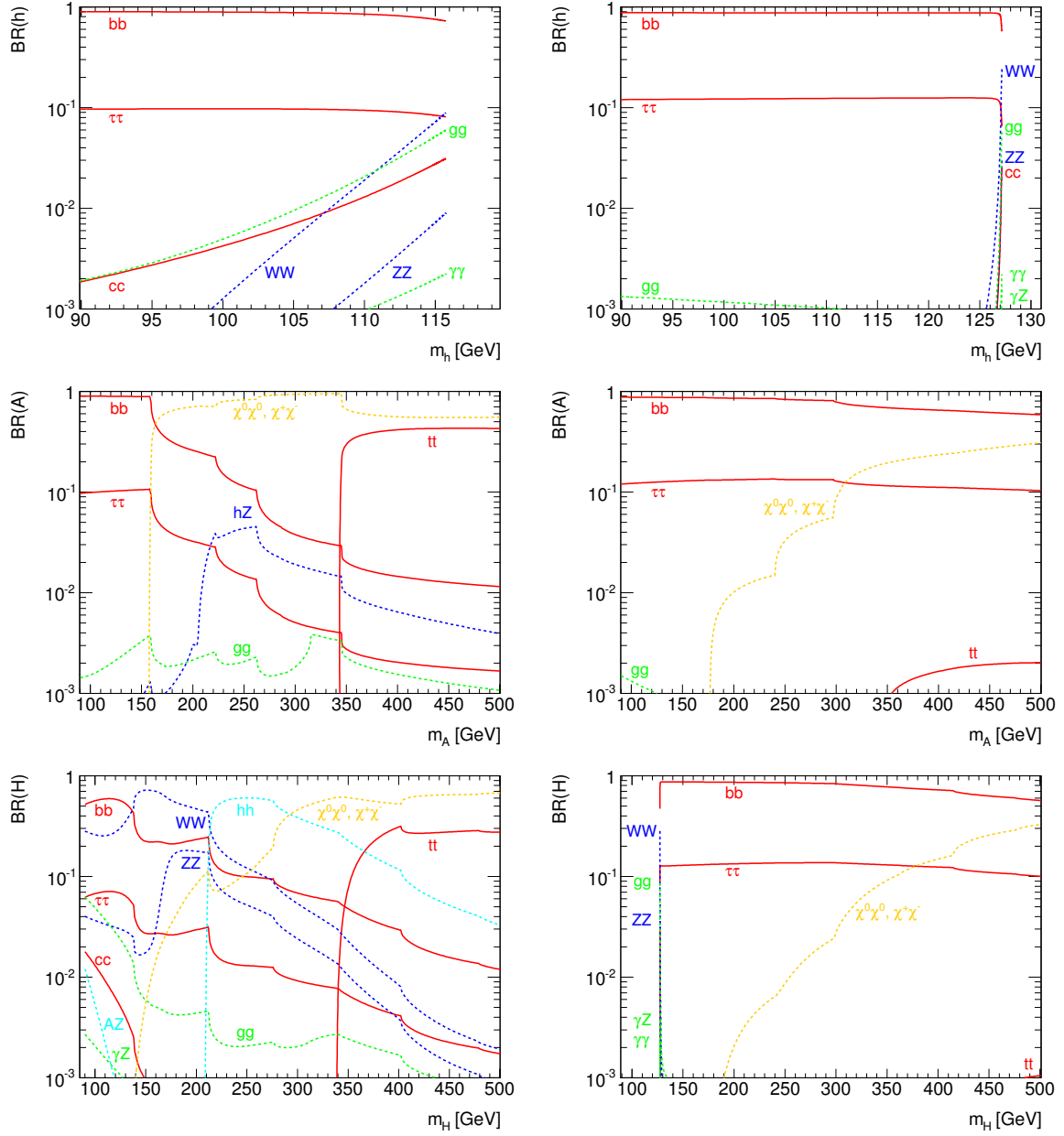


Figure 2.15.: The branching ratios for the decay of the Higgs bosons h (first row), A (second row) and H (third row) in the MSSM as a function of their masses for $\tan \beta = 3$ (left-hand column) and $\tan \beta = 30$ (right-hand column). The branching ratios have been calculated in the m_h^{\max} scenario with $\mu > 0$ with FEYNHIGGS [77] (schematically adapted from Reference [79]).

2.5.1. Observation of a Massive Particle Consistent With the Standard Model Higgs Boson

In 2012 the ATLAS and CMS collaborations presented evidence for the discovery of a new boson in the search for the Standard Model Higgs boson. The ATLAS collaboration published a measurement with a significance of 5.9σ and a measured mass of 126.0 ± 0.4 (stat.) ± 0.4 (syst.) GeV [80, 81]. The measurement of the CMS collaboration has a significance of 5.0σ and yields a mass of 125.3 ± 0.4 (stat.) ± 0.5 (syst.) GeV [82]. The measurements by the ATLAS and CMS collaborations are based on datasets corresponding to 4.8 fb^{-1} and 5.1 fb^{-1} at $\sqrt{s} = 7$ TeV and 5.8 fb^{-1} and 5.3 fb^{-1} at $\sqrt{s} = 8$ TeV for the measurements in the various decay channels, respectively. These results were later updated by measurements that use data corresponding to up to 25 fb^{-1} [83, 84, 85]. Measurements and searches have been performed for Higgs boson production in gluon fusion, vector-boson fusion and associated with the production of vector bosons. The decay channels $H \rightarrow ZZ \rightarrow 4\ell$, $H \rightarrow \gamma\gamma$, $H \rightarrow WW \rightarrow \ell\nu\ell\nu$, $H \rightarrow \tau\tau$ and $H \rightarrow b\bar{b}$ have been considered, however the highest sensitivity is obtained in the $H \rightarrow \gamma\gamma$, $H \rightarrow ZZ \rightarrow 4\ell$ and $H \rightarrow WW \rightarrow \ell\nu\ell\nu$ channels. The significance of the excess observed by the ATLAS collaboration is shown as a function of the Higgs boson mass in Figure 2.16 together with the signal strength for the VBF/VH and gluon-fusion/ $t\bar{t}H$ production processes for all considered decay channels. The ATLAS collaboration published a best estimate for the Higgs boson mass of

$$m_H = 125.5 \pm 0.2 \text{ (stat.) } {}^{+0.5}_{-0.6} \text{ (syst.) GeV [83]} \quad (2.110)$$

and the CMS collaboration of

$$m_H = 125.7 \pm 0.3 \text{ (stat.) } \pm 0.3 \text{ (syst.) GeV [85].} \quad (2.111)$$

The CDF and D0 collaborations at the Tevatron have observed an excess with a local significance of 3.3σ in the search for $VH \rightarrow Vb\bar{b}$ with $V = W, Z$ [86].

The compatibility of the discovered boson with supersymmetric models is investigated in References [87] and [88]. The observed boson is neutral and decays to W^+W^- and ZZ , so that it can be excluded that the discovered boson is the CP-odd A boson or one of the charged Higgs bosons. The assumption that the observed boson is the lightest CP-even Higgs boson, h , is compatible with the m_h^{max} scenario for $m_A > 130$ GeV and $4 < \tan\beta < 14$, depending on the value of m_A . The assumption that the observed boson is the heavier CP-even Higgs boson, H , is compatible with a smaller parameter range of the m_h^{max} scenario, namely $96 \text{ GeV} < m_A < 106 \text{ GeV}$ and $5 < \tan\beta < 11$, depending on m_A , if the signal strength for the $H \rightarrow \gamma\gamma$ decay channel is used as an additional constraint. The m_h^{max} scenario however was designed to maximise the h -boson mass. In consequence the parameters are optimised so that in parts of the parameter space $m_h > 125$ GeV is obtained and the exclusion region is larger than for general supersymmetric models. In Reference [78] new benchmark scenarios, which take the discovery of the new boson into account and optimise the model parameters accordingly, are proposed in the context of the constrained MSSM. The m_h^{mod} benchmark scenario for example is compatible with the hypothesis that the observed boson is the h boson over a wide range of the m_A - $\tan\beta$ parameter space. These new benchmark scenarios could not be considered in this thesis.

2.5.2. Searches for Neutral MSSM Higgs Bosons at LEP

Direct searches for the neutral MSSM Higgs bosons were performed by the LEP experiments ALEPH, DELPHI, L3 and OPAL. They were combined by the LEP Working Group for Higgs

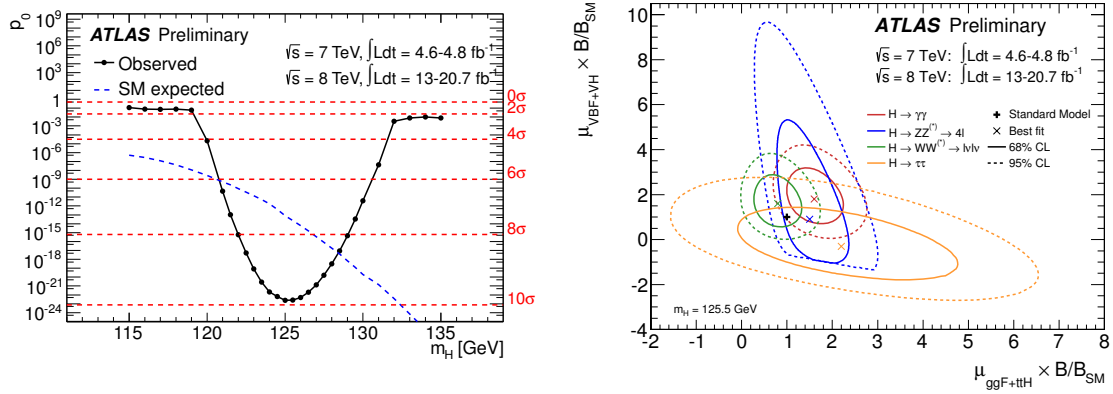


Figure 2.16.: The local probability p_0 for a background-only experiment to be more signal-like than the observation as a function of the Higgs bosons mass for the combination of all channels by the ATLAS collaboration is shown on the left-hand side. The median expected p_0 under the signal hypothesis is indicated by a dashed line and the observed p_0 by a solid line. On the right-hand side the likelihood contours are shown as a function of the signal strength for gluon-fusion/ $t\bar{t}H$ Higgs boson production and vector-boson associated/vector-boson fusion production for the considered search channels. The 68% and 95% confidence level contours are shown as full and dashed lines, respectively, together with the best fit to data (x) and the Standard Model expectation (+) (taken from Reference [84]).

Boson Searches and documented in Reference [89]. For the process $e^+e^- \rightarrow hZ_0$ searches are included for the Higgs boson decays to $b\bar{b}$ and Z boson decays to $q\bar{q}$, $\nu\bar{\nu}$, e^+e^- , $\mu^+\mu^-$ and $\tau^+\tau^-$ and for Higgs boson decays to $\tau^+\tau^-$ and Z -boson decays to $q\bar{q}$, $\nu\bar{\nu}$, $\tau^+\tau^-$ for centre-of-mass energies from 91 GeV to 209 GeV. In addition, constraints from the measured Z -boson decay width, the decay-channel independent search for $e^+e^- \rightarrow AZ$ and the search for light Higgs boson production in association with b quarks or τ leptons are considered. Limits have been derived from the combination of the search channels for various model assumptions. The limits on the parameter space of the m_h^{\max} scenario with $\mu > 0$ are shown in the m_h - $\tan\beta$ and m_A - $\tan\beta$ planes in Figure 2.17. For the derivation of the limits a top-quark mass of 174.3 GeV was assumed. The excluded region is expected to be larger for the updated value of the top-quark mass.

2.5.3. Searches for Neutral MSSM Higgs Bosons at the Tevatron

At the Tevatron $p\bar{p}$ collider, searches for neutral MSSM Higgs bosons have been performed by the CDF and the D0 collaborations using the Run II datasets with $\sqrt{s} = 1.96$ TeV. Searches for MSSM Higgs bosons produced in association with b quarks and decaying to $b\bar{b}$ were performed by the CDF and D0 experiments with data corresponding to an integrated luminosity of 2.6 fb^{-1} for CDF and 5.2 fb^{-1} for D0 [90]. Exclusion limits at the 95% confidence level are derived for the m_h^{\max} scenario with $\mu < 0$ and are shown in Figure 2.18. It should be noted that all other shown limits on the parameter space of the m_h^{\max} scenario are derived for $\mu > 0$.

Additional searches have been performed in the $\tau^+\tau^-$ decay channel by the CDF [91] and the D0 collaborations [92]. The CDF collaboration published results based on the $\tau_e\tau_\mu$, the $\tau_e\tau_{\text{had}}$ and the $\tau_\mu\tau_{\text{had}}$ decay channels and a dataset corresponding to an integrated luminosity

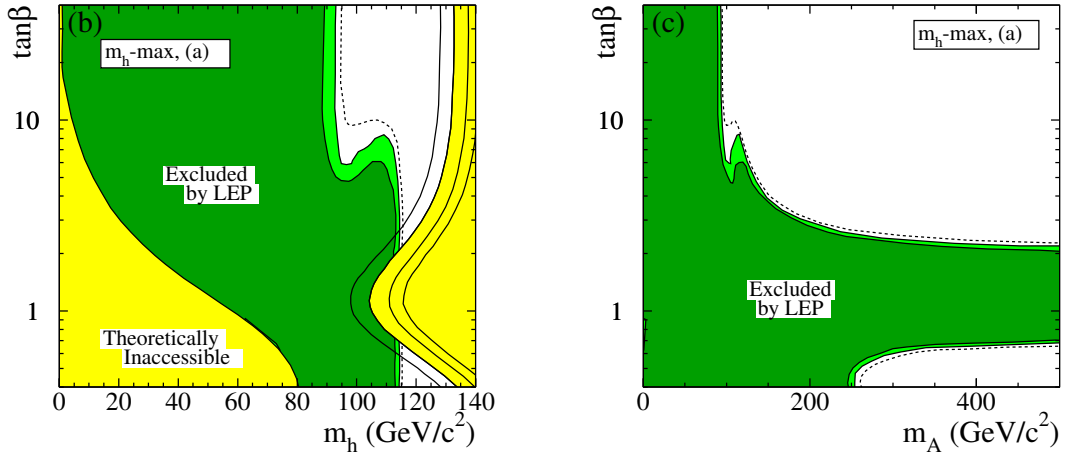


Figure 2.17.: Observed exclusion limits at the 95% confidence level (light-green) and the 99.7% confidence level (dark-green) for the m_h^{\max} benchmark scenarios as obtained by the LEP Working Group for Higgs Boson Searches. The exclusion is shown for the m_h - $\tan \beta$ (left-hand side) and the m_A - $\tan \beta$ (right-hand side) planes. The expected 95% confidence level exclusion is shown as a dashed line. In the figure on the left-hand side the upper boundary on m_h is indicated for four values of the top-quark mass $m_{\text{top}} = 169.3$ GeV, 174.3 GeV, 179.3 GeV and 183.0 GeV (taken from Reference [89]).

of 1.8 fb^{-1} . The symbols τ_e , τ_μ and τ_{had} denote a τ lepton decay into an electron, a muon and hadrons together with neutrinos, respectively. For the D0 publication searches in the $\tau_\mu \tau_{\text{had}}$ decay channel with and without associated b -jet are combined with the already mentioned search in final states with three b -jets. For the searches that require τ -lepton decays, data corresponding to an integrated luminosity of 7.3 fb^{-1} and for the search that requires three b -jets data corresponding to 5.2 fb^{-1} are used. In Figure 2.18 the 95% confidence level exclusion limits on the parameter space of the m_h^{\max} scenario with $\mu > 0$ are shown for the searches performed by the D0 collaboration. A search in the $\tau_{\text{had}} \tau_{\text{had}}$ decay channel was performed by the CDF collaboration [93]. The search is optimised for generic resonances decaying to $\tau^+ \tau^-$ and sensitivity to MSSM Higgs bosons is obtained.

2.5.4. Searches for Neutral MSSM Higgs Bosons at the LHC

In addition to the searches for Standard Model Higgs bosons, searches for neutral MSSM Higgs bosons have been performed by the ATLAS experiment in the $\tau^+ \tau^-$ channels with data corresponding to an integrated luminosity of 36 pb^{-1} [94] and 1.06 fb^{-1} [95]. The latter analysis was performed during the work for this thesis. The results are however not described in detail in this thesis as they are updated by those described in this thesis and published in References [96, 97]. In these analyses different di- τ mass reconstruction techniques are used and a detailed description of the techniques is available in Section 6.4. In the analysis using data corresponding to 36 pb^{-1} limits on MSSM Higgs bosons are derived using the effective di- τ mass distribution obtained in the $\tau_e \tau_\mu$ channel and the visible di- τ mass distribution obtained in the $\tau_e \tau_{\text{had}}$ and $\tau_\mu \tau_{\text{had}}$ channels. In the analysis using data corresponding to 1.06 fb^{-1} the effective di- τ mass is used for the $\tau_e \tau_\mu$ channel, the MMC mass for the $\tau_e \tau_{\text{had}}$

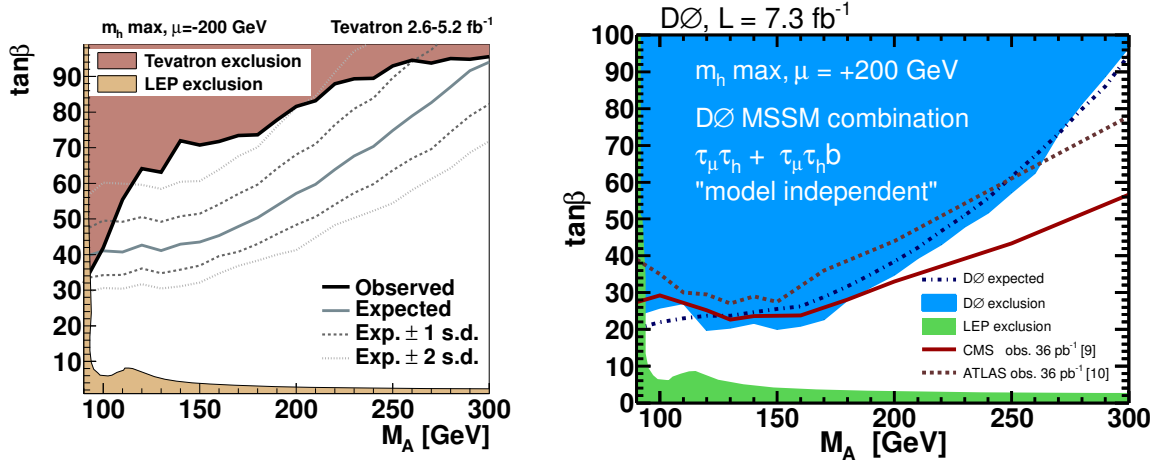


Figure 2.18.: Observed and expected exclusion limits at the 95% confidence level for the m_h^{\max} scenario as obtained from the combination of the searches for the b -quark associated $h/A/H \rightarrow b\bar{b}$ process performed by the CDF and D0 collaborations (left-hand side, taken from Reference [90]) and as obtained from the searches for $h/A/H \rightarrow \tau^+\tau^-$ with or without associated b quark by the D0 collaboration (right-hand side, taken from Reference [92]). The exclusion limit on the left-hand side was derived for the m_h^{\max} scenario with $\mu < 0$ and the one on the right-hand side for the m_h^{\max} scenario with $\mu > 0$.

and $\tau_\mu\tau_{\text{had}}$ channels and the visible mass for the $\tau_{\text{had}}\tau_{\text{had}}$ channel. For both analyses no specific selection that is targeted towards the b -quark associated production of MSSM Higgs bosons is applied. In addition, a search for the Higgs bosons from generic two-Higgs-doublet models was performed by the ATLAS collaboration in the $W^+W^- \rightarrow \ell\nu\ell\nu$ decay channel with $\ell = e, \mu$ [98]. The CMS collaboration published a search for MSSM Higgs bosons in the $\tau^+\tau^-$ decay channels [99, 100]. The exclusion limits of the searches for $h/A/H \rightarrow \tau\tau$ in the m_h^{\max} scenario are shown for the CMS analysis and the ATLAS analysis with $\int \mathcal{L} dt = 1.06 \text{ fb}^{-1}$ in Figure 2.19.

2.5.5. Searches for Charged MSSM Higgs Bosons

Direct searches for charged MSSM Higgs bosons have been performed for a wide variety of final states at the Tevatron and the LHC. For masses below approximately 150 GeV charged Higgs bosons could be produced in the decays $t \rightarrow H^+b$ and $\bar{t} \rightarrow H^- \bar{b}$. Searches for charged Higgs bosons have been performed at the Tevatron by the CDF collaboration in the $t\bar{t} \rightarrow b\bar{b}\ell\nu_\ell q\bar{q}$ channel by searching for a resonance from the $H^+ \rightarrow c\bar{s}$ decay in the di-jet mass [101] and by the D0 collaboration in the $t\bar{t} \rightarrow b\bar{b}\ell\nu_\ell \ell'\nu_{\ell'}$, the $t\bar{t} \rightarrow b\bar{b}\ell\nu_\ell q\bar{q}$ and the $t\bar{t} \rightarrow b\bar{b}\ell\nu_\ell \tau_{\text{had}}\nu_\tau$ decay channels [102] with $\ell = e, \mu$.

At the LHC, searches have been performed in samples of $t\bar{t}$ events by the ATLAS collaboration for the $H^+ \rightarrow c\bar{s}$ decay channel [103], based on the lepton universality (ratio of $t\bar{t}$ events with one light lepton and one hadronic τ -lepton decay and two light leptons) [104] and in the $H^+ \rightarrow \tau\nu$ decay channel [105]. The latter search was performed by the ATLAS and the CMS collaborations [106] in $t\bar{t}$ events that are selected in the light lepton + jets (ATLAS only), the $e+\mu$ (CMS only), the light lepton + hadronic τ -lepton decay and the hadronic τ -lepton decay + jets channels. For the m_h^{\max} scenario $\tan\beta$ values above 12-26 and between 1 and 2-6 are excluded for masses of the charged Higgs boson between 90 GeV and 150 GeV.

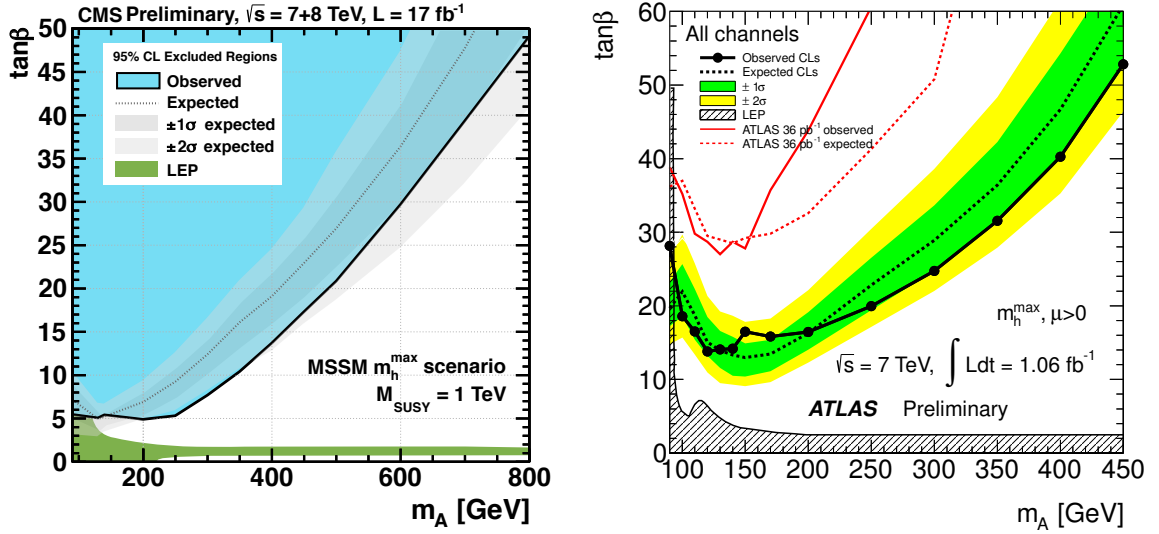


Figure 2.19.: Observed and expected exclusion limits at the 95% confidence level for the m_h^{\max} scenario with $\mu > 0$ as obtained by the searches for $h/A/H \rightarrow \tau\tau$ performed by the CMS (left-hand side, taken from Reference [100]) and ATLAS (right-hand side, taken from Reference [95]) collaborations. The CMS limit was obtained with $\sqrt{s} = 7$ TeV and $\sqrt{s} = 8$ TeV data that correspond to an integrated luminosity of 17 fb^{-1} . The ATLAS limit was obtained with $\sqrt{s} = 7$ TeV data that correspond to an integrated luminosity of 1.06 fb^{-1} .

2.5.6. Indirect Constraints on the Higgs Sector

Indirect constraints on generic or specific two-Higgs-doublet models, like the MSSM, are primarily due to quantum loops with non-Standard Model particles that influence an observable that can be measured with high precision. Examples of these high-precision variables are some of the branching ratios of B mesons that can be measured with the large datasets of the experiments BaBar [107], Belle [108] and LHCb [109] or the anomalous magnetic dipole momentum of the muon that is measured using muon storage rings. In this section B physics measurements of the decays $B_s \rightarrow \mu\mu$, $\bar{B} \rightarrow D^{(*)}\tau^-\bar{\nu}_\tau$ and $B^- \rightarrow \tau^-\bar{\nu}_\tau$ are discussed as well as the measurement of the anomalous magnetic moment of the muon. Additional constraints on the MSSM can arise from flavor-changing neutral current decays such as $B \rightarrow X_s\gamma$ [110]. Results from direct searches for supersymmetry at hadron colliders or searches for dark matter, such as XENON100 [111], are discussed in detail in References [112, 113, 114, 115] and the references therein.

The measurement of $B_s \rightarrow \mu\mu$

The leading-order Feynman diagrams for the decay $B_s \rightarrow \mu\mu$ are shown in Figure 2.20. For supersymmetric models and other models with an extended Higgs sector additional diagrams with charged or neutral Higgs bosons can exist and modify the branching ratio of $B_s \rightarrow \mu\mu$. Recently LHCb published evidence for the decay $B_s \rightarrow \mu\mu$ [116]. Thereafter measurements of the branching ratio of $B_s \rightarrow \mu\mu$ were performed by the CMS [117] and LHCb [118] collaborations. The LHCb collaboration measured the branching ratio

$$\text{BR}(B_s \rightarrow \mu\mu) = \left(2.9^{+1.1}_{-1.0} (\text{stat.})^{+0.3}_{-0.1} (\text{syst.})\right) \cdot 10^{-9}. \quad (2.112)$$

The value is consistent with the Standard Model branching ratio

$$\text{BR}(B_s \rightarrow \mu\mu)_{\text{SM}} = (3.23 \pm 0.27) \cdot 10^{-9} \quad [119]. \quad (2.113)$$

The couplings of the MSSM Higgs bosons are documented in Table 2.4. The coupling of the A boson to charged fermions, for example, is proportional to $\tan\beta$ and the branching ratio of $B_s \rightarrow \mu\mu$ is thus highly enhanced for high $\tan\beta$. The constraints on the MSSM parameter space depend on the supersymmetric model and are discussed in detail in Reference [115]. In general very high values of $\tan\beta$ are disfavored and for some parameter configurations values of $\tan\beta > 40$ can be excluded for $m_A < 1$ TeV. For lower values of m_A the excluded region in $\tan\beta$ increases.

The measurements of the decays $\bar{B} \rightarrow D^{(*)}\tau^-\bar{\nu}_\tau$ and $B^- \rightarrow \tau^-\bar{\nu}_\tau$

Measurements of the decays $\bar{B} \rightarrow D^{(*)}\tau^-\bar{\nu}_\tau$ and $B^- \rightarrow \tau^-\bar{\nu}_\tau$ are sensitive probes for models that predict charged Higgs bosons. The decay $\bar{B} \rightarrow D^{(*)}\tau^-\bar{\nu}_\tau$ includes the decays $B^- \rightarrow D^{0(*)}\tau^-\bar{\nu}_\tau$ and $\bar{B}^0 \rightarrow D^{+(*)}\tau^-\bar{\nu}_\tau$. The most important Feynman diagram for the decay is shown in Figure 2.20. If a charged Higgs boson exists additional Feynman diagrams, where the W boson is replaced by a charged Higgs boson, are present. As the coupling of charged Higgs bosons to τ leptons is enhanced for high $\tan\beta$ in such models the branching ratio of the decay $H^\pm \rightarrow \tau^\pm\nu_\tau$ can thus be enhanced. For the measurement of $\bar{B} \rightarrow D^{(*)}\tau^-\bar{\nu}_\tau$ the branching ratio is subject to large uncertainties, but the ratio of $\text{BR}(\bar{B} \rightarrow D^{(*)}\tau^-\bar{\nu}_\tau)$ and $\text{BR}(\bar{B} \rightarrow D^{(*)}\ell^-\bar{\nu}_\tau)$ with $\ell = e, \mu$, is predicted accurately for the Standard Model and models of new physics. This ratio, denoted by \mathcal{R} , has recently been measured by the BaBar experiment [120] as

$$\begin{aligned} \mathcal{R}(D) &= 0.440 \pm 0.058 \text{ (stat.)} \pm 0.042 \text{ (syst.)} \\ \mathcal{R}(D^*) &= 0.332 \pm 0.024 \text{ (stat.)} \pm 0.018 \text{ (syst.)} . \end{aligned} \quad (2.114)$$

The values

$$\begin{aligned} \mathcal{R}(D)_{\text{SM}} &= 0.296 \pm 0.016 \\ \mathcal{R}(D^*)_{\text{SM}} &= 0.252 \pm 0.003 \end{aligned} \quad (2.115)$$

are expected for the Standard Model [121]. The measurement corresponds to an excess with a significance of 2.0σ and 2.7σ , respectively.

The branching ratio $\text{BR}(B^- \rightarrow \tau^-\bar{\nu}_\tau)$ was measured by the Belle experiment with a semileptonic-tag [122] and a hadronic-tag method [123] and by the BaBar experiment with a hadronic-tag method [124]. The most precise measurement is based on the hadronic-tag method and was performed by the Belle experiment. It yields

$$\text{BR}(B^- \rightarrow \tau^-\bar{\nu}_\tau) = \left(0.72^{+0.27}_{-0.25} \text{ (stat.)} \pm 0.11 \text{ (syst.)}\right) \cdot 10^{-4}. \quad (2.116)$$

For the Standard Model the branching ratio

$$\text{BR}(B^- \rightarrow \tau^-\bar{\nu}_\tau)_{\text{SM}} = \left(0.73^{+0.12}_{-0.07}\right) \cdot 10^{-4} \quad (2.117)$$

is estimated based on a global fit to the CKM matrix elements [123, 125]. The impact of these measurements on the MSSM depends on the details of the signal hypothesis and is discussed in Reference [115].

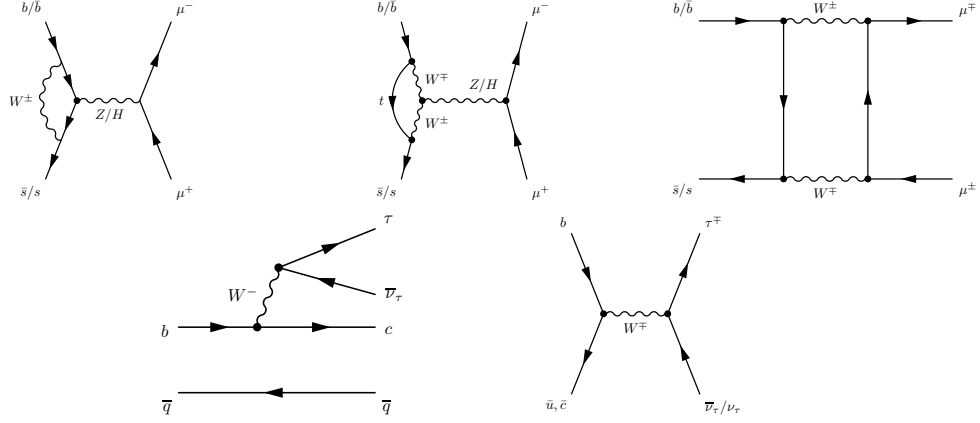


Figure 2.20.: Leading-order Feynman diagrams for the decay $B_s \rightarrow \mu\mu$ (first row), the decay $\bar{B} \rightarrow D^{(*)}\tau^-\bar{\nu}_\tau$ (second row, left-hand side) and the decay $B^- \rightarrow \tau^-\bar{\nu}_\tau$ (second row, right-hand side).

The measurement of the anomalous magnetic dipole moment of the muon

The anomalous magnetic dipole moment of the muon, $a_\mu = (g_\mu - 2)/2$, is the difference between the muon magnetic dipole moment, g_μ , and the tree-level prediction based on the Dirac equation $g_{\mu,\text{Dirac}} = 2$ due to quantum loop effects [126, 76]. The anomalous magnetic dipole moment is interesting because it can be accurately measured and new particles in quantum loops can affect its value. The anomalous magnetic moment was measured with an excellent precision in the decay of muons in a storage ring as $a_\mu^{\text{exp}} = (11,659,208.9 \pm 5.4 \pm 3.3) \cdot 10^{-10}$ [6]. For the Standard Model the value $a_\mu^{\text{SM}} = (11,659,180.2 \pm 4.9) \cdot 10^{-10}$ is expected and in consequence discrepancy with a significance of 3.6σ is observed⁵ [6].

In type II two-Higgs-doublet models the $A\bar{\mu}\mu$ coupling is enhanced by a factor of $\tan\beta$ and the contribution to a_μ can become sizable [76]. Using the requirement that the discrepancy between the measured and the calculated anomalous magnetic dipole moment should be smaller than 2σ , limits on two-Higgs-doublet models can be derived. However, due to the fact that also the expected value of a_μ for the Standard Model is discrepant from the measured value, the anomalous magnetic dipole moment measurement is used to motivate benchmark model scenarios rather than to exclude models.

⁵For the given value of a_μ^{SM} data from $e^+e^- \rightarrow \text{hadrons}$ events have been used. Alternatively data from $\tau \rightarrow \nu_\tau + \text{hadrons}$ decays can be used and a discrepancy of 1.8σ is observed.

3 The Large Hadron Collider and the ATLAS Experiment

With the Standard Model and models of new physics, such as supersymmetry¹, predictions for particle interactions at high energies can be calculated with good precision using perturbation theory. In order to probe the interactions at these energies particles have to be accelerated and collided. The highest-energy collider is the Large Hadron Collider (LHC) [1, 69], which provides proton–proton, proton–Pb and Pb–Pb collisions. The LHC is located in the laboratory of the European Organisation for Nuclear Research (CERN) in Geneva, Switzerland. It is built as a circular collider, a synchrotron, in a tunnel with a circumference of 26.7 km approximately 100 m below the ground. The LHC was initially designed to operate at an energy of 7 TeV per proton. Due to safety precautions after an electrical fault of a magnet interconnection on 19 September 2008 [127], the LHC was operated with a lower proton energy of 3.5 TeV in 2011 and 4 TeV in 2012. The LHC and the chain of pre-accelerators is described in more detail in Section 3.1.

The LHC ring is home to detectors built by seven collaborations. The ATLAS (A Toroidal LHC AparatuS) [128] and CMS (Compact Muon Solenoid) [129] collaborations use multi-purpose detectors which measure a large variety of Standard Model processes and search for new physics processes with an emphasis on the search for the Higgs boson and the measurement of its properties. While ATLAS and CMS were built for a similar physics programme, the design of the detectors is different. The ATLAS detector is described in Section 3.2. The data-taking and the running conditions of the LHC and the ATLAS detector are described in Section 3.3. With the ALICE experiment (A Large Ion Collider Experiment) [130] the physics of the quark-gluon plasma, a state where quarks and gluons are deconfined [131], is investigated. A quark-gluon plasma can be generated in Pb–Pb collisions and the ALICE detector is optimised for the high track multiplicities that are present in this environment. The LHCb (Large Hadron Collider beauty) experiment [109] was primarily built to study CP-violation in the interaction of b -hadrons and to indirectly search for new physics in rare b -hadron decays. LHCb is a forward detector and in order to resolve secondary vertices from b -hadron decays, a focus in the design of the LHCb detector was the construction of the high-precision tracking facilities. The LHCf (Large Hadron Collider forward) experiment [132] is a forward detector that is located 140 m away from ATLAS in the direction of the beam pipe. It was designed to measure the number and energy of neutral pions in the forward region. The spectrum of soft pions cannot be described with usual perturbation theory and is important to understand the nature of cosmic ray events in the atmosphere. The TOTEM (TOTal Elastic and diffractive cross section Measurement) experiment [133] measures the total elastic and diffractive cross section for proton–proton collisions. The MOEDAL (MONopole and EXotics Detector At the LHC) experiment [134] is used to perform a search for highly ionising stable massive particles like magnetic monopoles.

¹To obtain precise predictions from models of new physics usually a set of model parameters has to be assumed.

3.1. The Injector Chain and the Large Hadron Collider

With its 26.7 km circumference and a proton energy of 4 TeV the Large Hadron Collider is the largest and highest-energy man-made particle accelerator. For the highest-energy collisions two proton beams are used because accelerated proton beams and proton–proton collisions provide a good compromise between a low amount of energy loss due to synchrotron radiation compared to electron beams, a relatively clean environment compared to heavy-ion collisions and the protons for the collisions are easily attained compared to antiprotons or muons. Proton–proton collisions, however, provide a less clean environment than electron–positron collisions and a lower cross section for some of the interesting processes than proton–antiproton collisions. A schematic representation of the pre-accelerator complex and the LHC is shown in Figure 3.1.

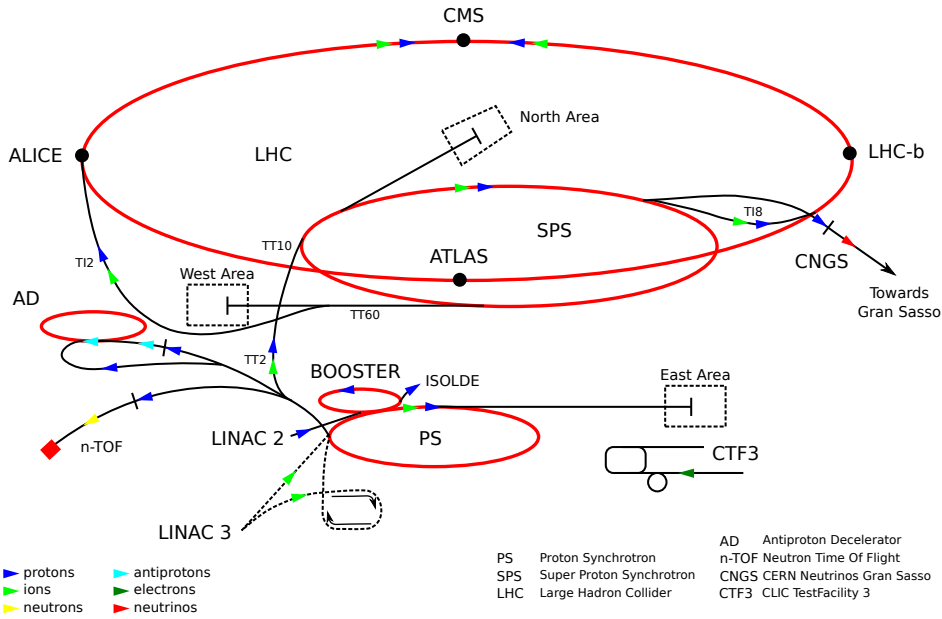


Figure 3.1.: Schematic representation of the CERN accelerator complex. Protons are created near the LINAC 2 (ejection energy 50 MeV) and transferred into the Proton Synchrotron Booster (ejection energy 1.5 GeV), the Proton Synchrotron (ejection energy 25 GeV), the Super Proton Synchrotron (ejection energy 450 GeV) and finally the Large Hadron Collider (design collision energy per beam 7 TeV). Lead ions are created near the LINAC 3 (ejection energy 4.2 MeV/nucleon) and transferred into the Low Energy Ion Ring (LEIR), where they are accumulated and cooled. From the LEIR storage ring (ejection energy 72 MeV/nucleon) lead ions are transferred into the PS (ejection energy 6 GeV/nucleon), the SPS (ejection energy 177 GeV/nucleon) and finally the LHC (collision energy 1.38 GeV per nucleon) [135] (taken from Reference [136]).

The protons are attained by ionising hydrogen gas with accelerated electrons. The protons are accelerated by 90 kV of direct voltage from a Cockcroft-Walton generator [137]. The protons are subsequently accelerated to 750 keV, focussed and bunched into packets by a radiofrequency quadrupole. After three stages of Alvarez structures [138] in the linear accelerator the protons have an energy of 50 MeV. The protons are accelerated to 1.4 GeV in four 25 m-radius rings that make up the Proton Synchrotron Booster (PSB). The number of protons in the accelerator and the structure of the packets is determined by the filling scheme.

For the harmonic-84 25 ns filling scheme² at design specifications, six bunches and one empty bucket from two batches are filled into the Proton Synchrotron (PS) with a circumference of 628 m. The used radiofrequency focusses the protons into a region in longitudinal direction, the bucket. All protons in a bucket are called a bunch. In the PS, the bunches from the PSB are split into 18 bunches and accelerated to 25 GeV. Before the bunches from three or four PS fills are extracted into the next pre-accelerator, the Super Proton Synchrotron (SPS), they are split into 72 bunches. These 72 neighboring bunches are called a bunch train. The SPS has a circumference of 6.9 km and accelerates protons to 450 GeV. The LHC ring is filled with twelve SPS fills, leading to 39 bunch trains with 2808 bunches per beam [135].

The LHC ring was built in a tunnel that was originally excavated for the Large Electron-Positron Collider (LEP). The two proton or the two Pb ion beams are contained in two different beam pipes. Due to possible interactions of the beam with particles in the beam pipe a vacuum with an H₂-equivalent gas density below 10¹⁵ m⁻³ [69] is required in order to ensure a beam lifetime of 100 hours. The beam is bent using 1232 dipole magnets with a length of 15 m per magnet. In order to provide a magnetic field with a flux density of 8 T the magnets are made from superconducting NbTi cables and are cooled to 1.9 K using superfluid helium. The beam is focussed and defocussed using superconducting quadrupole magnets with a length of 7 m. Sextupoles and a wide variety of other magnets are used for chromatic and higher-order corrections.

The proton or Pb ion beams are accelerated to 7 TeV or 1.38 GeV/nucleon, respectively, by a system of eight superconducting 400 MHz cavities per beam with an integrated field of 16 MV [1]. The beams are collided at the four interaction points inside the ATLAS, CMS, ALICE and LHCb detectors with a nominal crossing angle of 285 μ rad.

For a synchrotron in which proton beams are collided with negligible crossing angle the instantaneous luminosity can be approximated by

$$\mathcal{L} = \frac{fnN_1N_2}{2\pi\Sigma_x\Sigma_y}, \quad (3.1)$$

as outlined in Section 2.3. The revolution frequency of the beams in the storage ring is f , n is the number of colliding bunches, N_1 and N_2 are the numbers of protons per bunch for beam 1 and 2 and Σ_x and Σ_y characterise the beam widths [41]. The nominal design luminosity for collisions inside the ATLAS and CMS detectors is $\hat{\mathcal{L}} = 10^{34}$ cm⁻²s⁻¹ for two proton beams with 2808 bunches of $1.1 \cdot 10^{11}$ protons each [69].

3.2. The ATLAS Experiment

For the ATLAS experiment a general-purpose detector was built and is operated by the ATLAS collaboration. On Feb 10, 2013 the author list of the ATLAS collaboration consisted of 2911 scientists affiliated to 178 institutes from 37 countries [139]. The detector was constructed at the interaction point 1 of the LHC near Meyrin, Switzerland. The detector can record tracks from charged particles using the inner tracking detectors, energy deposits from neutral and charged particles due to strong or electromagnetic interactions with the calorimeters and hits from muons in the muon systems. One of the design goals of ATLAS was a good hermeticity and the ability to reconstruct particles that take part in the strong or electromagnetic interaction over the full range of the azimuthal angle and the maximum possible range of the pseudorapidity. Due to the presence of the beam pipe it is not possible

²The LHC filling scheme is subject to frequent changes. For other filling schemes the number of bunches and empty buckets can be different.

to reconstruct the longitudinal component of the total energy of the interaction products, however with a detector with good hermeticity the production of neutrinos and other stable particles that do not interact with the detector can be inferred using an imbalance of the transverse momentum.

The ATLAS detector [128] has a weight of approximately 7000 t, a height of 25 m and a length of 44 m. It is designed forward-backward symmetric. A schematic drawing of the ATLAS detector is shown in Figure 3.2. The following description of the ATLAS detector is based on References [140, 128].

3.2.1. The ATLAS Coordinate System

The ATLAS collaboration uses a right-handed cartesian coordinate system with its origin at the nominal interaction point in the centre of the detector. The z -axis points south-east along the beam axis, the x -axis points from the centre of the detector to the centre of the LHC ring and thus the y -axis points upwards. Alternative coordinates (r, ϕ, θ) are defined using $r = \sqrt{x^2 + y^2}$, the azimuthal angle $\phi = \arctan(y/x)$ and the polar angle $\theta = \arctan(r/z)$. Transverse momenta, p_T , correspond to the r -component of the momentum vector. The rapidity is defined as

$$y = \frac{1}{2} \ln \left(\frac{E + p_z}{E - p_z} \right). \quad (3.2)$$

Rapidity differences are invariant under Lorentz boosts in z -direction. For a particle with negligible mass the rapidity is equal to the pseudorapidity that is defined in terms of the polar angle θ as

$$\eta = -\ln \tan(\theta/2). \quad (3.3)$$

For pairs of particles originating from the detector centre a metric in η - ϕ space is defined by

$$\Delta R = \sqrt{\Delta\eta^2 + \Delta\phi^2}. \quad (3.4)$$

3.2.2. The Inner Detector

Tracks of charged particles are measured with the inner detector, which has a length of 6.2 m and a diameter of 2.1 m. It is comprised of the Pixel Detector, the Semiconductor Tracker (SCT) and the Transition Radiation Tracker (TRT). The inner detector is the closest detector to the interaction vertex and provides tracking capabilities for charged particles with $|\eta| < 2.5$. The Pixel and SCT detectors consist of semiconductor diodes in which electron-hole pairs are generated when highly-energetic charged particles traverse them. The electron or hole current can be measured at the electrodes of the diode. To reduce the noise the SCT and Pixel detectors are inside a cryostat where the temperature for the Pixel detector is kept at 0°C and for the SCT detector at -7°C using gaseous nitrogen [141]. In order to measure the transverse momenta of the charged particles the inner detector is enclosed in a solenoidal magnet which provides a 2 T magnetic field using superconducting NbTi/Cu cables. The solenoid has a diameter of 2.3 m and a length of 5.3 m. It is cooled to 4.2 K and resides in a cryostat together with the electromagnetic barrel calorimeter [142].

A schematic drawing of a quadrant of the inner the detector with the Pixel, SCT and TRT subdetectors, the solenoid and the corresponding dimensions is shown in Figure 3.3.

The Pixel detector

The Pixel detector is located very close to the beam pipe. As shown in Figure 3.3 it consists of three cylindrical layers in the barrel section and three discs in each end-cap section. The first

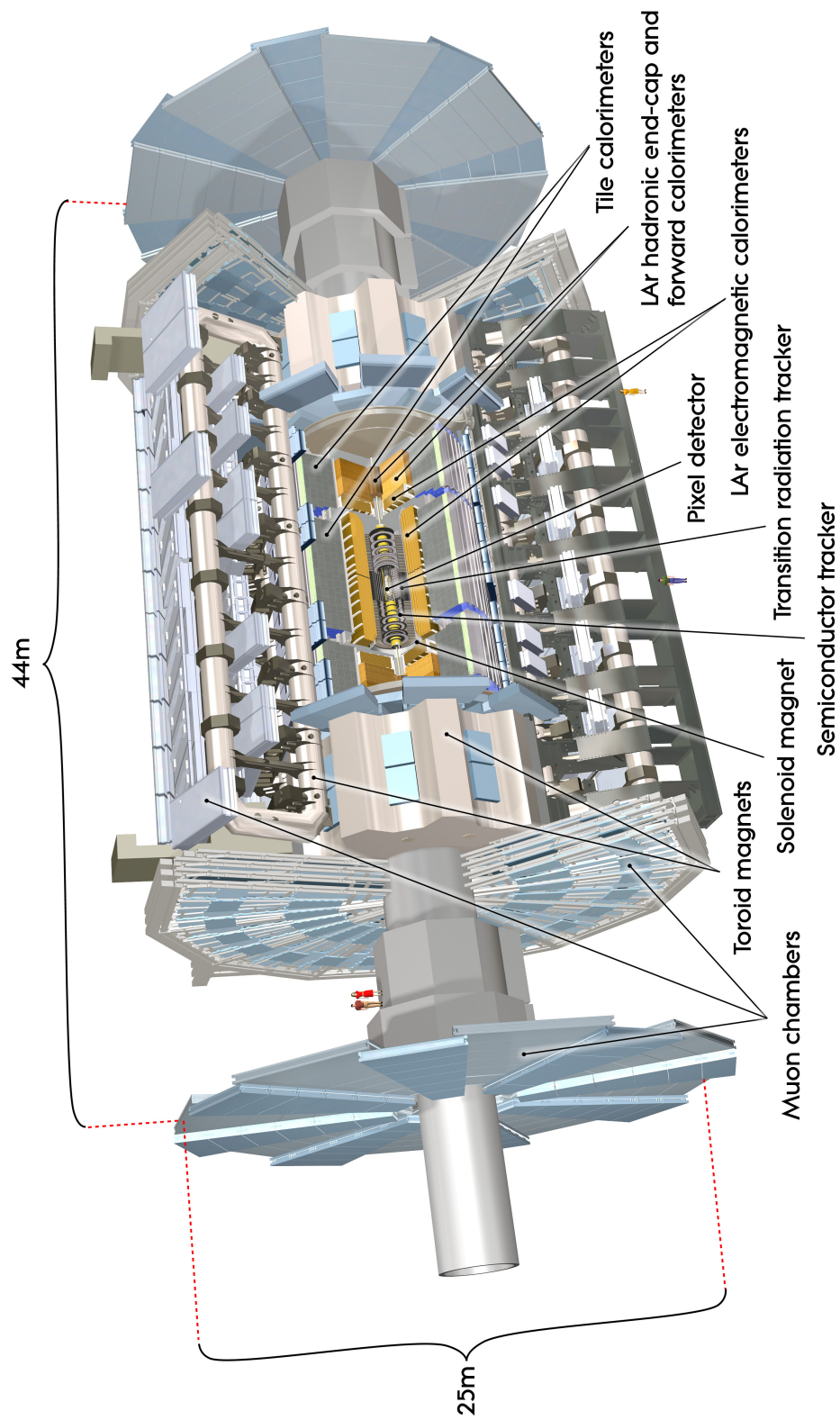


Figure 3.2.: Cut-away view of the ATLAS detector. The dimensions of the detector are 25 m in height and 44 m in length. The overall weight of the detector is approximately 7000 t (taken from Reference [128]).

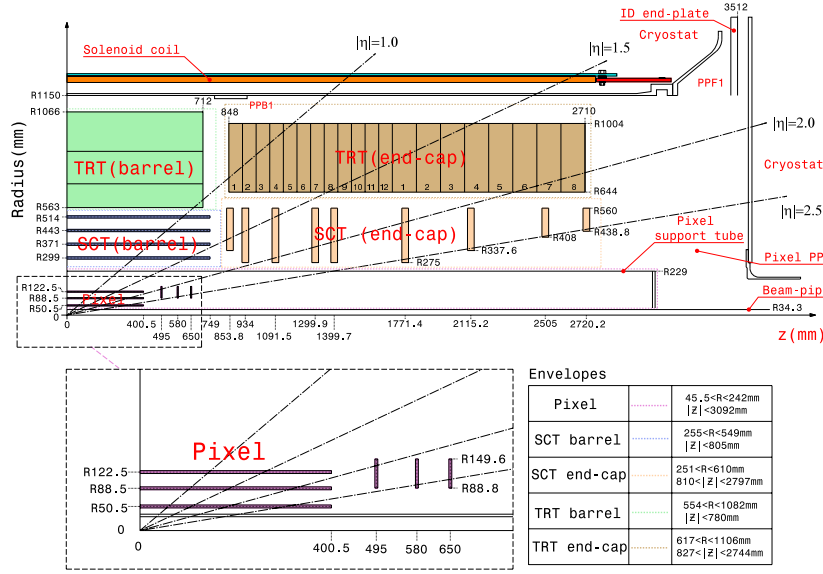


Figure 3.3.: Plan view of a quadrant of the inner detector showing each of the major detector elements. The lower part shows a zoom of the pixel region (taken from Reference [143]).

barrel layer is the B-layer and is located at $r = 5.05$ cm around the beam pipe. It provides important information for the reconstruction of the primary vertex as well as secondary vertices, that are used for instance to identify b -hadron decays. The Pixel detector is made of 80.4 million identical radiation-hard Si sensors on 1744 modules. The pixels are located on a $250 \mu\text{m}$ thick Si base and have a minimum size in $r - \phi \times z$ of $50 \times 400 \mu\text{m}^2$. They are arranged in an 18×160 matrix on a module and bump-bonded to 16 front-end electronics chips. The intrinsic precision of the hit measurement is $10 \mu\text{m}$ in $r - \phi$ -direction and $115 \mu\text{m}$ in z -direction. Due to the high cost of the pixel module production and the required space for the read-out electronics the pixel technology cannot be used in the intermediate and outer regions of the inner detector.

The Semiconductor Tracker

The SCT detector [128, 144] is a semiconductor strip detector with an active region of 63 m^2 . The barrel section is located around the pixel detector and consists of 2112 modules that are located in four cylindrical layers with a length of 153 cm at radii of 284 mm, 355 mm, 427 mm and 498 mm. The layers consist of 32, 40, 48 and 56 rows of twelve modules with a sensor length of 12.6 cm. The 1976 end-cap modules are mounted on nine disks at each side of the barrel from $|z| = 853.8 \text{ mm}$ to 2720.2 mm . The position of the layers and disks is shown in Figure 3.3. The end-cap wheels consist of an inner wheel made of 40 modules with a sensor length of 5.91 cm for wheels 2 – 6, a middle wheel with 40 modules with a sensor length of 11.6 cm for wheels 1 – 7 and a sensor length of 5.25 cm for wheel 8 (short middle modules). The outer wheel consists of 52 modules with a sensor length of 11.9 mm. A module consists of two sensors with 768 active strips each. The strips have a pitch of $80 \mu\text{m}$ and are rotated with respect to the base-board by $\pm 20 \text{ mrad}$ to provide a three-dimensional space-point for hits that are recorded on both sides. The precision for the resulting space-points is $17 \mu\text{m}$ in $r - \phi$ -direction and $580 \mu\text{m}$ in z -direction. The strips are produced from p-in-n silicon with a thickness of $285 \mu\text{m}$. The depletion region is enlarged with a bias voltage of 150 V to

increase the average charge collection per track. After irradiation the n-doped silicon bulk can effectively become p-type silicon, but with an increased bias voltage of up to 500 V the depleted region can be restored. The noise induced in the Si strips is reduced by operating the modules at temperatures between -10°C and -5°C . The signal is read out using aluminium electrodes that are capacitatively coupled to the p-type silicon bulk. Using twelve dedicated chips per module the signal is amplified, converted into an eight-bit digit and compared to a predefined threshold corresponding to approximately 6200 electron-hole pairs or 1 fC of charge to obtain a binary hit-no hit decision. The exact value of the threshold is determined in the calibration procedure using a charge injection mechanism. The calibration is described in detail in Chapter 4. The binary hit decision is stored in a pipeline for 132 bunch crossings. If a trigger signal is received on an optical link, the Tx fibre, the signal can be read out with two other optical links, the Rx fibres.

The Transition Radiation Tracker

The Transition Radiation Tracker uses straw tubes with a diameter of 4 mm to acquire tracking information for $|\eta| < 2$. The straw tubes are filled with a xenon-based gas mixture and contain a gold-plated tungsten wire as anode. Charged particles ionise the gas mixture and the resulting current can be measured. In addition, information about the particle type is obtained from transition radiation emitted in polypropylene/polyethylene fibres between the straws. The transition radiation can, for example, be used to separate electrons from pions. In the barrel the approximately 53,000 straws are 144 cm long and parallel to the beam axis, while in the end-caps the 320,000 straws are 37 cm long and radially oriented. No information of the hit position is obtained in the direction of the straw orientation other than whether the hit is in the upper or lower part of the straw. Thus the barrel of the TRT can only provide r - ϕ information. The intrinsic precision is $130\text{ }\mu\text{m}$ and on average 36 hits are expected per track.

3.2.3. The Calorimeter System

Calorimeters are used to measure the energy of electromagnetically and strongly interacting particles. In the calorimeters the incoming particles produce electromagnetic showers, a cascade of secondary photons, electrons or positrons, or hadronic showers, a cascade of hadrons and their decay products. To measure the energy of particles accurately the particles need to be stopped inside the calorimeter, so that the showers of particles are contained in the active region. This is not possible for particles such as muons or neutrinos. The measured size of the shower and the energy deposited can be related to the energy of the incoming particle.

A common calorimeter type is the sampling calorimeter, which is built using alternating layers of active sensors and absorbers. Electromagnetic calorimeters are used for precision measurements of electron and photon energies. The information from the electromagnetic calorimeter is combined with the information from the hadronic calorimeters to measure jets and hadronic τ -lepton decays. Missing transverse momentum created by undetected, stable particles can be measured using calorimeters with coverage for the full azimuthal angle and good pseudorapidity coverage.

The ATLAS calorimeters are predominantly sampling calorimeters where the energy is measured in active regions, while passive regions induce additional showering. The size of calorimeters is characterised in radiation and interaction lengths. A radiation length is the average distance over which a relativistic electron reduces its energy E to $1/e \times E$ using bremsstrahlung. An interaction length is the average distance over which the density of particles ρ is reduced to $1/e \times \rho$. For the ATLAS detector the energy determination using

calorimetry is complicated by the fact that the inner detector and the connected service infrastructure account for approximately 0.5 to 2 radiation lengths and 0.2 to 0.6 interaction lengths. The material distribution of the inner detector is shown in Figure 3.4.

For $0 < |\eta| < 1.8$ the electromagnetic and hadronic calorimeters are complemented by a presampler, a finely instrumented 11 mm thick liquid-argon layer, to reduce uncertainties due to energy lost in front of the calorimeters. The presampler is operated with a high voltage of 2000 V and has a segmentation of $\Delta\eta \times \Delta\phi = 0.025 \times 0.1$. Liquid argon is used because of its linear energy response and its radiation-hardness.

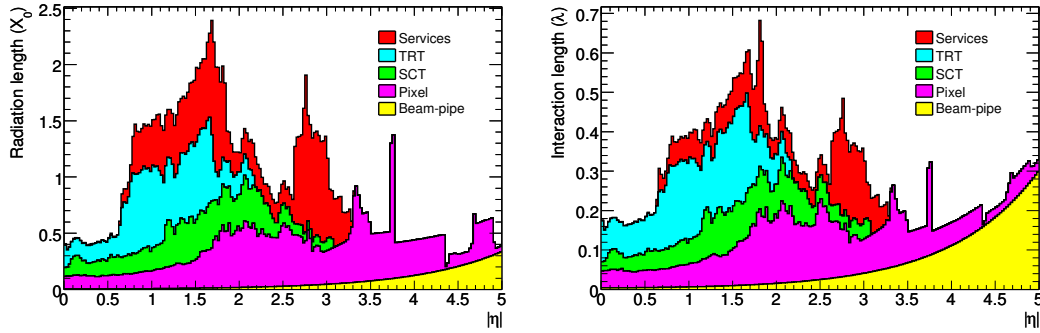


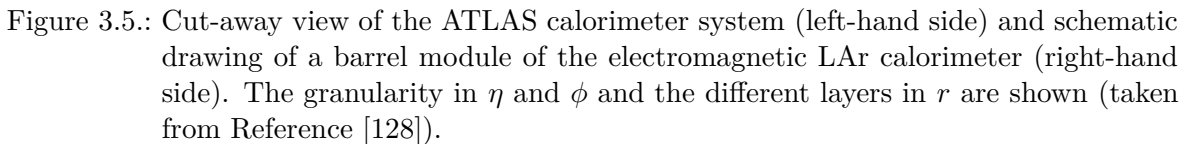
Figure 3.4.: Material distribution in radiation lengths (left-hand side) and interaction lengths (right-hand side) for the inner detector. The distribution is shown as a function of $|\eta|$ and averaged over ϕ . The contribution from the solenoid is not shown (taken from Reference [128]).

The electromagnetic calorimeter

The electromagnetic calorimeter is a lead/liquid-argon (LAr) sampling calorimeter with accordion-shaped electrodes and lead absorber plates. It is divided into a barrel part that covers the region $|\eta| < 1.475$ with a 4 mm gap at $|z| = 0$ and two end-caps that cover the region $1.375 < |\eta| < 3.2$. The barrel calorimeters extend to $|z| = 3.2$ m and from $r = 2.8$ m to $r = 4$ m. The end-cap calorimeters measure 63 cm in z -direction and extend from $r = 33$ cm to 209.8 cm.

The accordion shape, as shown in Figure 3.5, provides full coverage in the azimuthal direction and avoids cracks between segments. The 1024 absorbers in the barrel and the 2×768 absorbers in the end-caps are made of lead plates with a thickness of 1.53 mm for $|\eta| < 0.8$ and 1.13 mm for $|\eta| > 0.8$ to which stainless-steel sheets of 0.2 mm thickness are glued on each side. The gap, which is filled with liquid argon, is equipped with three conductive copper plates that are used as read-out electrodes. The outer layers are connected to 2000 V in the barrel and between 1000 V and 2500 V in the end-caps. The signal is read-out at the inner plate using capacitive coupling. The drift gaps are 2.1 mm wide and lead to a drift time of 450 ns.

As shown in Figure 3.5, modules in the barrel and the end-caps have three layers. The first layer predominantly has a high granularity of $\Delta\phi \times \Delta\eta = 0.1 \times 0.0031$ in the barrel and between $\Delta\phi \times \Delta\eta = 0.1 \times 0.0031$ and 0.1×0.1 in the end-caps. It is mainly used for γ/π^0 separation and calorimetric direction measurements. The measurement of the particle direction in the calorimeter is especially important for the four-momentum reconstruction of photons. The second layer contains the biggest part of the energy deposits and predominantly



The thickness of a barrel module is 22.3 radiation lengths in radial direction in the barrel and up to 38 radiation lengths in the end-caps. The material in front of the first calorimeter layers amounts to approximately 2 to 5 radiation lengths. For $|\eta| < 1.8$ an additional liquid-argon presampler is added to the electromagnetic calorimeter to reduce the uncertainties from the material in front of the calorimeters. The presampler consists of 11 mm (barrel) or 5 mm (end-cap) thick liquid-argon layers with two 2 mm gaps between a central read-out electrode and electrodes at 2000 V. With 7808 channels in the barrel and 1536 channels in the end-caps the presampler has a granularity of $\Delta\eta \times \Delta\phi = 0.025 \times 0.1$.

The hadronic calorimeter system consists of three types of detectors, the Tile Calorimeter, the Hadronic End-Cap Calorimeter and the Liquid-Argon Forward Calorimeter. The hadronic calorimeters have a coarser granularity than the electromagnetic calorimeters and are designed to measure the hadronic energy component of jets and the missing transverse momentum in the events.

The Tile Calorimeter is a hadronic calorimeter with an inner radius of 2.3 m, an outer radius of 4.3 m and a width of 5.8 m for the barrel section and 2.6 m for the extended barrel sections. In between the barrel and the extended barrel a gap of 60 cm has to be left for the LAr distribution pipes for the electromagnetic calorimeter and service infrastructure for the inner detector. The Tile Calorimeter covers $|\eta| < 1.7$ with approximately 4.7 interaction lengths. It is a sampling calorimeter that uses steel as passive material and scintillating polystyrene tiles in radial orientation as active material. The more than 460,000 polystyrene tiles emit ultraviolet scintillation light that is transported into photomultiplier tubes using wavelength shifting fibres with an emission peak at 476 nm. The fibres are grouped in three radial segments with 1.5, 4.1 and 1.8 interaction lengths at $\eta = 0$. The calorimeter is segmented

into 64 azimuthal wedge-shaped modules, the segmentation in η is 0.1 for the first two layers and 0.2 for the third layer.

The Hadronic End-Cap Calorimeter (HEC) is a sampling calorimeter that is made of two end-caps that cover the region $1.5 < |\eta| < 3.2$. The two end-caps extend from 47.5 cm (37.2 cm for the first nine plates) to 203 cm in radius and share a cryostat with the electromagnetic end-cap calorimeter and the forward calorimeter. Each end-cap is made of two wheels of 32 azimuthal wedge shaped modules. The modules in the first wheel are made of 25 copper plates with a thickness of 2.5 cm and in the second wheel of 17 copper plates with a thickness of 5 cm. In gaps of 8.5 mm, liquid argon is used as active material. An electric field is created by three electrodes and a voltage of 1800 V. The typical drift time for electrons is 430 ns. A total of 5632 read-out channels lead to a read-out cell size of $\Delta\eta \times \Delta\phi = 0.1 \times 0.1$ for $|\eta| < 2.5$ and 0.2×0.2 for $|\eta| > 2.5$.

The Liquid-Argon Forward Calorimeter (FCal) is located between 4.7 m and 6.1 m away from the interaction point in a cryostat with the other end-cap calorimeters. It covers the pseudorapidity range $3.1 < |\eta| < 4.9$ with a radius of 65 cm. The design of the FCal is optimised for high particle fluxes and to reduce cracks between the calorimeters. It consists of three layers, where the first layer is optimised for electromagnetic showers using copper as the passive medium, while the second and third layers use tungsten. All layers use liquid argon in small gaps to be able to withstand the high particle fluxes. The small gaps are created by drilling holes that are later filled with copper electrodes at potentials between 250 V and 500 V into the passive material. The Forward Calorimeter has 1762 read-out channels for 27.6 radiation and 2.6 interaction lengths in the first layer and approximately 90 radiation and 3.6 interaction lengths in the other layers.

3.2.4. The Muon Spectrometer

The ATLAS Muon Spectrometer was designed to efficiently reconstruct muons and trigger on muons in the outer part of the detector. It consists of different types of subdetectors, the Monitored Drift Tubes (MDT), the Cathode Strip Chambers (CSC), the Resistive Plate Chambers (RPC) and the Thin Gap Chambers (TGC) along with three superconducting air-core toroid magnets that provide a magnetic field for the regions with $|\eta| < 1.4$ and $1.6 < |\eta| < 2.7$. Each of the three toroids is made of eight coils which are in individual cryostats in the barrel toroid and in one cryostat in each of the end-caps. The toroids provide a magnetic field with a bending power, $\int B dl$, of 1.5 to 5.5 Tm in the barrel and 1 to 7.5 Tm in the end-cap. The magnetic flux density perpendicular to the muon direction is denoted by B . For $1.4 < |\eta| < 1.6$ the magnetic field is provided by both the end-cap and the barrel toroids. Schematic drawings of the ATLAS Muon Spectrometer and its components are shown in Figure 3.6.

Monitored Drift Tubes provide precision measurements for central muons with $|\eta| < 2.7$. In the barrel and end-caps 1150 chambers with 354,000 channels are installed. The chambers consist of two batches of three or four layers of drift tubes. The individual drift tubes are built from aluminium tubes with a 3 cm diameter and lengths ranging from 0.9 m to 6.2 m. They contain a tungsten-rhenium wire at a potential of 3080 V and are pressurised with a mixture of Ar and CO₂ gas (93%/7%). This leads to a gas gain of 2×10^4 and a maximum drift time from the wall to the wire of about 700 ns, thus making the Monitored Drift Tubes too slow for triggering. In the barrel they are installed in three concentric cylindrical shells around the beam axis at radii of 5 m, 7.5 m and 10 m. In the end-cap the Monitored Drift Tubes are installed in wheels perpendicular to the beam pipe located at $|z| = 7.4$ m, 10.8 m, 14 m and 21.5 m. All wires are oriented in ϕ -direction allowing for an efficient r - and η -

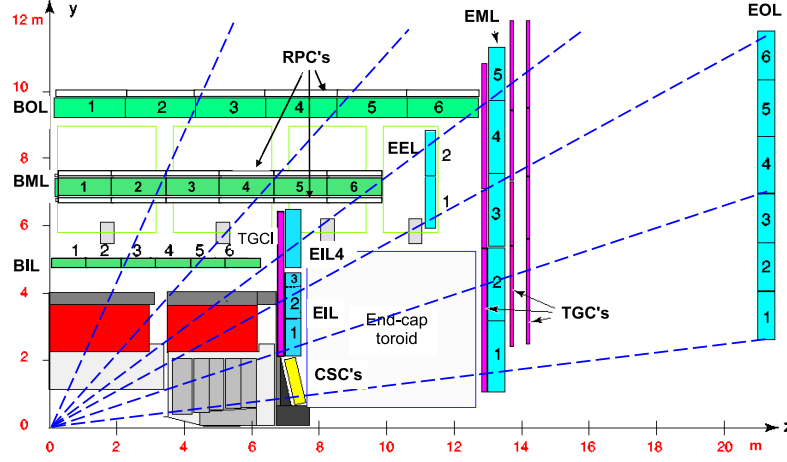


Figure 3.6.: Cross-section of the muon system in a plane containing the beam axis. Precision track measurements are provided by the Monitored Drift Tubes in the barrel (BIL, BML, BOL) and the end-cap (EIL, EEL, EML, EOL) and the Cathode Strip Chambers (CSC). Triggering capabilities are provided by the Resistive Plate Chambers (RPC) and the Thin Gap Chambers (TPC). The Tile barrel and the Tile extended barrel calorimeters are shown in red. The Liquid Argon, the Forward calorimeter and the toroids are shown in dark and light grey (taken from Reference [128]).

measurement. In order to meet the design specifications of the uncertainty on the muon momentum measurement, the uncertainty of the relative alignment of the muon chambers is reduced to less than $30 \mu\text{m}$ with the use of precision mechanical assembly techniques and an optical alignment system. The temperature and the local magnetic field are monitored for each chamber to determine the deformation of the muon detector.

Monitored Drift Tubes cannot be operated at hit rates above $150 \text{ cm}^{-2}\text{s}^{-1}$. These rates are exceeded in the first end-cap wheel at $|z| = 7.4 \text{ m}$ for $|\eta| > 2$, where consequently no Monitored Drift Tubes are installed. Instead 32 Cathode Strip Chambers with 31,000 channels are installed for $2.0 < |\eta| < 2.7$. Cathode Strip Chambers are multi-wire proportional chambers. The wires are oriented in radial direction and the two cathodes are segmented, so that one cathode is oriented parallel and one cathode perpendicular to the wires. The chambers are filled with an Ar/CO₂ gas mixture (80%/20%) that provides an average gain of 6×10^4 for a wire potential of 1900 V.

A total of 606 Resistive Plate Chambers with 373,000 channels are used for the triggering and the measurement of an additional coordinate for $|\eta| < 1.05$ and $|\eta| < 2.0$ for the innermost layer. The Resistive Plate Chambers are two gaseous parallel electrode-plate detectors with two resistive plates per detector. The plates are at a distance of 2 mm from each other and segmented, so that one plate can measure the coordinate ϕ and the other plate the coordinate η . In the electric field of 4.9 kV/mm, charged particles cause electron-ion avalanches in the gas mixture. Three cylindrical layers are mounted on the inner and outer side of the middle Muon Drift Tube layer and the outer side of the outer Muon Drift Tube layer.

In the forward region with $1.05 < |\eta| < 2.4$, a total of 3588 Thin Gap Chambers with 318,000 channels are used. Thin Gap Chambers are multi-wire proportional chambers with a gas gain of 3×10^5 for a wire potential of 2900 V. One coordinate is measured by the wire,

a second coordinate can be inferred from pickup strips that are perpendicular to the wires. Seven layers of Thin Gap Chambers are installed in two doublets and one triplet next to the inner layer of the Monitored Drift Tubes. All layers are installed in two concentric rings for $1.05 < |\eta| < 1.92$ and $1.92 < |\eta| < 2.4$.

3.2.5. The Luminosity Counters and the Forward Detectors

The integrated luminosity is determined with the the LUCID (Luminosity measurement using Cherenkov Integrating Detector) and the ALFA (Absolute Luminosity for ATLAS) detectors. In addition the Zero-Degree Calorimeter (ZDC) is located at $|z| = 140$ to determine the centrality in heavy-ion collisions [145].

The LUCID detectors are situated 17 m away from the interaction point in the direction of the beam axis at both sides of the ATLAS detector. They provide an online measurement of the instantaneous luminosity by measuring the number of inelastic p-p scatterings using an array of 20 radiation-hard Cherenkov tubes.

The ALFA detectors are situated 240 m away from the interaction point and measure the luminosity using the optical theorem that relates elastic scattering in the forward region with the full cross section. The ALFA detectors are scintillating fibre trackers that are located inside Roman Pots, special vacuum chambers that allow for closeness to the beam. As the ALFA detectors are not able to withstand the radiation conditions at the full instantaneous luminosity, they are only moved to the beam pipe for special runs with low instantaneous luminosity.

The luminosity detectors have been calibrated using van-der-Meer scans [146, 41], in which the overlap between the beams is changed in the vertical and horizontal plane.

3.2.6. The Trigger and Data Acquisition System

The trigger is implemented in a three-stage system consisting of the Level 1 (L1), the Level 2 (L2) and the Event Filter (EF) triggers. The L1 trigger is implemented in hardware using custom-made electronics. It reduces the event rate from the 40 MHz collision rate at a bunch spacing of 25 ns to 75 kHz. The L2 and the Event Filter triggers, together referred to as High Level Trigger (HLT), are predominantly implemented in software and run on a computing cluster. The performance of the L2 trigger, the EF trigger and the permanent data storage system has exceeded the initial requirements. Instead of L2 output rates of 3.5 kHz and EF output rates of 200 Hz, output rates of 5 kHz and 500 Hz have been reached, respectively [147]. The output rate is shared between different trigger chains. For trigger chains with too high output rate a prescaling can be applied. A prescale factor p that is associated with a trigger corresponds to the random acceptance of 1 out of p selected events.

The L1 trigger uses reduced hit and energy deposition information from electromagnetic and hadronic calorimeters and the muon systems to select muons, electromagnetic clusters (used as a proxy for electrons and photons), jets, hadronic τ -lepton decays, E_T^{miss} and large sum of the transverse energy in all cells. The L1 calorimeter trigger reads out 7000 projective trigger towers. Projective trigger towers are calorimeters that have a reduced granularity of $\Delta\eta \times \Delta\phi = 0.1 \times 0.1$ to allow for a fast read-out. The energy that is read-out from the L1 calorimeter trigger towers is normalised to the full expected transverse energy using a special calibration procedure. L1 electrons and photons are 2×2 trigger tower clusters in the electromagnetic calorimeter. Subsets of the towers have to exceed a threshold and the energy of the surrounding twelve trigger towers is required to be below an isolation-veto threshold. L1 hadronic τ -lepton decays are identified by using the same procedure on trigger towers from the electromagnetic and hadronic calorimeters. Jets are identified using E_T sums

within windows consisting of 4×4 , 6×6 and 8×8 trigger towers in the electromagnetic and hadronic calorimeters. For the identification of L1 muons, hits in pairs of the RPC and TPC detectors are used and a search for coincident hits within a road is performed. A road is a cone-like region that takes the track-bending in the magnetic field into account. The width of the road depends on the p_T threshold of the trigger item.

For the L2 trigger the event is reconstructed in Regions of Interest (RoI). The Regions of Interest are seeded by the L1 trigger and generally contain approximately 1% to 2% of the full event data. In these Regions of Interest detailed tracking, calorimeter and muon information is evaluated. For the EF trigger the full event is reconstructed. The event is subsequently sent to the permanent event storage and event reconstruction in the CERN Tier 0 by the Data Acquisition system (DAQ).

3.3. LHC Operation and ATLAS Data-Taking

On 10 September 2008 the first proton packet circulated the complete LHC synchrotron with the injection energy of 450 GeV [148]. However, nine days later a fault in the electrical connections between two magnets lead to a large helium leak into the tunnel that caused the destruction of several magnets [149, 150]. The LHC resumed operation with an energy of 450 GeV per proton in November 2009 and first collisions were produced [151, 152]. The data recorded with a centre-of-mass energy of $\sqrt{s} = 900$ GeV contain approximately 400,000 events corresponding to an integrated luminosity of $9 \mu\text{b}^{-1}$ [153]. A short run with a centre-of-mass energy of 2.36 TeV followed.

The beam energy was raised to 3.5 TeV in March 2010 [154] and the first $\sqrt{s} = 7$ TeV collisions were recorded at 30 March 2010 [155]. In 2010 proton–proton collision data corresponding to 48.1 pb^{-1} were delivered and 45.0 pb^{-1} were recorded [156]. After the proton–proton run the LHC was reconfigured and delivered the first heavy-ion Pb–Pb collisions [157].

The proton–proton collisions resumed in March 2011 and in the time until the end of October 2011 a total integrated luminosity of 5.61 fb^{-1} was delivered of which 5.25 fb^{-1} were recorded [158, 156]. During this time the LHC was able to set the world record beam intensity for hadron colliders [159]. The proton–proton runs were followed by heavy-ion runs in November and December 2011.

In April 2012 the first stable 4 TeV proton beams were present [160] and until December 2012 [161] a sample of proton collisions corresponding to a total integrated luminosity of 23.3 fb^{-1} were delivered and 21.7 fb^{-1} were recorded [156] for $\sqrt{s} = 8$ TeV. The first run of the LHC was concluded by proton–Pb collisions in January and February 2013.

The data used in this thesis were recorded during the 2011 LHC run with proton–proton collisions at a centre-of-mass energy of 7 TeV. The data-taking periods B2 to M from 22 March 2011 to 30 October 2011 with the runs 178044 to 191933 are used. A run is a period of data-taking during which no major part of the detector was shut down. A run usually lasts several hours. A data period is a collection of runs with a similar detector and trigger configuration and can last from some days to several weeks. Runs are divided into luminosity blocks, smaller time intervals in which the instantaneous luminosity is assumed to be constant. A luminosity block lasts approximately one minute.

For the presented analysis, data corresponding to an integrated luminosity of 4.7 fb^{-1} could be used after imposing the data-quality selection criteria that require all relevant detector subsystems used in the analysis to be operational. In Figure 3.7 the integrated luminosity of the considered run is shown as a function of the date and the peak instantaneous luminosity per LHC fill. The maximum instantaneous luminosity in the considered data sample was $2.65 \times 10^{33} \text{ cm}^{-2}\text{s}^{-1}$.

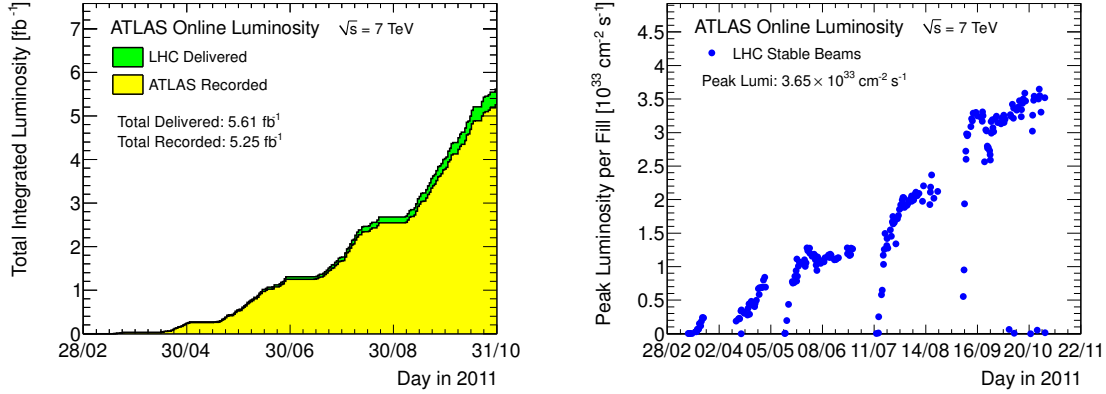


Figure 3.7.: Integrated luminosity that was delivered by the LHC (green) and recorded by ATLAS (yellow) during stable beams as a function of the day (left-hand side) and the maximum instantaneous luminosity per run delivered to ATLAS as a function of the day (right-hand side) for the $\sqrt{s} = 7$ TeV collisions that are analysed in this thesis (taken from Reference [156]).

An important property of the used data is the number of expected pile-up interactions which depends on the instantaneous luminosity and in particular on the bunch spacing. The data used was recorded with a bunch spacing of 50 ns inside a bunch train. The mean number of interactions per bunch crossing is shown in Figure 3.8. For the 2011 dataset 9.1 interactions per bunch crossing are expected on average.

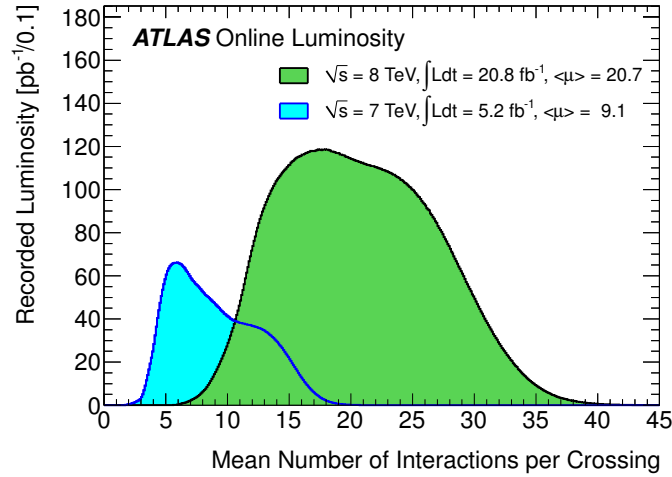


Figure 3.8.: Luminosity-weighted distribution of the mean number of interactions per bunch crossing for $\sqrt{s} = 7$ TeV and $\sqrt{s} = 8$ TeV data. The mean number of interactions per crossing is the mean of the Poisson distribution of the number of interactions per crossing calculated for each bunch with $\mu = \mathcal{L}_{\text{bunch}} \times \sigma_{\text{inel}} / f_r$, where $\mathcal{L}_{\text{bunch}}$ is the instantaneous luminosity per bunch, σ_{inel} is the inelastic cross section (71.5 mb for 7 TeV collisions and 73.0 mb for 8 TeV collisions), and f_r is the LHC revolution frequency. For n_{bunch} identical colliding bunches it is $\mathcal{L}_{\text{bunch}} = \mathcal{L} / n_{\text{bunch}}$, where \mathcal{L} is the instantaneous luminosity (taken from Reference [156]).

4 Calibration of the Semiconductor Tracker

When charged particles cross a silicon strip of the SCT sensors, electron–hole pairs are generated and a voltage is induced at the signal read-out electrode. For the reconstruction of charged particles a binary decision, whether a hit is identified or not, is recorded using a voltage threshold. The calibration of the Semiconductor Tracker includes the process of setting this threshold, the monitoring of electronic noise in the sensors and the masking of nonfunctional strips and modules. As only the binary decision for every strip is recorded, the calibration of the modules is a critical aspect for the successful operation of the SCT.

For this thesis work on the calibration of the SCT detector was performed as a contribution to the operation of the ATLAS detector. For the calibration several tests are performed. The response curve test, the trim range test and the noise occupancy test are described in detail in the following. For the reconstruction of physics objects from the hits in the tracking detectors, requirements on the number of hits and the number of holes, missing hits where hits are expected, are applied. The process of tagging a strip or module as non-functional, so that no hits are expected for this strip or module in the reconstruction of tracks, is called masking. In addition several digital and analogue tests as described in Reference [144] are performed to monitor the performance of the SCT sensors.

4.1. Response Curve Test

A minimum ionising particle is expected to create on average 25,000 electron–hole pairs in the 285 μm -thick silicon strips of the SCT sensors [144], corresponding to a charge of 4 fC for all created holes. The threshold for the detection of a hit is set to the voltage that allows for an identification of a charge of approximately 1 fC (6250 electrons) with a probability of 50%. This approach ensures a stable signal detection and results in a threshold that is well above the expected noise of approximately 1000 (short modules in inner and middle end-cap) to 1500 (long modules in the barrel, middle and outer end-cap) electrons is obtained. This threshold is set in the response curve test. A threshold scan is performed in which a charge is injected into the strips and the occupancy, the ratio of the number of recorded hits and the number of channels that were read out, is measured as a function of the threshold voltage, $V_{\text{threshold}}$. The measurement points are fit with a complementary error function,

$$O(V_{\text{threshold}}) = \text{erfc} \left(\left[V_{\text{threshold}} - Vt_{50} \right] / \left[\sqrt{2}\sigma \right] \right), \quad (4.1)$$

where O is the occupancy and the fit parameters are Vt_{50} , the threshold for which an occupancy of 50% is expected and σ , a measure for the output noise. An example of the performed fit is available in Reference [144]. For the response curve test the threshold scan is repeated for injected charges of 0.5 fC, 0.75 fC, 1.0 fC, 1.25 fC, 1.5 fC, 2 fC, 3 fC, 4 fC, 6 fC and 8 fC. The fit values obtained for Vt_{50} as a function of the injected charge are in turn fit with a quadratic function and the fitted value for Vt_{50} at 1 fC is used as the threshold for the binary hit decision.

The threshold setting can be validated with the faster three-point gain test. In the three-point gain test a threshold scan at injected charges of 1.5 fC, 2.0 fC and 2.5 fC is performed.

A fit with the function,

$$Vt_{50} = \text{offset} + \text{injected charge} \cdot \text{gain}, \quad (4.2)$$

follows. The offset, measured in mV, and the gain, measured in mV/fC, are reported. Strips with constantly high or low occupancy, fit failures and high or low offset or gain are masked and not used for the detection of charged particle hits. The input noise is calculated as the ratio of the output noise and the gain. The distribution of the average input noise, measured in electrons, is shown in Figure 4.1.

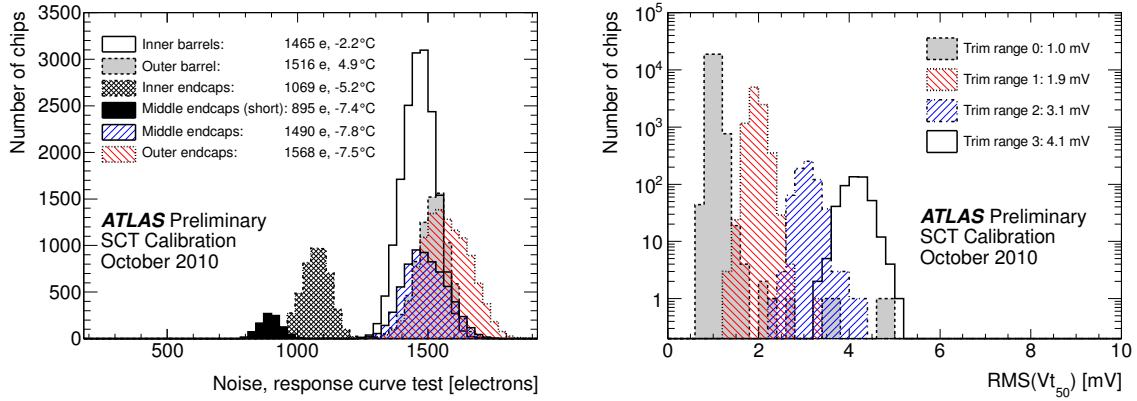


Figure 4.1.: The distribution of noise measured per chip is shown for the different parts of the SCT on the left-hand side [162]. The results are extracted from the response curve test (run 166544, scan 32, 2010-10-09). The temperatures given are measured by a sensor on the module hybrid and a correction obtained from a temperature simulation to account for differences between the measured temperature and the actual chip temperature is applied. On the right-hand side the distribution of the RMS of the measured Vt_{50} per chip for different settings of the trim range is shown. Vt_{50} is the threshold voltage at which the occupancy is 50%. The trim range is the possible reach of the channel-by-channel variations. It can be seen that for higher RMS, higher trim range settings are needed. The average RMS of Vt_{50} for a chip with a given trim range is shown in the legend.

4.2. Trim Range Test

In order to form the binary hit decision the amplified signal from the strips is compared with the Vt_{50} threshold. The Vt_{50} threshold is composed of a factor that is used for the whole chip and a factor used to compensate channel-by-channel variations. The component that is used for the whole chip is determined in the response curve test. The channel-by-channel variations are compensated using a 4-bit digital-to-analogue converter (DAC) setting, of which the analogue output maximum is the trim range: the higher the variations and in consequence the RMS of the measured Vt_{50} values per chip, the higher the trim range setting has to be. It is expected that the ageing process of the SCT modules will necessitate higher trim range settings in the future.

For the trim range test a charge of 1 fC is injected and threshold scans are performed for different DAC settings. For high trim range settings a high range of Vt_{50} values can be accommodated for the threshold voltage, however the accuracy of the set threshold voltage is

higher for low trim range settings. The optimal trim range is the lowest setting for which the highest number of channels can be successfully trimmed. Channels that cannot be trimmed for any trim range setting are masked.

In Figure 4.1 the distribution of the RMS of the measured V_{t50} thresholds per chip is shown for different settings of the trim range. It can be seen that for higher RMS, higher trim range settings are needed.

4.3. Noise Occupancy Test

For the noise occupancy test the occupancy is measured as a function of the threshold voltage corresponding to a charge specified in fC. No charge is injected and depending on the threshold voltage between $2 \cdot 10^3$ and 10^6 triggers are sent to accurately determine the occupancy. The logarithmic occupancy is shown in Figure 4.2. For Gaussian noise the occupancy follows a Gaussian cumulative distribution function (CDF). The standard deviation of the Gaussian CDF corresponds to the noise measured in electrons. To determine the noise a linear function is fitted to a graph of the logarithmic occupancy and the squared threshold using the least-squares method. Deviations from the linear behavior at high thresholds are a sign for non-Gaussian noise contributions. An example for this fit is available in Reference [144]. The noise as measured by the response curve test and the noise occupancy test is shown in Figure 4.3. It can be seen that the noise as measured by the noise occupancy test, where no charge is injected, is lower than the noise measured by the three-point gain test, where a charge is injected. This is consistent with the observation that the noise has a constant component and a component that depends on the injected charge.

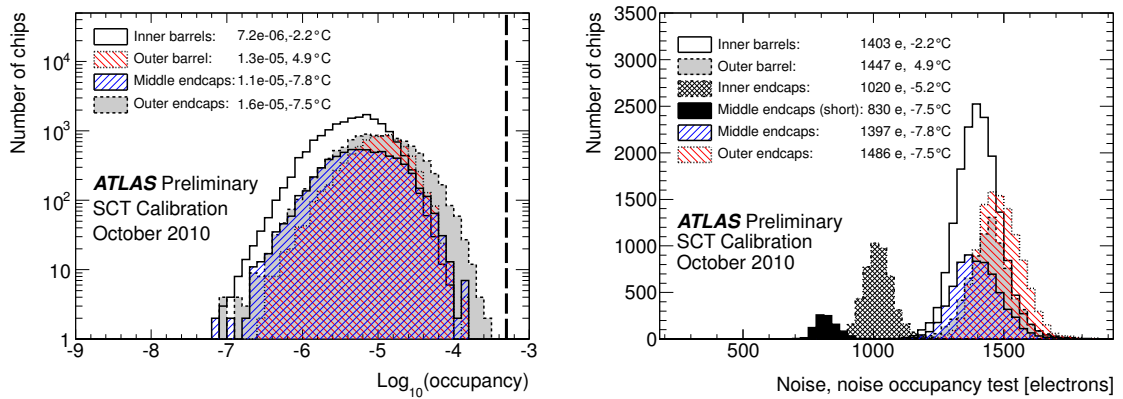


Figure 4.2.: On the left-hand side the distribution of the noise occupancy per chip is shown separately for the different parts of the SCT. On the right-hand side the distribution of the noise as measured by the noise occupancy test for each chip split up for the different parts of the SCT is shown [162]. The results are extracted from the noise occupancy test (run 166544, scan 42, 2010-10-09) in which the noise occupancy was measured with a threshold corresponding to 1 fC. The average occupancy and the average noise values are shown together with the temperatures. The temperatures given are measured by a sensor on the module hybrid and a correction obtained from a temperature simulation to account for differences between the measured temperature and the actual chip temperature is applied. The technical design report specification for the maximum noise occupancy of $5 \cdot 10^{-4}$ [163] is marked by the dashed line.

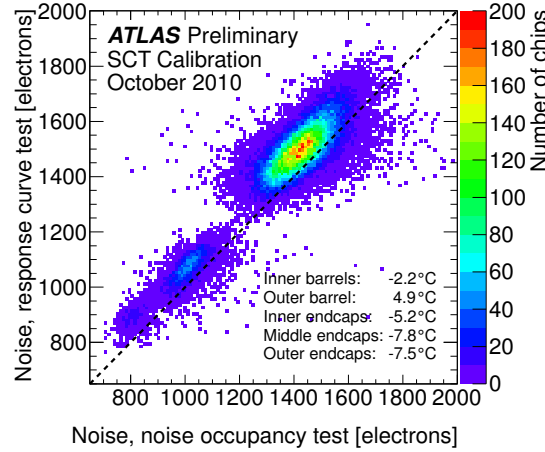


Figure 4.3.: The correlation of noise measured in the noise occupancy test (run 166544, scan 42, 2010-10-09) and the response curve test (run 166544, scan 32, 2010-10-09) is shown [162]. The temperatures given are measured by a sensor on the module hybrid and a correction obtained from a temperature simulation to account for differences between the measured temperature and the actual chip temperature is applied.

4.4. Summary of the Calibration Results

The described and referenced tests of the calibration are performed regularly on a daily, a weekly or a monthly basis depending on the test. The performance of the SCT as evaluated with the shown calibration data is within the limits set by the technical design report [163]. The noise measured in the response curve test and the noise occupancy test is constant over time. The noise is on average 1505 electrons as measured in the response curve test and 1432 electron as measured in the noise occupancy test at an average temperature of -3.1°C . The noise occupancy is $1.1 \cdot 10^{-5}$ for the long modules and below $5 \cdot 10^{-4}$ [163], the maximum noise occupancy specified by the technical design report, for all chips. The number of non-functional sensors is low enough so that no critical impact on the physics performance is expected. All results are in accordance with the values obtained during the module production and the expected ageing effects.

5 Object Reconstruction and Identification

In the object reconstruction and identification process, physics objects, such as electrons, muons, hadronic τ -lepton decays and jets, are identified and their momentum four-vectors and other properties are reconstructed based on detector-level information. Among other information the detector-level information consists of hits in the trackers and the muon system and energy deposits in the calorimeters. Dedicated reconstruction and identification algorithms for each kind of physics object are implemented within the ATHENA software framework [164]. Physics objects in simulated event samples are reconstructed with the same software as used for data. Reconstruction algorithms aim at an accurate reconstruction of the object four-momentum vector and provide object candidate reconstruction with the highest possible efficiency. Identification algorithms reduce the misidentification probability while trying to retain a high identification efficiency.

An important input for the reconstruction and identification of physics objects is provided by tracks of charged particles and vertices. A vertex is a reconstructed point of interaction from which several tracks emerge. Primary vertices are the points where the hard-scatter and the pile-up interactions originate. Secondary vertices are the points where long-lived particles like b hadrons decay. The reconstruction of tracks from charged particles and the reconstruction of primary and secondary vertices is described in Sections 5.1 and 5.2. In Section 5.3 the methods for the reconstruction of jets and the identification of jets initiated by the hadronisation of b quarks, the b -jets, are specified. The reconstruction and identification of hadronic decays of τ leptons is documented in Section 5.4. In Section 5.5 the reconstruction of electrons and muons is outlined. Finally in Section 5.6 the reconstruction of missing transverse momentum is described. Missing transverse momentum is used as a proxy for stable particles that cannot be directly reconstructed in the detector, e.g. neutrinos.

When two reconstructed objects that are selected by the described identification algorithms overlap geometrically within $\Delta R = \sqrt{\Delta\eta^2 + \Delta\phi^2} = 0.2$, where $\Delta\eta$ and $\Delta\phi$ are the absolute values of the pseudorapidity and azimuthal angle differences of the objects, only one of the objects is considered. The overlap is resolved by selecting muons, electrons, hadronic τ -lepton decays and jets in this order of priority.

5.1. Tracks

The track reconstruction is the process of forming charged-particle tracks based on the hits in the tracking detectors. Due to the acceptance of the tracking detectors in ATLAS the precise reconstruction of tracks is limited to $|\eta| < 2.5$ for the inner detector.

The ATLAS reconstruction software uses two different algorithms to reconstruct tracks, the INSIDE-OUT algorithm and the OUTSIDE-IN or BACK-TRACKING algorithm [165, 166]. For both algorithms the two-dimensional coordinates of the hits in the pixel detector are transformed into three-dimensional space points using the position of the pixel modules. For the SCT hits the one-dimensional coordinates from the two sides of a module that are glued together with a stereo angle are combined with the surface coordinates of the module to form three-dimensional space points. The TRT timing information is converted into drift circles around

the inner wire and track segments are formed by minimising the distance of the track segment to the drift circles.

The reconstruction of tracks by the INSIDE-OUT algorithm uses the three-dimensional space points in the pixel and SCT detectors as seeds to form tracks which are in turn extended to the TRT, where track segments that can be matched to the tracks in the silicon detectors are added to them. Combinations of at least three hits of which the associated vertex is compatible with the preliminary primary vertex found from two-hit combinations are referred to as seeds. The vertex formation is described in detail in Section 5.2. In addition seeds are required to have $p_T > 400$ GeV and may not be discarded by an ambiguity resolver that assigns hits exclusively to one track.

For the OUTSIDE-IN algorithm, track segments from the TRT are used as seeds and matched hits in the pixel and SCT detectors are added to them. While the INSIDE-OUT algorithm is targeted at the reconstruction of primary particles, particles that decay before they reach the pixel detector or in the pixel detector, the OUTSIDE-IN algorithm is targeted at the reconstruction of secondary particles, decay products of primary particles, such as electrons from photon conversions or particles from K_S decays. For both algorithms the tracks are finally refitted using the information about all assigned hits.

Tracks are selected using robust requirements defined by at least nine hits in the pixel and SCT detectors and no holes in the pixel detector. Holes are measurement points along the track where hits are expected, but not present. Missing hits in modules that are known to be inactive are counted as existing hits. For the identification of the hadronic decay of τ leptons special requirements for the associated tracks, as documented in Section 5.4, are used.

For every reconstructed track the impact parameters are determined. The transverse impact parameter, d_0 , is the distance of closest approach of the track to the primary vertex in the transverse plane. The longitudinal impact parameter, z_0 , is the longitudinal distance of the closest approach.

The efficiency of the track reconstruction as measured in simulated minimum-bias event data is shown in Figure 5.1. As the occupancy in the tracking detector rises with increasing number of interactions per bunch crossing a lower track reconstruction efficiency and more misidentified tracks from random hit combinations are expected for an increasing number of pile-up interactions. In Figure 5.1 it is shown that the track reconstruction efficiency is robust against more in-time pile-up interactions. The influence of out-of-time pile-up interactions is low as the pixel and SCT detectors have a read-out window of only 25 ns. Comparisons of the number of hits and the number of reconstructed tracks in simulation and data are available in Reference [166]. The number of hits in the tracking subdetectors agrees within 2% in data and simulation. The number of tracks as a function of the number of vertices is described with a 10% accuracy.

5.2. Vertices

Primary vertices, the vertices of the hard scatter and the pile-up interactions, are reconstructed with the ITERATIVE VERTEX FINDING procedure [168]. The tracks used for the vertex finding algorithm are required to fulfil quality criteria on the transverse momentum, the number of hits and the impact parameters in order to reject tracks from secondary vertices. The tracks are extrapolated to the point of closest approach to the beam spot centre, the centre of the region where collisions are expected based on measurements of the beam position. The vertex reconstruction algorithm is seeded by the maximum in the distribution of z -coordinates for this point. The vertex position is determined by an adaptive vertex fitting algorithm that refits the tracks using the constraint that they emerge from the vertex.

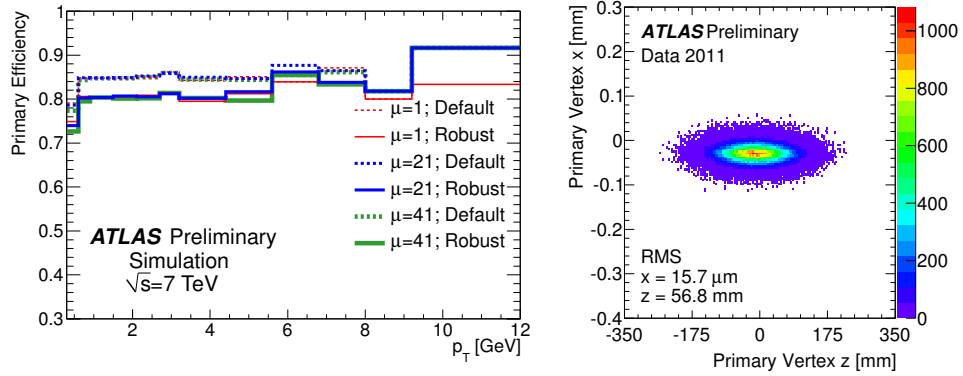


Figure 5.1.: On the left-hand side the reconstruction efficiency for primary tracks, the tracks corresponding to primary particles, is shown as a function of the transverse momentum of the track. The track reconstruction efficiency is measured in a sample of simulated minimum-bias events. It is shown for an average number of 1, 21 and 41 interactions per bunch crossing (taken from Reference [166]). The primary track reconstruction efficiency is the ratio of the number of reconstructed tracks and the number of primary particles with $p_T > 400$ GeV and $|\eta| < 2.5$. The robust requirements defined in Section 5.1 are compared with default requirements defined by at least seven hits in the pixel and SCT detectors and at most two holes in the pixel detector. On the right-hand side the two-dimensional distribution of the x - and z -coordinate for reconstructed primary vertices with greater than three tracks is shown (taken from Reference [167], the measurement is described in Reference [168]). Due to the symmetry of the detector and the accelerator the distribution of the y -coordinate is similar to the distribution of the x -coordinate.

The algorithm is based on a χ^2 fit with two degrees of freedom and downweights tracks that are outliers. Tracks that are incompatible with the vertex by more than 7σ , corresponding to $\chi^2 > 49$, are removed from the vertex. The procedure is repeated with all previously removed tracks until all tracks are associated with a vertex. Vertices to which only one track is assigned are discarded. The efficiency to reconstruct a primary vertex with at least two charged particles with $p_T > 400$ MeV and $|\eta| < 2.5$ varies slightly with the number of pile-up interactions per bunch crossing and is approximately 90% [166].

Based on the set of reconstructed primary vertices the primary signal vertex, the vertex of the hard scattering event, can be determined by selecting the vertex with the highest sum of the squared transverse momenta of the associated tracks, $\sum p_T^2$. All other reconstructed vertices are denoted pile-up vertices. The distribution of the x - and z -coordinate of the primary signal vertex is shown in Figure 5.1 (right-hand side).

5.3. Jets and Flavour Tagging

Jets are narrow clusterings of particles, calorimeter deposits or tracks that are reconstructed by jet algorithms as described in Section 5.3.1. Jets are reconstructed as a proxy for hadronised, high- p_T quarks or gluons. The calibration of the jet energy is described in Section 5.3.2. Flavour Tagging is the process of labelling jets as being initiated by the hadronisation of a quark of a specific flavour. In Section 5.3.3 the association of jets with b quarks, the b -tagging,

is described. Jets associated with hadronised b quarks and c quarks are called b -jets or c -jets, respectively. Jets due to the hadronisation of other quarks or gluons are referred to as light jets. Reconstructed jets can also stem from other sources, such as the hadronic decay of a τ leptons.

5.3.1. Jet Reconstruction

For most ATLAS analyses including the analysis presented in this thesis, jets are reconstructed using the anti- k_T algorithm [169] with a distance parameter of 0.4. Noise-suppressed topological clusters of calorimeter cells are used as input [170]. The reconstruction of topological cluster and the anti- k_T algorithm are described in the following.

Topological clusters are reconstructed with a cluster maker and a cluster splitter algorithm. The cluster maker algorithm creates a list of seeds from all calorimeter cells based on whether the signal-to-noise ratio of the cell energy and the expected RMS of the electronics noise is above a threshold t_{seed} . Neighbouring cells are added to the seed cells. If a cell is adjacent to two seed cells the seeds are merged if the signal-to-noise ratio is above the threshold $t_{\text{neighbour}}$ and the neighbour cell is added to the higher-energy cluster if the signal-to-noise ratio is above a threshold t_{cell} . The list of neighbour cells with $t > t_{\text{neighbour}}$ is used as the new seed list and the procedure is repeated iteratively until no further cells can be added to the seed list. For both the electromagnetic and the hadronic calorimeters $\{t_{\text{seed}}, t_{\text{neighbour}}, t_{\text{cell}}\} = \{4, 2, 0\}$ is used for the considered data-taking runs [171]. The cluster splitter algorithm is based on the cells obtained from the cluster maker algorithm. Cells are used as local maximum cluster seeds if the energy exceeds a threshold of 500 GeV and if the energy is higher than the energy of all neighbouring cells. The energy of the cells is calibrated at the electromagnetic scale, which was derived using the calorimeter response to electrons in test beam measurements. In addition, at least four neighbours are required to have a signal-to-noise ratio above t_{cell} . Cells that are adjacent to one seed cluster are added to the seed cluster and cells that are adjacent to more than one seed clusters are shared between the two highest- E_T energy clusters using weights that are proportional to $\exp(d_i)E_i$, where E_T is the transverse energy, E_i the total energy of the cluster and d_i the distance of the cluster centre and the considered cell. The neighbour list is used as the new seed list and this procedure is repeated until the neighbour list is empty. The four-vector of a topological cluster is defined by the energy sum, energy-weighted pseudorapidities and azimuthal angles of all associated calorimeter cells and a mass of zero is assumed.

The energy of the reconstructed clusters is calibrated using the Local Cluster Weighting scheme (LCW scheme) [172]. For the LCW scheme the electromagnetic scale calibration is used as the baseline calibration and energy corrections are derived using simulated single charged and neutral pion events. Clusters are classified as hadronic or electromagnetic based on the energy density and the shower depth. The corrections for charged and neutral pions are applied correspondingly. In addition, corrections for effects from the different response to electromagnetic and hadronic particles (“calorimeter non-compensation”), signal losses due to noise threshold effects and energy lost in non-instrumented regions are applied [173].

The anti- k_T algorithm with distance parameter $R = 0.4$ is run on the topological clusters using the FASTJET library [174]. The anti- k_T algorithm is a sequential recombination algorithm, for which all clusters are added to a list of proto-jets and the distance measures

$$d_{ij} = \min(k_{ti}^{2p}, k_{tj}^{2p}) \frac{\Delta_{ij}^2}{R^2} \quad \text{with} \quad \Delta_{ij}^2 = (y_i - y_j)^2 + (\phi_i - \phi_j)^2 \quad \text{and} \quad (5.1)$$

$$d_i = k_{ti}^{2p} \quad (5.2)$$

are calculated for every pair of proto-jets (d_{ij}) and every proto-jet (d_i). The variables k_{ti} , y_i and ϕ_i are the transverse energy, the rapidity and the azimuthal angle of the proto-jet i . The parameter p is fixed to -1 for the anti- k_T algorithm and $+1$ for the k_T algorithm. For $p = 0$ the Cambridge-Aachen algorithm is obtained. The minimum of the distances d_i and d_{ij} is determined and in the case that it is a distance between two proto-jets, the two proto-jets are merged. In the case that it is a distance d_i , the proto-jet i is removed from the list of proto-jets and considered a jet. The distances are recalculated and the procedure is repeated until no proto-jet remains. The momentum four-vector of the jet is defined as the sum of the momentum four-vectors of the clusters it consists of.

The anti- k_T algorithm was chosen because

- it is infrared safe, so that low-energy gluon emissions lead to the same jet (“low-energy limit”),
- it is collinear safe, so that clusters can be split into two collinear clusters without changing the resulting jet,
- it can be used at the parton-level, the particle-level and the cluster-level to enable the direct comparison of experimental and theoretical results,
- it produces quasi-circular jets in the η - ϕ plane,
- it is inexpensive in terms of computer resources.

The energy of jets is determined based on the energy reconstructed by the anti- k_T algorithm using the procedure described in Section 5.3.2. The other elements of the momentum four-vector are determined by the sum of the cluster four-momenta, which are corrected for the primary vertex position.

Jets are considered for the analysis if they have $p_T > 20$ GeV and $|\eta| < 4.5$. The jet vertex fraction is defined as the fraction of the transverse momentum of the jet from tracks that are matched to the primary vertex and all tracks [175]. For the calculation of the jet vertex fraction the transverse momentum of the jet is measured by the scalar sum of the transverse momenta of the associated tracks. With the requirement that jets with $|\eta| < 2.4$ have at least one associated track and that their jet vertex fraction is below 75% the number of jets originating from pile-up collisions is reduced.

Spurious jets can be caused by non pp -collision background, like

- beam-gas events, for which a beam proton collides with residual particles in the beam pipe,
- beam-halo events, for which a beam proton collides with the collimators, devices used to reduce the transverse beam width,
- cosmic ray muons and calorimeter noise, like sporadic noise bursts and coherent noise.

For the analysis presented in this thesis a set of so-called “looser selection requirements” for the quality of the jet signal as defined in Reference [176] is used. Sporadic noise bursts in the hadronic end-cap calorimeters are reduced by requirements on

- f_{HEC} , the fraction of energy in the hadronic end-cap calorimeters,
- $\langle Q \rangle$, the E^2 -weighted pulse quality of the calorimeter cells,

- f_Q^{HEC} , the fraction of the energy in HEC calorimeter cells with poor signal shape quality, and
- E_{neg} , the apparent negative energy due to the coupling of neighbouring cells.

Coherent noise in the electromagnetic calorimeter is reduced by requirements on

- the fraction of energy in the electromagnetic calorimeters,
- the pulse quality $\langle Q \rangle$ and
- the fraction of the energy from LAr calorimeter cells with poor signal shape quality f_Q^{LAr} .

Cosmic muons and beam background events are reduced by requirements on

- the electromagnetic energy fraction,
- the ratio of the scalar sum of the p_T of the tracks associated with the jet and the jet p_T and
- the maximum energy fraction in any single calorimeter layer.

An event is not considered for the analysis if any jet or τ_{had} candidate as defined in Section 5.4 with $p_T > 20$ GeV fails the selection requirements. This selection is 99.8% efficient for events without non-collision background.

For the period of data-taking from 30 April 2011 and 13 July 2011, corresponding to the run numbers 180614 to 185353, a crate controller in the LAr calorimeter failed. As a consequence it was not possible to get energy information from six front-end boards of the LAr calorimeter. To reject events where the jet energy and missing transverse momentum measurement is affected by this failure, events with jets with $p_T > 20$ GeV that point to the direction of the cells connected to the unusable front end boards are rejected.

5.3.2. Jet Energy Scale and Resolution

Building on the LCW calibration of the clusters a dedicated energy correction for jets is derived and documented in References [173, 177]. In the first step a correction of the energy for additional in-time and out-of-time pile-up interactions is applied [178]. This correction amounts to 370 MeV and 60 MeV per additional in-time and out-of-time pile-up interaction, respectively. The correction is derived from simulated event samples. An additional correction is obtained from the comparison of the reconstructed and the true jet energy as a function of η and p_T for isolated jets in simulated PYTHIA [179] di-jet event samples. The final correction is derived with in-situ techniques in event samples from the measured data. For the so-called p_T intercalibration [180] the p_T balance of events with two jets is used. Events with two central jets with $|\eta| < 0.8$ are used for the calibration of the energy of both jets. The p_T asymmetry of the jets is defined by the ratio of the difference of the transverse momenta and the average transverse momentum of the two jets. The average p_T asymmetry is determined as a function of jet pseudorapidity and the average p_T of the jets. Correction factors are derived based on the assumption that the average p_T asymmetry is zero. In events with one central and one non-central jet the average energy of the calibrated central jets is used to calibrate non-central jets.

In addition, events where a jet with $|\eta| < 1.2$ recoils against a Z boson, a photon or a system of lower- p_T jets are used for the energy calibration. When a jet recoils against a Z

boson which decays into e^+e^- , the transverse momentum of the Z boson is inferred from the momentum of the electrons. The jet response as a function of the transverse momentum of the Z boson is the ratio of the Z -boson and jet transverse momenta in data and simulation [181]. For events where a jet recoils against a photon the so-called MPF response is calculated. The MPF response is the ratio of the sum- E_T of all hadronic activity projected on the photon p_T vector and the photon p_T . The sum- E_T of all hadronic activity is determined by the sum- E_T of all clusters calibrated at the LCW scale [182]. Correction factors as a function of jet p_T are derived by minimising the χ^2 value based on the response in data and simulated event samples after applying the correction factors [173]. The jet energy scale for high- p_T jets is determined from the comparison of the response of a high- p_T jet and several recoiling low- p_T jets in data and simulation [183]. Prior to the comparison the low- p_T jets are calibrated with the methods described before. The obtained correction factors are applied to all jets. Depending on the transverse momentum of the jet the measurements from Z bosons, photons or the jet systems with the same transverse momenta are used irrespective of the pseudorapidity. The uncertainty of the jet energy calibration is approximately 1% for central jets with $40 \text{ GeV} < p_T < 500 \text{ GeV}$ and below 6% for all jets.

The jet energy resolution is determined in data recorded in the year 2011 using the di-jet balance method that was used for the determination of the jet energy scale and the bisector method described in Reference [184]. As the jet energy resolution is predominantly higher in data compared to simulation the jet energies in simulation are smeared. The momentum four-vector of jets is scaled with a random number that is generated using a Gaussian probability density function with mean 1 and standard deviation

$$\sigma = \sqrt{\sigma_{\text{data}}^2 - \sigma_{\text{MC}}^2}, \quad (5.3)$$

where σ_{data} and σ_{MC} are the relative jet energy resolutions measured in data and simulation.

5.3.3. Tagging of b -jets

The separation of b -jets from light and c -jets builds upon the high lifetime of b hadrons, which can lead to a reconstructed secondary vertex at the place where the b hadron decays. The charged B^\pm and the neutral B^0 mesons have mean lifetimes of $\tau = 1.641 \times 10^{-12} \text{ s}$ and $\tau = 1.519 \times 10^{-12} \text{ s}$ [6], respectively. These lifetimes lead to a mean decay length of $\beta\gamma c\tau = 791 \mu\text{m}$ and $\beta\gamma c\tau = 733 \mu\text{m}$ in a reference frame where the B meson has an energy of 10 GeV. On average the tracks that originate from a secondary vertex have a higher impact parameter compared to tracks from the primary vertex. A schematic illustration of a b -hadron decay is shown in Figure 5.2.

For ATLAS analyses a variety of b -tagging algorithms is provided. The IP3D algorithm uses the signed transverse impact parameter significance¹, d_0/σ_{d_0} , and the signed longitudinal impact parameter significance, z_0/σ_{z_0} , to build a likelihood ratio based on their distributions obtained for simulated b - and light jets.

For the SV1 algorithm, secondary vertices are reconstructed using a looser track selection compared to the other algorithms. The SV1 discriminant is a likelihood ratio based on the invariant mass of the tracks associated with the secondary vertex, the ratio of the sum of the energies of the tracks associated with the vertex and the sum of the energies of all tracks associated with the jet, the number of two-track vertices and the η - ϕ distance between the

¹The signed transverse impact parameter is positive if the track extrapolation crosses the jet direction in front of the primary vertex, and negative otherwise [186]. The signed longitudinal impact parameter is defined accordingly.

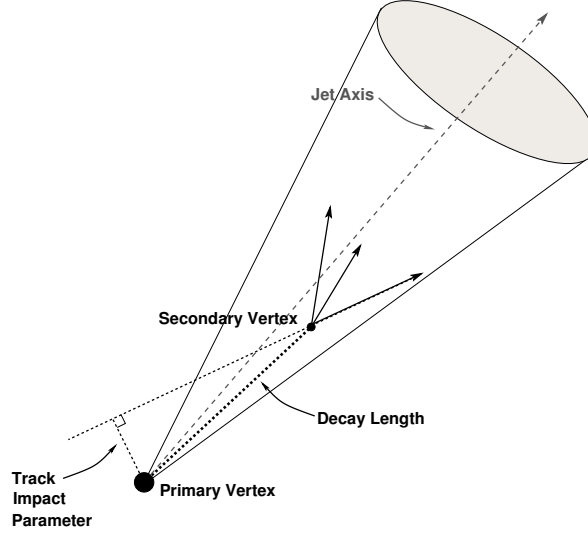


Figure 5.2.: Schematic illustration of a b -hadron decay. The b -hadron is produced at the primary vertex. The long-lived b hadron decays at the secondary vertex. On average tracks from the secondary vertex have a larger impact parameter significance with respect to the primary vertex compared to tracks from the primary vertex (taken from Reference [185]).

jet axis and the line joining the primary vertex and the secondary vertex [186]. For the first two variables correlations are considered.

The dominant decay of b hadrons proceeds through a transition of a b quark into a c quark since $|V_{cb}|^2 \gg |V_{ub}|^2$. The JETFITTER algorithm [187] tries to resolve the secondary vertex of the b -hadron decay and one or more tertiary vertices of the c -hadron decay. It is assumed that the two decay vertices and the primary vertex are on a straight line, the b -hadron flight axis, from which tracks emerge at the vertices. Using a Kalman filter technique the best position of the vertices based on the associated tracks is obtained. For the JETFITTERCOMBNN discriminant [188] the variables based on the vertices obtained from the JETFITTER algorithm, namely the number of vertices with at least two tracks, the total number of tracks at these vertices, the number of additional single-track vertices, the invariant mass of all charged particles that leave tracks attached to the decay chain, the energy ratio of these charged particles and the charged particles associated with the jet and the flight length significance, are combined using a neural network.

For the search for $h/A/H \rightarrow \tau_{\text{had}}\tau_{\text{had}}$ decays the MV1 algorithm [186], a neural network discriminant based on the IP3D, the SV1 and the JETFITTERCOMBNN discriminants is employed as it provides the best performance for the identification of b -jets and the rejection of light jets. A working point that provides an efficiency of 70% for identifying b -jets, as measured in a simulated sample of $t\bar{t}$ events, is used. The b -tag efficiency and the light and c -jet rejection, the inverse misidentification probability, are shown for the MV1 discriminant in Figure 5.3.

The efficiency of the b -tag algorithms is measured in data samples of semi-leptonic b -hadron decays, which are selected by requiring a muon that is close to a jet. For the p_T^{rel} method [189] templates of the p_T^{rel} variable, the momentum of the muon transverse to the combined muon and jet axis, are derived for simulated light-jet, c -jet and b -jet event samples. The templates are used to derive the b -tag efficiency in a fit to the data. For the SYSTEM 8 method [190] the sample is split into eight regions using requirements on the b -hadron lifetime, p_T^{rel} and

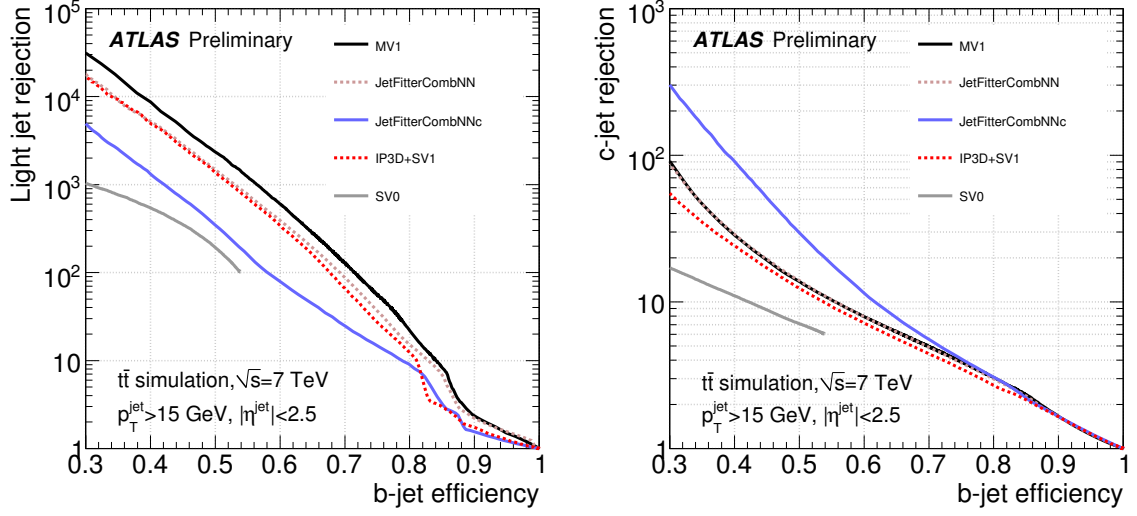


Figure 5.3.: Light-jet rejection (left-hand side) and c -jet rejection (right-hand side) as a function of the b -tag efficiency for different b -tag algorithms. The b -tag efficiency and the rejections have been measured in simulated $t\bar{t}$ events. For the MSSM analysis the MV1 algorithm with a b -tag efficiency of 70% is used. The discriminant JETFITTERCOMBNNC is similar to the JETFITTERCOMBNN discriminant, but trained to identify c -jets. The discriminant IP3D+SV1 is a combination of the IP3D and the SV1 discriminants (taken from Reference [189]).

whether a second b -tagged jet is present opposite to the considered jet. The second jet is considered opposite to the first jet if $|\pi - \Delta\phi| < 1$ holds. Using the assumption that the three variables are statistically independent, the b -tag efficiency can be extracted from a set of equations based on the number of events in each region. Combined data-to-simulation scale factors are derived for the measurement with the p_T^{rel} and the SYSTEM 8 method based on a likelihood method. The measured efficiencies and data-to-simulation scale factors are shown in Figure 5.4 for the MV1 discriminant with a 70% b -tag efficiency. The total uncertainties of the b -tag efficiency range from 5% to 19% [189]. The mistag probability for light jets is determined in data samples obtained with a single-jet trigger and the SV0 mass method, a template method based on the invariant mass of all particles associated with the secondary vertex, and the negative-tag method [191]. The negative-tag method uses the assumption that for tracks originating from the primary vertex the d_0/σ_{d_0} distribution is symmetric. A second version of the b -tag algorithm that reverses the sign of the impact parameter is created and the mistag efficiency is determined. If the assumption that the impact parameter distribution is symmetric holds, the original b -tag algorithm has the same mistag efficiency. The mistag probabilities are between 1% and 3%. For c -jets the mistag efficiency is measured in $D^{*+} \rightarrow D^0 (\rightarrow K^-\pi^+) \pi^+$ decays from data [192]. Data-to-simulation scale factors are between 1.4 and 1.6 with uncertainties between 0.4 and 0.5 for light jets and between 1.0 and 1.2 with uncertainties between 0.1 and 0.3 for c -jets.

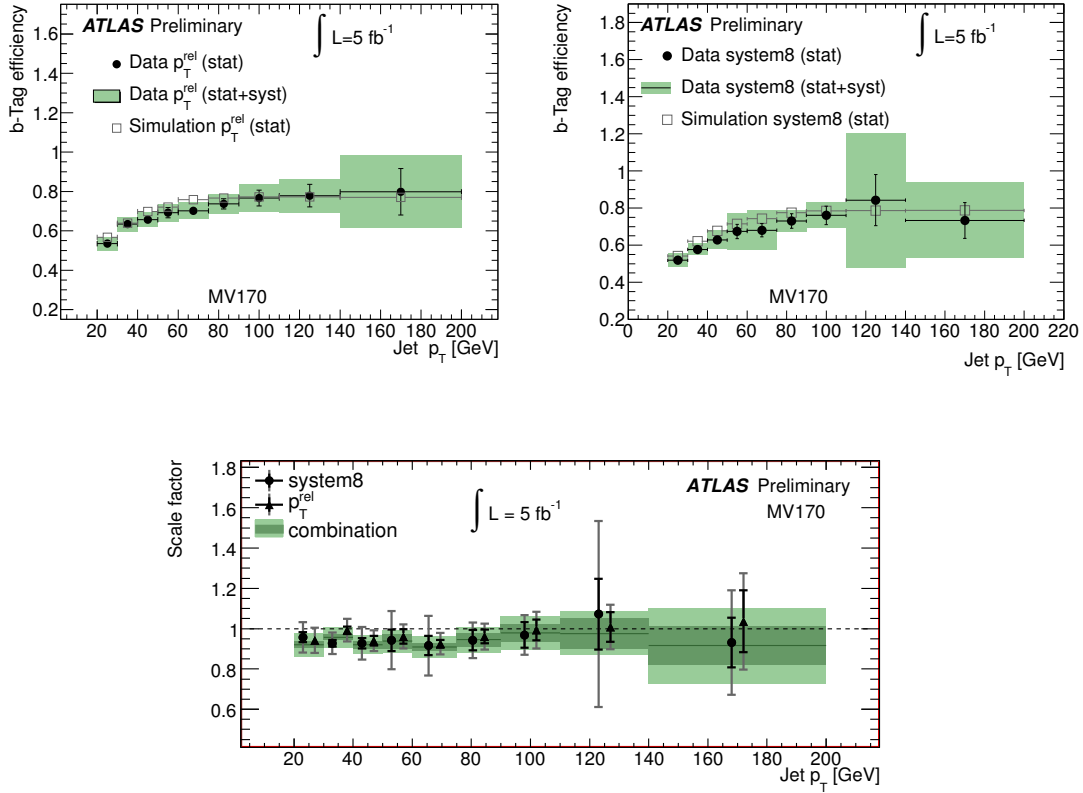


Figure 5.4.: The b -tag efficiencies as measured with the p_T^{rel} method (first row, left-hand side) and the SYSTEM 8 method (first row, right-hand side) are shown with data-to-simulation scale factors (second row) for the MV1 algorithm with an efficiency of 70%. All distributions are shown as a function of the transverse momentum of the jet. The b -tag efficiencies have been measured in data samples where a muon is matched to a jet (taken from Reference [189]).

5.4. τ Leptons

The identification of events with τ -leptons is an important part of the search for $h/A/H \rightarrow \tau_{\text{had}}\tau_{\text{had}}$ decays. However, it is not possible to identify τ leptons directly as they have a mean lifetime of

$$\tau = (290.6 \pm 1.0) \cdot 10^{-15} \text{ s} \quad [6]. \quad (5.4)$$

This corresponds to a mean decay length of $c\tau = 87.12 \mu\text{m}$ in the rest frame of the τ lepton and $\beta\gamma c\tau = 2.45 \text{ mm}$ in a reference frame where the τ lepton has an energy of 50 GeV. The dominant decay modes of a τ lepton are the leptonic decay into a charged lepton and neutrinos and the hadronic decay, predominantly into one or three charged pions, one neutrino and possibly neutral pions. The decay modes and their branching ratios are given in detail in Table 5.1. In the following the τ -lepton decay into an electron and neutrinos will be denoted by τ_e , the τ -lepton decay into a muon and neutrinos by τ_μ and the combination of the two leptonic decay modes of τ leptons is denoted by τ_{lep} . The hadronic decay mode of τ leptons refers to all decays including a neutrino and charged and neutral hadrons, primarily pions. The hadronic decay of a τ lepton is denoted by τ_{had} . The hadrons are the decay products that are visible in the detector and denoted by $\tau_{\text{had-vis}}$.

Decay mode	Branching ratio
$\tau^- \rightarrow e^- \bar{\nu}_e \nu_\tau$	$(17.83 \pm 0.04)\%$
$\tau^- \rightarrow \mu^- \bar{\nu}_\mu \nu_\tau$	$(17.41 \pm 0.04)\%$
$\tau^- \rightarrow \pi^- \pi^0 \nu_\tau$	$(25.52 \pm 0.09)\%$
$\tau^- \rightarrow \pi^- \nu_\tau$	$(10.83 \pm 0.06)\%$
$\tau^- \rightarrow \pi^- 2\pi^0 \nu_\tau$	$(9.30 \pm 0.11)\%$
$\tau^- \rightarrow K^* (892)^- \nu_\tau$	$(1.20 \pm 0.07)\%$
$\tau^- \rightarrow \pi^- 3\pi^0 \nu_\tau$	$(1.05 \pm 0.07)\%$
$\tau^- \rightarrow 2\pi^- \pi^+ \nu_\tau$	$(9.31 \pm 0.06)\%$
$\tau^- \rightarrow 2\pi^- \pi^+ \pi^0 \nu_\tau$	$(4.62 \pm 0.06)\%$

Table 5.1.: Dominant decay modes of τ^- leptons [6]. The combined leptonic branching ratio is approximately 35.2%, the hadronic one-prong branching ratio is approximately 49.5% and the hadronic three-prong branching ratio is approximately 15.2%.

The leptonic decay modes are usually identified with the standard electron and muon identification algorithms and an event-based missing transverse momentum requirement to differentiate events with leptonically decaying τ leptons from events with electrons or muons, but no neutrinos. Hadronic decays of τ leptons are identified as narrow jets with few tracks using the procedures described in the following sections in combination with an event-based missing transverse momentum requirement.

5.4.1. Reconstruction of Hadronic τ -Lepton Decays

The reconstruction of hadronic τ -lepton decays aims at the reconstruction of the visible decay products of hadronically decaying τ leptons. Hadronic τ -lepton decays are predominantly characterised by the presence of one or three tracks and energy deposits in the electromagnetic and hadronic calorimeters. Both the calorimeter deposits and the track system are narrow in η - ϕ space compared to jets from quark and gluon production. The dominant backgrounds to the τ_{had} identification arise from misidentified jets and electrons and, to a significantly lower extent, muons.

The reconstruction of hadronic τ -leptons decays is seeded by anti- k_T jets with distance parameter $R = 0.4$ based on topological clusters that have been calibrated using the Local Cluster Weighting scheme [172]. For the τ_{had} reconstruction anti- k_T jets are required to have $E_T > 10$ GeV and $|\eta| \leq 2.5$. Jets with $|\eta| > 2.5$ are not considered as no tracks which are available only within the acceptance of the tracking detectors can be associated [193]. The momentum four-vector of a hadronically decaying τ lepton is defined as the vectorial sum of the four-momenta of the visible decay products. The azimuthal angle of the τ_{had} candidate, ϕ , is determined by the seeding jet and the mass of the τ_{had} candidate is set to zero. The polar angle, θ , and the transverse energy of the τ_{had} candidate, E_T , are determined by the τ energy scale calibration as described in Section 5.4.2. The τ energy scale calibration corrects the jet energy to the expected energy for hadronic τ -lepton decays and corrects for poorly instrumented regions on a statistical basis.

Tracks within $\Delta R = 0.2$ around the seed-jet axis (“signal cone”) are associated with the τ_{had} candidate if they fulfil the requirements documented in Table 5.2 (right-hand side). In addition tracks in the “isolation annulus” of the τ_{had} candidate defined by $0.2 < \Delta R < 0.4$ are considered for some of the variables used in the identification process if they fulfil the

same requirements. The charge of the τ_{had} candidate is determined by the sum of the charges of the associated tracks. A schematic illustration of the track system of a τ_{had} candidate and the signal cone and isolation annulus is shown in Figure 5.5.

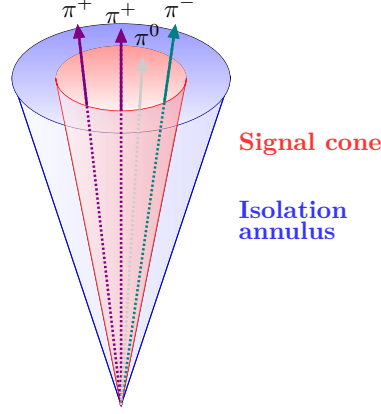


Figure 5.5.: Schematic illustration of a hadronic $\tau^+ \rightarrow \pi^+ \pi^+ \pi^- \pi^0$ decay. For the reconstruction tracks in the signal cone with $\Delta R < 0.2$ are associated to the τ_{had} candidate. As the track system of hadronic τ -lepton decays is narrow in η - ϕ space compared to jets from quark and gluon production, a low number of tracks is expected in the isolation annulus defined by $0.2 < \Delta R < 0.4$. In the illustration the signal cone is shown in red, the isolation annulus in blue and the visible τ -lepton decay products are indicated by arrows.

For the $\tau_{\text{had}}\tau_{\text{had}}$ analysis τ_{had} candidates are considered if they have $E_T > 20$ GeV, one or three tracks and charge q with $|q| = 1$. The requirements for the reconstruction of τ_{had} candidates are summarised together with the requirements for the identification of hadronically decaying τ leptons in Table 5.2 (left-hand side).

τ_{had} selection requirements	Track selection requirements
$E_T > 20$ GeV	$p_T > 1$ GeV
$ \eta < 2.5$	≥ 2 hits in pixel detector
1 or 3 tracks	≥ 7 hits in pixel and SCT detectors
Charge $ q = 1$	$ d_0 < 1$ mm
Fail electron veto	$ z_0 \sin \theta < 1.5$ mm
Fail muon veto	
Pass BDT medium τ_{had} identification	

Table 5.2.: Summary of the requirements used for the reconstruction and identification of hadronic τ -lepton decays (left-hand side) and tracks that can be matched to hadronic τ -lepton decays (right-hand side). The requirements “fail electron veto”, “fail muon veto” and “pass BDT medium τ_{had} identification” refer to the identification algorithms described in Section 5.4.3.

5.4.2. Energy Calibration for Hadronic τ -Lepton Decays

The hadronic τ energy scale calibration (TES) is aimed at an accurate description of the energy of the visible decay products of hadronic τ -lepton decays. The decay modes of hadronically decaying τ leptons have been shown in Table 5.1. As hadronic τ -lepton decays have a different fraction of neutral and charged pions than quark- or gluon-induced jets the jet energy calibration derived in Section 5.3.2 cannot be used and a special τ_{had} energy calibration has been derived in Reference [194].

The hadronic τ energy scale was derived using a deconvolution method based on the single-particle response after a correction for the energy contribution due to pile-up. The single-particle response is the ratio of the measured and the true energy of the considered particle, e.g. a pion. For particles with momentum $p < 20$ GeV and $|\eta| < 1.7$ or $p < 60$ GeV and $1.7 \leq |\eta| \leq 2.5$ the response is determined using an E/p measurement in minimum-bias data and the measured energy of the particles in simulation is corrected to the expected energy from data. For $|\eta| < 0.8$ and $p \geq 20$ GeV the measurement of the response in combined test beam data is used. For particles with larger pseudorapidities or transverse momenta the response is obtained from simulated $Z/\gamma^* \rightarrow \tau^+\tau^-$, $Z' \rightarrow \tau^+\tau^-$ and $W \rightarrow \tau\nu$ event samples. The single-particle energy calibration and its uncertainties are propagated to the energies of the hadronic τ -lepton decays using simulated event samples. With the ATLAS calorimeter simulation it is possible to link calorimeter energy deposits to the particles that are responsible for the deposit. The calorimeter deposits of a hadronic τ -lepton decay are calibrated using the single-particle response of the particles that are linked to the deposit. Calibration constants are obtained as a function of the τ_{had} pseudorapidity and transverse momentum separately for one- and multi-prong τ_{had} candidates. Uncertainties are obtained by comparing the nominal energy scale to the energy scale obtained for a detector simulation with additional dead material (“material modelling uncertainty”), by comparing the nominal energy scale to the energy scale obtained with a different underlying event model (“underlying event uncertainty”) and by comparing the energy scale for different average numbers of pile-up vertices (“pile-up uncertainty”). The uncertainties of the single particle response measurements are divided into measurement uncertainties (“single-particle response uncertainty”) and uncertainties due to the numerical inversion of the calibration constants (“non-closure uncertainty”). The τ energy scale and its uncertainties were successfully validated in a sample of $Z/\gamma^* \rightarrow \tau_\mu\tau_{\text{had}}$ events in data.

The uncertainties of the energy scale for one-prong and multi-prong hadronic τ -lepton decays with $|\eta| < 0.3$ are shown in Figure 5.6 together with the individual uncertainty components. The combined energy scale uncertainty is documented with the coarser binning that is used for the search for $h/A/H \rightarrow \tau_{\text{had}}\tau_{\text{had}}$ decays in Table 5.3.

5.4.3. Identification of Hadronic τ -Lepton Decays

The discrimination of hadronic τ -lepton decays and jets initiated by quarks and gluons in the $\tau_{\text{had}}\tau_{\text{had}}$ analysis is based on the following variables:

- Track radius,

$$R_{\text{track}} = \frac{\sum_{i \in \{\text{tracks}\}} [p_{T,i} \Delta R_i]}{\sum_{i \in \{\text{tracks}\}} p_{T,i}}, \quad (5.5)$$

where the sum includes all tracks in a cone with size $\Delta R = 0.4$ around the τ_{had} candidate. The transverse momentum of track i is $p_{T,i}$ and ΔR_i the distance in η - ϕ space between track i and the τ_{had} candidate.

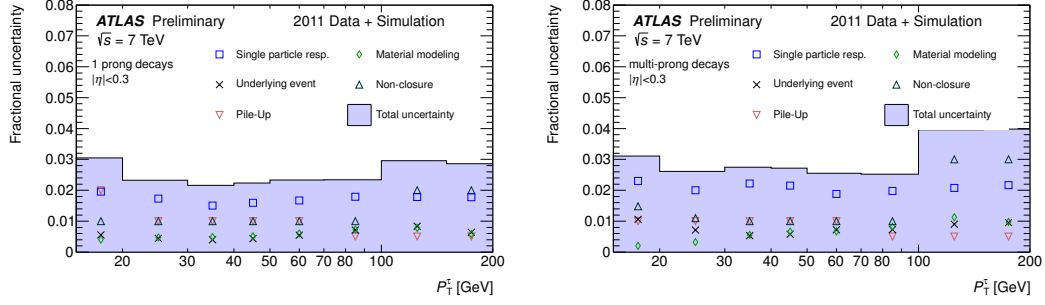


Figure 5.6.: Energy scale uncertainty for one-prong (left-hand side) and multi-prong (right-hand side) hadronic τ -lepton decays with $|\eta| < 0.3$ as a function of the transverse momentum of the hadronic τ -lepton decay. The individual contributions to the uncertainty are shown as markers and the combined uncertainty is shown as filled band (taken from Reference [194]).

$\tau_{\text{had}} p_T$	$ \eta \leq 0.3$	$0.8 < \eta \leq 1.3$		$ \eta > 1.6$	
		$0.3 < \eta \leq 0.8$	$1.3 < \eta \leq 1.6$		
One-prong τ_{had} decays					
$15 \text{ GeV} < p_T < 20 \text{ GeV}$	3.0%	3.0%	3.0%	3.5%	3.0%
$20 \text{ GeV} < p_T < 50 \text{ GeV}$	2.5%	2.5%	2.5%	3.0%	2.5%
$p_T > 50 \text{ GeV}$	3.0%	3.0%	3.0%	3.5%	3.0%
Multi-prong τ_{had} decays					
$15 \text{ GeV} < p_T < 20 \text{ GeV}$	3.0%	3.5%	5.0%	4.5%	3.0%
$20 \text{ GeV} < p_T < 50 \text{ GeV}$	3.0%	3.0%	3.5%	3.5%	2.5%
$p_T > 50 \text{ GeV}$	3.5%	3.0%	3.0%	3.0%	3.0%

Table 5.3.: Uncertainty of the energy scale for hadronic τ -lepton decays. The uncertainties are shown for one- and multi-prong τ_{had} decays as a function of the $\tau_{\text{had}} p_T$ and the τ_{had} pseudorapidity. The uncertainties are assumed to be independent of the τ_{had} identification level [194].

- Highest- p_T track momentum fraction,

$$f_{\text{track}} = \frac{p_{T,1}^{\text{track}}}{p_T^\tau}, \quad (5.6)$$

where $p_{T,1}$ is the p_T of the highest- p_T core track and p_T^τ is the transverse momentum of the τ_{had} candidate.

- Core energy fraction,

$$f_{\text{core}} = \frac{\sum_{i \in \{\text{cells}\}} [\theta(0.1 - \Delta R_i) E_{T,i}]}{\sum_{i \in \{\text{cells}\}} E_{T,i}}, \quad (5.7)$$

where the sum includes all cells that are part of the clusters seeding the τ_{had} candidate. The Heaviside function $\theta(0.1 - \Delta R_i)$ ensures that only core cells, cells with $\Delta R_i <$

0.1, are used for the numerator. The transverse energy of cell i is calibrated at the electromagnetic scale and denoted by $E_{T,i}$. The distance between cell i and the τ_{had} candidate in η - ϕ space is denoted by ΔR_i .

- Number of tracks in the isolation annulus, $N_{\text{track}}^{\text{iso}}$.
- Calorimetric radius,

$$R_{\text{Cal}} = \frac{\sum_{i \in \{\text{cells}\}} [E_{T,i} \Delta R_i]}{\sum_{j \in \{\text{cells}\}} E_{T,j}}, \quad (5.8)$$

where the sum runs over all cells that are part of the clusters seeding the τ_{had} candidate and have a distance to the τ_{had} candidate axis of $\Delta R_i < 0.4$.

- Cluster mass,

$$m_{\text{eff.clusters}} = \sqrt{\left(\sum_{i \in \{\text{clusters}\}} E_i \right)^2 - \left(\sum_{i \in \{\text{clusters}\}} \mathbf{p}_i \right)^2}, \quad (5.9)$$

where the sum includes only the N highest- E_T clusters of the seed jet calibrated at the LCW energy scale to minimise pile-up effects. N is defined by

$$N = \text{ceil} \left(\left(\sum_{i \in \{\text{clusters}\}} E_{T,i} \right)^2 / \sum_{i \in \{\text{clusters}\}} E_{T,i}^2 \right), \quad (5.10)$$

where the sum includes all clusters that are associated with the τ_{had} candidate. The ceil function maps a real number to the smallest following integer.

- Mass of the track system,

$$m_{\text{tracks}} = \sqrt{\left(\sum_{i \in \{\text{tracks}\}} E_i \right)^2 - \left(\sum_{i \in \{\text{tracks}\}} \mathbf{p}_i \right)^2}, \quad (5.11)$$

where the sum includes all tracks associated to the τ_{had} candidate with $\Delta R_i < 0.4$ between the track and the τ_{had} momentum four-vector. The variables E_i and \mathbf{p}_i are the energy and the momentum three-vector of track i (this variable is used for multi-prong τ_{had} identification only).

- Transverse flight path significance, S_T^{flight} , the fraction of the decay length of the secondary vertex in the transverse plane and its uncertainty (this variable is used for multi-prong τ_{had} identification only),
- Highest- p_T track impact parameter significance, $S_{\text{lead track}}$, the significance of the distance of closest approach of the track to the primary vertex in the transverse plane, d_0 (variable is used for one-prong τ_{had} identification only).
- Three highest- E_T clusters energy ratio, the ratio of the sum of the energies of the three highest- E_T clusters and the energy of all clusters associated with the τ_{had} candidate.
- the maximum ΔR between a core track and the τ_{had} candidate axis, ΔR_{max} (this variable is used for multi-prong τ_{had} identification only).

The distributions of the variables $N_{\text{track}}^{\text{iso}}$ and R_{Cal} is shown in Figure 5.7 for hadronic τ -lepton decays and a sample of events that is dominated by jets initiated by quarks and gluons. The distributions of the other other variables are available in Reference [195]. The information from the distribution of these variables is combined in two discriminants based on a likelihood function and a boosted decision tree (BDT) [193, 195], however in this thesis only the BDT discriminant is used. With a decision tree an event is classified as signal- or background-like with a series of binary decisions based on requirements on the input variables and whether the resulting subsets are more signal- or background-like. Several decision trees are created sequentially based on event samples where previously misidentified events receive a higher weight. Finally the output of the individual trees is combined to form the boosted decision tree discriminant [196].

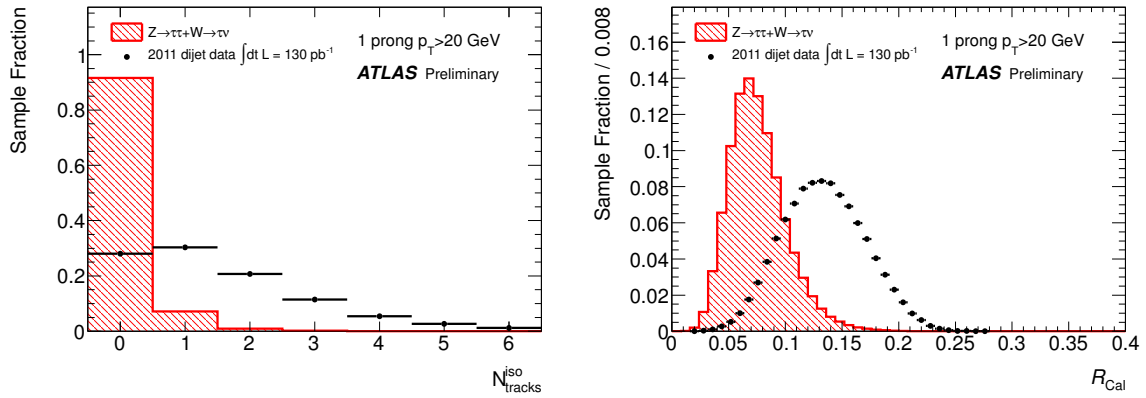


Figure 5.7.: Distribution of the number of tracks in the isolation annulus, $N_{\text{track}}^{\text{iso}}$ (left-hand side), and the calorimetric radius, R_{Cal} (right-hand side), for one-prong hadronic τ -lepton decays and a di-jet selection in data. The di-jet selection in data is dominated by events with jets initiated by quarks and gluons. The distributions of these variables are used together with the distributions of nine other variables to derive the boosted decision tree discriminant with which hadronic τ -lepton decays are differentiated from jets initiated by quarks and gluons (taken from Reference [195]).

The BDT discriminant was optimised using hadronic τ -lepton decays from simulated $Z/\gamma^* \rightarrow \tau^+\tau^-$, $W \rightarrow \tau\nu$ and $Z' \rightarrow \tau^+\tau^-$ events as signal and jets from a di-jet event rejection sample in 2011 data as background. The inverse background efficiency (background rejection) is shown as a function of the τ_{had} identification efficiency in Figure 5.8. The τ_{had} identification efficiency is defined as the ratio of the number of identified hadronic τ -lepton decays that are matched to a true hadronic τ -lepton decay with $p_T > 20$ GeV and $|\eta| < 2.5$ within $\Delta R = 0.2$ and the number true hadronic τ -lepton decays with the same requirements. It is measured in samples of simulated $Z/\gamma^* \rightarrow \tau^+\tau^-$, $W \rightarrow \tau\nu$ and $Z' \rightarrow \tau^+\tau^-$ events. The inverse jet-to- τ_{had} misidentification efficiency is defined as the ratio of the number of τ_{had} candidates that are reconstructed and identified and the number of reconstructed τ_{had} candidates in a di-jet selection applied to data. For the τ_{had} analysis loose, medium and tight working points are used. The working points are defined by a signal efficiency of 60%, 50% and 30% for one-prong and 65%, 55% and 35% for multi-prong τ_{had} candidates. The requirement on the BDT score is evaluated as a function of the transverse momentum of the τ_{had} candidate and the number of vertices in the event.

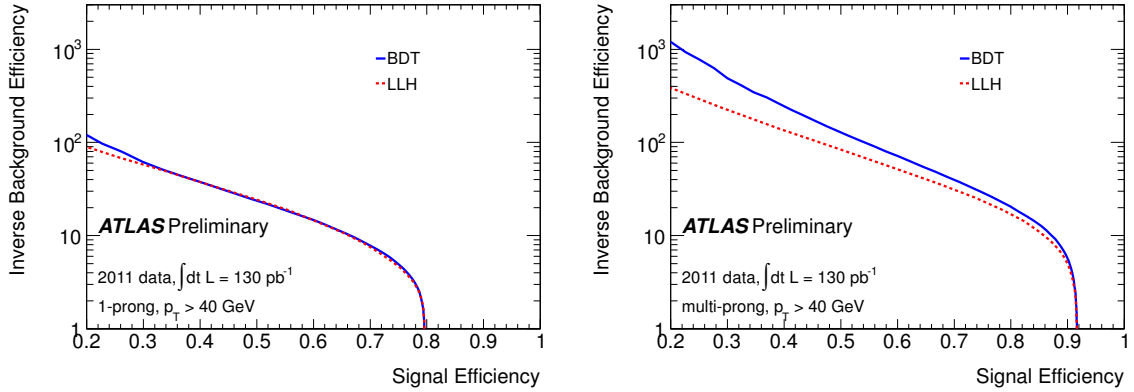


Figure 5.8.: The inverse jet-to- τ_{had} misidentification probability as a function of the τ_{had} identification efficiency is shown for the boosted decision tree discriminant (BDT) and the likelihood discriminant (LLH) and for one-prong (left-hand side) and multi-prong (right-hand side) τ_{had} candidates with $p_T > 40$ GeV. For the $\tau_{\text{had}}\tau_{\text{had}}$ analysis loose, medium and tight working points are defined with a signal efficiency of 60%, 50% and 30% for one-prong and 65%, 55% and 35% for multi-prong τ_{had} candidates (taken from Reference [193]).

Electrons can resemble one-prong hadronic τ -lepton decays if they feature sufficient energy deposits in the hadronic calorimeters and a compact energy cluster is associated. A boosted-decision-tree discriminant based on variables such as the electromagnetic energy fraction and the track radius of the τ_{had} candidate is used to reject electrons that are misidentified as hadronic one-prong τ -lepton decays. The details of the discriminant and the input variables are available in Reference [193]. The electron veto requirement has a signal efficiency of 85%.

In addition to the discriminants that are defined to reject misidentified electrons and jets a muon veto is defined. Muons can be misidentified as hadronic τ -lepton decays if an independent calorimeter cluster from pile-up jets or a collinear photon radiation is associated with the muon or if the muon deposits a substantial amount of energy in the calorimeters. The muon veto uses the electromagnetic energy fraction and the fact that in most cases the muon momentum and the muon's measured energy deposits differ significantly to reject these objects. The signal efficiency for this veto is approximately 96% and the rejection 55% for medium BDT τ_{had} identification requirements.

5.4.4. Measurement of the Identification Efficiency of Hadronic τ -Lepton Decays

The efficiency of the identification of hadronic τ lepton decays is measured in data using a sample of $Z/\gamma^* \rightarrow \tau_\mu \tau_{\text{had}}$ and $W \rightarrow \tau_{\text{had}} \nu$ events with a tag-and-probe method. For a tag-and-probe method events of a distinct type, e.g. $Z/\gamma^* \rightarrow \tau_\mu \tau_{\text{had}}$ or $W \rightarrow \tau_{\text{had}} \nu$ events, are selected using only information from a subset of the reconstructed objects, the so-called “tag”, e.g. the leptonic τ -lepton decay or the missing transverse energy, so that an unbiased measurement can be performed with the objects that have not been used in the selection of the event sample, the so-called “probe”, e.g. an additional hadronic τ -lepton decay.

The details of the selection, the background estimation and the efficiency measurement are documented in References [193, 195]. The $Z/\gamma^* \rightarrow \tau_\mu \tau_{\text{had}}$ events are selected with a single-muon trigger and an isolated muon. Additional requirements on the p_T of the muon, the

transverse mass of the muon and the missing transverse momentum system, the azimuthal angles between the τ_{had} candidate and the the missing transverse momentum and the muon and the missing transverse momentum and the invariant mass of the visible τ_{had} decay products and the muon are applied. The $W \rightarrow \tau_{\text{had}}\nu$ event sample is selected with an E_T^{miss} trigger, an electron and muon veto and requirements on the missing transverse momentum, the azimuthal angle between the τ_{had} candidate and the missing transverse momentum. Events are selected if at least one τ_{had} candidate is present and the transverse mass of the τ_{had} candidate and the missing transverse momentum system is consistent with W boson production. Because of the selection $W + \geq 1$ jet events are enhanced in the $W \rightarrow \tau_{\text{had}}\nu$ event sample. The multi-jet background, the background from exclusive quark and gluon production in strong interaction, in the $Z/\gamma^* \rightarrow \tau_\mu\tau_{\text{had}}$ event sample is estimated using a two-dimensional side-band extrapolation method and the background from W -boson production is estimated using a one-dimensional sideband extrapolation. The methods used are similar to the ones described for the search for $h/A/H \rightarrow \tau_{\text{had}}\tau_{\text{had}}$ decays in Section 7.1.3. For the $W \rightarrow \tau_{\text{had}}\nu$ event sample the background is estimated using templates of the distributions of the number of tracks for the signal process and the background processes. The individual contributions of the signal and background processes are obtained by fitting the relative contributions of the templates to the number of tracks distribution in data.

The efficiency of the τ_{had} identification is measured by comparing the number of events that pass the selection and have an additional τ_{had} candidate with and without the τ_{had} identification requirements in data and simulated event samples. A p_T -binned and a p_T -inclusive measurement is performed. The results of the measurement in the $Z/\gamma^* \rightarrow \tau_\mu\tau_{\text{had}}$ event sample are shown in Figure 5.9. The efficiencies determined in simulated event samples are

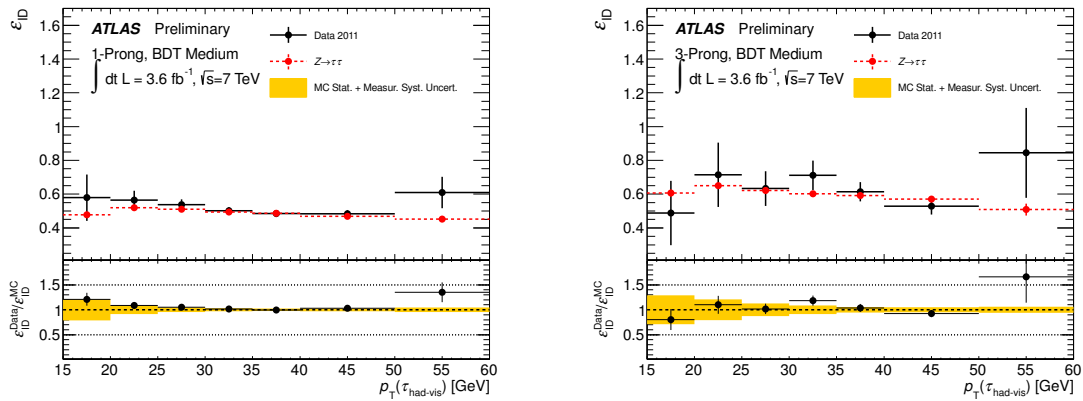


Figure 5.9.: Measurement of the hadronic τ -lepton identification efficiency in $Z/\gamma^* \rightarrow \tau_\mu\tau_{\text{had}}$ events for one-prong τ_{had} candidates (left-hand side) and three-prong τ_{had} candidates (right-hand side). The measured identification efficiency is shown for the BDT medium identification working point together with the systematic and statistical uncertainties for the measurement in data and the statistical uncertainties for the measurement using simulated events. The ratio of the efficiencies measured in data and simulated events is shown at the bottom (taken from Reference [193]).

consistent with the efficiencies determined in data for all measurements and no correction factors need to be applied to simulated events. The uncertainties of the measurements are dominated by the uncertainty of the multi-jet background estimate and the statistical uncer-

tainty. For each τ_{had} identification level the uncertainty of the more precise measurement is used as the final uncertainty. These uncertainties are shown in Table 5.4.

In this thesis the jet-to- τ_{had} misidentification probability is measured together with the corresponding misidentification probability at the trigger level. This measurement is documented in Section 6.5.3 and the results are shown in Figure 6.29.

Identification level	One-prong τ_{had} decays	Three-prong τ_{had} decays
BDT loose	4%	8%
BDT medium	5%	8%
BDT tight	4%	7%

Table 5.4.: Uncertainty of the identification efficiency for hadronic τ -lepton decays. The uncertainties are valid for hadronic τ -lepton decays with $p_T > 22$ GeV. For hadronic τ -lepton decays with $20 \text{ GeV} < p_T < 22 \text{ GeV}$ the uncertainties are doubled. The measurement of the efficiencies is described in detail in Reference [193].

5.5. Electrons and Muons

Electrons and muons are not used directly in the search for $h/A/H \rightarrow \tau_{\text{had}}\tau_{\text{had}}$. However, a veto on electrons and muons is applied to remove backgrounds with real electrons and muons, such as $Z/\gamma^* \rightarrow \ell^+\ell^-$ and $W \rightarrow \ell\nu$. The reconstruction and identification of electrons and muons is described in Sections 5.5.1 and 5.5.2, respectively.

5.5.1. Electron Reconstruction and Identification

For the reconstruction of electrons, clusters are created from longitudinal towers in the electromagnetic calorimeter using a sliding-window algorithm with a window size of 0.075×0.125 in η - ϕ space. Electron candidates are energy clusters in the electromagnetic calorimeter that are matched to a track. For the matching, tracks are extrapolated to the middle layer of the calorimeters. Tracks are matched if the difference between the cluster centre and the track pseudorapidity and azimuthal angle fulfil $\Delta\eta < 0.05$ and $\Delta\phi < 0.05$ or $\Delta\phi < 0.1$. The size of the $\Delta\phi$ window is 0.05 on the side to which the track bends in the magnetic field and 0.1 on the other side where the energy from bremsstrahlung losses is expected. In the case that more than one track is matched to an electron, tracks with silicon hits are preferred and the one with smallest ΔR between the track and the cluster is chosen.

Electrons are selected if they have a transverse energy $E_T > 15 \text{ GeV}$ and meet quality requirements based on the detector conditions and on whether high-noise cells are part of the energy cluster. The pseudorapidity of the cluster and the track has to lie within $|\eta| < 2.47$, but outside the transition region between the barrel and end-cap calorimeters defined by $|\eta| \in [1.37, 1.52]$. The energy of electrons is recalibrated to take into account different cluster sizes in the barrel and the end-cap, energy leakage and energy losses in front of the calorimeter.

For the identification of electrons the medium identification requirements, which correspond to a jet rejection factor of approximately 5000, are used. They include requirements on the shower shape in the electromagnetic calorimeter, the hadronic leakage, the electromagnetic calorimeter strip layer energy and shower width, the track quality and the track-cluster matching. More details about the electron reconstruction and identification are documented in Reference [197].

The efficiency of the electron identification algorithm was measured with a tag-and-probe method in $Z/\gamma^* \rightarrow e^+e^-$ and $W \rightarrow e\nu_e$ events from data using the method described in Reference [197]. In $Z/\gamma^* \rightarrow e^+e^-$ events one electron is used to select the events and the reconstruction and identification efficiency is measured using the other electron. The selection of $W \rightarrow e\nu_e$ events is primarily based on requirements on the missing transverse momentum and the transverse mass of the electron- E_T^{miss} system. Correction factors for the simulation and their uncertainties have been derived from the comparison of the reconstruction and identification efficiencies in data and simulated event samples. The energy scale is initially calibrated with simulated event samples and single-particle test beam measurements. The final calibration is derived from $Z/\gamma^* \rightarrow e^+e^-$, $J/\Psi \rightarrow e^+e^-$ with the methods described in Reference [197]. In $Z/\gamma^* \rightarrow e^+e^-$ and $J/\Psi \rightarrow e^+e^-$ events the di-electron mass is reconstructed as a function of the p_T -dependent calibration constants for the electron energy scale and a likelihood based the difference of the measured and the known Z -boson and J/Ψ -meson mass is minimised to obtain the most probable values of the calibration constants. In addition, the energy resolution was measured in $Z/\gamma^* \rightarrow e^+e^-$ events. In $W \rightarrow e\nu_e$ events the W -boson mass can not be reconstructed due to the unknown neutrino momentum and the variable E/p , the ratio of the energy measured in the calorimeters and the momentum measured in the tracking systems, is compared in simulation and data to cross-check the energy calibration.

5.5.2. Muon Reconstruction and Identification

For the muon reconstruction used in this thesis, track segments in the muon chambers are reconstructed with pattern matching algorithms and matched to hits in the trigger chambers. Two or more track segments in the muon system are combined to form a track that is subsequently matched to an inner detector track to form the so-called combined STACO muons [198, 199]. For the quality of the track fits, $\chi^2 < 150$ is required for five degrees of freedom [200]. Energy losses and scattering in the calorimeters are taken into account. The information of the reconstructed momentum in the muon system and the inner detector is combined by using the weighted average of the two independent measurements. The combination of the muon-spectrometer track properties with the information of the inner-detector track improves the momentum resolution at momenta lower than 100 GeV and allows for a rejection of secondary muons from π/K decays using the vertex information. In the barrel, the inner-detector measurement dominates the combination for $p_T \leq 80$ GeV and for $p_T \approx 100$ GeV the inner-detector and muon-spectrometer measurements feature comparable uncertainties.

Muons are required to have $p_T > 10$ GeV and $|\eta| < 2.5$. In addition, a good track has to be associated to the muon. A good track consists of a hit in the B -layer of the pixel detector if the track passes functional B -layer sensors, at least one hit in the pixel detector, ≥ 6 hits in the SCT detector and < 3 holes in the pixel and SCT detectors. Missing hits in sensors that are known to be non-functional are counted as existing hits.

For the reconstruction of the missing transverse momentum stand-alone muons, which are reconstructed solely based on information from the muon spectrometer, are used in addition to combined muons [199].

The muon reconstruction efficiency was measured in $Z/\gamma^* \rightarrow \mu^+\mu^-$ and $J/\Psi \rightarrow \mu^+\mu^-$ events with a tag-and-probe method, where one muon is used to select the event and the reconstruction efficiency is measured for the second muon [199, 200]. The average muon reconstruction efficiency is 0.928 ± 0.002 .

The muon momentum resolution is measured in $Z/\gamma^* \rightarrow \mu^+\mu^-$ and $W \rightarrow \mu\nu$ events in

data and simulation and the simulation is corrected to the value obtained from data [201]. In $Z/\gamma^* \rightarrow \mu^+\mu^-$ events the invariant di-muon mass is used while for $W \rightarrow \mu\nu$ events the difference between the momentum measurements in the inner detector and the muon spectrometer is used to determine the momentum resolution.

5.6. Missing Transverse Momentum

The reconstruction of missing transverse momentum, E_T^{miss} , is important in events with stable particles that cannot be reconstructed in the detector, e.g. neutrinos from τ -lepton decays in $Z/\gamma^* \rightarrow \tau^+\tau^-$ events. The missing transverse momentum of an event is defined as the negative vectorial sum of the transverse momenta of all particles in the event. In the ATLAS reconstruction process, calorimeter cells are associated with reconstructed objects in the following order: electrons, photons, hadronically decaying τ leptons, jets and muons. Cells that are not associated with any such object are accounted for in the so-called CELLOUT term. The total missing transverse momentum is the combination of all individual missing transverse momentum terms for the different object types,

$$E_x^{\text{miss}} = E_x^{\text{miss},e} + E_x^{\text{miss},\gamma} + E_x^{\text{miss},\tau} + E_x^{\text{miss},\text{jets}} + E_x^{\text{miss},\text{softjets}} + E_x^{\text{miss},\text{calo},\mu} + E_x^{\text{miss},\text{CellOut}} + E_x^{\text{miss},\mu} \quad [202], \quad (5.12)$$

where each term is the sum of the energy of the cells associated with the objects. The mentioned sum of cell energies is defined by

$$E_x^{\text{miss,term}} = - \sum_{i=1}^{N_{\text{cell}}^{\text{term}}} E_i \sin \theta_i \cos \phi_i, \\ E_y^{\text{miss,term}} = - \sum_{i=1}^{N_{\text{cell}}^{\text{term}}} E_i \sin \theta_i \sin \phi_i, \quad (5.13)$$

where E_i is the energy of cell i . The variables θ_i and ϕ_i are the azimuthal angle and the polar angle of the calorimeter cell centre and $N_{\text{cell}}^{\text{term}}$ is the number of cells that contribute to the considered E_T^{miss} term. Equation 5.12 holds for the y-component of the missing transverse momentum accordingly. Only cells associated with electrons, photons or topological clusters associated with hadronically decaying τ leptons, jets and muons or unassociated clusters are used to suppress the influence of energy from noise in non-clustered cells. The terms $E_x^{\text{miss},e}$ and $E_x^{\text{miss},\gamma}$ are obtained from cells associated with medium electrons or tight photons with $p_T > 10$ GeV, the energy is calibrated with the electron energy calibration for the electron term or at the electromagnetic scale for the photon term. The term $E_x^{\text{miss},\tau}$ is reconstructed from cells associated with hadronic τ -lepton decays with medium τ_{had} identification requirements and $p_T > 10$ GeV. The energy is calibrated with the LCW scheme. The terms $E_x^{\text{miss},\text{softjets}}$, $E_x^{\text{miss},\text{jets}}$ are composed of the energy of cells associated with anti- k_T jets with radius parameter 0.6 and $7 \text{ GeV} < p_T < 20 \text{ GeV}$ and $p_T > 20 \text{ GeV}$, respectively. The cell energies are calibrated with the LCW scheme. For jets with $p_T > 20$ GeV the jet energy calibration is applied in addition. The $E_x^{\text{miss},\text{CellOut}}$ term is calculated from the cells of topoclusters that are not associated with any object. The energy is calibrated using the LCW scheme or from the transverse momentum of tracks associated with the cell. In addition, energy from tracks that do not reach the calorimeter is added. $E_x^{\text{miss},\mu}$ is the negative sum of the momenta of combined muons with $|\eta| < 2.5$ and stand-alone muons with $2.5 < |\eta| < 2.7$. For muons that are matched to a jet with $\Delta R < 0.3$ the $E_x^{\text{miss},\text{calo}}$ term contains the energy

of the associated cells and the $E_x^{\text{miss},\mu}$ term the difference between the cell energies and the muon energy.

The performance of the E_T^{miss} reconstruction is studied in $Z/\gamma^* \rightarrow \ell^+\ell^-$ and $W \rightarrow \ell\nu$ events in References [202, 203]. In Figure 5.10 the distribution of the missing transverse energy in $Z \rightarrow \mu\mu$ and $W \rightarrow e\nu$ events is shown.

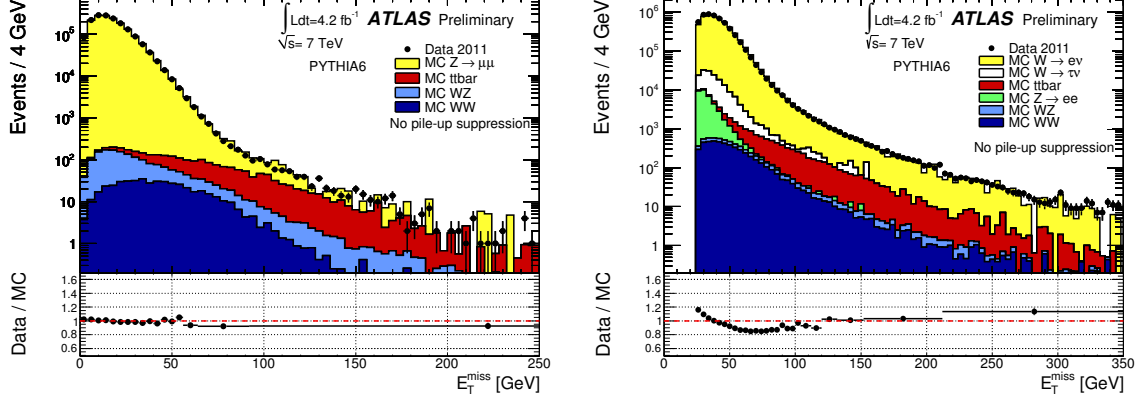


Figure 5.10.: Distribution of the missing transverse energy as measured in a data sample of $Z \rightarrow \mu\mu$ (left-hand side) and $W \rightarrow e\nu$ (right-hand side) events. The data are compared to the background expectation obtained from event samples that were simulated with the PYTHIA generator. In $Z \rightarrow \mu\mu$ events the missing transverse energy is primarily due to non-reconstructed objects and energy mismeasurements, while in $W \rightarrow e\nu$ events genuine missing transverse energy due to the undetected neutrino is expected (taken from Reference [203]).

6 The Search for the Higgs Bosons $h/A/H$ in the $\tau_{\text{had}}\tau_{\text{had}}$ Decay Channel

In this chapter a search for the neutral Higgs bosons $h/A/H$ predicted by two-Higgs-doublet models is described. The search is performed in the $h/A/H \rightarrow \tau_{\text{had}}\tau_{\text{had}}$ channel with two hadronically decaying τ leptons. In Sections 6.1 and 6.2 an overview of the signal and background processes and the corresponding simulated event samples is presented. In Section 6.3 the event selection is introduced and in Section 6.4 the calculation of the final discrimination variable, the mass of the $\tau_{\text{had}}\tau_{\text{had}}$ resonance, is described. The event selection is optimised to discriminate Higgs bosons from background processes, however the sensitivity towards the Higgs bosons from general two-Higgs-doublet models is retained. The methods for the estimation of the event yields for signal and background processes are described in Section 6.5. The systematic uncertainties of the event yields and the di- τ mass distributions are discussed in Section 6.6. The results of the search are shown in Section 6.7.

6.1. Signal Processes and Event Samples

Even though the described search is designed to be as model-independent as possible, i.e. it was attempted to be sensitive to generic two-Higgs-doublet models, the sensitivity of the search can only be evaluated for a limited set of signal hypotheses. For this analysis an MSSM signal hypothesis and generic Higgs boson production process in the context of a two-Higgs-doublet model are considered. In both cases it is assumed that Higgs bosons can be produced in the b -quark annihilation process, as discussed in Section 6.1.1, and the gluon-fusion process, as discussed in Section 6.1.2.

6.1.1. Simulation of Higgs Boson Production in b -quark Annihilation

The couplings of the Higgs bosons to fermions and gauge bosons are proportional to their masses, as shown in Table 2.4 for the MSSM. The coupling to b quarks is especially large and therefore Higgs boson production in b -quark annihilation is an important process over a wide range of parameters of supersymmetric models. The most important Feynman diagrams for the production of Higgs bosons in b -quark annihilation are shown in Figure 6.1. Event samples with CP-even Higgs bosons that are produced in b -quark annihilation and that decay to $\tau_{\text{had}}\tau_{\text{had}}$ were generated for masses from 100 GeV to 150 GeV in steps of 10 GeV, for 170 GeV and from 200 GeV to 500 GeV in steps of 50 GeV. Compared to the experimental mass resolution the natural width of the Higgs boson is negligible and the value of the width for the m_h^{max} parameter point with the considered m_A and $\tan\beta = 20$ is used for all values of $\tan\beta$. For the simulation of the Higgs boson production and decay the SHERPA generator [204] is used together with the parton distribution functions CTEQ6L1 [47]. The SHERPA generator features the automated generation of all tree-level matrix elements of the type “2 partons $\rightarrow \tau\tau + n$ partons” with $n \leq 3$ additional partons. Loop processes and couplings of the Higgs boson to quarks other than b quarks are not considered. The SHERPA generator uses its own hadronisation model and parton shower implementation and

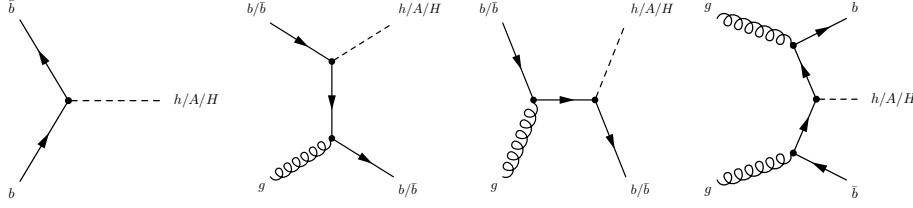


Figure 6.1.: Feynman diagrams for the perturbative partonic processes implemented in the SHERPA generator that is used for the production of the event sample with Higgs boson production in b -quark annihilation. The complete list of perturbative partonic processes, as documented in Table 6.1, can be derived by the addition of gluon radiations, radiated gluons that split into $q\bar{q}$ pairs and a quark or antiquark that radiates one of the incoming gluons. The decay of the Higgs bosons is not included in these diagrams.

the overlap between the partons produced in the parton shower and the partons produced based on the fixed-order calculation is resolved using the CKKW algorithm [59, 60].

The probability for the different $2 \text{ partons} \rightarrow \tau\tau + n \text{ partons}$ processes is shown in Table 6.1. In approximately 55% the parton final state consists of one b quark and two τ -lepton decays and in 36% of the cases a second b quark is present. In the following, Higgs boson production in b -quark annihilation will be denoted by $b\bar{b}h/A/H$, irrespective of the number of b quarks in the final state of the fixed-order calculation.

Process	Leading order in α_S	Fraction
$gb/\bar{b} \rightarrow A(\rightarrow \tau\tau)b/\bar{b}$	1	31.9 %
$gb/\bar{b} \rightarrow A(\rightarrow \tau\tau)b/\bar{b}g$	2	9.2 %
$q_4/\bar{q}_4b/\bar{b} \rightarrow A(\rightarrow \tau\tau)b/\bar{b}q_4/\bar{q}_4$	2	2.2 %
$gb/\bar{b} \rightarrow A(\rightarrow \tau\tau)b/\bar{b}gg$	3	5.3 %
$gb/\bar{b} \rightarrow A(\rightarrow \tau\tau)b/\bar{b}q_5\bar{q}_5$	3	3.2 %
$q_4/\bar{q}_4b/\bar{b} \rightarrow A(\rightarrow \tau\tau)b/\bar{b}q_4/\bar{q}_4g$	3	3.5 %
<hr/>		
$gg \rightarrow A(\rightarrow \tau\tau)b\bar{b}$	2	22.8 %
$gg \rightarrow A(\rightarrow \tau\tau)b\bar{b}g$	3	8.9 %
$q_4/\bar{q}_4g \rightarrow A(\rightarrow \tau\tau)q_4/\bar{q}_4b\bar{b}$	3	4.6 %
<hr/>		
$b\bar{b} \rightarrow A(\rightarrow \tau\tau)$	0	1.1 %
$b\bar{b} \rightarrow A(\rightarrow \tau\tau)g$	1	4.4 %

Table 6.1.: Perturbative partonic processes used for the generation of Higgs boson production in b -quark annihilation with the SHERPA generator and the fraction of the corresponding cross section of the full cross section. All partonic processes with a cross section fraction $\geq 1\%$ in the SHERPA $m_A = 300$ GeV event sample are shown with $q_4 \in \{u, d, c, s\}$ and $q_5 \in \{u, d, c, s, b\}$. For every process SHERPA generates only the tree-level Feynman diagrams. “Leading order in α_S ” refers to the order of α_S of the tree-level Feynman diagram.

The distribution of the generated transverse momenta of the τ leptons and the highest- p_T b -jet is shown in Figure 6.2. The distributions are obtained from the generated particle-level information of the Higgs boson event samples that were produced with masses of $m_H =$

150 GeV and $m_H = 300$ GeV. The same distributions are shown for $m_H = 200$ GeV in Figure 6.8 (left-hand side). The anti- k_T jet algorithm with distance parameter $R = 0.4$ is applied to the stable generated particles and jets are considered b -jets if they are matched to a true b quark with $p_T > 5$ GeV within $\Delta R = 0.3$. They are required to have $|\eta| < 2.5$ and to be separated from hadronic τ -lepton decays.

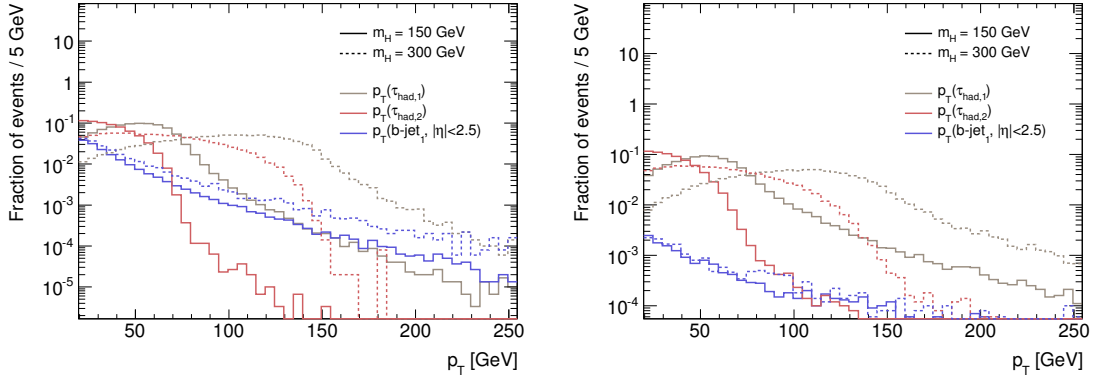


Figure 6.2.: Distribution of the generated visible transverse momentum of the highest- p_T τ lepton, second-highest- p_T τ lepton and highest- p_T generator-level b -jet for events with Higgs boson production in b -quark annihilation (left-hand side) and gluon fusion (right-hand side). The samples were generated with Higgs boson masses of $m_H = 150$ GeV and $m_H = 300$ GeV. The distributions are obtained from simulated samples produced with the generators SHERPA and POWHEG.

6.1.2. Simulation of Higgs Boson Production in Gluon Fusion

Higgs bosons do not couple directly to gluons. However, at orders higher or equal to α_S^2 gluons can effectively couple to Higgs bosons via a quark loop as shown in the Feynman diagrams in Figure 6.3. CP-even Higgs boson production in gluon fusion is simulated using

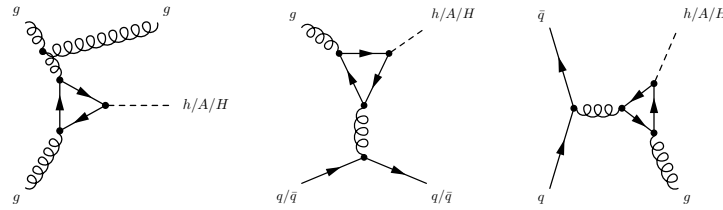


Figure 6.3.: The 2 partons $\rightarrow h/A/H + 1$ parton processes as implemented in the POWHEG generator that is used to generate the gluon-fusion Higgs boson production event samples. All shown processes have squared amplitudes proportional to α_S^3 . In the $m_H = 300$ GeV sample the $gg \rightarrow Hg$ process is used in 74.2% of the events, the $gq/\bar{q} \rightarrow Hq/\bar{q}$ process in 25.7% and the $q\bar{q} \rightarrow Hg$ process in 0.1%.

the POWHEG generator [61] with the Feynman diagrams from Figure 6.3. Event samples are produced using the same set of Higgs boson masses and the same width that are used for the b -quark annihilation event samples. Gluon radiation from quarks in the loop is not considered. For the $gb/\bar{b} \rightarrow h/H/Ab/\bar{b}$ and the $b\bar{b} \rightarrow h/H/Ag$ processes Feynman diagrams are implemented in the SHERPA (without quark loop) and the POWHEG (with quark loop)

generator. The interference between the Feynman diagrams is not considered. The CTEQ6.6 parton distribution functions [48] are used together with the multi-parton interaction model, the parton shower and the hadronisation model from PYTHIA [179]. The p_T spectrum of the Higgs boson obtained at NLO in α_S with POWHEG differs from the NNLL+NLO prediction obtained with HQT [205] for low- p_T Higgs bosons. Therefore, the Higgs boson p_T spectrum in POWHEG is reweighted to the spectrum obtained with HQT.

The distributions of the generated visible transverse momenta of the τ leptons and a possible b -jet are shown in Figure 6.2 (right-hand side) for Higgs boson masses of $m_H = 150$ GeV and $m_H = 300$ GeV.

6.1.3. The MSSM Signal Hypothesis

As described in Section 2.2.7 the m_h^{max} benchmark scenario is used to represent a larger class of supersymmetric models. For the search for $h/A/H \rightarrow \tau_{\text{had}}\tau_{\text{had}}$ decays signal hypotheses with $110 \text{ GeV} \leq m_A \leq 500 \text{ GeV}$ and $5 < \tan\beta < 60$ are considered. For lower masses the efficiency of the event selection described in Section 6.3 is too small and it is not possible to generate enough simulated events to achieve a reasonable statistical uncertainty of the event yield for the signal hypothesis. For masses significantly larger than 500 GeV the lower bound of the $\tan\beta$ exclusion is above $\tan\beta = 50$. For $\tan\beta \gg 50$ the third-generation Yukawa couplings become comparable and the electroweak symmetry breaking is more difficult if a universal $m_{H_{u,d}}^2$, as in the constrained MSSM, exists [206]. In addition $\tan\beta > 60$ is disfavored by the recent results of the $B_s \rightarrow \mu\mu$ analysis that are described in Section 2.5.6. Low values of $\tan\beta$, i.e. $\tan\beta < 5$, are close to the exclusion bound obtained from the searches at the LEP collider [89] (see Figure 2.17) and no exclusion is expected from the ATLAS search for MSSM Higgs bosons.

The masses, couplings and branching ratios of the Higgs bosons in the m_h^{max} scenario are calculated with FEYNHIGGS [77]. The masses are shown as a function of m_A in Figure 2.13. The dominant mechanisms for the production of MSSM Higgs bosons are b -quark annihilation and gluon-fusion production. For high values of $\tan\beta$ Higgs boson production in vector-boson fusion and in association with a W or Z boson has a small cross section compared to the other production channels and is not considered for this analysis. For Higgs boson production in b -quark annihilation the four-flavour [207, 208] and five-flavour scheme BBH@NLO cross section calculations [209] have been combined by the LHC Cross Section Working Group [72] with the ‘‘Santander matching scheme’’ described in Reference [210]. The cross sections for Higgs boson production in gluon fusion have been calculated with HIGLU [211] and GGH@NNLO [212].

As discussed in Sections 6.1.1 and 6.1.2 event samples for CP-even Higgs boson are generated. For a given m_h^{max} parameter point and the corresponding masses of the Higgs bosons $h/A/H$, the simulated signal samples of Higgs boson production in b -quark annihilation and gluon fusion with Higgs boson mass closest to the calculated values of m_h , m_A and m_H are scaled to the appropriate cross sections. The event samples for CP-even Higgs boson production are also employed for CP-odd Higgs boson production. The differences between the calculated Higgs boson natural widths and the generated Higgs boson width are negligible compared to the experimental mass resolution and neglected.

6.1.4. The Generic Higgs Boson Production Model

For the generic Higgs boson production model no specific cross sections and branching ratios are assumed and inference in the form of discovery significances or exclusion limits is made on the cross section for Higgs boson production multiplied with the branching ratio for the decay into $\tau^+\tau^-$ separately for the gluon-fusion and the b -quark annihilation processes. Only

one Higgs boson, ϕ , is considered and the difference between CP-even and CP-odd Higgs bosons is neglected. The intrinsic width of the Higgs boson mass is negligible compared to the experimental mass resolution and the value from the m_h^{\max} scenario with $\tan\beta = 20$ is used.

6.2. Background Processes and Event Samples

The search for Higgs bosons in the $\tau_{\text{had}}\tau_{\text{had}}$ decay channel builds on the identification of events with two hadronic τ -lepton decays and possibly accompanying b -jets. The reconstruction and identification of hadronic τ -lepton decays and b -jets was described in Sections 5.4 and 5.3. Identified hadronic τ -lepton decays can stem from τ leptons that are produced in the hard-scattering process, primarily in the decay of vector bosons, and from other objects that are misidentified as hadronic τ -lepton decays. Misidentified hadronic τ -lepton decays are primarily jets and to a lower extent electrons that pass the τ_{had} -identification criteria.

In Figure 6.4 the cross sections for different Standard Model benchmark processes are shown together with the cross section for the production of the MSSM Higgs bosons A and H in the m_h^{\max} scenario with $m_A = 300$ GeV and $\tan\beta = 20$. The relevant background processes for the search for $h/A/H \rightarrow \tau_{\text{had}}\tau_{\text{had}}$ are the production of at least two jets in QCD interactions, referred to as multi-jet production, the production of a W or Z boson, the production of top quarks and the production of two vector bosons, referred to as diboson production. It can be seen in Figure 6.4 that the cross sections for some of the background processes are larger than the one of the signal process by many orders of magnitude.

For the MSSM Higgs boson signal hypothesis also additional events from the production of squarks and gluinos are expected to contribute to the selected sample of signal candidate events. Two hadronic τ -lepton decays can be present in events with neutralino, chargino or $\tilde{\tau}$ production. Additional b quarks might be present if the gauginos stem from squark decays. While the phenomenology of MSSM Higgs bosons can be described by a small number of parameters, the phenomenology of general MSSM particle production is much richer and in practice it is not possible to consider this background for all parameter configurations of the MSSM. As supersymmetric particles have not been observed in searches for supersymmetry in events with at least one hadronic τ -lepton decay [214] and other searches for supersymmetry, it is assumed that the cross section for these events is several orders of magnitude lower than the production cross section of the most important other backgrounds. In the following, backgrounds from the production of sparticles are neglected. In the case of a discovery of an excess of events in a search for supersymmetry, the background from supersymmetric particle production has to be investigated in detail.

6.2.1. Multi-jet Production

The production of multi-jet events in QCD processes with at least one jet with $p_T > 20$ GeV occurs with a rate roughly eight orders of magnitude larger than the hypothesised production rate of the MSSM Higgs bosons A and H for $m_A = 300$ GeV and $\tan\beta = 20$ [215]. The dominant Feynman diagrams for the 2 partons \rightarrow 2 partons multi-jet production process are shown in Figure 6.5. The signature of multi-jet production is very different from that of the signal and no isolated high- p_T τ leptons are produced in multi-jet events. With the methods for the identification of hadronic τ -lepton decays this background can be efficiently reduced, but its high production rate means that events from multi-jet production constitute a significant background even for low jet-to- τ_{had} misidentification probabilities. The measurement of the jet-to- τ_{had} misidentification probability at the trigger and object selection level

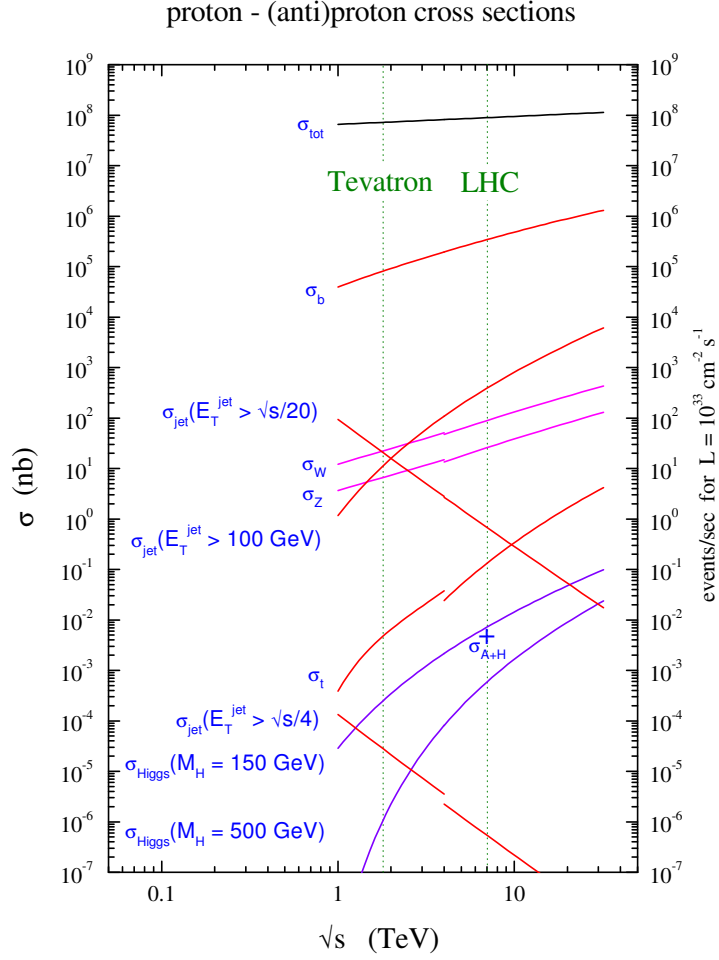


Figure 6.4.: Standard Model cross sections for different processes in $p\bar{p}$ collisions for centre-of-mass energies $\sqrt{s} < 4$ TeV and pp collisions for $\sqrt{s} > 4$ TeV (figure adapted from Reference [213]). Tevatron refers to the Tevatron Run II centre-of-mass energy of 1.96 TeV, LHC to the centre-of-mass energy of 7 TeV for the 2011 data-taking of the LHC. The total cross section is σ_{tot} and σ_{Higgs} is the cross section for the production of a Standard Model Higgs boson. The cross section for the production of the MSSM Higgs bosons A or H , σ_{A+H} , is shown for $\sqrt{s} = 7$ TeV and the parameter point $m_A = 300$ GeV, $\tan\beta = 20$ with a blue marker (+).

is documented for a sample of jets produced in association with a W boson in Section 6.5.3. The misidentification probability is approximately 3‰ for the medium τ_{had} identification requirements and 2‰ for the tight τ_{had} identification requirements. Therefore the multi-jet background is reduced by approximately 5 to 6 orders of magnitude by the τ_{had} identification criteria in the trigger and object selection. However, the jet-to- τ_{had} identification probability is highly dependent on the transverse momentum of the jet and whether the jet is initiated by the hadronisation of a quark or a gluon. Thus the misidentification probabilities are only an order-of-magnitude estimate. Due to the low selection efficiency for multi-jet background, a good understanding of the jet-to- τ_{had} misidentification probability at the trigger and event selection level and the properties of the misidentified jets is critical for an accurate estimation of the background from multi-jet production.

The estimation of the multi-jet background with simulated event samples was investigated.

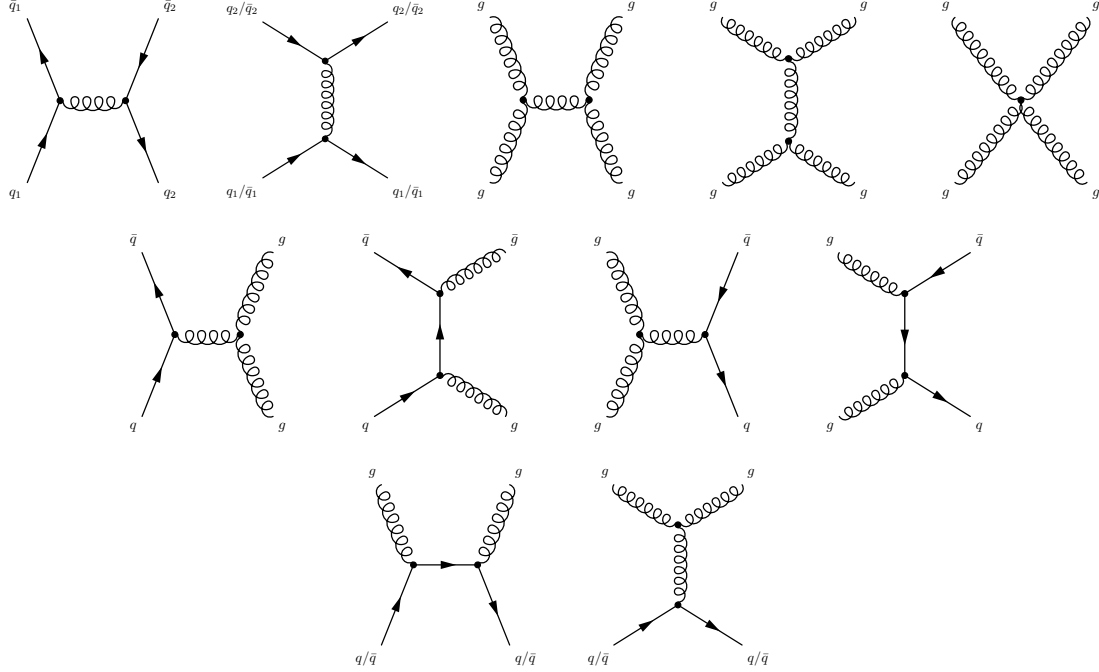


Figure 6.5.: Leading-order of α_S 2 partons \rightarrow 2 partons Feynman diagrams for di-jet production in proton-proton collisions.

The large cross section, however, makes the simulation of events computationally expensive. The application of event filters and the factorisation of the kinematic event selection and the τ_{had} identification criteria were investigated, but had to be discarded. Instead the data-driven background estimation technique described in Section 6.5.1 was developed to estimate the multi-jet background contribution.

6.2.2. Production of Z/γ^* and W Bosons

The production of Z bosons and off-shell photons, γ^* , which decay into two τ leptons which in turn decay hadronically is the most important source of non-reducible background. The kinematic properties are similar for $Z/\gamma^* \rightarrow \tau^+\tau^-$ and signal events, especially for low Higgs boson masses, and the di- τ mass distribution for signal events has its maximum on the tail of the distribution for Z -boson events. The branching ratio of $Z/\gamma^* \rightarrow \tau^+\tau^-$, $Z/\gamma^* \rightarrow e^+e^-$ and $Z/\gamma^* \rightarrow \mu^+\mu^-$ decays is approximately 3.37% [6] for each of the decay channels. Events with Z bosons that decay into electrons, muons or τ leptons which in turn decay leptonically can be strongly suppressed by a veto on identified electrons or muons and the identification criteria for hadronic τ -lepton decays.

The production of Z/γ^* bosons is simulated with the ALPGEN generator [216] for the $\tau^+\tau^-$, $\mu^+\mu^-$ and e^+e^- decay channels. The set of parton distribution functions CTEQ6L1 [47] is used together with the multi-parton interaction model from the JIMMY generator [66] and the parton shower and the hadronisation model from HERWIG [217]. For the decay into τ leptons, event samples with $10 \text{ GeV} < m_{\tau\tau} < 40 \text{ GeV}$ (“low-mass Drell-Yan process”), $m_{\tau\tau} > 40 \text{ GeV}$ (“resonant Z -boson production”) and three samples with $150 \text{ GeV} < m_{\tau\tau} < 250 \text{ GeV}$, $250 \text{ GeV} < m_{\tau\tau} < 400 \text{ GeV}$ and $m_{\tau\tau} > 400 \text{ GeV}$ (“high-mass Drell-Yan process”) were generated. For the sample of high-mass Drell-Yan events a larger number of events per expected event is produced in order to reduce the statistical uncertainty for events with high- p_T τ leptons. As events with $m_{\tau\tau} > 150 \text{ GeV}$ are included in the event samples with

the resonant Z -boson production and high-mass Drell-Yan production, the events from the first sample are removed using generator-level information. For the decay into electrons and muons only the low-mass Drell-Yan process and the resonant Z -boson production are simulated and no overlap removal is needed. All samples are additionally split into event samples including the $2 \rightarrow 2$, $2 \rightarrow 3$, $2 \rightarrow 4$, $2 \rightarrow 5$, $2 \rightarrow 6$ and $2 \rightarrow 7$ partons Feynman diagrams with two leptons in the final state. Loop contributions are not considered and the overlap between events with partons from the parton shower and partons from the fixed-order calculation is removed with the MLM matching procedure [58]. The Feynman diagrams for Z -boson production in the $2 \rightarrow 2$ and $2 \rightarrow 3$ partons processes are shown in Figure 6.6.

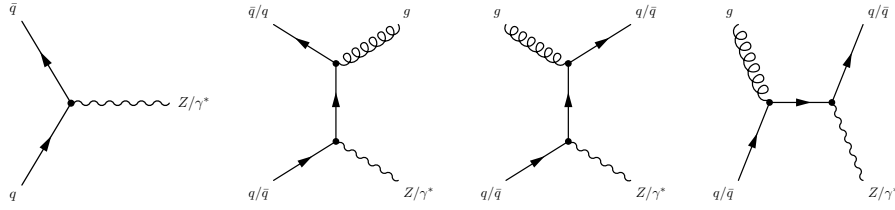


Figure 6.6.: Subset of the Feynman diagrams for the production of Z bosons in proton–proton collisions as used in the ALPGEN generator. Only the tree-level Feynman diagrams with no or one additional parton are shown.

In the event samples described above only quarks of the first two generations are used in the fixed-order calculation and it is assumed that their mass is negligible. Special event samples for the production of $Z/\gamma^* b\bar{b}$ with up to 3 additional light quarks and gluons in the fixed-order calculation are simulated. The most important Feynman diagrams for this event sample are shown in Figure 6.7. The overlap with events where heavy flavour quarks are produced in the parton shower is removed based on generator-level information with the HFOR tool [218].

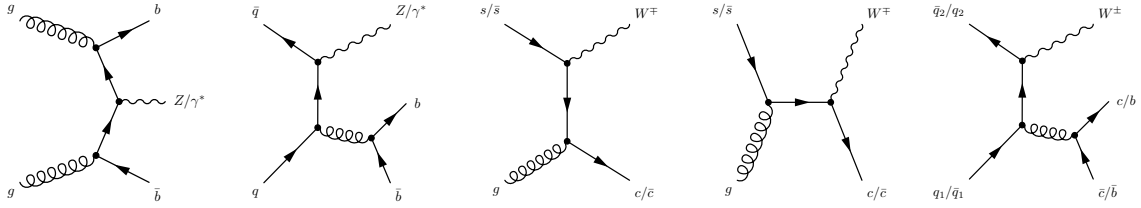


Figure 6.7.: Subset of the Feynman diagrams for the production of a Z boson in association with a $b\bar{b}$ pair or a W -boson in association with a c quark, a $c\bar{c}$ pair or a $b\bar{b}$ pair in proton–proton collisions as used in the ALPGEN generator. Only tree-level Feynman diagrams with no additional partons are shown. Feynman diagrams where the Z boson is radiated off a final state quark are not shown.

Distributions of the visible transverse momenta of the τ leptons and the highest- p_T b -jet are shown together with the di- τ invariant mass for $Z/\gamma^* \rightarrow \tau^+\tau^-$ events and a comparison to distributions from events with Higgs boson production in Figure 6.8. The distributions are obtained from the generated particle-level information of the event samples that are simulated with ALPGEN. The anti- k_T jet algorithm with distance parameter $R = 0.4$ is run on the stable generated particles. Jets are considered b -jets if they are matched to a true b quark with $p_T > 5$ GeV within $\Delta R = 0.3$. They are required to have $|\eta| < 2.5$ and to be separated from hadronic τ -lepton decays. The invariant mass is calculated based on generated information,

consequently only the intrinsic resolution is included. Experimentally the dominant source of the mass resolution is the missing information about the momentum four-vector of the neutrinos in the mass reconstruction. For the search documented in this thesis instead of the invariant mass which can not be reconstructed unambiguously in events with neutrinos, a mass reconstruction technique, which uses inference on the neutrino four-vectors, the Missing Mass Calculator (MMC), is used. The MMC technique is described in detail in Section 6.4. It can be seen in Figure 6.8 that $Z/\gamma^* \rightarrow \tau^+\tau^-$ events can be discriminated from events with Higgs boson production based on the lower p_T of the hadronic τ -lepton decays and the lower reconstructed di- τ mass. Additional discrimination is achieved in events with b -jets.

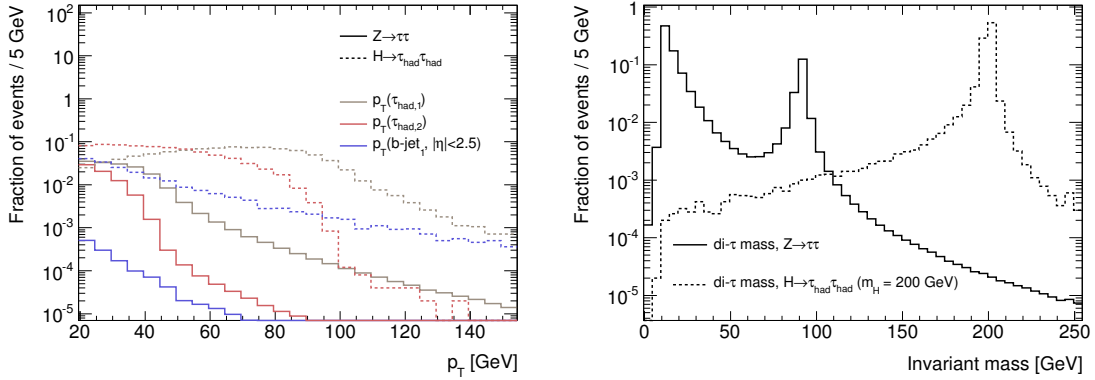


Figure 6.8.: Distributions of the generated visible transverse momenta of the highest- p_T hadronic τ -lepton decay, the second highest- p_T hadronic τ -lepton decay and the highest- p_T generator-level b -jet together with the distribution of the generated invariant mass of the two τ leptons for $Z/\gamma^* \rightarrow \tau^+\tau^-$ and $h/A/H \rightarrow \tau_{\text{had}}\tau_{\text{had}}$ simulated event samples. For the $h/A/H \rightarrow \tau_{\text{had}}\tau_{\text{had}}$ event sample $m_H = 200$ GeV is used. The distributions are obtained from ALPGEN samples of $Z/\gamma^* \rightarrow \tau^+\tau^-$ events and events with Higgs bosons produced in b -quark annihilation with the SHERPA generator. Additional information about the reconstruction of the shown quantities is provided in Section 6.2.2.

The production of a W boson is an important background to the search for $h/A/H \rightarrow \tau_{\text{had}}\tau_{\text{had}}$ decays if the W boson decays into a τ lepton which in turn decays hadronically and an additional jet is misidentified as a hadronic τ -lepton decay. Additional b -jets can stem from associated heavy-flavour quark production. The branching ratio of $W^+ \rightarrow \tau^+\nu_\tau$ is approximately 11.25% [6]. Events with a W boson that decays into an electron or a muon do not constitute a relevant source of background.

The production of W bosons with positive and negative electric charge is simulated with the ALPGEN generator [216] for the $\tau\nu_\tau$, $\mu\nu_\mu$ and $e\nu_e$ decay channels. The parton distribution functions CTEQ6L1 [47] are used together with the multi-parton interaction model from the JIMMY generator [66] and the parton shower and the hadronisation model from HERWIG [217]. Samples with up to five additional quarks or gluons in the final state of the fixed-order calculation are simulated. The most important Feynman diagrams for W -boson production are shown in Figure 6.9.

Similar to the event samples for the production of Z bosons, no b quarks are included in the final state of the fixed-order calculation and all other quarks, including c quarks, are assumed to be massless. Special simulated event samples for the production of a W boson in association with a c/\bar{c} quark, a $c\bar{c}$ pair or a $b\bar{b}$ pair together with up to three additional

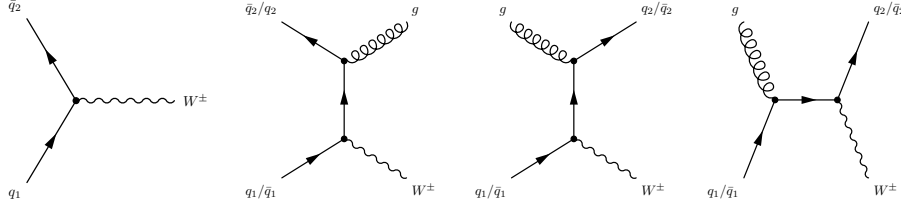


Figure 6.9.: Subset of the Feynman diagrams for the production of W bosons in proton–proton collisions as used in the ALPGEN generator. Only the tree-level Feynman diagrams with no or one additional parton are shown.

partons (four additional partons for Wc/\bar{c} production) in the final state of the fixed-order calculation are generated. The overlap with the light flavour event samples is removed with the HFOR tool [218].

The cross sections for W - and Z -boson production with $40 \text{ GeV} < m_{\ell\ell} < 2 \text{ TeV}$ and $\ell = e, \mu, \tau$ are calculated in Reference [219] at next-to-next-to-leading (NNLO) order of perturbative QCD with the cross-section calculators FEWZ [220] and ZWPROD [221] and the parton distribution functions MSTW2008 [50]. The results and their uncertainties due to parton distribution function and the scale parameter uncertainties are documented in Table 6.2. The cross sections for the processes corresponding to the individual event samples are obtained by multiplying the ratio of the ALPGEN cross section for the considered sample and the total ALPGEN cross section with the total cross section as obtained with ZWPROD.

For the Z/γ^* -boson event samples with $m_{\ell\ell} < 40 \text{ GeV}$ and $\ell = e, \mu, \tau$ it is assumed that the ratio of the ALPGEN and the NNLO cross section is comparable to the one obtained for the events with $m_{\ell\ell} > 40 \text{ GeV}$. For the search for $h/A/H \rightarrow \tau_{\text{had}}\tau_{\text{had}}$ decays, a cross-section uncertainty of $\pm 5\%$ is assigned for all event samples with W - and Z/γ^* -boson production.

Process	Cross section	Scale uncertainty	PDF uncertainty	Total uncertainty
$Z/\gamma^* \rightarrow \tau^+\tau^-$	1.07 nb	+0.5% −0.7%	+4.5% −3.9%	+4.5% −4.0%
$W^+ \rightarrow \tau^+\nu_\tau$	6.16 nb	+0.5% −0.8%	+4.9% −4.1%	+4.9% −4.2%
$W^- \rightarrow \tau^-\bar{\nu}_\tau$	4.30 nb	+0.6% −0.8%	+4.4% −4.2%	+4.4% −4.3%

Table 6.2.: Cross sections and their uncertainties for Z - and W -boson production at pp colliders at $\sqrt{s} = 7 \text{ TeV}$. The quoted cross sections include the decay branching ratio into $\tau^+\tau^-$, $\tau^+\nu_\tau$ or $\tau^-\bar{\nu}_\tau$. For the decays into e^+e^- , $e^+\nu_e$, $e^-\bar{\nu}_e$ and $\mu^+\mu^-$, $\mu^+\nu_\mu$, $\mu^-\bar{\nu}_\mu$ the same cross sections are used. The term “Scale uncertainty” refers to uncertainties that are derived from variations of the renormalisation and factorisation scale by factors of 1/2 and 2. The term “PDF uncertainty” denotes the 90% confidence level uncertainty of the set of parton distribution functions MSTW2008 and the “total uncertainty” is the quadratic sum of the scale and PDF uncertainties.

Distributions of the important kinematic variables of $W \rightarrow \tau\nu$ events and a comparison with events with Higgs boson production can be found in Figure 6.10. The main rejection of $W \rightarrow \tau\nu$ events is achieved with the hadronic τ -lepton decay identification as one jet has to be misidentified as a hadronic τ -lepton decay. Additional rejection can be based on requirements on the visible τ_{had} p_T . It can be seen that $W \rightarrow \tau\nu$ events lead to a broad di- τ mass spectrum.

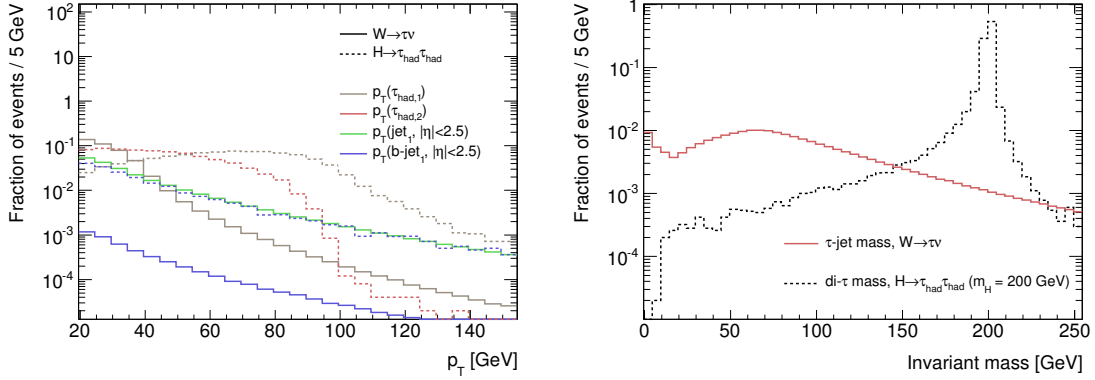


Figure 6.10.: Distributions of the generated visible transverse momenta of the highest- p_T hadronic τ -lepton decay, the highest- p_T generator-level jet, the highest- p_T generator-level b -jet for $W \rightarrow \tau\nu$ and $h/A/H \rightarrow \tau_{\text{had}}\tau_{\text{had}}$ simulated event samples together with the distributions of the generated invariant mass of the highest- p_T τ lepton and the highest- p_T generator-level jet for $W \rightarrow \tau\nu$ and the di- τ mass for $h/A/H \rightarrow \tau_{\text{had}}\tau_{\text{had}}$ simulated event samples. For the $h/A/H \rightarrow \tau_{\text{had}}\tau_{\text{had}}$ event sample $m_H = 200$ GeV is used. If $W \rightarrow \tau\nu$ events pass the event selection, the highest- p_T jet is expected to be misidentified as a hadronic τ -lepton decay. The distributions are obtained from ALPGEN simulated samples of $W \rightarrow \tau\nu$ events and events with Higgs bosons produced in b -quark annihilation with the SHERPA generator. Additional information about the reconstruction of the shown quantities is provided in Section 6.2.2.

6.2.3. Production of Top-Quark Pairs and Single Top Quarks

In events with $t\bar{t}$ production the top-quark pair decays via $t\bar{t} \rightarrow b\bar{b}W^+W^-$ with a high branching fraction. In global fits of the Standard Model reported in Reference [6]

$$V_{tb} = 0.999146^{+0.000021}_{-0.000046} \quad (6.1)$$

and thus $\text{BR}(t\bar{t} \rightarrow b\bar{b}W^+W^-) > 99\%$ are obtained. The production of top-quark pairs is a relevant background if either two hadronically decaying τ leptons are produced in the decay of the W bosons or at least one jet is misidentified as a hadronic τ -lepton decay. In the search channel with an identified b -jet, the fraction of the background from $t\bar{t}$ is enhanced due to the existence of a b quark with significant transverse momentum in the top-quark decay chain.

Simulated event samples for $t\bar{t}$ production are generated with a top-quark mass of $m_{\text{top}} = 172.5$ GeV with the MC@NLO generator [62] in next-to-leading order of α_S . Events are produced with top-quark decays into a W boson, a b quark or light quark and all W -boson decay channels. The leading-order Feynman diagrams for $t\bar{t}$ production are shown in Figure 6.11. The parton distribution functions CT10 [49] are used together with the multi-parton interaction model from the JIMMY generator [66] and the parton shower and hadronisation model from HERWIG [217].

The cross section for top-quark pair production is calculated at approximate next-to-leading order of α_S with the resummation of next-to-next-to-leading order logarithms with the HATHOR tool [222, 223] and the CTEQ6.6 parton distribution functions [48]. The results are documented in Table 6.3. Uncertainties have been derived from variations of the factorisation and renormalisation scales and PDF variations. For the $h/A/H \rightarrow \tau_{\text{had}}\tau_{\text{had}}$ analysis a

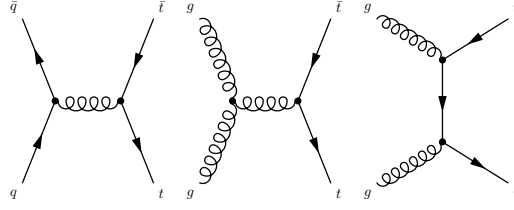


Figure 6.11.: Leading-order of α_S Feynman diagrams contributing to the matrix element of the MC@NLO generator for $t\bar{t}$ production in proton–proton collisions. In the left-hand and middle Feynman diagrams the s-channel production and in the right-hand Feynman diagram the t-channel production are shown. The next-to-leading order of α_S Feynman diagrams that contribute to the perturbative partonic process implemented in MC@NLO are not shown.

conservative $t\bar{t}$ production cross-section uncertainty of $\pm 10\%$ is used.

Single-top production can be a background to the search for $h/A/H \rightarrow \tau_{\text{had}}\tau_{\text{had}}$ decays if the top quark is produced in association with a W boson (Wt -channel), where the top quark decays via $t \rightarrow bW$ and the two W bosons decay into τ leptons which in turn decay hadronically. An additional contribution is due to the production of one hadronically decaying τ lepton accompanied by a jet that is misidentified as a hadronic τ -lepton decay in the s-channel, t-channel or Wt -production. Because of the b quark in a $t \rightarrow bW$ decay, the fraction of the single-top production background is increased in the search channels where a b -jet is required.

The simulation of single-top production for a top-quark mass of 172.5 GeV is performed with the ACERMC generator [224] together with the multi-parton interaction model, the parton shower and the hadronisation model of PYTHIA [179]. The Feynman diagrams for the hard-scattering processes used in the ACERMC generator are shown in Figure 6.12. The phase space overlap between the diagrams in the t-channel is removed [225]. The modified leading order parton distribution functions MRST2007 [51] are used. For the Wt -production channel all W -boson decay channels are considered, for the s- and t-channel production only the decay of the W boson into an electron, a muon or a τ lepton is considered. The contribution of the decay channels where the W boson decays into quarks to the final event yield is negligible.

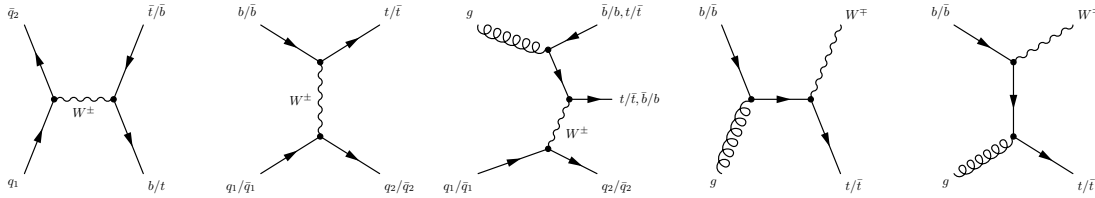


Figure 6.12.: Leading-order and next-to-leading order of α_S Feynman diagrams for the perturbative partonic processes implemented in ACERMC for single-top production in proton–proton collisions. The first diagram shows the s-channel production, the second and third diagrams show the t-channel production and the fourth and fifth diagrams show the Wt -channel production.

The cross sections for single-top production have been calculated in References [226, 227, 228] at next-to-leading order accuracy with the resummation of next-to-next-to-leading logarithms, so that approximate next-to-next-to-leading order precision is achieved. The parton

distribution functions MSTW2008 [50] are used. Uncertainties have been derived from variations of the factorisation and renormalisation scales and PDF variations. The results and the uncertainties of the calculations are shown in Table 6.3. For the $h/A/H \rightarrow \tau_{\text{had}}\tau_{\text{had}}$ analysis a conservative single-top production cross-section uncertainty of $\pm 10\%$ is used. For the estimate of the single-top background with s- and t-channel production a branching ratio of $\text{BR}(W \rightarrow \ell\nu) = 0.324$, where $\ell = e, \mu, \tau$, is used.

Process	Cross section	Scale uncertainty	PDF uncertainty	Total uncertainty
$t\bar{t}$	164.57 pb	$+4.3\%$ -4.0%	$+7.0\%$ -9.6%	$+8.2\%$ -10.4%
t , s-channel	3.19 pb	$\pm 1.9\%$	$+4.1\%$ -3.1%	$+4.4\%$ -3.8%
\bar{t} , s-channel	1.44 pb	$\pm 0.7\%$	$+4.2\%$ -4.9%	$+4.2\%$ -4.9%
t , t-channel	41.92 pb	$\pm 2.0\%$	$+3.8\%$ -0.5%	$+4.3\%$ -2.1%
\bar{t} , t-channel	22.65 pb	$\pm 2.2\%$	$+3.0\%$ -4.0%	$+3.7\%$ -4.6%
$W^\mp t/\bar{t}$	15.74 pb	$\pm 2.5\%$	$+7.0\%$ -7.2%	$+7.4\%$ -7.7%

Table 6.3.: Cross sections and their uncertainties for the production of single top quarks and top-quark pairs in pp collisions with $\sqrt{s} = 7$ TeV. The cross sections and uncertainties have been calculated as described in Section 6.2.3 and do not include decay branching ratios.

In the following the combination of the background from $t\bar{t}$ and single-top production is referred to as top background. Distributions of the important kinematic variables of events with top-quark production and a comparison to events with Higgs boson production can be found in Figure 6.13. Events with top-quark production can be selected in the search for $h/A/H \rightarrow \tau_{\text{had}}\tau_{\text{had}}$ decays if either two hadronic τ -lepton decays are present or if one hadronic τ -lepton decay is accompanied by the misidentification of a jet as a hadronic τ -lepton decay. In events with two hadronic τ -lepton decays one of the decays usually has low transverse momentum, however misidentified jets can lead to events with two high- p_T τ_{had} candidates. In a sample where one additional b -jet is required the top background can be reduced by an upper limit on the transverse momentum of the b -jet. Events with $t\bar{t}$ and single-top production feature a broad, non-resonant di- τ mass spectrum.

6.2.4. Diboson Production

Diboson production includes the production of W^+W^- , $W^\pm Z$ and ZZ pairs. The most important leading-order Feynman diagrams are shown in Figure 6.14. Diboson production can be a relevant background to the search for $h/A/H \rightarrow \tau_{\text{had}}\tau_{\text{had}}$ decays if at least two hadronically decaying τ leptons stem from the two gauge bosons.

For the background estimation diboson production is simulated at next-to-leading order of α_S with the MC@NLO generator [62] for all decay channels where at least one vector boson decays into an electron, a muon or a τ lepton. W - and Z -boson production with electroweak radiation of a second vector boson from the decay products of the first vector boson and the decay channel where both vector bosons decay into quarks are not simulated. The contribution to the final background expectation of the decay channel into four quarks is considered negligible.

The parton distribution functions CT10 [49] are used together with the multi-parton interaction model from the JIMMY generator [66] and the parton shower and hadronisation model from HERWIG [217]. For the W^+W^- production process on- and off-shell W bosons

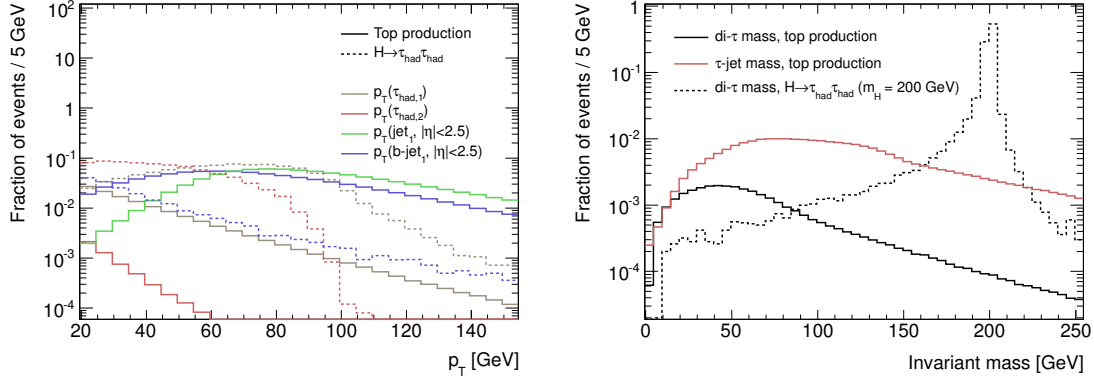


Figure 6.13.: Distributions of the generated visible transverse momenta of the highest- p_T hadronic τ -lepton decay, the second highest- p_T hadronic τ -lepton decay, the highest- p_T generator-level jet, the highest- p_T generator-level b -jet together with the distributions of the generated invariant mass of the two highest p_T τ leptons and the highest- p_T τ lepton and the highest- p_T generator-level jet for samples of top decays from $t\bar{t}$ and single-top production and $h/A/H \rightarrow \tau_{\text{had}}\tau_{\text{had}}$ simulated event samples. For the $h/A/H \rightarrow \tau_{\text{had}}\tau_{\text{had}}$ event sample $m_H = 200$ GeV is used. If events with top decays pass the event selection either two hadronic τ -lepton decays are present or the highest- p_T jet is expected to be misidentified as a hadronic τ -lepton decay. The distributions are obtained from event samples that were simulated with the MC@NLO and ACERMC generators and samples with Higgs bosons produced in b -quark annihilation that were simulated the SHERPA generator. Additional information about the reconstruction of the shown quantities is provided in Section 6.2.2.

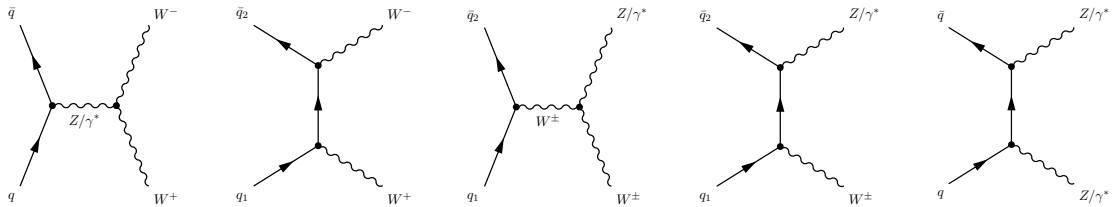


Figure 6.14.: Leading-order of α_S Feynman diagrams for W^+W^- , $W^\pm Z$ and ZZ pair production in pp collisions. The higher-order gluon-induced vector boson pair production processes are not shown in this figure.

are considered, while for the $W^\pm Z$ and ZZ production processes only on-shell W and Z bosons are considered.

The cross sections for vector boson pair production are calculated in Reference [219] with the parton-level Monte Carlo program MCFM [229], the MSTW2008 parton distribution functions [50] at next-to-leading order of α_S . For Z -boson production $66 \text{ GeV} < m_{\ell\ell} < 116 \text{ GeV}$ is used, while for W -boson production no such requirement is employed. Uncertainties have been derived from variations of the factorisation and renormalisation scale and PDF variations. The results are shown in Table 6.4. For the $h/A/H \rightarrow \tau_{\text{had}}\tau_{\text{had}}$ analysis a conservative cross-section uncertainty of $\pm 7\%$ is used for all processes with diboson production.

The contribution of gluon-induced W -boson pair production as described in Reference [230]

Process	Cross section	Scale uncertainty	PDF uncertainty	Total uncertainty
W^+W^-	44.92 pb	+3.6% -2.9%	+4.2% -3.5%	+5.5% -4.5%
W^+Z	11.50 pb	+5.5% -4.2%	+4.3% -3.4%	+7.0% -5.5%
W^-Z	6.47 pb	+5.7% -4.3%	+4.3% -4.0%	+7.1% -5.9%
ZZ	5.64 pb	+2.6% -2.1%	+4.3% -3.5%	+5.0% -4.1%

Table 6.4.: Cross sections and their uncertainties for diboson production in pp collisions at $\sqrt{s} = 7$ TeV [219]. The quoted cross sections do not include the vector boson decay branching ratios.

was estimated with the acceptance for leading order of α_S W^+W^- production and the cross section for $gg \rightarrow W^+W^-$. It was found to contribute approximately 2.9% [219] to the background from W^+W^- production. Gluon-induced Z -boson pair production as described in Reference [231] contributes approximately 5.7% [219] to the background from ZZ production. Due to the small background from gluon-induced diboson production this contribution is neglected.

Distributions of the important kinematic variables for diboson events and a comparison to events with Higgs boson production can be found in Figure 6.15. Diboson events can be discriminated from events with Higgs bosons with the same variables that are used for electroweak single-boson production. The di- τ invariant mass spectrum has a resonant component if both τ leptons are produced in the decay of the same Z boson and a non-resonant component for other backgrounds.

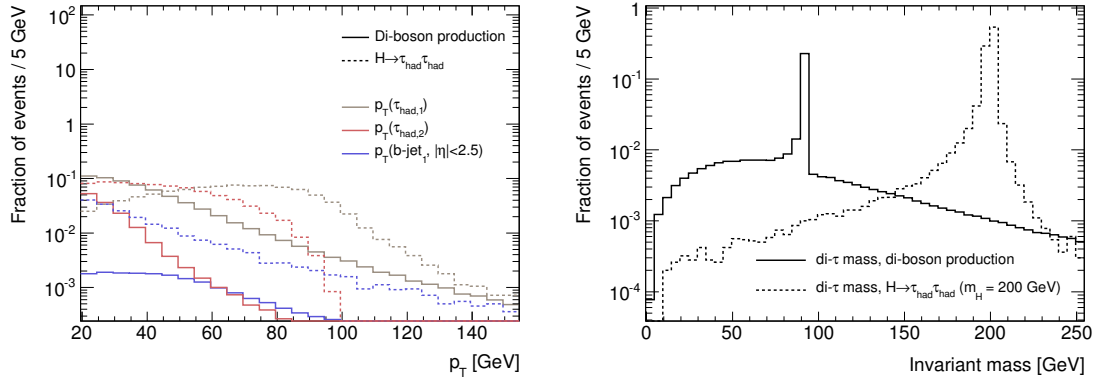


Figure 6.15.: Distributions of the generated visible transverse momenta of the highest- p_T hadronic τ -lepton decay, the second highest- p_T hadronic τ -lepton decay, the highest- p_T generator-level b -jet together with the distribution of the generated invariant mass of the two τ leptons for W^+W^- , $W^\pm Z$, ZZ and $h/A/H \rightarrow \tau_{\text{had}}\tau_{\text{had}}$ simulated event samples. For the $h/A/H \rightarrow \tau_{\text{had}}\tau_{\text{had}}$ event sample $m_H = 200$ GeV is used. The distributions are obtained from MC@NLO simulated event samples and events with Higgs bosons produced in b -quark annihilation with the SHERPA generator. Additional information about the reconstruction of the shown quantities is given in Section 6.2.2. The low width of the resonance peak at the Z -boson mass is an artefact of the generation process, in which only on-shell ZZ production is simulated.

6.3. Event Selection

Based on the signal and background topologies described in Sections 6.1 and 6.2 a set of selection criteria is established to increase the ratio of the signal and background event yields. The event selection was derived following the concept of “semi-blind analysis optimisation”. In particle physics searches, control and signal regions are defined. Signal regions are data samples with high signal-to-background event yield ratio and are optimised to discriminate the signal-and-background and the background-only hypothesis. Control regions are usually disjoint from the signal region, have low signal-to-background event yield ratios and are used to validate background estimation techniques. Contrary to a “blind analysis optimisation” in a semi-blind analysis optimisation, collision data in control regions is used to derive the selection criteria and to validate the background estimation techniques. The number of events after the selection and the distribution of the final discriminating variable, the di- τ mass, in the signal region is not viewed until the selection criteria and the methods for the background estimation are fixed in order to avoid a selection bias from the observed data. In this section, first the on-line selection of the data sample with a di- τ_{had} trigger is described, then the off-line selection criteria are described.

6.3.1. Data Sample and Trigger

In the majority of events with Higgs bosons that decay into two τ leptons which in turn decay hadronically, no high- p_T electrons or muons are present. Therefore, the trigger for this analysis has to be based on the more complex triggers for hadronic τ -lepton decays and the single-lepton triggers cannot be used. On average, the reconstructed jets that can be matched to hadronic τ -lepton decays are more narrow in η - ϕ space compared to jets that are initiated by the hadronisation of quarks or gluons. At level 1 the τ trigger uses electromagnetic and hadronic calorimeter trigger towers to calculate the energy in a so-called core region in order to form an L1 τ cluster. The core region consists of four trigger towers and has a size of $\Delta\eta \times \Delta\phi = 0.2 \times 0.2$. For the $h/A/H \rightarrow \tau_{\text{had}}\tau_{\text{had}}$ analysis an L1 trigger that requires one τ cluster with at least 8 GeV of energy in the core region and one different cluster with at least 11 GeV of energy in the core region (trigger item L1_2TAU8_TAU11) is used for the data-recording periods prior to September 2011 (periods B2 to K). For the data-recording periods after September 2011 (periods L and M) a trigger with one cluster with at least 11 GeV of energy and one different cluster with at least 15 GeV of energy is used (trigger item L1_2TAU11_TAU15).

The level 2 decision is based on calorimeter and tracking information in the Regions of Interest seeded by the L1 trigger. For all data periods two hadronic τ -lepton decays with $p_T > 29$ GeV and $p_T > 20$ GeV, medium τ_{had} identification level and between 1 and 4 tracks are required. In the event filter selection two hadronic τ -lepton decays with $p_T > 29$ GeV and $p_T > 20$ GeV, medium τ_{had} identification level and 1 to 3 tracks are required [232]. The event filter triggers used before (EF_tau29_medium1_tau20_medium1 for periods B2 to K) and after September 2011 (EF_tau29T_medium1_tau20T_medium1 for periods L and M) are identical, apart from the different level 1 seed triggers. For an instantaneous luminosity of $\mathcal{L} = 1.5 \cdot 10^{33} \text{ cm}^{-2}\text{s}^{-1}$ the rate of the triggers is approximately 12 Hz for the trigger used before and 10 Hz for the trigger used after September 2011.

The distribution of the visible p_T of the τ_{had} candidates in an event sample with Higgs boson production in b -quark annihilation is shown for $m_H = 120$ GeV in Figure 6.16. Evidently the choice of the τ_{had} p_T thresholds for the trigger has a crucial impact on the signal efficiency. In a sample of events with Higgs boson production with $m_H = 120$ GeV the signal efficiency

of the trigger is approximately 9.5% and for Higgs boson production with $m_H = 200$ GeV approximately 22%. For background events the trigger efficiencies are 2% for $Z/\gamma^* + \text{jets}$ and top-quark production, 0.2% for $W + \text{jets}$ production and 9% for diboson production.

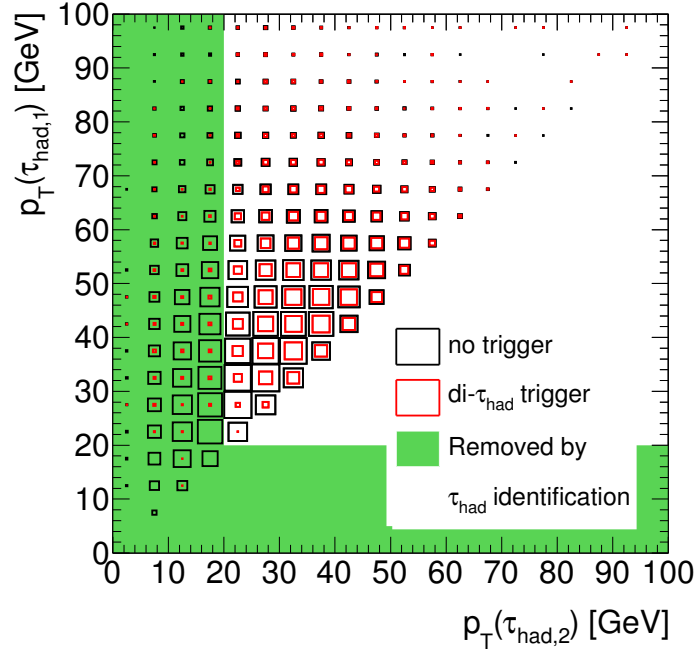


Figure 6.16.: The distribution of the transverse momentum of the highest and second highest- p_T τ_{had} candidate is shown as obtained from a sample of Higgs boson production in b -quark annihilation with $m_H = 120$ GeV. It is shown for events that are selected by a di- τ_{had} trigger (EF_tau29_medium1_tau20_medium1) and all events. The τ_{had} candidates are selected with the requirements defined in Section 5.4 and medium τ_{had} identification requirements. For the reconstruction of τ_{had} candidates a minimum transverse momentum of 20 GeV is required, however no further p_T selection is applied. The area coloured in green shows the p_T region in which at most one hadronic τ -lepton decay can be reconstructed. In the event sample with two hadronic τ -lepton decays with $p_T > 20$ GeV and medium τ_{had} identification requirements the efficiency of the trigger is approximately 36%.

The use of a single- τ_{had} trigger and di- τ_{had} triggers with different thresholds was studied. In the latest run in October 2011 (run 191933) the lowest unprescaled single hadronic τ -lepton decay trigger (EF_tau125_medium1) requires a transverse momentum of 125 GeV at the event filter level. This in turn results in a too low signal efficiency. Different di- τ_{had} triggers similarly lead to a lower signal efficiency or prevent the estimation of the multi-jet background with the method described in Section 6.5.1.

With the described di- τ_{had} triggers a data sample of pp collisions at $\sqrt{s} = 7$ TeV corresponding to an integrated luminosity of $\int \mathcal{L} dt = (4.60 \pm 0.18) \text{ fb}^{-1}$ can be selected for the analysis. The sample consists of data recorded from March 22, 2011 to October 30, 2011. The corresponding run numbers, triggers and the integrated luminosity are shown in Table 6.5. Only luminosity blocks where all detector parts are working and where no major data quality defects are present are selected using the so-called Good Runs List (GRL). Data quality defects are assigned to all collisions in a luminosity block if problems in a subdetector or the

Period	Runs	Trigger p_T thresholds		$\int \mathcal{L} dt / \text{pb}^{-1}$
		L2 and EF	L1	
B2	178044 - 178109	29 GeV, 20 GeV	11 GeV, 8 GeV	11.7
D	179725 - 180481	29 GeV, 20 GeV	11 GeV, 8 GeV	159.8
E	180614 - 180776	29 GeV, 20 GeV	11 GeV, 8 GeV	48.2
F	182013 - 182519	29 GeV, 20 GeV	11 GeV, 8 GeV	134.5
G	182726 - 183462	29 GeV, 20 GeV	11 GeV, 8 GeV	531.3
H	183544 - 184169	29 GeV, 20 GeV	11 GeV, 8 GeV	256.5
I	185353 - 186493	29 GeV, 20 GeV	11 GeV, 8 GeV	320.7
J	186516 - 186755	29 GeV, 20 GeV	11 GeV, 8 GeV	223.5
K	186873 - 187815	29 GeV, 20 GeV	11 GeV, 8 GeV	554.9
L	188921 - 190343	29 GeV, 20 GeV	15 GeV, 11 GeV	1367.5
M	190608 - 191933	29 GeV, 20 GeV	15 GeV, 11 GeV	991.7
All	178044 - 191933			4600.3

Table 6.5.: Data periods, corresponding run ranges, used di- τ_{had} trigger p_T thresholds and corresponding integrated luminosity.

reconstruction of objects are detected during or shortly after the data-taking. In this thesis the mentioned integrated luminosities refer to the values after the data with quality defects were removed.

6.3.2. Additional Data Quality Requirements

To ensure that only events from pp collisions are selected, the reconstruction of at least one vertex with four or more associated tracks is required. No requirement on the impact parameters of the tracks is applied. Occasionally events contain localised high-energy calorimeter deposits that do not originate from proton-proton collisions, but from sporadic discharges in the hadronic end-cap calorimeter, coherent noise in the electromagnetic calorimeter or hard bremsstrahlung from cosmic-ray muons. These events are rare, but create high-energy tails in the E_T^{miss} distribution [233]. Events with jets with a transverse energy exceeding 20 GeV that result from these effects are removed with dedicated event cleaning requirements [234]. In addition, events with data integrity errors or noise bursts in the LAr calorimeter are vetoed. From 30 April 2011 to 28 June 2011 (runs 180614 to 184169) six front-end boards of the electromagnetic calorimeter read-out system were non-functional. As a consequence the calorimeter channels corresponding to the region with $\phi \in [-0.74, -0.64]$ and $\eta \in [0, 1.4]$ could not be read out. Jets that point into this dead region can be mismeasured and lead to missing transverse momentum. Consequently events within this data-taking period and with jets with $p_T > 20$ GeV, $-0.1 < \eta < 1.5$ and $-0.9 < \phi < -0.5$ are vetoed in data and simulation.

6.3.3. Electron and Muon Vetoes

As the $h/A/H \rightarrow \tau_{\text{had}}\tau_{\text{had}}$ signal process does not lead to high- p_T electrons or muons, events with high- p_T electrons and muons are vetoed in order to suppress background from $Z/\gamma^* \rightarrow e^+e^-/\mu^+\mu^-$ and $W \rightarrow e\nu/\mu\nu$ decays in single-boson, diboson or top-quark produc-

tion. In addition, this requirement ensures that the event samples that are selected for the MSSM Higgs boson search in other final states, i.e. $h/A/H \rightarrow \mu\mu$, $h/A/H \rightarrow \tau_{\text{lep}}\tau_{\text{lep}}$ and $h/A/H \rightarrow \tau_{\text{lep}}\tau_{\text{had}}$, are orthogonal and hence statistical independence can be assumed for the combination of the results. Electrons are selected according to Section 5.5.1 and events are vetoed if at least one electron with $p_T > 15$ GeV is identified. Muons are selected according to Section 5.5.2 and events are vetoed if at least one muon with $p_T > 10$ GeV is identified.

6.3.4. Selection of the Hadronic τ -lepton Decays

The most important part of the event selection is the selection of two hadronic τ -lepton decays. Candidates for hadronic τ -lepton decays are considered if they can be matched to a trigger-level τ_{had} candidate within $\Delta R = 0.2$. The matched trigger-level τ_{had} candidate is required to induce a single- τ_{had} trigger with a p_T threshold of 20 GeV (EF_tau20_medium1 or EF_tau20T_medium1 depending on the data-taking period). At least one of the two τ_{had} candidates is required to be matched to a trigger-level τ_{had} candidate that fulfils the requirements of a single- τ_{had} trigger with a 29 GeV threshold (EF_tau29_medium1 or EF_tau29T_medium1). The efficiency of the single- τ_{had} triggers is shown in Figure 6.27 as a function of the τ_{had} transverse momentum. The efficiency is steeply rising for $20 \text{ GeV} < p_T < 30 \text{ GeV}$ for the 20 GeV trigger threshold and for $30 \text{ GeV} < p_T < 40 \text{ GeV}$ for the 29 GeV trigger threshold. In order to avoid problems with threshold effects from the p_T selection of the τ_{had} trigger, the τ_{had} candidates are required to have $p_T > 45$ GeV for the highest- p_T τ_{had} candidate and $p_T > 30$ GeV for the second highest- p_T τ_{had} candidate.

Hadronic τ -lepton decays can be identified with a boosted decision tree discriminant with three different working points, the “loose”, “medium” and “tight” working points. They are defined with τ_{had} identification efficiencies of 60%, 50% and 30% for one-prong and 65%, 55% and 35% for multi-prong τ_{had} candidates. It should be noted that the medium τ_{had} identification requirements used by the τ_{had} trigger are less stringent compared to the medium τ_{had} identification requirements of the off-line identification. The method with which the multi-jet background is estimated requires the selection of events in control regions that are based on the τ_{had} identification requirements and statistically independent from the signal region. Events in the signal region can be selected with any combination of the loose, medium and tight identification requirements for the two τ_{had} candidates. However, if for one of the two hadronic τ -lepton decays only loose requirements are used, the number of events in the control regions is too low for a reliable estimation of the multi-jet background which is described in Section 6.5.1. In consequence for the signal region selection it is possible to require that both τ_{had} candidates pass the medium τ_{had} identification level (“medium-and-medium”), one candidate passes the medium τ_{had} identification level and one the tight τ_{had} identification level (“medium-and-tight”) or both candidates pass the tight τ_{had} identification level (“tight-and-tight”).

The τ_{had} identification process requires that τ_{had} candidates have one or three associated tracks and charge $\pm 1e$, however there is no requirement on the charge product of the two τ -leptons. Because the two τ leptons are produced in the decay of a neutral Higgs boson for signal, they are required to have opposite charge. This requirement reduces the background from jets that are misidentified as hadronic τ -lepton decays for which same-charge events are expected more often than for events with hadronic τ -lepton decays from neutral resonances.

A good discrimination between signal and background can be provided by a kinematic selection that uses the transverse momenta of the two selected τ_{had} candidates and the missing transverse momentum in the event. In signal events missing transverse momentum is expected due to the two neutrinos in the final state, while multi-jet events are not a sig-

nificant source of high- p_T neutrinos and are expected to have low E_T^{miss} . The distribution of the transverse momenta of the two highest- p_T hadronic τ -lepton decays and the missing transverse momentum is shown in Figure 6.17 after the selection of two τ_{had} candidates with opposite charge. One of the τ_{had} candidates is required to pass the tight and one the medium τ_{had} identification requirements. The requirements of the kinematic selection are optimised after the event sample is split into two separate subsamples with the procedure described in the following section.

6.3.5. Categorisation into Events With and Without b -jet

After the selection described above the event sample is split into two orthogonal subsamples, the b -tagged and the b -vetoed subsamples. Events are considered for the b -tagged sample if the highest- p_T jet is b -tagged and satisfies $20 \text{ GeV} < p_T < 50 \text{ GeV}$; events are considered for the b -vetoed sample if either there is no additional jet, the highest- p_T jet has $p_T > 50 \text{ GeV}$ or the highest- p_T jet is not b -tagged. In the following this selection step is referred to as the b -jet requirement. The p_T distributions of the highest- p_T jet and the variable MV1 which is used for the discrimination of light and b -jets and described in Section 5.3.3, is shown in Figure 6.18. In the b -vetoed sample the requirement on the highest- p_T hadronic τ -lepton decay is tightened to $p_T > 60 \text{ GeV}$, in the b -tagged sample $p_T > 45 \text{ GeV}$ is required. In both subsamples $E_T^{\text{miss}} > 25 \text{ GeV}$ is required and one hadronic τ -lepton decay needs to fulfil the tight and the other hadronic τ -lepton decay the medium τ_{had} identification requirements (medium-and-tight).

The τ_{had} transverse momentum, the missing transverse momentum and the τ_{had} identification requirements have been optimised separately for the b -tagged and the b -vetoed selection with a sample of events with Higgs boson production for $m_A = 200 \text{ GeV}$. For the three different choices of the hadronic τ -lepton identification levels, medium-and-medium, medium-and-tight, tight-and-tight, the requirements on the p_T of the highest- p_T and the second highest- p_T hadronic τ -lepton decay and the missing transverse momentum are optimised with TMVA [196] and the expected cross-section exclusion at the 95% confidence level is compared for the different τ_{had} identification levels. The calculation of the expected cross-section exclusion is described in Section 7. It is expected that approximately these results hold for a wide variety of signal hypotheses. The results of this optimisation procedure are summarised in Table 6.6.

Selection requirement	b -tagged selection	b -vetoed selection
τ_{had} identification level	medium-and-tight	
p_T of the highest- p_T τ_{had} candidate	$> 45 \text{ GeV}$	$> 60 \text{ GeV}$
p_T of the second highest- p_T τ_{had} candidate	$> 30 \text{ GeV}$	
Missing transverse momentum	$> 25 \text{ GeV}$	
Charge product	-1 (opposite charge)	

Table 6.6.: Summary of the requirements used for the selection of the two hadronic τ -lepton decays for the b -tagged and the b -vetoed event samples. In addition to the shown requirements events have to be selected by a di- τ_{had} trigger and the hadronic τ -lepton decays are required to be matched with the trigger-level τ_{had} decays. The values of the τ_{had} identification and p_T requirements and the E_T^{miss} requirement have been obtained from the optimisation procedure described in Section 6.3.5.

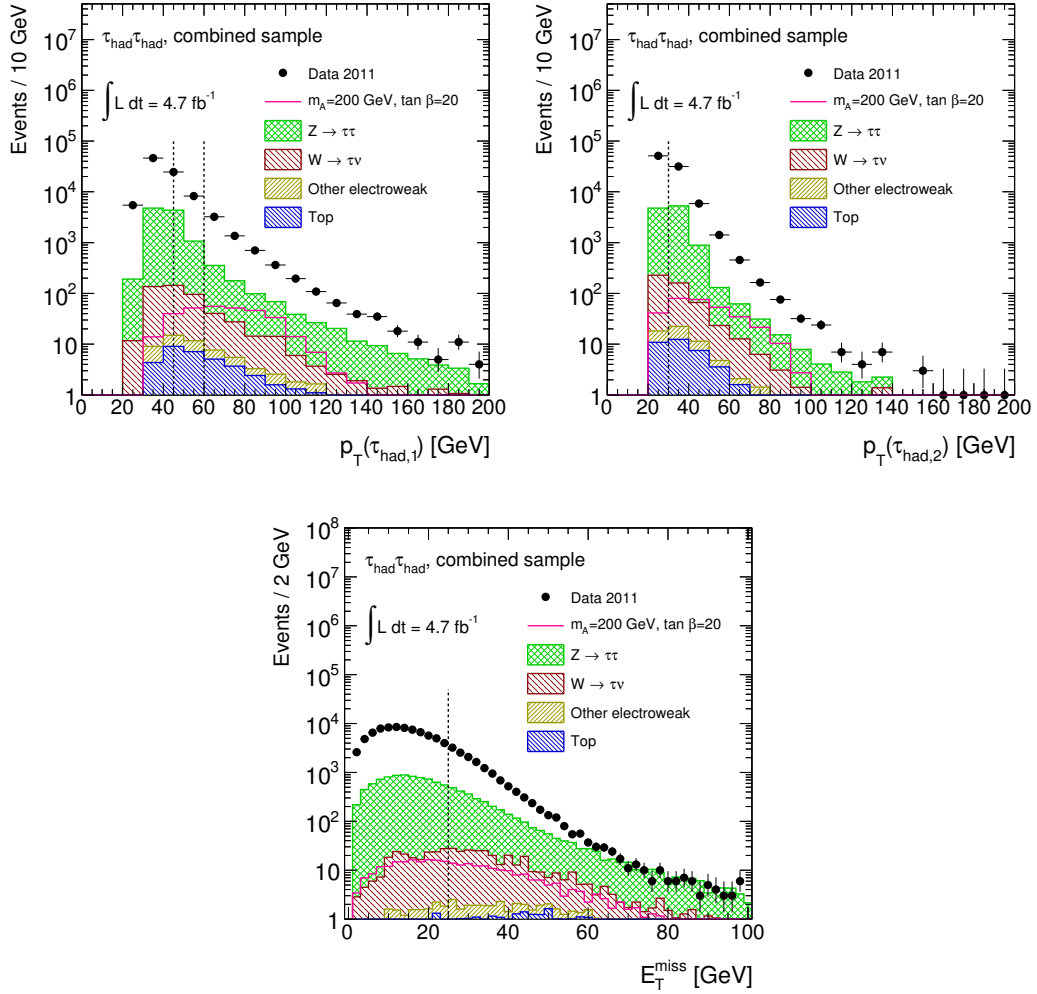


Figure 6.17.: Distribution of the transverse momentum of the two highest- p_T τ_{had} candidates (first row) and the missing transverse momentum (second row) after a selection in which the trigger, the data quality selections, the object vetoes, two hadronic τ -lepton decays that pass tight and medium τ_{had} identification levels and have opposite charge and the convergence of the di- τ_{had} mass calculation with the Missing Mass Calculator as described in Section 6.4 are required. This corresponds to the event selection described in Sections 6.3.1 to 6.3.4 and the MMC convergence with the exception of the p_T requirements for the hadronic τ -lepton decays and the missing transverse momentum. The data are compared with the expectation from backgrounds other than multi-jet production and an added hypothetical MSSM signal ($m_A = 150$ GeV, $\tan \beta = 20$). At this step of the selection no significant signal contribution is expected. The difference between data and the shown backgrounds can be attributed to the multi-jet background. The selection requirements on the shown variables are obtained in the optimisation procedure that is outlined in Section 6.3.4. For the highest- p_T hadronic τ -lepton decay $p_T > 45$ GeV is required in the b -tagged channel and $p_T > 60$ GeV in the b -vetoed channel. For the second highest- p_T hadronic τ -lepton decay $p_T > 30$ GeV and for the missing transverse momentum $E_T^{\text{miss}} > 25$ GeV is required. These values are shown by dashed vertical lines.

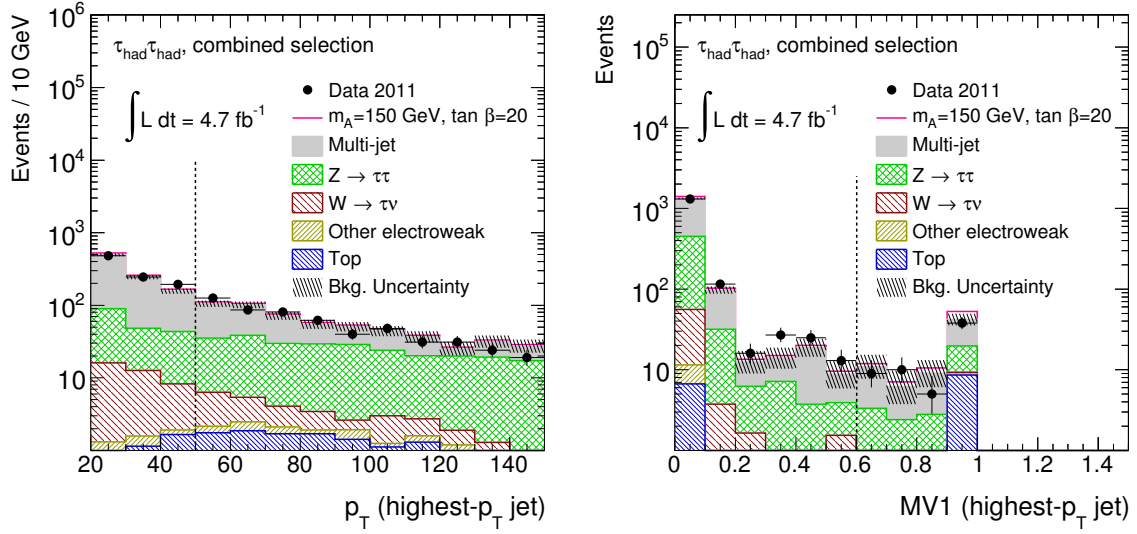


Figure 6.18.: Distribution of the variables used for the categorisation of the selected events. The transverse momentum of the highest- p_T jet is shown on the left-hand side and the variable used for the discrimination of light and b -jets, MV1, is shown for the highest- p_T jet on the right-hand side. The data are compared to the background expectation and an added hypothetical MSSM signal with $m_A = 150$ GeV and $\tan \beta = 20$ after the complete selection with the exception of the categorisation into the b -tagged and b -vetoed subsamples. The background uncertainty is shown as a hatched band and includes statistical and systematic uncertainties. The selection requirements for the b -tagged selection, $p_T < 50$ GeV for the highest- p_T jet and MV1 discriminant > 0.601713 , corresponding to a b -jet identification efficiency of approximately 70% in simulated $t\bar{t}$ events, are shown as dashed lines.

The expected number of events for data, signal and background processes is shown in Table 6.7 after each of the selection requirements to illustrate the effect of the event selection on the event yields for the background and signal processes. The methods with which these expected signal and background event yields are obtained are described in Section 6.5.

6.4. Mass Reconstruction for Di- τ Final States

When τ leptons decay, a final state with missing transverse momentum due to neutrinos is produced. In the search for $h/A/H \rightarrow \tau\tau$ decays the mass of the di- τ system is used to discriminate events with Higgs boson production from background events. In the case that a new Higgs boson is discovered the di- τ mass is used to determine the mass of the Higgs boson. The background is composed of processes with a di- τ_{had} resonance, like $Z/\gamma^* \rightarrow \tau^+\tau^-$ production, and processes without a di- τ_{had} resonance, like multi-jet production. A reliable mass reconstruction with a small resolution is important to obtain a good discrimination between signal and backgrounds. An accurate mass reconstruction of the di- τ system is challenging due to the inability to reconstruct the neutrino four-momenta. Different di- τ mass reconstruction methods have been studied and are presented in the following section. The simplest method is the calculation of the “visible mass” for which the value of the missing

	Data	$b\bar{b}\phi \rightarrow \tau_{\text{had}}\tau_{\text{had}}$	$g\bar{g} \rightarrow \phi \rightarrow \tau_{\text{had}}\tau_{\text{had}}$	$W + \text{jets}$	$Z/\gamma^* + \text{jets}$	Top	Diboson
No selection	-	4721 \pm 21	5316 \pm 14	(15386 \pm 4) $\times 10^4$	(6958.1 \pm 3.0) $\times 10^4$	(9429 \pm 4) $\times 10^2$	47280 \pm 90
Trigger and GRL	3.0 $\times 10^7$	1061 \pm 10	740 \pm 5	(2182 \pm 7) $\times 10^2$	(15920 \pm 10) $\times 10^2$	19220 \pm 50	4151 \pm 20
Event cleaning	3.0 $\times 10^7$	1034 \pm 10	720 \pm 5	(2128 \pm 6) $\times 10^2$	(15317 \pm 9) $\times 10^2$	18310 \pm 40	4017 \pm 19
Muon veto	2.9 $\times 10^7$	1017 \pm 10	717 \pm 5	(2089 \pm 6) $\times 10^2$	(15284 \pm 9) $\times 10^2$	15500 \pm 40	3753 \pm 19
Electron veto	2.8 $\times 10^7$	1006 \pm 10	710 \pm 5	62430 \pm 340	(1015.4 \pm 2.1) $\times 10^2$	5056 \pm 33	369 \pm 6
First τ_{had} candidate	6.4 $\times 10^6$	813 \pm 9	570 \pm 5	20410 \pm 180	44150 \pm 120	1282 \pm 10	173.8 \pm 2.9
First τ_{had} $p_T > 45$ GeV	1.5 $\times 10^6$	669 \pm 8	391 \pm 4	8210 \pm 110	11350 \pm 60	648 \pm 6	91.4 \pm 2.0
First τ_{had} identification	9.4 $\times 10^5$	567 \pm 7	335.5 \pm 3.4	6990 \pm 100	9720 \pm 50	531 \pm 6	79.1 \pm 1.9
Second τ_{had} candidate	92301	261 \pm 5	163.9 \pm 2.4	477 \pm 18	4220 \pm 40	57.3 \pm 1.5	25.9 \pm 1.1
Second τ_{had} $p_T > 30$ GeV	63710	239 \pm 5	141.5 \pm 2.3	321 \pm 14	2948 \pm 30	43.2 \pm 1.3	19.8 \pm 0.9
Second τ_{had} identification	25910	180 \pm 4	107.9 \pm 2.0	201 \pm 11	2227 \pm 26	30.3 \pm 1.1	14.8 \pm 0.8
Opposite charge	15555	179 \pm 4	107.2 \pm 2.0	174 \pm 10	2189 \pm 26	27.9 \pm 1.1	13.5 \pm 0.8
$E_T^{\text{miss}} > 25$ GeV	3241	95.0 \pm 3.0	51.2 \pm 1.3	122 \pm 9	758 \pm 14	24.3 \pm 1.0	9.7 \pm 0.6
MMC convergence	3205	94.6 \pm 3.0	50.7 \pm 1.3	106.3 \pm 8.0	749 \pm 14	18.8 \pm 0.9	7.8 \pm 0.6
≥ 1 b -jet with $p_T < 50$ GeV	27	4.4 \pm 0.6	0.38 \pm 0.12	0.5 \pm 0.4	4.0 \pm 1.2	1.65 \pm 0.24	0.013 \pm 0.035
no b -jet with $p_T < 50$ GeV	3178	90.3 \pm 2.9	50.2 \pm 1.3	106 \pm 8	746 \pm 14	17.2 \pm 0.9	7.8 \pm 0.6
First τ_{had} $p_T > 60$ GeV	1223	76.9 \pm 2.7	34.7 \pm 1.0	52 \pm 5	298 \pm 8	11.2 \pm 0.7	4.9 \pm 0.5

Table 6.7.: The observed number of events in data and the expected number of signal and background events for the individual selection steps of the search for $h/A/H \rightarrow \tau_{\text{had}}\tau_{\text{had}}$ decays. The data are compared with the background expectation and a hypothetical MSSM signal ($m_A = 200$ GeV and $\tan\beta = 20$). The background and signal event yields are estimated with the methods described in Section 6.5. Simulated event yields are normalised to the total integrated luminosity, 4.6 fb $^{-1}$. Due to the estimation method the background expectation for events with multi-jet production cannot be calculated at each of the selection steps. The event yield for multi-jet production after all selection steps is documented in Section 6.5.1. The given uncertainties are the statistical uncertainties of the simulated event samples.

transverse momentum is not used. For the “effective mass” the missing transverse momentum in x - and y -direction is used, but no inference on the missing transverse momentum in z -direction is attempted. For the “collinear mass approximation” the neutrino four-momenta are inferred using the assumption that the neutrinos are collinear with the visible τ -lepton decay products. Finally, the “Missing Mass Calculator” attempts to reconstruct the neutrino four-momenta without the assumption of collinearity, but based on probability density functions for the τ -lepton decay kinematics.

6.4.1. Visible Mass, Effective Mass and Transverse Mass

The visible mass is the invariant mass of the visible products of the two τ -lepton decays. It is defined by

$$(m_{\tau\tau}^{\text{vis}})^2 = (E_{\text{vis},1} + E_{\text{vis},2})^2 - (\vec{p}_{\text{vis},1} + \vec{p}_{\text{vis},2})^2 \quad (6.2)$$

$$= m_{\text{vis},1}^2 + m_{\text{vis},2}^2 + 2 \cdot (E_{\text{vis},1}E_{\text{vis},2} - \vec{p}_{\text{vis},1}\vec{p}_{\text{vis},2}) \quad (6.3)$$

$$\approx 2E_{\text{vis},1}E_{\text{vis},2}(1 - \cos \Delta\alpha), \quad (6.4)$$

where $E_{\text{vis},i}$, $m_{\text{vis},i}$, $\vec{p}_{\text{vis},i}$, $i = 1, 2$, are the energies, masses and momentum three-vectors of the visible τ -lepton decay products. The three-dimensional angular difference between the momentum vectors of the two τ_{had} candidates is denoted by $\Delta\alpha$. The approximation used in the derivation of Equation 6.4 is valid in the limit $m_{\text{vis},1} \ll E_{\text{vis},1}$ and $m_{\text{vis},2} \ll E_{\text{vis},2}$.

The effective mass is the invariant mass of the visible products of the two τ -lepton decays and the missing transverse momentum in x - and y -direction. It is defined by

$$(m_{\tau\tau}^{\text{eff}})^2 = (E_{\text{vis},1} + E_{\text{vis},2} + E_T^{\text{miss}})^2 - (\vec{p}_{\text{vis},1} + \vec{p}_{\text{vis},2} + \vec{p}_T^{\text{miss}})^2, \quad (6.5)$$

where $\vec{p}_T^{\text{miss}} = (E_x^{\text{miss}}, E_y^{\text{miss}}, 0)^T$. For the effective mass the mass of the di- τ system is calculated under the assumption that the missing four-momentum vector is entirely due to produced neutrinos and that it has a negligible mass and z -component. The distribution of the visible and the effective mass of the two τ_{had} candidates is shown for a Higgs boson event sample with $m_H = 300$ GeV and $H \rightarrow \tau_{\text{had}}\tau_{\text{had}}$ decays in Figure 6.19.

The transverse mass is defined by

$$m_T = \sqrt{E_T^2 - \vec{p}_T^2}, \quad (6.6)$$

where E_T and \vec{p}_T are the transverse components of the four-momentum vector of the sum of the visible decay products of the two τ leptons and the missing transverse momentum. In practice the transverse mass is more often used to differentiate W -boson decays with one τ -lepton from other processes than for the di- τ mass reconstruction. In this case, E_T and \vec{p}_T are the transverse components of the four-momentum vector of the visible part of the decay, e.g. an electron, a muon or a hadronic τ -lepton decay and the missing transverse momentum. If the mass of the system of the visible decay products and the mass of the system of the invisible decay products is negligible compared to the energy, the transverse mass can be approximated by

$$m_T^2 \approx 2E_{\text{vis}}E_T^{\text{miss}}(1 - \cos \Delta\phi), \quad (6.7)$$

where E_{vis} is the energy of the visible decay products and $\Delta\phi$ the angle between the three-vector of the visible decay products in the transverse plane, $\vec{p}_{T,\text{vis}}$, and the missing transverse momentum three-vector.

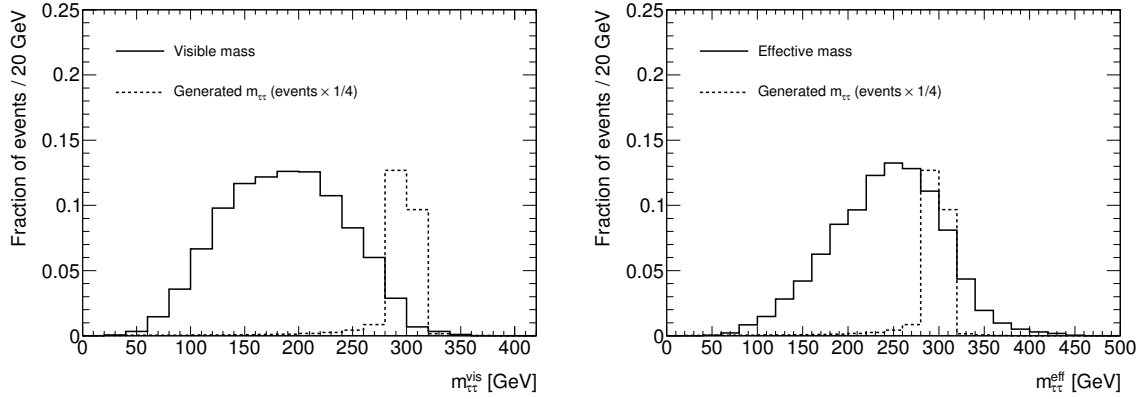


Figure 6.19.: The distribution of the visible mass (left-hand side) and the effective mass (right-hand side) from a $H \rightarrow \tau_{\text{had}}\tau_{\text{had}}$ event sample with $m_H = 300$ GeV is compared with the generated di- τ mass. The distribution of the di- τ mass has been scaled down. In the considered event sample the visible mass estimator has a bias of -114 GeV and a estimated standard deviation of 55 GeV. The effective mass estimator has a bias of -59 GeV and an estimated standard deviation of 60 GeV.

6.4.2. Collinear Mass Approximation

In the mass reconstruction method based on the collinear mass approximation it is attempted to reconstruct the momentum vector of the neutrinos in order to gain additional discrimination between the signal and background and to obtain a less-biased estimator of the Higgs boson mass. For the collinear mass approximation it is assumed that the missing transverse momentum is completely due to the neutrinos from the τ -lepton decays and that each neutrino is emitted collinear to the corresponding τ lepton and in consequence collinear to their visible decay products. The collinear mass approximation was first proposed in Reference [235] for topologies in which the transverse momentum of the resonance can be inferred from the p_T of a recoiling jet. However, in practice it is mostly used in cases where the missing transverse momentum is measured. Typical values for the angle between the neutrino and the τ -lepton three-momentum vectors, $\Delta\theta_{3D}$, and the ratio of the reconstructed missing transverse momentum and the missing transverse momentum due to neutrinos (“true missing transverse momentum”) are shown in Figure 6.20. The collinear mass approximation is applicable for small angles $\Delta\theta_{3D}$ and similar values of the true and the reconstructed missing transverse momenta.

With the missing transverse momentum,

$$\vec{p}_T^{\text{miss}} = (E_x^{\text{miss}}, E_y^{\text{miss}})^T, \quad (6.8)$$

and the directions of the visible decay products of the τ leptons in the transverse plane, \vec{e}_1 and \vec{e}_2 , the neutrino energies $E_{\nu,1}$ and $E_{\nu,2}$ can be calculated in the collinear mass approximation with

$$\vec{p}_T^{\text{miss}} = E_{\nu,1} \cdot \vec{e}_1 + E_{\nu,2} \cdot \vec{e}_2 \quad (6.9)$$

$$\Leftrightarrow \begin{pmatrix} E_x^{\text{miss}} \\ E_y^{\text{miss}} \end{pmatrix} = \begin{pmatrix} \sin\theta_1 \cos\phi_1 & \sin\theta_2 \cos\phi_2 \\ \sin\theta_1 \sin\phi_1 & \sin\theta_2 \sin\phi_2 \end{pmatrix} \begin{pmatrix} E_{\nu,1} \\ E_{\nu,2} \end{pmatrix}. \quad (6.10)$$

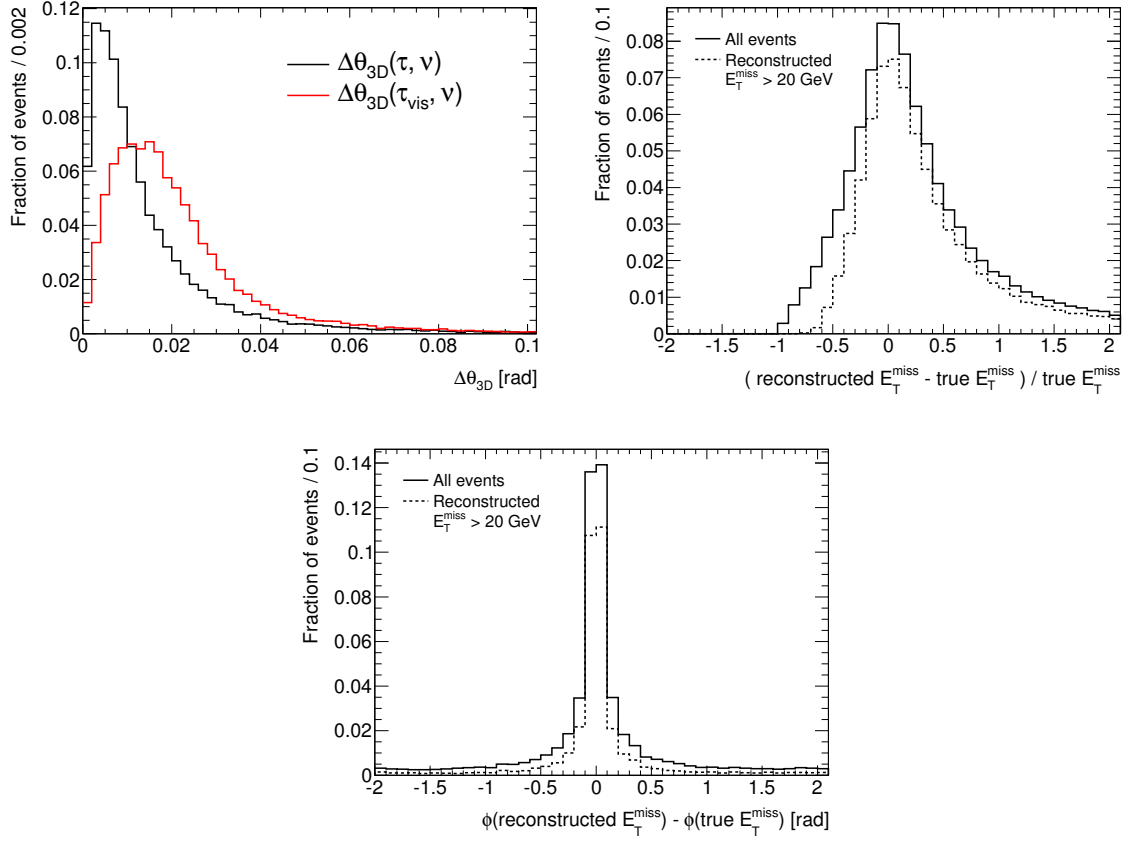


Figure 6.20.: Distributions of the angle between the τ -lepton and the neutrino three-momentum vectors and the angle between the three-momentum vectors of the visible decay products of the τ lepton and the neutrino (left-hand side), the relative difference of the reconstructed and the true missing transverse momentum (middle) and the difference between the azimuthal angle of the reconstructed and the true missing transverse momentum (right-hand side) as measured in a $H \rightarrow \tau_{\text{had}}\tau_{\text{had}}$ sample of simulated events with $m_H = 300$ GeV. The true missing transverse momentum is calculated from the neutrino four-momentum vectors which are obtained from generator-level information. The reconstructed missing transverse momentum is based on simulated detector response.

With the obtained neutrino energies the collinear mass and the fraction of the energies of the visible and all τ -lepton decay products, X_1 and X_2 , can be calculated as

$$X_1 = \frac{E_{\text{vis},1}}{E_{\text{vis},1} + E_{\nu,1}} \quad (6.11)$$

$$X_2 = \frac{E_{\text{vis},2}}{E_{\text{vis},2} + E_{\nu,2}} \quad (6.12)$$

$$(m_{\tau\tau}^{\text{col}})^2 = \left(\frac{E_{\text{vis},1}}{X_1} + \frac{E_{\text{vis},2}}{X_2} \right)^2 - \left(\frac{\vec{p}_{\text{vis},1}}{X_1} + \frac{\vec{p}_{\text{vis},2}}{X_2} \right)^2 \quad (6.13)$$

$$\approx \frac{m_{\text{vis}}^2}{X_1 X_2}, \quad (6.14)$$

where $E_{\text{vis},1}$, $E_{\text{vis},2}$ and $\vec{p}_{\text{vis},1}$, $\vec{p}_{\text{vis},2}$ are the energies and the transverse momentum three-

vectors of the visible τ -lepton decay products. Depending on the measured directions of the missing transverse momentum and the visible τ -lepton decay products, $E_{\nu,1}, E_{\nu,2} < 0$ is a possible result. Based on the equivalence

$$X_i < 0 \Leftrightarrow E_{\nu,1} < 0 \wedge |E_{\nu,i}| > E_{\text{vis},i}, \quad (6.15)$$

$$X_i > 1 \Leftrightarrow E_{\nu,1} < 0 \wedge |E_{\nu,i}| < E_{\text{vis},i}, \quad (6.16)$$

all solutions with positive neutrino energies can be selected by the requirement $0 \leq X_1 \leq 1$, $0 \leq X_2 \leq 1$. In Figure 6.21 the distributions of X_1 and X_2 as measured in an event sample of simulated $H \rightarrow \tau_{\text{had}}\tau_{\text{had}}$ decays is shown. The determinant of the matrix defined in Equation 6.10 is $-\sin\theta_1 \sin\theta_2 \sin(\phi_1 - \phi_2)$ and in consequence the relative uncertainty of the neutrino energies and thus the collinear mass has a pole for $\sin\theta_1 \rightarrow 0$, $\sin\theta_2 \rightarrow 0$ and $\sin\Delta\phi = \sin(\phi_1 - \phi_2) \rightarrow 0$. Due to the detector acceptance no hadronic τ -lepton decays with $\sin\theta_1 \rightarrow 0$, $\sin\theta_2 \rightarrow 0$ can be reconstructed, but as shown in Figure 6.22 the mass resolution is poor for $\Delta\phi \rightarrow \pi$ (“back-to-back τ -lepton decays”). As the signal and background event samples are dominated by events with back-to-back τ -lepton decays, the collinear mass resolution is poor if no further requirements are applied to the event sample. A requirement on a maximum $\Delta\phi$, however, has a low efficiency. In the considered $m_H = 300$ GeV signal event sample an efficiency of approximately 46% is obtained. In Figure 6.22 the distribution of the collinear mass is shown with and without the requirement on $\Delta\phi$. In addition, the mass distribution is shown after the requirement that the neutrino energies are positive. The requirement on $\Delta\phi$ reduces the standard deviation of the mass distribution and the bias of the mass estimator significantly.

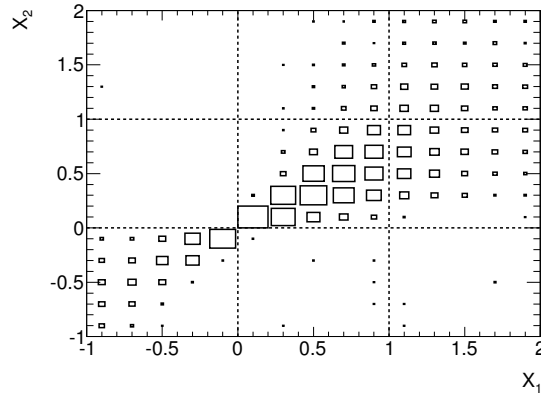


Figure 6.21.: Distribution of the ratios of the neutrino energies and the energies from the visible and invisible τ -lepton decay products, X_1 and X_2 , in an event sample of $H \rightarrow \tau_{\text{had}}\tau_{\text{had}}$ decays with $m_H = 300$ GeV. The quantities X_1 and X_2 are the neutrino- τ -lepton energy ratios for the τ_{had} candidates with higher and lower visible transverse momentum, respectively. Dashed lines indicate the region for solutions with positive neutrino energies, $0 \leq X_1 \leq 1$, $0 \leq X_2 \leq 1$.

6.4.3. Missing Mass Calculator

The Missing Mass Calculator technique (MMC) [236] is a more sophisticated version of the collinear approximation. The most important improvement over the collinear approximation stems from the fact that the requirement of collinearity of the neutrinos and the visible τ -lepton decay products is relaxed. Instead a scan over the variables that correspond to the

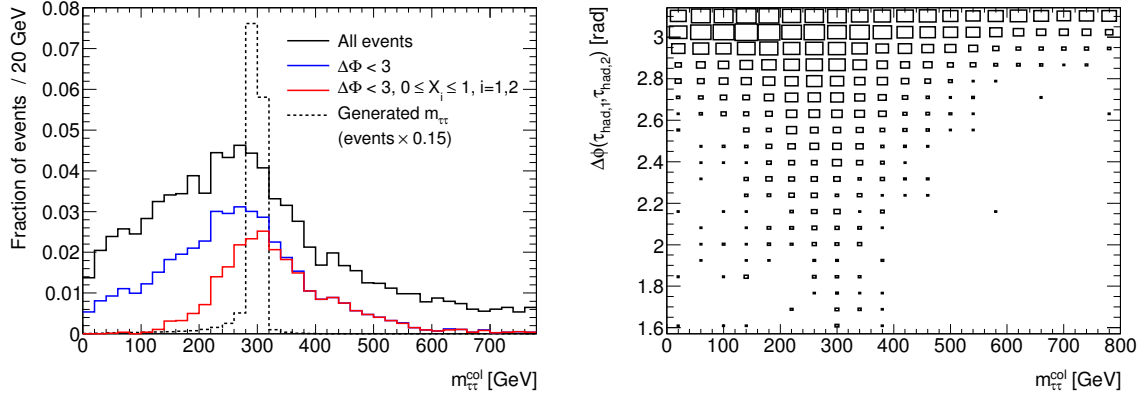


Figure 6.22.: Distribution of the collinear mass calculated with and without the $\Delta\phi < 3.0$ and $0 \leq X_1 \leq 1$, $0 \leq X_2 \leq 1$ requirements and the generated invariant mass of the two τ leptons (left-hand side) and the collinear mass distribution as a function of the azimuthal angle between the two hadronic τ -lepton decays $\Delta\phi$ (right-hand side) in a sample of events with $H \rightarrow \tau_{\text{had}}\tau_{\text{had}}$ production in b -quark annihilation with $m_H = 300$ GeV. The bias of the collinear mass estimator is 209 GeV, -34 GeV and 43 GeV with an estimated standard deviation of 613 GeV, 138 GeV and 122 GeV for the full sample, the sample with the $\Delta\phi$ requirement and the sample with the $\Delta\phi$, X_1 and X_2 requirements, respectively.

unknown components of the neutrino four-vectors is performed and the masses calculated in the scan are weighted based on a probability density function for the τ -lepton decay kinematics.

For the MMC mass reconstruction technique it is assumed that the neutrinos from the τ -lepton decays fully account for the missing transverse momentum and that the reconstructed τ -lepton four-momentum vectors have an invariant mass that corresponds to the τ -lepton mass, $m_\tau = 1.777$ GeV [6]. The reconstructed τ -lepton four-momentum vectors are the four-momentum vector sum of the neutrinos and the visible decay products corresponding to the first and second τ -lepton decay. These assumptions lead to the following system of equations for the most general case where both τ leptons decay leptonically:

$$\begin{aligned}
 E_x^{\text{miss}} + \alpha_x \sigma_x &= p_{\nu,1} \sin \theta_{\nu,1} \cos \phi_{\nu,1} + p_{\nu,2} \sin \theta_{\nu,2} \cos \phi_{\nu,2} \\
 E_y^{\text{miss}} + \alpha_y \sigma_y &= p_{\nu,1} \sin \theta_{\nu,1} \sin \phi_{\nu,1} + p_{\nu,2} \sin \theta_{\nu,2} \sin \phi_{\nu,2} \\
 m_\tau^2 &= m_{\nu,1}^2 + m_{\text{vis},1}^2 + 2\sqrt{p_{\text{vis},1}^2 + m_{\text{vis},1}^2} \sqrt{p_{\nu,1}^2 + m_{\nu,1}^2} \\
 &\quad - 2p_{\text{vis},1}p_{\nu,1} \cos \Delta\theta_{3D,1} \\
 m_\tau^2 &= m_{\nu,2}^2 + m_{\text{vis},2}^2 + 2\sqrt{p_{\text{vis},2}^2 + m_{\text{vis},2}^2} \sqrt{p_{\nu,2}^2 + m_{\nu,2}^2} \\
 &\quad - 2p_{\text{vis},2}p_{\nu,2} \cos \Delta\theta_{3D,2} .
 \end{aligned} \tag{6.17}$$

Here $p_{\text{vis},i}$ and $m_{\text{vis},i}$ are the momentum and the invariant mass of the visible decay products of the τ lepton i ($i = 1, 2$), $p_{\nu,i}$, $m_{\nu,i}$, $\theta_{\nu,i}$, $\phi_{\nu,i}$, are the momentum, the mass, the polar and the azimuthal angle of the neutrino system from the decay of τ lepton i . The angle between the momentum vectors of the neutrino system and the visible decay products of τ lepton i is denoted by $\Delta\theta_{3D,i}$. The four-momentum vector of the neutrino system i is the vectorial sum of the neutrino four-momentum vectors associated with the decay of τ lepton i . The

quantities E_x^{miss} and E_y^{miss} are the x - and y -components of the missing transverse momentum vector and σ_x and σ_y their uncertainties. The symbols α_x and α_y denote nuisance parameters that describe the deviation from the nominal missing transverse momentum measurement. For the less general cases where a τ leptons decays hadronically only one neutrino is present in the decay and the mass of the neutrino system $m_{\nu,i}$ can be set to 0.

The general system of four equations shown in Equation 6.17 has ten unknowns, α_x, α_y and the two four-momentum vectors of the neutrino systems. In a scan over

- $\alpha_x, \alpha_y \in [-3, 3]$ in 30 steps,
- the azimuthal angle between the visible and the invisible decay products of τ lepton i , $\Delta\phi_i \in [-0.2, 0.2]$ for $i = 1, 2$, in 39 steps and if applicable
- the mass of the neutrino systems, $m_{\nu,i} \in [0, m_\tau - m_{\text{vis},i}]$ for $i = 1, 2$, in 10 steps,

the mass of the di- τ system is calculated. For every solution a probability is calculated based on $\alpha_x, \alpha_y, \theta_{3D,1}, \theta_{3D,2}$ and the energy of the neutrino system and the visible decay products. The probability for α_x and α_y is calculated with a standard normal distribution. The probability density function for $\theta_{3D,1}$ and $\theta_{3D,2}$ is measured as a function of the decay type (leptonic decay, hadronic one-prong decay or hadronic three-prong decay) and the τ -lepton momentum in simulated $Z \rightarrow \tau\tau$ events and is shown in Figure 6.23.

The MMC mass of a di- τ event is the maximum of the distribution of di- τ masses obtained in the described scan. For some events it is not possible to find a solution for $m_{\tau\tau}$ due to the limited parameter range used in the scan. In consequence the efficiency of the MMC mass calculation, i.e. the ratio of the number of events for which the MMC finds a solution and the number of events for which the calculation was attempted, is below 100%.

For the $\tau_{\text{had}}\tau_{\text{had}}$ final state, the MMC technique has an efficiency above 98% for signal event samples with mass $m_H < 250$ GeV and for Z -boson background processes after the event selection without the categorisation into the b -tagged and b -vetoed selection. The efficiency is above 80% for signal events with $250 \text{ GeV} < m_H < 500$ GeV. The efficiency for non- Z backgrounds varies from 80% (diboson production) to 87% (W boson production). The MMC mass distribution is shown for a Higgs boson event sample with $m_H = 300$ GeV as a function of $\Delta\phi$, the azimuthal angle between the two hadronic τ -lepton decays, and integrated over $\Delta\phi$ in Figure 6.24. Compared to the collinear approximation the MMC mass distribution has a lower standard deviation for high $\Delta\phi$.

6.5. Signal and Background Estimation

In the following section the estimation of the event yields for the signal and the background processes is described. Apart from the background from multi-jet production the event yields for all signal and background processes are estimated based on the simulated event samples described in Sections 6.1 and 6.2. The estimation of the multi-jet background from control regions in collision data is described in Section 6.5.1.

Simulated events are subject to the same selection procedure as used for collision data. In order to avoid a bias on the event yield estimate the simulated event samples are corrected for known problems and the obtained event yield is validated with data where possible. These corrections are described in the following sections. Compared to collision data the simulated event samples are produced with a slightly different distribution of the number of pile-up interactions. The simulated events are reweighted with the procedure described in Section 2.3.8. The corrections for different trigger responses and jet-to- τ_{had} misidentification

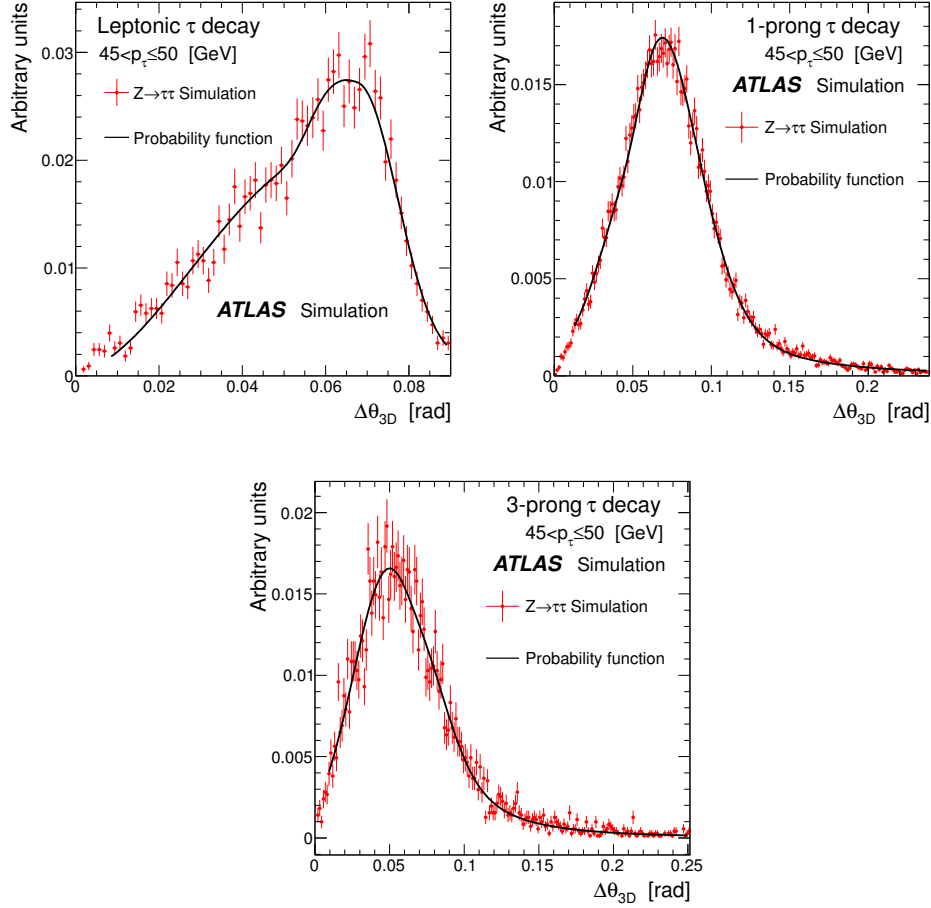


Figure 6.23.: Angular distance distributions [95] between the neutrino and the visible decay products for τ leptons as used in the calculation of the MMC mass. The three distributions have been obtained for τ leptons that decay into a lepton and two neutrinos (first row, left-hand side), τ leptons that decay into one charged hadron, ≥ 0 neutral hadrons and a neutrino (first row, right-hand side) and τ leptons that decay into three charged hadrons, ≥ 0 neutral hadrons and a neutrino (second row). The shown distributions have been obtained from τ leptons with momentum $45 \text{ GeV} < p_\tau \leq 50 \text{ GeV}$ from simulated $Z \rightarrow \tau\tau$ events. The solid black lines show the fitted probability density functions used in the MMC calculations.

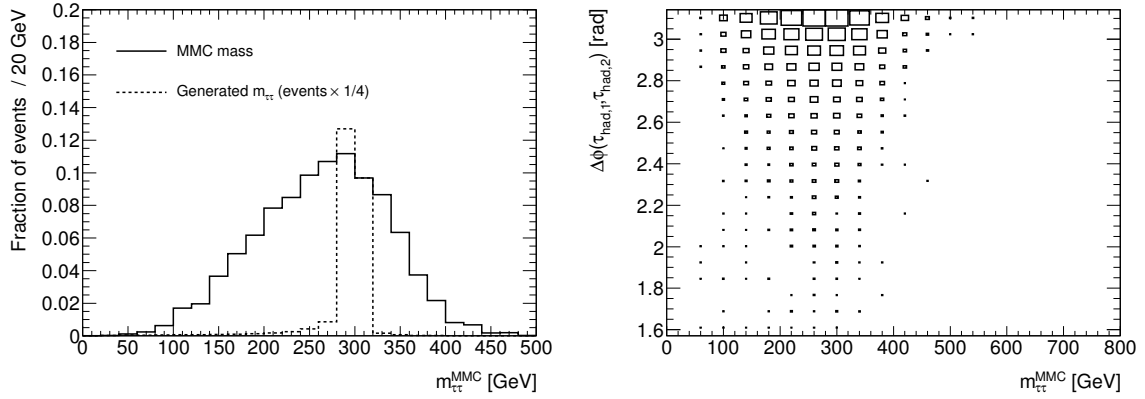


Figure 6.24.: Distribution of the MMC mass and the generated invariant mass of the two τ leptons (left-hand side) and the MMC mass distribution as a function of the azimuthal angle between the two hadronic τ -lepton decays, $\Delta\phi$, (right-hand side) in a sample of events with $H \rightarrow \tau_{\text{had}}\tau_{\text{had}}$ production in b -quark annihilation with $m_H = 300$ GeV. In the considered event sample the MMC mass estimator has a bias of -36 GeV and an estimated standard deviation of 71 GeV. In the figure on the right-hand side it can be seen that the width of the mass distribution is significantly smaller and has a significantly lower dependence on $\Delta\phi$ compared to the distribution of the collinear mass which is shown in Figure 6.22.

probabilities in simulated and collision data event samples are documented in Sections 6.5.2 and 6.5.3. The event samples with Z - and W -boson production are validated with hybrid data–simulation event samples, the so-called τ -embedded data samples, that are described in Section 6.5.4. In the event selection the event sample is split into two subsamples based on the identification of a b -jet. The efficiency of this requirement is measured in collision data and correction factors for simulated events are derived in Section 6.5.5. Finally, the combined background estimates are compared with collision data for distributions other than the MMC mass distribution in Section 6.5.6.

6.5.1. Estimation of the Multi-jet Background

The multi-jet background is estimated from data with a multi-sideband method based on three control regions, the so-called “ABCD method”. In the following section the principle of an ABCD method is introduced, the method is applied to the search for $h/A/H \rightarrow \tau_{\text{had}}\tau_{\text{had}}$ decays and the assumptions used in the method are verified.

The ABCD method

The ABCD method is a technique to estimate the event yield and the distribution of a random variable X_3 for a background from experimental data. For this purpose two random variables X_1 and X_2 that are used in the selection of the signal region are selected in addition to the random variable X_3 . The combined probability density function for X_1 , X_2 and X_3 is denoted by $f(X_1, X_2, X_3)$. For all selection requirements that define the signal region, i.e. $A_1 < X_1 < B_1$ and $A_2 < X_2 < B_2$, the variables X_1 and X_2 can be transformed into X'_1 , X'_2 , such that $X'_1 < B'_1$ and $X'_2 < B'_2$. It is therefore – without loss of generality –

assumed that the projection of the signal region onto X_1 and X_2 is defined by $X_1 < B_1$ and $X_2 < B_2$. Based on the signal region selection three control regions, labelled B, C and D, that are orthogonal to the signal region A with their corresponding distributions for X_3 are defined by

$$\begin{aligned}
\text{Region A: } X_1 < B_1, X_2 < B_2 &\Rightarrow N_A f_3^A(X_3) = N \int_{-\infty}^{B_1} \int_{-\infty}^{B_2} f(X_1, X_2, X_3) dX_1 dX_2, \\
\text{Region B: } X_1 > B_1, X_2 < B_2 &\Rightarrow N_B f_3^B(X_3) = N \int_{B_1}^{\infty} \int_{-\infty}^{B_2} f(X_1, X_2, X_3) dX_1 dX_2, \\
\text{Region C: } X_1 < B_1, X_2 > B_2 &\Rightarrow N_C f_3^C(X_3) = N \int_{-\infty}^{B_1} \int_{B_2}^{\infty} f(X_1, X_2, X_3) dX_1 dX_2, \\
\text{Region D: } X_1 > B_1, X_2 > B_2 &\Rightarrow N_D f_3^D(X_3) = N \int_{B_1}^{\infty} \int_{B_2}^{\infty} f(X_1, X_2, X_3) dX_1 dX_2,
\end{aligned} \tag{6.18}$$

where N_i is the number of events for the considered background in region i , $N = N_A + N_B + N_C + N_D$ and

$$\begin{aligned}
f_3^i(X_3) &= \frac{N}{N_i} \int_{\text{Region } i} f(X_1, X_2, X_3) d^2(X_1 X_2) \\
&= \frac{\int_{\text{Region } i} f(X_1, X_2, X_3) d^2(X_1 X_2)}{\int_{-\infty}^{\infty} \left[\int_{\text{Region } i} f(X_1, X_2, X_3) d^2(X_1 X_2) \right] dX_3}
\end{aligned} \tag{6.19}$$

is the probability density function for X_3 in region i with $i = A, B, C, D$. An example of the signal and control region definition is shown in Figure 6.25. If the random variables X_1 and X_2 are independent, it is

$$f(X_1, X_2, X_3) = f_1(X_1, X_3) \cdot f_2(X_2, X_3) \tag{6.20}$$

and Equation 6.18 can be written as

$$\begin{aligned}
N_A f_3^A(X_3) &= N I_1(X_3) I_2(X_3), \\
N_B f_3^B(X_3) &= N (1 - I_1(X_3)) I_2(X_3), \\
N_C f_3^C(X_3) &= N I_1(X_3) (1 - I_2(X_3)), \\
N_D f_3^D(X_3) &= N (1 - I_1(X_3)) (1 - I_2(X_3))
\end{aligned} \tag{6.21}$$

with

$$I_1(X_3) = \int_{-\infty}^{B_1} f_1(X_1, X_3) dX_1, \quad I_2(X_3) = \int_{-\infty}^{B_2} f_2(X_2, X_3) dX_2. \tag{6.22}$$

In consequence the distribution of events in the signal region is

$$N_A f_3^A(X_3) = \frac{N_B f_3^B(X_3) \cdot N_C f_3^C(X_3)}{N_D f_3^D(X_3)}. \tag{6.23}$$

If $f_3^C(X_3) = f_3^D(X_3)$ holds for all considered values of X_3 , Equation 6.23 can be further simplified to

$$N_A = \frac{N_B \cdot N_C}{N_D} \quad \text{and} \quad f_3^A(X_3) = f_3^B(X_3). \quad (6.24)$$

Alternatively, $f_3^A(X_3) = f_3^C(X_3)$ holds if $f_3^B(X_3) = f_3^D(X_3)$ for all considered values of X_3 .

Implementation of the ABCD method for the search for $h/A/H \rightarrow \tau_{\text{had}}\tau_{\text{had}}$ decays

In the $h/A/H \rightarrow \tau_{\text{had}}\tau_{\text{had}}$ analysis the variable X_3 of which the probability density function has to be estimated is the MMC mass. The electric-charge product of the hadronic τ -lepton decays is chosen as variable X_1 and the variable X_2 is a boolean variable based on whether the τ_{had} candidates fulfil the τ_{had} identification requirements. As the hadronic τ -lepton decays are required to have charge $|q| = 1$, the electric-charge product is either +1 (“same sign”) or -1 (“opposite sign”). The τ_{had} identification variable has two states “pass ID” and “fail ID”. The state “pass ID” refers to events where one τ_{had} candidate fulfils the tight and the other τ_{had} candidate fulfils at least the medium τ_{had} identification requirements. The state “fail ID” refers to events in which the two τ_{had} candidates fulfil the loose τ_{had} identification requirements, but do not satisfy the selection of the “pass ID” category. The signal and control regions are then given by:

- signal region A: opposite-sign charges and τ_{had} identification requirements fulfilled,
- control region B: same-sign charges and τ_{had} identification requirements fulfilled,
- control region C: opposite-sign charges and τ_{had} identification requirements failed,
- control region D: same-sign charges and τ_{had} identification requirements failed.

The definition of the signal and control regions is illustrated in Figure 6.25.

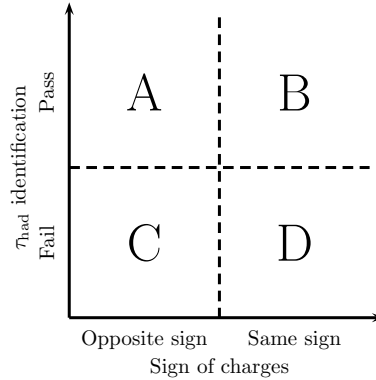


Figure 6.25.: Signal and control regions for the estimation of the multi-jet background for the $h/A/H \rightarrow \tau_{\text{had}}\tau_{\text{had}}$ analysis: Events are categorised according to the product of the electric charges of the two τ_{had} candidates and the τ_{had} identification level. “Pass τ_{had} identification” refers to events where one τ_{had} candidate passes the tight and the other passes the medium τ_{had} identification requirements. “Fail τ_{had} identification” refers to all events in which the two τ_{had} decays pass the loose τ_{had} identification requirements but do not satisfy the requirements of the “pass τ_{had} identification” category. Region A is the signal region.

Considering the definition of the BDT score that is used for the identification of hadronic τ -lepton decays it is rational to assume that the τ_{had} identification level and the electric-charge product are independent. This assumption is validated in Section 6.5.1 to the extent that this is possible.

In the following, N_i^{QCD} refers to the number of multi-jet events in region i , N_i^{data} is the number of observed events in region i for collision data, N_i^{other} is the expected number of events in region i from background processes other than multi-jet production and N_i^{signal} is the expected number of signal events in region i . The numbers of multi-jet events in regions B, C and D, N_i^{QCD} , $i = \text{B, C, D}$, are needed in Equation 6.24 and cannot be measured directly. They can, however, be inferred from the numbers of observed events in data and the event yields for the other background and signal processes with

$$N_i^{\text{QCD}} = N_i^{\text{data}} - N_i^{\text{signal}} - N_i^{\text{other}} \quad \text{for } i = \text{B, C, D}. \quad (6.25)$$

For Equation 6.25 a signal hypothesis is assumed, e.g. for the background-only hypothesis it is $N_i^{\text{signal}} = 0$.

The numbers of events in the control regions for the signal and the remaining background processes, N_i^{signal} and N_i^{other} , $i = \text{B, C, D}$, are estimated with simulated event samples and the methods described in Section 6.5, but applied to the control regions instead of the signal region. The numbers of events in the signal and control regions for data and simulation are documented in Tables 6.8 and 6.9 for the b -vetoed and the b -tagged event selections, respectively.

For the b -vetoed selection the MMC mass distributions in regions B and D, the regions with same-charge τ_{had} decays, are assumed to be equal and hence the MMC mass distribution in the signal region can be obtained from region C, the region with opposite-charge τ_{had} decays that fail the medium-and-tight τ_{had} identification criteria. Alternatively, the MMC mass distribution in the signal region could be obtained from region B, however this leads to a larger statistical uncertainty.

Based on Equations 6.24, 6.25 and the event yields in the control regions from Table 6.8 the number of events expected from multi-jet background for the b -vetoed selection signal region is

$$n_{\text{QCD}}^{b\text{-vetoed}} = 870 \pm 40 \quad (6.26)$$

for the background-only hypothesis. The quoted uncertainty is computed with the statistical uncertainties of the event yields for data and simulated background in the control regions.

For the b -tagged selection the MMC mass distribution in regions C and D, the regions with failed medium-and-tight τ_{had} identification criteria, are assumed to be equal. With this assumption the MMC mass distribution in the signal region can be obtained from region B, the region with same-charge τ_{had} decays and passed medium-and-tight τ_{had} identification criteria.

The jet-to- τ_{had} misidentification probability is different for b - and light jets. In consequence the ratio of events from $b\bar{b}$ and $q_3\bar{q}_3$ production, where q_3 is a light quark, is different for events that pass and events that fail the medium-and-tight τ_{had} identification criteria. Compared to $q_3\bar{q}_3$ events, $b\bar{b}$ events have a smaller angular difference $\Delta\phi$ between the two τ_{had} candidates for the b -tagged selection. Therefore the shape of the $\Delta\phi$ distribution and thus also the shape of the MMC mass distribution is different in regions that pass and fail the medium-and-tight τ_{had} identification criteria. The $\Delta\phi$ distribution for $b\bar{b}$ events is different from $q_3\bar{q}_3$ events as in $b\bar{b}$ events preferentially one b quark can be associated with the identified b -jet. The hadronisation of the other b quark can lead to a jet that is misidentified as a hadronic τ -lepton decay and the second hadronic τ -lepton decay stems from an accompanying jet that is

	A	B	C	D
	OS, pass ID	SS, pass ID	OS, fail ID	SS, fail ID
Collision data	1223	710	3110	2325
$b\bar{b}h/A/H \rightarrow \tau_{\text{had}}\tau_{\text{had}}$	23.4 ± 0.6	0.14 ± 0.05	13.27 ± 0.21	0.155 ± 0.030
$gg \rightarrow h/A/H \rightarrow \tau_{\text{had}}\tau_{\text{had}}$	3.89 ± 0.10	0.034 ± 0.009	2.154 ± 0.031	0.0163 ± 0.0008
$Z/\gamma^* + \text{jets}$	298 ± 8	7.8 ± 0.9	159.2 ± 2.4	10.5 ± 0.5
$W + \text{jets}$	52 ± 5	6.9 ± 1.5	62.0 ± 2.3	9.5 ± 0.5
Top	11.2 ± 0.7	0.79 ± 0.13	8.55 ± 0.21	0.88 ± 0.07
Di-boson	4.9 ± 0.5	0.43 ± 0.10	2.47 ± 0.11	0.213 ± 0.024

Table 6.8.: Observed number of events in collision data and expected number of events from simulation for the b -vetoed selection in the signal region and the three control regions used for the multi-jet background estimation with the ABCD method. “OS” and “SS” refer to events with opposite-charge and same-charge τ_{had} decays, “pass ID” and “fail ID” refer to events that pass and fail the medium-and-tight τ_{had} identification criteria, respectively. The full event selection except for the criteria that define the control regions (electric-charge product, τ_{had} identification) is applied. For the simulated signal event samples $m_A = 200$ GeV and $\tan \beta = 20$ is used. The quoted uncertainties are statistical.

misidentified. In events with jets from gluons and light quarks only, no such preference can be observed.

The event yields in the signal and the control regions used for the multi-jet background estimation in the b -tagged channel are shown in Table 6.9. Based on Equations 6.24, 6.25 and the event yields in the control regions from Table 6.9 the number of events expected from multi-jet background for the b -tagged selection is

$$n_{\text{QCD}}^{b\text{-tagged}} = 19 \pm 5 \quad (6.27)$$

for the background-only hypothesis. The quoted uncertainty is computed with the statistical uncertainties of the event yields for data and simulated background in the control regions.

Validation of the multi-jet background estimation

In summary the ABCD method as used for the search for $h/A/H \rightarrow \tau_{\text{had}}\tau_{\text{had}}$ is applicable if

- the random variables τ_{had} identification and τ_{had} charge product are independent and
- the probability density functions $f_3(m_{\tau\tau}^{\text{MMC}})$ are equal in regions B and D for the b -vetoed event sample and in regions C and D for the b -tagged event sample.

In addition, a large contamination of the control regions with events from backgrounds other than multi-jet background leads to a large uncertainty of the multi-jet background event yield due to the subtraction of the non-multi-jet background from the data according to Equation 6.25. It is shown in Tables 6.8 and 6.9 that the highest fraction of non-multi-jet background is expected in region C, where opposite charge τ_{had} decays and failed τ_{had} identification are required. For the background-only hypothesis these fractions amount to 6.8% and 4.0% for the b -tagged and the b -vetoed selections, respectively. Therefore, the uncertainty of n_{QCD} due to the subtraction of background event yields is small.

Even though the τ_{had} charge product and the τ_{had} identification variables are expected and assumed to be independent, in practice it is not possible to prove this assumption. However,

	A	B	C	D
	OS, pass ID	SS, pass ID	OS, fail ID	SS, fail ID
Collision data	27	22	73	73
$b\bar{b}h/A/H \rightarrow \tau_{\text{had}}\tau_{\text{had}}$	1.83 ± 0.16	0	0.98 ± 0.06	0
$gg \rightarrow h/A/H \rightarrow \tau_{\text{had}}\tau_{\text{had}}$	0.029 ± 0.009	0	0.0177 ± 0.0029	0
$Z/\gamma^* + \text{jets}$	4.0 ± 1.2	0	6.2 ± 0.4	0
$W + \text{jets}$	0.5 ± 0.4	0	0.41 ± 0.16	0
Top	1.65 ± 0.25	0.08 ± 0.06	1.12 ± 0.08	0.123 ± 0.030
Di-boson	0.014 ± 0.035	0.006 ± 0.006	0	0.018 ± 0.012

Table 6.9.: Observed number of events in collision data and expected number of events from simulation for the b -tagged selection in the signal region and the three control regions used for the multi-jet background estimation with the ABCD method. “OS” and “SS” refer to events with opposite-charge and same-charge τ_{had} decays, “pass ID” and “fail ID” refer to events that pass and fail the medium-and-tight τ_{had} identification criteria, respectively. The full event selection except for the criteria defining the control regions (electric-charge product, τ_{had} identification) is applied. For the simulated signal event samples $m_A = 200$ GeV and $\tan \beta = 20$ is used. The quoted uncertainties are statistical.

if the variables are independent, the distribution of the τ_{had} identification variable is identical for events with opposite-charge and same-charge τ_{had} candidates. In Figure 6.26 the BDT jet score that is used for the identification of the highest- p_T and the second highest- p_T τ_{had} candidates is shown for multi-jet events with opposite-charge and same-charge τ_{had} candidates. These distributions are obtained by subtracting the distributions of all backgrounds other than multi-jet production from the corresponding distributions in collision data. The compatibility of the distributions for same-charge and opposite-charge τ_{had} candidates is evaluated with a Kolmogorov-Smirnov test. Based on the histograms probabilities of 60.7% (highest- p_T τ_{had} decay, b -tagged selection), 99.9% (highest- p_T τ_{had} decay, b -vetoed selection), 99.4% (second highest- p_T τ_{had} decay, b -tagged selection) and 47.1% (second highest- p_T τ_{had} decay, b -vetoed selection) are obtained.

The probability density function for the MMC mass for multi-jet events in regions B and D for the b -vetoed selection and in regions C and D for the b -tagged selection are shown in Figure 6.26. A Kolmogorov-Smirnov test yields probabilities of 99.7% and 97.7% for the b -tagged and the b -vetoed selections, respectively. The results of the Kolmogorov-Smirnov tests confirm that the ABCD method is applicable.

6.5.2. Trigger Correction Factors

Events that are considered for the search for $h/A/H \rightarrow \tau_{\text{had}}\tau_{\text{had}}$ decays are selected by a di- τ_{had} trigger whose selection criteria are partly implemented in hardware. Due to the high background rate from multi-jet events, the selection of τ_{had} decays at the trigger level is difficult. Not all variables that are used for the trigger selection are modelled at a satisfactory level in simulation. To avoid a bias on the background estimation from a mis-modelled trigger efficiency in simulation, the trigger efficiency is measured in collision data. In simulation it is corrected to the value obtained from data.

By design the efficiency of τ_{had} triggers is significantly different for τ_{had} decays and jets that are misidentified as τ_{had} decays. Therefore, different measurements have to be performed. Jets that are misidentified as τ_{had} decays are initiated by the hadronisation of either quarks

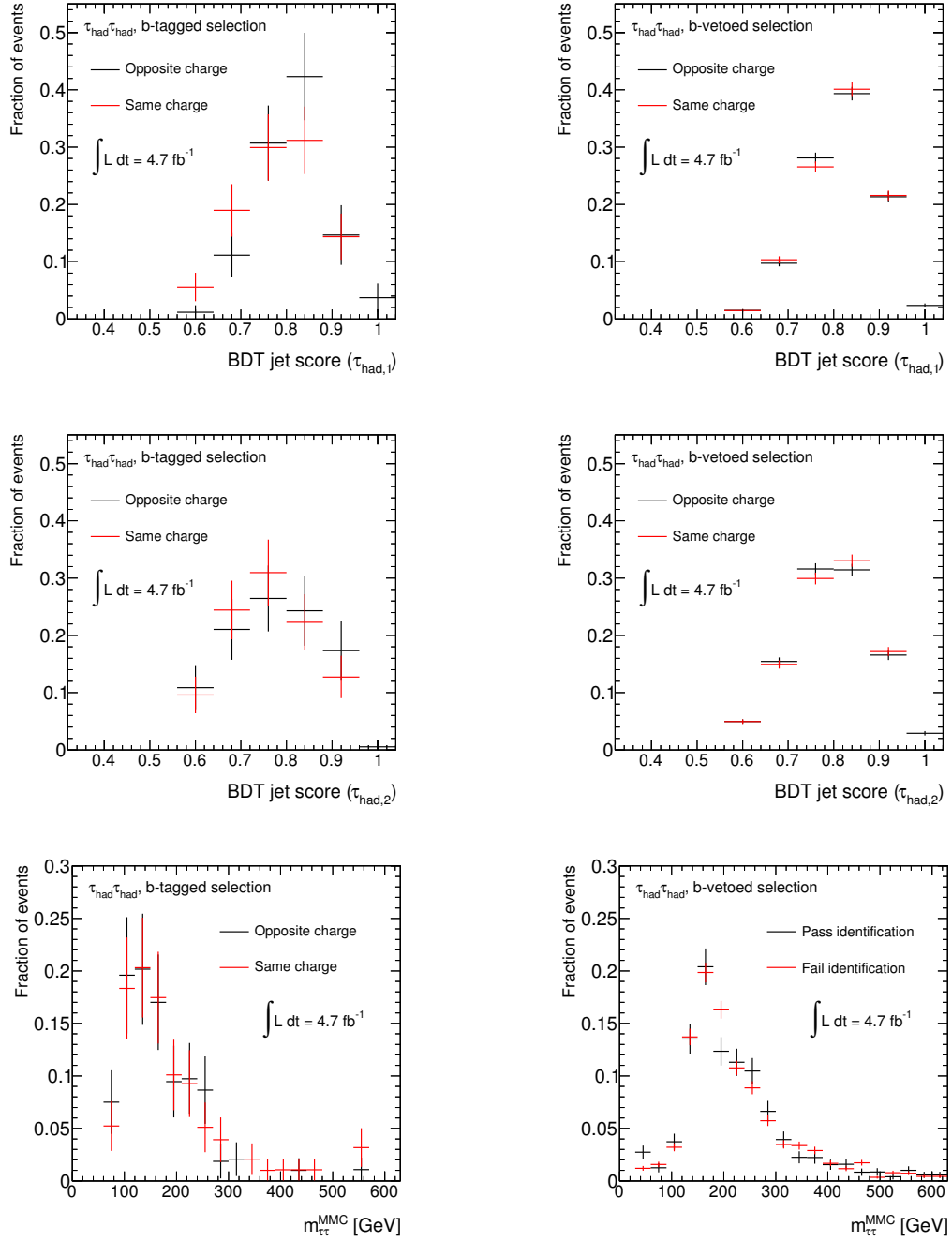


Figure 6.26.: The tests of the applicability of the ABCD method as described in Section 6.5.1 are shown. In the first row the BDT jet score used for the τ_{had} identification of the highest- p_T τ_{had} candidate for the b -tagged (left-hand side) and the b -vetoed (right-hand side) selection is compared for events with opposite-charge and same-charge τ_{had} decays. The background from events other than multi-jet production and signal was subtracted. The same distributions are shown for the second highest- p_T hadronic τ -lepton decay in the second row. In the third row the MMC mass distribution in regions C and D is compared for the b -tagged selection (left-hand side) and in regions B and D for the b -vetoed selection (right-hand side).

or gluons. For this thesis an inclusive measurement that averages over differences associated with the initiating parton is performed.

The efficiency of the di- τ_{had} trigger is determined with a tag-and-probe method. For an unbiased measurement of the di- τ_{had} trigger efficiency with a tag-and-probe method, events with two τ_{had} decays have to be selected without using the information from the two hadronic τ -lepton decays. With the available collision data it is not possible to select such an event sample with a sufficient number of events and a high enough purity.

However, the di- τ_{had} trigger decision is based on two single- τ_{had} trigger items and if the efficiency of single- τ_{had} trigger items can be measured and the single- τ_{had} trigger items are independent, the efficiency of the di- τ_{had} trigger can be calculated. The di- τ_{had} trigger with p_T thresholds of 29 GeV and 20 GeV (e.g. `EF_tau29_medium1_tau20_medium1`) is composed of the single- τ_{had} triggers with corresponding p_T thresholds (`EF_tau29_medium1` and `EF_tau20_medium1`). The two trigger items are independent if

$$P(p_T(\tau_1) > 29 \text{ GeV}, p_T(\tau_2) > 20 \text{ GeV}) = P(p_T(\tau_1) > 29 \text{ GeV}) \cdot P(p_T(\tau_2) > 20 \text{ GeV}), \quad (6.28)$$

where $p_T(\tau_1) > 29 \text{ GeV}$, $p_T(\tau_2) > 20 \text{ GeV}$ denotes the event that τ_{had} decays 1 and 2 are selected by the trigger with p_T thresholds of 29 GeV and 20 GeV, respectively, and P is the probability for the event to happen¹. Events are selected by the di- τ_{had} trigger if either of the τ_{had} candidates is selected by the trigger with 29 GeV threshold and the other by the trigger with 20 GeV threshold. Consequently the probability that the two τ_{had} decays are selected by the di- τ_{had} trigger, $P_{\text{di-}\tau_{\text{had}}}(\tau_1, \tau_2)$, is

$$\begin{aligned} P_{\text{di-}\tau_{\text{had}}}(\tau_1, \tau_2) &= P(p_T(\tau_1) > 29 \text{ GeV}) \cdot P(p_T(\tau_2) > 29 \text{ GeV}) \\ &\quad + P(p_T(\tau_1) > 29 \text{ GeV}) \cdot P(20 \text{ GeV} < p_T(\tau_2) < 29 \text{ GeV}) \\ &\quad + P(20 \text{ GeV} < p_T(\tau_1) < 29 \text{ GeV}) \cdot P(p_T(\tau_2) > 29 \text{ GeV}) \end{aligned} \quad (6.29)$$

$$\begin{aligned} &= P(p_T(\tau_1) > 29 \text{ GeV}) \cdot P(p_T(\tau_2) > 20 \text{ GeV}) \\ &\quad + P(p_T(\tau_1) > 20 \text{ GeV}) \cdot P(p_T(\tau_2) > 29 \text{ GeV}) \\ &\quad - P(p_T(\tau_1) > 29 \text{ GeV}) \cdot P(p_T(\tau_2) > 29 \text{ GeV}). \end{aligned} \quad (6.30)$$

Here the probability that τ_{had} decay i is selected by the 20 GeV threshold trigger, but not the 29 GeV trigger, is denoted by $P(20 \text{ GeV} < p_T(\tau_i) < 29 \text{ GeV})$. Studies with simulated $Z/\gamma^* \rightarrow \tau_{\text{had}}\tau_{\text{had}}$ and $h/A/H \rightarrow \tau_{\text{had}}\tau_{\text{had}}$ events [237] have shown that the two single- τ_{had} trigger items used for the di- τ_{had} trigger are independent. The independence of the single- τ_{had} trigger items permits the use of single- τ_{had} correction factors for each of the hadronic τ -lepton decays (“factorisation”).

For the single- τ_{had} triggers that were used (i.e. `EF_tau29T_medium1`, `EF_tau20T_medium1`, `EF_tau29_medium1`, `EF_tau20_medium1`) the measurement of the efficiencies for hadronic τ -lepton decays is documented in Reference [232]. For the measurement, samples of $Z/\gamma^* \rightarrow \tau_\mu\tau_{\text{had}}$ and $W \rightarrow \tau_{\text{had}}\nu$ events are selected in collision data. These data samples correspond to an integrated luminosity of 3.6 fb^{-1} and 4.7 fb^{-1} , respectively. The $Z/\gamma^* \rightarrow \tau_\mu\tau_{\text{had}}$ events are selected in the same way as the control samples in Section 5.4.4 with a single-muon trigger and requirements on the p_T of an isolated muon, the transverse mass of the muon and E_T^{miss} system, the azimuthal angle between the τ_{had} candidate, the muon and the missing transverse momentum and the visible mass of the τ_{had} candidate and the muon. The $W \rightarrow \tau_{\text{had}}\nu$ event sample is selected with an E_T^{miss} trigger, an electron and muon veto and

¹In this context, τ_1 and τ_2 do not refer to the highest- p_T and second highest- p_T τ_{had} candidate, but an arbitrary, but fixed labelling is introduced.

requirements on the reconstructed E_T^{miss} , the azimuthal angle between the τ_{had} candidate and the missing transverse momentum and the transverse mass. The transverse mass is calculated from the momentum vector of the τ_{had} candidate and the E_T^{miss} vector.

For the efficiencies of the single- τ_{had} triggers and their uncertainties consistent results are obtained from the measurements based on the samples of $Z/\gamma^* \rightarrow \tau_\mu \tau_{\text{had}}$ and $W \rightarrow \tau_{\text{had}} \nu$ events in collision data and simulation. Correction factors for simulation are derived based on the measurements with $Z/\gamma^* \rightarrow \tau_\mu \tau_{\text{had}}$ and $W \rightarrow \tau_{\text{had}} \nu$ event samples individually and based on the combination measurements. The efficiencies of the single- τ_{had} triggers used in the data-taking before September 2011 (i.e. EF_tau20_medium1 and EF_tau29_medium1) are shown in Figure 6.27 for the measurement in the $Z/\gamma^* \rightarrow \tau_\mu \tau_{\text{had}}$ event sample together with correction factors that are derived from the ratio of the efficiencies as measured in collision data and simulated events for the $Z/\gamma^* \rightarrow \tau_\mu \tau_{\text{had}}$ and the $W \rightarrow \tau_{\text{had}} \nu$ event samples. The efficiencies and correction factors for the single- τ_{had} triggers used in the data-taking after September 2011 are comparable to results for the corresponding triggers used before September 2011.

The efficiencies of the single- τ_{had} triggers for jets that are misidentified as hadronic τ -lepton decays are measured together with the off-line jet-to- τ_{had} misidentification probabilities. This measurement is described in Section 6.5.3.

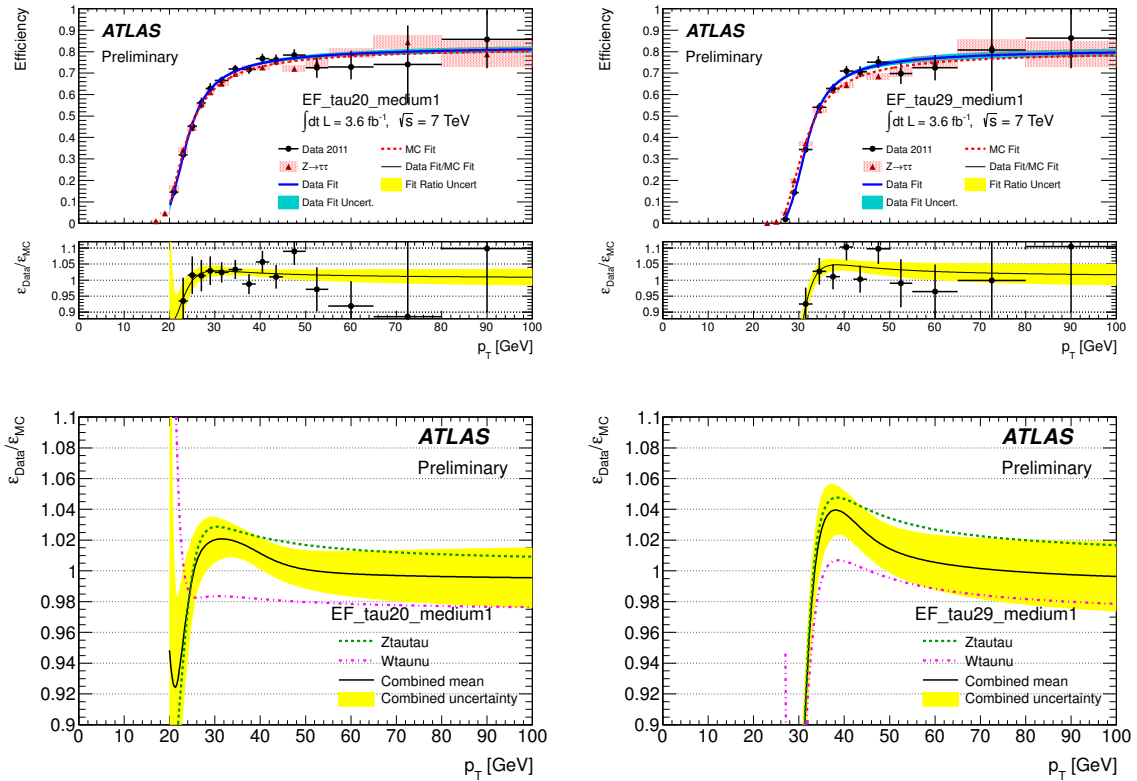


Figure 6.27.: Efficiencies of the single- τ_{had} triggers with p_T thresholds of 20 GeV (left-hand side, first row) and 29 GeV (right-hand side, first row) as measured in the $Z/\gamma^* \rightarrow \tau_\mu \tau_{\text{had}}$ event sample and correction factors for the same triggers (second row) as measured in the $Z/\gamma^* \rightarrow \tau_\mu \tau_{\text{had}}$ and $W \rightarrow \tau_{\text{had}} \nu$ event samples. The efficiencies and correction factors are shown for the single- τ_{had} triggers used in the data-taking before September 2011, i.e. EF_tau20_medium1 and EF_tau29_medium1 (taken from Reference [232]).

6.5.3. Estimation of the Background From Events With Misidentified Jets

After the selection, events with jets that are misidentified as hadronic τ -lepton decays are expected from multi-jet production, W +jets production and to a significantly smaller extent from $t\bar{t}$ and single-top production. The contribution from $Z/\gamma^* \rightarrow \tau^+\tau^-$ +jets events is small compared to the other background sources. The description of the variables that are used to identify hadronic τ -lepton decays in simulated events is insufficient for misidentified jets. The probability that jets are misidentified as hadronic τ -lepton decays, the jet-to- τ_{had} misidentification probability, is significantly higher in simulation than in data. The estimation of the background from multi-jet production is described in Section 6.5.1. Apart from the subtraction of the other backgrounds, the estimation of the multi-jet background does not depend on simulation and is thus not affected by the observed difference between simulation and data. All other backgrounds are estimated using simulation and corrections have to be applied for the jet-to- τ_{had} misidentification probability.

The jet-to- τ_{had} misidentification probability is measured together with the trigger efficiency for jets with a tag-and-probe method in data. For this purpose a sample of $W \rightarrow \mu\nu$ +jets events is selected in data. Events are primarily selected based on information about the muon. The jet-to- τ_{had} misidentification probability is measured for the accompanying jets. It depends on whether a jet is initiated by the hadronisation of a quark or a gluon. Ideally, the misidentification probability should be measured separately for quark- and gluon-initiated jets. It is, however, not possible to distinguish quark- and gluon-initiated jets in data at a high enough confidence level. For this reason the jet-to- τ_{had} misidentification probability is measured in an event sample that has the same fraction of jets initiated by the hadronisation of quarks or gluons, the so-called quark-gluon fraction, as the dominant background to the search for $h/A/H \rightarrow \tau_{\text{had}}\tau_{\text{had}}$ decays for which the misidentification probability is important in the background estimation. This background is dominated by $W \rightarrow \tau_{\text{had}}\nu$ +jets events and contains additional events which primarily stem from top-quark production. A sample of $W \rightarrow \mu\nu$ +jets events can be selected easily and has the same quark-gluon fraction as a $W \rightarrow \tau_{\text{had}}\nu$ +jets event sample.

The $W \rightarrow \mu\nu$ +jets event sample is selected with a single-muon trigger with a p_T threshold of 18 GeV (i.e. `EF_mu18_MG` before and `EF_mu18_MG_medium` after run 180776). The standard data quality and event cleaning procedure described in Section 6.3.2 is applied. Events with one isolated muon with $p_T > 20$ GeV are selected with medium muon identification requirements. To ensure the isolation of the muon, both calorimeter and track isolation criteria are used. A muon is calorimeter-isolated if the calorimetric energy in a cone of $\Delta R = 0.2$ around the muon excluding the clusters associated with the muon itself is below 4% of the transverse momentum of the muon. A muon is track-isolated if in a cone of radius $\Delta R = 0.4$ at most one track with $p_T > 1$ GeV is present in addition to the track associated to the muon itself. A veto against electrons with $p_T > 15$ GeV is complemented by requirements that the transverse mass of the muon- E_T^{miss} system is above 40 GeV and the missing transverse momentum is above 25 GeV.

The expected number of signal and background events in this event sample is estimated from simulation for all processes except for multi-jet production. The estimation of the backgrounds closely follows the procedures that are used for the search for $h/A/H \rightarrow \tau_{\text{had}}\tau_{\text{had}}$ decays. The multi-jet background is estimated with an ABCD method. Similar to the method described in Section 6.5.1 a signal region and three control regions are defined based on whether the missing transverse momentum is above 25 GeV or below 20 GeV and whether both muon-isolation requirements are satisfied or not. Events with $20 \text{ GeV} < E_T^{\text{miss}} < 25 \text{ GeV}$ are not considered to obtain clearly separated control regions.

The number of events in data and the expected number of signal and background events is shown in Table 6.10 after each of the selection steps. In Figure 6.28 the distributions of the muon transverse momentum and the transverse mass of the muon- E_T^{miss} system are shown after the full selection.

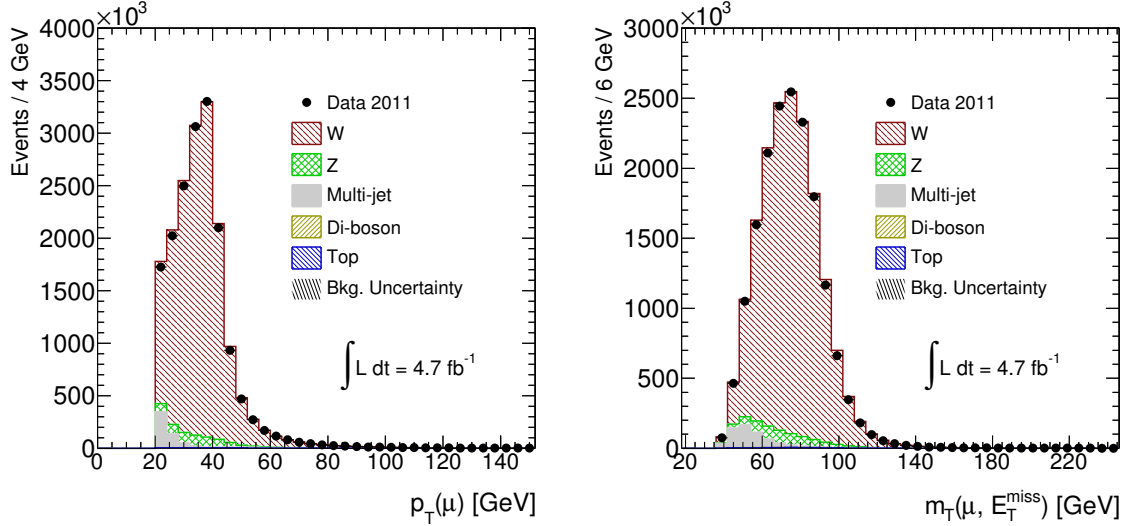


Figure 6.28.: Distributions of the transverse momentum of the selected muon (left-hand side) and the transverse mass of the muon and the missing transverse momentum (right-hand side) for the $W \rightarrow \mu\nu$ control region used in the measurement of the jet-to- τ_{had} misidentification probability. The background uncertainties include statistical uncertainties only.

The jet-to- τ_{had} misidentification probability for a given single- τ_{had} trigger and a certain τ_{had} identification level is measured in a sample without τ_{had} decays as the ratio of the number of τ_{had} candidates that induce a positive trigger decision and pass the requirements for the considered τ_{had} identification level and the number of all τ_{had} candidates. To obtain a pure event sample without τ_{had} decays the background from $Z/\gamma^* \rightarrow \tau^+\tau^-$ and diboson production is subtracted from the data. The background from $Z/\gamma^* \rightarrow \mu^+\mu^-$ production is not subtracted as for these events a similar jet-to- τ_{had} misidentification rate as for $W \rightarrow \mu\nu$ events is expected.

In the hypothetical case that the top background contains only misidentified τ_{had} decays the top background would not be subtracted, while in the hypothetical case that the top background contains only correctly identified τ_{had} decays the background would need to be subtracted. In reality the events from the top background can be misidentified τ_{had} decays or correctly identified τ_{had} decays, but the exact fraction of correctly identified τ_{had} decays is unknown without a detailed measurement. It is conservatively assumed that this fraction is $50\% \pm 50\%$. For the nominal value of the jet-to- τ_{had} misidentification probability 50% of the top background is subtracted and a systematic uncertainty on the jet-to- τ_{had} misidentification probability is obtained by subtracting the complete top background and by not subtracting the top background at all. The obtained systematic uncertainty is small and therefore no significant influence of the exact value of the fraction of correctly identified τ_{had} decays in top background is expected.

For the measurement of the jet-to- τ_{had} misidentification probability τ_{had} candidates are considered if they have a minimum p_T of 20 GeV and one or three associated tracks. The misidentification probability is measured as a function of the transverse momentum of the τ_{had} can-

	Data	$W + \text{jets}$	$Z/\gamma^* + \text{jets}$	Top	Diboson
Trigger/GRL	3.34×10^7	$(2.4981 \pm 0.0015) \times 10^7$	$(4.2380 \pm 0.0029) \times 10^6$	171860 ± 120	16070 ± 50
Event cleaning	3.34×10^7	$(2.3727 \pm 0.0015) \times 10^7$	$(4.0353 \pm 0.0028) \times 10^6$	142490 ± 110	14880 ± 50
One muon	3.34×10^7	$(2.3422 \pm 0.0015) \times 10^7$	$(4.0138 \pm 0.0028) \times 10^6$	140360 ± 110	14740 ± 50
Muon $p_T > 20$ GeV	3.34×10^7	$(2.1930 \pm 0.0014) \times 10^7$	$(3.7002 \pm 0.0024) \times 10^6$	129910 ± 100	14180 ± 40
Muon calorimeter isolation	2.12×10^7	$(2.0601 \pm 0.0014) \times 10^7$	$(3.5223 \pm 0.0024) \times 10^6$	101340 ± 70	13390 ± 40
Muon track isolation	2.00×10^7	$(2.0140 \pm 0.0013) \times 10^7$	$(3.4475 \pm 0.0024) \times 10^6$	94250 ± 70	12950 ± 40
Second-muon veto	2.00×10^7	$(2.0125 \pm 0.0013) \times 10^7$	$(1.3494 \pm 0.0015) \times 10^6$	78070 ± 60	8840 ± 40
Electron veto	2.00×10^7	$(2.0121 \pm 0.0013) \times 10^7$	$(1.3406 \pm 0.0015) \times 10^6$	71780 ± 60	7060 ± 40
$m_T > 40$ GeV	2.00×10^7	$(1.8350 \pm 0.0013) \times 10^7$	862200 ± 1200	56440 ± 50	5829 ± 35
$E_T^{\text{miss}} > 25$ GeV	1.70×10^7	$(1.6010 \pm 0.0012) \times 10^7$	648900 ± 1000	51210 ± 50	5069 ± 32

Table 6.10.: Number of events after each of the requirements for the selection of the $W \rightarrow \mu\nu$ +jets control region that is used to determine the jet-to- τ_{had} misidentification probability. The observed event yields in data are compared to the expected event yields for simulated event samples of W -boson, Z -boson, top and diboson production. The latter event yields are normalised to the integrated luminosity of 4.66 fb^{-1} . After all selection steps the expected event yield for multi-jet production is $580,000 \pm 10,000$.

didate for all considered single- τ_{had} triggers (i.e. `EF_tau29T_medium1`, `EF_tau20T_medium1`, `EF_tau29_medium1`, `EF_tau20_medium1`) and the τ_{had} identification levels loose, medium and tight. In addition, measurements without trigger requirement are performed for all three τ_{had} identification levels. The measured jet-to- τ_{had} misidentification probabilities are shown in Figure 6.29 for the medium τ_{had} identification level with and without requiring a single- τ_{had} trigger with a p_T threshold of 20 GeV (`EF_tau20T_medium1`) as an example. The results of the measurement of the jet-to- τ_{had} misidentification probabilities are available for other single- τ_{had} triggers and τ_{had} identification levels in Appendix B.2.

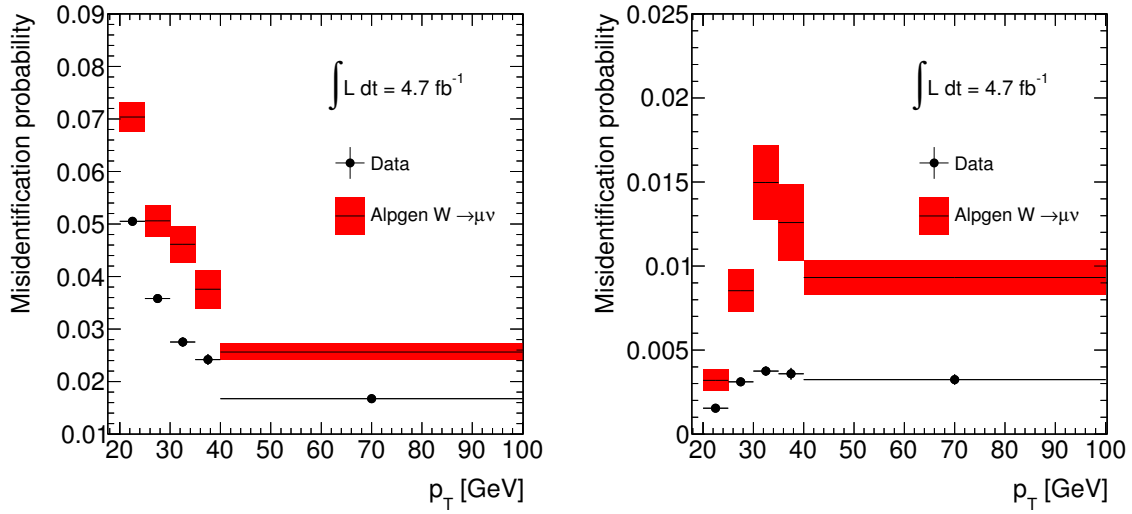


Figure 6.29.: Jet-to- τ_{had} misidentification probability for the off-line and the off-line and trigger selection as measured in data and simulation with the tag-and-probe method in the $W \rightarrow \mu\nu$ event sample. On the left-hand side the off-line jet-to- τ_{had} misidentification probability is shown for the medium τ_{had} identification level, no trigger decision is required. On the right-hand side the combined trigger and off-line jet-to- τ_{had} misidentification probability is shown for a single- τ_{had} trigger with a p_T threshold of 20 GeV (`EF_tau20T_medium1`) and the medium τ_{had} identification level. The uncertainties include statistical uncertainties and systematic uncertainties originating from the subtraction of the background distributions.

For all simulated samples weights are applied to the events that contain selected τ_{had} decays that cannot be matched to a true τ_{had} decay, an electron or a muon in order to correct the jet-to- τ_{had} misidentification probability in simulation to the corresponding probability in data. These weights are computed as the ratio of the jet-to- τ_{had} misidentification probabilities as measured in data and simulation. They depend on the transverse momentum of the τ_{had} candidate, the τ_{had} identification level and the associated single- τ_{had} trigger item. If several single- τ_{had} trigger items are associated, the item with the highest- p_T threshold is used. The measured correction factors are shown for the single- τ_{had} triggers used after September 2011 (i.e. `EF_tau20T_medium1` and `EF_tau29T_medium1`) in Figure 6.30. The correction factors for the single- τ_{had} triggers used before September 2011 are comparable. They are shown in Appendix B.2.

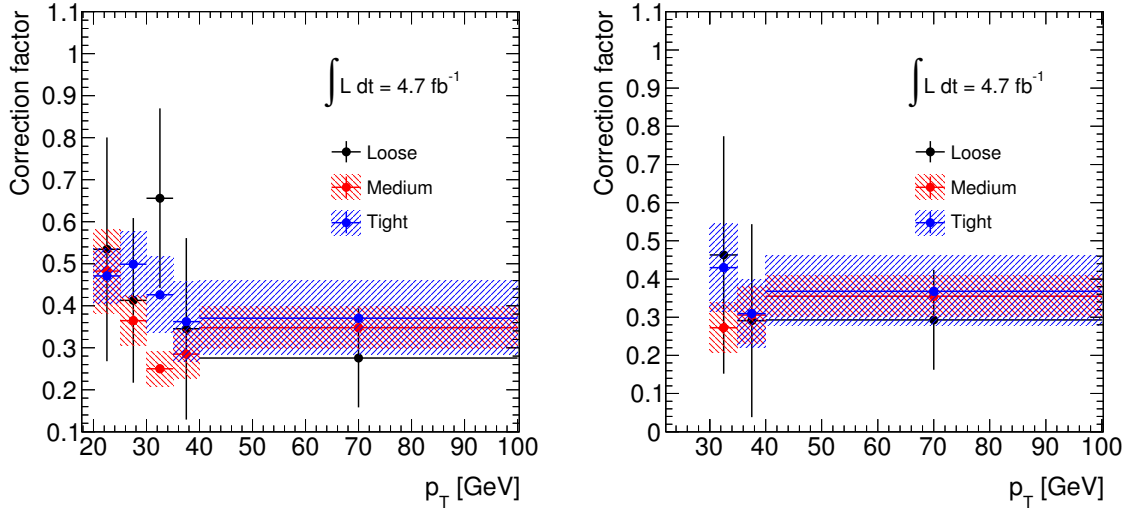


Figure 6.30.: Ratio of the jet-to- τ_{had} misidentification probabilities for the off-line and trigger selection as measured in data and simulation with the tag-and-probe method in the $W \rightarrow \mu\nu + \text{jets}$ event sample. On the left-hand side the ratio of the jet-to- τ_{had} misidentification probabilities is shown for a single- τ_{had} trigger with a p_T threshold of 20 GeV (EF_tau20T_medium1) and the τ_{had} identification levels loose, medium and tight. On the right-hand side the ratio of the jet-to- τ_{had} misidentification probabilities is shown for a single- τ_{had} trigger with a p_T threshold of 29 GeV (EF_tau29T_medium1) and the same τ_{had} identification levels. These ratios are applied as correction factors to simulated events that contain jets which are misidentified as τ_{had} decays. The uncertainties include statistical uncertainties and systematic uncertainties from the subtraction of the backgrounds.

6.5.4. Studies With τ -embedded $Z/\gamma^* \rightarrow \mu^+\mu^-$ and $W \rightarrow \mu\nu$ Data

The expected event yields for the $Z/\gamma^* \rightarrow \tau^+\tau^-$ and $W \rightarrow \tau\nu$ backgrounds are estimated with simulated event samples. The correction factors that have been described in the previous sections are applied. In the following, the production of samples of τ -embedded $Z/\gamma^* \rightarrow \mu^+\mu^-$ and $W \rightarrow \mu\nu$ data events using the so-called “embedding technique” [238] is described. The τ -embedded $Z/\gamma^* \rightarrow \mu^+\mu^-$ and $W \rightarrow \mu\nu$ event samples are modified data samples created by removing the muons from the event and replacing them by simulated τ leptons. With the event samples that were obtained with the embedding technique the simulated $Z/\gamma^* \rightarrow \tau^+\tau^-$ and $W \rightarrow \tau\nu$ event samples that are employed for this analysis are validated.

The $Z/\gamma^* \rightarrow \mu^+\mu^-$ and $W \rightarrow \mu\nu$ event samples that are used for the production of the τ -embedded $Z/\gamma^* \rightarrow \mu^+\mu^-$ and $W \rightarrow \mu\nu$ data are selected from collision data using the requirements reported in Table 6.11. For the $Z/\gamma^* \rightarrow \mu^+\mu^-$ selection a purity of 97% is obtained. The main background is multi-jet production with enriched heavy-flavour quark production. The contribution from $t\bar{t}$ production is approximately 0.1%. For the $W \rightarrow \mu\nu$ selection a purity of 90% and 92% is obtained depending on the W -boson charge. After the full event selection the main background is multi-jet production with a contribution of 2% to 3%. Additional backgrounds stem from $Z/\gamma^* \rightarrow \mu^+\mu^-$ and $W \rightarrow \tau\nu$ production with a contribution of approximately 3% and for each process. The multi-jet background stems mainly from heavy-quark decays. A background contribution of approximately 0.4%

Selection requirement	$Z/\gamma^* \rightarrow \mu^+\mu^-$ events	$W \rightarrow \mu\nu$ events
Trigger	single-muon trigger and data quality requirements	
Muons	at least two muons	exactly one muon
	medium identification	
	$p_{T,\mu} > 20 \text{ GeV}$ isolation: $\sum_{i=0}^{n_{\text{tracks}}} p_{T,\text{track } i} / p_{T,\mu} < 0.2$	
Invariant di-muon mass	$m_{\mu\mu} > 55 \text{ GeV}$	-
Missing transverse momentum	-	$E_T^{\text{miss}} > 25 \text{ GeV}$
Transverse mass	-	$m_T(\mu, E_T^{\text{miss}}) > 40 \text{ GeV}$

Table 6.11.: Summary of the requirements for the selection of the data samples that are used for the production of τ -embedded $Z/\gamma^* \rightarrow \mu^+\mu^-$ and $W \rightarrow \mu\nu$ events. For the single-muon trigger the trigger with the lowest available muon p_T threshold is used. The number of tracks with $p_T > 1 \text{ GeV}$ in a cone with $\Delta R = 0.2$ around the muon track is referred to as n_{tracks} . The transverse momentum of track i is $p_{T,\text{track } i}$ and the two muons in the $Z/\gamma^* \rightarrow \mu^+\mu^-$ selection are required to share a common primary vertex. The transverse mass $m_T(\mu, E_T^{\text{miss}})$ is calculated based on the muon and the E_T^{miss} four-momentum vectors.

is expected from $t\bar{t}$ production [239]. Possible background from Higgs boson production is found to be negligible for the $Z/\gamma^* \rightarrow \mu^+\mu^-$ and the $W \rightarrow \mu\nu$ selections.

For each of the considered events the four-vectors of the selected muons are determined and a so-called mini-event is simulated. A mini-event is an event with one or two τ leptons that feature the same energy and three-momentum direction and the same production vertex as the reconstructed muons from data. The absolute value of the τ -lepton three-momentum, however, has to be different from the absolute value of the three-momentum of the corresponding muon by a factor of $\sqrt{E_\mu^2 - m_\tau^2} / |\vec{p}_\mu|$ to account for the different τ -lepton and muon masses. The τ leptons are decayed using TAUOLA [65], final state radiation is simulated with PHOTOS [55]. For the mini-event no underlying event is simulated. As the mini-event is merged with the corresponding event in data, the simulation of the underlying event in the mini-event would lead to an inadequate amount of underlying event activity. The complete detector simulation is performed for the mini-event, but the calorimeter noise is switched off during the digitisation of the mini-event to avoid an inadequate amount of noise.

To facilitate the merging of the mini-event and the reconstructed $Z/\gamma^* \rightarrow \mu^+\mu^-$ or $W \rightarrow \mu\nu$ data event, all hits associated with the tracks of the selected muons are removed from the reconstructed $Z/\gamma^* \rightarrow \mu^+\mu^-$ or $W \rightarrow \mu\nu$ data event. To subtract the energy deposition of the muons a second mini-event with muons that feature the same kinematics as the muons reconstructed in data is simulated and the calorimeter energy deposits of the simulated muons are subtracted from the reconstructed $Z/\gamma^* \rightarrow \mu^+\mu^-$ or $W \rightarrow \mu\nu$ data event at the cell level. After the subtraction of the $Z/\gamma^* \rightarrow \mu^+\mu^-$ or $W \rightarrow \mu\nu$ energy deposits and track hits, the track hits and calorimeter cells of the simulated $\tau^+\tau^-$ or τ^\pm mini-event are added to the $Z/\gamma^* \rightarrow \mu^+\mu^-$ or $W \rightarrow \mu\nu$ data event. The resulting $Z/\gamma^* \rightarrow \tau^+\tau^-$ and $W \rightarrow \tau\nu$ hybrid events are subject to the event reconstruction, in which all objects are re-reconstructed. For technical reasons it is not possible to simulate trigger decisions in τ -embedded data events.

The τ -embedding method is based on the assumptions that clean $Z/\gamma^* \rightarrow \mu^+\mu^-$ and $W \rightarrow \mu\nu$ event samples can be selected from data and that the $h/A/H \rightarrow \tau\tau$ event selection does not significantly increase the contribution of the non- Z or non- W backgrounds. It is necessary to assume that the kinematic properties of a $Z/\gamma^* \rightarrow \tau^+\tau^-$ ($W \rightarrow \tau\nu$) and a $Z/\gamma^* \rightarrow \mu^+\mu^-$ ($W \rightarrow \mu\nu$) event with rescaled muon momenta are similar. In addition, it is assumed that the embedding procedure does not introduce a bias of the event selection efficiency.

For the τ -embedded sample without the $h/A/H \rightarrow \tau_{\text{had}}\tau_{\text{had}}$ event selection it was shown before that the contamination with background is at an acceptable level. For the τ -embedded $Z/\gamma^* \rightarrow \mu^+\mu^-$ data the top background fraction after the b -tagged selection is increased to below 2.2% and after the b -vetoed selection to below 1%. The contribution of multi-jet production events to the τ -embedded samples is estimated to be below the relative contribution in the sample before the event selection. For the τ -embedded $W \rightarrow \mu\nu$ data the contribution of the top background is up to 20% for the b -tagged selection and below 3% for the b -vetoed selection. The backgrounds from $Z/\gamma^* \rightarrow \mu^+\mu^-$ and $W \rightarrow \tau\nu$ production are expected to contribute roughly at the same level before and after the selection. Multi-jet production is expected to contribute less to the background event yield after the selection than before. For the b -vetoed selection the purity of the τ -embedded event sample is acceptable. For the b -tagged selection, however, the contribution of the top background in the τ -embedded $W \rightarrow \mu\nu$ sample is increased to a degree that forbids the use of the τ -embedded $W \rightarrow \mu\nu$ sample in this channel. For top background the efficiency of the requirement of one b -jet with $20 \text{ GeV} < p_T < 50 \text{ GeV}$ is higher than for $W \rightarrow \mu\nu$ events and in consequence the expectation of the selection efficiency would be biased towards higher values if the τ -embedded $W \rightarrow \mu\nu$ data was employed.

An important step in the validation of the τ -embedded data is the embedding of a simulated $Z/\gamma^* \rightarrow \mu^+\mu^-$ or $W \rightarrow \mu\nu$ mini-event – instead of a simulated $Z/\gamma^* \rightarrow \tau^+\tau^-$ or $W \rightarrow \tau\nu$ mini-event – into a $Z/\gamma^* \rightarrow \mu^+\mu^-$ and $W \rightarrow \mu\nu$ data event and the subsequent comparison of the hybrid events to the data events. In this step the merging procedure can be validated without significant influence of the background composition and the rescaling of the muon momentum four-vectors to obtain the correct τ -lepton kinematics.

The advantage of the τ -embedded event samples is that the underlying event, associated jet production and any interactions apart from the decay of the Z or W boson are obtained from data. However, it is not possible to simulate the trigger decisions in the reconstruction of the hybrid event. In the $h/A/H \rightarrow \tau_{\text{had}}\tau_{\text{had}}$ analysis a di- τ_{had} trigger is used for the selection of the data sample. As the di- τ_{had} trigger uses similar variables for the background suppression as the off-line τ_{had} identification, it cannot be ensured that the trigger efficiency and its correlation with the off-line selection can be modelled correctly with the τ -embedded data. It is therefore not possible to estimate the background from W - and Z -boson production with the τ -embedded data. The τ -embedded data are, however, used to validate the ALPGEN simulation samples.

The shape of the distributions of several variables is compared between the τ -embedded $Z/\gamma^* \rightarrow \mu^+\mu^-$ data and the simulated $Z/\gamma^* \rightarrow \tau^+\tau^-$ samples after the b -tagged and the b -vetoed selection with the exception of the di- τ_{had} trigger requirement and the requirement that the τ_{had} decays are matched to trigger-level τ_{had} decays. The results of this comparison are shown in Figures 6.31 and 6.32. Since the event samples for the b -tagged selection suffer from a low number of events, the comparison is additionally performed for a selection without b -jet requirement. Additional comparisons are performed for a looser selection where only loose τ_{had} identification levels and p_T thresholds of 20 GeV are required for the τ_{had} decays. These comparisons are shown in Appendix B.3.

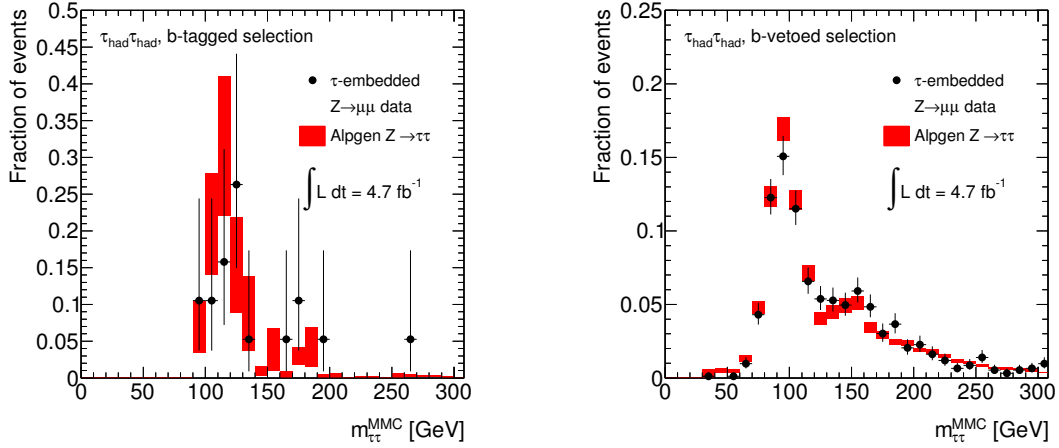


Figure 6.31.: Validation of the simulated $Z/\gamma^* \rightarrow \tau^+\tau^-$ event samples. The distributions of the MMC mass are shown for the τ -embedded $Z/\gamma^* \rightarrow \mu^+\mu^-$ data and the simulated $Z/\gamma^* \rightarrow \tau^+\tau^-$ event samples after the b -tagged (left-hand side) and the b -vetoed (right-hand side) selections as described in Section 6.5.4. The shown uncertainties are statistical.

Due to the low number of selected events a meaningful comparison of the τ -embedded $W \rightarrow \mu\nu$ data and the ALPGEN $W \rightarrow \tau\nu$ event samples is not possible for the complete selection of the b -vetoed and the b -tagged channels. Instead a looser selection that requires loose identification levels for the τ_{had} decays and reduced p_T requirements for every reconstructed τ_{had} decay that is matched to a true τ_{had} decay within a distance of $\Delta R = 0.4$. The requirement on the charge product of the τ_{had} decays is dropped and $m_T(\mu, E_T^{\text{miss}}) > 40$ GeV is required to ensure that the τ -embedded $W \rightarrow \mu\nu$ sample is not biased towards higher transverse masses or transverse momenta of the τ_{had} decays compared to the simulated event sample. The resulting comparisons are shown in Figure 6.33 and Appendix B.4. The simulated event sample cannot be compared with the τ -embedded event samples for the b -tagged selection due to an expected bias from the higher efficiency of the b -jet requirement for background from $t\bar{t}$ and single-top production in the $W \rightarrow \mu\nu$ selection in data. A correction of this bias might be possible in principle, but due to the complexity of the production of the τ -embedded event sample a correction cannot be derived for this thesis.

6.5.5. Estimation of the Fraction of Events With Identified b -jet

It is known that the p_T spectra of additional b -jets are not well described in event samples that are simulated with the ALPGEN generator. In the selection of the $h/A/H \rightarrow \tau_{\text{had}}\tau_{\text{had}}$ analysis the data sample is split according to whether a b -jet with $20 \text{ GeV} < p_T < 50 \text{ GeV}$ is identified or not. In the following, the measurement of the efficiency of this selection step, the fraction of events with identified b -jet, is described for the $Z/\gamma^* \rightarrow \tau^+\tau^-$ and $W \rightarrow \tau\nu$ backgrounds. Correction factors for the simulated event samples are measured with $W \rightarrow \mu\nu$ data or τ -embedded $Z/\gamma^* \rightarrow \mu^+\mu^-$ data and applied for event samples with all leptonic W -boson decays and all Z -boson decays to charged leptons.

Measurement of the fraction of events with identified b -jet for $Z/\gamma^* \rightarrow \tau^+\tau^-$ events

The efficiency of the b -jet requirement for $Z/\gamma^* \rightarrow \tau^+\tau^-$ events is measured in the τ -embedded $Z/\gamma^* \rightarrow \mu^+\mu^-$ data sample. In order to obtain an unbiased measurement it is necessary that

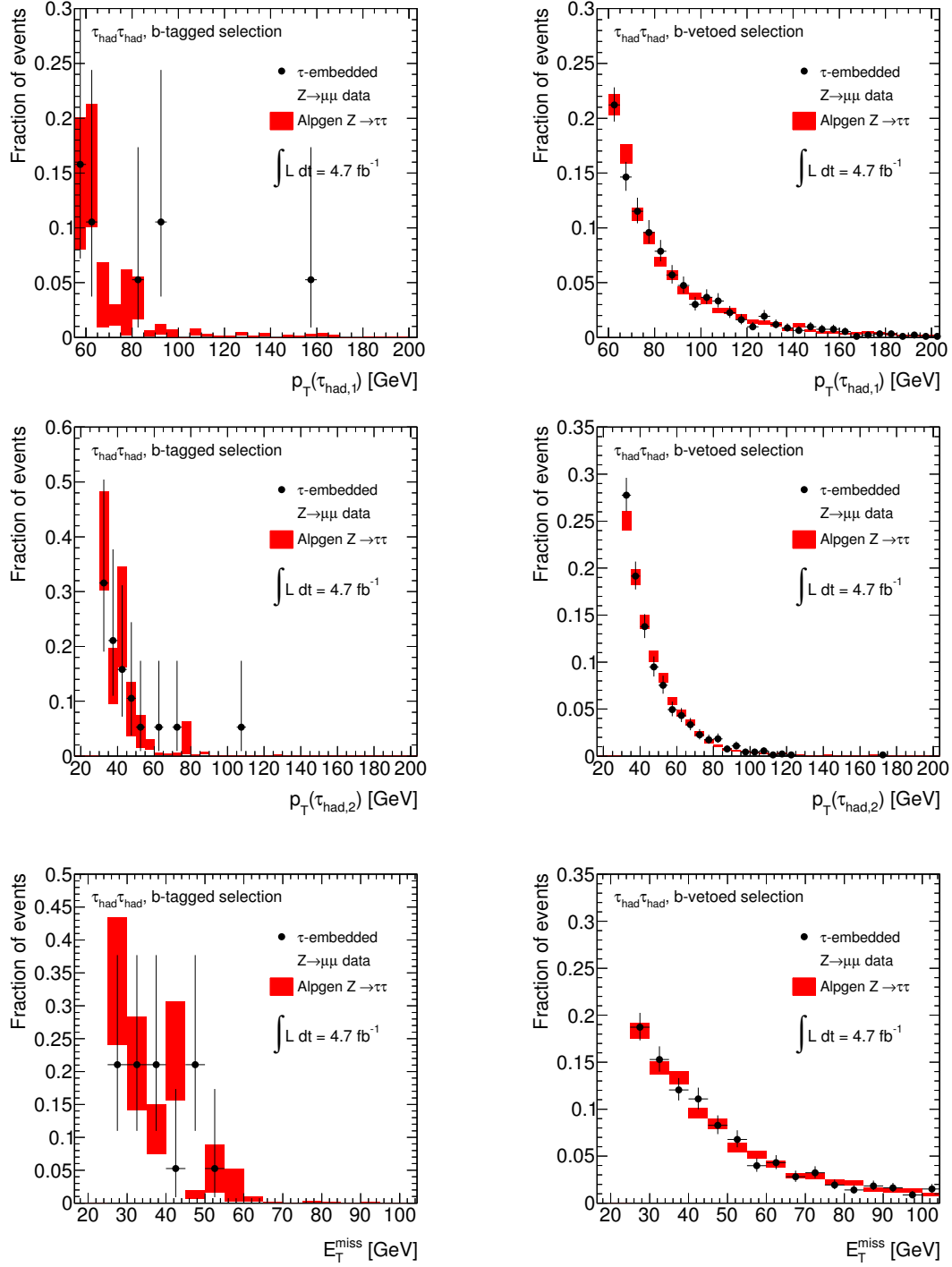


Figure 6.32.: Validation of the simulated $Z/\gamma^* \rightarrow \tau^+\tau^-$ event samples. The distributions of the transverse momenta of the highest- p_T (first row) and second highest- p_T (second row) hadronic τ -lepton decays and the missing transverse momentum (third row) are shown for the τ -embedded $Z/\gamma^* \rightarrow \mu^+\mu^-$ data and the simulated $Z/\gamma^* \rightarrow \tau^+\tau^-$ event samples. The distributions are shown after the b -tagged (left-hand side) and the b -vetoed (right-hand side) selections as described in Section 6.5.4. The shown uncertainties are statistical.

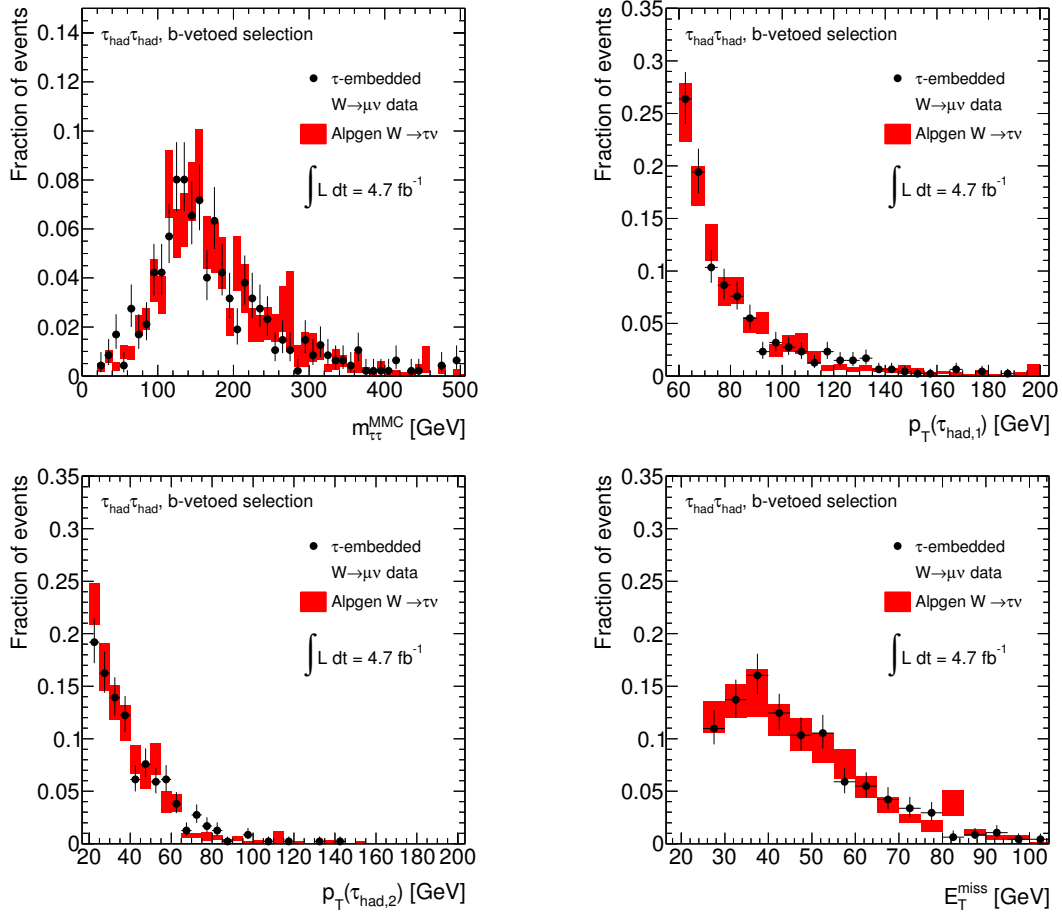


Figure 6.33.: Validation of the simulated $W \rightarrow \tau\nu$ event samples. The distributions of the MMC mass (first row, left-hand side), the p_T of the highest- p_T (first row, right-hand side) and second highest- p_T (second row, left-hand side) hadronic τ -lepton decays and the missing transverse momentum (second row, right-hand side) are shown for the τ -embedded $W \rightarrow \mu\nu$ data and the $W \rightarrow \tau\nu$ event samples. The distributions are shown after the selection described in Section 6.5.4. The shown uncertainties are statistical.

the selected $Z/\gamma^* \rightarrow \mu^+\mu^-$ data sample has the same fraction of events with identified b -jets with $20 \text{ GeV} < p_T < 50 \text{ GeV}$ as the $Z/\gamma^* \rightarrow \tau^+\tau^-$ data. As the b -jet spectrum is independent of the Z -boson decay channel, the same b -jet spectrum is expected in $Z/\gamma^* \rightarrow \mu^+\mu^-$ and $Z/\gamma^* \rightarrow \tau^+\tau^-$ data events. As mentioned in Section 6.5.4, the background from other processes in the selected $Z/\gamma^* \rightarrow \mu^+\mu^-$ event sample is small, in particular only low background from top production is expected.

In the τ -embedded $Z/\gamma^* \rightarrow \mu^+\mu^-$ data samples and the simulated $Z/\gamma^* \rightarrow \tau^+\tau^-$ event samples the complete event selection apart from the trigger requirement is applied. In the τ -embedded samples 2766 events are observed after the full selection. In 19 events a b -jet with $20 \text{ GeV} < p_T < 50 \text{ GeV}$ is identified. In the simulated $Z/\gamma^* \rightarrow \tau^+\tau^-$ event samples 345 ± 9 events are selected after the MMC calculation, in 8.7 ± 1.3 events a b -jet is identified.

The ratios of the efficiencies of the b -jet requirement that are obtained in the τ -embedded

data and the simulated event samples are

$$k_b^Z = 1.24 \pm 0.34 \quad (6.31)$$

for the sample of events with identified b -jet and

$$k_{\text{no } b}^Z = 1.00 \pm 0.04 \quad (6.32)$$

for the sample of events without identified b -jet. The quoted uncertainties are derived from the statistical uncertainties of the τ -embedded $Z/\gamma^* \rightarrow \mu^+\mu^-$ and the simulated $Z/\gamma^* \rightarrow \tau^+\tau^-$ event samples with a binomial calculation. The uncertainty of the correction factor for the b -vetoed selection is found to be small compared to all other uncertainties and is therefore neglected.

Measurement of the fraction of events with identified b -jet for $W \rightarrow \tau\nu$ events

After the selection of the $W \rightarrow \mu\nu$ data for the τ -embedded event samples there is a significant background from $t\bar{t}$ production and other events. The relative contributions of these backgrounds are further increased by the analysis selection criteria. Thus the purity of τ -embedded $W \rightarrow \mu\nu$ data sample is significantly lower than the purity of the corresponding τ -embedded $Z/\gamma^* \rightarrow \mu^+\mu^-$ data sample. Compared to $W \rightarrow \mu\nu$ events the b -jet requirement has a higher efficiency in $t\bar{t}$ events. Therefore the measured efficiency is biased and the τ -embedded event samples cannot be used for $W \rightarrow \tau\nu$ events in the background selection.

Instead, the efficiency of the requirement of at least one b -jet is measured in a $W \rightarrow \mu\nu$ event sample in data and in a simulated $W \rightarrow \tau\nu$ event sample. The $W \rightarrow \mu\nu$ event sample has a similar background composition and level as the τ -embedded $W \rightarrow \mu\nu$ data. However, the background to the $W \rightarrow \mu\nu$ event sample is known more precisely and is subtracted before the efficiency is measured.

The ratio of the efficiencies measured in data and simulation is used as a correction factor for simulation. The efficiency is expected to be independent of the decay channel of the W boson and hence the derived correction factors can be applied to the simulated $W \rightarrow \tau_{\text{had}}\nu$ event samples. In the $h/A/H \rightarrow \tau_\mu\tau_{\text{had}}$ analysis [240], where one τ lepton decays into a muon and neutrinos and one τ lepton hadronically, a control region that is dominated by W -boson production is defined based on an identified muon, an additional identified hadronic τ -lepton decay and the requirement $70 \text{ GeV} < m_T(\mu, E_T^{\text{miss}}) < 110 \text{ GeV}$. As the jet-to- τ_{had} misidentification probability is not well described in the $W \rightarrow \mu\nu$ and $W \rightarrow \tau\nu$ simulated event samples a correction factor for the W -boson background is measured by comparing the ratio of the number of events in data, where the contribution of non- W background is subtracted based on the expectation in simulated event samples, and the number of events in the simulated W -boson event samples. The correction factor is given by

$$k_W = \frac{n_{\text{data}} - n_{\text{other,MC}}}{n_{W,\text{MC}}}, \quad (6.33)$$

where n_{data} is the number of events selected in data, $n_{W,\text{MC}}$ is the number of expected $W \rightarrow \tau\nu$ and $W \rightarrow \mu\nu$ events and $n_{\text{other,MC}}$ is the number of events expected from other processes. The numbers $n_{W,\text{MC}}$ and $n_{\text{other,MC}}$ are obtained from simulated event samples.

In this measurement

$$k_W = 0.531 \pm 0.012 \quad (6.34)$$

is obtained. After requiring a b -jet the correction factor is re-measured and

$$k_W^{b\text{-tag}} = 0.54 \pm 0.16 \quad (6.35)$$

is obtained. The ratio

$$k_b^W = \frac{k_W^{b\text{-tag}}}{k_W} \quad (6.36)$$

is a measure of the ratio of the b -jet requirement efficiencies in data and simulated event samples. The measured value is

$$k_b^W = 1.01 \pm 0.31 \quad (6.37)$$

and therefore no correction factor is applied to the $W \rightarrow \tau_{\text{had}}\nu$ simulated event samples in the channel with at least one identified b -jet. The uncertainty of this measurement is used as the systematic uncertainty for the efficiency of the b -jet requirement. The measured ratio can be converted into a correction factor on the simulated $W \rightarrow \tau_{\text{had}}\nu$ event sample in the channel without identified b -jet. This correction was measured as

$$k_{\text{no } b}^W = 1.000 \pm 0.031. \quad (6.38)$$

The uncertainty of the correction factor is negligible compared to all other systematic uncertainties.

6.5.6. Validation and Results of the Combined Background Estimate

Based on the background estimation methods described in the previous sections the expected distributions of several important variables are compared to those observed in data. In Figure 6.34 the distributions of the transverse momenta of the highest- p_T and the second highest- p_T hadronic τ -lepton decays and the missing transverse momentum are shown. In Figure 6.35 the distributions of the azimuthal angle between the highest- p_T and second highest- p_T hadronic τ -lepton decays, the electric-charge product of the hadronic τ -lepton decays and the transverse momentum of the di- τ resonance as reconstructed by the MMC algorithm are shown. In Figure 6.36 the BDT jet scores for the identification of hadronic τ -lepton decays are shown for the highest- p_T and second highest- p_T τ_{had} candidate together with the number of additional jets per event. The distributions of further variables are shown in Appendix B.5. All distributions are shown separately for the b -tagged and the b -vetoed selections. All the considered distributions show a good agreement of the data with the estimated background at the level that is expected based on the estimated uncertainties. The good consistency of the data and the background expectation provides confidence that the contributions of all important background processes are estimated with a sufficient accuracy.

6.6. Systematic Uncertainties

In the last section the background estimation procedures were introduced, however these estimates cannot be perfect and the associated statistical and systematic uncertainties need to be quantified. Uncertainties are statistical if, under the assumption that only this uncertainty exists, for a large number of measurements the average result of the measurements approaches the true value. For this analysis the measurement result is the event yield and the MMC mass distribution after the event selection for the signal region and the multi-jet control regions. Statistical uncertainties from auxiliary measurements, such as the measurement of the jet-to- τ_{had} misidentification probability in the $W \rightarrow \mu\nu$ control region, are treated as systematic uncertainties. The statistical uncertainty can be calculated from the number of events in the simulated event samples for all backgrounds except for the multi-jet background. The statistical uncertainty of the multi-jet background is calculated based on the number of events

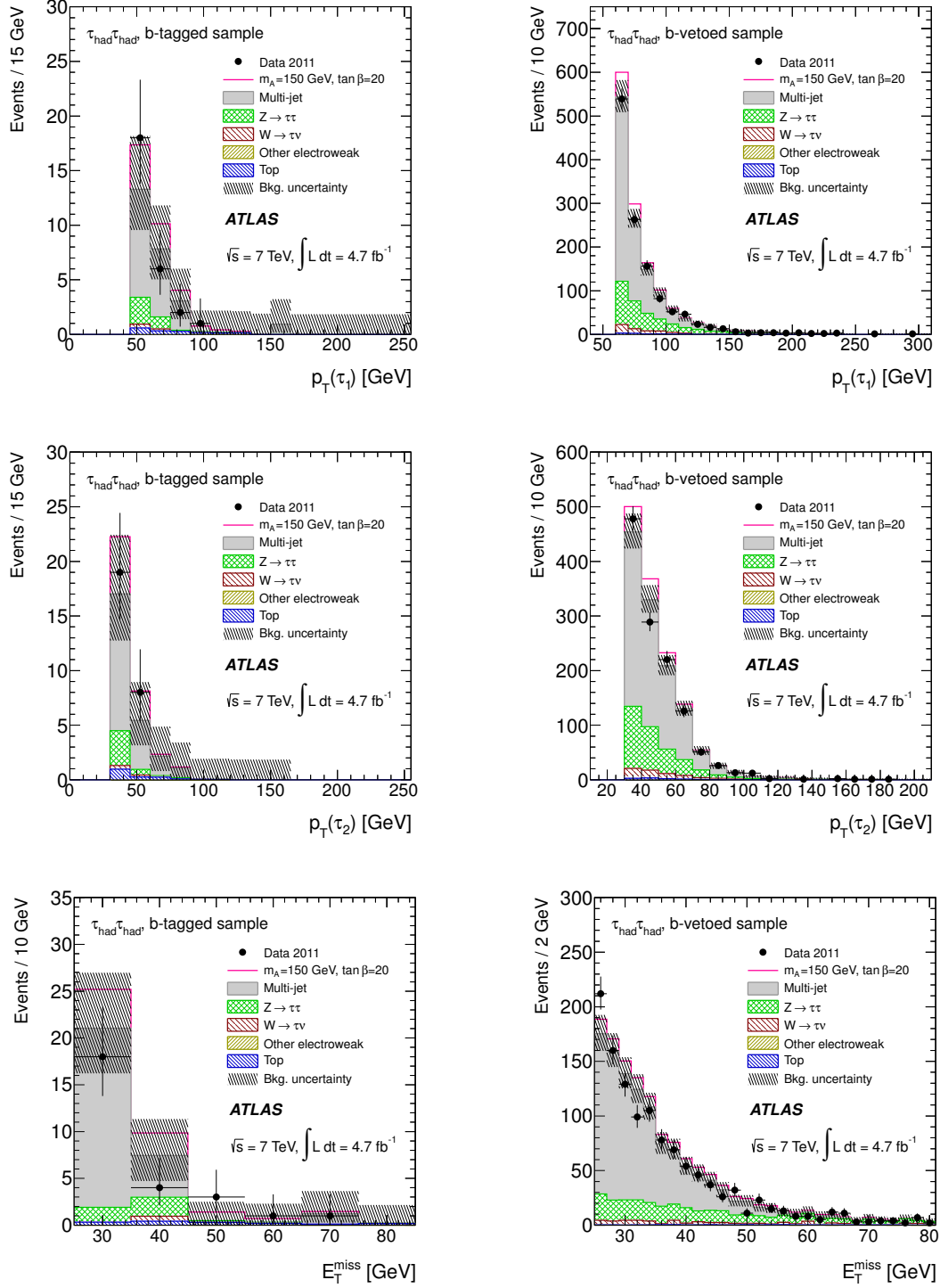


Figure 6.34.: Distributions of the transverse momenta of the highest- p_T (first row) and the second highest- p_T (second row) hadronic τ -lepton decays together with the distributions of the missing transverse momentum (third row) for the b -tagged (left-hand column) and the b -vetoed (right-hand column) selections. The data are compared with the background expectation and an added hypothetical MSSM signal with $m_A = 150$ GeV and $\tan \beta = 20$. The background uncertainties include statistical and systematic uncertainties.

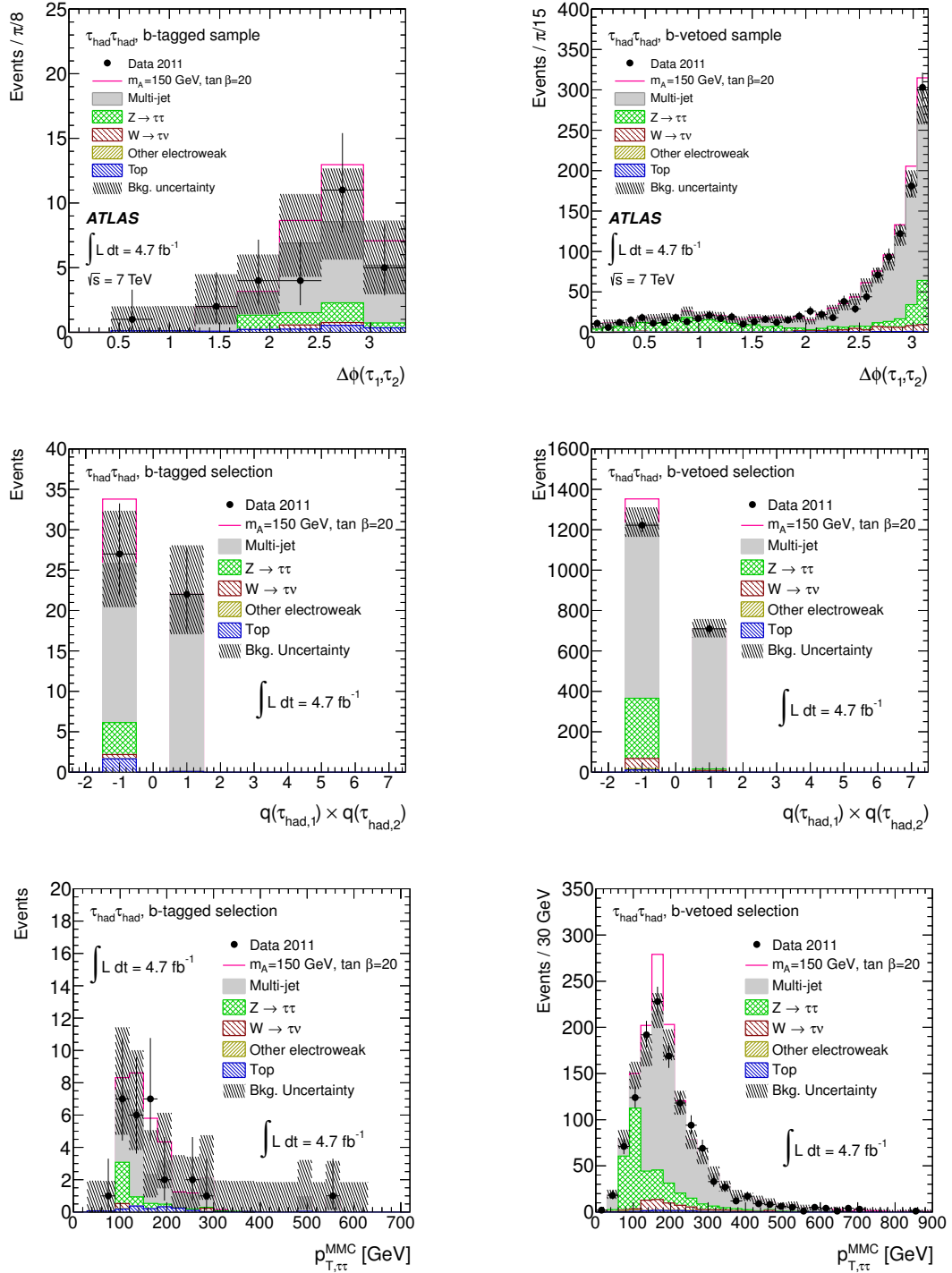


Figure 6.35.: Distributions of the azimuthal angle between the two hadronic τ -lepton decays, $\Delta\phi$ (first row), the charge product of the two hadronic τ -lepton decays (second row) and the p_T of the di- τ resonance as reconstructed by the MMC algorithm (third row) for the b -tagged (left-hand column) and the b -vetoed (right-hand column) selections. The data are compared with the background expectation and an added hypothetical MSSM signal with $m_A = 150 \text{ GeV}$ and $\tan \beta = 20$. The background uncertainties include statistical and systematic uncertainties.

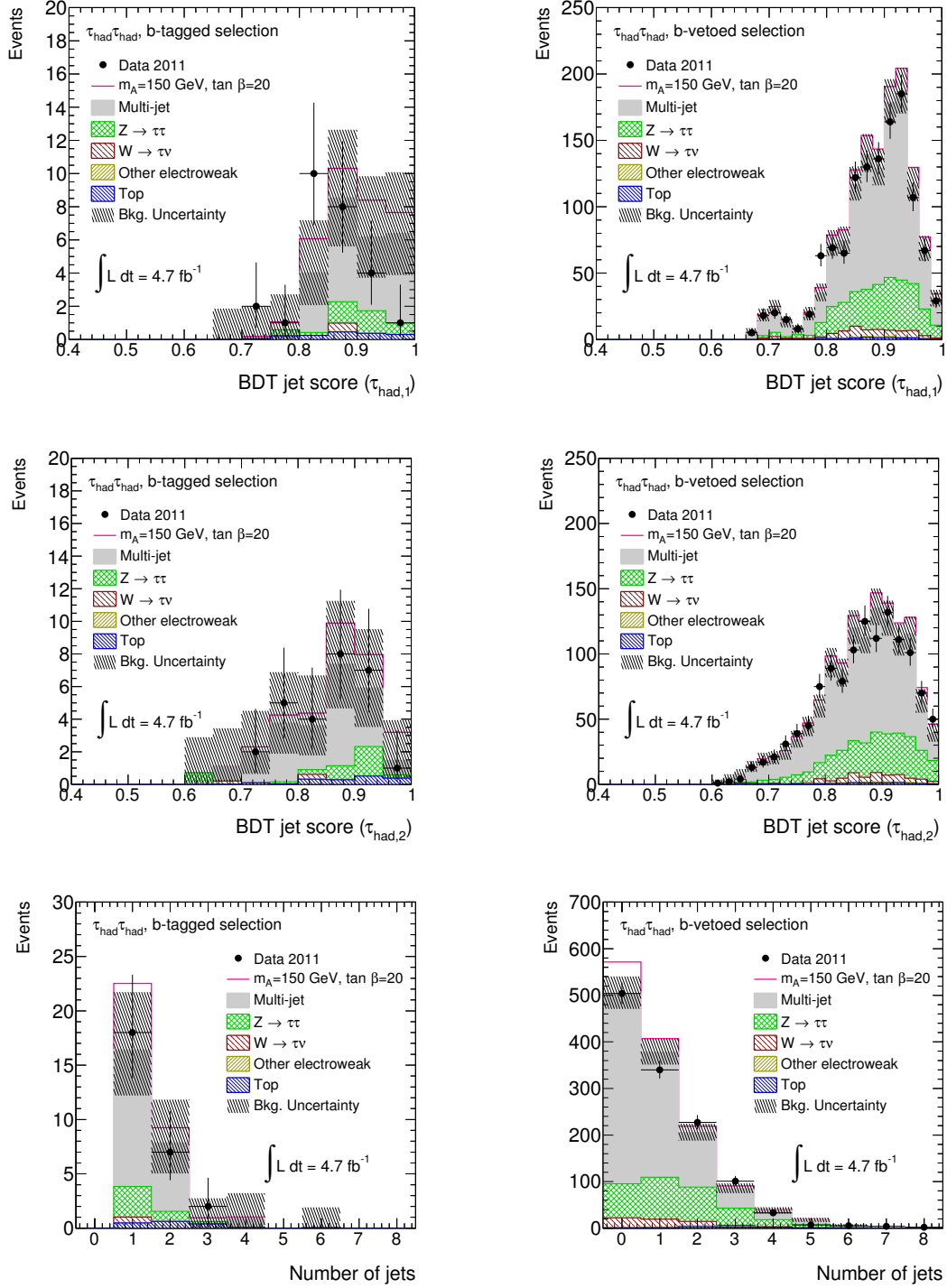


Figure 6.36.: Distributions of the BDT jet scores used for the identification of hadronic τ -lepton decays for the highest- p_T (first row) and the second highest- p_T (second row) hadronic τ -lepton decays together with distributions of the number of jets per event (third row) for the b -tagged (left-hand column) and the b -vetoed (right-hand column) selections. The data are compared with the background expectation and an added hypothetical MSSM signal with $m_A = 150$ GeV and $\tan \beta = 20$. The background uncertainties include statistical and systematic uncertainties.

in the control regions in data and simulation. The estimation of the multi-jet background is directly implemented into the limit setting likelihood function with the statistical methods described in Section 7.

Uncertainties are systematic if, under the assumption that only this uncertainty exists, a large number of measurements does not reduce the expectation value of the uncertainty. In the following section first the uncertainties related to particle-level distributions and later the experimental uncertainties will be discussed. Systematic uncertainties for simulated event samples also affect the estimate of the multi-jet background as the non-multi-jet background in the control regions is subtracted.

6.6.1. Systematic Uncertainties for Generator-level Distributions

For the production of simulated event samples, properties of generator-level particles such as their momenta are obtained with Monte Carlo methods. This information is passed to the detector simulation of which the results are in turn used in the event reconstruction. The uncertainty of the generator-level information can be divided into an inclusive cross-section uncertainty, which does not depend on the event selection, and an acceptance uncertainty, which depends on the event selection.

For the determination of the acceptance uncertainty various settings of the event generators are modified and the effect on the event selection efficiency is studied. As the simulation of the detector response is computationally expensive it is not possible to simulate enough events for all variations that need to be considered. Instead, only the particle-level information from the generator is simulated and an event selection on generator level is performed. With this event selection it is tried to mimic the selection described in Section 6.3. Due to the limited computing resources it is also not possible to generate event samples for all backgrounds with the generators that are used for the nominal event sample. For example, the acceptance uncertainty for the top background is determined with the generator ACERMC [224] instead of MC@NLO [62] as $t\bar{t}$ event samples have been generated with ACERMC by the ATLAS central production system. It is assumed that the resulting acceptance uncertainty is of comparable size for the two generators.

In accordance with the event selection described in Section 6.3, for the event selection on generator-level information events with electrons with $|\eta| < 2.5$ and $p_T > 15$ GeV or muons with $|\eta| < 2.5$ and $p_T > 10$ GeV are vetoed. Events are required to have one hadronic τ -lepton decay with $|\eta| < 2.5$ and $p_T > 45$ GeV (b -tagged selection) or $p_T > 60$ GeV (b -vetoed selection) and an additional hadronic τ -lepton decay with $|\eta| < 2.5$ and $p_T > 30$ GeV.

In addition to true hadronic τ -lepton decays, particle jets are considered identified hadronic τ -lepton decays with a p_T -dependent event weight, w_τ , that is equal to the measured jet-to- τ_{had} misidentification probability. With a weight, $1 - w_\tau$, a jet is not considered as a hadronic τ -lepton decay. Instead of the rejection or acceptance of an event based on the jet-to- τ_{had} misidentification probability, event weights are used to minimise the statistical uncertainty of the obtained event samples. For the b -tagged selection events are considered if the highest- p_T jet with $|\eta| < 2.5$ is a b -jet with $20 \text{ GeV} < p_T < 50 \text{ GeV}$. Jets are dismissed if an identified hadronic τ -lepton decay is within $\Delta R = 0.4$. A jet is considered a b -jet if it can be matched to a b quark with $p_T > 7 \text{ GeV}$ within $\Delta R = 0.4$. A weight of $w_b = 0.7$ is used to account for the identification efficiency of approximately 70%. Jets that cannot be matched to a b quark are considered as identified b -jets with a p_T -dependent weight w_b that is obtained from the measurement of the b -jet misidentification probability for light quarks. In events with an associated weight due to the b -jet identification efficiency, the light jet misidentification probability or the jet-to- τ_{had} misidentification probability, the event weights are multiplied.

The acceptance uncertainty for a systematic variation is the difference of the number of events in the sample with the systematic variation and the nominal event sample after the described selection.

Cross-section uncertainties

The uncertainties of the cross sections depend on the details of the methods that are used for their calculation. In most cases the largest uncertainty contribution results from the uncertainty from the factorisation and renormalisation scales and the parton distribution functions. For the background processes the cross-section uncertainties and their sources were reported in detail in Section 6.2. The cross-section uncertainties considered for this analysis are summarised in Table 6.12.

Process	Table	Uncertainty
W, Z	6.2	$\pm 5\%$
$t\bar{t}$, single-top	6.3	$\pm 10\%$
Diboson	6.4	$\pm 7\%$

Table 6.12.: Uncertainties on the cross sections for the production of W -boson, Z -boson, $t\bar{t}$, single-top and diboson events as used in the $h/A/H \rightarrow \tau_{\text{had}}\tau_{\text{had}}$ analysis. More detailed information on the cross-section uncertainties is given in the referenced tables.

For the signal processes no cross-section uncertainty is considered for the generic Higgs boson production model as the cross section is the parameter of interest in the statistical analysis. In the MSSM signal model the signal cross-section uncertainty depends on the model parameters and is shown in Figure 6.37 for $\tan\beta = 20$ as a function of m_A and for $m_A = 200$ GeV as a function of $\tan\beta$. The cross-section uncertainty for Higgs boson production in b -quark annihilation is obtained with the so-called “Santander matching” prescription [210]. For the cross-section uncertainty for Higgs boson production in gluon fusion, variations of the renormalisation and factorisation scales are considered in addition to variations of the parton distribution functions within their 68% confidence level uncertainties.

Acceptance uncertainty for the event samples with Higgs boson production in b -quark annihilation

The event samples for Higgs boson production in b -quark annihilation are produced with the SHERPA generator [204]. For the nominal event sample up to three partons are considered for the fixed-order calculation in addition to the Higgs boson decay products. The uncertainty of the acceptance due to the number of partons in the fixed-order calculation is derived from a comparison of event samples with up to two and up to three additional partons used in the fixed-order calculation. The uncertainty derived with this method is between 0.5% and 3.0% for the b -tagged selection and below 0.5% for the b -vetoed selection. It is small compared to the total acceptance uncertainty. Therefore, the acceptance uncertainty for all other systematic variations can be derived from samples with two additional partons and applied to samples with three additional partons in order to reduce the required amount of computing resources. The overlap between events with partons produced in the parton shower and the fixed-order calculation is resolved with the CKKW algorithm [59, 60] with

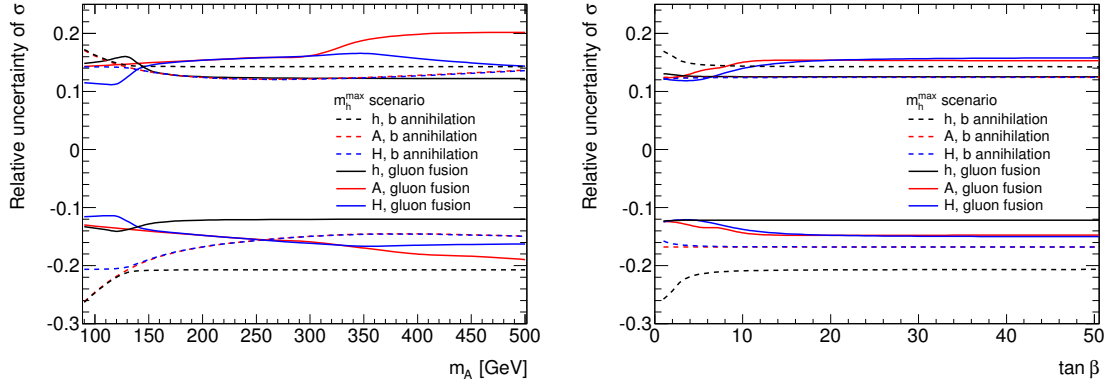


Figure 6.37.: Systematic uncertainties of the cross section for Higgs boson production in b -quark annihilation and gluon fusion. In the figure on the left-hand side the cross-section uncertainty is shown as a function of the CP-odd Higgs boson mass, m_A , for $\tan \beta = 20$ and on the right-hand side the cross-section uncertainty is shown as a function of $\tan \beta$ for $m_A = 200$ GeV. The cross-section uncertainties have been calculated by the LHC Cross Section Working Group [72].

scale parameter

$$\sqrt{20 \text{ GeV}/\sqrt{s}}. \quad (6.39)$$

The systematic uncertainty due to the scale parameter is derived from the comparison of event samples with the nominal scale parameter and the scale parameters

$$\sqrt{15 \text{ GeV}/\sqrt{s}} \quad \text{and} \quad \sqrt{30 \text{ GeV}/\sqrt{s}}. \quad (6.40)$$

The factorisation scale is varied by factors of 0.5 and 2, while the renormalisation scale is varied by factors of 0.9 and 1.1 in order to determine the associated uncertainty. The underlying event activity is increased by changing the non-diffractive cross section by $\pm 12\%$. In the nominal event sample b quarks are assumed to be massless; the uncertainty due to this assumption is derived by comparing the nominal event sample to an event sample with massive b quarks. The parton distribution functions CTEQ6L1 [47] are used for the nominal event sample; the corresponding uncertainty is derived by comparing the nominal event sample to an event sample with the parton distribution functions CTEQ6.6M [48]. A part of this uncertainty can be attributed to the fact that for CTEQ6L1 the value of the strong coupling constant is $\alpha_S(m_Z) = 0.130$ and for CTEQ6.6M $\alpha_S(m_Z) = 0.118$, where m_Z is the mass of the Z boson.

The uncertainties that result from these systematic variations are documented in Table 6.13. The combined systematic uncertainty is dominated by the uncertainty due to the CKKW matching uncertainty, the factorisation and renormalisation scale uncertainties and the uncertainties of the parton distribution functions. For the b -tagged selection an uncertainty of $^{+15\%}_{-18\%}$ is used for $m_\phi < 200$ GeV and $\pm 14\%$ for $m_\phi \geq 200$ GeV, where m_ϕ is the Higgs boson mass and $\phi = h, A, H$. For the b -vetoed selection $^{+10\%}_{-14\%}$ is used for $m_\phi < 150$ GeV and $^{+1.5\%}_{-1.9\%}$ for $m_\phi \geq 150$ GeV.

Source	120 GeV		150 GeV		200 GeV		300 GeV	
	b -tag	b -veto	b -tag	b -veto	b -tag	b -veto	b -tag	b -veto
≤ 2 additional partons for matrix element								
	0.6 %	0.0 %	1.2 %	0.5 %	2.5 %	-0.4 %	3.0 %	-0.2 %
CKKW matching scale								
$\sqrt{15 \text{ GeV}/\sqrt{s}}$	-12.8 %	-9.4 %	-13.0 %	-0.5 %	-10.5 %	0.8 %	-8.8 %	1.1 %
$\sqrt{30 \text{ GeV}/\sqrt{s}}$	14.9 %	9.7 %	15.1 %	-0.5 %	13.5 %	-1.0 %	13.0 %	-1.7 %
Factorisation scale								
$\times 0.5$	-3.0 %	-6.4 %	-4.4 %	-1.2 %	-4.0 %	0.1 %	-2.9 %	-0.2 %
$\times 2.0$	-9.9 %	-9.8 %	-9.1 %	-0.5 %	-6.4 %	0.9 %	-6.8 %	1.0 %
Renormalisation scale								
$\times 0.9$	2.7 %	2.3 %	-0.5 %	0.1 %	1.7 %	-0.1 %	0.2 %	0.0 %
$\times 1.1$	0.0 %	2.6 %	-0.7 %	0.0 %	0.8 %	0.3 %	0.0 %	-0.1 %
Underlying event activity								
More	0.7 %	0.6 %	0.0 %	0.0 %	0.0 %	0.0 %	0.3 %	0.0 %
Less	0.0 %	0.4 %	0.8 %	0.0 %	0.0 %	0.0 %	0.3 %	0.0 %
Massive b -quarks								
	-2.0 %	-3.4 %	-4.5 %	-0.8 %	-1.7 %	0.4 %	-1.3 %	-0.1 %
Parton distribution functions								
CTEQ6.6M	-5.2 %	-1.6 %	-6.4 %	-1.2 %	-5.7 %	-1.0 %	-5.6 %	-0.9 %
Total uncertainty								
	+15.2 % -17.1 %	+10.1 % -14.1 %	+15.2 % -17.7 %	+0.5 % -1.5 %	+13.8 % -13.7 %	+1.3 % -1.5 %	+13.3 % -12.5 %	+1.5 % -1.9 %

Table 6.13.: Systematic generator uncertainties of the event selection efficiency for Higgs boson production in b -quark annihilation as obtained for the SHERPA generator. Event samples with Higgs boson masses of 120 GeV, 150 GeV, 200 GeV and 300 GeV are considered and results are shown for the b -tagged and b -vetoed selections. The systematic variations are described in Section 6.6.1. A value of the systematic uncertainty of 0.0% refers to an absolute value of the systematic uncertainty below 0.05%.

Acceptance uncertainty for the event samples with Higgs boson production in gluon fusion

The samples of events with Higgs boson production in gluon fusion are generated with POWHEG [61]. The systematic uncertainties of the event selection efficiency due to the renormalisation and factorisation scales are quantified using variations of the nominal renormalisation and factorisation scale $\mu_F = \mu_R = m_\phi$, where m_ϕ is the Higgs boson mass, by a factor of 0.5 and 2.0. The systematic uncertainty for the underlying event tune is derived by comparing the selection efficiency in event samples that are produced with the AUET2B LO** [67] and the PERUGIA 2011 [68] tunes. Event samples with more and with less initial and final state radiation from the parton shower algorithm are produced following the recommendations by the ATLAS collaboration and the parton shower uncertainty is derived based on them. Finally, the systematic uncertainty for the parton distribution functions is obtained

by comparing event samples produced with the CT10 [49] and the MSTW2008NLO68CL [50] parton distribution functions. The systematic uncertainties that are obtained for the b -vetoed event selection are documented in Table 6.14. The dominant source of uncertainty is the uncertainty connected with the parton distribution functions. As the signal yield for gluon-fusion events is negligible compared to the yield for b -quark associated production for the b -tagged selection, no systematic uncertainty is determined for this subsample.

Source	b -vetoed channel
Renormalisation and factorisation scales	
$\times 0.5$	0.3 %
$\times 2.0$	0.8 %
Underlying event model tune	
PERUGIA 2011	0.6 %
Initial state radiation	
More	0.0 %
Less	0.4 %
Final state radiation	
More	-0.1 %
Less	0.4 %
Parton distribution functions	
MSTW2008NLO68CL	1.7 %
Total uncertainty	$+2.1\%$ -0.1%

Table 6.14.: Systematic generator uncertainties of the event selection efficiency for Higgs boson production in gluon fusion as obtained for the POWHEG generator. Event samples with Higgs boson masses of 120 GeV are considered and results are shown for the b -vetoed selection. The systematic variations are described in Section 6.6.1. A value of the systematic uncertainty of 0.0% refers to an absolute value of the systematic uncertainty below 0.05%.

Acceptance uncertainty for the event samples with Z/γ^* - and W -boson production

The largest background estimated with simulated data is the $Z/\gamma^* \rightarrow \tau^+\tau^-$ background. For the production of the $Z/\gamma^* \rightarrow \tau^+\tau^-$ and $W \rightarrow \tau\nu$ event samples the ALPGEN generator [216] is used. As soft and collinear partons are produced by parton showering a minimum transverse momentum for partons of $p_T > 20$ GeV and a minimum separation between two partons of $\Delta R > 0.7$ is required for partons from the fixed-order calculation. The systematic uncertainty connected to the overlap removal between parton shower and fixed-order calculation partons is obtained by comparing the event yields in the nominal sample and a sample with the requirements $p_T > 12$ GeV and $\Delta R > 0.4$. The parton shower of HERWIG [217] is used to obtain information for partons with k_T below the parton shower threshold. The systematic uncertainty that covers uncertainties due to this approach is derived by varying k_T by factors of 0.5 and 2. The overlap between events with partons from the parton shower and partons used in the fixed-order calculation is removed with the MLM matching procedure [58]. For the MLM matching jets based on partons from the parton shower and the fixed-order calculation

are matched to the partons from the fixed-order calculation. Parton shower jets are required to have $p_T > 20$ GeV and need to have a separation of $\Delta R = 0.7$. The systematic uncertainty connected to the matching algorithm is derived by comparing the nominal event sample to event samples where $p_T > 15$ GeV or $\Delta R = 0.4$ are required instead. In addition, the systematic uncertainties obtained from variations of the renormalisation and factorisation scales are considered. The scale parameter Q is defined by

$$Q^2 = q_{\text{fac}}^2 \left(m_V^2 + \sum_{i=1}^{n_{\text{partons}}} (m_i^2 + p_{T,i}^2) \right), \quad (6.41)$$

where the nominal value of q_{fac} is 1, m_V is the mass of the Z boson or W boson, respectively, m_i and $p_{T,i}$ are the mass and transverse momentum of parton i and n_{partons} is the number of partons excluding the W - or Z -boson decay products. The systematic uncertainty due to this choice is quantified by comparing the event yield with this scale definition to the event yield with the scale $Q^2 = m_V^2$ (“iqopt2”). The systematic uncertainty due to the factorisation and renormalisation scale choice is derived by comparing the nominal event yields to event yields where the scales are varied by factors of 0.5 and 2. These variations are achieved by changing the factor q_{fac} in Equation 6.41. Finally, the systematic uncertainty due to the choice of the parton distribution functions is obtained by comparing the event yield with the nominal parton distribution functions CTEQ6L1 [47] to the event yield with the parton distribution functions MRST2001J [241].

The resulting systematic uncertainties for the ALPGEN Z - and W -boson production event samples are shown in Table 6.15. The uncertainties are reported for the combination of all subsamples with 0 to 5 additional partons. For the Z -boson production event sample the systematic uncertainty is dominated by the event sample with no additional parton from the fixed-order calculation for the b -vetoed and one additional parton for the b -tagged selection. For the W -boson production event samples usually one τ_{had} decay is a misidentified jet that is initiated by the hadronisation of a quark or gluon, so that the systematic uncertainty is dominated by the subsample with one additional parton for the b -vetoed selection and two additional partons for the b -tagged selection. The combined systematic uncertainty is dominated by the uncertainties associated to the MLM matching, which have a high dependence on the number of additional partons from the fixed-order calculation.

Acceptance uncertainty for the event samples with top-quark production

The background from events with top-quark production is dominated by $t\bar{t}$ production which is simulated with the MC@NLO generator. The systematic uncertainties are determined for the ACERMC event samples and it is assumed that the sizes of the various systematic uncertainties are similar for MC@NLO. In order to evaluate the uncertainty connected with the underlying event model the nominal model AUET2B LO** [67] is exchanged with the PERUGIA 2011 tune [68]. An event sample is produced where colour-reconnection effects are turned off and the PERUGIA 2011 tune is used. The more conservative systematic uncertainty of the uncertainties in which the underlying event model is varied is used. In addition, event samples with approximately 10% more or less underlying event activity, as quantified by the charged-particle multiplicity and the average p_T of the highest- p_T jet from the underlying event, are produced. Event samples with more or less initial and final state radiation from the parton shower are produced following the same procedure as outlined for the event samples with Higgs boson production in gluon fusion. The more conservative uncertainty from varying the initial and final state radiation independently and coherently is used. A separate, but similar variation of the PYTHIA parton shower parameters is called “more/less parton

Source	Z/γ^* -boson production		W -boson production	
	b -tag	b -veto	b -tag	b -veto
Matrix element				
Parton $p_T > 12$ GeV	1.4 %	-2.8 %	-11.9 %	-3.9 %
Parton $\Delta R > 0.4$	8.4 %	-1.1 %	-2.0 %	-1.1 %
Parton shower k_T factor				
$\times 0.5$	10.3 %	-0.9 %	-5.2 %	-1.7 %
$\times 2$	9.6 %	-0.4 %	2.0 %	1.8 %
MLM matching				
$p_T = 15$ GeV	7.1 %	-3.8 %	-24.7 %	-24.2 %
$\Delta R = 0.4$	40.9 %	15.9 %	-6.5 %	6.9 %
Scale definition				
	14.5 %	-0.1 %	-1.6 %	3.6 %
Renormalisation and factorisation scales: Q^2 scale				
$\times 0.5$	5.2 %	-3.8 %	0.4 %	2.8 %
$\times 2$	-4.4 %	-8.7 %	-3.4 %	-1.9 %
Parton distribution functions				
MRST2001J	-2.6 %	-5.4 %	3.0 %	7.0 %
Total uncertainty				
	+46.3% -5.1%	+15.9% -11.4%	+3.6% -29.0%	+11.0% -25.2%

Table 6.15.: Systematic generator uncertainties of the event selection efficiency for Z/γ^* - and W -boson production as obtained for the ALPGEN generator. Results are shown for the b -tagged and b -vetoed selections. The systematic variations are described in Section 6.6.1.

shower”. Even though the initial and final state radiation and the parton shower systematic uncertainties quantify similar underlying systematic uncertainties, they are both considered following a conservative approach. The uncertainty connected with the parton distribution functions is obtained by comparing MC@NLO event samples with the CT10 [49] and the MSTW2008 [50] parton distribution functions.

The resulting systematic uncertainties are shown in Table 6.16. The total uncertainty is dominated by the uncertainties connected with the underlying event and the initial and final state radiation from the parton shower.

6.6.2. Experimental Uncertainties

In the following the systematic uncertainties connected with the reconstruction and identification of objects based on detector information and the measurement of the integrated luminosity are described. These systematic uncertainties include uncertainties of the reconstruction and identification efficiencies and energy calibration uncertainties. The intrinsic uncertainties of the methods used for the estimation of backgrounds from data are described in Section 6.5. In this section the given uncertainties for the multi-jet background are only an approximate result and exact for the case that the event yields in data do not constrain the nuisance parameters introduced in Section 7.2. The final uncertainty for multi-jet production

Source	b -tagged channel	b -vetoed channel
Underlying event activity		
PERUGIA 2011	-11.9 %	1.0 %
No colour reconnection	-12.5 %	1.0 %
More	-1.5 %	-0.2 %
Less	1.3 %	-0.5 %
Parton shower		
More	-0.5 %	1.1 %
Less	2.1 %	-3.9 %
Initial state radiation		
More	-16.3 %	4.7 %
Less	13.9 %	-2.9 %
Final state radiation		
More	9.6 %	0.1 %
Less	-10.1 %	-1.7 %
Initial and final state radiation		
More	-6.8 %	3.9 %
Less	2.7 %	-5.5 %
Parton distribution functions		
MSTW2008	1.4 %	0.5 %
Total uncertainty		
	+17.1% -22.9%	+5.0% -6.8%

Table 6.16.: Systematic generator uncertainties of the event selection efficiency for $t\bar{t}$ production as obtained for the ACERMC generator. Results are shown for the b -tagged and b -vetoed selections. The systematic variations are described in Section 6.6.1. The “no colour reconnection” variation includes the change of the underlying event model to PERUGIA 2011. For the total uncertainty the more conservative variation of PERUGIA 2011 and no colour reconnection is used. Similarly, the more conservative choice of varying the parton shower initial and final state radiation independently and varying it coherently is used.

is obtained indirectly from the uncertainties of the other background processes in the data control samples used for the estimation of the multi-jet background.

Uncertainty of the integrated luminosity

The procedure used to determine the integrated luminosity and its uncertainty is described in Reference [242]. An overview of the used detector components is available in Section 3.2.5. For the dataset used in this analysis and recorded in 2011 the relative uncertainty for the integrated luminosity is 3.9%, so that

$$\int \mathcal{L} dt = (4.66 \pm 0.18) \text{ fb}^{-1}. \quad (6.42)$$

The luminosity uncertainty affects all signal and background event yields that are estimated from simulation.

Uncertainties of the τ_{had} identification efficiency and the jet-to- τ_{had} misidentification probability

The measurement of the identification efficiency for hadronic τ -lepton decays is described in Section 5.4, the measurement of the trigger efficiency in Section 6.5.2 and the measurement of the jet-to- τ_{had} misidentification probability in Section 6.5.3. The results of these measurements are p_T -dependent correction factors and their uncertainties. The uncertainties for the τ_{had} identification efficiency correction factors are determined as a function of the number of associated tracks and the transverse momentum of the τ_{had} candidate. They are shown in Table 5.4. The uncertainty of the trigger efficiency measurement is shown for the single- τ_{had} triggers used before September 2011 (i.e. `EF_tau29_medium1` and `EF_tau20_medium1`) in Figure 6.27 and Reference [232]. The uncertainty of the jet-to- τ_{had} misidentification probability is reported in Section 6.5.3 and Appendix B.2.

For the background estimation a correction factor that depends on the p_T of the hadronic τ -lepton decay, the matched trigger and whether the τ_{had} decay is correctly identified or a misidentified jet is applied to the event weight. The event weight is the product of the correction factors for all hadronic τ -lepton decays that have been identified in the event. In order to derive the systematic uncertainties for the event yield of the analysis the correction factors are varied within their $\pm 1\sigma$ uncertainties and the resulting event yields are compared with the nominal one. The results are shown in Table 6.17. Due to the relatively small number of events in the simulated event samples the systematic uncertainty for the b -tagged selection was determined in an event sample where a jet with $20 \text{ GeV} < p_T < 50 \text{ GeV}$ is required, but no requirement on the b -jet identification variables is applied. With this approach the number of available events is increased, but no influence on the expectation value of the uncertainties is expected. For the backgrounds with hadronic τ -lepton decays the dominating efficiency uncertainty is the τ_{had} identification uncertainty. For the $W + \text{jets}$ background the uncertainty of the jet-to- τ_{had} misidentification probability is dominant.

The effect of the uncertainty of the electron-to- τ_{had} misidentification probability was studied, but due to the low number of events with electrons that are misidentified as hadronic τ -lepton decays after the selection requirements this uncertainty is neglected.

Uncertainties of the b -jet identification efficiency and the misidentification probability

The measurement of the b -jet identification efficiency and the c - and light-jet misidentification probabilities is described in Section 5.3.3. For signal events and background events from top and diboson production the resulting uncertainty of the event yield is determined with the same procedure that was used for the τ_{had} identification efficiency with the exception that the complete selection is applied in the b -tagged channel. The results are shown in Table 6.18. The dominant source of uncertainty is the b -jet identification efficiency. For the gluon-fusion signal event sample and the diboson event sample large uncertainties have been measured for the misidentification probability. In these event samples the b -jet requirement has a low efficiency and consequently the systematic uncertainties have a large statistical uncertainty. A comparison of the systematic uncertainties for these event samples to the statistical uncertainty of the measurement suggests that the uncertainties of the gluon-fusion Higgs boson production and the diboson production event samples are high due to a statistical fluctuation. Due to the low number of expected events for these backgrounds for the b -tagged selection the size of the uncertainty has no significant influence on the final result.

For the background from W - and Z -boson production the efficiency of the b -jet requirement

b -tagged selection						
$b\bar{b}h/A/H$	$gg \rightarrow h/A/H$	$Z/\gamma^* \rightarrow \tau^+\tau^-$	$W + \text{jets}$	Top	Diboson	Multi-jet
200 GeV	200 GeV					
τ_{had} trigger efficiency						
$+4.8\%$ -4.7%	$+4.7\%$ -4.6%	$+4.5\%$ -4.4%	$\pm 2.2\%$	$+4.3\%$ -4.2%	$+4.8\%$ -4.2%	$\mp 0.2\%$
τ_{had} identification efficiency						
$+10.5\%$ -9.9%	$+10.4\%$ -9.9%	$+10.5\%$ -10.0%	$\pm 5.0\%$	$+9.8\%$ -9.3%	$+11.4\%$ -10.8%	$\mp 0.5\%$
Jet-to- τ_{had} misidentification probability						
$\pm 0.0\%$	$\pm 0.1\%$	$\pm 0.6\%$	$+21.1\%$ -21.0%	$+3.8\%$ -3.6%	$\pm 0.5\%$	$\mp 0.6\%$
b -vetoed selection						
$b\bar{b}h/A/H$	$gg \rightarrow h/A/H$	$Z/\gamma^* \rightarrow \tau^+\tau^-$	$W + \text{jets}$	Top	Diboson	Multi-jet
200 GeV	200 GeV					
τ_{had} trigger efficiency						
$+4.9\%$ -4.8%	$+4.9\%$ -4.8%	$+4.8\%$ -4.7%	$\pm 2.2\%$	$+4.1\%$ -4.0%	$+5.0\%$ -4.8%	$\mp 0.4\%$
τ_{had} identification efficiency						
$+10.5\%$ -10.0%	$+10.4\%$ -9.9%	$+10.5\%$ -10.0%	$\pm 5.0\%$	$+9.4\%$ -9.0%	$+10.7\%$ -10.1%	$\mp 0.8\%$
Jet-to- τ_{had} misidentification probability						
$\pm 0.0\%$	$\pm 0.0\%$	$\pm 0.4\%$	$\pm 21.7\%$	$+6.0\%$ -5.9%	$\pm 0.7\%$	$\mp 1.0\%$

Table 6.17.: Uncertainties on the event yield due to the uncertainties of the τ_{had} trigger efficiency, the τ_{had} identification efficiency and the jet-to- τ_{had} misidentification probability. The uncertainties are shown for signal and background processes and the b -tagged and b -vetoed selections. The uncertainties for the background from multi-jet production are an approximate result. A value of the systematic uncertainty of 0.0% refers to an absolute value of the systematic uncertainty below 0.05%.

$b\bar{b}h/A/H$	$gg \rightarrow h/A/H$	Top	Diboson	Multi-jet
200 GeV	200 GeV			
b -jet identification efficiency				
$\pm 5.2\%$	$\pm 1.7\%$	$\pm 5.5\%$	$\pm 0.0\%$	$\mp 0.0\%$
c -to- b -jet misidentification probability				
$\pm 0.5\%$	$\pm 4.1\%$	$\pm 0.1\%$	$\pm 35.9\%$	$\mp 0.1\%$
Light-to- b -jet misidentification probability				
± 4.2	$\pm 21.0\%$	$\pm 0.0\%$	$\pm 3.3\%$	$\mp 0.1\%$

Table 6.18.: Uncertainties on the event yield resulting from the b -jet identification efficiency uncertainty, the c -to- b -jet and the light-to- b -jet misidentification probability uncertainty. The uncertainties are shown for signal and background processes and the b -tagged selection. The uncertainties for the background from multi-jet production are an approximate result. A value of the systematic uncertainty of 0.0% refers to an absolute value of the systematic uncertainty below 0.05%.

is measured in data. The measurement is described in Section 6.5.5. The correction factors

$$k_b^Z = 1.24 \pm 0.34 \quad \text{and} \quad k_b^W = 1.01 \pm 0.31 \quad (6.43)$$

are measured and the corresponding systematic uncertainties are taken into account.

Energy scale uncertainties

The energy scale for jets and hadronic τ -lepton decays was measured in References [173, 177, 194] and described in Sections 5.3.2 and 5.4.2. To derive an uncertainty on the event yield for backgrounds estimated from simulation the energies of jets and τ_{had} decays are varied within their nominal $\pm 1\sigma$ uncertainty values based on the jet and τ_{had} energy scale measurements by scaling the momentum four-vector of the jet or τ_{had} decay accordingly. The event yield for changed jet and τ_{had} energies is compared with the nominal event yield to derive the event yield uncertainty. As the energy calibration for hadronic τ -lepton decays is based on the energy of the seed jet, the energies of jets and τ_{had} decays are varied coherently. The jet and τ_{had} energy change is propagated to the missing transverse momentum vector by subtracting the changed and adding the original jet or τ_{had} momentum vector².

An additional uncertainty is derived for the jet energy resolution which was measured and documented in Reference [184]. With the procedure described in Section 5.3.2 the jet four-momentum vectors in simulation are scaled with a random factor of which the Gaussian probability density function is designed so that the jet energy resolution after the correction is the nominal $+1\sigma$ uncertainty value of the measured jet energy resolution in data. The energy change is again propagated to the missing transverse momentum vector with the procedure described above. The event yield uncertainty is derived by comparing the number of events in this modified event sample and the nominal event sample.

The uncertainty of the missing transverse momentum due to energy uncertainties of the objects that are not identified in the main analysis is assessed by varying the terms for the soft-jet energy, $E_T^{\text{miss,softjets}}$, and the energy from unassociated clusters, $E_T^{\text{miss,CellOut}}$. To derive an uncertainty due to the varying pile-up conditions the energies of the clusters associated with any of the two terms are varied by $\pm 6.6\%$. The cluster and soft-jet energy uncertainty of the event yield is derived by applying an energy scale factor for the clusters associated with any of the two terms. The scale factor is between 1.09 and 1.11 for the up-ward variation and between 0.91 and 0.89 for the down-ward variation of the energies of the clusters associated with soft jets. For the unassociated cluster the scale factors depend on the sum- E_T of the soft-jet or CELLOUT term and is between 1.12 and 1.16 for the up-ward variation and 0.88 and 0.84 for the down-ward variation.

The resulting event yield uncertainties due to energy scale variations are shown in Table 6.19. The energy scale uncertainty is dominated by the component derived from the jet and τ_{had} energy variations.

Electron and muon identification efficiency and energy scale uncertainties

Electron and muon reconstruction and identification efficiencies have been measured with a tag-and-probe method in data samples of leptonic W - and Z -boson decays in References [197, 199]. The electron identification efficiency uncertainties are 3% to 6%, while

²For the calculation of the missing transverse momentum it is considered that muons or other objects might not deposit their full energy in the calorimeters and a weight is applied to the energy of the object to account for this. The weights are obtained from the E_T^{miss} composition map and are also considered for the described systematic variation of the missing transverse energy. The E_T^{miss} composition map describes the relative contribution of the identified objects to the missing transverse momentum.

b -tagged selection						
$b\bar{b}h/A/H$	$gg \rightarrow h/A/H$	$Z/\gamma^* \rightarrow \tau^+\tau^-$	$W + \text{jets}$	Top	Diboson	Multi-jet
200 GeV	200 GeV					
Jet and τ_{had} energy scale						
+39.9%	+19.2%	+59.5%	+21.0%	-9.1%	+31.2%	-2.9%
-17.5%	-11.6%	-34.8%	-11.0%	-4.1%	-10.7%	+1.5%
Jet energy resolution						
3.2%	-3.5%	1.5%	0.8%	2.5%	-1.3%	-0.1%
Cluster and soft jet energy scale						
+6.4%	+6.3%	+21.1%	+3.8%	+5.3%	+8.5%	-0.7%
-2.4%	-4.9%	-13.0%	-6.2%	-1.9%	+1.0%	+0.6%
Missing transverse energy uncertainty due to pile-up						
+2.2%	+3.2%	+7.1%	+3.3%	-0.2%	+0.1%	$\mp 0.3\%$
-1.0%	-2.1%	-5.5%	-1.3%	-1.8%	+3.4%	
b -vetoed selection						
$b\bar{b}h/A/H$	$gg \rightarrow h/A/H$	$Z/\gamma^* \rightarrow \tau^+\tau^-$	$W + \text{jets}$	Top	Diboson	Multi-jet
200 GeV	200 GeV					
Jet and τ_{had} energy scale						
+7.1%	+6.9%	+16.0%	+14.4%	+6.1%	+14.7%	-1.6%
-7.2%	-3.9%	-12.9%	-13.6%	-5.6%	-7.9%	+1.2%
Jet energy resolution						
0.8%	0.0%	-0.5%	-0.3%	0.0%	0.5%	0.1%
Cluster and soft jet energy scale						
+4.8%	+6.3%	+5.4%	+5.3%	+2.8%	+2.8%	$\mp 0.4\%$
-4.6%	-4.2%	-5.2%	-4.3%	-0.8%	-4.4%	
Missing transverse energy uncertainty due to pile-up						
+1.6%	+2.3%	+1.6%	+2.9%	-0.2%	+1.6%	-0.3%
-2.9%	-1.4%	-3.1%	-1.1%	-0.9%	-1.5%	+0.2%

Table 6.19.: Uncertainties on the event yield due to the jet and τ_{had} energy scale uncertainties, the cluster and soft-jet energy scale uncertainties and the missing transverse momentum uncertainty due to pile-up. The uncertainties are shown for signal and background processes and the b -tagged and b -vetoed selections. The uncertainties for the background from multi-jet production is an approximate result. A value of the systematic uncertainty of 0.0% refers to an absolute value of the systematic uncertainty below 0.05%.

the muon identification efficiency uncertainty is below 1.8%. In the $h/A/H \rightarrow \tau_{\text{had}}\tau_{\text{had}}$ analysis an electron and muon veto is used and electron and muon identification inefficiencies would need to be considered. Uncertainties for the identification inefficiency have not been measured. The systematic uncertainty was studied for the approximation that the identification inefficiency uncertainty is small compared with the identification inefficiency. With this approximation the systematic uncertainties have been found to be considerably below the sizable statistical uncertainties and could not be measured. The electron energy scale uncertainties [197] are typically below 3% and the muon energy scale uncertainties below 1%. The effect of changing the electron and muon energy scales within their uncertainties is studied and found to be negligible. Due to the low expected background from events with electrons or muons and the small absolute values of the uncertainties, these systematic uncertainties are neglected.

6.7. Results

For the b -tagged and b -vetoed event selections described in Section 6.3 the numbers of events in data and the expected signal and background event yields, as estimated with the methods described in Section 6.5, are shown in Table 6.20. The distributions of the discriminating variable used to extract the signal, the di- τ mass as calculated with the MMC algorithm, are shown for the data and the expected distributions for the signal and background processes in Figure 6.38. For the signal the m_h^{max} benchmark scenario with the parameter $m_A = 150$ GeV and $\tan\beta = 20$ is assumed. For this parameter point the CP-odd Higgs boson A has a mass of 150 GeV and the CP-even Higgs bosons h and H have masses of 129 GeV and 151 GeV. The cross section times branching ratio for the production of one of the Higgs bosons and the subsequent decay to $\tau\tau$ is 7.1 pb and 4.4 pb for the production in b -quark annihilation and gluon fusion, respectively.

For the b -tagged and the b -vetoed selections the background is dominated by events with multi-jet production, where two quark- or gluon-induced jets are misidentified as hadronic τ -lepton decays. Even though the jet-to- τ_{had} misidentification probability is only about 5%, events with multi-jet production constitute a significant background due to the large production cross section. The uncertainty of the multi-jet background is dominated by the statistical uncertainty due to the low numbers of events in the control regions. The second-largest background contribution is due to events with $Z/\gamma^* \rightarrow \tau^+\tau^-$ production. The background from $Z/\gamma^* \rightarrow \tau^+\tau^-$ production is estimated with simulated event samples. The uncertainty is dominated by the jet and τ_{had} energy scale uncertainties, the theoretical generator uncertainty and the uncertainty of the τ_{had} identification efficiency. For the b -tagged selection the uncertainty of the b -jet requirement is also an important contribution.

The observed event yields are compatible with the expected yields from Standard Model background processes within their uncertainties and the MMC mass distributions in data show no obvious sign of an excess of events over the background expectation.

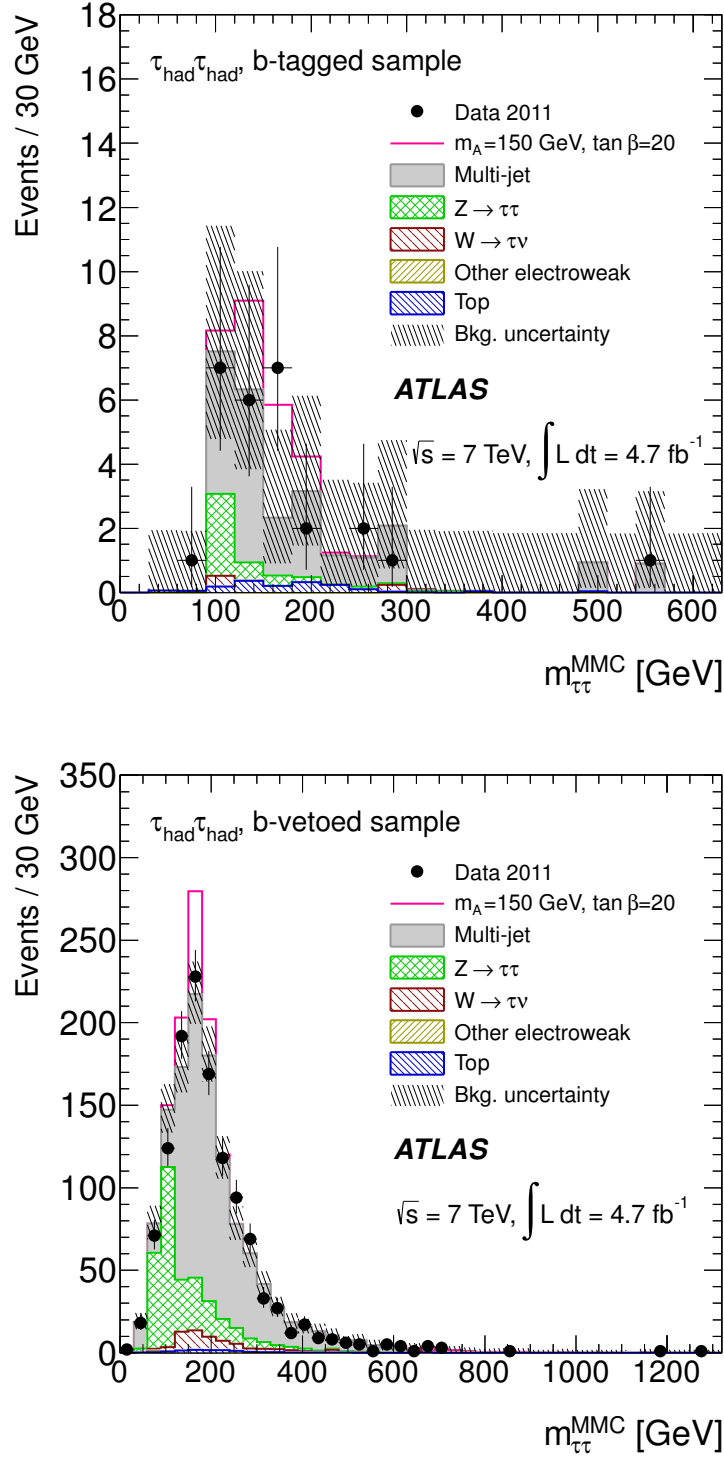


Figure 6.38.: Di- τ mass distributions as calculated with the MMC algorithm for the $h/A/H \rightarrow \tau_{\text{had}}\tau_{\text{had}}$ final state. The MMC mass is shown for the b -tagged (upper figure) and b -vetoed (lower figure) samples. The data are compared with the background expectation and an added hypothetical MSSM signal with $m_A = 150$ GeV and $\tan\beta = 20$. The background uncertainty includes statistical and systematic uncertainties.

	b -tagged sample		b -vetoed sample
Multi-jet	19 ± 5	± 1	$870 \pm 40 \pm 20$
$Z/\gamma^* \rightarrow \tau^+ \tau^-$	4.0 ± 1.2	$^{+3.3}_{-1.9}$	$300 \pm 10 \begin{smallmatrix} +80 \\ -70 \end{smallmatrix}$
W + jets	0.5 ± 0.4	$^{+0.2}_{-0.3}$	$52 \pm 5 \begin{smallmatrix} +16 \\ -20 \end{smallmatrix}$
Top	1.7 ± 0.3	± 0.5	$11.2 \pm 0.7 \pm 2.0$
Diboson	$0.013 \pm 0.035 \pm 0.004$		$4.9 \pm 0.5 \pm 0.9$
Total	25 ± 5	± 2	$1230 \pm 40 \begin{smallmatrix} +70 \\ -60 \end{smallmatrix}$
Signal $m_A = 150 \text{ GeV}, \tan \beta = 20$			
$b\bar{b}(h/A/H \rightarrow \tau\tau)$	7.7 ± 0.6	$^{+3.3}_{-3.2}$	$73 \pm 2 \begin{smallmatrix} +21 \\ -20 \end{smallmatrix}$
$gg \rightarrow h/A/H \rightarrow \tau\tau$	0.50 ± 0.18	$^{+0.18}_{-0.15}$	$47 \pm 2 \begin{smallmatrix} +13 \\ -11 \end{smallmatrix}$
Data	27		1223

Table 6.20.: The observed number of events in data and the expected number of signal and background events for the b -tagged and b -vetoed selections of the $h/A/H \rightarrow \tau_{\text{had}}\tau_{\text{had}}$ channel. The simulated event yields are normalised to the total integrated luminosity of 4.6 fb^{-1} . The data are compared with the background expectation and an added hypothetical MSSM signal ($m_A = 150 \text{ GeV}$ and $\tan \beta = 20$). Because of the subtraction of the $Z/\gamma^* \rightarrow \tau^+ \tau^-$ background in the control regions used in the multi-jet background estimation the uncertainties of the $Z/\gamma^* \rightarrow \tau^+ \tau^-$ and the multi-jet backgrounds are anti-correlated.

7 Statistical Analysis of the Results of the Search for $h/A/H$

No obvious excess of data events above the background expectation is observed in the $m_{\tau\tau}^{\text{MMC}}$ distributions of the search for $h/A/H \rightarrow \tau_{\text{had}}\tau_{\text{had}}$ decays. Also in the other searches for neutral MSSM Higgs bosons carried out in ATLAS in the $h/A/H \rightarrow \mu\mu$, $h/A/H \rightarrow \tau_e\tau_\mu$ and $h/A/H \rightarrow \tau_{\text{lep}}\tau_{\text{had}}$ channels no evidence for the presence of a signal is visible. The expected and observed event yields in all the $h/A/H \rightarrow \mu\mu$ and $h/A/H \rightarrow \tau\tau$ search channels are combined to derive exclusion limits for two-Higgs-doublet models. As discussed in Section 6.1 for this analysis MSSM signal hypotheses based on the m_h^{max} scenario and a model with generic Higgs boson production in b -quark annihilation and gluon fusion are considered. In Section 7.1 the selection, the background estimation and the results of the search for $h/A/H$ are briefly described for the channels that have not been studied in Section 6. A more detailed description is available in References [96, 243, 240]. In Section 7.2 the likelihood function used in the employed hypothesis tests is described and in Section 7.3 the hypothesis tests themselves are discussed. The inputs to the limit derivation procedure and the results of the minimisation that is used in the limit setting procedure are validated in Section 7.4. The obtained exclusion limits and p -values for deviations from the background-only expectation are reported in Section 7.5.

7.1. Results of the $h/A/H \rightarrow \mu\mu$ and $\tau\tau$ Search Channels

The results of the search for $h/A/H \rightarrow \tau_{\text{had}}\tau_{\text{had}}$ decays are combined with the results of the searches for $h/A/H \rightarrow \mu\mu$, $h/A/H \rightarrow \tau_e\tau_\mu$ and $h/A/H \rightarrow \tau_{\text{lep}}\tau_{\text{had}}$ decays. In this section the selection of these search channels is briefly described together with the methods for the background estimation and the obtained results. The sensitivity of the search channels towards the MSSM signal hypothesis or the model with generic Higgs boson production varies as a function of the mass of the CP-odd Higgs boson, m_A . For the combination of the results the $\mu\mu$, $\tau_e\tau_\mu$ and $\tau_{\text{had}}\tau_{\text{had}}$ channels are considered for a signal hypothesis only if they provide relevant sensitivity. The channels and the model parameter range in which they are considered for the combination of the results is given in Table 7.1.

7.1.1. Results of the Search for $h/A/H \rightarrow \mu\mu$ Decays

The search for $h/A/H \rightarrow \mu\mu$ decays profits from the precise reconstruction of muon momenta in ATLAS and thus a good resolution of the di-muon mass. It is, however, complicated by the low branching ratio of $h/A/H \rightarrow \mu\mu$ and the large number of background events from the $Z/\gamma^* \rightarrow \mu\mu$ process. The branching ratio of $h/A/H \rightarrow \mu\mu$ for the m_h^{max} parameter point $m_A = 150$ GeV, $\tan\beta = 20$ is 0.038%, 0.041% and 0.041% for the Higgs bosons h , A and H , respectively.

Events in this search channel are selected by a single-muon trigger with a transverse momentum threshold of 18 GeV. At the reconstruction level two isolated muons with $p_T > 20$ GeV

Decay channel	Model parameter range
$h/A/H \rightarrow \mu\mu$	$m_A \in [120 \text{ GeV}, 300 \text{ GeV}], \quad \tan \beta \in [3, 60]$
$h/A/H \rightarrow \tau_e \tau_\mu$	$m_A \in [90 \text{ GeV}, 300 \text{ GeV}], \quad \tan \beta \in [3, 60]$
$h/A/H \rightarrow \tau_{\text{lep}} \tau_{\text{had}}$	$m_A \in [90 \text{ GeV}, 500 \text{ GeV}], \quad \tan \beta \in [3, 60]$
$h/A/H \rightarrow \tau_{\text{had}} \tau_{\text{had}}$	$m_A \in [110 \text{ GeV}, 500 \text{ GeV}], \quad \tan \beta \in [3, 60]$

Table 7.1.: Higgs boson decay channels used for the search for $h/A/H \rightarrow \mu\mu$ and $\tau\tau$ and parameter range of the m_h^{max} scenario in which the results of the channel are considered. The sensitivities of the search channels towards the MSSM signal hypothesis vary as a function of the mass of the CP-odd Higgs boson, m_A . For the combination of the search results only channels with relevant sensitivity are considered. For the model with generic Higgs boson production the range of m_A holds for the Higgs boson mass, m_ϕ , correspondingly.

and $p_T > 15 \text{ GeV}$ are required. The selected muons must have opposite charges and in addition the invariant mass of the two muons, $m_{\mu\mu}$, is required to be above 70 GeV. Due to the absence of neutrinos in the final state, the expected missing transverse momentum, E_T^{miss} , is low and events with $E_T^{\text{miss}} < 40 \text{ GeV}$ are selected. After the described selection the event sample is split into a subsample of events with identified b -jet, the b -tagged sample, and a subsample of events without identified b -jet, the b -vetoed sample.

The background is estimated with a fit to the sidebands of the $m_{\mu\mu}$ distribution. The background is parameterised by a Gaussian function that is convolved with a sum of terms representing the propagator of the Z boson, the propagator of the photon and the $Z\text{--}\gamma^*$ interference term. The signal model is parameterised as the sum of a Landau function and a Breit-Wigner function, which is convolved with a Gaussian kernel that reflects the experimental resolution. For the fit a search window, which depends on the considered signal point, is defined and the fit is performed only outside of the search window. It is defined by the condition that di-muon masses are included in the search window if the signal event yield is 10% of the signal peak height, e.g. $m_{\mu\mu} \in [134, 152] \text{ GeV}$ for $m_A = 150 \text{ GeV}$, $\tan \beta = 20$. Similarly the full fit range depends on the signal point, e.g. $m_{\mu\mu} \in [108, 200] \text{ GeV}$ for $m_A = 150 \text{ GeV}$, $\tan \beta = 20$. The signal expectation is obtained by fitting the described signal function to simulated events. For signal hypotheses with parameters for which no simulated samples exist the signal expectation is obtained by interpolation between the fit results from the available samples.

The statistical interpretation of the results of this search is based on the distribution of the mass of the di-muon system, $m_{\mu\mu}$, in the search window. For the likelihood function defined in Section 7.2 the distributions are required to be in the form of binned histograms. The di-muon mass is rebinned for the b -tagged subsample into bins of 2 GeV for signal hypotheses with $m_A \leq 125 \text{ GeV}$, 4 GeV for $125 \text{ GeV} < m_A \leq 150 \text{ GeV}$ and 5 GeV for $m_A > 150 \text{ GeV}$. For the b -vetoed subsample the bin widths are 1 GeV for $m_A \leq 200 \text{ GeV}$ and 2 GeV for $m_A > 200 \text{ GeV}$. The $m_{\mu\mu}$ distribution is shown for data, background and the signal point $m_A = 150 \text{ GeV}$, $\tan \beta = 40$ for the b -tagged and b -vetoed samples in Figure 7.1. For the combination of the results the $h/A/H \rightarrow \mu\mu$ channel is considered for signal hypotheses with $120 \text{ GeV} \leq m_A \leq 300 \text{ GeV}$. For lower masses the sensitivity is decreased by the large background from resonant $Z/\gamma^* \rightarrow \mu\mu$ production, for higher masses the expected signal contribution is low.

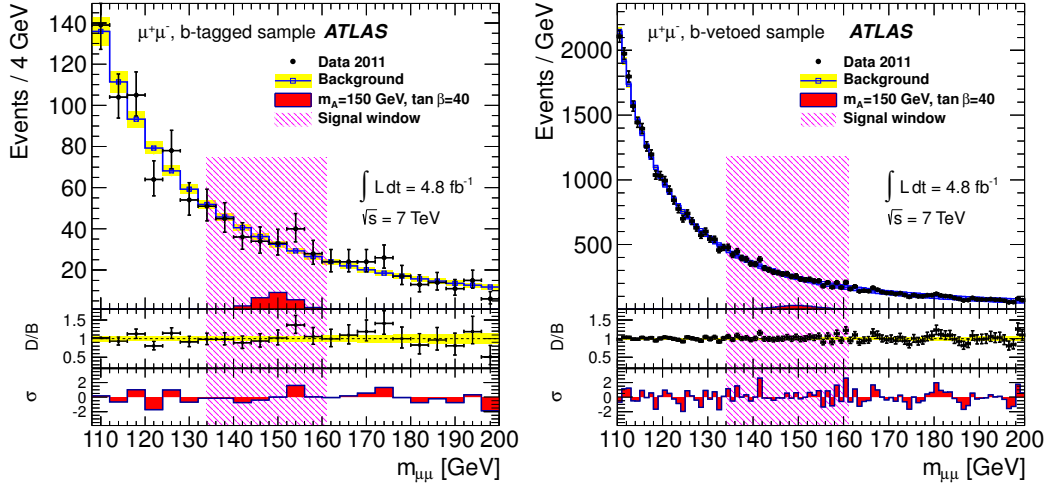


Figure 7.1.: The invariant di-muon mass distribution for data and expected distributions for signal and background from sideband fits to the data are shown for the signal point with $m_A = 150$ GeV and $\tan\beta = 40$ and the b -tagged (left-hand side) and the b -vetoed (right-hand side) samples of the $h/A/H \rightarrow \mu\mu$ channel. The ratio of the data and the expected background, labelled D/B , and the bin-by-bin significances of the deviations of the data from the background expectation, labelled σ , are shown beneath. For the signal point with $m_A = 150$ GeV and $\tan\beta = 40$ the signal window corresponds to the interval $134 \text{ GeV} < m_{\mu\mu} \leq 162 \text{ GeV}$ and the fit of the background model is performed in the sidebands corresponding to the interval $110 \text{ GeV} < m_{\mu\mu} \leq 200 \text{ GeV}$, but excluding the signal window.

7.1.2. Results of the Search for $h/A/H \rightarrow \tau_e\tau_\mu$ Decays

Events in the $h/A/H \rightarrow \tau_e\tau_\mu$ channel are selected with a single-electron trigger with a p_T threshold of 20 GeV or 22 GeV depending on the run, a single-muon trigger with a p_T threshold of 18 GeV or a combined electron–muon trigger with p_T thresholds of 10 GeV for the electron and 6 GeV for the muon. One isolated electron with $p_T > 15$ GeV and one isolated muon with opposite charge and $p_T > 10$ GeV is required. The mass of the electron–muon system has to fulfil $m_{e\mu} > 30$ GeV. The event sample is split into a b -tagged and a b -vetoed subsample depending on whether or not there is an identified b -jet.

The top and diboson backgrounds are reduced with requirements¹ on the absolute sum of the electron, muon and the missing transverse momenta, the absolute sum of the transverse momenta of all jets and the azimuthal angles between the electron and muon, the electron and the missing transverse momentum and the muon and the missing transverse momentum.

The main background from $Z/\gamma^* \rightarrow \tau^+\tau^-$ production is estimated with τ -embedded $Z/\gamma^* \rightarrow \mu^+\mu^-$ data. The $t\bar{t}$ background is estimated from simulated event samples that are normalised in a control region in data. For the selection of the $t\bar{t}$ control region, instead of the requirement on H_T in the nominal selection, a second b -jet is required. The multi-jet background is estimated with an ABCD method. The control regions of the ABCD method

¹The requirements are $E_T^{\text{miss}} + p_T^e + p_T^\mu < 125 \text{ GeV}$ ($< 150 \text{ GeV}$), $\Delta\phi(e, \mu) > 2.0$ (> 1.6) and $\cos\Delta\phi(E_T^{\text{miss}}, e) + \cos\Delta\phi(E_T^{\text{miss}}, \mu) > -0.2$ (> -0.4) for the b -tagged (b -vetoed) subsamples. In the b -tagged sample in addition the absolute sum of the transverse energies of all jets, H_T , is required to be below 100 GeV.

are defined based on the charge product of the electron and the muon and whether both leptons are isolated or not isolated. The event yields for all other backgrounds are estimated with simulated event samples.

The statistical analysis of the results obtained in this channel is based on the MMC mass distributions, which are shown in Reference [96] for the b -tagged and the b -vetoed subsamples. The likelihood function described in Section 7.2 is constructed based on the binned MMC mass distributions that are shown in Figure 7.2. The binned MMC mass distributions in Figure 7.2 are obtained from the MMC mass distributions in Reference [96] with the non-linear bin number–MMC mass relations which are documented in Appendix C.1. For the stability of the limit setting machinery a minimum number of events per bin is needed. To achieve this, non-linear bin number–MMC mass relations are necessary as the number of events falls off quickly for high MMC masses. Due to the non-linearity of the bin number–MMC mass relations the number of events is shown as a function of the bin number in Figure 7.2 instead of the MMC mass. For the combination of the results the $h/A/H \rightarrow \tau_e \tau_\mu$ channel is used for signal hypotheses with $m_A \leq 300$ GeV. For signal hypothesis with larger m_A the sensitivity of this channel is too low to exclude relevant regions in $\tan \beta$.

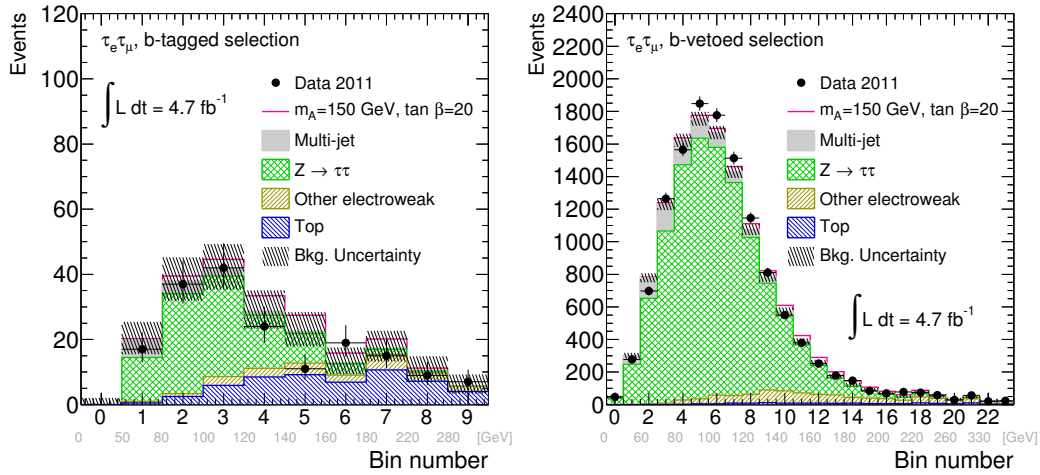


Figure 7.2.: Di- τ mass distributions as calculated with the MMC algorithm for the b -tagged (left-hand side) and b -vetoed (right-hand side) samples of the $h/A/H \rightarrow \tau_e \tau_\mu$ channel. The distributions are shown in the binned versions used to construct the likelihood function in Section 7.2. The binned mass distributions are obtained with non-linear bin number–MMC mass relations. The MMC mass values corresponding to the bins are indicated in grey on a non-linear axis. The data are compared with the background expectation and an added hypothetical MSSM signal ($m_A = 150$ GeV, $\tan \beta = 20$). The background from diboson, $Z/\gamma^* \rightarrow e^+e^-/\mu^+\mu^-$, W + jets and single-top processes is combined and labelled “Other electroweak”.

7.1.3. Results of the Search for $h/A/H \rightarrow \tau_{\text{lep}} \tau_{\text{had}}$ Decays

Events in the $h/A/H \rightarrow \tau_{\text{lep}} \tau_{\text{had}}$ search channel are selected with a single-muon trigger with a p_T threshold of 18 GeV or a single-electron trigger with a p_T threshold of 20 GeV or 22 GeV, depending on the data-taking period. One isolated electron with $p_T > 25$ GeV or one isolated muon with $p_T > 20$ GeV and no additional lepton with $p_T > 15$ GeV or $p_T > 10$ GeV in

the case of an electron or muon, respectively, are required. In addition a reconstructed hadronic τ -lepton decay with medium τ_{had} identification requirements and opposite charge to the identified electron or muon is demanded. The transverse mass of the lepton and the missing transverse momentum,

$$m_T = \sqrt{2p_T^{\text{lep}} E_T^{\text{miss}} (1 - \cos \Delta\phi)}, \quad (7.1)$$

where p_T^{lep} is the transverse momentum of the identified lepton, E_T^{miss} the missing transverse momentum and $\Delta\phi$ the angle between p_T^{lep} and E_T^{miss} , is required to be below 30 GeV to remove background from W -boson production. After this selection the sample is split into the b -tagged subsample with the highest- p_T jet within $|\eta| < 2.5$ being a b -jet with $20 \text{ GeV} < p_T < 50 \text{ GeV}$ and the orthogonal b -vetoed subsample. In the b -vetoed subsample in addition $E_T^{\text{miss}} > 20 \text{ GeV}$ is required to remove backgrounds without intrinsic E_T^{miss} , such as multi-jet, $Z/\gamma^* \rightarrow e^+e^-$ and $Z/\gamma^* \rightarrow \mu^+\mu^-$ production.

The $Z/\gamma^* \rightarrow \tau^+\tau^-$ background is estimated with τ -embedded $Z/\gamma^* \rightarrow \mu^+\mu^-$ events from data. The background from $Z/\gamma^* \rightarrow e^+e^-$ and $Z/\gamma^* \rightarrow \mu^+\mu^-$ production is estimated from simulation, where a correction for the number of b -jets, which is measured in the τ -embedded $Z/\gamma^* \rightarrow \mu^+\mu^-$ data, is applied. The background from W -boson production is estimated from simulation. For the majority of the background from W -boson production the hadronic τ -lepton decay is due to a misidentified jet. As a result of the problems with the description of the jet-to- τ_{had} misidentification probability in simulation a normalisation factor is derived in a control region, for which the full selection is applied and the m_T selection is replaced by the requirement $70 \text{ GeV} < m_T < 110 \text{ GeV}$. The top background is estimated from simulation and normalised in a control region, where the full selection, apart from the m_T requirement, is applied. In addition the second highest- p_T jet within $|\eta| < 2.5$ is required to be an identified b -jet. The background from multi-jet production is estimated with an ABCD method based on the charge product of the electron or muon and the hadronic τ -lepton decay and the isolation of the electron or muon. All other background event yields are estimated with simulated event samples.

The statistical analysis of the results obtained in this channel is based on the MMC mass distributions, which are shown in Reference [96] for the b -tagged and the b -vetoed subsamples of the $\tau_e\tau_{\text{had}}$ and the $\tau_\mu\tau_{\text{had}}$ channels. The MMC mass distributions are shown in Figures 7.3 and 7.4 in the binned form that is used to construct the likelihood function described in Section 7.2. The binned mass distributions are obtained with the non-linear bin number–MMC mass relations that are documented in Appendix C.1. Due to the non-linearity of the bin number–MMC mass relations the number of events is shown as a function of the bin number in Figures 7.3 and 7.4 instead of the MMC mass. In contrast to the other channels, the $h/A/H \rightarrow \tau_{\text{lep}}\tau_{\text{had}}$ channels provides significant sensitivity for all considered mass hypotheses and are thus used for the combination of the results for all mass hypotheses.

7.1.4. Results of the Search for $h/A/H \rightarrow \tau_{\text{had}}\tau_{\text{had}}$ Decays

The search for $h/A/H \rightarrow \tau_{\text{had}}\tau_{\text{had}}$ decays was discussed in detail in Chapter 6. The statistical analysis is based on the MMC mass distributions for the b -tagged and b -vetoed event samples as shown in Figure 6.38. The MMC mass distributions are rebinned with the non-linear bin number–MMC mass relations, which are documented in Appendix C.1, into the form that is used to construct the likelihood function described in Section 7.2. The result is shown in Figure 7.5. Due to the non-linearity of the bin number–MMC mass relations the number of events is shown as a function of the bin number in Figure 7.5 instead of the MMC

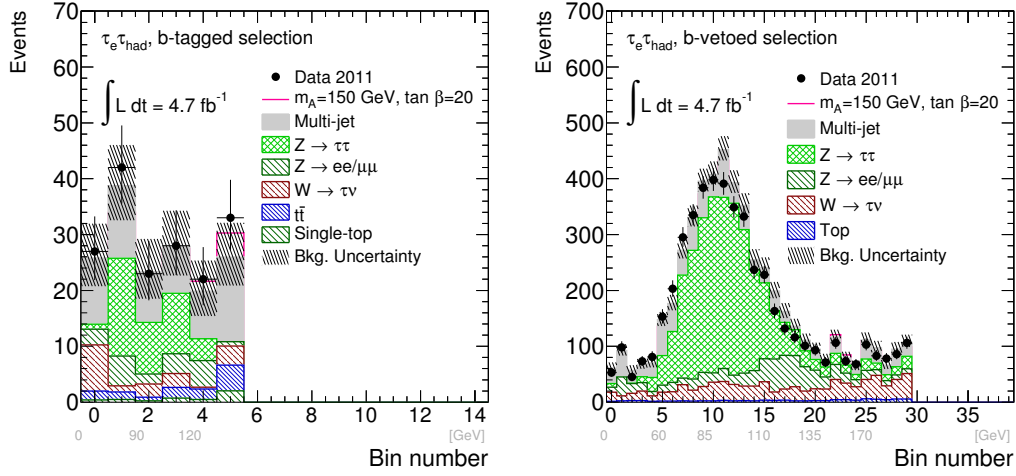


Figure 7.3.: Di- τ mass distributions as calculated with the MMC algorithm for the b -tagged (left-hand side) and b -vetoed (right-hand side) samples of the $h/A/H \rightarrow \tau_e \tau_{\text{had}}$ channel. The distributions are shown in the binned versions used to construct the likelihood function in Section 7.2. The binned mass distributions are obtained with non-linear bin number–MMC mass relations. The MMC mass values corresponding to the bins are indicated in grey on a non-linear axis. The data are compared with the background expectation and an added hypothetical MSSM signal ($m_A = 150 \text{ GeV}$, $\tan \beta = 20$).

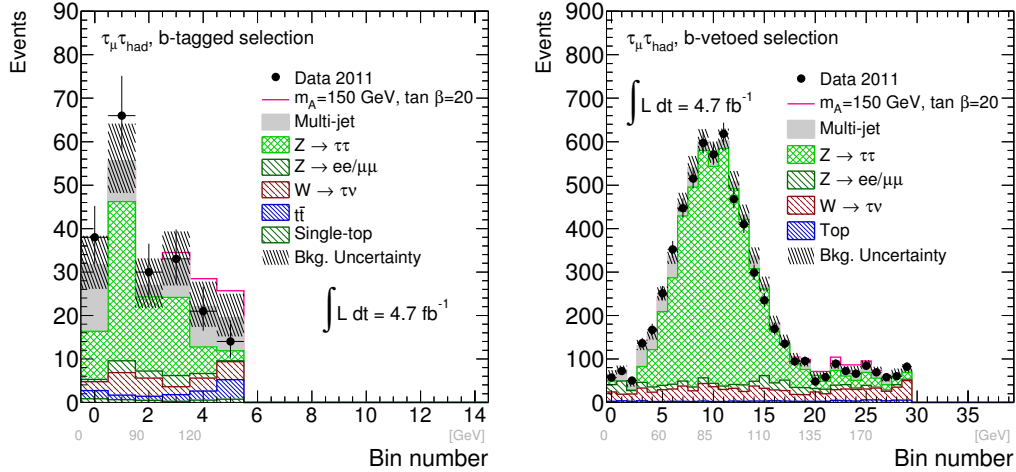


Figure 7.4.: Di- τ mass distributions as calculated with the MMC algorithm for the b -tagged (left-hand side) and b -vetoed (right-hand side) samples of the $h/A/H \rightarrow \tau_\mu \tau_{\text{had}}$ channel. The distributions are shown in the binned versions used to construct the likelihood function in Section 7.2. The binned mass distributions are obtained with non-linear bin number–MMC mass relations. The MMC mass values corresponding to the bins are indicated in grey on a non-linear axis. The data are compared with the background expectation and an added hypothetical MSSM signal ($m_A = 150 \text{ GeV}$, $\tan \beta = 20$).

mass. The $h/A/H \rightarrow \tau_{\text{had}}\tau_{\text{had}}$ channels are considered in the combination of the results for $m_A \geq 110$ GeV. For lower signal masses the sensitivity of this channel is low and the efficiency of the selection is too low to obtain reliable results based on the available number of simulated signal events.

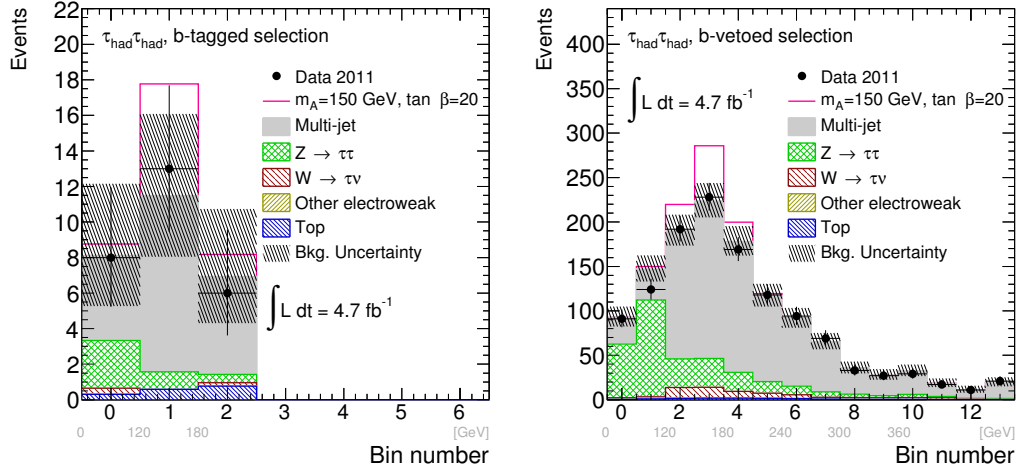


Figure 7.5.: Di- τ mass distributions as calculated with the MMC algorithm for the b -tagged (left-hand side) and b -vetoed (right-hand side) samples of the $h/A/H \rightarrow \tau_{\text{had}}\tau_{\text{had}}$ channel. The distributions are shown in the binned versions used to construct the likelihood function in Section 7.2. The binned mass distributions are obtained with non-linear bin number–MMC mass relations. The MMC mass values corresponding to the bins are indicated in grey on a non-linear axis. The data are compared with the background expectation and an added hypothetical MSSM signal ($m_A = 150$ GeV, $\tan \beta = 20$). The background from diboson and $Z/\gamma^* \rightarrow e^+e^-/\mu^+\mu^-$ processes is combined and labelled “Other electroweak”.

7.2. Definition of the Likelihood Function

For the statistical analysis of the data the HISTFACTORY tool [244] is used together with the ROOT packages ROOSTATS [245] and ROOFIT [246] in order to obtain a likelihood function based on the histograms shown in Figures 7.1 to 7.5 and the systematic uncertainties. The likelihood function is a measure for the consistency of the data with the signal-and-background hypothesis as a function of the signal strength, μ . In Section 7.3 the hypothesis tests, in which the likelihood function is used, are described. In the following derivation of the likelihood function, N denotes the number of observed events in data for the combination of all considered channels, b and μs the number of expected background and signal events for the signal strength μ , $f_B(m)dm$ and $f_S(m)dm$ are the background and signal probability density functions that describe the probability for an event that passes the selection to have an MMC mass $m_0 \in [m, m + dm)$. The number of expected signal events for the nominal signal expectation is s . The signal strength μ is uniquely determined by the condition that the expected number of signal events is μs , so that $\mu = 1$ corresponds to the nominal signal strength. The probability density to obtain N events with masses $\{m_1, \dots, m_N\}$ can be described with the probability density function of a marked Poisson process (MPP). Given a Poisson process $X(t)$ with rate $\lambda > 0$, where each event has an associated random variable

m_i with a common distribution function, a marked Poisson process is the sequence of pairs $(W_1, m_1), \dots, (W_N, m_N)$, where W_i are the points in time of the occurrence of event i , the so-called waiting time [247]. For a mixture of signal and background the combined probability density function, f_C , for m_i is

$$f_C(m_i) = \frac{\mu s f_S(m_i) + b f_B(m_i)}{\mu s + b}. \quad (7.2)$$

Thus the probability density function to obtain N events with MMC masses $\{m_1, \dots, m_N\}$ is

$$\mathcal{P}_{\text{MPP}}(\{m_1, \dots, m_N\}|\mu) = \text{Poisson}(N|b + \mu s) \prod_{i=1}^N \frac{\mu s f_S(m_i) + b f_B(m_i)}{b + \mu s}, \quad (7.3)$$

where $\text{Poisson}(n|\lambda) = \frac{\lambda^n e^{-\lambda}}{n!}$ and the best estimator for λ , which is $b + \mu s$, is used. As the background estimation and the observed numbers of events are based on histograms, the best estimators for the functions f_B and f_S are

$$f_B(m_i) = \frac{b_j}{b \Delta_j} \quad \text{and} \quad f_S(m_i) = \frac{s_j}{s \Delta_j}. \quad (7.4)$$

The MMC mass m_i and bin number j are related by the non-linear MMC mass–bin number relation, the number of observed events in bin j with bin width Δ_j is N_j , the number of signal events is s_j and the number of background events is b_j , so that

$$N = \sum_{j=1}^{n_{\text{bins}}} N_j, \quad b = \sum_{j=1}^{n_{\text{bins}}} b_j, \quad s = \sum_{j=1}^{n_{\text{bins}}} s_j, \quad (7.5)$$

where n_{bins} is the number of bins. With this definition the probability density function from Equation 7.3 can be written as

$$\begin{aligned} \mathcal{P}_{\text{MPP}}(\{m_1, \dots, m_N\}|\mu) &= \text{Poisson}(N|b + \mu s) \prod_{i=1}^N \frac{b f_B(m_i) + \mu s f_S(m_i)}{b + \mu s} \\ &= \frac{(b + \mu s)^N e^{-(b + \mu s)}}{N!} \prod_{j=1}^{n_{\text{bins}}} \left[\frac{1}{\Delta_j^{N_j}} \frac{(b_j + \mu s_j)^{N_j}}{(b + \mu s)^{N_j}} \right] \\ &= \frac{1}{N!} \prod_{j=1}^{n_{\text{bins}}} \left[\frac{N_j!}{\Delta_j^{N_j}} \right] \cdot \prod_{j=1}^{n_{\text{bins}}} \left[\frac{(b_j + \mu s_j)^{N_j} e^{-(b_j + \mu s_j)}}{N_j!} \right] \\ &= \mathcal{N} \cdot \prod_{j=1}^{n_{\text{bins}}} \text{Poisson}(N_j|b_j + \mu s_j), \end{aligned} \quad (7.6)$$

where \mathcal{N} is a normalisation factor that depends on the number of observed events and the bin widths only. For the analysis of the data an extended maximum likelihood method [248] is used and the negative logarithmic likelihood (NLL) is defined as

$$\begin{aligned} -\ln \mathcal{L}_{\text{MPP}}(\mu) &= -\ln \mathcal{P}_{\text{MPP}}(\{m_1, \dots, m_N\}|\mu) \\ &= \sum_{j=1}^{n_{\text{bins}}} [b_j + \mu s_j + \ln N_j! - N_j \ln(\mu s_j + b_j)] - \ln \mathcal{N}. \end{aligned} \quad (7.7)$$

The term $-\ln \mathcal{N}$ changes only the value of the minimum of $-\ln \mathcal{L}_{\text{MPP}}$, but not its position. In the following the term $-\ln \mathcal{N}$ and the corresponding factor in \mathcal{P}_{MPP} are neglected and only the binned variants of the probability density functions $f_B(m_i)$ and $f_S(m_i)$ are used.

The case of $n_{\text{ch}} > 1$ search channels or additional auxiliary measurements can be formulated in the above-described formalism if the bin contents b_j , s_j and N_j are redefined to include the bin contents of all search channels and auxiliary measurements. The vectors of the bin contents for background b_j , signal s_j and data N_j are defined to contain the bin contents from all channels and the bin contents are inserted sequentially, i.e. with the number of bins in search channel k , $n_{\text{bins},k}$, and the binned background expectation for bin i of channel k , $b_{k,i}$, the vector of the expected number of background events is

$$\mathbf{b} = \left(b_{1,1}, \dots, b_{1,n_{\text{bins},1}}, b_{2,1}, \dots, b_{2,n_{\text{bins},2}}, \dots, b_{n_{\text{ch}},1}, \dots, b_{n_{\text{ch}},n_{\text{bins},n_{\text{ch}}}} \right)^T \quad (7.8)$$

and in the example of three channels with two bins each

$$\mathbf{b} = (b_{1,1}, b_{1,2}, b_{2,1}, b_{2,2}, b_{3,1}, b_{3,2})^T. \quad (7.9)$$

The binned signal expectation s_j and the binned number of data events N_j are defined accordingly. All vectors have n_{bins} elements, where

$$n_{\text{bins}} = \sum_{k=1}^{n_{\text{ch}}} n_{\text{bins},k}. \quad (7.10)$$

7.2.1. Nuisance Parameters for Systematic Uncertainties

The estimates of the binned background and signal expectations, b_j and s_j , are subject to systematic uncertainties such as the τ_{had} identification efficiency and the τ_{had} energy scale uncertainties. The systematic uncertainties considered for the $h/A/H \rightarrow \tau_{\text{had}}\tau_{\text{had}}$ channels and their effect on the signal and background expectations are described in detail in Section 6.6 and for the other channels in References [96, 240, 243].

For every relevant systematic uncertainty a nuisance parameter is introduced. A nuisance parameter is a parameter of a statistical model that is not of primary interest for the analysis, but influences the values of the relevant parameters. The background and signal expectations depend on the nuisance parameters and can be written as $b_j(\{\alpha_i\}_{i=1}^{n_{\text{syst}}})$ and $s_j(\{\alpha_i\}_{i=1}^{n_{\text{syst}}})$, where $\{\alpha_i\}_{i=1}^{n_{\text{syst}}}$ is the set of nuisance parameters $\alpha_1, \dots, \alpha_{n_{\text{syst}}}$ and n_{syst} is the number of nuisance parameters used to model the systematic uncertainties. In the following the background and signal expectations are defined such that a value of the nuisance parameter of $\alpha_i = 0$ corresponds to the nominal value of the signal and background expectation and $\alpha_i = \pm 1$ to a shift of the corresponding systematic uncertainty by $\pm 1\sigma$.

Every systematic uncertainty can be split into a part that affects only the normalisation of the combined event yield and a part that affects only the shape of the binned discriminating distribution, i.e. the MMC mass distribution. The functional form of $b_j(\{\alpha_i\}_{i=1}^{n_{\text{syst}}})$ for the part that affects only the shape of the distribution is obtained by piecewise linear interpolation and for the part that affects only the normalisation by piecewise exponential interpolation between the MMC mass distributions that are expected for the $\pm 1\sigma$ variations of the systematic uncertainty and the nominal distribution [249]. The term piecewise interpolation refers to the fact that the interpolation for $\alpha_i > 0$ is independent from the interpolation for $\alpha_i < 0$. With the nuisance parameter α_i , the nominal background expectation for bin j , h_j^0 , and the $\pm 1\sigma$ variations of the background expectation in bin j for the systematic uncertainty i ,

$h_j^{i,+}$ and $h_j^{i,-}$, the modified background expectation $b_j(\{\alpha_i\}_{i=1}^{n_{\text{syst}}})$ can be written as

$$b_j(\{\alpha_i\}_{i=1}^{n_{\text{syst}}}) = \left[h_j^0 + \sum_{i=1}^{n_{\text{syst}}} L_{i,j}(\alpha_i) \right] \cdot \left[\prod_{i=1}^{n_{\text{syst}}} E_i(\alpha_i) \right] \quad \text{with} \quad (7.11)$$

$$L_{i,j}(\alpha_i) = \begin{cases} \alpha_i (N_i^+ h_j^{i,+} - h_j^0) & \text{for } \alpha_i \geq 0, \\ \alpha_i (h_j^0 - N_i^- h_j^{i,-}) & \text{for } \alpha_i < 0, \end{cases} \quad (7.12)$$

$$N_i^+ = \sum_{j=1}^{n_{\text{bins}}} h_j^0 / \sum_{j=1}^{n_{\text{bins}}} h_j^{i,+}, \quad (7.13)$$

$$N_i^- = \sum_{j=1}^{n_{\text{bins}}} h_j^0 / \sum_{j=1}^{n_{\text{bins}}} h_j^{i,-}, \quad (7.14)$$

$$E_i(\alpha_i) = \begin{cases} \left(\sum_{j=1}^{n_{\text{bins}}} h_j^{i,+} / \sum_{j=1}^{n_{\text{bins}}} h_j^0 \right)^{\alpha_i} & \text{for } \alpha_i \geq 0, \\ \left(\sum_{j=1}^{n_{\text{bins}}} h_j^0 / \sum_{j=1}^{n_{\text{bins}}} h_j^{i,-} \right)^{\alpha_i} & \text{for } \alpha_i < 0. \end{cases} \quad (7.15)$$

The linear interpolation between the nominal MMC mass distribution and the MMC mass distributions for the $\pm 1\sigma$ variations of the considered systematic uncertainty is defined in Equation 7.12. The MMC mass distributions for the $\pm 1\sigma$ variations are normalised to the expected nominal event yield with the normalisation factors N_i^+ and N_i^- , so that only the shape difference is subject to the linear interpolation. The exponential interpolation between the integrated event yield for the nominal event expectation and the expectations for the $\pm 1\sigma$ variations is defined in Equation 7.15. The modified signal expectation, $s_j(\{\alpha_i\}_{i=1}^{n_{\text{syst}}})$, is defined accordingly.

For the $h/A/H \rightarrow \tau_{\text{had}}\tau_{\text{had}}$ channel the following nuisance parameters are introduced:

- 1 nuisance parameter for the uncertainty of the integrated luminosity,
- 3 nuisance parameters for the uncertainties of the τ_{had} identification efficiency, the τ_{had} trigger efficiency and the jet-to- τ_{had} misidentification probability,
- 2 nuisance parameters for the uncertainties of the measured fraction of events with identified b -jet for the backgrounds with W - and Z -boson production in the b -tagged channel,
- 3 nuisance parameters for the uncertainties of the b -tag efficiency and the light-jet and c -jet mistag probability for the backgrounds other than the backgrounds with single W - and Z -boson production in the b -tagged channel,
- 1 nuisance parameters for the jet and τ_{had} energy scale uncertainty,
- 6 nuisance parameters for the cross-section uncertainties of the backgrounds with Z -boson production, W -boson production, top-quark production, diboson production and signal production in b -quark annihilation and gluon fusion,
- 7 nuisance parameters for the theory uncertainty of the acceptance for the search in the b -tagged and b -vetoed channel separately for the background with Z -boson production, W -boson production, top-quark production, and signal production in b -quark annihilation and gluon fusion.

If multiple nuisance parameters affect only the normalisation of one background process, they are merged into one nuisance parameter to avoid unnecessary degrees of freedom. For example, the uncertainties of the b -jet fraction measurement and the acceptance uncertainty based on theory predictions are merged for the backgrounds with W - and Z -boson production and thus the number of nuisance parameters is different from the initial number of uncorrelated systematic uncertainties.

If not explicitly mentioned only one nuisance parameter is introduced per systematic uncertainty for all search channels and a coherent variation for all search channels is performed. In addition to the nuisance parameters for the $h/A/H \rightarrow \tau_{\text{had}}\tau_{\text{had}}$ channels, the following nuisance parameters are introduced for the $h/A/H \rightarrow \mu\mu$, the $h/A/H \rightarrow \tau_e\tau_\mu$ and the $h/A/H \rightarrow \tau_{\text{lep}}\tau_{\text{had}}$ channels:

- 3 nuisance parameters for the systematic uncertainties of the τ -embedded $Z/\gamma^* \rightarrow \mu^+\mu^-$ data,
- 1 nuisance parameter for uncertainty of the electron-to- τ_{had} misidentification probability,
- 4 nuisance parameters for the electron and muon identification efficiency, energy scale and resolution uncertainties,
- 14 nuisance parameters for the signal and background fit uncertainties in the $h/A/H \rightarrow \mu\mu$ channels,
- 6 nuisance parameters for the data-driven estimation of the top and multi-jet backgrounds for the $h/A/H \rightarrow \tau_e\tau_\mu$ channels,
- 4 nuisance parameters for the data-driven estimation of the multi-jet background for the $h/A/H \rightarrow \tau_{\text{lep}}\tau_{\text{had}}$ channels,
- 2 nuisance parameters for the cross-section uncertainties for single-top production and other processes with a small background contribution,
- 14 nuisance parameters for the theory uncertainties on the acceptance for all channels separately for the Z -boson, W -boson, top-quark ($t\bar{t}$, single-top), diboson, b -associated signal and gluon-fusion signal production processes, if the backgrounds are not normalised by data-driven methods.

In total these are 70 nuisance parameters. The nuisance parameters are described in more detail in Appendix C.2. They are further constrained by the addition of the factor

$$\mathcal{L}_{\text{syst}} = \prod_{i=1}^{n_{\text{syst}}} \text{Gaussian}(\alpha_i|0,1) , \quad (7.16)$$

to the likelihood function. The function $\text{Gaussian}(x|\mu, \sigma)$ represents a Gaussian distribution with mean μ and variance σ^2 . In the frequentist approach that is used for the limit setting the Gaussian terms cannot be interpreted as a prior, but should be interpreted as the information from the auxiliary measurement of the size of the systematic uncertainty. It is assumed that all parameters from the auxiliary measurement apart from the value of α_i are uncorrelated to the nuisance parameters in the main measurement, so that the likelihood function of the auxiliary measurement can be summarised by $\text{Gaussian}(\alpha_i|0,1)$.

7.2.2. Nuisance Parameters for Statistical Uncertainties

If the relative statistical uncertainty of the background expectation in bin j exceeds 5%, a nuisance parameter γ_k is introduced to account for this statistical uncertainty². This statistical uncertainty is primarily due to a small number of simulated events or events in a control region. In the following the number of introduced nuisance parameters γ_k is denoted by n_{stat} and the number of introduced nuisance parameters per channel is given in Table 7.2.

The modified background expectation is redefined as

$$\begin{aligned} b_j(\{\alpha_i\}_{i=1}^{n_{\text{syst}}}, \gamma_k) &= \gamma_k b_j(\{\alpha_i\}_{i=1}^{n_{\text{syst}}}) \\ &= \gamma_k \left[h_j^0 + \sum_{i=1}^{n_{\text{syst}}} L_{i,j}(\alpha_i) \right] \cdot \left[\prod_{i=1}^{n_{\text{syst}}} E_i(\alpha_i) \right], \end{aligned} \quad (7.17)$$

where h_j^0 , $L_{i,j}(\alpha_i)$ and $E_i(\alpha_i)$ are defined as in Section 7.2.1, Equations 7.12 and 7.15, respectively. Statistical uncertainties of the signal yield are not considered, i.e. for s_j Equation 7.11 holds. The Monte Carlo simulation is interpreted as an auxiliary random process of which the number of events, n_{MC}^j , can be estimated with

$$\sigma_{\text{stat}}^j = \frac{\sqrt{n_{\text{MC}}^j}}{n_{\text{MC}}^j} \Leftrightarrow n_{\text{MC}}^j = \left(\sigma_{\text{stat}}^j \right)^{-2}, \quad (7.18)$$

where σ_{stat}^j is the relative statistical uncertainty for bin j . A constraint term can be constructed from the probability to get n_{MC}^j events from a Poisson process with mean $\gamma_k n_{\text{MC}}^j$. For event samples with a non-constant weight distribution n_{MC}^j corresponds to an effective number of events for an event sample with a constant weight distribution. As n_{MC}^j is not necessarily an integer number, the Poisson constraint term is replaced by a constraint term based on a Gamma distribution with shape parameter $\gamma = n_{\text{MC}}^j + 1$, location parameter $\mu = 0$ and scale parameter $\beta = 1/n_{\text{MC}}^j$, so that

$$\mathcal{L}_{\text{stat}} = \prod_{k=1}^{n_{\text{stat}}} \text{Gamma} \left(\gamma_k \middle| n_{\text{MC}}^j + 1, 0, 1/n_{\text{MC}}^j \right), \quad (7.19)$$

where

$$\text{Gamma}(x|\gamma, \mu, \beta) = \frac{\left(\frac{x-\mu}{\beta} \right)^{\gamma-1} \exp\left(-\frac{x-\mu}{\beta} \right)}{\beta \Gamma(\gamma)} \quad (7.20)$$

and $\Gamma(x) = \int_0^\infty t^{x-1} \exp(-t) dt$ is the Gamma function. The constraint term can be written as

$$C \frac{\gamma_k^{n_{\text{MC}}^j} \exp(-\gamma_k)}{\Gamma(n_{\text{MC}}^j + 1)}, \quad (7.21)$$

where C is a constant factor, which can be neglected as it will not affect the position of the minimum of the negative log-likelihood.

²As the statistical uncertainty in a bin can be lower than 5%, in which case no nuisance parameter is introduced, a different index k is introduced for the statistical nuisance parameters and it is $k \leq j$.

Channel	<i>b</i> -tagged channel		<i>b</i> -vetoed channel	
	Number of bins	Number of γ_i	Number of bins	Number of γ_i
$h/A/H \rightarrow \mu\mu$	32	0	62	0
$h/A/H \rightarrow \tau_e\tau_\mu$	13	12	28	12
$h/A/H \rightarrow \tau_e\tau_{\text{had}}$	8	8	32	31
$h/A/H \rightarrow \tau_\mu\tau_{\text{had}}$	8	8	32	21
$h/A/H \rightarrow \tau_{\text{had}}\tau_{\text{had}}$	6	6	17	15

Table 7.2.: Number of bins of the discriminating distributions that are used for the derivation of the exclusion limits and number of introduced nuisance parameters that account for the statistical uncertainty of the simulated event yields. For the $h/A/H \rightarrow \tau\tau$ channels the number of bins and nuisance parameters is independent of the considered Higgs boson mass, for the $h/A/H \rightarrow \mu\mu$ channels the results for the search optimised for $m_A = 120$ GeV are shown. For the combination of all channels 113 nuisance parameters are introduced to account for statistical uncertainties in 238 bins.

7.2.3. Nuisance Parameters for Backgrounds Normalised in Control Regions

In the $h/A/H \rightarrow \tau_e\tau_\mu$ and $h/A/H \rightarrow \tau_{\text{lep}}\tau_{\text{had}}$ channels the event yield of the top background is normalised in a control region. This normalisation is implemented in the likelihood function by introducing a linear dependence of the number of events in the signal and the control regions on a nuisance parameter τ that is only constrained by the event yields in the signal and control regions.

The estimation of the background from multi-jet production is implemented in a similar way. In the $h/A/H \rightarrow \tau_{\text{had}}\tau_{\text{had}}$ *b*-vetoed channel for example, the multi-jet background estimate is obtained by introducing three unconstrained nuisance parameters. The number of multi-jet events in region C is parameterised by τ_{shape} , τ_D parameterises the number of multi-jet events in region D and τ_{ratio} parameterises the ratio of the number of multi-jet events in regions B and D, so that

$$\begin{aligned}
n_{\text{QCD}}^B &= \tau_D \tau_{\text{ratio}} , \\
n_{\text{QCD}}^C &= \tau_{\text{shape}} , \\
n_{\text{QCD}}^D &= \tau_D ,
\end{aligned} \tag{7.22}$$

where n_{QCD}^X is the number of multi-jet events in region X . The number of multi-jet events in the signal region, n_{QCD}^A , is given by

$$n_{\text{QCD}}^A = n_{\text{QCD}}^C \frac{n_{\text{QCD}}^B}{n_{\text{QCD}}^D} = \tau_{\text{shape}} \tau_{\text{ratio}} . \tag{7.23}$$

The shape of the $m_{\tau\tau}^{\text{MMC}}$ distribution for multi-jet events is constant and taken from region C. For the $h/A/H \rightarrow \tau_{\text{had}}\tau_{\text{had}}$ *b*-tagged channel the parameterisation of n_{QCD}^B and n_{QCD}^C is interchanged and the shape is obtained from region B. In the following, the set of unconstrained nuisance parameters will be denoted as $\{\tau_i\}_{i=1}^{n_{\text{uncon}}}$ and the modified background expectation is

$$b_j(\{\alpha_i\}_{i=1}^{n_{\text{syst}}}, \gamma_k, \{\tau_i\}_{i=1}^{n_{\text{uncon}}}) = \gamma_k \left[h_j^0(\{\tau_i\}_{i=1}^{n_{\text{uncon}}}) + \sum_{i=1}^{n_{\text{syst}}} L_{i,j}(\alpha_i) \right] \cdot \left[\prod_{i=1}^{n_{\text{syst}}} E_i(\alpha_i) \right] . \tag{7.24}$$

7.2.4. Functional Form of the Likelihood

In the last sections the different parts of the likelihood function were described. If all information is combined, the likelihood function is given by

$$\begin{aligned}
\mathcal{L}(\mu, \boldsymbol{\theta}) &= \mathcal{L}_{\text{MPP}}(\mu, \{\alpha_i\}_{i=1}^{n_{\text{syst}}}, \{\gamma_i\}_{i=1}^{n_{\text{stat}}}, \{\tau_i\}_{i=1}^{n_{\text{uncon}}}) \cdot \mathcal{L}_{\text{syst}}(\{\alpha_i\}_{i=1}^{n_{\text{syst}}}) \cdot \mathcal{L}_{\text{stat}}(\{\gamma_i\}_{i=1}^{n_{\text{stat}}}) \\
&= \prod_{j=1}^{n_{\text{bins}}} \text{Poisson}(N_j | b_j(\{\alpha_i\}_{i=1}^{n_{\text{syst}}}, \{\gamma_i\}_{i=1}^{n_{\text{stat}}}, \{\tau_i\}_{i=1}^{n_{\text{uncon}}}) + \mu s_j(\{\alpha_i\}_{i=1}^{n_{\text{syst}}})) \cdot \\
&\quad \prod_{k=1}^{n_{\text{syst}}} \text{Gaussian}(\alpha_k | 0, 1) \cdot \\
&\quad \prod_{l=1}^{n_{\text{stat}}} \text{Gamma}\left(\gamma_l \left| \left(\sigma_{\text{stat}}^{k_l}\right)^{-2} + 1, 0, \left(\sigma_{\text{stat}}^{k_l}\right)^2\right.\right), \tag{7.25}
\end{aligned}$$

where s_j and b_j are defined as in Equations 7.11 and 7.24 and $\boldsymbol{\theta}$ is a vector containing all nuisance parameters. The parameter k_l refers to the number of the bin corresponding to γ_l .

7.3. Hypothesis Tests

For discrimination between a signal-and-background hypothesis, $H_{\mu S+B}$, and a background-only hypothesis, H_B , a test statistic that can be used in a hypothesis test is defined. A test statistic t is a number (or a small set of numbers) that summarises the outcome of a random process. Without loss of generality it is assumed that the expectation value of t , $E[t]$, is larger for H_B than for $H_{\mu S+B}$. With the value of the test statistic obtained in data, t_{μ}^{obs} , and the probability density function for t assuming the background-only hypothesis, $f(t|H_B)$, a p-value for the hypothesis H_B , can be calculated

$$p_0 = \int_{-\infty}^{t_{\mu}^{\text{obs}}} f(t_{\mu}|H_B) dt_{\mu} = 1 - \int_{t_{\mu}^{\text{obs}}}^{\infty} f(t_{\mu}|H_B) dt_{\mu}. \tag{7.26}$$

This p-value is the probability to obtain the value of the test statistic t_{μ}^{obs} or a lower value under the assumption that no signal exists. It can be translated into a Gaussian significance, Z_0 , with

$$Z_0 = \Phi^{-1}(1 - p_0), \tag{7.27}$$

where Φ^{-1} is the inverse cumulative function of a standard Gaussian distribution. It should be noted that formally t_{μ}^{obs} and p_0 are functions of the signal strength μ used for the signal-and-background hypothesis. The confidence level for the background-only hypothesis is defined as $\text{CL}_b = 1 - p_0$. In particle physics the background-only hypothesis is typically rejected if $Z_0 > 5$, which corresponds to $p_0 < 2.87 \cdot 10^{-7}$. With the probability density function for t_{μ} assuming the signal-and-background hypothesis, $f(t_{\mu}|H_{\mu S+B})$, the p-value for the signal-and-background hypothesis can be calculated with

$$p_{\mu} = \int_{t_{\mu}^{\text{obs}}}^{\infty} f(t_{\mu}|H_{\mu S+B}) dt_{\mu} \tag{7.28}$$

and the hypothesis is typically rejected at the 95% confidence level corresponding to $p_\mu < 5\%$ ($Z_\mu > 1.64$). According to the Neyman-Pearson lemma [250], the optimal test statistic in the absence of systematic uncertainties is the likelihood ratio,

$$Q_\mu = \frac{\mathcal{L}_{\text{MPP}}(\mu)}{\mathcal{L}_{\text{MPP}}(\mu = 0)}, \quad (7.29)$$

or any monotonic function of Q_μ , such as $t_\mu = -2 \ln Q_\mu$. The probability density function of Q_μ under the signal-and-background and the background-only hypotheses can be determined with Monte Carlo pseudo experiments (“toy experiments”) that are generated with the procedure described in Section 7.3.1.

For the CL_{s+b} limit the confidence level CL_{s+b} is defined by

$$\text{CL}_{s+b} = p_\mu \quad (7.30)$$

and all signal strengths greater or equal to the signal strength that corresponds to $p_\mu = 0.05$ are considered excluded. It should be noted that there are cases where the observed value of the test statistic is incompatible with the background-only hypothesis and a large set of signal-and-background hypotheses. In these cases the exclusion of signal-and-background hypotheses can be perceived as unnatural.

7.3.1. Calculation of Exclusion Limits and Discovery Significances

To overcome the fact that the compatibility of the data with the event yield expectation for the background-only hypothesis has no influence on the exclusion of the signal-and-background hypothesis in the earlier described hypothesis test, the CL_s procedure [251] is used for this analysis. The CL_s value is defined as

$$\text{CL}_s = \frac{p_\mu}{1 - p_0} = \frac{\text{CL}_{s+b}}{\text{CL}_b} \quad (7.31)$$

and a signal-and-background hypothesis is excluded at the 95% confidence level if $\text{CL}_s < 0.05$. While the CL_s values cannot be interpreted as a probability, the definition of CL_s is formally equivalent to the result of a Bayesian calculation, as outlined in Reference [252]. An illustration of the CL_s procedure is shown in Figure 7.6.

For signal-and-background hypotheses that depend on a parameter, i.e. in this analysis the signal strength μ , it is in general not possible to define a single optimal test statistic. The test statistic for the exclusion limit is defined as

$$\tilde{q}_\mu = \begin{cases} -2 \ln \left(\frac{\mathcal{L}(\mu, \hat{\boldsymbol{\theta}}_\mu)}{\mathcal{L}(0, \hat{\boldsymbol{\theta}}_0)} \right) & \text{if } \hat{\mu} < 0, \\ -2 \ln \left(\frac{\mathcal{L}(\mu, \hat{\boldsymbol{\theta}}_\mu)}{\mathcal{L}(\hat{\mu}, \hat{\boldsymbol{\theta}})} \right) & \text{if } 0 \leq \hat{\mu} \leq \mu, \\ 0 & \text{if } \hat{\mu} > \mu, \end{cases} \quad (7.32)$$

with the likelihood function \mathcal{L} as defined in Equation 7.25 [253]. The symbols $\hat{\mu}$ and $\hat{\boldsymbol{\theta}}$ refer to the values of μ and $\boldsymbol{\theta}$ that are obtained in the unconditional minimisation of $-\ln \mathcal{L}(\mu, \boldsymbol{\theta})$ and $\hat{\boldsymbol{\theta}}_\mu$ refers to the values of $\boldsymbol{\theta}$ that are obtained in the conditional minimisation of $-\ln \mathcal{L}(\mu, \boldsymbol{\theta})$ for a constant signal strength μ . In the case of the MSSM analysis negative signal strengths are not physical solutions and the test statistic is evaluated at $\hat{\mu} = 0$ for negative signal strengths. For probed signal strengths μ lower than the signal strength obtained in the minimisation, $\hat{\mu}$, the test statistic is set to 0, the minimal and most signal-like value possible. It should be

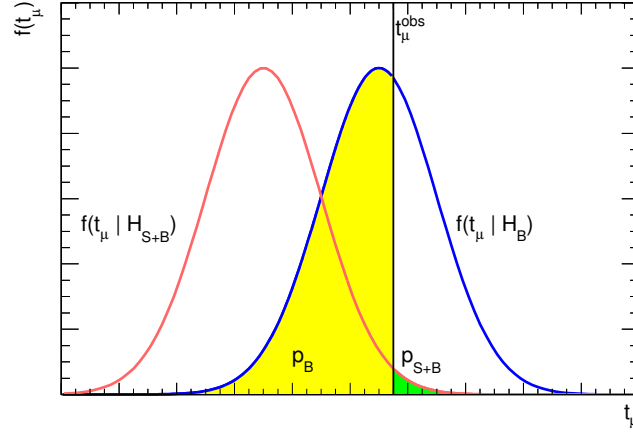


Figure 7.6.: Illustration of the CL_s procedure. The probability density functions for t_μ under the signal-and-background hypothesis $H_{\mu S+B}$ and the background-only hypothesis H_B are shown with red and blue lines, respectively. The vertical black line represents the value of the test statistic that is observed in data, t_μ^{obs} . The green and yellow areas represent the probability of the signal-and-background hypothesis p_μ and the background-only hypothesis p_0 . An arbitrary normalisation is used for the x- and y-axes.

noted that the test statistic is not a function of the ratio of the signal-and-background and the background-only hypothesis, but the ratio of the likelihood functions of the tested signal-and-background hypothesis and the most likely signal-and-background hypothesis. According to the Neyman-Pearson lemma this test statistic is optimal with respect to the signal-and-background hypothesis that is closest to the observed data in the absence of systematic uncertainties. Based on this definition of the test statistic a similar test statistic can be used for the exclusion of signal-and-background hypotheses and the background-only hypothesis.

If an excess over the background expectation is observed in data its significance with respect to a tested signal-and-background hypothesis needs to be quantified. The test statistic for the calculation of local discovery significances is given by

$$q_0 = \begin{cases} -2 \ln \left(\frac{\mathcal{L}(0, \hat{\theta}_0)}{\mathcal{L}(\hat{\mu}, \hat{\theta})} \right) & \text{if } \hat{\mu} \geq 0, \\ 0 & \text{if } \hat{\mu} < 0. \end{cases} \quad (7.33)$$

The term local refers to the fact that the significance is calculated for only one tested signal-and-background hypothesis. The calculation of the significance of an excess in data for experiments in which more than one signal-and-background hypothesis is tested, the global significance, is discussed in Section 7.3.3.

The probability density functions of \tilde{q}_μ and q_0 can be obtained with pseudo experiments or asymptotic formulae. For the generation of pseudo experiments both the measured distribution of the MMC mass and the outcome of the auxiliary measurements that constrain the nuisance parameters are randomised. Using $\mu = 1$ for the signal-and-background hypothesis and $\mu = 0$ for the background-only hypothesis, the pseudo-data N_j are generated by drawing a random number with a Poisson probability function centred around $\mu s_j(\hat{\theta}_\mu) + b_j(\hat{\theta}_\mu)$. For the signal and background expectations the values of the nuisance parameters obtained in the conditional minimisation of the likelihood function for $\mu = 1$ (signal-and-background hypothesis) or $\mu = 0$ (background-only hypothesis) are used. The outcome of the auxiliary

measurement that constrains a nuisance parameter with a Gaussian constraint term, α_i , is randomised by drawing a random number δ_{α_i} with a Gaussian $(\delta_{\alpha_i}|0, 1)$ probability density function and subsequent centring of the constraint term at δ_{α_i} , so that Equation 7.16 is replaced by

$$\mathcal{L}_{\text{syst}} = \prod_{i=1}^{n_{\text{syst}}} \text{Gaussian}(\alpha_i | \delta_{\alpha_i}, 1) . \quad (7.34)$$

For the nuisance parameters with a constraint term in the form of a Gamma distribution, a random number δ_{α_i} is drawn using a Gamma distribution as probability density function and the Gamma distribution constraint term is centred around δ_{α_i} . This change of the functional form of the test statistic should be interpreted as a randomisation of the data yield of the auxiliary measurements and thus it represents a change of the term that summarises the measurement rather than a change of the test statistic definition itself.

In addition, asymptotic formulae exist for the probability density functions of \tilde{q}_μ and q_0 . The asymptotic formulae have been derived with the Wald approximation [254] and Wilks' theorem [255] in Reference [253]. Based on the probability density function of \tilde{q}_μ the signal strength that is excluded at the 95% confidence level can be calculated without the simulation of pseudo experiments. With the probability density function for q_0 the p-value of the background-only hypothesis, p_0 , and thus the Gaussian discovery significance, Z_0 , can be calculated. In the presented MSSM analysis the asymptotic formulae are used. The results are cross-checked with the results from pseudo experiments for one m_A -tan β signal point in Section 7.4.3.

7.3.2. Characterisation of the Experimental Sensitivity

The sensitivity of an analysis is described by the expected limit on the signal strength and its one and two standard deviation values. The expected limit is defined as the lowest signal strength that can be excluded assuming that the value of the test statistic in data is equal to the median of the test statistic expected for the background-only hypothesis. The median of the test statistic can be obtained by simulating pseudo experiments for the background-only hypothesis. The $\pm 1\sigma$ and $\pm 2\sigma$ values of the expected limit can be obtained from the values of the test statistic that correspond to the 2.3% (-2σ), 15.9% (-1σ), 84.1% ($+1\sigma$) and 97.7% ($+2\sigma$) quantiles. In practice the median of the test statistic under the background-only hypothesis can be approximated by the value of the test statistic obtained for the Asimov dataset [253]. For this analyses, as for most ATLAS and CMS analyses, the Asimov dataset is defined as the dataset where the observed distributions are replaced by the expected distributions with a signal strength $\mu = 0$ and the nuisance parameter values obtained from the conditional minimisation with data and $\mu = 0$.

7.3.3. Calculation of Trial Factors

For independent signal hypotheses the probability to find an excess with a given significance or higher significance increases with the number of tested signal hypotheses. The calculation of the discovery significance, however, is independent of the number of different probed signal hypotheses. For this reason the resulting p-value denotes the probability for the case that only one signal hypothesis is considered and the resulting significance is called a local significance. The global significance corresponds to the probability of finding an excess with a given significance or a higher significance in any of the probed signal hypotheses. The global

significance is the significance for the test statistic

$$q_{\text{global}} = \sup_{m \in \mathcal{M}} [q_0(m)] , \quad (7.35)$$

where \mathcal{M} is the parameter space of all tested signal hypotheses. The trial factor is the ratio of the global and the local p_0 values.

It is shown in References [256] and [257] that for the cases where Wilks' theorem holds, the trial factor can be related to the Euler characteristics of an excursion set A_c defined by

$$A_c = \{m \in \mathcal{M} : q_0(m) > c\} . \quad (7.36)$$

In the case of a one-dimensional vector space of signal hypothesis parameters the Euler characteristics are the upcrossings of level c ; in the case of a two-dimensional vector space the Euler characteristics are given by the vertices, edges and faces of the excursion set. An upcrossing³ of level c occurs at m_0 if $\epsilon > 0$ exists, so that for all $m \in [m_0 - \epsilon, m_0)$, it is $q(m) < c$ and $q(m_0) = c$. Vertices, edges and faces of the excursion set are defined in Reference [257].

For the one-dimensional case the global p_0 -value is given by

$$P(q_{\text{global}} > c) \approx P(q_{\text{local}} > c) + E[N(c)] , \quad (7.37)$$

where $E[N(c)]$ is the expectation value for the number of upcrossings of level c . The number of upcrossings at level c can be measured at a lower level c_0 and the expectation value at the higher level is

$$E[N(c)] = E[N(c_0)] \exp \left[\frac{1}{2} (c_0 - c) \right] . \quad (7.38)$$

If the level c_0 is chosen as $c_0 = 0$, $q_0 = 0$ corresponds to $\mu = \hat{\mu}$ and the number of upcrossings can be determined from the $\hat{\mu}(m)$ function. For the multi-dimensional case the calculation of the trial factor is described in Reference [257].

7.4. Validation of the Likelihood Function

In Section 7.2 the construction of the likelihood function based on the expected and observed event yields and the systematic and statistical uncertainties was described. Due to the complexity of the likelihood function a validation procedure that is described in this section follows the construction of the likelihood function. In the validation procedure the interpolation and extrapolation for the bin content vectors for nuisance parameter changes. Due to the number of nuisance parameters used in the statistical model the minimisation of the negative log-likelihood is complicated and the results are reviewed. In addition the excluded limits based on the asymptotic formula are compared with the results from pseudo experiments. Due to the large number of considered distributions it is not possible to document the validation results for all nuisance parameters in this thesis. The full set of validation results is shown in Reference [258].

7.4.1. Validation of the Model for the Systematic Uncertainties

To model the uncertainties that affect the shape of the $m_{\tau\tau}^{\text{MMC}}$ distribution the shapes of the distribution for the nominal value and the distributions for the $\pm 1\sigma$ values of the nuisance

³Schematically an upcrossing exists if a function intersects a constant from below.

parameter are interpolated and extrapolated as described in Section 7.2.1. For the minimisation the range $[-5\sigma, +5\sigma]$ is considered. The results of the extrapolation procedure are validated at $\alpha_i = \pm 5$ for all channels and nuisance parameters. In Figure 7.7 the results of the extrapolation are shown for the jet and τ_{had} energy scale and the jet-to- τ_{had} misidentification probability nuisance parameters for the $\tau_{\text{had}}\tau_{\text{had}}$ b -vetoed channel as an example.

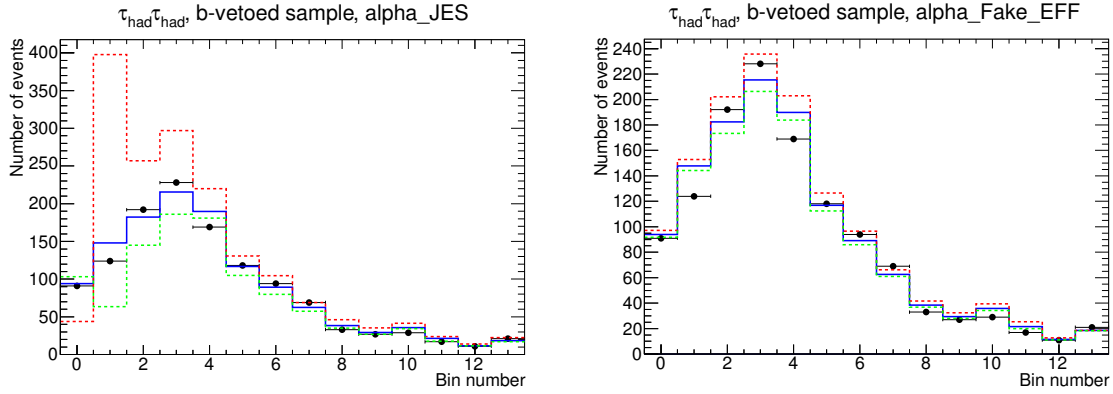


Figure 7.7.: Validation of the extrapolation procedure used to model systematic uncertainties. On the left-hand side the MMC mass distributions for the nominal (solid blue line) and $\pm 5\sigma$ values (red and green dashed lines) of the jet and τ_{had} energy scale uncertainty nuisance parameter, α_{JES} , are shown together with the number of events in data (black markers) for the $\tau_{\text{had}}\tau_{\text{had}}$ b -vetoed channel. On the right-hand side the same distributions are shown for the nuisance parameter for the uncertainty of the jet-to- τ_{had} misidentification probability, $\alpha_{\text{Fake_EFF}}$. The fact that the data points are outside the $\pm 5\sigma$ range does not indicate a problem, but shows that the difference between the background expectation and the data cannot be attributed to the considered systematic uncertainty alone.

7.4.2. Validation of the Likelihood Minimisation Procedure

For the validation of the values of the nuisance parameters obtained in the minimisation procedure several automated checks have been implemented to warn if values $\hat{\alpha}_i$ with $|\hat{\alpha}_i| > 3$ are obtained for nuisance parameters that model systematic uncertainties. In addition, the obtained values of α_i are validated for the unconditional minimisation and the conditional minimisation with $\mu = 0$ and $\mu = 1$. High values of $\hat{\alpha}_i$ are possibly a sign of problems with finding the correct minimum. The results are shown in Table C.2.

The obtained value of $\hat{\alpha}_i$ as a function of the signal strength parameter μ is checked and shown for two nuisance parameters as an example in Figure 7.8. In Figure 7.9 the obtained value of the test statistic is shown as a function of the signal strength. The functional dependence of the nuisance parameter estimate and the test statistic on μ is a good indicator for competing local minima. In the case of competing local minima, $\hat{\alpha}_i$ would be discontinuous as a function μ . In the validation discontinuities are observed (see for example Figure 7.9), however they are small and are attributed to the low number of events in data and simulation for some bins of the distribution. In Figure 7.10 the mutual correlations of the nuisance parameters and the signal strength is shown. High absolute values of the correlations are investigated and the nuisance parameters are replaced by a single nuisance parameter in cases where unphysical degrees of freedom are detected.

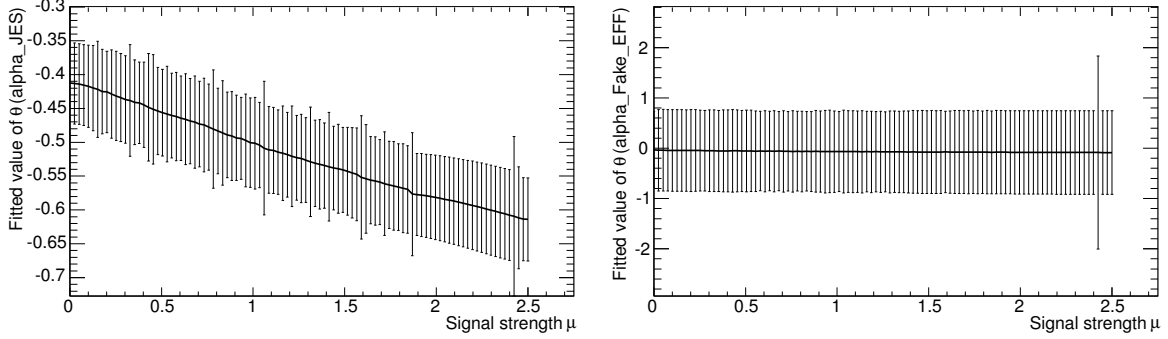


Figure 7.8.: Values and uncertainties of the nuisance parameters that model the jet and τ_{had} energy scale uncertainty (left-hand side) and the uncertainty of the jet-to- τ_{had} misidentification probability (right-hand side) as obtained from the conditional minimisation of the negative log-likelihood for fixed signal strength parameter μ . The functional dependence on μ is a good indicator for competing local minima, in which case $\hat{\alpha}_i$ as a function of μ is discontinuous. A complete set of figures for all nuisance parameters is available in Reference [258].

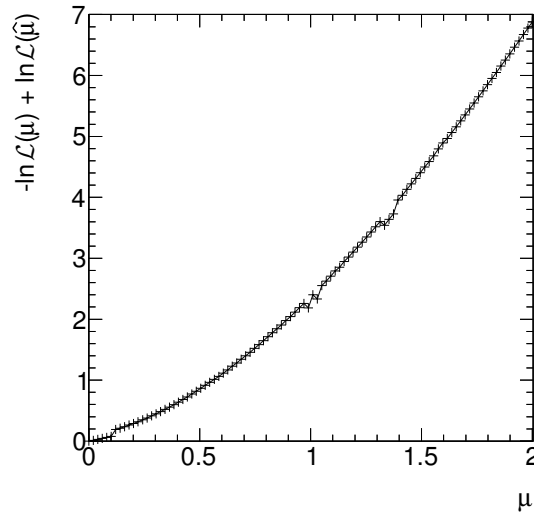


Figure 7.9.: Value of the negative log-likelihood ratio $t_\mu/2 = -\ln \mathcal{L}(\mu) + \ln \mathcal{L}(\hat{\mu})$ obtained from the conditional minimisation for fixed signal strength parameter μ . The shown functional dependence is used as an indicator for minimisation procedures which are too-localised and an unnatural dependence on the start values, which would result in a discontinuous dependence. A small discontinuity can be seen at $\mu \approx 0.1$. However, the differences in t_μ and the fitted nuisance parameter values are small and it was checked that the influence on the final result is negligible.

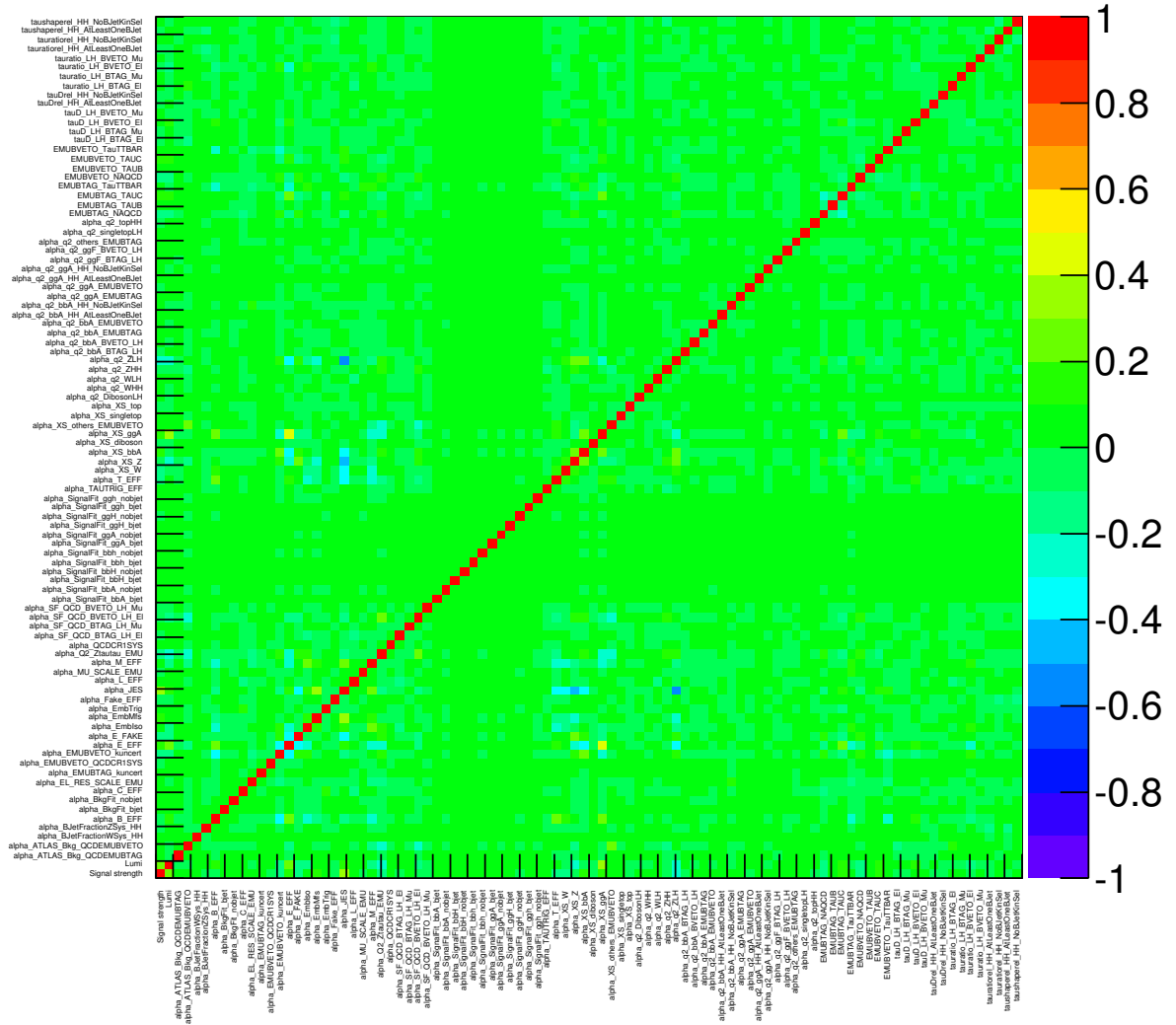


Figure 7.10.: Mutual correlations of the estimators for the signal strength $\hat{\mu}$ and the nuisance parameters $\hat{\alpha}_i$ that correspond to systematic uncertainties. The estimators for the correlations are obtained from the unconditional minimisation.

7.4.3. Comparison to Results Obtained From Pseudo Experiments

In Section 7.5 exclusion limits are shown based on the asymptotic formula. For the validation of these results, 5000 Monte Carlo pseudo experiments⁴ are generated for the parameter point $m_A = 130$ GeV, $\tan \beta = 10$ and each of the signal strengths $\mu = 0.7, 0.8, 0.9, 1.05, 1.1$ and 1.6 . The obtained probability density function for \tilde{q}_μ is shown for $\mu = 1.05$ in Figure 7.11. Based on the probability density functions the observed CL_s values can be calculated with Equations 7.26, 7.28 and 7.31. The observed CL_s values are shown for the considered signal strengths in Table 7.3 together with the 95% confidence level limit on μ . In Figure 7.12 two examples for the distribution of the values of the nuisance parameters obtained in the minimisation of the negative log-likelihood are shown.

⁴The number of pseudo experiments varies between approximately 3600 and 5000 depending on the signal hypothesis.

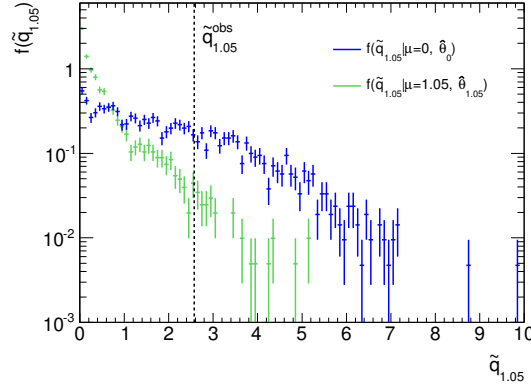


Figure 7.11.: Probability density functions $f(\tilde{q}_\mu | \mu, \hat{\theta}_\mu)$ for $\mu = 1.05$ as obtained with pseudo experiments. The observed test statistic in data, $\tilde{q}_\mu^{\text{obs}}$, is also shown. The CL_s value is 0.034 ± 0.005 .

μ	CL_s
0.70	0.137 ± 0.011
0.80	0.090 ± 0.009
0.90	0.068 ± 0.008
1.05	0.034 ± 0.005
1.10	0.028 ± 0.005
1.60	0.0044 ± 0.0020

Table 7.3.: Observed CL_s values for the point $m_A = 130$ GeV, $\tan \beta = 10$ and variable signal strength parameter are shown as calculated with pseudo experiments. The uncertainty is based on the number of generated pseudo experiments. The 95% confidence level observed limit on the signal strength μ as calculated with piecewise linear interpolation is 0.979 ± 0.020 . The observed 95% confidence limit obtained with the asymptotic approximation is 0.87. The difference between the observed limits obtained from pseudo experiments and the asymptotic approximation corresponds to approximately 50% of the difference between the expected limit and the 1σ value of the expected limit.

7.5. Results of the Calculation of Exclusion Limits

No obvious excess of events above the background-only expectation is observed in the data of the $\tau_{\text{had}}\tau_{\text{had}}$ channels and the other considered channels. Exclusion limits at the 95% confidence level are obtained with the frequentist method described in Section 7.3 and the likelihood function described in Section 7.2. These limits are shown in Sections 7.5.2 and 7.5.3. In Section 7.5.4 discovery significances are documented and in Section 7.5.1 the binned MMC mass distributions are shown with the nominal nuisance parameters and the nuisance parameters obtained from the limit setting procedure.

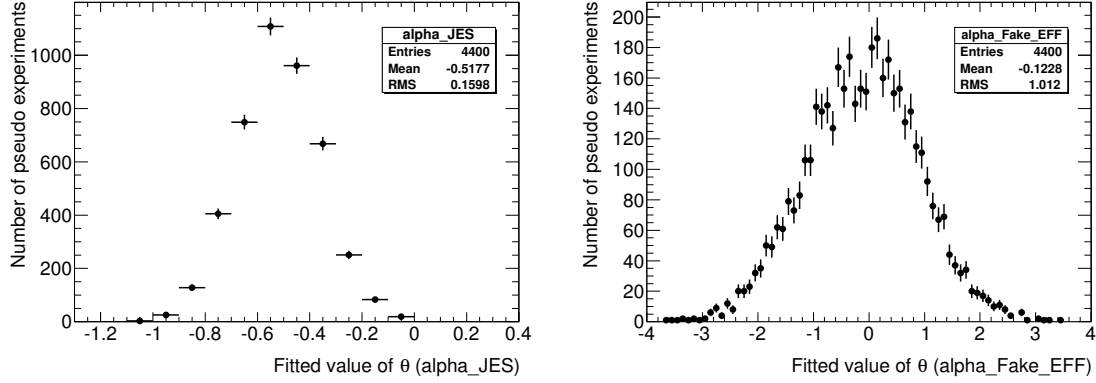


Figure 7.12.: Distribution of the value of the nuisance parameters for the jet and τ_{had} energy scale uncertainty (left-hand side) and the uncertainty of the jet-to- τ_{had} misidentification probability (right-hand side) obtained in the minimisation of the negative log-likelihood for pseudo experiments. The distribution of the values for the jet and τ_{had} energy scale shows that the data are able to constrain the nuisance parameter significantly, while this is not possible in the case of the jet-to- τ_{had} misidentification probability. The corresponding distributions for all other nuisance parameters are available in Reference [258].

7.5.1. Event Yield and MMC Mass Distributions for the $h/A/H \rightarrow \tau_{\text{had}}\tau_{\text{had}}$ Channel After the Minimisation Procedure

The event yields and the $m_{\tau\tau}^{\text{MMC}}$ and $m_{\mu\mu}$ distributions for the different background processes depend on the nuisance parameters according to Equation 7.11. In the test statistic the values of the likelihood function for the conditional and the unconditional minimisation are used. The MMC mass distributions are documented for the $\tau_{\text{had}}\tau_{\text{had}}$ channels with the nominal values of the nuisance parameters and the values from the conditional minimisation of the test statistic for $\mu = 0$ in Figure 7.13. The best estimators for the nuisance parameters that are derived in the conditional minimisation of the negative log-likelihood for $\mu = 0$ are documented in Table C.2. The resulting integrated event yields are shown in Table 7.4. As the control regions for the multi-jet background estimation are directly modelled in the likelihood function, it is not possible to assign uncertainties to the multi-jet production in an unambiguous way. Due to the modelling of statistical uncertainties in the likelihood function only the statistical uncertainty of the combined background mass distribution is available after the minimisation procedure. The statistical uncertainties of the individual background processes, as shown in Figure 7.13 and Table 7.4, are obtained by reducing the relative statistical uncertainty for each background coherently until the combined statistical uncertainty is at the level obtained from the minimisation procedure.

7.5.2. Exclusion Limit on the Parameter Space of the Minimal Supersymmetric Standard Model

For limits on the parameter space of the MSSM, the signal model is constructed based on the m_h^{max} scenario with Higgs mixing parameter $\mu > 0$ [75] according to the description in Section 6.1. With the production cross section for $h/A/H$ and the decay branching ratio for $h/A/H \rightarrow \tau\tau$ the event samples with Higgs boson masses that are closest to m_h , m_A and

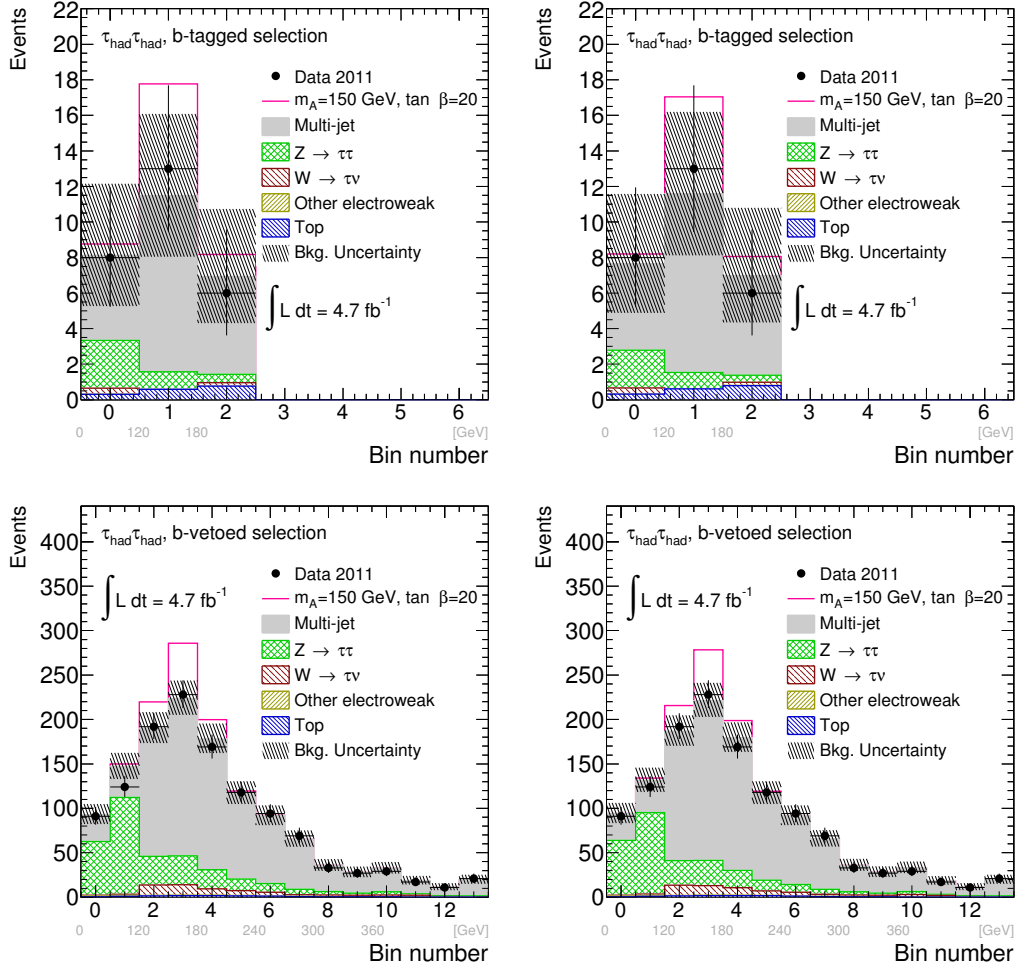


Figure 7.13.: Final mass distributions for the $h/A/H \rightarrow \tau_{\text{had}}\tau_{\text{had}}$ channels before (left-hand side) and after (right-hand side) the minimisation procedure. The final observable for the b -tagged (first row) and b -vetoed sample (second row) is the reconstructed di- τ invariant mass, $m_{\tau\tau}^{\text{MMC}}$, with a binning which is detailed in Appendix C.1. The data are compared with the background expectation and an hypothetical MSSM signal ($m_A = 150$ GeV, $\tan \beta = 20$). The background from diboson and $Z/\gamma^* \rightarrow e^+e^-/\mu^+\mu^-$ processes is combined and labelled “Other electroweak”. For all background processes the nuisance parameters have been set to the nominal values (“before minisation”) or to their best estimators obtained from the conditional minimisation of the negative log-likelihood (“after minimisation”) for all $h/A/H \rightarrow \mu\mu/\tau\tau$ search channels with $\mu = 0$, as documented in Table C.2. For the signal $\mu = 1$ is used.

	b -tagged sample		b -vetoed sample	
	Before minimisation	After minimisation	Before minimisation	After minimisation
Multi-jet	19±5 ±1	21±4 ±4	870±40 ±20	896±23 ±26
$Z/\gamma^* \rightarrow \tau^+\tau^-$	4.0±1.2 $^{+3.3}_{-1.9}$	3.5±0.9 ±0.8	300±10 $^{+80}_{-70}$	268±6 ±21
W + jets	0.5±0.4 $^{+0.2}_{-0.3}$	0.52±0.33 $^{+0.18}_{-0.23}$	52±5 $^{+16}_{-20}$	53±4 $^{+11}_{-15}$
Top	1.7±0.3 ±0.5	1.7±0.2 ±0.4	11.2±0.7±2.0	11.5±1.6±1.4
Diboson	0.013±0.035±0.004	0.013±0.030±0.001	4.9±0.5±0.9	4.7±0.4±0.4
Total	25±5 ±2	26±4 ±4	1230±40 $^{+70}_{-60}$	1230±20 ±40
Signal $m_A = 150$ GeV, $\tan\beta = 20$				
$b\bar{b}(h/A/H \rightarrow \tau\tau)$	7.7±0.6 $^{+3.3}_{-3.2}$	6.7±0.5 $^{+1.4}_{-1.8}$	73±2 $^{+21}_{-20}$	68±2 $^{+10}_{-14}$
$gg \rightarrow h/A/H \rightarrow \tau\tau$	0.50±0.18 $^{+0.18}_{-0.15}$	0.50±0.17 ±0.08	47±2 $^{+13}_{-11}$	43±1 $^{+7}_{-6}$
Data	27	27	1223	1223

Table 7.4.: The observed number of events in data and the expected numbers of signal and background events for the b -tagged and b -vetoed selection of the $h/A/H \rightarrow \tau\tau$ channel before and after the minimisation procedure. The simulated event yields are normalised to the total integrated luminosity of the data, 4.6 fb^{-1} . The data are compared with the background expectation and an hypothetical MSSM signal ($m_A = 150$ GeV and $\tan\beta = 20$). The event yields labelled “before minimisation” are obtained for nominal nuisance parameters and have been shown in Table 6.20. For the event yields labelled “after minimisation” the nuisance parameters have been set to their best estimators obtained from the conditional minimisation of the negative log-likelihood with $\mu = 0$ for all channels. The values of the nuisance parameters are documented in Table C.2. Due to the method for the multi-jet background estimation it is not possible to directly compare the uncertainties of the multi-jet estimate before and after the minimisation procedure. For the signal $\mu = 1$ is used.

m_H are weighted and combined. For a given m_A and various discrete $\tan\beta$ hypotheses the excluded signal strength, $\mu_{95\%}$, is calculated and the value of $\tan\beta$ that is excluded at the 95% confidence level is obtained by interpolating between the values of $\tan\beta$ with excluded signal strengths that are slightly higher or lower than 1. The results for the $\tau_{\text{had}}\tau_{\text{had}}$ final state and the statistical combination of all channels are shown in Figure 7.14.

The tightest constraint for the combination of all channels is at $m_A = 130$ GeV, where values of $\tan\beta > 9.3$ are excluded. The expected exclusion for the same point is $\tan\beta > 10.3$. The exclusion of the parameter space is significantly increased in comparison to earlier results by the ATLAS Collaboration [94, 95] and complementary to the excluded region from searches at LEP [89]. A significant portion of the parameter space of the m_h^{max} benchmark model that is not excluded is still compatible with the assumption that the newly discovered particle at the LHC is one of the neutral CP-even MSSM Higgs bosons [87, 88].

The tightest constraint for the $\tau_{\text{had}}\tau_{\text{had}}$ channels, i.e. the combination of the b -tagged and the b -vetoed $\tau_{\text{had}}\tau_{\text{had}}$ channels, is at $m_A = 170$ GeV, where values of $\tan\beta > 18.4$ are excluded. The expected exclusion for this point is $\tan\beta > 17.9$. For the b -vetoed (b -tagged) $\tau_{\text{had}}\tau_{\text{had}}$ channel the tightest constraint is at $m_A = 170$ GeV ($m_A = 200$ GeV), where values of $\tan\beta > 18.6$ ($\tan\beta > 32.3$) are excluded. The expected exclusion is $\tan\beta > 18.3$ ($\tan\beta > 34.6$).

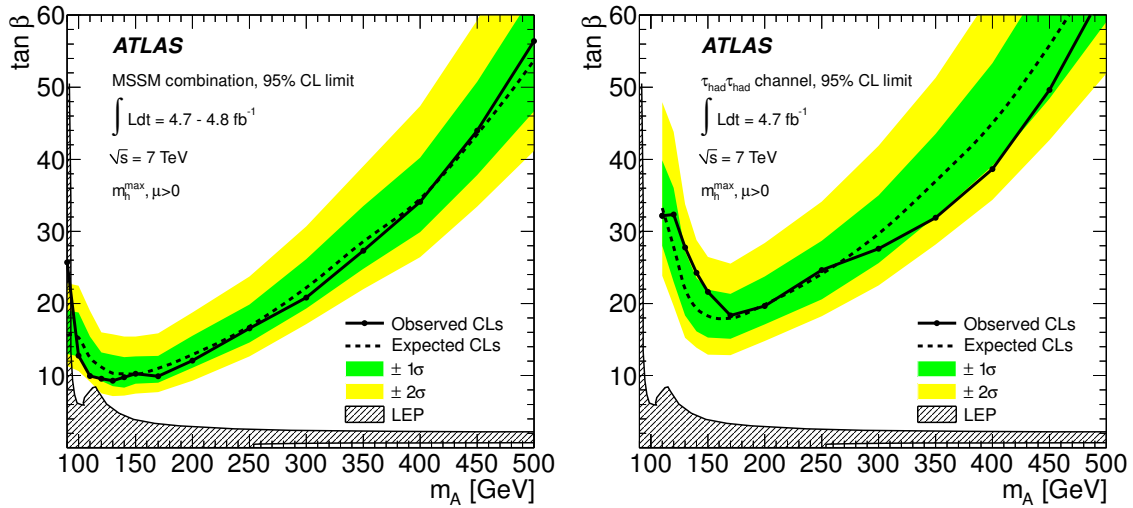


Figure 7.14.: Expected (dashed line) and observed (solid line) 95% confidence level limits on $\tan\beta$ as a function of m_A for the statistical combination of all channels (left-hand side) and the $\tau_{\text{had}}\tau_{\text{had}}$ channels (right-hand side), i.e. the combination of the b -tagged and b -vetoed $\tau_{\text{had}}\tau_{\text{had}}$ channels. The $\pm 1\sigma$ and $\pm 2\sigma$ uncertainty bands for the expected limit are shown as green and yellow bands. Values of $\tan\beta$ greater than the shown lines are excluded. The 95% confidence level exclusion region from neutral MSSM Higgs boson searches performed at LEP [89] is shown as a hatched area.

In Figure 7.15 the exclusion limits of the $\mu\mu$, $\tau_e\tau_\mu$, $\tau_{\text{lep}}\tau_{\text{had}}$ and the $\tau_{\text{had}}\tau_{\text{had}}$ channels and b -tagged and b -vetoed $\tau_{\text{had}}\tau_{\text{had}}$ channels are shown individually. The combined exclusion is dominated by the $\tau_{\text{lep}}\tau_{\text{had}}$ channel for the full range of considered signal hypotheses. For masses around $m_A = 100$ GeV the combination with the $\tau_e\tau_\mu$ channels is able to improve the limit; for masses $m_A > 200$ GeV the combination with the $\tau_{\text{had}}\tau_{\text{had}}$ channels is able

to improve the limit from the $\tau_{\text{lep}}\tau_{\text{had}}$ channels alone. Compared to the background from $Z/\gamma^* \rightarrow \tau^+\tau^-$ production the background from multi-jet production decreases faster as a function of m_A . For this reason the $\tau_{\text{had}}\tau_{\text{had}}$ channels are more important for the combination of the results for signal hypotheses with high values of m_A and especially for high values of m_A the $\tau_{\text{had}}\tau_{\text{had}}$ channels improve the combined limit significantly. The combined exclusion limit for the $\tau_{\text{had}}\tau_{\text{had}}$ channels is dominated by the sensitivity in the b -vetoed channel. The same observation holds for the $\mu\mu$, the $\tau_e\tau_\mu$ and the $\tau_{\text{lep}}\tau_{\text{had}}$ channels.

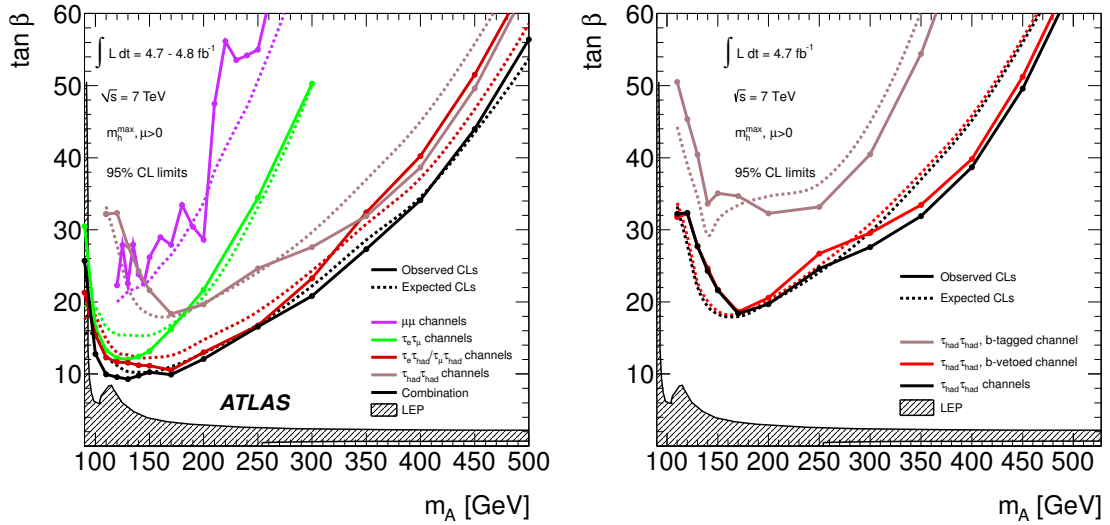


Figure 7.15.: Expected (dashed lines) and observed (solid lines) 95% confidence level limits on $\tan\beta$ as a function of m_A for the statistical combination of all channels and the combination of the $\mu\mu$, $\tau_e\tau_\mu$, $\tau_{\text{lep}}\tau_{\text{had}}$ and $\tau_{\text{had}}\tau_{\text{had}}$ channels individually are shown on the left-hand side. The 95% confidence level limits for the expected limit and the observed limit the b -vetoed and b -tagged $\tau_{\text{had}}\tau_{\text{had}}$ channels and their statistical combination are shown on the right-hand side. The 95% confidence level exclusion region from neutral MSSM Higgs boson searches performed at LEP [89] is shown as a hatched area.

7.5.3. Exclusion Limits on the Cross Section and Branching Ratio

The search results are further interpreted in the more generic case of a single scalar boson ϕ that is produced in either the gluon-fusion or the b -quark annihilation production mode. Exclusion limits for the production cross section times the branching ratio for a Higgs boson decaying to $\mu\mu$ or $\tau\tau$ are obtained as a function of the Higgs boson mass for the combination of all considered channels and for each channel individually. In Figure 7.16 the 95% confidence level limits for the generic Higgs production are shown for the combination of the $\tau_{\text{had}}\tau_{\text{had}}$ channels and all channels. The different sensitivities to the gluon-fusion and the b -quark annihilation production modes are due to the b -tagged channels of which the sensitivities towards the gluon-fusion production mode are negligible.

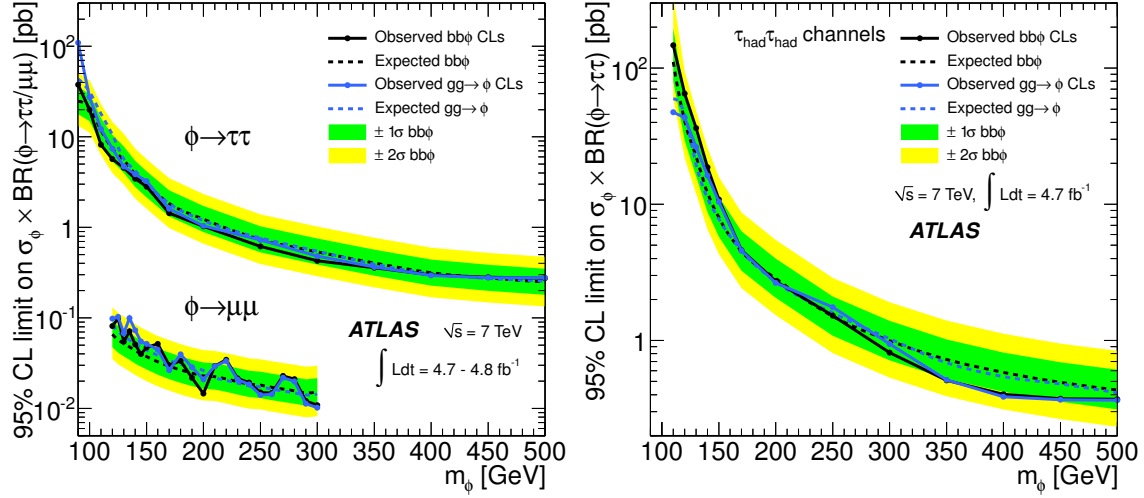


Figure 7.16.: Expected (dashed line) and observed (solid line) 95% confidence level limits on the cross section for Higgs boson production in gluon fusion and b -quark annihilation times the branching ratio into τ and μ pairs, respectively, along with the $\pm 1\sigma$ and $\pm 2\sigma$ uncertainty bands for the expected limit. The combinations of all $\tau\tau$ and $\mu\mu$ channels are shown on the left-hand side. On the right-hand side the combination of the b -tagged and b -vetoed $\tau_{\text{had}}\tau_{\text{had}}$ channels is shown. The difference in the exclusion limits obtained for the gluon-fusion and the b -quark annihilation production modes is due to the low sensitivity from the b -tagged samples towards the gluon-fusion production mode.

7.5.4. Discovery Significances for the Minimal Supersymmetric Standard Model

To obtain discovery significances the local p_0 -values are calculated with the test statistic defined in Equation 7.33. The lowest p_0 -value for the combination of the b -tagged and b -vetoed $\tau_{\text{had}}\tau_{\text{had}}$ channels is 0.097 at $m_A = 140$ GeV. This corresponds to a deviation of 1.3σ . For the other channels the lowest p_0 -values are 0.014 (2.2σ) at $m_A = 125$ GeV for the $\mu\mu$ channel, 0.014 (2.2σ) at $m_A = 90$ GeV for the $\tau_e\tau_\mu$ channel and 0.067 (1.5σ) at $m_A = 90$ GeV for the $\tau_{\text{lep}}\tau_{\text{had}}$ channel. The lowest local p_0 -value for the statistical combination of all channels is 0.004 (2.7σ) at $m_A = 90$ GeV. The significance of this excess is below 2σ , after considering the look-elsewhere effect that is – as discussed in Section 7.3.3 – quantified by the trial factor in the range $90 \text{ GeV} \leq m_A \leq 500 \text{ GeV}$ and $5 \leq \tan\beta \leq 60$ [256, 257]. The observed and expected local p_0 -values and the corresponding significances are shown as a function of the CP-odd Higgs boson mass, m_A , for $\tan\beta = 20$ and the combination of all and the combination of the b -tagged and b -vetoed $\tau_{\text{had}}\tau_{\text{had}}$ channels in Figure 7.17. The observed local p_0 -value is the value obtained in data and the expected local p_0 -value is the value expected under the signal-and-background hypothesis, $H_{\mu S+B}$.

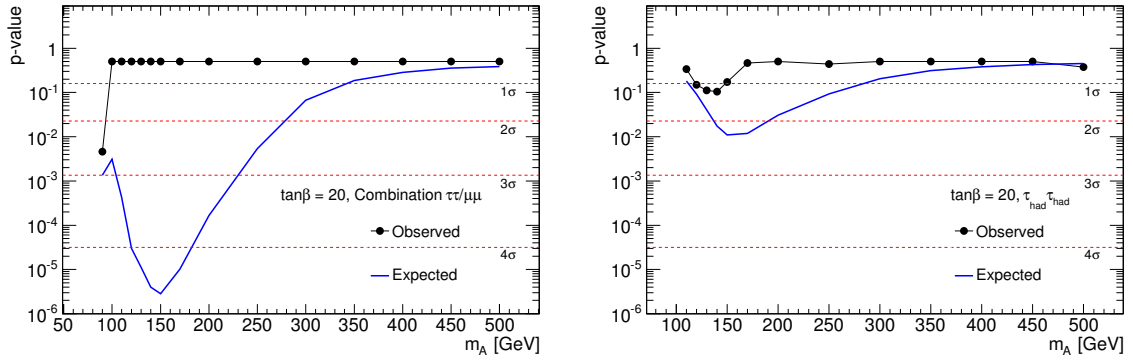


Figure 7.17.: Observed and expected local p_0 -values as a function of m_A for the statistical combination of all search channels (left-hand side) and the combination of the b -tagged and b -vetoed $\tau_{\text{had}}\tau_{\text{had}}$ channels (right-hand side). The expected local- p_0 values refer to the expected value of p_0 under the signal-and-background hypothesis with signal strength $\mu = 1$. Red dashed lines show the local p_0 -values corresponding to significances of $1, 2, 3$ and 4σ . The signal hypothesis is based on the m_h^{max} scenario with $\tan\beta = 20$. The observed local p_0 -values and significances exhibit only a minor dependence on $\tan\beta$ as there is only a small influence of $\tan\beta$ on the shape of the signal mass distribution.

The first LHC proton–proton collisions in November 2009 marked the beginning of a new era of particle physics at the high-energy frontier. The outstanding result of the searches at the LHC is the discovery of a new boson by the ATLAS [2] and CMS [3] collaborations in July 2012. The measurements of the cross sections for the different production mechanisms and the spin of the new boson are consistent with the Standard Model Higgs boson hypothesis. It is, however, still possible that the observed boson stems from an extended Higgs sector, such as the two-doublet Higgs sector of the Minimal Supersymmetric Standard Model. The two Higgs doublets of the MSSM lead to five physical Higgs bosons, the electrically neutral Higgs bosons h , A and H and the electrically charged Higgs bosons H^\pm .

In this thesis a search for the neutral MSSM Higgs bosons h , A and H in the decay channel with two hadronically decaying τ leptons is documented. The search exploits the possibility that the Higgs boson couplings to down-type fermions can be enhanced in two-Higgs-doublet models and focusses on Higgs boson production in gluon fusion and b -quark annihilation. For the two production mechanisms separate event samples are selected by requiring two hadronic τ -lepton decays and one identified b -jet for the b -tagged event sample and two hadronic τ -lepton decays and no identified b -jet for the b -vetoed event sample. The search is based on proton–proton collisions at a centre-of-mass energy $\sqrt{s} = 7$ TeV. The collisions have been recorded with the ATLAS detector at the LHC in 2011 and correspond to an integrated luminosity of $\int \mathcal{L} dt = 4.6 \text{ fb}^{-1}$.

Events with $h/A/H \rightarrow \tau_{\text{had}}\tau_{\text{had}}$ decays are acquired with a di- τ_{had} trigger and hadronic τ -lepton decays are identified using tracking and calorimeter information. The di- τ_{had} mass is reconstructed with the Missing Mass Calculator (MMC) [236]. In the MMC algorithm a scan over all possible neutrino four-momenta is performed. The solutions for the di- τ mass are weighted based on the obtained and the expected τ -lepton decay kinematics and the missing transverse momentum. The MMC mass is the most probable di- τ mass. The full event selection has an efficiency of $6 \cdot 10^{-4}$ and $6 \cdot 10^{-3}$ for events with Higgs boson production in b -quark annihilation with $m_A = 150$ GeV for the b -tagged and b -vetoed selections, respectively. For events with Z -boson production the selection efficiency is $6 \cdot 10^{-8}$ and $4 \cdot 10^{-6}$.

The dominant background processes are multi-jet production in strong interaction and $Z/\gamma^* \rightarrow \tau^+\tau^-$ production. A smaller contribution to the background is expected from the $W \rightarrow \tau\nu$ +jets, $t\bar{t}$ and single-top production processes. The background events contain hadronic τ -lepton decays or jets that are initiated by the hadronisation of quarks or gluons and misidentified as hadronic τ -lepton decays. The background from multi-jet production is estimated from data with a multi-sideband method, the ABCD method. All other background yields are estimated using simulated event samples. Correction factors for the jet-to- τ_{had} misidentification probability have been measured in data and applied to simulation. The estimate of the backgrounds with Z - and W -boson production is cross-checked with event samples of τ -embedded $Z/\gamma^* \rightarrow \mu^+\mu^-$ and $W \rightarrow \mu\nu$ data.

In collision data 27 events are observed in the b -tagged channel, where 25 ± 5 (stat.) ± 2 (syst.) background events are expected and 8.2 ± 0.6 (stat.) ± 3.5 (syst.) additional events are predicted for the m_h^{max} signal hypothesis with $m_A = 150$ GeV and $\tan \beta = 20$. For the b -vetoed channel 1223 events are found in collision data. For background processes 1230 ± 40 (stat.) ± 70 (syst.)

events are expected and for the m_h^{\max} signal hypothesis 120 ± 2 (stat.) ± 32 (syst.) events are predicted. The distributions of the di- τ mass for the b -tagged and b -vetoed channels exhibit no obvious excess of data events compared with the background expectation.

The statistical interpretation of the search is based on two classes of signal hypotheses: MSSM Higgs boson production based on the m_h^{\max} scenario and the more model-independent case of a single scalar boson, ϕ , produced in either the gluon-fusion or b -quark annihilation production mode. The results of the search for $h/A/H \rightarrow \tau_{\text{had}}\tau_{\text{had}}$ decays are combined with the results of the searches for $h/A/H \rightarrow \mu\mu$, $h/A/H \rightarrow \tau_e\tau_\mu$ and $h/A/H \rightarrow \tau_{\text{lep}}\tau_{\text{had}}$ decays. Based on the MMC mass distributions 95% confidence level exclusion limits are derived with the frequentist CL_s procedure [251] using a likelihood ratio test statistic. In the m_h^{\max} scenario the tightest constraint for the $\tau_{\text{had}}\tau_{\text{had}}$ channel is at $m_A = 170$ GeV, where values of $\tan\beta > 18.8$ are excluded, the expected exclusion for the same value of m_A is $\tan\beta > 18.1$. The tightest constraint for all $h/A/H \rightarrow \mu\mu$ and $\tau\tau$ channels is at $m_A = 130$ GeV, where values of $\tan\beta > 9.3$ are excluded, the expected exclusion is $\tan\beta > 10.3$.

Especially for high Higgs boson masses the background from multi-jet production in the $\tau_{\text{had}}\tau_{\text{had}}$ channels is low and the sensitivity is comparable to the one obtained from the combination of the $\tau_e\tau_{\text{had}}$ and the $\tau_\mu\tau_{\text{had}}$ channels. The region in the m_A - $\tan\beta$ plane of the m_h^{\max} scenario that is excluded by the combination of all search channels is significantly increased with respect to previous searches in the $\tau\tau$ decay channels [95, 94]. It is comparable to the region excluded by the CMS collaboration for the same amount of data [99]. Newer results by the CMS collaboration with an increased dataset exclude a larger region [100].

The search presented in this thesis is published together with the other searches for $h/A/H \rightarrow \mu\mu$ and $h/A/H \rightarrow \tau\tau$ decays in Reference [96]. The analysis presented in this thesis is the first search for Higgs bosons or other new resonances in the $\tau_{\text{had}}\tau_{\text{had}}$ channel at the LHC¹. Subsequently searches for Standard Model Higgs bosons [259] and generic heavy resonances [260] have been conducted in the $\tau_{\text{had}}\tau_{\text{had}}$ channel. These searches have been influenced by the search for MSSM Higgs bosons in the $\tau_{\text{had}}\tau_{\text{had}}$ channel, but have since developed methods that are tailored to the searches for the Standard Model Higgs boson or generic heavy resonances.

After the discovery of a boson with a mass near 125 GeV, the focus of attention is on the question about the nature of this boson. The search for MSSM Higgs bosons provides important insight into whether the discovered boson can be a Higgs boson that is described by a two-Higgs-doublet model. Even though a large region of the parameter space of the m_h^{\max} scenario is excluded, a significant part of the parameter space is still compatible with the results of the performed searches for Higgs bosons from extended Higgs sectors. For the future the used benchmark scenario will be modified to include the newly discovered boson. Additional information could be obtained from two-Higgs-doublet benchmark models with a parameterised mixing angle of the h and H bosons, α . The recorded dataset of proton-proton collision at $\sqrt{s} = 8$ TeV and a significantly increased integrated luminosity of approximately 20 fb^{-1} together with the increased centre-of-mass energy of $\sqrt{s} = 13$ TeV after the shutdown of the LHC will provide the possibility to further probe the parameter space of two-Higgs-doublet models and determine the nature of the electroweak symmetry breaking.

¹Preliminary results of the search for the MSSM Higgs bosons $h/A/H$ in the $\tau_{\text{had}}\tau_{\text{had}}$ decay channel were first published in Reference [95]. This result was obtained as part of the work for this thesis. The search documented in this thesis and published in Reference [96] uses refined methods for the event selection and the background estimation compared with the result in Reference [95].

A Auxiliary Information for the Theory Overview

In this appendix auxiliary information for the theory overview is documented.

A.1. The Dirac and Gell-Mann Matrices

The Dirac matrices γ^μ used in Chapter 2 are defined in the Dirac basis as

$$\gamma^0 = \begin{pmatrix} \mathbb{1} & 0 \\ 0 & -\mathbb{1} \end{pmatrix}, \quad \gamma^i = \begin{pmatrix} 0 & \sigma^i \\ -\sigma^i & 0 \end{pmatrix}, \quad i \in \{1, 2, 3\}, \quad (\text{A.1})$$

where $\mathbb{1}$ is the 2×2 identity matrix and σ^i are the Pauli matrices as defined by

$$\sigma^1 = \begin{pmatrix} 0 & 1 \\ 1 & 0 \end{pmatrix}, \quad \sigma^2 = \begin{pmatrix} 0 & -i \\ i & 0 \end{pmatrix}, \quad \sigma^3 = \begin{pmatrix} 1 & 0 \\ 0 & -1 \end{pmatrix}. \quad (\text{A.2})$$

In the Weyl basis the Dirac matrices are

$$\gamma^0 = \begin{pmatrix} 0 & \mathbb{1} \\ \mathbb{1} & 0 \end{pmatrix}, \quad \gamma^i = \begin{pmatrix} 0 & \sigma^i \\ -\sigma^i & 0 \end{pmatrix}, \quad i \in \{1, 2, 3\}, \quad (\text{A.3})$$

so that the first two components of a spinor Ψ correspond to the two-component field with left-handed chirality and the second two components to the field with right-handed chirality.

The Gell-Mann matrices are a representation of the generators of the $\text{SU}(3)$ algebra. They are defined as

$$\begin{aligned} \lambda_1 &= \begin{pmatrix} 0 & 1 & 0 \\ 1 & 0 & 0 \\ 0 & 0 & 0 \end{pmatrix}, & \lambda_2 &= \begin{pmatrix} 0 & -i & 0 \\ i & 0 & 0 \\ 0 & 0 & 0 \end{pmatrix}, & \lambda_3 &= \begin{pmatrix} 1 & 0 & 0 \\ 0 & -1 & 0 \\ 0 & 0 & 0 \end{pmatrix}, & \lambda_4 &= \begin{pmatrix} 0 & 0 & 1 \\ 0 & 0 & 0 \\ 1 & 0 & 0 \end{pmatrix}, \\ \lambda_5 &= \begin{pmatrix} 0 & 0 & -i \\ 0 & 0 & 0 \\ i & 0 & 0 \end{pmatrix}, & \lambda_6 &= \begin{pmatrix} 0 & 0 & 0 \\ 0 & 0 & 1 \\ 0 & 1 & 0 \end{pmatrix}, & \lambda_7 &= \begin{pmatrix} 0 & 0 & 0 \\ 0 & 0 & -i \\ 0 & i & 0 \end{pmatrix}, & \lambda_8 &= \frac{1}{\sqrt{3}} \begin{pmatrix} 1 & 0 & 0 \\ 0 & 1 & 0 \\ 0 & 0 & -2 \end{pmatrix}. \end{aligned} \quad (\text{A.4})$$

For the Gell-Mann matrices

$$[\lambda_a, \lambda_b] = if_{abc}\lambda_c \quad (\text{A.5})$$

holds, where the structure constants f_{abc} are completely antisymmetric and the components are

$$f_{123} = 1, \quad f_{147} = f_{246} = f_{257} = f_{345} = \frac{1}{2}, \quad f_{156} = f_{367} = -\frac{1}{2}, \quad f_{458} = f_{678} = \frac{\sqrt{3}}{2}. \quad (\text{A.6})$$

A.2. The QCD Lagrange Density Function

In Section 2.1.4 the theory of quantum chromodynamics is introduced and the corresponding Lagrange density function is documented. In this section the Lagrange density function is documented in the form of kinetic, mass and interaction terms. The Lagrange density function is

$$\begin{aligned}
\mathcal{L}_{\text{QCD}} &= \sum_f \bar{q}_{f,\alpha} (i\not{D} - m_f) q_f^\alpha - \frac{1}{4} G_a^{\mu\nu} G_{a\mu\nu} \\
&= \underbrace{\sum_f \bar{q}_{f,\alpha} (i\not{D} - m_f) q_f^\alpha - \frac{1}{4} (\partial^\mu G_a^\nu - \partial^\nu G_a^\mu) (\partial_\mu G_{a\nu} - \partial_\nu G_{a\mu})}_{\text{kinetic and mass term}} \\
&\quad - \underbrace{\frac{gS}{2} \sum_f \bar{q}_f^\alpha \not{A}_a (\lambda_a)_{\alpha\beta} q_f^\beta}_{\text{quark-gluon interaction}} \\
&\quad + \underbrace{\frac{gS}{2} f_{abc} (\partial^\mu G_a^\nu - \partial^\nu G_a^\mu) G_{b\mu} G_{c\nu}}_{\text{3-gluon interaction}} \\
&\quad + \underbrace{\frac{g_S^2}{4} f_{abc} f_{ade} G_b^\mu G_c^\nu G_{d\mu} G_{e\nu}}_{\text{4-gluon interaction}}, \tag{A.7}
\end{aligned}$$

where all symbols are defined as in Section 2.1.4. As QCD is a non-abelian gauge theory, a 3- and 4-gluon interaction term exists in addition to the quark-gluon interaction term.

A.3. Lagrange Density Function of the Glashow-Weinberg-Salam Model

The Glashow-Weinberg-Salam model is described in Section 2.1.5 and the spontaneous breaking of the electroweak symmetry is described in Section 2.1.6. In this section, the Lagrange density function is shown in terms of the fields $W^{i\mu}$ and B^μ :

$$\begin{aligned}
\mathcal{L}_{\text{EW}} &= i\bar{E}_L \not{D} E_L + i\bar{\nu}_R \not{D} \nu_R + i\bar{e}_R \not{D} e_R - \frac{1}{4} W_{\mu\nu}^i W^{i\mu\nu} - \frac{1}{4} B_{\mu\nu} B^{\mu\nu} \\
&= i\bar{E}_L \not{\partial} E_L + i\bar{\nu}_R \not{\partial} \nu_R + i\bar{e}_R \not{\partial} e_R \\
&\quad - \frac{1}{4} (\partial_\mu W_\nu^i - \partial_\nu W_\mu^i) (\partial^\mu W^{\nu i} - \partial^\nu W^{\mu i}) - \frac{1}{4} (\partial_\mu B_\nu - \partial_\nu B_\mu) (\partial^\mu B^\nu - \partial^\nu B^\mu) \\
&\quad - g'y_1 \bar{E}_L \not{B} E_L - g'y_2 \bar{\nu}_R \not{B} \nu_R - g'y_3 \bar{e}_R \not{B} e_R - g\bar{E}_L \not{W} E_L \\
&\quad + \frac{g}{4} \epsilon^{ijk} (\partial_\mu W_\nu^i - \partial_\nu W_\mu^i) W^{j\mu} W^{k\nu} + \frac{g}{4} \epsilon^{ijk} W^{j\mu} W^{k\nu} (\partial_\mu W_\nu^i - \partial_\nu W_\mu^i) \\
&\quad - \frac{g^2}{4} \epsilon^{ijk} \epsilon^{ilm} W^{j\mu} W^{k\nu} W_\mu^l W_\nu^m, \tag{A.9}
\end{aligned}$$

(A.10)

The Lagrange density function in terms of the fields corresponding to the mass eigenstates of the gauge bosons, $W^{\pm\mu}$, Z^μ and A^μ is:

$$\begin{aligned}
\mathcal{L}_{\text{EW}} = & i\bar{E}_L \not{\partial} E_L + i\bar{\nu}_R \not{\partial} \nu_R + i\bar{e}_R \not{\partial} e_R - \frac{1}{4} W_{\mu\nu}^i W^{i\mu\nu} - \frac{1}{4} B_{\mu\nu} B^{\mu\nu} \\
& - \bar{E}_L \left\{ \left[g' y_1 \cos \theta_W + g \frac{\sigma_3}{2} \sin \theta_W \right] \not{A} + \left[-g' y_1 \sin \theta_W + g \frac{\sigma_3}{2} \cos \theta_W \right] \not{Z} \right\} E_L \\
& - \bar{\nu}_R \left[y_2 g' \cos \theta_W \not{A} - y_2 g' \sin \theta_W \not{Z} \right] \nu_R - \bar{e}_R \left[y_3 g' \cos \theta_W \not{A} - y_3 g' \sin \theta_W \not{Z} \right] e_R \\
& - \frac{g}{\sqrt{2}} \bar{\nu}_{e,L} \not{W}^+ e_L - \frac{g}{\sqrt{2}} \bar{e}_L \not{W}^- \nu_{e,L} \\
& - ig \cos \theta_W \left\{ (\partial^\mu W^{-\nu} - \partial^\nu W^{-\mu}) W_\mu^+ Z_\nu - (\partial^\mu W^{+\nu} - \partial^\nu W^{+\mu}) W_\mu^- Z_\nu \right. \\
& \left. + W_\mu^- W_\nu^+ (\partial^\mu Z^\nu - \partial^\nu Z^\mu) \right\} \\
& - ig \sin \theta_W \left\{ (\partial^\mu W^{-\nu} - \partial^\nu W^{-\mu}) W_\mu^+ A_\nu - (\partial^\mu W^{+\nu} - \partial^\nu W^{+\mu}) W_\mu^- A_\nu \right. \\
& \left. + W_\mu^- W_\nu^+ (\partial^\mu A^\nu - \partial^\nu A^\mu) \right\} \\
& - \frac{g^2}{2} \left\{ (W_\mu^+ W^{-\mu})^2 - W_\mu^+ W^{+\mu} W_\nu^- W^{-\nu} \right\} \\
& - g^2 \cos^2 \theta_W \left\{ W_\mu^+ W^{-\mu} Z_\nu Z^\nu - W_\mu^+ Z^\mu W_\nu^- Z^\nu \right\} \\
& - g^2 \sin^2 \theta_W \left\{ W_\mu^+ W^{-\mu} A_\nu A^\nu - W_\mu^+ A^\mu W_\nu^- A^\nu \right\} \\
& - g^2 \sin \theta_W \cos \theta_W \left\{ 2W_\mu^+ W^{-\mu} Z_\nu A^\nu - W_\mu^+ Z^\mu W_\nu^- A^\nu - W_\mu^+ A^\mu W_\nu^- Z^\nu \right\} . \quad (\text{A.11})
\end{aligned}$$

The notation from Section 2.1.5 is used.

B Auxiliary Figures for the Background Estimation

The methods for the estimation of the event yield and the distribution of the $\text{di-}\tau_{\text{had}}$ mass for background processes are described in Section 6.5. In this appended section additional material for the validation of the background estimation methods is shown. In Section B.1 additional information for the multi-jet background estimate is provided and in Section B.2 additional figures for the measurement of the jet-to- τ_{had} misidentification probabilities are available. Comparison of the background estimate based on the τ -embedded data samples and the ALPGEN simulated event samples are shown in Sections B.3 and B.4. In Section B.5 additional distributions for the validation of the combined background estimate with data are shown.

B.1. Estimation of the Multi-jet Background

The background from multi-jet production in QCD interactions is estimated from data with a multi-sideband method, the ABCD method. This method is described in detail in Section 6.5.1. For the estimation of the background from multi-jet production it is necessary to assume that the two variables that are used to define the control regions, the charge product of the τ_{had} candidates and the τ_{had} identification level, are independent. In addition, it is necessary to assume that the probability density functions for the MMC mass for multi-jet events in regions B and D, the regions with same-charge τ_{had} decays, for the b -vetoed selection and in regions C and D, the “fail ID” regions, for the b -tagged selection are identical. Comparisons of the probability density function are shown in Section 6.5.1. In Figures B.1 and B.2 the probability density functions for multi-jet background are shown as a function of other variables for events with opposite-charge τ_{had} decays and same-charge τ_{had} -decays for the b -tagged and b -vetoed selections. The same probability density functions are shown in Figure B.3 for the “fail ID” and “pass ID” regions of the b -vetoed selection. For the b -tagged channel it is known that the probability density functions of kinematic variables are not identical in the “fail ID” and “pass ID” regions and consequently the MMC mass shape is taken from the region with same-charge τ_{had} decays.

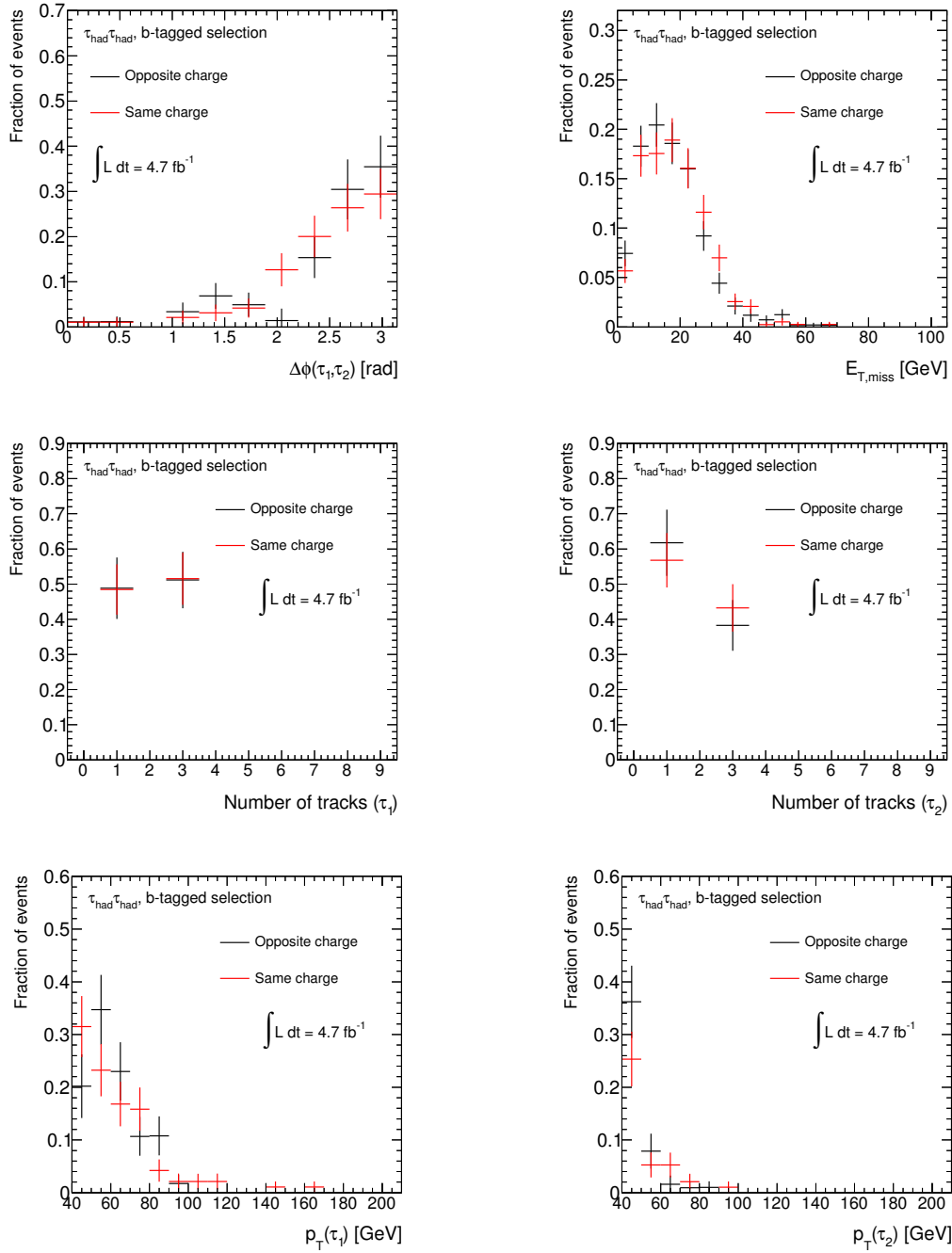


Figure B.1.: Tests for the applicability of the ABCD method as described in Section 6.5.1 are shown. In the first row the azimuthal angle between the τ_{had} decays, $\Delta\phi$, is shown on the left-hand side and the missing transverse momentum on the right-hand side for events with opposite-charge and same-charge τ_{had} decays that pass the b -tagged selection. The background from events other than multi-jet production and signal was subtracted. The same distributions are shown for the number of tracks (second row) and the transverse momenta (third row) of the highest- p_T (left-hand side) and the second highest- p_T (right-hand side) hadronic τ -lepton decay.

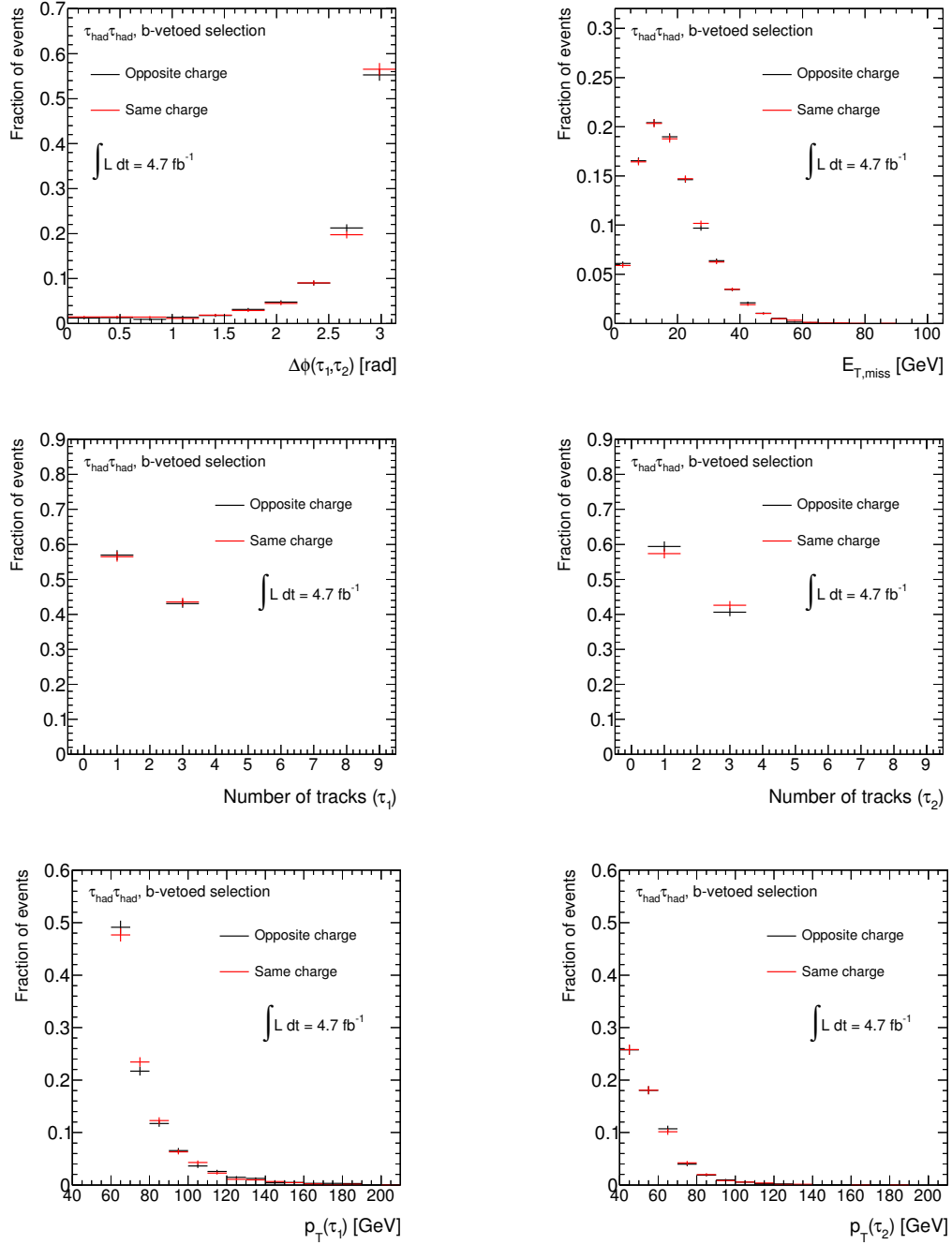


Figure B.2.: Tests for the applicability of the ABCD method as described in Section 6.5.1 are shown. In the in the first row the azimuthal angle between the τ_{had} decays, $\Delta\phi$, is shown on the left-hand side and the missing transverse momentum on the right-hand side for events with opposite-charge and same-charge τ_{had} decays that pass the b -vetoed selection. The background from events other than multi-jet production and signal was subtracted. The same distributions are shown for the number of tracks (second row) and the transverse momenta (third row) of the highest- p_T (left-hand side) and the second highest- p_T (right-hand side) hadronic τ -lepton decay.

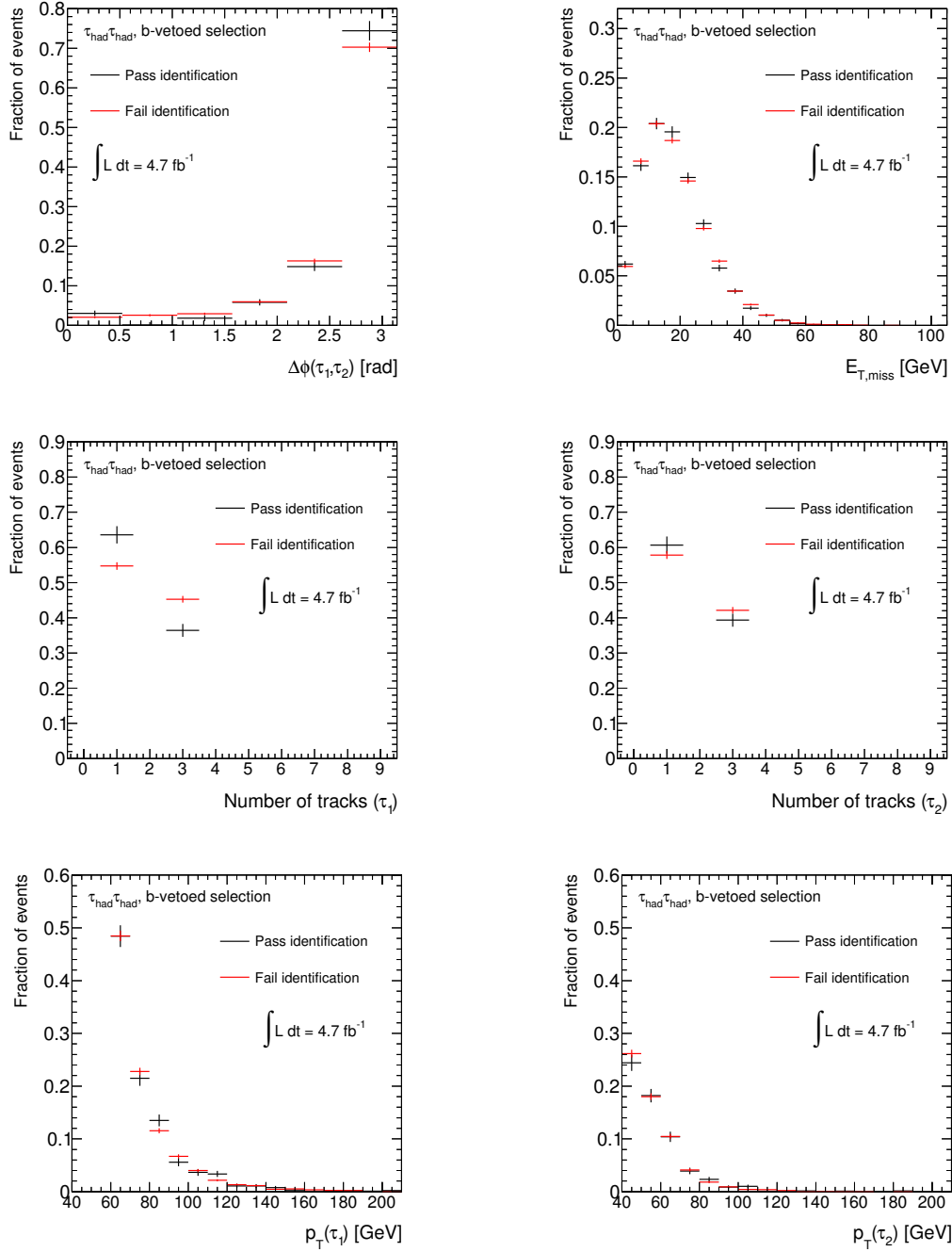


Figure B.3.: Tests for the applicability of the ABCD method as described in Section 6.5.1 are shown. In the in the first row the azimuthal angle between the τ_{had} decays, $\Delta\phi$, is shown on the left-hand side and the missing transverse momentum on the right-hand side for events which pass or fail the τ_{had} identification requirements of the b -vetoed selection. The background from events other than multi-jet production and signal was subtracted. The same distributions are shown for the number of tracks (second row) and the transverse momenta (third row) of the highest- p_T (left-hand side) and the second highest- p_T (right-hand side) hadronic τ -lepton decay.

B.2. Estimation of the Background From Events With Misidentified Jets

The measurement of jet-to- τ_{had} misidentification probability as a function of the transverse momentum of the τ_{had} candidate is described in Section 6.5.3. In Figures B.4 the jet-to- τ_{had} misidentification probabilities are shown for the measurement without trigger requirement and the loose and tight τ_{had} identification levels. The measurements for the single- τ_{had} triggers with p_T thresholds of 20 GeV and 29 GeV are shown for the loose, medium and tight identification requirements in Figures B.5, B.6 and B.7.

From the measurements of the jet-to- τ_{had} misidentification probabilities in collision data and simulated event samples correction factors for the simulated event samples are derived and shown as a function of the τ_{had} transverse momentum for the loose, medium and tight τ_{had} identification requirements and the single- τ_{had} triggers that were used in the data-taking before September 2011 in Figure B.8.

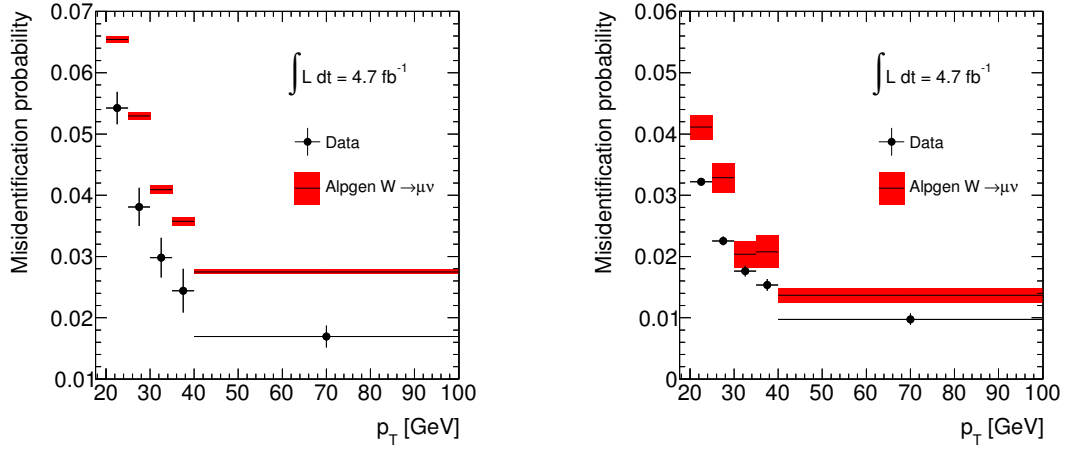


Figure B.4.: Jet-to- τ_{had} misidentification probabilities for the off-line selection as measured in data and simulation with the tag-and-probe method in the $W \rightarrow \mu\nu$ event sample. The jet-to- τ_{had} misidentification probabilities are shown for the loose (left-hand side) and the tight (right-hand side) τ_{had} identification levels, no trigger decision is required. The uncertainties include statistical uncertainties and systematic uncertainties from the subtraction of the backgrounds.

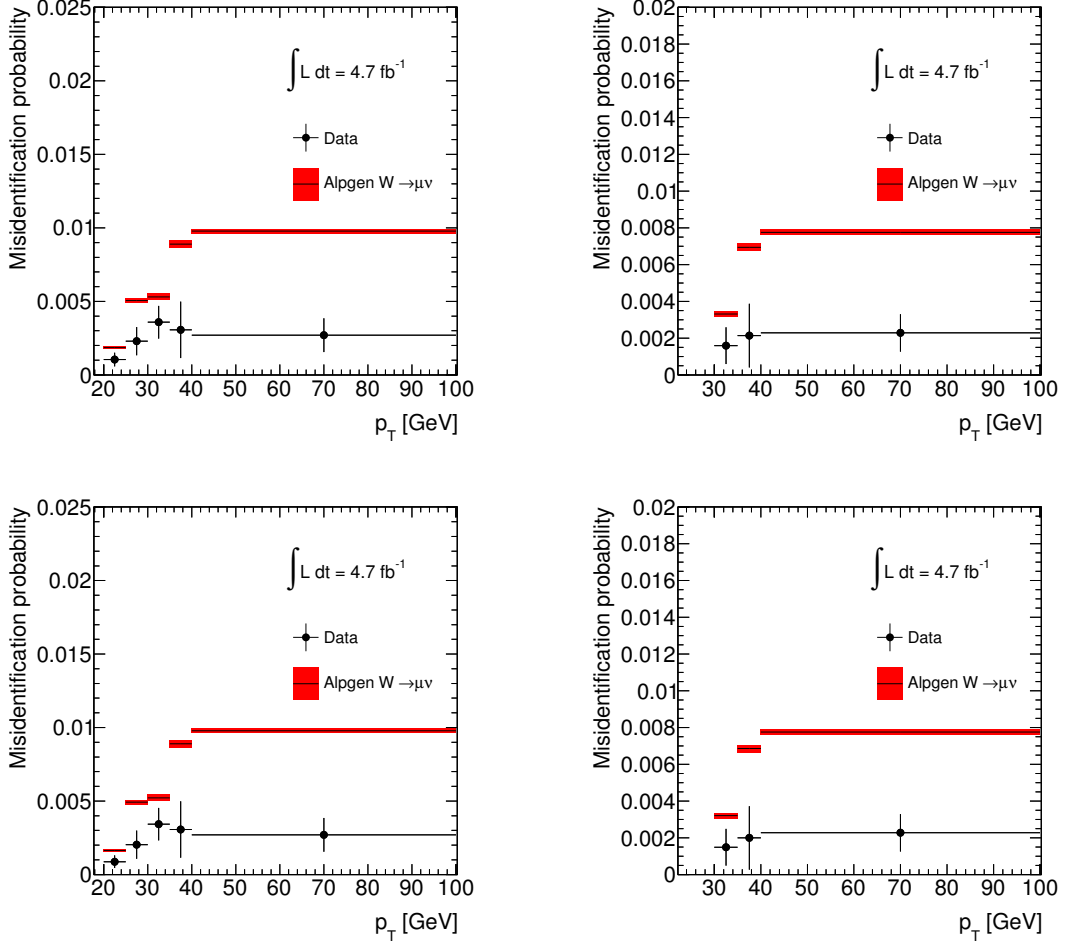


Figure B.5.: Jet-to- τ_{had} misidentification probabilities for the off-line and trigger selection as measured in data and simulation with the tag-and-probe method in the $W \rightarrow \mu\nu$ event sample. The jet-to- τ_{had} misidentification probabilities are shown for the loose τ_{had} identification level with the trigger `EF_tau20_medium1` (left-hand side, first row), the trigger `EF_tau29_medium1` (right-hand side, first row), the trigger `EF_tau20T_medium1` (left-hand side, second row) and the trigger `EF_tau29T_medium1` (right-hand side, second row). The uncertainties include statistical uncertainties and systematic uncertainties from the subtraction of the backgrounds.

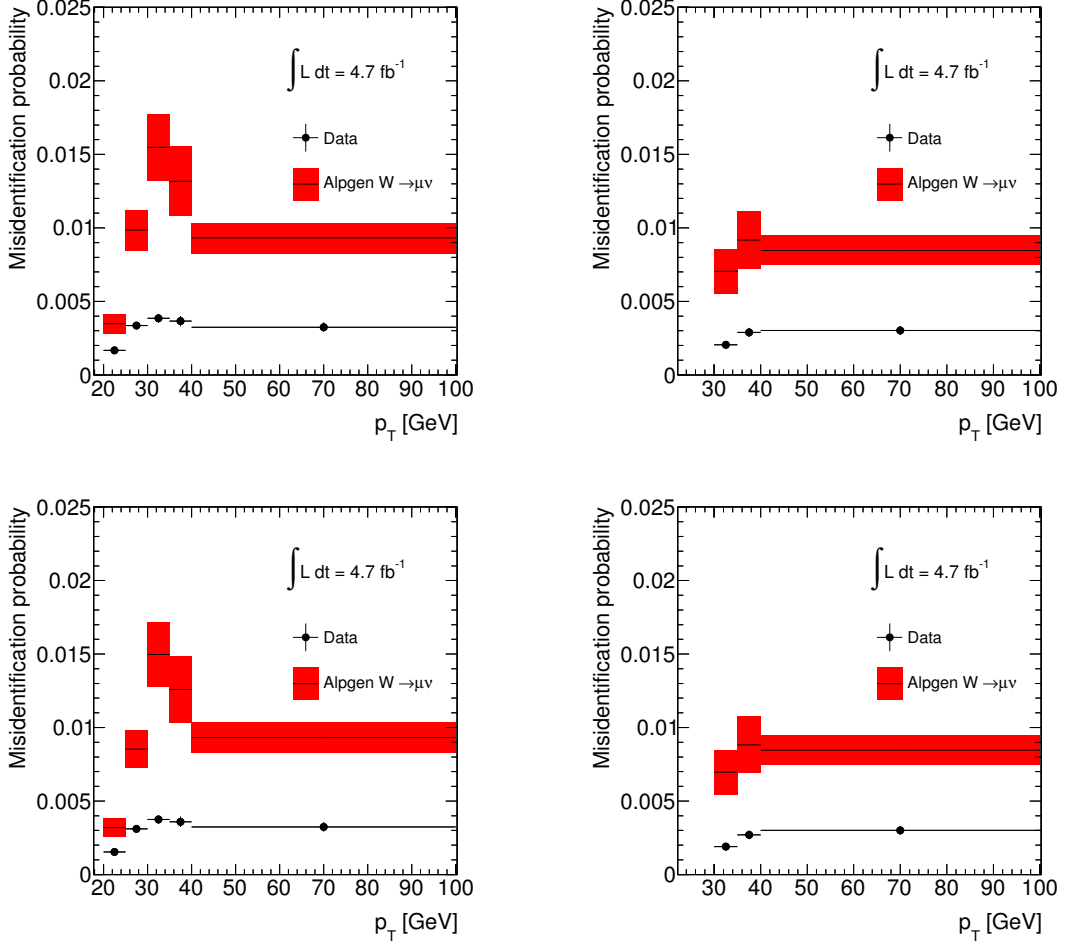


Figure B.6.: Jet-to- τ_{had} misidentification probabilities for the off-line and trigger selection as measured in data and simulation with the tag-and-probe method in the $W \rightarrow \mu\nu$ event sample. The jet-to- τ_{had} misidentification probabilities are shown for the medium τ_{had} identification level with the trigger EF_tau20_medium1 (left-hand side, first row), the trigger EF_tau29_medium1 (right-hand side, first row), the trigger EF_tau20T_medium1 (left-hand side, second row) and the trigger EF_tau29T_medium1 (right-hand side, second row). The uncertainties include statistical uncertainties and systematic uncertainties from the subtraction of the backgrounds.

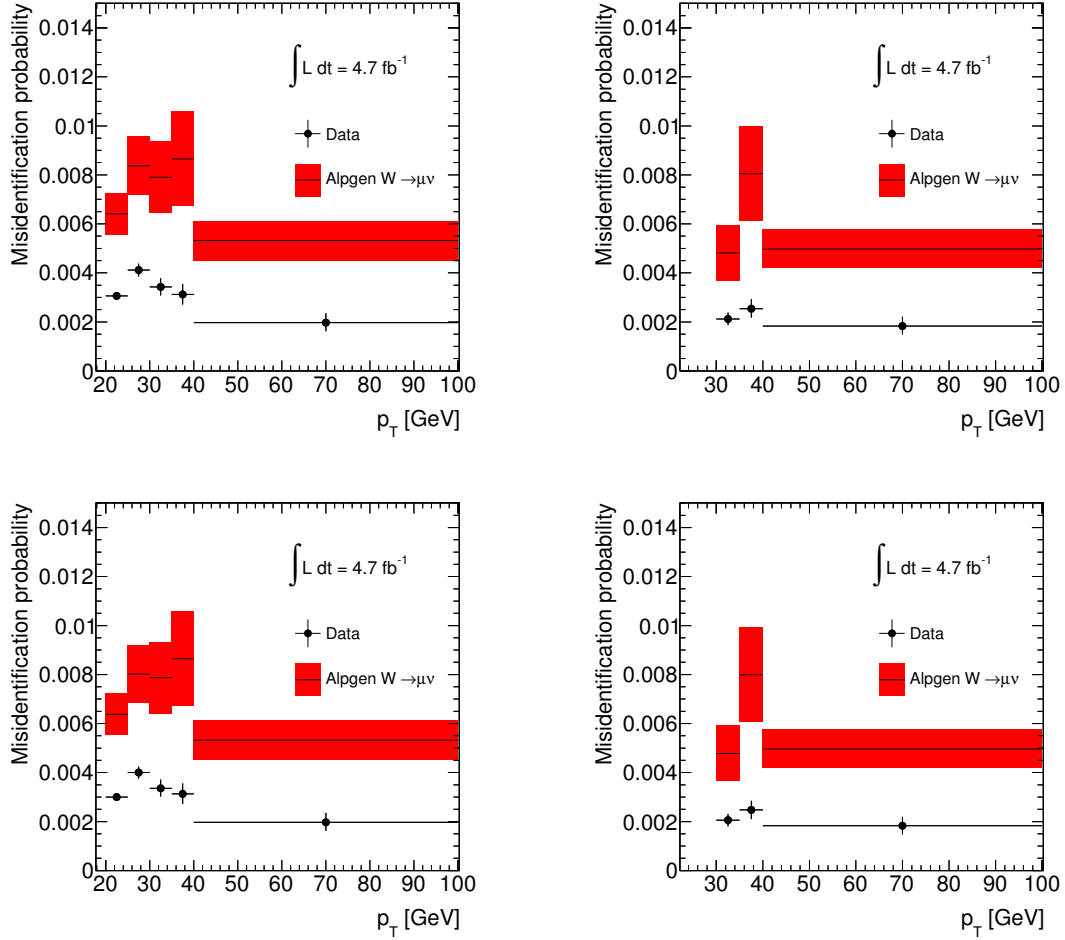


Figure B.7.: Jet-to- τ_{had} misidentification probabilities for the off-line and trigger selection as measured in data and simulation with the tag-and-probe method in the $W \rightarrow \mu\nu$ event sample. The jet-to- τ_{had} misidentification probabilities are shown for the tight τ_{had} identification level with the trigger `EF_tau20_medium1` (left-hand side, first row), the trigger `EF_tau29_medium1` (right-hand side, first row), the trigger `EF_tau20T_medium1` (left-hand side, second row) and the trigger `EF_tau29T_medium1` (right-hand side, second row). The uncertainties include statistical uncertainties and systematic uncertainties from the subtraction of the backgrounds.

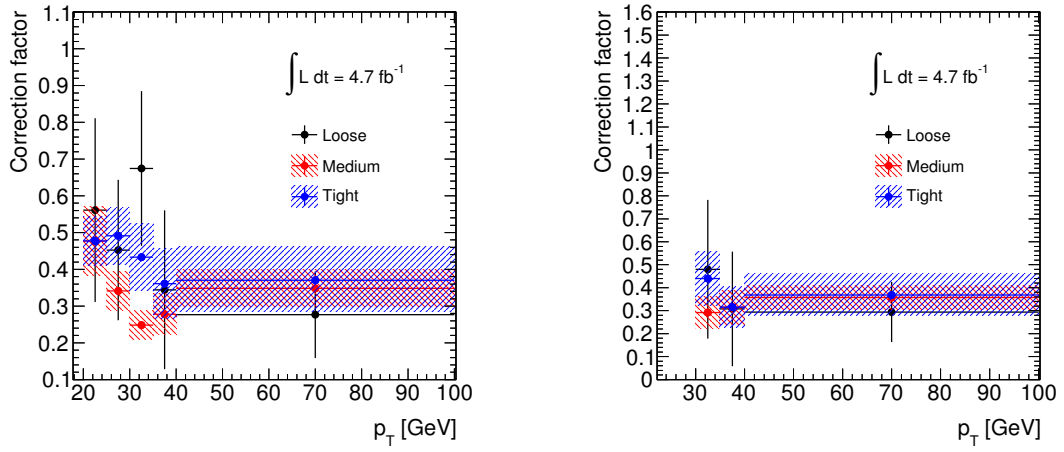


Figure B.8.: Ratio of the jet-to- τ_{had} misidentification probabilities for the off-line and trigger selection as measured in data and simulation with the tag-and-probe method in the $W \rightarrow \mu\nu$ event sample. On the left-hand side the ratios of the jet-to- τ_{had} misidentification probabilities are shown for the trigger `EF_tau20_medium1` and the τ_{had} identification levels loose, medium and tight. On the right-hand side the ratios of the jet-to- τ_{had} misidentification probabilities are shown for the trigger `EF_tau29_medium1` and the same τ_{had} identification levels. The shown ratios are applied as correction factors to simulation events with jets that are misidentified as a τ_{had} decay. The uncertainties include statistical uncertainties and systematic uncertainties from the subtraction of the backgrounds.

B.3. Comparison of τ -embedded $Z/\gamma^* \rightarrow \mu^+\mu^-$ Data and Simulated $Z/\gamma^* \rightarrow \tau^+\tau^-$ Events

The construction of the samples of τ -embedded $Z/\gamma^* \rightarrow \mu^+\mu^-$ events is described in Section 6.5.4. The event samples are employed to validate the ALPGEN samples of simulated $Z/\gamma^* \rightarrow \tau^+\tau^-$ events. Comparisons of the distributions of the pseudorapidities and the azimuthal angles of the two highest- p_T τ_{had} candidates are shown in Figures B.9 and B.10. In Figures B.11 and B.12 comparisons of the distributions of the azimuthal angle of the missing transverse momentum, the visible mass of the two τ_{had} candidates, the azimuthal angle difference between the two τ_{had} candidates and the transverse momentum of the highest- p_T jet are shown.

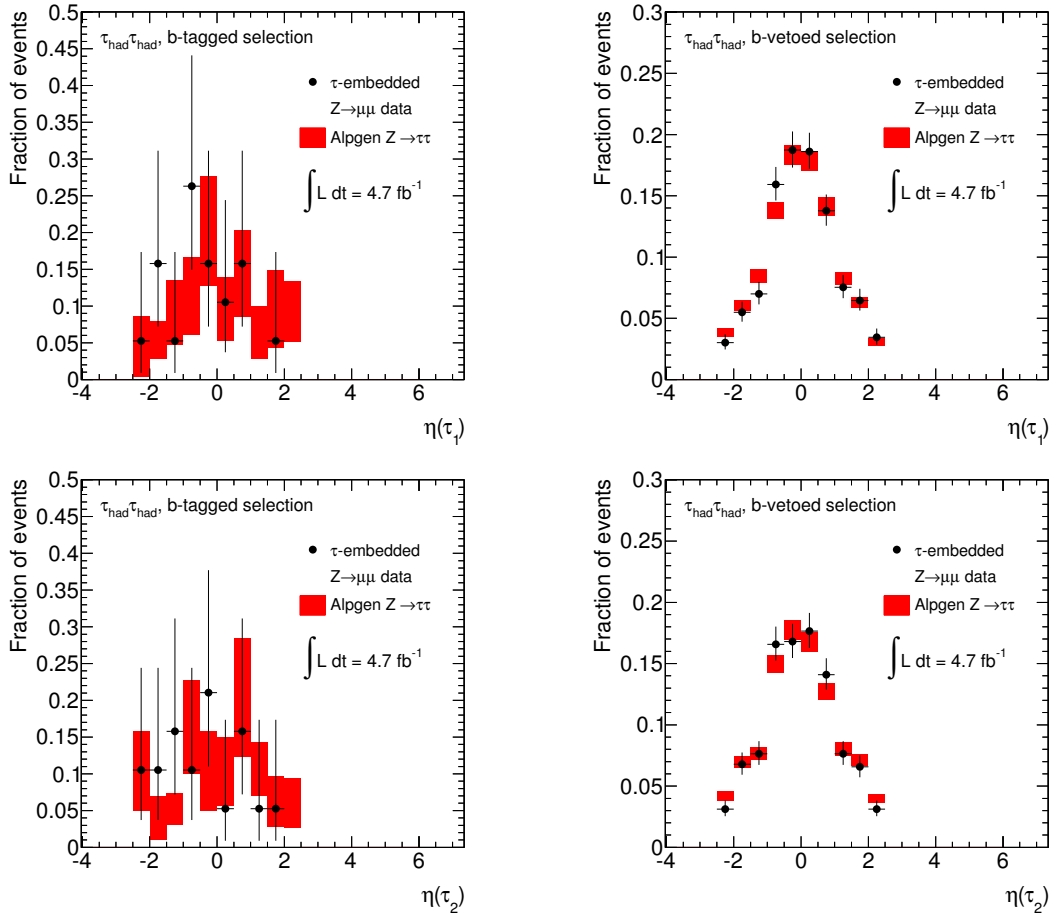


Figure B.9.: Validation of the simulated samples of Z -boson production. The pseudorapidity of the highest- p_T (first row) and the second highest- p_T (second row) hadronic τ -lepton decays is shown for the τ -embedded $Z/\gamma^* \rightarrow \mu^+\mu^-$ data samples and the ALPGEN simulated $Z/\gamma^* \rightarrow \tau^+\tau^-$ event samples. The distributions are shown after the b -tagged (left-hand side) and b -vetoed (right-hand side) selections as described in Section 6.5.4. The shown uncertainties are statistical uncertainties.

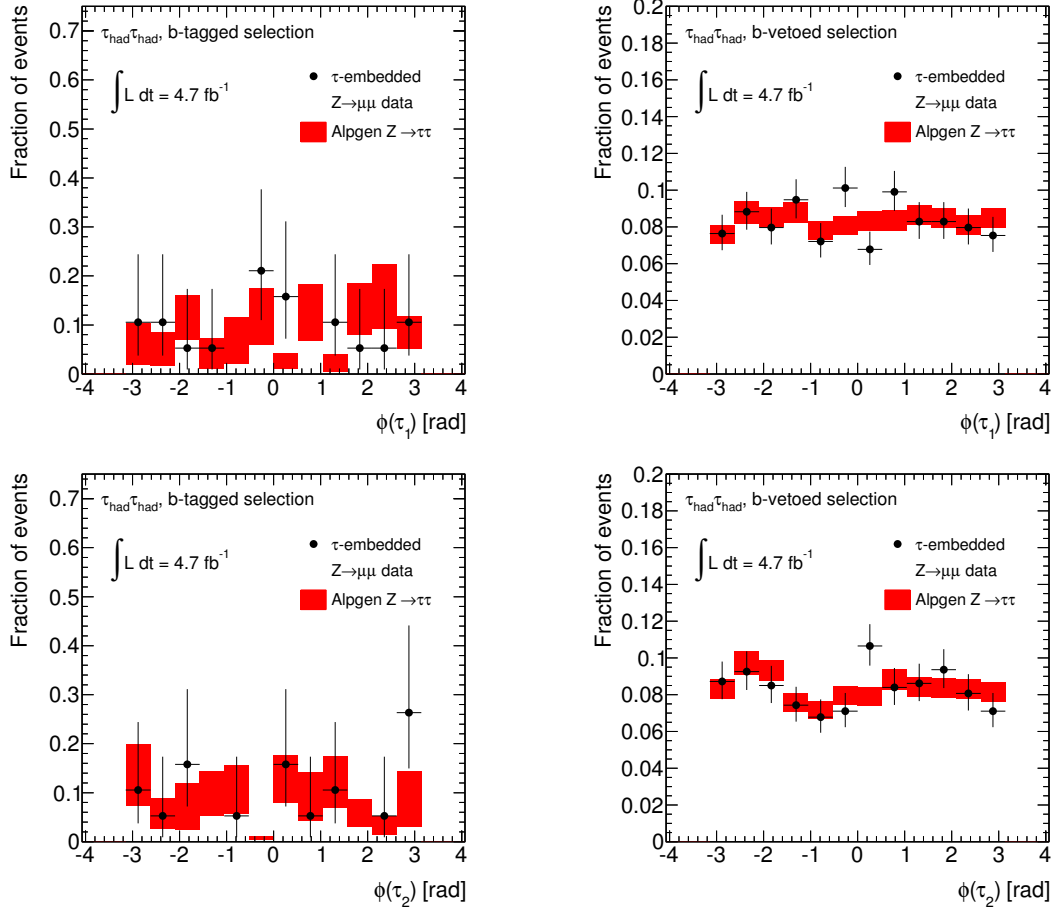


Figure B.10.: Validation of the simulated samples of Z -boson production. The azimuthal angle, ϕ , of the highest- p_T (first row) and the second highest- p_T (second row) hadronic τ -lepton decays are shown for the τ -embedded $Z/\gamma^* \rightarrow \mu^+\mu^-$ data samples and the ALPGEN simulated $Z/\gamma^* \rightarrow \tau^+\tau^-$ event samples. The distributions are shown after the b -tagged (left-hand side) and b -vetoed (right-hand side) selections as described in Section 6.5.4. The shown uncertainties are statistical uncertainties.

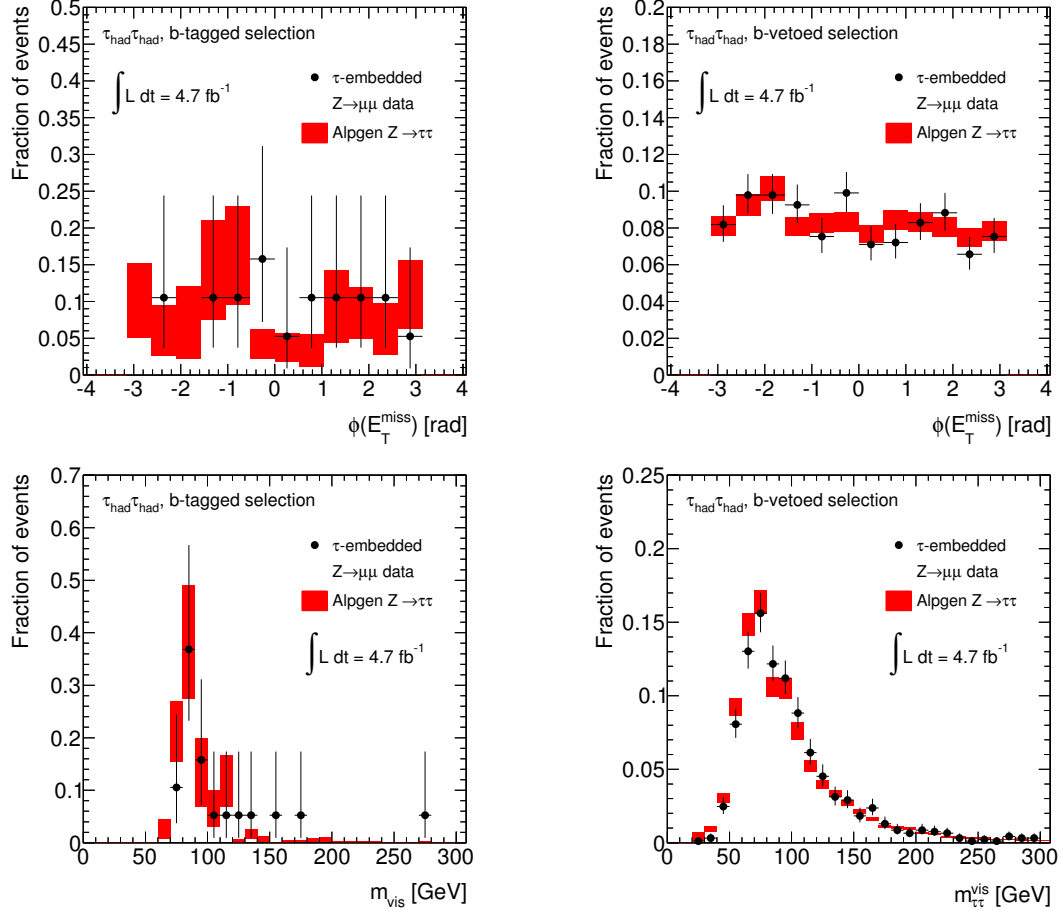


Figure B.11.: Validation of the simulated samples of Z -boson production. The azimuthal angle of the missing transverse momentum (first row) and the visible mass of the two τ_{had} candidates (second row) are shown for the τ -embedded $Z/\gamma^* \rightarrow \mu^+\mu^-$ data samples and the ALPGEN simulated $Z/\gamma^* \rightarrow \tau^+\tau^-$ event samples. The distributions are shown after the b -tagged (left-hand side) and b -vetoed (right-hand side) selections as described in Section 6.5.4. The shown uncertainties are statistical uncertainties.

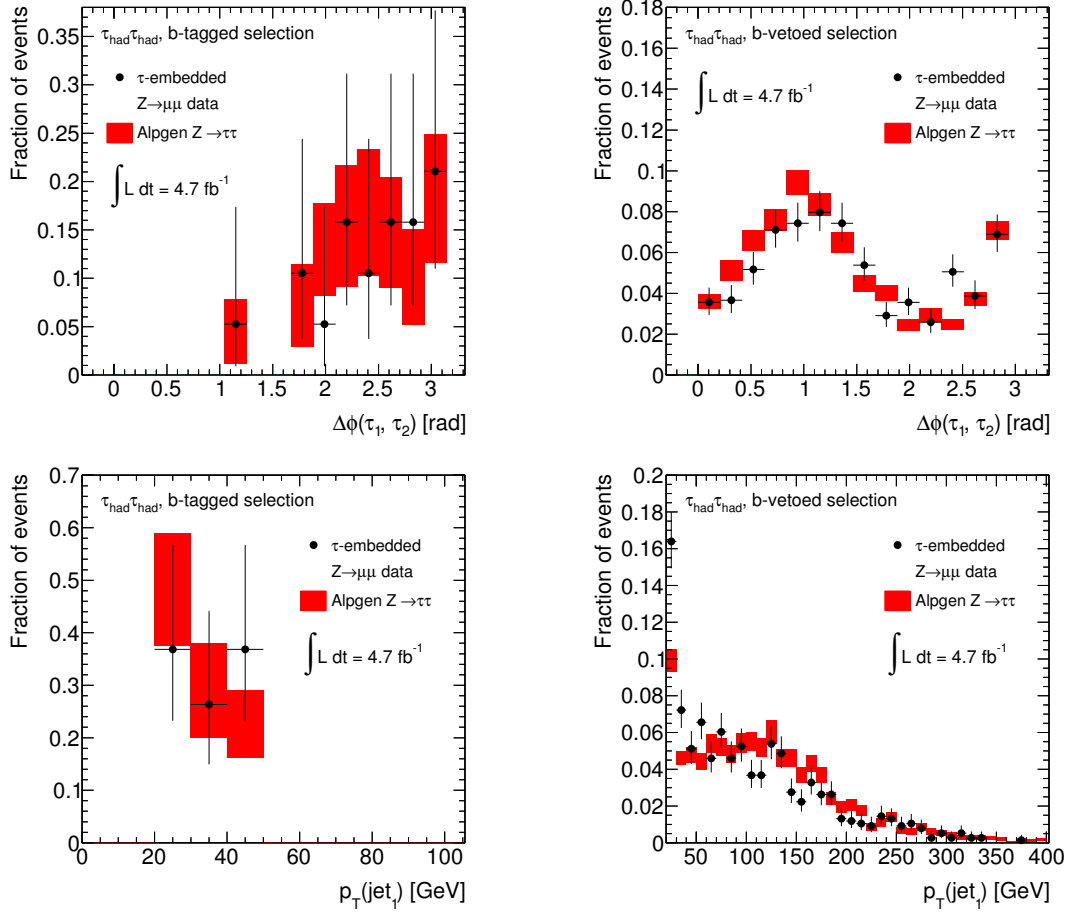


Figure B.12.: Validation of the simulated samples of Z -boson production. The difference of the azimuthal angle of the two highest- p_T τ_{had} candidates (first row) and the transverse momentum of the highest- p_T jet (second row) is shown for the τ -embedded $Z/\gamma^* \rightarrow \mu^+\mu^-$ data samples and the ALPGEN simulated $Z/\gamma^* \rightarrow \tau^+\tau^-$ event samples. The distributions are shown after the b -tagged (left-hand side) and b -vetoed (right-hand side) selections as described in Section 6.5.4. The shown uncertainties are statistical uncertainties.

B.4. Comparison of τ -embedded $W \rightarrow \mu\nu$ Data and Simulated $W \rightarrow \tau\nu$ Events

As for the τ -embedded $Z/\gamma^* \rightarrow \mu^+\mu^-$ data, the τ -embedded $W \rightarrow \mu\nu$ data are employed to validate the ALPGEN samples of simulated $W \rightarrow \tau\nu$ events. Comparisons of the distributions of the pseudorapidities and the azimuthal angles of the two highest- p_T τ_{had} candidates are shown in Figure B.13. In Figure B.14 comparisons of the distributions of the azimuthal angle of the missing transverse momentum, the visible mass of the two τ_{had} candidates, the azimuthal angle difference between the two τ_{had} candidates and the transverse momentum of the highest- p_T jet are shown.

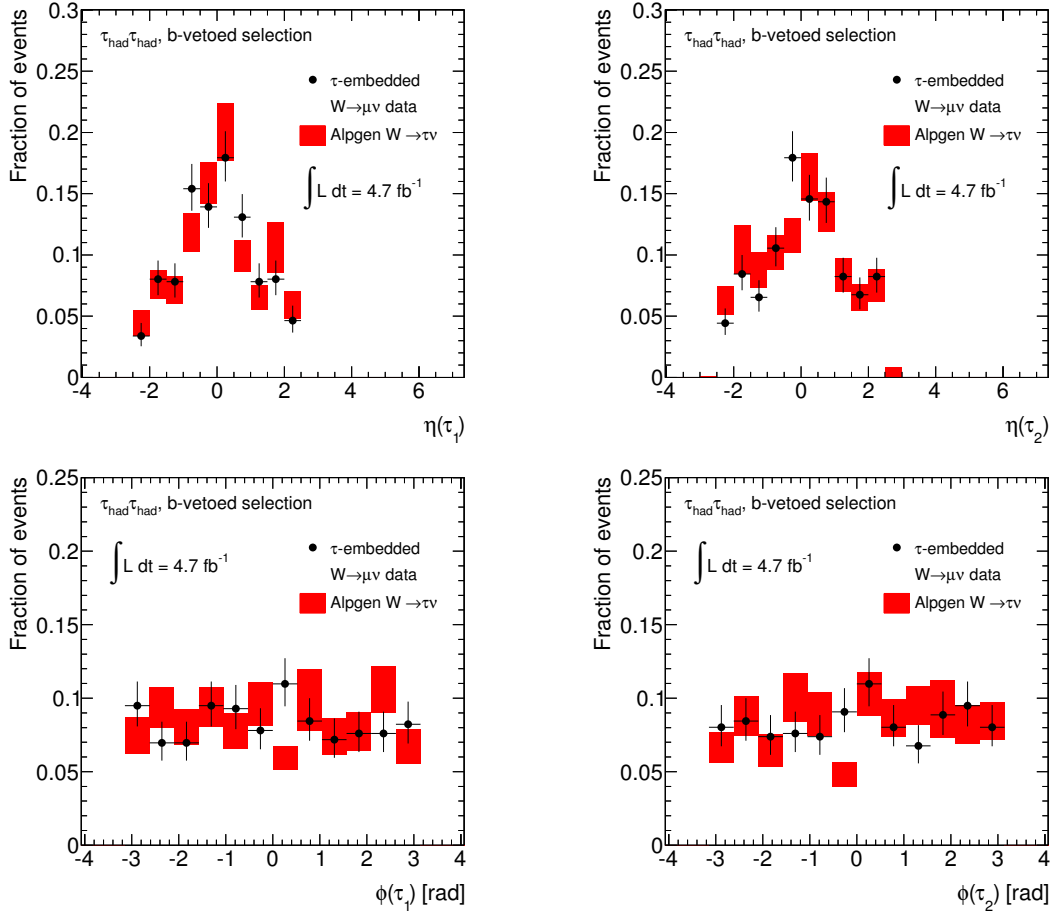


Figure B.13.: Validation of the simulated samples of W -boson production. The pseudorapidities (first row) and azimuthal angles, ϕ (second row), of the highest- p_T (left-hand side) and the second highest- p_T (right-hand side) hadronic τ -lepton decays are shown for the τ -embedded $W \rightarrow \mu\nu$ data samples and the ALPGEN simulated $W \rightarrow \tau\nu$ event samples. The distributions are shown after the looser b -vetoed selection as described in Section 6.5.4. The shown uncertainties are statistical uncertainties.

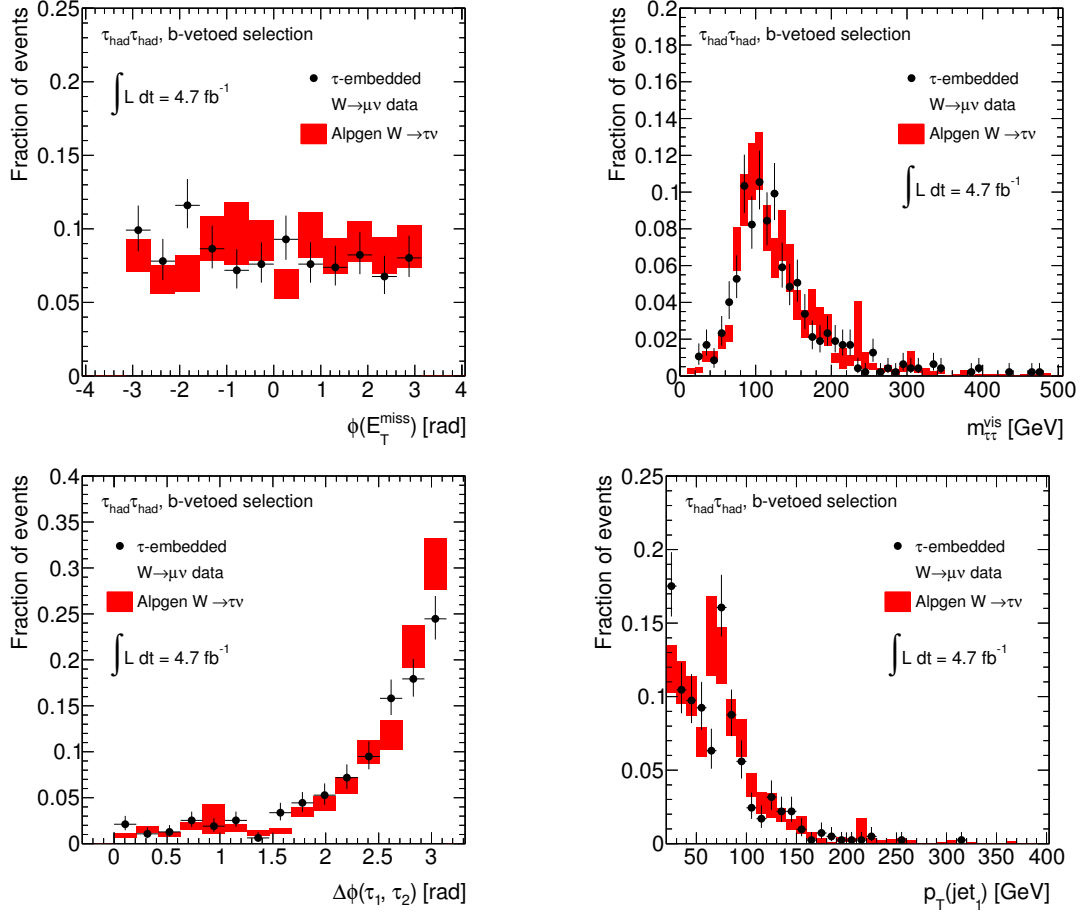


Figure B.14.: Validation of the simulated samples of W -boson production. The azimuthal angle of the missing transverse momentum (first row, left-hand side), the visible mass of the two τ_{had} candidates (first row, right-hand side), the azimuthal angle between the two τ_{had} candidates (second row, left-hand side) and the transverse momentum of the highest- p_T jet (second row, right-hand side) are shown for the τ -embedded $W \rightarrow \mu\nu$ data samples and the ALPGEN simulated $W \rightarrow \tau\nu$ event samples. The distributions are shown after the looser b -vetoed selection as described in Section 6.5.4. The shown uncertainties are statistical uncertainties.

B.5. Validation of the Combined Background Estimate

Based on the background estimation methods described in Section 6.5 the expected distributions of several important variables are compared to those observed in data. The distributions for the most important variables are shown in Section 6.5.6. In Figures B.15 and B.16 the pseudorapidities and the azimuthal angles of the two highest- p_T τ_{had} candidates are shown. In Figure B.17 the distributions of the azimuthal angle of the missing transverse energy are reported. The distributions of the number of tracks and the highest fulfilled set of τ_{had} identification requirements is documented in Figures B.18 and B.19. Finally in Figures B.20 and B.21 the distributions of the visible mass and the collinear mass are available. All distributions are shown for the b -tagged and the b -vetoed subsamples.

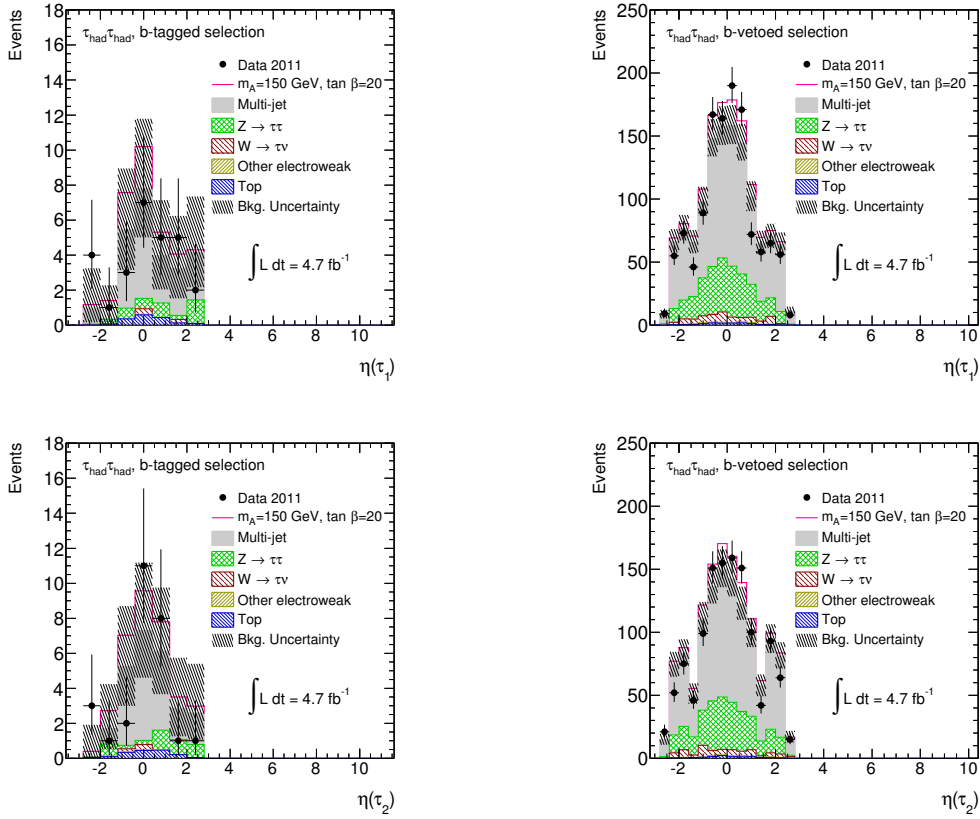


Figure B.15.: Distributions of the pseudorapidities of the highest- p_T (first row) and the second highest- p_T (second row) hadronic τ lepton decays for the b -tagged (left-hand column) and the b -vetoed (right-hand column) selections. The data are compared to the background expectation and an added hypothetical MSSM signal with $m_A = 150$ GeV and $\tan \beta = 20$. The background uncertainties include statistical and systematic uncertainties.

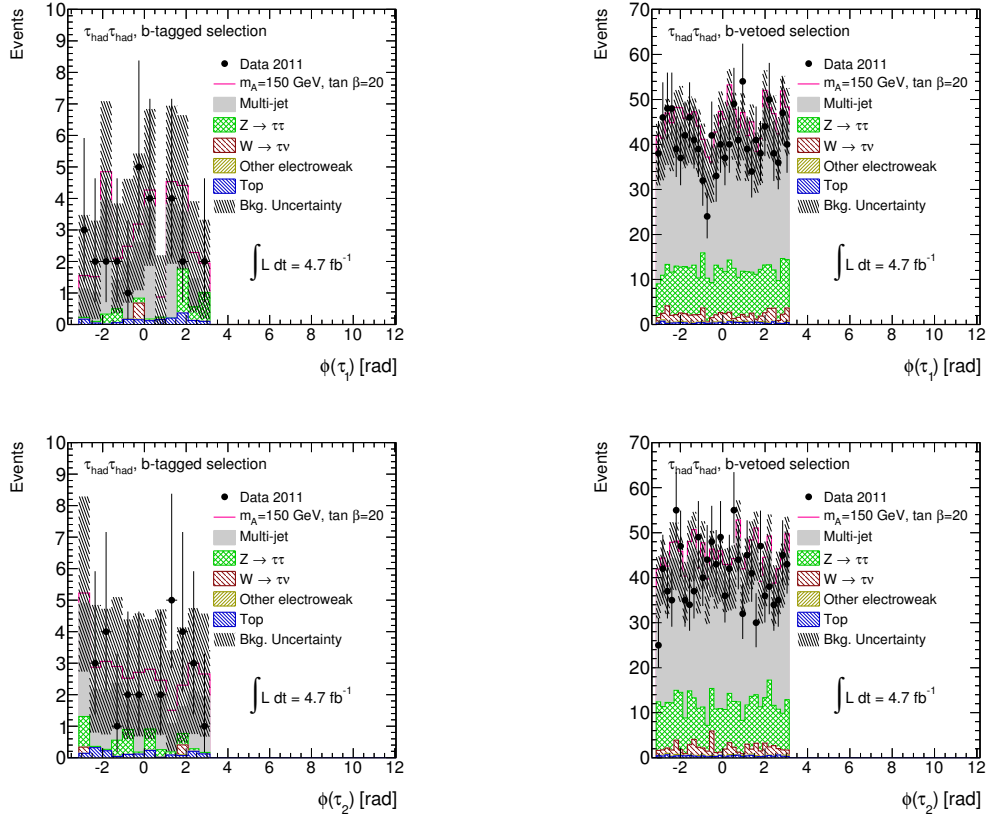


Figure B.16.: Distributions of the azimuthal angles, ϕ , of the highest- p_T (first row) and the second highest- p_T (second row) hadronic τ lepton decays for the b -tagged (left-hand column) and the b -vetoed (right-hand column) selections. The data are compared to the background expectation and an added hypothetical MSSM signal with $m_A = 150$ GeV and $\tan \beta = 20$. The background uncertainties include statistical and systematic uncertainties.

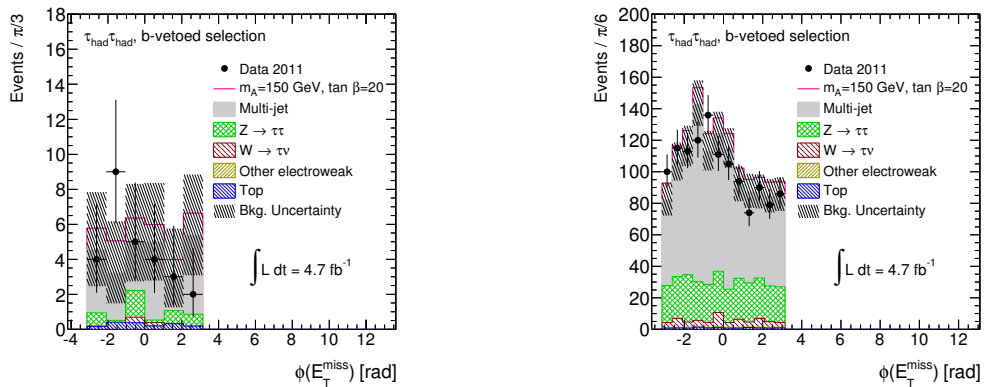


Figure B.17.: Distributions of the azimuthal angle of the missing transverse momentum vector for the b -tagged (left-hand column) and the b -vetoed (right-hand column) selections. The data are compared to the background expectation and an added hypothetical MSSM signal with $m_A = 150$ GeV and $\tan \beta = 20$. The background uncertainties include statistical and systematic uncertainties.

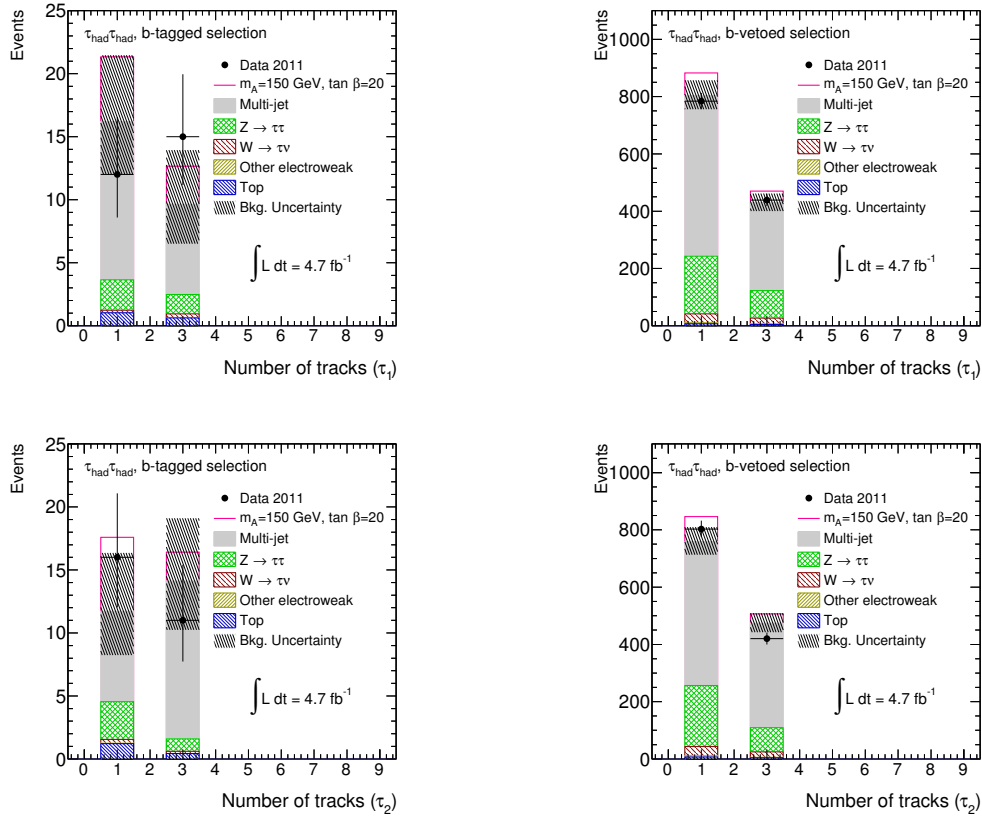


Figure B.18.: Distribution of the number of associated tracks to the highest- p_T (first row) and the second highest- p_T (second row) hadronic τ lepton decays for the b -tagged (left-hand column) and the b -vetoed (right-hand column) selections. The data are compared to the background expectation and an added hypothetical MSSM signal with $m_A = 150 \text{ GeV}$ and $\tan\beta = 20$. The background uncertainties include statistical and systematic uncertainties.

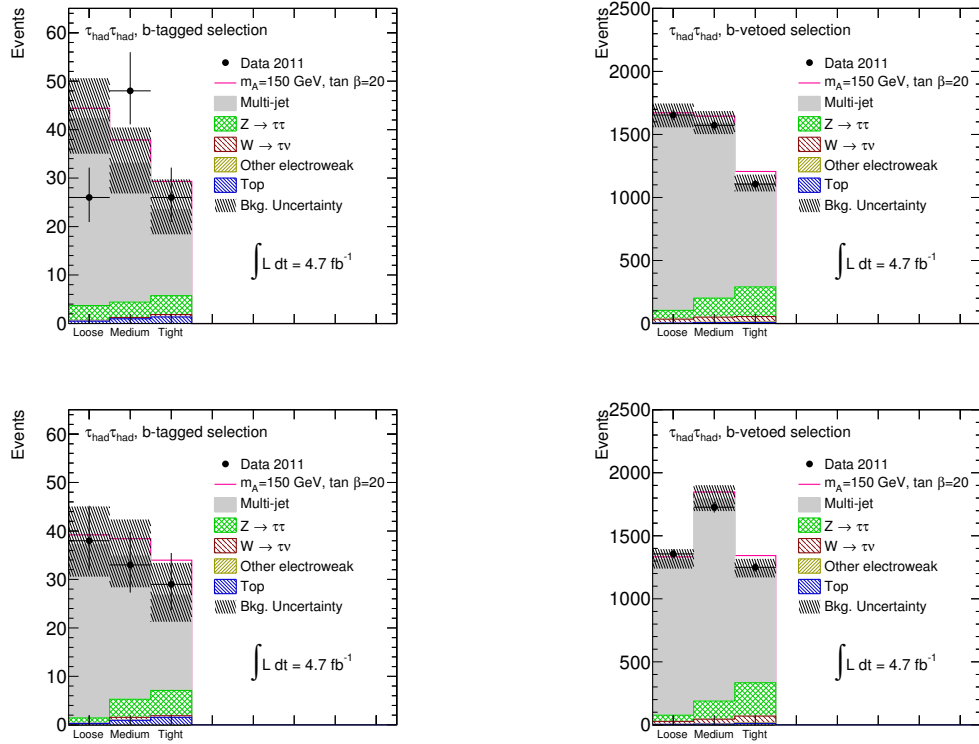


Figure B.19.: Distributions of the passed identification levels for the highest- p_T (first row) and the second highest- p_T (second row) hadronic τ lepton decay for the b -tagged (left-hand column) and the b -vetoed (right-hand column) selections. “Loose”, “Medium” and “Tight” refers to hadronic τ -lepton decays that pass the respective identification requirements, but not the requirements of the stricter identification levels. The data are compared to the background expectation and an added hypothetical MSSM signal with $m_A = 150 \text{ GeV}$ and $\tan \beta = 20$. The background uncertainties include statistical and systematic uncertainties.

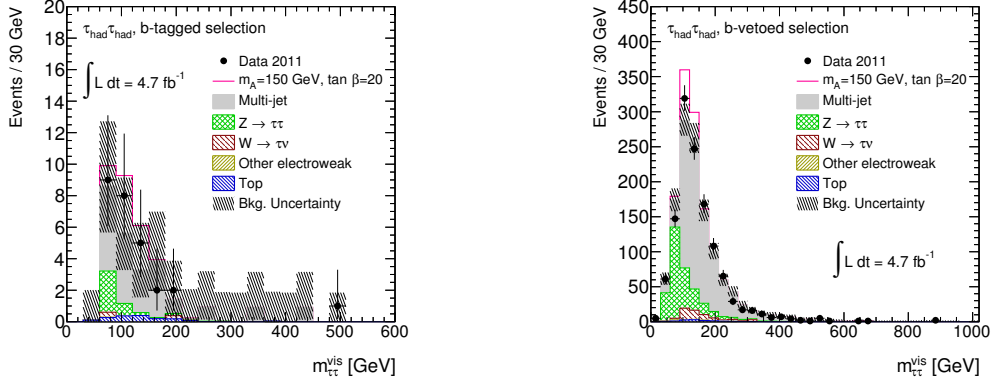


Figure B.20.: Distributions of the visible mass based on the four-vectors of the two selected hadronic τ -lepton decays for the b -tagged (left-hand column) and the b -vetoed (right-hand column) selections. The data are compared to the background expectation and an added hypothetical MSSM signal with $m_A = 150$ GeV and $\tan\beta = 20$. The background uncertainties include statistical and systematic uncertainties.

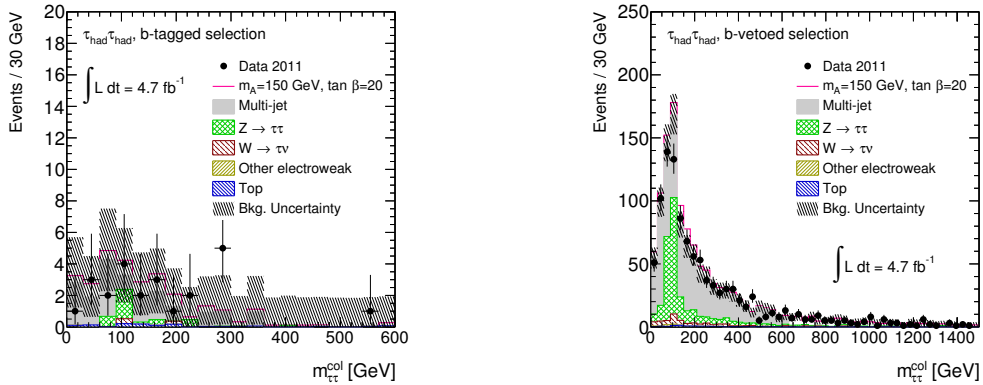


Figure B.21.: Distributions of the collinear mass based on the four-vectors of the two selected hadronic τ -lepton decays and the missing transverse momentum vector for the b -tagged (left-hand column) and the b -vetoed (right-hand column) selections. The data are compared to the background expectation and an added hypothetical MSSM signal with $m_A = 150$ GeV and $\tan\beta = 20$. The background uncertainties include statistical and systematic uncertainties.

C Auxiliary Information for the Statistical Analysis

As no obvious excess of data events above the background expectation is observed in the di- τ_{had} mass distributions of the $h/A/H \rightarrow \tau_{\text{had}}\tau_{\text{had}}$ channels, exclusion limits are derived in Section 7. The observed excesses of data in the di- τ_{had} mass distribution are quantified with p-values. The hypothesis tests described in Section 7.3 are using a likelihood ratio test statistic defined in Equation 7.32 for the calculation of exclusion limits and in Equation 7.33 for the calculation of p-values. The likelihood function is calculated from binned histograms of MMC mass distributions. The binning of these histograms is detailed in Section C.1. To model systematic uncertainties and statistical uncertainties of the background estimation methods, the likelihood function defined in Equation 7.25 depends on nuisance parameters. The names and functions of all nuisance parameters are described in Section C.2. For the calculation of the test statistic the values of the negative logarithmic likelihood function are minimised with respect to the nuisance parameters. In most cases the likelihood ratio is a ratio of the value obtained from the conditional minimisation for fixed signal strength μ and the value obtained from the unconditional minimisation with unconstrained signal strength μ . The values of the nuisance parameters in an exemplary minimisation are shown Section C.3.

C.1. Binning of the Mass Distributions

For the statistical analysis of the results of the search for MSSM Higgs bosons, the distributions of the invariant mass of the di-muon system and the MMC mass are rebinned with a non-linear MMC mass–bin number relationship. A non-linear relationship is necessary in the $h/A/H \rightarrow \tau\tau$ channels to retain the sensitivity in regions with a high number of expected events in addition to removing the influence from statistical fluctuations of the number of events in background templates for regions with a low number of expected events.

For the $h/A/H \rightarrow \mu\mu$ channel the di-muon mass is rebinned for the b -tagged subsample into bins of 2 GeV for signal hypotheses with $m_A < 125$ GeV, 4 GeV for $125 \text{ GeV} < m_A \leq 150$ GeV and 5 GeV for $m_A > 150$ GeV. For the b -vetoed subsample the bin widths are 1 GeV for $m_A \leq 200$ GeV and 2 GeV for $m_A > 200$ GeV. The non-linear MMC mass–bin number relationships for the $h/A/H \rightarrow \tau\tau$ channels are documented in Table C.1.

Bin number	$h/A/H \rightarrow \tau_e \tau_\mu$		$h/A/H \rightarrow \tau_{\text{lep}} \tau_{\text{had}}$		$h/A/H \rightarrow \tau_{\text{had}} \tau_{\text{had}}$	
	b -tagged	b -vetoed	b -tagged	b -vetoed	b -tagged	b -vetoed
0	[0, 50]	[0, 50]	[0, 70]	[0, 20]	[0, 120]	[0, 90]
1	[50, 80]	[50, 60]	[70, 90]	[20, 40]	[120, 180]	[90, 120]
2	[80, 100]	[60, 70]	[90, 100]	[40, 50]	[180, ∞]	[120, 150]
3	[100, 120]	[70, 80]	[100, 120]	[50, 55]		[150, 180]
4	[120, 140]	[80, 90]	[120, 150]	[55, 60]		[180, 210]
5	[140, 160]	[90, 100]	[150, ∞]	[60, 65]		[210, 240]
6	[160, 180]	[100, 110]		[65, 70]		[240, 270]
7	[180, 220]	[110, 120]		[70, 75]		[270, 300]
8	[220, 280]	[120, 130]		[75, 80]		[300, 330]
9	[280, ∞]	[130, 140]		[80, 85]		[330, 360]
10		[140, 150]		[85, 90]		[360, 420]
11		[150, 160]		[90, 95]		[420, 480]
12		[160, 170]		[95, 100]		[480, 540]
13		[170, 180]		[100, 105]		[540, ∞]
14		[180, 190]		[105, 110]		
15		[190, 200]		[110, 115]		
16		[200, 210]		[115, 120]		
17		[210, 220]		[120, 125]		
18		[220, 240]		[125, 130]		
19		[240, 260]		[130, 135]		
20		[260, 280]		[135, 140]		
21		[280, 330]		[140, 145]		
22		[330, 380]		[145, 150]		
23		[380, ∞]		[150, 160]		
24				[160, 170]		
25				[170, 180]		
26				[180, 200]		
27				[200, 225]		
28				[225, 250]		
29				[250, ∞]		

Table C.1.: Binning of the MMC mass histograms in the signal regions for the statistical analysis. All intervals are given in units of GeV. The size of the bins is optimised to have a compromise between a low statistical uncertainty for the background and signal templates and a high sensitivity to the signal and background hypothesis. In the control regions only one bin per control region is considered.

C.2. Names and Functions of the Nuisance Parameters

In this section the names and functions of the used nuisance parameters are documented. Nuisance parameters with names of the form **alpha_** model the systematic uncertainties described in Section 6.6, while nuisance parameters with names of the form **gamma_** are used to model the statistical uncertainties of the background estimation methods if it exceeds 5% for the combination of all backgrounds in a given bin of the mass distribution. Other nuisance parameters are used for the implementation of event yield relations between signal and control regions for the top and multi-jet background estimation methods (e.g. the nuisance parameter **tauratiorel_HH_NoBJetKinSel**).

The used nuisance parameters and their functions are:

μ : Signal strength parameter

Lumi: Luminosity uncertainty, a value of the nuisance parameter of 1 corresponds to the nominal luminosity measurement. For the luminosity uncertainty of 3.9% a value of the nuisance parameters of 1.039 and 0.961 corresponds to a $\pm 1\sigma$ effect.

alpha_ATLAS_Bkg_QCDEMUBTAG: Uncertainty from the estimation of the multi-jet background for the $h/A/H \rightarrow \tau_e \tau_\mu$ b -tagged selection.

alpha_ATLAS_Bkg_QCDEMUBVETO: Uncertainty from the estimation of the multi-jet background for the $h/A/H \rightarrow \tau_e \tau_\mu$ b -vetoed selection.

alpha_BJetFractionWSys_HH: Uncertainty from the measurement of the fraction of b -jets and the theoretical acceptance uncertainty for W events for the $h/A/H \rightarrow \tau_{\text{had}} \tau_{\text{had}}$ b -tagged channel, the uncertainties have been combined in order to avoid unnecessary degrees of freedom.

alpha_BJetFractionZSys_HH: Uncertainty from the measurement of the fraction of b -jets and the theoretical acceptance uncertainty for Z events for the $h/A/H \rightarrow \tau_{\text{had}} \tau_{\text{had}}$ b -tagged channel, the uncertainties have been combined in order to avoid unnecessary degrees of freedom.

alpha_B_EFF: Uncertainty of the b -jet identification efficiency for correctly identified b -jets.

alpha_BkgFit_bjet: Uncertainty of the fit results of the background in the $h/A/H \rightarrow \mu\mu$ b -tagged channel.

alpha_BkgFit_nobjet: Uncertainty of the fit results of the background in the $h/A/H \rightarrow \mu\mu$ b -vetoed channel.

alpha_C_EFF: Uncertainty of the c -to- b -jet misidentification probability.

alpha_EL_RES_SCALE_EMU: Uncertainty of the electron energy scale and resolution in the $h/A/H \rightarrow \tau_e \tau_\mu$ channel.

alpha_EMUBTAG_QCDCR1SYS: Uncertainty on the multi-jet background in the top control region of the $h/A/H \rightarrow \tau_e \tau_\mu$ b -tagged channel.

alpha_EMUBTAG_kuncert: Uncertainty on the extrapolation factor from the top control region of the $h/A/H \rightarrow \tau_e \tau_\mu$ b -tagged channel.

alpha_EMUBVETO_QCDCR1SYS: Uncertainty on the multi-jet background in the top control region of the $h/A/H \rightarrow \tau_e \tau_\mu$ b -vetoed channel.

alpha_EMUBVETO_kuncert: Uncertainty on the extrapolation factor from the top control region of the $h/A/H \rightarrow \tau_e \tau_\mu$ b -vetoed channel.

alpha_E_EFF: Uncertainty of the electron identification efficiency.

alpha_E_FAKE: Uncertainty of the electron-to- τ_{had} misidentification probability

alpha_EmbIso: Uncertainty of the τ -embedded $Z/\gamma^* \rightarrow \mu^+ \mu^-$ data obtained by removing the isolation requirement for the selection of $Z/\gamma^* \rightarrow \mu^+ \mu^-$ data events.

alpha_EmbMfs: Uncertainty of the τ -embedded $Z/\gamma^* \rightarrow \mu^+ \mu^-$ data obtained by changing the subtraction of energy deposits of the $Z/\gamma^* \rightarrow \mu^+ \mu^-$ mini-event.

alpha_EmbTrig: Uncertainty of the normalisation of τ -embedded $Z/\gamma^* \rightarrow \mu^+ \mu^-$ data due to the trigger efficiency.

alpha_Fake_EFF: Uncertainty of the jet-to- τ_{had} misidentification probability.

alpha_JES: Uncertainty of the jet and τ_{had} energy scale, the energy scale uncertainty of clusters and soft jets and the missing transverse energy uncertainty due to pile-up.

alpha_L_EFF: Uncertainty of the light-jet-to- b -jet misidentification probability.

alpha_MU_SCALE_EMU: Uncertainty of the muon energy scale.

alpha_M_EFF: Uncertainty of the muon identification efficiency.

alpha_SF_QCD_BTAG_LH_El: Uncertainty on the estimation of the multi-jet background in the $h/A/H \rightarrow \tau_e \tau_{\text{had}}$ b -tagged channel.

alpha_SF_QCD_BTAG_LH_Mu: Uncertainty on the estimation of the multi-jet background in the $h/A/H \rightarrow \tau_\mu \tau_{\text{had}}$ b -tagged channel.

alpha_SF_QCD_BVETO_LH_El: Uncertainty on the estimation of the multi-jet background in the $h/A/H \rightarrow \tau_e \tau_{\text{had}}$ b -vetoed channel.

alpha_SF_QCD_BVETO_LH_Mu: Uncertainty on the estimation of the multi-jet background in the $h/A/H \rightarrow \tau_\mu \tau_{\text{had}}$ b -vetoed channel.

alpha_SignalFit_bbA_bjet: Uncertainty of the fit results for the b -quark annihilation A -boson production in the $h/A/H \rightarrow \mu\mu$ b -tagged channel.

alpha_SignalFit_bbA_nobjjet: Uncertainty of the fit results for the b -quark annihilation A -boson production in the $h/A/H \rightarrow \mu\mu$ b -vetoed channel.

alpha_SignalFit_bbH_bjet: Uncertainty of the fit results for the b -quark annihilation H -boson production in the $h/A/H \rightarrow \mu\mu$ b -tagged channel.

alpha_SignalFit_bbH_nobjjet: Uncertainty of the fit results for the b -quark annihilation H -boson production in the $h/A/H \rightarrow \mu\mu$ b -vetoed channel.

alpha_SignalFit_bbh_bjet: Uncertainty of the fit results for the b -quark annihilation h -boson production in the $h/A/H \rightarrow \mu\mu$ b -tagged channel.

alpha_SignalFit_bbh_nobjjet: Uncertainty of the fit results for the b -quark annihilation h -boson production in the $h/A/H \rightarrow \mu\mu$ b -vetoed channel.

- alpha_SignalFit_ggA_bjet:** Uncertainty of the fit results for the gluon-fusion A -boson production in the $h/A/H \rightarrow \mu\mu$ b -tagged channel.
- alpha_SignalFit_ggA_nobjjet:** Uncertainty of the fit results for the gluon-fusion A -boson production in the $h/A/H \rightarrow \mu\mu$ b -vetoed channel.
- alpha_SignalFit_ggH_bjet:** Uncertainty of the fit results for the gluon-fusion H -boson production in the $h/A/H \rightarrow \mu\mu$ b -tagged channel.
- alpha_SignalFit_ggH_nobjjet:** Uncertainty of the fit results for the gluon-fusion H -boson production in the $h/A/H \rightarrow \mu\mu$ b -vetoed channel.
- alpha_SignalFit_ggh_bjet:** Uncertainty of the fit results for the gluon-fusion h -boson production in the $h/A/H \rightarrow \mu\mu$ b -tagged channel.
- alpha_SignalFit_ggh_nobjjet:** Uncertainty of the fit results for the gluon-fusion h -boson production in the $h/A/H \rightarrow \mu\mu$ b -vetoed channel.
- alpha_TAUTRIG_EFF:** Uncertainty of the τ_{had} trigger efficiency for correctly identified τ_{had} decays in the $h/A/H \rightarrow \tau_{\text{had}}\tau_{\text{had}}$ channel.
- alpha_T_EFF:** Uncertainty of the τ_{had} identification efficiency.
- alpha_XS_W:** Theoretical cross-section uncertainty for W -boson production.
- alpha_XS_Z:** Theoretical cross-section uncertainty for Z -boson production.
- alpha_XS_bbA:** Theoretical cross-section uncertainty for signal events produced in b -quark annihilation.
- alpha_XS_diboson:** Theoretical cross-section uncertainty for the production of di-boson events.
- alpha_XS_ggA:** Theoretical cross-section uncertainty for gluon-fusion signal event production.
- alpha_XS_others_EMUBVETO:** Theoretical cross-section uncertainty for the production of other processes in the $h/A/H \rightarrow \tau_e\tau_\mu$ b -vetoed channel.
- alpha_XS_singletop:** Theoretical cross-section uncertainty for the production of single-top events
- alpha_XS_top:** Theoretical cross-section uncertainty for the production of $t\bar{t}$ events.
- alpha_q2_WHH:** Theoretical acceptance uncertainty for events with W -boson production for the $h/A/H \rightarrow \tau_{\text{had}}\tau_{\text{had}}$ b -vetoed channel.
- alpha_q2_WLH:** Theoretical acceptance uncertainty for events with W -boson production for the $h/A/H \rightarrow \tau_{\text{lep}}\tau_{\text{had}}$ channels.
- alpha_q2_ZHH:** Theoretical acceptance uncertainty for events with Z -boson production for the $h/A/H \rightarrow \tau_{\text{had}}\tau_{\text{had}}$ b -vetoed channel.
- alpha_q2_ZLH:** Theoretical acceptance uncertainty for events with Z -boson production for the $h/A/H \rightarrow \tau_{\text{lep}}\tau_{\text{had}}$ channels.

alpha_q2_Ztautau_EMU: Theoretical acceptance uncertainty for events with Z -boson production for the $h/A/H \rightarrow \tau_e \tau_\mu$ channel.

alpha_q2_bbA_BTAG_LH: Theoretical acceptance uncertainty for the production of signal events in b -quark annihilation for the $h/A/H \rightarrow \tau_{\text{lep}} \tau_{\text{had}}$ b -tagged channel.

alpha_q2_bbA_BVETO_LH: Theoretical acceptance uncertainty for the production of signal events in b -quark annihilation for the $h/A/H \rightarrow \tau_{\text{lep}} \tau_{\text{had}}$ b -vetoed channel.

alpha_q2_bbA_EMUBTAG: Theoretical acceptance uncertainty for the production of signal events in b -quark annihilation for the $h/A/H \rightarrow \tau_e \tau_\mu$ b -tagged channel.

alpha_q2_bbA_EMUBVETO: Theoretical acceptance uncertainty for the production of signal events in b -quark annihilation for the $h/A/H \rightarrow \tau_e \tau_\mu$ b -vetoed channel.

alpha_q2_bbA_HH_AtLeastOneBJet: Theoretical acceptance uncertainty for the production of signal events in b -quark annihilation for the $h/A/H \rightarrow \tau_{\text{had}} \tau_{\text{had}}$ b -tagged channel.

alpha_q2_bbA_HH_NoBJetKinSel: Theoretical acceptance uncertainty for the production of signal events in b -quark annihilation for the $h/A/H \rightarrow \tau_{\text{had}} \tau_{\text{had}}$ b -vetoed channel.

alpha_q2_ggA_EMUBTAG: Theoretical acceptance uncertainty for the production of signal events in gluon fusion for the $h/A/H \rightarrow \tau_e \tau_\mu$ b -vetoed channel.

alpha_q2_ggA_EMUBVETO: Theoretical acceptance uncertainty for the production of signal events in gluon fusion for the $h/A/H \rightarrow \tau_e \tau_\mu$ b -vetoed channel.

alpha_q2_ggA_HH_AtLeastOneBJet: Theoretical acceptance uncertainty for the production of signal events in gluon fusion for the $h/A/H \rightarrow \tau_{\text{had}} \tau_{\text{had}}$ b -tagged channel.

alpha_q2_ggA_HH_NoBJetKinSel: Theoretical acceptance uncertainty for the production of signal events in gluon fusion for the $h/A/H \rightarrow \tau_{\text{had}} \tau_{\text{had}}$ b -vetoed channel.

alpha_q2_ggF_BTAG_LH: Theoretical acceptance uncertainty for the production of signal events in gluon fusion for the $h/A/H \rightarrow \tau_{\text{lep}} \tau_{\text{had}}$ b -tagged channel.

alpha_q2_ggF_BVETO_LH: Theoretical acceptance uncertainty for the production of signal events in gluon fusion for the $h/A/H \rightarrow \tau_{\text{lep}} \tau_{\text{had}}$ b -vetoed channel.

alpha_q2_others_EMUBTAG: Theoretical acceptance uncertainty for the production of other events for the $h/A/H \rightarrow \tau_e \tau_\mu$ b -tagged channel.

alpha_q2_singletopLH: Theoretical acceptance uncertainty for the production of single-top events for the $h/A/H \rightarrow \tau_{\text{lep}} \tau_{\text{had}}$ channel.

alpha_q2_topHH: Theoretical acceptance uncertainty for the production of top events for the $h/A/H \rightarrow \tau_{\text{had}} \tau_{\text{had}}$ channel.

EMUBTAG_NAQCD: Parameter used in the estimation of the multi-jet background for the $h/A/H \rightarrow \tau_e \tau_\mu$ b -tagged channel.

EMUBTAG_TAUB: Parameter used in the estimation of the multi-jet background for the $h/A/H \rightarrow \tau_e \tau_\mu$ b -tagged channel.

EMUBTAG_TAUC: Parameter used in the estimation of the multi-jet background for the $h/A/H \rightarrow \tau_e \tau_\mu$ b -tagged channel.

EMUBTAG_TauTTBAR: Parameter used in the estimation of the top background for the $h/A/H \rightarrow \tau_e \tau_\mu$ b -tagged channel.

EMUBVETO_NAQCD: Parameter used in the estimation of the multi-jet background for the $h/A/H \rightarrow \tau_e \tau_\mu$ b -vetoed channel.

EMUBVETO_TAUB: Parameter used in the estimation of the multi-jet background for the $h/A/H \rightarrow \tau_e \tau_\mu$ b -vetoed channel.

EMUBVETO_TAUC: Parameter used in the estimation of the multi-jet background for the $h/A/H \rightarrow \tau_e \tau_\mu$ b -vetoed channel.

EMUBVETO_TauTTBAR: Parameter used in the estimation of the top background for the $h/A/H \rightarrow \tau_e \tau_\mu$ b -vetoed channel.

tauD_LH_BTAG_El: Parameter used in the estimation of the multi-jet background for the $h/A/H \rightarrow \tau_e \tau_{\text{had}}$ b -tagged channel.

tauD_LH_BTAG_Mu: Parameter used in the estimation of the multi-jet background for the $h/A/H \rightarrow \tau_\mu \tau_{\text{had}}$ b -tagged channel.

tauD_LH_BVETO_El: Parameter used in the estimation of the multi-jet background for the $h/A/H \rightarrow \tau_e \tau_{\text{had}}$ b -vetoed channel.

tauD_LH_BVETO_Mu: Parameter used in the estimation of the multi-jet background for the $h/A/H \rightarrow \tau_\mu \tau_{\text{had}}$ b -vetoed channel.

tauDrel_HH_AtLeastOneBJet: Number of events in the control region D used in the estimation of the multi-jet background for the $h/A/H \rightarrow \tau_{\text{had}} \tau_{\text{had}}$ b -tagged channel.

tauDrel_HH_NoBJetKinSel: Number of events in the control region D used in the estimation of the multi-jet background for the $h/A/H \rightarrow \tau_{\text{had}} \tau_{\text{had}}$ b -vetoed channel.

tauratio_LH_BTAG_El: Parameter used in the estimation of the multi-jet background for the $h/A/H \rightarrow \tau_e \tau_{\text{had}}$ b -tagged channel.

tauratio_LH_BTAG_Mu: Parameter used in the estimation of the multi-jet background for the $h/A/H \rightarrow \tau_e \tau_{\text{had}}$ b -tagged channel.

tauratio_LH_BVETO_El: Parameter used in the estimation of the multi-jet background for the $h/A/H \rightarrow \tau_e \tau_{\text{had}}$ b -tagged channel.

tauratio_LH_BVETO_Mu: Parameter used in the estimation of the multi-jet background for the $h/A/H \rightarrow \tau_e \tau_{\text{had}}$ b -tagged channel.

tauratiorel_HH_AtLeastOneBJet: Ratio of the number of events in the control regions C and D used in the estimation of the multi-jet background for the $h/A/H \rightarrow \tau_{\text{had}} \tau_{\text{had}}$ b -tagged channel.

tauratiorel_HH_NoBJetKinSel: Ratio of the number of events in the control regions B and D used in the estimation of the multi-jet background for the $h/A/H \rightarrow \tau_{\text{had}} \tau_{\text{had}}$ b -vetoed channel.

taushaperel_HH_AtLeastOneBJet: Number of events in the control region B used in the estimation of the multi-jet background for the $h/A/H \rightarrow \tau_{\text{had}}\tau_{\text{had}}$ b -vetoed channel.

taushaperel_HH_NoBJetKinSel: Number of events in the control region C used in the estimation of the multi-jet background for the $h/A/H \rightarrow \tau_{\text{had}}\tau_{\text{had}}$ b -vetoed channel.

C.3. Validation of the Nuisance Parameter Values Obtained in the Likelihood Minimisation Procedure

The values of the nuisance parameters obtained in the minimisation of the negative logarithmic likelihood function based on all $\mu\mu$ and $\tau\tau$ channels are documented for the unconditional minimisation and the conditional minimisation with $\mu = 0$ in Table C.2. For the nuisance parameters with names of the form **alpha_** a value of ± 1 can be interpreted as a change of the nominal distribution to the distribution that corresponds to the $\pm 1\sigma$ value of the uncertainty. For the other nuisance parameters such an interpretation is not possible.

Nuisance parameter name	μ unconstrained	$\mu = 0$
μ	0.00 ± 0.20	constant
EMUBTAG_NAQCD	15.52 ± 0.24	15.70 ± 0.15
EMUBTAG_TAUB	0.547 ± 0.008	0.547 ± 0.009
EMUBTAG_TAUC	511 ± 8	505 ± 4
EMUBTAG_TauTTBAR	1.17 ± 0.10	1.16 ± 0.10
EMUBVETO_NAQCD	980.7 ± 2.9	982.3 ± 2.2
EMUBVETO_TAUB	0.5011 ± 0.0018	0.5011 ± 0.0019
EMUBVETO_TAUC	138.4 ± 0.4	138.19 ± 0.30
EMUBVETO_TauTTBAR	1.22 ± 0.11	1.21 ± 0.06
Lumi	1.018 ± 0.017	1.014 ± 0.010
alpha_ATLAS_Bkg_QCDEMUBTAG	-0.5 ± 0.9	-0.5 ± 1.1
alpha_ATLAS_Bkg_QCDEMUBVETO	-1.3 ± 0.5	-1.7 ± 0.5
alpha_BJetFractionWSys_HH	0.0 ± 1.0	0.0 ± 1.0
alpha_BJetFractionZSys_HH	0.1 ± 1.1	0.1 ± 0.8
alpha_B_EFF	0.13 ± 0.34	0.13 ± 0.23
alpha_BkgFit_bjet	0.1 ± 0.6	0.1 ± 0.6
alpha_BkgFit_nobjet	-0.08 ± 0.30	-0.08 ± 0.29
alpha_C_EFF	0.1 ± 0.9	0.1 ± 0.6
alpha_EL_RES_SCALE_EMU	-0.1 ± 0.7	-0.1 ± 0.8
alpha_EMUBTAG_kuncert	0.0 ± 1.0	0.0 ± 1.0
alpha_EMUBVETO_QCDCR1SYS	0.0 ± 1.0	0.0 ± 1.0
alpha_EMUBVETO_kuncert	0.1 ± 0.4	0.13 ± 0.26
alpha_E_EFF	-0.17 ± 0.32	-0.01 ± 0.28
alpha_E_FAKE	-0.09 ± 0.25	-0.1 ± 0.4
alpha_EmbIso	0.0 ± 0.5	0.1 ± 0.4
alpha_EmbMfs	-0.29 ± 0.18	0.28 ± 0.19
alpha_EmbTrig	-0.1 ± 1.2	-0.2 ± 0.6
alpha_Fake_EFF	0.0 ± 0.9	0.0 ± 0.8
alpha_JES	-0.53 ± 0.07	-0.41 ± 0.14
alpha_L_EFF	0.1 ± 1.0	0.2 ± 1.0
alpha_MU_SCALE_EMU	0.0 ± 1.2	0.0 ± 0.9
alpha_M_EFF	0.3 ± 0.5	0.3 ± 0.4

continued on next page

<i>continued from previous page</i>		
Nuisance parameter name	μ unconstrained	$\mu = 0$
alpha_Q2_Ztautau_EMU	0.45 ± 0.26	0.48 ± 0.19
alpha_QCDCR1SYS	0.1 ± 1.0	0.1 ± 1.0
alpha_SF_QCD_BTAG_LH_El	0.4 ± 0.8	0.5 ± 0.7
alpha_SF_QCD_BTAG_LH_Mu	-0.1 ± 1.0	0.0 ± 0.9
alpha_SF_QCD_BVETO_LH_El	0.2 ± 0.5	0.1 ± 0.5
alpha_SF_QCD_BVETO_LH_Mu	0.3 ± 0.9	0.2 ± 0.8
alpha_SignalFit_bbA_bjet	0.0 ± 1.0	0.0 ± 1.0
alpha_SignalFit_bbA_nobjjet	0.0 ± 1.0	0.0 ± 1.0
alpha_SignalFit_bbH_bjet	0.0 ± 1.0	0.0 ± 1.0
alpha_SignalFit_bbH_nobjjet	0.0 ± 1.0	0.0 ± 1.0
alpha_SignalFit_bbh_bjet	0.0 ± 1.0	0.0 ± 1.0
alpha_SignalFit_bbh_nobjjet	0.0 ± 1.0	0.0 ± 1.0
alpha_SignalFit_ggA_bjet	0.0 ± 1.0	0.0 ± 1.0
alpha_SignalFit_ggA_nobjjet	0.0 ± 1.0	0.0 ± 1.0
alpha_SignalFit_ggH_bjet	0.0 ± 1.0	0.0 ± 1.0
alpha_SignalFit_ggH_nobjjet	0.0 ± 1.0	0.0 ± 1.0
alpha_SignalFit_ggh_bjet	0.0 ± 1.0	0.0 ± 1.0
alpha_SignalFit_ggh_nobjjet	0.0 ± 1.0	0.0 ± 1.0
alpha_TAUTRIG_EFF	-0.1 ± 0.7	-0.2 ± 0.8
alpha_T_EFF	-0.31 ± 0.25	-0.31 ± 0.30
alpha_XS_W	0.8 ± 0.7	0.7 ± 0.7
alpha_XS_Z	0.25 ± 0.29	0.31 ± 0.17
alpha_XS_bbA	0.0 ± 1.0	0.0 ± 1.0
alpha_XS_diboson	0.1 ± 1.0	0.1 ± 1.0
alpha_XS_ggA	0.1 ± 0.7	0.0 ± 1.0
alpha_XS_others_EMUBVETO	-0.7 ± 0.6	-0.5 ± 0.6
alpha_XS_singletop	0.1 ± 1.0	0.1 ± 1.0
alpha_XS_top	0.5 ± 0.8	0.5 ± 0.9
alpha_q2_DibosonLH	0.0 ± 1.0	0.0 ± 1.0
alpha_q2_WHH	0.0 ± 0.9	0.0 ± 0.9
alpha_q2_WLH	0.1 ± 1.0	0.1 ± 0.9
alpha_q2_ZHH	-0.4 ± 0.5	-0.5 ± 0.5
alpha_q2_ZLH	0.03 ± 0.13	-0.17 ± 0.12
alpha_q2_bbA_BTAG_LH	0.0 ± 1.1	0.0 ± 1.0
alpha_q2_bbA_BVETO_LH	0.0 ± 1.2	0.0 ± 1.0
alpha_q2_bbA_EMUBTAG	0.0 ± 0.9	0.0 ± 1.0
alpha_q2_bbA_EMUBVETO	0.0 ± 1.0	0.0 ± 1.0
alpha_q2_bbA_HH_AtLeastOneBJet	0.0 ± 1.1	0.0 ± 1.0
alpha_q2_bbA_HH_NoBJetKinSel	0.0 ± 1.1	0.0 ± 1.0
alpha_q2_ggA_EMUBTAG	0.0 ± 1.0	0.0 ± 1.0
alpha_q2_ggA_EMUBVETO	-0.01 ± 0.07	0.0 ± 1.0
alpha_q2_ggA_HH_AtLeastOneBJet	0.0 ± 1.0	0.0 ± 1.0
<i>continued on next page</i>		

<i>continued from previous page</i>		
Nuisance parameter name	μ unconstrained	$\mu = 0$
alpha_q2_ggA_HH_NoBJetKinSel	-0.00 ± 0.35	0.0 ± 1.0
alpha_q2_ggF_BTAG_LH	0.0 ± 0.5	0.0 ± 1.0
alpha_q2_ggF_BVETO_LH	0.0 ± 1.1	0.0 ± 1.0
alpha_q2_others_EMUBTAG	-0.3 ± 1.0	-0.3 ± 1.0
alpha_q2_singletopLH	0.0 ± 1.0	0.0 ± 1.0
alpha_q2_topHH	0.0 ± 1.0	0.0 ± 1.0
gamma_stat_BTAG_regionB_El_bin_0	1.1 ± 0.8	1.1 ± 0.8
gamma_stat_BTAG_regionB_Mu_bin_0	1.02 ± 0.24	1.02 ± 0.24
gamma_stat_BTAG_regionD_El_bin_0	1.0 ± 0.5	1.0 ± 0.4
gamma_stat_BTAG_regionD_Mu_bin_0	1.02 ± 0.24	1.02 ± 0.24
gamma_stat_BVETO_regionB_El_bin_0	1.01 ± 0.20	1.01 ± 0.19
gamma_stat_BVETO_regionD_El_bin_0	1.02 ± 0.29	1.02 ± 0.29
gamma_stat_BVETO_regionD_Mu_bin_0	1.00 ± 0.06	1.00 ± 0.06
gamma_stat_Compl_el_bin_0	0.92 ± 0.09	0.92 ± 0.10
gamma_stat_Compl_el_bin_1	1.22 ± 0.11	1.23 ± 0.09
gamma_stat_Compl_el_bin_10	1.03 ± 0.04	1.027 ± 0.035
gamma_stat_Compl_el_bin_12	0.99 ± 0.04	0.98 ± 0.04
gamma_stat_Compl_el_bin_13	0.99 ± 0.05	1.01 ± 0.04
gamma_stat_Compl_el_bin_14	0.99 ± 0.06	1.00 ± 0.05
gamma_stat_Compl_el_bin_15	1.00 ± 0.06	1.02 ± 0.05
gamma_stat_Compl_el_bin_16	0.92 ± 0.06	0.92 ± 0.06
gamma_stat_Compl_el_bin_17	0.89 ± 0.06	0.89 ± 0.06
gamma_stat_Compl_el_bin_18	1.03 ± 0.08	1.02 ± 0.07
gamma_stat_Compl_el_bin_19	0.98 ± 0.09	0.99 ± 0.07
gamma_stat_Compl_el_bin_2	0.88 ± 0.09	0.88 ± 0.10
gamma_stat_Compl_el_bin_20	1.13 ± 0.12	1.10 ± 0.08
gamma_stat_Compl_el_bin_21	1.05 ± 0.13	1.05 ± 0.09
gamma_stat_Compl_el_bin_22	0.95 ± 0.09	0.96 ± 0.07
gamma_stat_Compl_el_bin_23	1.01 ± 0.12	1.01 ± 0.09
gamma_stat_Compl_el_bin_24	1.07 ± 0.13	1.08 ± 0.09
gamma_stat_Compl_el_bin_25	0.98 ± 0.08	0.97 ± 0.07
gamma_stat_Compl_el_bin_26	0.93 ± 0.07	0.92 ± 0.08
gamma_stat_Compl_el_bin_27	1.28 ± 0.12	1.27 ± 0.08
gamma_stat_Compl_el_bin_28	0.95 ± 0.07	0.95 ± 0.08
gamma_stat_Compl_el_bin_29	1.06 ± 0.08	1.05 ± 0.07
gamma_stat_Compl_el_bin_3	1.33 ± 0.14	1.33 ± 0.09
gamma_stat_Compl_el_bin_4	1.31 ± 0.12	1.31 ± 0.08
gamma_stat_Compl_el_bin_5	1.12 ± 0.07	1.11 ± 0.06
gamma_stat_Compl_el_bin_6	1.25 ± 0.07	1.23 ± 0.05
gamma_stat_Compl_el_bin_7	1.10 ± 0.05	1.09 ± 0.04
gamma_stat_Compl_el_bin_8	1.04 ± 0.04	1.04 ± 0.04
gamma_stat_Compl_el_bin_9	0.99 ± 0.04	0.99 ± 0.04
<i>continued on next page</i>		

<i>continued from previous page</i>		
Nuisance parameter name	μ unconstrained	$\mu = 0$
gamma_stat_Compl_mu_bin_0	0.89±0.09	0.89±0.10
gamma_stat_Compl_mu_bin_1	1.01±0.09	1.00±0.08
gamma_stat_Compl_mu_bin_16	1.00±0.06	1.01±0.05
gamma_stat_Compl_mu_bin_17	1.00±0.08	1.01±0.06
gamma_stat_Compl_mu_bin_18	1.01±0.08	1.00±0.07
gamma_stat_Compl_mu_bin_19	1.09±0.09	1.10±0.06
gamma_stat_Compl_mu_bin_2	1.31±0.15	1.31±0.11
gamma_stat_Compl_mu_bin_20	0.84±0.12	0.85±0.11
gamma_stat_Compl_mu_bin_21	1.07±0.13	1.05±0.09
gamma_stat_Compl_mu_bin_22	1.07±0.09	1.08±0.08
gamma_stat_Compl_mu_bin_23	1.02±0.11	1.03±0.08
gamma_stat_Compl_mu_bin_24	0.98±0.10	0.96±0.09
gamma_stat_Compl_mu_bin_25	1.01±0.09	1.01±0.07
gamma_stat_Compl_mu_bin_26	1.00±0.09	1.00±0.08
gamma_stat_Compl_mu_bin_27	1.07±0.10	1.07±0.09
gamma_stat_Compl_mu_bin_28	0.93±0.08	0.93±0.09
gamma_stat_Compl_mu_bin_29	1.08±0.09	1.08±0.08
gamma_stat_Compl_mu_bin_3	1.05±0.07	1.03±0.06
gamma_stat_Compl_mu_bin_4	1.10±0.06	1.09±0.05
gamma_stat_Compl_mu_bin_5	0.98±0.04	0.98±0.04
gamma_stat_EM_EMUBTAG_B_bin_0	1.0±0.4	1.0±0.4
gamma_stat_EM_EMUBTAG_C_bin_0	1.01±0.16	1.01±0.16
gamma_stat_EM_EMUBTAG_D_bin_0	1.01±0.22	1.01±0.22
gamma_stat_EM_EMUBTAG_SR_bin_1	0.97±0.11	0.97±0.12
gamma_stat_EM_EMUBTAG_SR_bin_2	0.99±0.08	0.99±0.08
gamma_stat_EM_EMUBTAG_SR_bin_3	1.00±0.07	1.00±0.07
gamma_stat_EM_EMUBTAG_SR_bin_4	0.97±0.08	0.97±0.08
gamma_stat_EM_EMUBTAG_SR_bin_5	0.91±0.08	0.91±0.09
gamma_stat_EM_EMUBTAG_SR_bin_6	1.07±0.11	1.07±0.09
gamma_stat_EM_EMUBTAG_SR_bin_7	0.99±0.08	0.99±0.08
gamma_stat_EM_EMUBTAG_SR_bin_8	0.99±0.08	0.99±0.08
gamma_stat_EM_EMUBTAG_SR_bin_9	1.02±0.11	1.02±0.10
gamma_stat_EM_EMUBVETO_B_bin_0	1.00±0.07	1.00±0.07
gamma_stat_EM_EMUBVETO_C_bin_0	1.00±0.09	1.00±0.09
gamma_stat_EM_EMUBVETO_D_bin_0	1.01±0.12	1.01±0.11
gamma_stat_EM_EMUBVETO_SR_bin_0	1.02±0.07	1.01±0.07
gamma_stat_EM_EMUBVETO_SR_bin_13	0.99±0.06	0.99±0.05
gamma_stat_EM_EMUBVETO_SR_bin_15	0.96±0.06	0.97±0.06
gamma_stat_EM_EMUBVETO_SR_bin_16	0.99±0.08	0.98±0.07
gamma_stat_EM_EMUBVETO_SR_bin_17	1.07±0.06	1.07±0.04
gamma_stat_EM_EMUBVETO_SR_bin_19	1.03±0.09	1.04±0.08
gamma_stat_EM_EMUBVETO_SR_bin_20	0.98±0.05	0.98±0.06
<i>continued on next page</i>		

<i>continued from previous page</i>		
Nuisance parameter name	μ unconstrained	$\mu = 0$
gamma_stat_EM_EMUBVETO_SR_bin_22	0.99±0.06	0.99±0.06
gamma_stat_EM_EMUBVETO_SR_bin_23	1.00±0.06	1.00±0.06
gamma_stat_HH_AtLeastOneBJet_Denominator_bin_0	1.0±0.4	1.0±0.4
gamma_stat_HH_AtLeastOneBJet_Numerator_bin_0	1.01±0.20	1.01±0.20
gamma_stat_HH_AtLeastOneBJet_Shape_bin_0	1.1±0.7	1.1±0.7
gamma_stat_HH_AtLeastOneBJet_Signal_bin_0	1.08±0.32	1.07±0.26
gamma_stat_HH_AtLeastOneBJet_Signal_bin_1	1.3±0.4	1.34±0.27
gamma_stat_HH_AtLeastOneBJet_Signal_bin_2	0.73±0.25	0.73±0.27
gamma_stat_HH_NoBJetKinSel_Denominator_bin_0	1.01±0.10	1.01±0.10
gamma_stat_HH_NoBJetKinSel_Numerator_bin_0	1.01±0.11	1.01±0.11
gamma_stat_HH_NoBJetKinSel_Signal_bin_0	0.99±0.05	1.00±0.05
gamma_stat_HH_NoBJetKinSel_Signal_bin_10	0.92±0.11	0.92±0.12
gamma_stat_HH_NoBJetKinSel_Signal_bin_11	0.88±0.17	0.88±0.19
gamma_stat_HH_NoBJetKinSel_Signal_bin_12	0.99±0.21	0.99±0.22
gamma_stat_HH_NoBJetKinSel_Signal_bin_13	1.08±0.17	1.08±0.15
gamma_stat_HH_NoBJetKinSel_Signal_bin_2	1.06±0.07	1.06±0.05
gamma_stat_HH_NoBJetKinSel_Signal_bin_3	1.06±0.07	1.06±0.05
gamma_stat_HH_NoBJetKinSel_Signal_bin_4	0.96±0.05	0.96±0.05
gamma_stat_HH_NoBJetKinSel_Signal_bin_5	1.02±0.07	1.02±0.07
gamma_stat_HH_NoBJetKinSel_Signal_bin_6	1.05±0.08	1.05±0.08
gamma_stat_HH_NoBJetKinSel_Signal_bin_7	1.06±0.09	1.06±0.08
gamma_stat_HH_NoBJetKinSel_Signal_bin_8	0.95±0.11	0.95±0.11
gamma_stat_HH_NoBJetKinSel_Signal_bin_9	0.97±0.13	0.97±0.14
gamma_stat_bTaggedDef_el_bin_0	0.97±0.17	0.97±0.16
gamma_stat_bTaggedDef_el_bin_1	1.03±0.13	1.05±0.11
gamma_stat_bTaggedDef_el_bin_2	0.93±0.14	0.94±0.14
gamma_stat_bTaggedDef_el_bin_3	1.01±0.15	1.01±0.13
gamma_stat_bTaggedDef_el_bin_4	1.09±0.21	1.09±0.16
gamma_stat_bTaggedDef_el_bin_5	1.30±0.19	1.29±0.13
gamma_stat_bTaggedDef_mu_bin_0	1.12±0.14	1.14±0.12
gamma_stat_bTaggedDef_mu_bin_1	1.12±0.10	1.13±0.08
gamma_stat_bTaggedDef_mu_bin_2	1.10±0.16	1.11±0.13
gamma_stat_bTaggedDef_mu_bin_3	1.01±0.13	1.02±0.11
gamma_stat_bTaggedDef_mu_bin_4	0.97±0.16	0.97±0.14
gamma_stat_bTaggedDef_mu_bin_5	0.81±0.13	0.81±0.14
tauD_LH_BTAG_El	170±9	170±9
tauD_LH_BTAG_Mu	2690±40	2690±40
tauD_LH_BVETO_El	1716±29	1717±29
tauD_LH_BVETO_Mu	20630±100	2630±100
tauDrel_HH_AtLeastOneBJet	1.00±0.09	1.00±0.09
tauDrel_HH_NoBJetKinSel	1.001±0.018	1.001±0.018
tauratio_LH_BTAG_El	1.00±0.07	1.00±0.07

continued on next page

<i>continued from previous page</i>		
Nuisance parameter name	μ unconstrained	$\mu = 0$
tauratio_LH_BTAg_Mu	1.024 ± 0.020	1.024 ± 0.019
tauratio_LH_BVETO_El	1.059 ± 0.024	1.058 ± 0.023
tauratio_LH_BVETO_Mu	1.157 ± 0.008	1.157 ± 0.007
tauratiorel_HH_AtLeastOneBJet	1.02 ± 0.12	1.01 ± 0.12
tauratiorel_HH_NoBJetKinSel	1.010 ± 0.028	1.009 ± 0.026
taushaperel_HH_AtLeastOneBJet	1.02 ± 0.18	1.02 ± 0.16
taushaperel_HH_NoBJetKinSel	1.010 ± 0.018	1.009 ± 0.016

Table C.2.: Values of the nuisance parameters obtained in the unconditional (signal strength μ unconstrained) and the conditional likelihood minimisation procedure for $\mu = 0$. The term **Lumi** refers to the parameter with which the luminosity uncertainty is modelled. The name of nuisance parameters that model systematic uncertainties starts with **alpha_** and a value of 0 is the nominal value. Values of ± 1 correspond to $\pm 1\sigma$ variations. The values of the 113 nuisance parameters with which the uncertainty due to limited number of events in the simulated samples is modelled starts with **gamma_**. The nominal value is 1 and a 5% upward fluctuation in a bin corresponds to the value 1.05. The other nuisance parameters are used to relate event yields in the signal and control regions in the estimation of the top and multi-jet backgrounds.

Bibliography

- [1] O. Brüning *et al.*, *LHC Design Report Volume 1: The LHC Main Ring*, Tech. Rep. CERN-2004-003-V-1, CERN, Geneva, 2004.
- [2] ATLAS Collaboration, G. Aad *et al.*, *Observation of a new particle in the search for the Standard Model Higgs boson with the ATLAS detector at the LHC*, Phys. Lett. **B716** (2012) 1–29, [arXiv:1207.7214 \[hep-ex\]](#).
- [3] CMS Collaboration, S. Chatrchyan *et al.*, *Observation of a new boson at a mass of 125 GeV with the CMS experiment at the LHC*, Phys. Lett. **B716** (2012) 30–61, [arXiv:1207.7235 \[hep-ex\]](#).
- [4] S. P. Martin, *A Supersymmetry primer*, [arXiv:hep-ph/9709356 \[hep-ph\]](#).
- [5] Planck Collaboration, P. A. R. Ade *et al.*, *Planck 2013 results. XVI. Cosmological parameters*, [arXiv:1303.5076 \[astro-ph.CO\]](#).
- [6] Particle Data Group, J. Beringer *et al.*, *Review of Particle Physics*, Phys. Rev. D **86** (2012) 010001.
- [7] S. W. Herb *et al.*, *Observation of a Dimuon Resonance at 9.5 GeV in 400-GeV Proton-Nucleus Collisions*, Phys. Rev. Lett. **39** (1977) 252–255.
- [8] CDF Collaboration, F. Abe *et al.*, *Observation of Top Quark Production in $\bar{p}p$ Collisions with the Collider Detector at Fermilab*, Phys. Rev. Lett. **74** (1995) 2626–2631.
- [9] D0 Collaboration, S. Abachi *et al.*, *Search for High Mass Top Quark Production in $p\bar{p}$ Collisions at $\sqrt{s} = 1.8$ TeV*, Phys. Rev. Lett. **74** (1995) 2422–2426.
- [10] DONUT Collaboration, K. Kodama *et al.*, *Observation of tau neutrino interactions*, Phys. Lett. **B504** (2001) 218–224, [arXiv:hep-ex/0012035 \[hep-ex\]](#).
- [11] A. Pich, *The Standard Model of Electroweak Interactions in Proceedings of the 2010 European School of High-Energy Physics*, Raseborg, Finland, 2012. [arXiv:1201.0537 \[hep-ph\]](#).
- [12] F. Halzen and A. D. Martin, *Quarks and Leptons: An Introductory Course in Modern Particle Physics*, Wiley, 1984.
- [13] M. E. Peskin and D. V. Schroeder, *An Introduction to Quantum Field Theory*, Westview Press, 1995.
- [14] F. J. Ynduráin, *Limits on the mass of the gluon*, Phys. Lett. **B345** (1995) 524–526.
- [15] Y. Nambu, *Quasi-Particles and Gauge Invariance in the Theory of Superconductivity*, Phys. Rev. **117** (1960) 648–663.

- [16] J. Goldstone, *Field theories with Superconductor solutions*, Il Nuovo Cimento **19** (1961) 154–164.
- [17] J. Goldstone, A. Salam, and S. Weinberg, *Broken Symmetries*, Phys. Rev. **127** (1962) 965–970.
- [18] N. Cabibbo, *Unitary Symmetry and Leptonic Decays*, Phys. Rev. Lett. **10** (1963) 531–533.
- [19] M. Kobayashi and T. Maskawa, *CP-Violation in the Renormalizable Theory of Weak Interaction*, Prog. Theor. Phys. **49** no. 2, (1973) 652–657.
- [20] Z. Maki, M. Nakagawa, and S. Sakata, *Remarks on the unified model of elementary particles*, Prog. Theor. Phys. **28** (1962) 870–880.
- [21] A. Romanino, *Neutrino Physics in Proceedings of the 2010 European School of High-Energy Physics*, Raseborg, Finland, 2012. [arXiv:1201.6158 \[hep-ph\]](#).
- [22] WMAP Collaboration, G. Hinshaw *et al.*, *Nine-Year Wilkinson Microwave Anisotropy Probe (WMAP) Observations: Cosmological Parameter Results*, [arXiv:1212.5226 \[astro-ph.CO\]](#).
- [23] Planck Collaboration, P. A. R. Ade *et al.*, *Planck 2013 results. I. Overview of products and scientific results*, [arXiv:1303.5062 \[astro-ph.CO\]](#).
- [24] H. Kurki-Suonio, *Physics of the Cosmic Microwave Background and the Planck Mission in Proceedings of the 2010 European School of High-Energy Physics*, Raseborg, Finland, 2012. [arXiv:1012.5204 \[astro-ph.CO\]](#).
- [25] A. D. Sakharov, *Violation of CP invariance, C asymmetry, and baryon asymmetry of the universe*, Pis'ma Zh. Eksp. Teor. Fiz. **5** (1967) 32–35.
- [26] F.-K. Guo and U.-G. Meissner, *Baryon electric dipole moments from strong CP violation*, JHEP **1212** (2012) 097, [arXiv:1210.5887 \[hep-ph\]](#).
- [27] M. E. Peskin, *Beyond the Standard Model*, [arXiv:hep-ph/9705479 \[hep-ph\]](#).
- [28] S. Coleman and J. Mandula, *All Possible Symmetries of the S Matrix*, Phys. Rev. **159** (1967) 1251–1256.
- [29] R. Haag, J. T. Lopuszański, and M. Sohnius, *All Possible Generators of Supersymmetries of the S-Matrix*, Nucl. Phys. **B88** (1975) 257–274.
- [30] H. P. Nilles, *Supersymmetry, Supergravity and Particle Physics*, Phys. Rept. **110** (1984) 1–162.
- [31] J. Wess and B. Zumino, *Supergauge Invariant Extension of Quantum Electrodynamics*, Nucl. Phys. **B78** (1974) 1.
- [32] M. Drees, *Supersymmetric dark matter: Relic density and detection*, [arXiv:hep-ph/9402211 \[hep-ph\]](#).
- [33] J. F. Gunion *et al.*, *The Higgs Hunter's Guide*, Frontiers in Physics, Perseus Pub., 2000.
- [34] M. Trodden, *Electroweak Baryogenesis: A Brief Review*, [arXiv:hep-ph/9805252 \[hep-ph\]](#).

- [35] R. D. Peccei and H. R. Quinn, *CP Conservation in the Presence of Instantons*, Phys. Rev. Lett. **38** (1977) 1440–1443.
- [36] R. D. Peccei and H. R. Quinn, *Constraints Imposed by CP Conservation in the Presence of Instantons*, Phys. Rev. **D16** (1977) 1791–1797.
- [37] S. Davidson and H. E. Haber, *Basis-independent methods for the two-Higgs-doublet model*, Phys. Rev. **D72** (2005) 035004, [arXiv:hep-ph/0504050 \[hep-ph\]](#), Erratum-ibid. **D72** (2002) 099902.
- [38] D. Kominis, *The Phenomenology of the CP-odd scalar in two-doublet models*, Nucl. Phys. **B427** (1994) 575–613, [arXiv:hep-ph/9402339 \[hep-ph\]](#).
- [39] J. F. Gunion and H. E. Haber, *CP-conserving two-Higgs-doublet model: The Approach to the decoupling limit*, Phys. Rev. **D67** (2003) 075019, [arXiv:hep-ph/0207010 \[hep-ph\]](#).
- [40] M. Maniatis *et al.*, *Stability and symmetry breaking in the general two-Higgs-doublet model*, Eur. Phys. J. **C48** (2006) 805–823, [arXiv:hep-ph/0605184 \[hep-ph\]](#).
- [41] ATLAS Collaboration, *Improved Luminosity Determination in pp Collisions at $\sqrt{s} = 7$ TeV using the ATLAS Detector at the LHC*, Tech. Rep. ATLAS-CONF-2012-080, CERN, Geneva, 2012.
- [42] J. C. Collins, D. E. Soper, and G. F. Sterman, *Factorization of Hard Processes in QCD*, Adv. Ser. Direct. High Energy Phys. **5** (1988) 1–91, [arXiv:hep-ph/0409313 \[hep-ph\]](#).
- [43] P. Z. Skands, *QCD for Collider Physics in Proceedings of the 2010 European School of High-Energy Physics*, Raseborg, Finland, 2012. [arXiv:1104.2863 \[hep-ph\]](#).
- [44] Y. L. Dokshitzer, *Calculation of the Structure Functions for Deep Inelastic Scattering and e^+e^- Annihilation by Perturbation Theory in Quantum Chromodynamics*, Sov. Phys. JETP **46** (1977) 641–653.
- [45] V. N. Gribov and L. N. Lipatov, *Deep inelastic $e p$ scattering in perturbation theory*, Sov. J. Nucl. Phys. **15** (1972) 438–450.
- [46] G. Altarelli and G. Parisi, *Asymptotic Freedom in Parton Language*, Nucl. Phys. **B126** (1977) 298.
- [47] J. Pumplin *et al.*, *New generation of parton distributions with uncertainties from global QCD analysis*, JHEP **0207** (2002) 012, [arXiv:hep-ph/0201195 \[hep-ph\]](#).
- [48] P. M. Nadolsky *et al.*, *Implications of CTEQ global analysis for collider observables*, Phys. Rev. **D78** (2008) 013004, [arXiv:0802.0007 \[hep-ph\]](#).
- [49] H.-L. Lai *et al.*, *New parton distributions for collider physics*, Phys. Rev. **D82** (2010) 074024, [arXiv:1007.2241 \[hep-ph\]](#).
- [50] A. D. Martin *et al.*, *Parton distributions for the LHC*, Eur. Phys. J. **C63** (2009) 189–285, [arXiv:0901.0002 \[hep-ph\]](#).
- [51] A. Sherstnev and R. S. Thorne, *Parton distributions for LO generators*, Eur. Phys. J. **C55** (2008) 553–575, [arXiv:0711.2473 \[hep-ph\]](#).

- [52] A. D. Martin *et al.*, *MSTW PDFs: key plots*, <http://mstwpdf.hepforge.org/plots/plots.html>, accessed 18-Jun-2013.
- [53] M. Drees, P. Roy, and R. Godbole, *Theory And Phenomenology of Sparticles: An Account of Four-dimensional N=1 Supersymmetry in High Energy Physics*, World Scientific, 2004.
- [54] M. Dobbs and J. B. Hansen, *The HepMC C++ Monte Carlo event record for High Energy Physics*, Comput. Phys. Commun. **134** (2001) 41–46.
- [55] E. Barberio, B. van Eijk, and Z. Wąs, *PHOTOS - a universal Monte Carlo for QED radiative corrections in decays*, Comput. Phys. Commun. **66** (1991) 115–128.
- [56] A. Buckley *et al.*, *General-purpose event generators for LHC physics*, Phys. Rept. **504** (2011) 145–233, [arXiv:1101.2599 \[hep-ph\]](#).
- [57] S. Schumann and F. Krauss, *A Parton shower algorithm based on Catani-Seymour dipole factorisation*, JHEP **0803** (2008) 038, [arXiv:0709.1027 \[hep-ph\]](#).
- [58] J. Alwall *et al.*, *Comparative study of various algorithms for the merging of parton showers and matrix elements in hadronic collisions*, Eur. Phys. J. **C53** (2008) 473–500, [arXiv:0706.2569 \[hep-ph\]](#).
- [59] S. Catani *et al.*, *QCD matrix elements + parton showers*, JHEP **0111** (2001) 063, [arXiv:hep-ph/0109231 \[hep-ph\]](#).
- [60] F. Krauss, *Matrix elements and parton showers in hadronic interactions*, JHEP **0208** (2002) 015, [arXiv:hep-ph/0205283 \[hep-ph\]](#).
- [61] S. Alioli *et al.*, *NLO Higgs boson production via gluon fusion matched with shower in POWHEG*, JHEP **0904** (2009) 002, [arXiv:0812.0578 \[hep-ph\]](#).
- [62] S. Frixione and B. R. Webber, *Matching NLO QCD computations and parton shower simulations*, JHEP **0206** (2002) 029, [arXiv:hep-ph/0204244 \[hep-ph\]](#).
- [63] S. Catani, Y. L. Dokshitzer, M. Olsson, G. Turnock, and B. R. Webber, *New clustering algorithm for multi-jet cross-sections in e^+e^- annihilation*, Phys. Lett. **B269** (1991) 432–438.
- [64] B. Andersson *et al.*, *Parton Fragmentation and String Dynamics*, Phys. Rept. **97** (1983) 31–145.
- [65] S. Jadach, J. H. Kühn, and Z. Wąs, *TAUOLA - a library of Monte Carlo programs to simulate decays of polarized τ leptons*, Comput. Phys. Commun. **64** (1990) 275–299.
- [66] J. M. Butterworth, J. R. Forshaw, and M. H. Seymour, *Multiparton interactions in photoproduction at HERA*, Z. Phys. **C72** (1996) 637–646, [arXiv:hep-ph/9601371 \[hep-ph\]](#).
- [67] ATLAS Collaboration, *ATLAS tunes of PYTHIA 6 and Pythia 8 for MC11*, Tech. Rep. ATL-PHYS-PUB-2011-009, CERN, Geneva, 2011.
- [68] P. Z. Skands, *Tuning Monte Carlo generators: The Perugia tunes*, Phys. Rev. **D82** (2010) 074018, [arXiv:1005.3457 \[hep-ph\]](#).

- [69] L. Evans and P. Bryant, *LHC Machine*, JINST **3** (2008) S08001.
- [70] GEANT4, S. Agostinelli *et al.*, *GEANT4: A Simulation toolkit*, Nucl. Instrum. Meth. **A506** (2003) 250–303.
- [71] I. Bird *et al.*, *LHC computing Grid: Technical Design Report*, Tech. Rep. CERN-LHCC-2005-024, CERN, Geneva, 2005.
- [72] LHC Higgs Cross Section Working Group, S. Dittmaier *et al.*, *Handbook of LHC Higgs cross sections: 1. Inclusive observables*, arXiv:1101.0593 [hep-ph].
- [73] LHC Higgs Cross Section Working Group, S. Dittmaier *et al.*, *LHC Higgs Cross Section Working Group Twiki*, <https://twiki.cern.ch/twiki/bin/view/LHCPhysics/CrossSections>, accessed 15-Jun-2013.
- [74] M. Carena *et al.*, *Suggestions for improved benchmark scenarios for Higgs boson searches at LEP2*, arXiv:hep-ph/9912223 [hep-ph].
- [75] M. Carena *et al.*, *Suggestions for benchmark scenarios for MSSM Higgs boson searches at hadron colliders*, Eur. Phys. J. **C26** (2003) 601, arXiv:hep-ph/0202167 [hep-ph].
- [76] F. Jegerlehner and A. Nyffeler, *The muon $g-2$* , Phys. Rept. **477** (2009) 1–110, arXiv:0902.3360 [hep-ph].
- [77] M. Frank *et al.*, *The Higgs boson masses and mixings of the complex MSSM in the Feynman-diagrammatic approach*, JHEP **0702** (2007) 047, arXiv:hep-ph/0611326 [hep-ph].
- [78] M. Carena, S. Heinemeyer, O. Stål, C. E. M. Wagner, and G. Weiglein, *MSSM Higgs Boson Searches at the LHC: Benchmark Scenarios after the Discovery of a Higgs-like Particle*, arXiv:1302.7033 [hep-ph].
- [79] A. Djouadi, *The Anatomy of electro-weak symmetry breaking. II. The Higgs bosons in the minimal supersymmetric model*, Phys. Rept. **459** (2008) 1–241, arXiv:hep-ph/0503173 [hep-ph].
- [80] ATLAS Collaboration, G. Aad *et al.*, *Observation of a new particle in the search for the Standard Model Higgs boson with the ATLAS detector at the LHC*, Phys. Lett. **B716** (2012) 1–29, arXiv:1207.7214 [hep-ex].
- [81] ATLAS Collaboration, G. Aad *et al.*, *A Particle Consistent with the Higgs Boson Observed with the ATLAS Detector at the Large Hadron Collider*, Science **338** (2012) 1576–1582, <http://cds.cern.ch/record/1511050>.
- [82] CMS Collaboration, S. Chatrchyan *et al.*, *Observation of a new boson at a mass of 125 GeV with the CMS experiment at the LHC*, Phys. Lett. **B716** (2012) 30–61, arXiv:1207.7235 [hep-ex].
- [83] ATLAS Collaboration, *Combined measurements of the mass and signal strength of the Higgs-like boson with the ATLAS detector using up to 25 fb⁻¹ of proton-proton collision data*, Tech. Rep. ATLAS-CONF-2013-014, CERN, Geneva, 2013.
- [84] ATLAS Collaboration, *Combined coupling measurements of the Higgs-like boson with the ATLAS detector using up to 25 fb⁻¹ of proton-proton collision data*, Tech. Rep. ATLAS-CONF-2013-034, CERN, Geneva, 2013.

- [85] CMS Collaboration, *Combination of standard model Higgs boson searches and measurements of the properties of the new boson with a mass near 125 GeV*, Tech. Rep. CMS-PAS-HIG-13-005, CERN, Geneva, 2013.
- [86] CDF Collaboration, D0 Collaboration, T. Aaltonen *et al.*, *Evidence for a particle produced in association with weak bosons and decaying to a bottom-antibottom quark pair in Higgs boson searches at the Tevatron*, Phys. Rev. Lett. **109** (2012) 071804, arXiv:1207.6436 [hep-ex].
- [87] S. Heinemeyer, O. Stål, and G. Weiglein, *Interpreting the LHC Higgs search results in the MSSM*, Phys. Lett. **B710** (2012) 201–206, arXiv:1112.3026 [hep-ph].
- [88] A. Arbey *et al.*, *The Higgs sector of the phenomenological MSSM in the light of the Higgs boson discovery*, JHEP **1209** (2012) 107, arXiv:1207.1348 [hep-ph].
- [89] ALEPH Collaboration, DELPHI Collaboration, L3 Collaboration, OPAL Collaboration, LEP Working Group for Higgs Boson Searches, S. Schael *et al.*, *Search for neutral MSSM Higgs bosons at LEP*, Eur. Phys. J. **C47** (2006) 547–587, arXiv:hep-ex/0602042 [hep-ex].
- [90] CDF Collaboration, D0 Collaboration, T. Aaltonen *et al.*, *Search for neutral Higgs bosons in events with multiple bottom quarks at the Tevatron*, Phys. Rev. **D86** (2012) 091101, arXiv:1207.2757 [hep-ex].
- [91] CDF Collaboration, T. Aaltonen *et al.*, *Search for Higgs Bosons Predicted in Two-Higgs-Doublet Models via Decays to Tau Lepton Pairs in 1.96 TeV $p\bar{p}$ Collisions*, Phys. Rev. Lett. **103** (2009) 201801, arXiv:0906.1014 [hep-ex].
- [92] D0 Collaboration, V. M. Abazov *et al.*, *Search for Higgs bosons of the minimal supersymmetric standard model in $p\bar{p}$ collisions at $\sqrt{s} = 1.96$ TeV*, Phys. Lett. **B710** (2012) 569–577, arXiv:1112.5431 [hep-ex].
- [93] CDF Collaboration, D. Acosta *et al.*, *Search for New Physics Using High-Mass Tau Pairs from 1.96 TeV $p\bar{p}$ Collisions*, Phys. Rev. Lett. **95** (2005) 131801, arXiv:hep-ex/0506034 [hep-ex].
- [94] ATLAS Collaboration, G. Aad *et al.*, *Search for neutral MSSM Higgs bosons decaying to $\tau^+\tau^-$ pairs in proton-proton collisions at $\sqrt{s} = 7$ TeV with the ATLAS detector*, Phys. Lett. **B705** (2011) 174–192, arXiv:1107.5003 [hep-ex].
- [95] ATLAS Collaboration, *Search for neutral MSSM Higgs bosons decaying to $\tau^+\tau^-$ pairs in proton-proton collisions at $\sqrt{s} = 7$ TeV with the ATLAS detector*, Tech. Rep. ATLAS-CONF-2011-132, CERN, Geneva, 2011.
- [96] ATLAS Collaboration, G. Aad *et al.*, *Search for the neutral Higgs bosons of the Minimal Supersymmetric Standard Model in pp collisions at $\sqrt{s} = 7$ TeV with the ATLAS detector*, JHEP **1302** (2013) 095, arXiv:1211.6956 [hep-ex].
- [97] ATLAS Collaboration, *Search for neutral MSSM Higgs bosons in $\sqrt{s} = 7$ TeV pp collisions with the ATLAS detector*, Tech. Rep. ATLAS-CONF-2012-094, CERN, Geneva, 2012.
- [98] ATLAS Collaboration, *Search for Higgs bosons in Two-Higgs-Doublet models in the $H \rightarrow WW \rightarrow e\nu\mu\nu$ channel with the ATLAS detector*, Tech. Rep. ATLAS-CONF-2013-027, CERN, Geneva, 2013.

- [99] CMS Collaboration, S. Chatrchyan *et al.*, *Search for neutral Higgs bosons decaying to tau pairs in pp collisions at $\sqrt{s} = 7$ TeV*, Phys. Lett. **B713** (2012) 68–90, [arXiv:1202.4083 \[hep-ex\]](#).
- [100] CMS Collaboration, *Search for MSSM Neutral Higgs Bosons Decaying to Tau Pairs in pp Collisions*, Tech. Rep. CMS-PAS-HIG-12-050, CERN, Geneva, 2012.
- [101] CDF Collaboration, T. Aaltonen *et al.*, *Search for Charged Higgs Bosons in Decays of Top Quarks in $p\bar{p}$ Collisions at $\sqrt{s} = 1.96$ TeV*, Phys. Rev. Lett. **103** (2009) 101803, [arXiv:0907.1269 \[hep-ex\]](#).
- [102] D0 Collaboration, V. M. Abazov *et al.*, *Search for charged Higgs bosons in top quark decays*, Phys. Lett. **B682** (2009) 278–286, [arXiv:0908.1811 \[hep-ex\]](#).
- [103] ATLAS Collaboration, G. Aad *et al.*, *Search for a light charged Higgs boson in the decay channel $H^+ \rightarrow c\bar{s}$ in $t\bar{t}$ events using pp collisions at $\sqrt{s} = 7$ TeV with the ATLAS detector*, Eur. Phys. J. **C73** (2013) 2465, [arXiv:1302.3694 \[hep-ex\]](#).
- [104] ATLAS Collaboration, G. Aad *et al.*, *Search for charged Higgs bosons through the violation of lepton universality in $t\bar{t}$ events using pp collision data at $\sqrt{s} = 7$ TeV with the ATLAS experiment*, JHEP **1303** (2013) 076, [arXiv:1212.3572 \[hep-ex\]](#).
- [105] ATLAS Collaboration, G. Aad *et al.*, *Search for charged Higgs bosons decaying via $H^+ \rightarrow \tau\nu$ in top quark pair events using pp collision data at $\sqrt{s} = 7$ TeV with the ATLAS detector*, JHEP **1206** (2012) 039, [arXiv:1204.2760 \[hep-ex\]](#).
- [106] CMS Collaboration, S. Chatrchyan *et al.*, *Search for a light charged Higgs boson in top quark decays in pp collisions at $\sqrt{s} = 7$ TeV*, JHEP **1207** (2012) 143, [arXiv:1205.5736 \[hep-ex\]](#).
- [107] BaBar Collaboration, B. Aubert *et al.*, *The BaBar Detector: Upgrades, Operation and Performance*, [arXiv:1305.3560 \[physics.ins-det\]](#).
- [108] Belle Collaboration, A. Abashian *et al.*, *The Belle detector*, Nucl. Instrum. Meth. **A479** (2002) 117–232.
- [109] LHCb Collaboration, *LHCb Technical Design Report: Reoptimized Detector Design and Performance*, Tech. Rep. CERN-LHCC-2003-030, CERN, Geneva, 2003.
- [110] BaBar Collaboration, J. Lees *et al.*, *Measurement of $B(B \rightarrow X_s\gamma)$, the $B \rightarrow X_s\gamma$ photon energy spectrum, and the direct CP asymmetry in $B \rightarrow X_{s+d}\gamma$ decays*, Phys. Rev. **D86** (2012) 112008, [arXiv:1207.5772 \[hep-ex\]](#).
- [111] XENON100 Collaboration, E. Aprile *et al.*, *The XENON100 Dark Matter Experiment*, Astropart. Phys. **35** (2012) 573–590, [arXiv:1107.2155 \[astro-ph.IM\]](#).
- [112] ATLAS Collaboration, G. Aad *et al.*, *ATLAS Supersymmetry (SUSY) searches*, <https://twiki.cern.ch/twiki/bin/view/AtlasPublic/SupersymmetryPublicResults>, accessed 17-Jun-2013.
- [113] CMS Collaboration, S. Chatrchyan *et al.*, *CMS Supersymmetry Physics Results*, <https://twiki.cern.ch/twiki/bin/view/CMSPublic/PhysicsResultsSUS>, accessed 17-Jun-2013.

- [114] XENON100 Collaboration, E. Aprile *et al.*, *Dark Matter Results from 225 Live Days of XENON100 Data*, Phys. Rev. Lett. **109** (2012) 181301, [arXiv:1207.5988 \[astro-ph.CO\]](#).
- [115] W. Altmannshofer, M. Carena, N. R. Shah, and F. Yu, *Indirect Probes of the MSSM after the Higgs Discovery*, JHEP **1301** (2013) 160, [arXiv:1211.1976 \[hep-ph\]](#).
- [116] LHCb Collaboration, R. Aaij *et al.*, *First Evidence for the Decay $B_s^0 \rightarrow \mu^+ \mu^-$* , Phys. Rev. Lett. **110** (2013) 021801, [arXiv:1211.2674 \[hep-ex\]](#).
- [117] CMS Collaboration, S. Chatrchyan *et al.*, *Measurement of the $B_s^0 \rightarrow \mu^+ \mu^-$ branching fraction and search for $B^0 \rightarrow \mu^+ \mu^-$ with the CMS Experiment*, [arXiv:1307.5025 \[hep-ex\]](#), submitted to Phys. Rev. Lett.
- [118] LHCb collaboration, R. Aaij *et al.*, *Measurement of the $B_s^0 \rightarrow \mu^+ \mu^-$ branching fraction and search for $B^0 \rightarrow \mu^+ \mu^-$ decays at the LHCb experiment*, [arXiv:1307.5024 \[hep-ex\]](#), submitted to Phys. Rev. Lett.
- [119] A. J. Buras, J. Girrbach, D. Guadagnoli, and G. Isidori, *On the Standard Model prediction for $\mathcal{B}(B_{s,d} \rightarrow \mu^+ \mu^-)$* , Eur. Phys. J. **C72** (2012) 2172, [arXiv:1208.0934 \[hep-ph\]](#).
- [120] BaBar Collaboration, J. P. Lees *et al.*, *Evidence for an Excess of $\bar{B} \rightarrow D^{(*)} \tau^- \bar{\nu}_\tau$ Decays*, Phys. Rev. Lett. **109** (2012) 101802, [arXiv:1205.5442 \[hep-ex\]](#).
- [121] S. Fajfer, J. F. Kamenik, and I. Nišandžić, *On the $B \rightarrow D^* \tau \bar{\nu}_\tau$ Sensitivity to New Physics*, Phys. Rev. **D85** (2012) 094025, [arXiv:1203.2654 \[hep-ph\]](#).
- [122] Belle Collaboration, K. Hara *et al.*, *Evidence for $B^- \rightarrow \tau^- \bar{\nu}_\tau$ with a semileptonic tagging method*, Phys. Rev. **D82** (2010) 071101, [arXiv:1006.4201 \[hep-ex\]](#).
- [123] Belle Collaboration, I. Adachi *et al.*, *Measurement of $B^- \rightarrow \tau^- \bar{\nu}_\tau$ with a Hadronic Tagging Method Using the Full Data Sample of Belle*, Phys. Rev. Lett. **110** (2013) 131801, [arXiv:1208.4678 \[hep-ex\]](#).
- [124] BaBar Collaboration, J. Lees *et al.*, *Evidence of $B \rightarrow \tau \nu$ decays with hadronic B tags*, [arXiv:1207.0698 \[hep-ex\]](#), submitted to Phys. Rev. D.
- [125] CKMfitter Group, J. Charles *et al.*, *CP violation and the CKM matrix: Assessing the impact of the asymmetric B factories*, Eur. Phys. J. **C41** (2005) 1–131, [arXiv:hep-ph/0406184 \[hep-ph\]](#), preliminary results as of winter 2012, <http://ckmfitter.in2p3.fr>.
- [126] D. Stöckinger, *The muon magnetic moment and supersymmetry*, J. Phys. **G34** (2007) R45–R92, [arXiv:hep-ph/0609168 \[hep-ph\]](#).
- [127] L. Rossi, *Superconductivity: its role, its success and its setbacks in the Large Hadron Collider of CERN*, Supercond. Sci. Technol. **23** (2010) 034001.
- [128] ATLAS Collaboration, G. Aad *et al.*, *The ATLAS Experiment at the CERN Large Hadron Collider*, JINST **3** (2008) S08003.
- [129] CMS Collaboration, S. Chatrchyan *et al.*, *The CMS experiment at the CERN LHC*, JINST **3** (2008) S08004.

- [130] ALICE Collaboration, K. Aamodt *et al.*, *The ALICE experiment at the CERN LHC*, JINST **3** (2008) S08002.
- [131] P. Braun-Munzinger and J. Stachel, *The quest for the quark-gluon plasma*, Nature **448** (2007) 302–309.
- [132] LHCf Collaboration, O. Adriani *et al.*, *The LHCf detector at the CERN Large Hadron Collider*, JINST **3** (2008) S08006.
- [133] TOTEM Collaboration, G. Anelli *et al.*, *The TOTEM experiment at the CERN Large Hadron Collider*, JINST **3** (2008) S08007.
- [134] MoEDAL Collaboration, *Technical Design Report of the MoEDAL Experiment*, Tech. Rep. CERN-LHCC-2009-006, CERN, Geneva, 2009.
- [135] M. Benedikt *et al.*, *LHC Design Report Volume 3: The LHC Injector Chain*, Tech. Rep. CERN-2004-003-V-3, CERN, Geneva, 2004.
- [136] Wikipedia, *File:Cern-accelerator-complex.svg*, <http://en.wikipedia.org/wiki/File:Cern-accelerator-complex.svg>, accessed 20-December-2012.
- [137] J. D. Cockcroft and E. T. S. Walton, *Experiments with High Velocity Positive Ions, Further Developments in the Method of Obtaining High Velocity Positive Ions*, Proc. Roy. Soc. Lond. **A136** (1932) 619–630.
- [138] S. Y. Lee, *Accelerator physics*, World Scientific Publishing Co., 2004.
- [139] ATLAS Collaboration, G. Aad *et al.*, *Measurement of the cross-section for W boson production in association with b -jets in pp collisions at $\sqrt{s} = 7$ TeV with the ATLAS detector*, arXiv:1302.2929 [hep-ex].
- [140] ATLAS Collaboration, *ATLAS Detector and Physics Performance: Technical Design Report*, Tech. Rep. CERN-LHCC-99-014, CERN, Geneva, 1999.
- [141] D. Attree *et al.*, *The evaporative cooling system for the ATLAS inner detector*, JINST **3** (2008) P07003.
- [142] A. Yamamoto *et al.*, *The ATLAS central solenoid*, Nucl. Instrum. Meth. **A584** (2008) 53–74.
- [143] ATLAS Collaboration, G. Aad *et al.*, *A study of the material in the ATLAS inner detector using secondary hadronic interactions*, JINST **7** (2012) P01013, arXiv:1110.6191 [hep-ex].
- [144] B. M. Demirkoz, *Construction and Performance of the ATLAS SCT Barrels and Cosmic Tests*, PhD thesis, Oxford Univ., Oxford, 2007.
- [145] ALICE Collaboration, A. Toia, *Bulk Properties of Pb-Pb collisions at $\sqrt{s_{NN}} = 2.76$ TeV measured by ALICE*, J. Phys. **G38** (2011) 124007, arXiv:1107.1973 [nucl-ex].
- [146] S. van der Meer, *Calibration of the Effective Beam Height in the ISR*, Tech. Rep. CERN-ISR-PO-68-31, CERN, Geneva, 1968.
- [147] R. Hauser, *The ATLAS Data Acquisition and High Level Trigger Systems: Experience and Upgrade Plans*, Tech. Rep. ATL-DAQ-PROC-2012-073, CERN, Geneva, 2012.

- [148] CERN Press Office, *First beam in the LHC - accelerating science*, <http://press.web.cern.ch/press-releases/2008/09/first-beam-lhc-accelerating-science>, accessed 13-May-2013.
- [149] CERN Press Office, *Incident in LHC sector 3-4*, <http://press.web.cern.ch/press-releases/2008/09/incident-lhc-sector-3-4>, accessed 13-May-2013.
- [150] CERN Press Office, *CERN releases analysis of LHC incident*, <http://press.web.cern.ch/press-releases/2008/10/cern-releases-analysis-lhc-incident>, accessed 13-May-2013.
- [151] CERN Press Office, *The LHC is back*, <http://press.web.cern.ch/press-releases/2009/11/lhc-back>, accessed 13-May-2013.
- [152] CERN Press Office, *Two circulating beams bring first collisions in the LHC*, <http://press.web.cern.ch/press-releases/2009/11/two-circulating-beams-bring-first-collisions-lhc>, accessed 13-May-2013.
- [153] ATLAS Collaboration, G. Aad *et al.*, *Performance of the ATLAS detector using first collision data*, JHEP **1009** (2010) 056, arXiv:1005.5254 [hep-ex].
- [154] CERN Press Office, *CERN sets date for first attempt at 7 TeV collisions in the LHC*, <http://press.web.cern.ch/press-releases/2010/03/cern-sets-date-first-attempt-7-tev-collisions-lhc>, accessed 13-May-2013.
- [155] CERN Press Office, *LHC research programme gets underway*, <http://press.web.cern.ch/press-releases/2010/03/lhc-research-programme-gets-underway>, accessed 13-May-2013.
- [156] ATLAS Collaboration, G. Aad *et al.*, *ATLAS Twiki: Luminosity Public Results*, <https://twiki.cern.ch/twiki/bin/view/AtlasPublic/LuminosityPublicResults>, accessed 31-May-2013.
- [157] CERN Press Office, *CERN completes transition to lead-ion running at the LHC*, <http://press.web.cern.ch/press-releases/2010/11/cern-completes-transition-lead-ion-running-lhc>, accessed 13-May-2013.
- [158] CERN Press Office, *LHC proton run for 2011 reaches successful conclusion*, <http://press.web.cern.ch/press-releases/2011/10/lhc-proton-run-2011-reaches-successful-conclusion>, accessed 13-May-2013.
- [159] CERN Press Office, *LHC sets world record beam intensity*, <http://press.web.cern.ch/press-releases/2011/04/lhc-sets-world-record-beam-intensity>, accessed 13-May-2013.
- [160] CERN Press Office, *LHC physics data taking gets underway at new record collision energy of 8TeV*, <http://press.web.cern.ch/press-releases/2012/04/lhc-physics-data-taking-gets-underway-new-record-collision-energy-8tev>, accessed 13-May-2013.
- [161] CERN Press Office, *The first LHC protons run ends with new milestone*, <http://press.web.cern.ch/press-releases/2012/12/first-lhc-protons-run-ends-new-milestone>, accessed 13-May-2013.

- [162] ATLAS Collaboration, G. Aad *et al.*, *ATLAS Twiki: Approved SCT Plots*, <https://twiki.cern.ch/twiki/bin/view/AtlasPublic/ApprovedPlotsSCT>, accessed 18-Feb-2013.
- [163] ATLAS Collaboration, *ATLAS inner detector : Technical Design Report 2*, Tech. Rep. CERN-LHCC-97-017, CERN, Geneva, 1997.
- [164] ATLAS Collaboration, *ATLAS Computing: Technical Design Report*, Tech. Rep. CERN-LHCC-2005-022, CERN, Geneva, 2005.
- [165] T. Cornelissen *et al.*, *Concepts, Design and Implementation of the ATLAS New Tracking (NEWT)*, Tech. Rep. ATL-SOFT-PUB-2007-007, CERN, Geneva, 2007.
- [166] ATLAS Collaboration, *Performance of the ATLAS Inner Detector Track and Vertex Reconstruction in the High Pile-Up LHC Environment*, Tech. Rep. ATLAS-CONF-2012-042, CERN, Geneva, 2012.
- [167] ATLAS Collaboration, G. Aad *et al.*, *ATLAS Twiki: Tracking Performance Public Results*, <https://twiki.cern.ch/twiki/bin/view/AtlasPublic/InDetTrackingPerformanceApprovedPlots>, accessed 31-May-2013.
- [168] ATLAS Collaboration, *Performance of primary vertex reconstruction in proton-proton collisions at $\sqrt{s} = 7$ TeV in the ATLAS experiment*, Tech. Rep. ATLAS-CONF-2010-069, CERN, Geneva, 2010.
- [169] M. Cacciari, G. P. Salam, and G. Soyez, *The anti- k_t jet clustering algorithm*, JHEP **0804** (2008) 063, [arXiv:0802.1189 \[hep-ph\]](#).
- [170] W. Lampl *et al.*, *Calorimeter Clustering Algorithms: Description and Performance*, Tech. Rep. ATL-LARG-PUB-2008-002, CERN, Geneva, 2008.
- [171] ATLAS Collaboration, G. Aad *et al.*, *Measurement of inclusive jet and dijet cross sections in proton-proton collisions at 7 TeV centre-of-mass energy with the ATLAS detector*, Eur. Phys. J. **C71** (2011) 1512, [arXiv:1009.5908 \[hep-ex\]](#).
- [172] T. Barillari *et al.*, *Local Hadronic Calibration*, Tech. Rep. ATL-LARG-PUB-2009-001-2, CERN, Geneva, 2008.
- [173] ATLAS Collaboration, *Jet energy scale and its systematic uncertainty in proton-proton collisions at $\sqrt{s}=7$ TeV with ATLAS 2011 data*, Tech. Rep. ATLAS-CONF-2013-004, CERN, Geneva, 2013.
- [174] M. Cacciari, G. P. Salam, and G. Soyez, *FastJet user manual*, Eur. Phys. J. **C72** (2012) 1896, [arXiv:1111.6097 \[hep-ph\]](#).
- [175] D0 Collaboration, V. M. Abazov *et al.*, *Measurement of the $p\bar{p} \rightarrow t\bar{t}$ production cross section at $\sqrt{s} = 1.96$ TeV in the fully hadronic decay channel*, Phys. Rev. **D76** (2007) 072007, [arXiv:hep-ex/0612040 \[hep-ex\]](#).
- [176] ATLAS Collaboration, *Selection of jets produced in proton-proton collisions with the ATLAS detector using 2011 data*, Tech. Rep. ATLAS-CONF-2012-020, CERN, Geneva, 2012.

- [177] ATLAS Collaboration, G. Aad *et al.*, *Jet energy measurement with the ATLAS detector in proton-proton collisions at $\sqrt{s} = 7$ TeV*, Eur. Phys. J. **C73** (2013) 2304, [arXiv:1112.6426 \[hep-ex\]](#).
- [178] ATLAS Collaboration, *Pile-up corrections for jets from proton-proton collisions at $\sqrt{s} = 7$ TeV in ATLAS in 2011*, Tech. Rep. ATLAS-CONF-2012-064, CERN, Geneva, 2012.
- [179] T. Sjöstrand, S. Mrenna, and P. Z. Skands, *PYTHIA 6.4 physics and manual*, JHEP **0605** (2006) 026, [arXiv:hep-ph/0603175 \[hep-ph\]](#).
- [180] ATLAS Collaboration, *In situ jet pseudorapidity intercalibration of the ATLAS detector using dijet events in $\sqrt{s}=7$ TeV proton-proton 2011 data*, Tech. Rep. ATLAS-CONF-2012-124, CERN, Geneva, 2012.
- [181] ATLAS Collaboration, *Probing the measurement of jet energies with the ATLAS detector using Z+jet events from proton-proton collisions at $\sqrt{s} = 7$ TeV*, Tech. Rep. ATLAS-CONF-2012-053, CERN, Geneva, 2012.
- [182] ATLAS Collaboration, *Probing the measurement of jet energies with the ATLAS detector using photon+jet events in proton-proton collisions at $\sqrt{s} = 7$ TeV*, Tech. Rep. ATLAS-CONF-2012-063, CERN, Geneva, 2012.
- [183] ATLAS Collaboration, *TeV-scale jet energy calibration using multijet events including close-by jet effects at the ATLAS experiment*, Tech. Rep. ATLAS-CONF-2013-003, CERN, Geneva, 2013.
- [184] ATLAS Collaboration, G. Aad *et al.*, *Jet energy resolution in proton-proton collisions at $\sqrt{s} = 7$ TeV recorded in 2010 with the ATLAS detector*, Eur. Phys. J. **C73** (2013) 2306, [arXiv:1210.6210 \[hep-ex\]](#).
- [185] ATLAS Collaboration, *Performance of the ATLAS Secondary Vertex b-tagging Algorithm in 7 TeV Collision Data*, Tech. Rep. ATLAS-CONF-2010-042, CERN, Geneva, 2010.
- [186] ATLAS Collaboration, *Commissioning of the ATLAS high-performance b-tagging algorithms in the 7 TeV collision data*, Tech. Rep. ATLAS-CONF-2011-102, CERN, Geneva, 2011.
- [187] G. Piacquadio and C. Weiser, *A new inclusive secondary vertex algorithm for b-jet tagging in ATLAS*, J. Phys. Conf. Ser. **119** (2008) 032032.
- [188] G. Piacquadio, *Identification of b-jets and investigation of the discovery potential of a Higgs boson in the $WH \rightarrow l\nu b\bar{b}$ channel with the ATLAS experiment*, PhD thesis, Freiburg Univ., Freiburg, 2010.
- [189] ATLAS Collaboration, *Measurement of the b-tag Efficiency in a Sample of Jets Containing Muons with 5 fb^{-1} of Data from the ATLAS Detector*, Tech. Rep. ATLAS-CONF-2012-043, CERN, Geneva, 2012.
- [190] ATLAS Collaboration, *b-Jet Tagging Efficiency Calibration using the System8 Method*, Tech. Rep. ATLAS-CONF-2011-143, CERN, Geneva, 2011.

- [191] ATLAS Collaboration, *Measurement of the Mistag Rate of b-tagging algorithms with 5 fb^{-1} of Data Collected by the ATLAS Detector*, Tech. Rep. ATLAS-CONF-2012-040, CERN, Geneva, 2012.
- [192] ATLAS Collaboration, *b-jet tagging calibration on c-jets containing D^{*+} mesons*, Tech. Rep. ATLAS-CONF-2012-039, CERN, Geneva, 2012.
- [193] ATLAS Collaboration, *Performance of the Reconstruction and Identification of Hadronic τ Decays in ATLAS with 2011 Data*, Tech. Rep. ATLAS-CONF-2012-142, CERN, Geneva, 2012.
- [194] ATLAS Collaboration, *Determination of the tau energy scale and the associated systematic uncertainty in proton-proton collisions at $\sqrt{s}=7\text{ TeV}$ with the ATLAS detector at the LHC in 2011*, Tech. Rep. ATLAS-CONF-2012-054, CERN, Geneva, 2012.
- [195] ATLAS Collaboration, *Performance of the Reconstruction and Identification of Hadronic Tau Decays with ATLAS*, Tech. Rep. ATLAS-CONF-2011-152, CERN, Geneva, 2011.
- [196] A. Hoecker *et al.*, *TMVA - Toolkit for Multivariate Data Analysis*, PoS **ACAT** (2007) 040, [arXiv:physics/0703039](#) [PHYSICS].
- [197] ATLAS Collaboration, G. Aad *et al.*, *Electron performance measurements with the ATLAS detector using the 2010 LHC proton-proton collision data*, Eur. Phys. J. **C72** (2012) 1909, [arXiv:1110.3174](#) [hep-ex].
- [198] S. Hassani *et al.*, *A muon identification and combined reconstruction procedure for the ATLAS detector at the LHC using the (MUONBOY, STACO, MuTag) reconstruction packages*, Nucl. Instrum. Meth. **A572** (2007) 77–79.
- [199] ATLAS Collaboration, *Muon reconstruction efficiency in reprocessed 2010 LHC proton-proton collision data recorded with the ATLAS detector*, Tech. Rep. ATLAS-CONF-2011-063, CERN, Geneva, 2011.
- [200] ATLAS Collaboration, *A measurement of the ATLAS muon reconstruction and trigger efficiency using J/ψ decays*, Tech. Rep. ATLAS-CONF-2011-021, CERN, Geneva, 2011.
- [201] ATLAS Collaboration, *ATLAS Muon Momentum Resolution in the First Pass Reconstruction of the 2010 p-p Collision Data at $\sqrt{s} = 7\text{ TeV}$* , Tech. Rep. ATLAS-CONF-2011-046, CERN, Geneva, 2011.
- [202] ATLAS Collaboration, G. Aad *et al.*, *Performance of missing transverse momentum reconstruction in proton-proton collisions at $\sqrt{s} = 7\text{ TeV}$ with ATLAS*, Eur. Phys. J. **C72** (2012) 1844, [arXiv:1108.5602](#) [hep-ex].
- [203] ATLAS Collaboration, *Performance of Missing Transverse Momentum Reconstruction in ATLAS with 2011 Proton-Proton Collisions at $\sqrt{s} = 7\text{ TeV}$* , Tech. Rep. ATLAS-CONF-2012-101, CERN, Geneva, 2012.
- [204] T. Gleisberg *et al.*, *Event generation with SHERPA 1.1*, JHEP **0902** (2009) 007, [arXiv:0811.4622](#) [hep-ph].
- [205] G. Bozzi *et al.*, *Transverse-momentum resummation and the spectrum of the Higgs boson at the LHC*, Nucl. Phys. **B737** (2006) 73–120, [arXiv:hep-ph/0508068](#) [hep-ph].

- [206] W. Altmannshofer and D. M. Straub, *Viability of MSSM scenarios at very large $\tan\beta$* , JHEP **1009** (2010) 078, [arXiv:1004.1993](#) [hep-ph].
- [207] S. Dittmaier, M. Krämer, and M. Spira, *Higgs radiation off bottom quarks at the Fermilab Tevatron and the CERN LHC*, Phys. Rev. **D70** (2004) 074010, [arXiv:hep-ph/0309204](#) [hep-ph].
- [208] S. Dawson *et al.*, *Exclusive Higgs boson production with bottom quarks at hadron colliders*, Phys. Rev. **D69** (2004) 074027, [arXiv:hep-ph/0311067](#) [hep-ph].
- [209] R. V. Harlander and W. B. Kilgore, *Higgs boson production in bottom quark fusion at next-to-next-to-leading order*, Phys. Rev. **D68** (2003) 013001, [arXiv:hep-ph/0304035](#) [hep-ph].
- [210] R. Harlander, M. Krämer, and M. Schumacher, *Bottom-quark associated Higgs-boson production: reconciling the four- and five-flavour scheme approach*, [arXiv:1112.3478](#) [hep-ph].
- [211] M. Spira, *HIGLU: A Program for the Calculation of the Total Higgs Production Cross Section at Hadron Colliders via Gluon Fusion including QCD Corrections*, [arXiv:hep-ph/9510347](#) [hep-ph].
- [212] R. V. Harlander and W. B. Kilgore, *Next-to-Next-to-Leading Order Higgs Production at Hadron Colliders*, Phys. Rev. Lett. **88** (2002) 201801, [arXiv:hep-ph/0201206](#) [hep-ph].
- [213] J. M. Campbell, J. W. Huston, and W. J. Stirling, *Hard interactions of quarks and gluons: a primer for LHC physics*, Rep. Prog. Phys. **70** (2007) 89, [arXiv:hep-ph/0611148](#) [hep-ph].
- [214] ATLAS Collaboration, G. Aad *et al.*, *Search for supersymmetry in events with large missing transverse momentum, jets, and at least one tau lepton in 7 TeV proton-proton collision data with the ATLAS detector*, Eur. Phys. J. **C72** (2012) 2215, [arXiv:1210.1314](#) [hep-ex].
- [215] ATLAS Collaboration, G. Aad *et al.*, *Measurement of inclusive jet and dijet production in pp collisions at $\sqrt{s} = 7$ TeV using the ATLAS detector*, Phys. Rev. **D86** (2012) 014022, [arXiv:1112.6297](#) [hep-ex].
- [216] M. L. Mangano *et al.*, *ALPGEN, a generator for hard multiparton processes in hadronic collisions*, JHEP **0307** (2003) 001, [arXiv:hep-ph/0206293](#) [hep-ph].
- [217] G. Corcella *et al.*, *HERWIG 6: an event generator for hadron emission reactions with interfering gluons (including supersymmetric processes)*, JHEP **0101** (2001) 010, [arXiv:hep-ph/0011363](#) [hep-ph].
- [218] S. Allwood-Spires *et al.*, *Monte Carlo samples used for top physics*, Tech. Rep. ATL-PHYS-INT-2010-132, CERN, Geneva, 2010.
- [219] J. Butterworth *et al.*, *Single Boson and Diboson Production Cross Sections in pp Collisions at $\sqrt{s}=7$ TeV*, Tech. Rep. ATL-COM-PHYS-2010-695, CERN, Geneva, 2010.
- [220] C. Anastasiou *et al.*, *High precision QCD at hadron colliders: Electroweak gauge boson rapidity distributions at next-to-next-to leading order*, Phys. Rev. **D69** (2004) 094008, [arXiv:hep-ph/0312266](#) [hep-ph].

- [221] R. Hamberg, W. van Neerven, and T. Matsuura, *A Complete calculation of the order α_s^2 correction to the Drell-Yan k -factor*, Nucl. Phys. **B359** (1991) 343–405, Erratum-ibid. **B644** (2002) 403–404.
- [222] S. Moch and P. Uwer, *Theoretical status and prospects for top-quark pair production at hadron colliders*, Phys. Rev. **D78** (2008) 034003, [arXiv:0804.1476 \[hep-ph\]](#).
- [223] M. Beneke *et al.*, *Threshold expansion of the $gg(q\bar{q}) \rightarrow Q\bar{Q} + X$ cross section at $\mathcal{O}(\alpha_s^4)$* , Phys. Lett. **B690** (2010) 483–490, [arXiv:0911.5166 \[hep-ph\]](#).
- [224] B. P. Kersevan and E. Richter-Was, *The Monte Carlo event generator AcerMC versions 2.0 to 3.8 with interfaces to PYTHIA 6.4, HERWIG 6.5 and ARIADNE 4.1*, Comput. Phys. Commun. **184** (2013) 919–985, [arXiv:hep-ph/0405247 \[hep-ph\]](#).
- [225] B. P. Kersevan and I. Hinchliffe, *A consistent prescription for the production involving massive quarks in hadron collisions*, JHEP **0609** (2006) 033, [arXiv:hep-ph/0603068 \[hep-ph\]](#).
- [226] N. Kidonakis, *Next-to-next-to-leading logarithm resummation for s -channel single top quark production*, Phys. Rev. **D81** (2010) 054028, [arXiv:1001.5034 \[hep-ph\]](#).
- [227] N. Kidonakis, *Next-to-next-to-leading-order collinear and soft gluon corrections for t -channel single top quark production*, Phys. Rev. **D83** (2011) 091503, [arXiv:1103.2792 \[hep-ph\]](#).
- [228] N. Kidonakis, *Two-loop soft anomalous dimensions for single top quark associated production with a W^- or H^-* , Phys. Rev. **D82** (2010) 054018, [arXiv:1005.4451 \[hep-ph\]](#).
- [229] J. M. Campbell and R. K. Ellis, *Update on vector boson pair production at hadron colliders*, Phys. Rev. **D60** (1999) 113006, [arXiv:hep-ph/9905386 \[hep-ph\]](#).
- [230] T. Binoth *et al.*, *Gluon-induced W -boson pair production at the LHC*, JHEP **0612** (2006) 046, [arXiv:hep-ph/0611170 \[hep-ph\]](#).
- [231] T. Binoth, N. Kauer, and P. Mertsch, *Gluon-induced QCD corrections to $pp \rightarrow ZZ \rightarrow \ell\bar{\ell}'\ell'$* , [arXiv:0807.0024 \[hep-ph\]](#).
- [232] ATLAS Collaboration, *Performance of the ATLAS tau trigger in 2011*, Tech. Rep. ATLAS-CONF-2013-006, CERN, Geneva, 2013.
- [233] ATLAS Collaboration, *Measurement of the $W \rightarrow \ell\nu$ production cross-section and observation of $Z \rightarrow \ell\ell$ production in proton-proton collisions at $\sqrt{s} = 7$ TeV with the ATLAS detector*, Tech. Rep. ATLAS-CONF-2010-051, CERN, Geneva, 2010.
- [234] ATLAS Collaboration, *Data-Quality Requirements and Event Cleaning for Jets and Missing Transverse Energy Reconstruction with the ATLAS Detector in Proton-Proton Collisions at a Center-of-Mass Energy of $\sqrt{s} = 7$ TeV*, Tech. Rep. ATLAS-CONF-2010-038, CERN, Geneva, 2010.
- [235] R. K. Ellis *et al.*, *Higgs decay to $\tau^+\tau^-$: A possible signature of intermediate mass Higgs bosons at high energy hadron colliders*, Nucl. Phys. **B297** (1988) 221–243.
- [236] A. Elagin *et al.*, *A new mass reconstruction technique for resonances decaying to $\tau\tau$* , Nucl. Instrum. Meth. **A654** (2011) 481–489, [arXiv:1012.4686 \[hep-ex\]](#).

- [237] E. Barberio *et al.*, *Search for neutral MSSM Higgs bosons in the decay mode $H \rightarrow \tau^+\tau^- \rightarrow \tau_h\tau_h + 2$ neutrinos in proton-proton collisions at $\sqrt{s} = 7$ TeV with the ATLAS experiment*, Tech. Rep. ATL-COM-PHYS-2011-937, CERN, Geneva, 2011.
- [238] N. Möser *et al.*, *Estimation of $Z \rightarrow \tau\tau$ Background in VBF $H \rightarrow \tau\tau$ Searches from $Z \rightarrow \mu\mu$ Data using an Embedding Technique*, Tech. Rep. ATL-COM-PHYS-2009-446, CERN, Geneva, 2009.
- [239] ATLAS Collaboration, G. Aad *et al.*, *Measurement of the inclusive W^\pm and Z/γ^* cross sections in the e and μ decay channels in pp collisions at $\sqrt{s} = 7$ TeV with the ATLAS detector*, Phys. Rev. **D85** (2012) 072004, [arXiv:1109.5141 \[hep-ex\]](#).
- [240] S. Thoma, *Search for the neutral Higgs Bosons of the Minimal Supersymmetric Standard Model in the $\tau_{\text{lep}}\tau_{\text{had}}$ decay mode with the ATLAS experiment*, PhD thesis, Freiburg Univ., Freiburg, 2012.
- [241] A. D. Martin *et al.*, *MRST2001: Partons and α_s from precise deep inelastic scattering and Tevatron jet data*, Eur. Phys. J. **C23** (2002) 73–87, [arXiv:hep-ph/0110215 \[hep-ph\]](#).
- [242] ATLAS Collaboration, *Luminosity Determination in pp Collisions at $\sqrt{s} = 7$ TeV using the ATLAS Detector in 2011*, Tech. Rep. ATLAS-CONF-2011-116, CERN, Geneva, 2011.
- [243] H. von Radziewski, *Search for Neutral Higgs Bosons of the Minimal Supersymmetric Standard Model in the $\tau_e\tau_\mu$ Decay Mode at $\sqrt{s} = 7$ TeV with the ATLAS Detector*, PhD thesis, Freiburg Univ., Freiburg, 2013, to be submitted.
- [244] K. Cranmer *et al.*, *HistFactory: A tool for creating statistical models for use with RooFit and RooStats*, Tech. Rep. CERN-OPEN-2012-016, New York U., New York, 2012.
- [245] L. Moneta *et al.*, *The RooStats Project*, PoS **ACAT2010** (2010) 057, [arXiv:1009.1003 \[physics.data-an\]](#).
- [246] W. Verkerke and D. Kirkby, *The RooFit toolkit for data modeling*, eConf **C0303241** (2003) MOLT007, [arXiv:physics/0306116 \[physics\]](#).
- [247] M. A. Pinsky and S. Karlin, *An Introduction to Stochastic Modeling*, ch. Poisson Processes. Elsevier Science, 4th ed., 2011.
- [248] R. Barlow, *Extended maximum likelihood*, Nucl. Instrum. Meth. **A297** (1990) 496–506.
- [249] K. Cranmer, *HistFactory User Guide (ROOT 5.32) Draft 5*, <https://twiki.cern.ch/twiki/pub/RooStats/WebHome/HistFactoryLikelihood.pdf>, accessed 11-Feb-2013.
- [250] J. Neyman and E. S. Pearson, *On the Problem of the Most Efficient Tests of Statistical Hypotheses*, Phil. Trans. R. Soc. Lond. **A231** (1933) 289–337.
- [251] A. L. Read, *Presentation of search results: The CL_s technique*, J. Phys. **G28** (2002) 2693–2704.
- [252] S. Dittmaier and M. Schumacher, *The Higgs Boson in the Standard Model - From LEP to LHC: Expectations, Searches, and Discovery of a Candidate*, Prog. Part. Nucl. Phys. **70** (2013) 1–54, [arXiv:1211.4828 \[hep-ph\]](#).

-
- [253] G. Cowan *et al.*, *Asymptotic formulae for likelihood-based tests of new physics*, Eur. Phys. J. **C71** (2011) 1554, [arXiv:1007.1727 \[physics.data-an\]](#).
- [254] A. Wald, *Tests of Statistical Hypotheses Concerning Several Parameters When the Number of Observations is Large*, Trans. Amer. Math. Soc. **54** (1943) 426–482.
- [255] S. S. Wilks, *The Large-Sample Distribution of the Likelihood Ratio for Testing Composite Hypotheses*, Ann. Math. Statist. **9** (1938) 60–62.
- [256] E. Gross and O. Vitells, *Trial factors or the look elsewhere effect in high energy physics*, Eur. Phys. J. **C70** (2010) 525–530, [arXiv:1005.1891 \[physics.data-an\]](#).
- [257] O. Vitells and E. Gross, *Estimating the significance of a signal in a multi-dimensional search*, Astropart. Phys. **35** (2011) 230–234, [arXiv:1105.4355 \[astro-ph.IM\]](#).
- [258] ATLAS Collaboration, CMS Collaboration, LHC Higgs Combination Group, *Procedure for the LHC Higgs boson search combination in Summer 2011*, Tech. Rep. ATL-PHYS-PUB-2011-011, CERN, Geneva, 2011.
- [259] ATLAS Collaboration, G. Aad *et al.*, *Search for the Standard Model Higgs boson in the H to $\tau^+\tau^-$ decay mode in $\sqrt{s} = 7$ TeV pp collisions with ATLAS*, JHEP **1209** (2012) 070, [arXiv:1206.5971 \[hep-ex\]](#).
- [260] ATLAS Collaboration, G. Aad *et al.*, *A search for high-mass resonances decaying to $\tau^+\tau^-$ in pp collisions at $\sqrt{s} = 7$ TeV with the ATLAS detector*, Phys. Lett. **B719** (2013) 242–260, [arXiv:1210.6604 \[hep-ex\]](#).

Acknowledgements

I want start with expressing my gratitude to my advisor Prof. Jochen Dingfelder. Thank you for taking the time whenever it was needed and for creating a very productive and supportive environment. I have enjoyed the time as your student and appreciate your support. I am obliged to Prof. Karl Jakobs for the inclusion to his group and his support in situations where I needed it. I thank Prof. Markus Schumacher for his help in all matters of the MSSM analysis and the helpful and informative discussions. I am grateful to Prof. Sunil Somalwar for introducing me to particle physics and his advice in many fields. I am indebted to Christina Skorek for the support in all administrative matters and all the nice words.

The great companionship and support during the research and publication phases by Christoph Anders and Sascha Thoma make me grateful. I would like to thank them, Will Davey, Holger von Radziewski, Nikolaos Rompotis, Federico Scutti, John Stakely Keller, Sebastian Stern and the ATLAS groups in Freiburg and Bonn for their support and collaboration. I had a good time sharing the office during the time of the thesis writing with Felix Bühner, who was a great partner in mastering the computer administration tasks.

I am grateful for the proofreading of this thesis to Jochen Dingfelder, Christoph Anders, Sascha Thoma, Georges Aad, Felix Bühner, Will Davey, Mirjam Fehling-Kaschek, Florian Kiß, Stan Lai, Kristin Lohwasser, Evelyn Schmidt and Iacopo Vivarelli. I would like to thank all friends and colleagues at Freiburg, Bonn and CERN for the time I was able to experience with them, especially Christoph, Daniel, Dennis, Duc, Felix, Georges, Kristin, Liv, Marc, Mirjam, Nils, Priscilla, Sascha and Stefan.

I want to thank my family, Benedikt, Christine and Manfred, for supporting me and being able to judge what is important in life – and what is not. Vielen Dank.